ZEOLITE AS NATURAL GAS ADSORBENTS

(ZEOLIT SEBAGAI PENJERAP GAS ASLI)

KHAIRUL SOZANA NOR KAMARUDIN
HANAPI BIN MAT
HALIMATON HAMDAN

FAKULTI KEJURUTERAAN KIMIA DAN KEJURUTERAAN SUMBER ASLI
UNIVERSITI TEKNOLOGI MALAYSIA

Lampiran 20

UTM/RMC/F/0024(1998)

UNIVERSITI TEKNOLOGI MALAYSIA

BORANG PENGESAHAN
LAPORAN AKHIR PENYELIDIKAN

TAJUK PROJEK : **ZEOLIT SEBAGAI PENJERAP GAS ASLI**

Saya **DR. KHAIRUL SOZANA NOR BINTI KAMARUDIN**

Mengaku membenarkan Laporan Akhir Penyelidikan ini disimpan di Perpustakaan Universiti Teknologi Malaysia dengan syarat-syarat kegunaan seperti berikut :

1. Laporan Akhir Penyelidikan ini adalah hakmilik Universiti Teknologi Malaysia.
2. Perpustakaan Universiti Teknologi Malaysia dibenarkan membuat salinan untuk tujuan rujukan sahaja.
3. Perpustakaan dibenarkan membuat penjualan salinan Laporan Akhir Penyelidikan ini bagi kategori TIDAK TERHAD.
4. * Sila tandakan (✓)

☐	SULIT	(Mengandungi maklumat yang berdarjah keselamatan atau Kepentingan Malaysia seperti yang termaktub di dalam AKTA RAHSIA RASMI 1972).
☐	TERHAD	(Mengandungi maklumat TERHAD yang telah ditentukan oleh Organisasi/badan di mana penyelidikan dijalankan).
✓	TIDAK TERHAD	

TANDATANGAN KETUA PENYELIDIK

DR. KHAIRUL SOZANA NOR BINTI KAMARUDIN

Nama & Cop Ketua Penyelidik

Tarikh: 11 hb. JUNE 2007

CATATAN : * ***Jika Laporan Akhir Penyelidikan ini SULIT atau TERHAD, sila lampirkan surat daripada pihak berkuasa/organisasi berkenaan dengan menyatakan sekali sebab dan tempoh laporan ini perlu dikelaskan sebagai SULIT dan TERHAD.***

2007

ACKNOWLEDGEMENT

The financial support from the Ministry of Science, Technology and Innovation (MOSTI) on the project (Project No. 09-02-06-0057/SR0005/09-08/VOT 74512) is gratefully acknowledged.

ABSTRACT

ZEOLITE AS NATURAL GAS ADSORBENTS

(Keywords: Zeolite; Modification; Adsorption; Metal Cation, Metal Oxides, Amines)

Zeolites are inorganic crystalline materials with uniform sized pores of molecular dimensions. Many researchers have proved that zeolite has good adsorption characteristics, which has potential to be use as an adsorbent in gas separation process and adsorptive gas storage. Since 1980s, zeolite properties were found that it could be tailored and modified for specific application. The modified zeolites lead to the positive development in vast applications from catalyst, adsorbent to nanoparticle technology. This research studies the adsorptive characteristics of various adsorbents such as zeolite A, X, Y, mordenite and ZSM-5 as well as mesoporous materials such as MCM-41 and SBA-15. The study was carried out using gases such as N_2, CO_2, and CH_4. The modifications was carried out by introducing various types of substance or modifying agent onto/into selected adsorbents using several modification methods in order to enhance the adsorptive capacity of the adsorbents. The performance of the adsorbents for adsorptive natural gas storage was also investigated. The structures of the adsorbents were characterized by powder X-Ray Diffraction (XRD), Micromeritics ASAP 2000, Fourier Transform Infrared (FTIR) spectroscopy and Scanning Electron Microscope (SEM). The adsorption equilibrium and kinetic study of gases on the modified samples have been analyzed using Thermogravimetric Analyzer (TGA). Gas adsorption characteristics of zeolites were evaluated based on the adsorption capacity, adsorption isotherms, heat of adsorption, uptake rate of the adsorbates, and FTIR spectra of gas-zeolite interactions. It was found that cage-type zeolites such as NaX and NaY are better adsorbents than channel-type zeolites. Results also revealed that types of metal cation, metal oxide, amine, loading concentration, calcination temperature, duration of calcination process, adsorption temperature and pressure as well as the modification techniques greatly affect the modified zeolite adsorbent structural and gas adsorption characteristics. In general, modification can enhance the adsorption characteristics of adsorbents. The adsorption measurements have revealed that exchanging Na^+ with some metal cation enhanced the adsorption capacity of methane. The addition metal oxides can also increases the adsorption of gases. Addition of MgO to NaY increases the adsorption capacity of CO_2, meanwhile, HgO-NaY has higher adsorption of N_2 and CH_4 than NaY itself. The study also showed that CO_2 adsorption on microporous and mesoporous silica improved as amine grafted onto its surface. The isosteric heat of adsorption that measured using TGA and gases adsorption bands that observed in FTIR spectra also demonstrate that the adsorbates interact with adsorbents. At higher pressure (up to

500 psi), the study showed that in order to get high methane storage and delivery capacity, adsorbents with large accessible surface area, high pore volume and high packing density are needed. Amount of methane remain adsorbed after discharging was influence by the adsorbent pore volume. These findings enable us to elucidate the fundamental question about the structural and adsorptive characteristics of natural gas on modified zeolites as well as other porous materials such as MCM-41 and SBA-15.

Key Researchers:

Dr. Khairul Sozana Nor Binti Kamarudin
Associate Professor Dr. Hanapi Bin Mat
Professor Dr. Halimaton Hamdan
Chieng Yu Yuan
Chua Chung Lieh
Barry Tan Joon Liang

Email: sozana@fkkksa.utm.my
Tel. No.: +607-5535482
Fax No.: +607-5581463
Vote No.: 74512

ABSTRAK

ZEOLIT SEBAGAI PENJERAP GAS ASLI

(Kata Kunci: Zeolit;Pengubahsuaian; Penjerapan; Kation Logam; Logam Oksida; Amin)

Zeolit adalah bahan berhablur tak organik dengan saiz liang berdimensi molekul yang seragam. Ramai penyelidik telah membuktikan bahawa zeolit mempunyai ciri-ciri penjerapan yang baik, yang berpotensi untuk digunakan sebagai penjerap dalam proses pemisahan gas dan pengstoran gas secara penjerapan. Sejak 1980s, didapati bahawa sifat-sifat zeolit dapat diubahsuaikan untuk kegunaan tertentu. Zeolit yang telah diubahsuai telah membawa kepada perkembangan yang positif dalam pelbagai bidang, dari pemangkin, penjerap ke teknologi nanopartikel. Kajian ini mengkaji cirri penjerapan pelbagai jenis penjerap seperti zeolit A, X, Y, mordenite and ZSM-5 serta bahan mesoporos seperti MCM-41 dan SBA-15. Kajian ini dijalankan menggunakan gas N_2, CO_2, and CH_4. Pengubahsuaian dijalankan dengan menambahkan beberapa jenis bahan atau agen pengubah kepada bahan penjerap terpilih menggunakan beberapa kaedah pengubahsuaian untuk meningkatkan kapasiti penjerapan bahan penjerap. Keupayaan penjerapan untuk penstoran gas asli juga dikaji. Struktur bahan penjerap ditentukan dengan menggunakan Pembelauan X-Ray (XRD), Micromeritics ASAP 2000, spektroskopi Pengubah Fourier Infra Merah (FTIR) dan Mikroskop Imbasan Elektron (SEM). Kajian keseimbangan penjerapan dan kinetik gas untuk sampel yang telah diubahsuai turut dianalisis dengan menggunakan Penganalisa Termogravimetrik (TGA). Ciri-ciri penjerapan zeolit dinilai berdasarkan kepada kapasiti penjerapan, penjerapan isoterma, haba penjerapan, kadar penjerapan zat terjerap, dan spectra FTIR interaksi gas-zeolit. Hasil kajian ini mendapati zeolit jenis sesangkar seperti NaX dan NaY mempu menjerap dengan lebih baik berbanding zeolit jenis sesalur. Keputusan juga mendapati bahawa jenis kation logam, oksida logam, amina, kepekatan masukan, suhu pemanasan, jangka masa pemanasan, suhu dan tekanan penjerapan serta teknik pengubahsuaian membawa kesan yang ketara terhadap struktur penjerap dan ciri-ciri penjerapan gas. Secara umum, pengubahsuaian boleh meningkatkan cirri-ciri penjerapan bahan penjerap. Pengukuran penjerapan telah menunjukkan penukaran Na^+ dengan beberapa kation logam telah meningkatkan kapasiti penjerapan metana. Penambahan logam oksida juga boleh meningkatkan penjerapan gas-gas lain. Penambahan MgO pada NaY meningkatkan kapasiti penjerapan CO_2 manakala HgO-NaY berupaya menjerap N_2 dan CH_4 melebihi keupayaan NaY. Kajian ini juga menunjukkan penjerapan CO_2 keatas silica mikroporos dan mesoporos meningkat apabila amina diserakkan diatas permukaan bahan penjerap. Keputusan haba

penjerapan yang diukur menggunakan TGA dan spektra penjerapan gas daripada ukuran FTIR turut menunjukkan bahawa molekul gas berinteraksi dengan penjerap. Pada tekanan lebih tinggi (500 psi), kajian ini menunjukkan bahan penjerap yang mempunyai luas permukaan yang besar, isipadu liang, dan ketumpatan terpadat yang tinggi diperlukan untuk memperoleh penstoran dan kapasiti penghantaran metana yang tinggi. Jumlah metana yang tinggal di dalam sel selepas operasi pengeluaran dipengaruhi oleh isipadu liang bahan penjerap. Berasaskan jisim, NiO-MCM-41 mempunyai kapasiti pensoran yang tertinggi. Hasil penemuan ini membolehkan kita memahami persoalan asas mengenai struktur dan ciri-ciri penjerapan gas asli keatas zeolit serta bahan silica poros terubahsuai yang lain seperti MCM-41 dan SBA-15.

Penyelidik Utama:

Dr. Khairul Sozana Nor Binti Kamarudin
Associate Profesor Dr. Hanapi Bin Mat
Profesor Dr. Halimaton Hamdan
Chieng Yu Yuan
Chua Chung Lieh
Barry Tan Joon Liang

Email: sozana@fkkksa.utm.my
Tel. No.: +607-5535482
Fax No.: +607-5581463
Vote No.: 74512

TABLE OF CONTENTS

CHAPTER	TITLE	PAGE
	TITLE PAGE	i
	ACKNOWLEDGEMENTS	ii
	ABSTRACT	iii
	ABSTRAK	v
	TABLE OF CONTENTS	vii
	LIST OF TABLES	xiv
	LIST OF FIGURES	xix
	LIST OF SYMBOLS	xxxiv
	LIST OF ABBREVIATIONS	xxxvi
1	**INTRODUCTION**	
	1.1 Background	1
	1.2 Objectives and Scopes	5
	1.3 Thesis Outline	7
	1.4 Summary	8

2 LITERATURE REVIEW

2.1 Zeolite Adsorbent 9

2.1.1 Introduction to zeolite 9

2.1.2 Zeolite structure and properties 14

2.1.3 Development of zeolite adsorbent 16

2.1.4 Natural gas adsorbents 24

2.1.4.1 Carbon dioxide removal 26

2.1.4.2 Adsorption as CO_2 removal method 27

2.1.4.3 CO_2 Adsorbents 29

2.2 Gas Adsorption 30

2.2.1 Introduction 30

2.2.2 Adsorption parameters 34

2.2.3 Adsorption equilibrium 35

2.2.3.1 Adsorption equilibrium isotherm 35

2.2.3.2 Adsorption equilibrium model 39

2.2.3.3 Heat of adsorption 42

2.2.4 Adsorption kinetics 44

2.3.4.1 Initial gas uptake rate 44

2.3.4.2 Diffusion rate constant 46

2.2.5 Gas adsorption mechanisms 48

2.2.5.1 Diffusion effects 48

2.2.5.2 Surface interaction 49

2.2.5.3 Adsorption at supercritical conditions 52

2.2.6 High pressure adsorption 54

2.3 Potential Applications of Silica Based Adsorbents 64

2.4 Summary 67

3 MATERIALS AND METHODS

3.1 Introduction 68

3.2 Materials 70

3.2.1 General chemicals 70

3.2.2 Zeolites 71
3.2.3 Gases 71
3.3 Synthesis and Modification Procedures 72
3.3.1 Zeolite synthesis procedures 72
3.3.2 Mesoporous material synthesis procedures 72
3.3.3 Zeolite modification procedures 73
3.3.3.1 Cation exchange technique 74
3.3.3.2 Thermal dispersion techniques 75
3.3.3.3 Incipient wetness impregnation technique 76
3.3.3.4 Amine wet impregnation procedures 76
3.4 Zeolite Characterization Procedures 77
3.4.1 Structural characterization 77
3.4.2 Physical properties characterization 81
3.4.3 Morphological characterization 82
3.5 Gas Adsorption Measurements 83
3.5.1 Gas adsorption isotherm measurement 83
3.5.2 Gas adsorption kinetic measurements 84
3.5.3 Heat of adsorption measurements 85
3.3.4 Gas-solid interaction measurements 85
3.6 Adsorption Isotherm Model Constant Estimation 86
3.7 High Pressure Adsorption Measurement 89
3.7.1 Adsorptive gas storage 89
3.7.2 Experimental procedures 94
3.7.3 Estimation of methane stored, delivered, and adsorbed 97
3.8 Summary 98

4 GAS ADSORPTION CHARACTERISTICS OF STRUCTURALLY DIFFERENT ZEOLITES

4.1 Introduction 99
4.2 Properties of Zeolites 103
4.2.1 Structural determination 103
4.2.2 Physicochemical properties of zeolites 109

4.3 Adsorption Equilibrium 114
4.3.1 Gas adsorption capacity 114
4.3.1.1 Effect of different types of structure 114
4.3.1.2 Effect of pore system 117
4.3.1.3 Effect of pore size 118
4.3.1.4 Effect of surface area and pore volume on gas adsorption 112
4.3.1.5 Effect of crystallinity 120
4.3.1.6 Effect of Si/Al ratio 120
4.3.2 Gas adsorption isotherms 129
4.3.3 Heat of adsorption 138
4.4 Gas Adsorption Kinetics 140
4.4.1 Gas adsorption uptake curve 140
4.4.2 Initial adsorption rate 144
4.4.3 Adsorption equilibrium time 150
4.4.4 Gas diffusivity 155
4.4.4.1 Bulk phase gas diffusivity 155
4.4.4.2 Internal zeolite pore diffusivity 156
4.4.4.3 Diffusional time constant 162
4.5 Gas – Zeolite Interaction 164
4.6 Gas Adsorption Mechanism of Different Zeolite Structural Frameworks 176
4.7 Summary 182

5 GAS ADSORPTION CHARACTERISTICS OF METAL CATION EXCHANGED ZEOLITES

5.1 Introduction 185
5.2 Properties of Metal Cation Exchanged Zeolites 188
5.2.1 Introduction to metal cations 188
5.2.2 Structural determination of metal cation exchanged zeolites 190
5.2.3 Physicochemical properties of metal cation exchanged zeolites 198
5.3 Gas Adsorption Equilibrium 205

5.3.1 Gas adsorption capacity 206
5.3.2 Gas adsorption isotherms 215
5.3.3 Heat of adsorption 227
5.4 Gas Adsorption Kinetics 229
5.4.1 Gas adsorption uptake curve 230
5.4.2 Initial adsorption rate 234
5.4.3 Adsorption equilibrium time 238
5.4.4 Gas diffusivity 244
5.4.4.1 Bulk phase gas diffusivity 244
5.4.4.2 Internal pore diffusivity 244
5.4.4.3 Diffusional time constant 248
5.5 Gas - Zeolite Interactions 250
5.6 Gas Adsorption Mechanism of Metal Cation Exchanged Zeolites 260
5.7 Summary 264

6 GAS ADSORPTION CHARACTERISTICS OF METAL OXIDE BASED ZEOLITES

6.1 Introduction 266
6.2 Structural Characteristics and Properties of Metal Oxide based zeolites 267
6.2.1 Effect of various metal oxides 267
6.2.2 Effect of copper oxide loading concentration 286
6.2.3 Effect of calcination temperature 292
6.2.4 Effect of duration of calcination process 295
6.2.5 Effect of modification techniques 298
6.3 Gas Adsorption Characteristics 301
6.3.1 Adsorption equilibrium 301
6.3.1.1 Effect of various metal oxides 301
6.3.1.2 Effect of loading concentration 306
6.3.1.3 Effect of calcination temperature 308
6.3.1.4 Effect of calcination time 309
6.3.1.5 Effect of modification techniques 310

6.3.2 Heat of adsorption 312
6.3.2.1 Effect of different adsorbate 312
6.3.2.2 Effect of different metal oxide 315
6.3.3 Adsorption kinetics 316
6.3.3.1 Initial gas uptake rate 316
6.3.3.2 Diffusion rate constant 319
6.3.4 Gas-zeolite interactions 325
6.3.4.1 Interaction of N_2 on metal oxide modified zeolite 325
6.3.4.2 Interaction of CO_2 on metal oxide modified zeolite 331
6.3.4.3 Interaction of CH_4 on metal oxide modified Na-Y zeolite 335
6.4 Summary 340

7 AMINE MODIFIED POROUS SILICA AS CO_2 ADSORBENTS

7.1 Introduction 341
7.2 Structural Characteristics and Properties 342
7.2.1 Effect of various amine 342
7.2.2 Effect of metal loading 349
7.2.3 Effect of amine on microporous materials 351
7.2.4 Effect of amine concentration 354
7.3 Carbon Dioxide Adsorption Characteristics 355
7.3.1 Effect of various amine 356
7.3.2 Effect of support materials 361
7.3.3 Effect of amine concentration 366
7.3.4 Effect of temperature 369
7.3.4.1 Adsorption temperature 370
7.3.4.2 Heating temperature 372
7.4 Gas-Solid Interaction 375
7.4.1 Interaction of CO2 on various amine modified MCM-41 376
7.4.2 Interaction of CO2 modified MCM-41 at various pressure 378

7.5 Summary 380

8 ZEOLITE AS ADSORPTIVE METHANE STORAGE ADSORBENT

8.1 Introduction 382
8.2 Microporous and Mesoporous Silica 383
8.2.1 Methane adsorption characteristics 383
8.2.2 Methane adsorption isotherms 387
8.2.3 Methane adsorptive storage characteristics 393
8.2.3.1 Charging phase 393
8.2.3.2 Discharging phase
8.3 Modified Microporous and Mesoporous Silica 400
8.3.1 Methane adsorption characteristics 400
8.3.2 Methane adsorption isotherms 406
8.3.3 Methane adsorptive storage characteristics 411
8.3.3.1 Charging phase 411
8.3.3.2 Discharging phase 412
8.4 Summary 415

9 CONCLUSIONS

9.1 Introduction 416
9.2 Summary of Research Findings 417
9.3 Recommendation for Future Work 422
9.4 Concluding Remarks 425

REFERENCES 427

LIST OF TABLES

TABLE NO.	TITLE	PAGE
2.1	Properties of natural zeolites (Sand and Mumpton, 1978)	11
2.2	Properties of synthetic zeolites (Frost and Sullivan, 2001)	12
2.3	Studies on natural zeolites (Ma and Lee, 1978)	18
2.4	Modification techniques and the effect on zeolite properties	23
2.5	Typical composition of natural gas (Anon, 2005)	25
2.6	Studies on zeolite based adsorbent	32
2.7	Six IUPAC classified isotherms and corresponding hypothetical differential enthalpy of adsorption isotherm (Llewellyn and Maurin, 2005)	37
2.8	Summary of existing adsorption models	41
3.1	The cations used and products obtained from metal cation exchange method.	74
3.2	The assignment of FTIR bands in zeolites (Flanigen *et al*., 1971)	81
3.3	Methods of plotting gas adsorption data and calculating the constants	88
3.4	ANG vessel specification	89
3.5	Measuring and controlling equipment	91
4.1	Structural framework and pore network of zeolites.	101
4.2	The peaks position of cage type zeolites obtained from XRD data.	106
4.3	The physical properties of faujasite type zeolites calculated from XRD data.	112

4.4	The physical properties of channel type zeolite calculated from nitrogen adsorption data.	112
4.5	The physical properties and chemical composition of faujasite-type zeolite calculated from XRD data.	113
4.6	The fraction of surface coverage for methane and carbon dioxide on different zeolites.	125
4.7	The relative crystallinity and the amount of methane and carbon dioxide adsorbed on faujasite structures.	127
4.8	The Si/Al ratio and unit cell parameter of faujasite structures.	128
4.9	The model constants calculated from the fitting of methane adsorption isotherm for different zeolites.	136
4.10	The model constants calculated from the fitting of carbon dioxide adsorption isotherm for different zeolites.	137
4.11	The enthalpy and entropy change in the adsorption of methane and carbon dioxide on selected zeolites.	139
4.12	The initial adsorption rate of methane and carbon dioxide on different types of zeolites.	144
4.13	The adsorption equilibrium time and adsorption capacity of methane and carbon dioxide on different zeolites.	151
4.14	The Knudsen number (N_{Kn}) and diffusion characteristics in zeolite pore systems based on average pore diameter.	158
4.15	The Knudsen diffusivity of methane and carbon dioxide inside the zeolite pores.	159
4.16	The diffusional characteristics of methane for different zeolite structures.	161
4.17	The diffusional characteristics of carbon dioxide for different zeolite structures.	161
4.18	The diffusional time constants of methane and carbon dioxide at 323 K and 137 kPa.	163
4.19	The peak position of v_3 and v_4 bands and area of the adsorbed methane.	170
4.20	The peak position of v_3 and v_4 bands and area of the adsorbed carbon dioxide.	173

5.1	The properties of cations used for metal cation exchanged treatment.	189
5.2	The peak positions of the alkali metal cation exchanged zeolites obtained from XRD data.	194
5.3	The peak positions of the alkaline earth metal cation exchanged zeolites obtained from XRD data.	194
5.4	The peak positions of the transition metal cation exchanged zeolites obtained from XRD data.	195
5.5	The physical properties of metal cation exchanged zeolites calculated from nitrogen adsorption data.	203
5.6	The physical properties and chemical composition of metal exchanged zeolites calculated from XRD data.	204
5.7	The surface coverage of methane and carbon dioxide for metal cation exchanged zeolites.	214
5.8	The model constants calculated from the best fitting of methane adsorption isotherm for metal exchanged zeolites.	224
5.9	The model constants calculated from the best fitting of carbon dioxide adsorption isotherm for metal exchanged zeolites.	226
5.10	The enthalpy and entropy change in the adsorption of methane and carbon dioxide.	229
5.11	The initial adsorption rate and equilibrium time of metal cation exchanged zeolites.	235
5.12	The adsorption equilibrium time of methane and carbon dioxide adsorbed on metal cation exchanged zeolites	239
5.13	The Knudsen number (N_{Kn}) and diffusional characteristics of metal cation exchanged zeolites.	245
5.14	The diffusional characteristics of metal cation exchanged zeolites.	246
5.15	Knudsen diffusivity of methane and carbon dioxide inside metal cation exchanged zeolites.	247
5.16	The diffusional time constants of methane and	249

	carbon dioxide adsorption at 323 K and 137 kPa.	
5.17	The peak position and area of the peaks for adsorbed methane.	256
5.18	The peak position and area of the peaks for adsorbed carbon dioxide.	259
6.1	Structural characterization of metal oxide modified Na-Y zeolites	268
6.2	Physical properties of metal oxides (Náray-Szabo, 1969)	273
6.3	Surface area and pore size characterization of metal oxide modified NaY	276
6.4	Effect of loading concentration on the structure characteristics of CuO modified Na-Y zeolite samples	289
6.5	Effect of calcination temperature on the structure characteristics of CuO modified Na-Y zeolite samples at 2.25wt.% loading	293
6.6	Effect of calcination time on the structure characteristics of CuO modified Na-Y zeolite samples at 2.25wt.% loading	295
6.7	Effect of duration calcination to physical properties characteristics of CuO modified Na-Y zeolite samples at 2.25 wt% loading.	296
6.8	Surface area and pore size characterization of CuO/NaY and Ga_2O_3/NaY	300
6.9	Gases adsorption capacity of adsorbents studied at 323.15 K and 138 kPa	302
6.10	Enthalpy and entropy of gases adsorption	315
6.11	Equilibrium adsorption time requirement for adsorbents studied	318
6.12	Gases adsorption kinetics for various adsorbents	323
7.1	Physical properties of metal oxides (Náray-Szabo, 1969)	350
7.2	Structural characterization of metal oxide modified Na-Y zeolites	
7.3	Equilibrium adsorption time requirement for different	352

	amines modified MCM-41.	
7.4	Equilibrium adsorption time requirement for MEA modified on different mesoporous and microporous supports	366
8.1	Methane adsorption storage at various pressures	383
8.2	Methane adsorption capacity (V/V) of different adsorbents at various pressures	384
8.3	Amount methane adsorbed (mol/kg) for SBA-15 and MCM-41	387
8.4	Constant of Freundlich isotherm model for methane adsorption onto various adsorbent (0 – 500 psi)	390
8.5	Langmuir parameters for various adsorbents	392
8.6	Amount of methane desorbed at various pressure for different type adsorbents	397
8.7	Methane delivery capacity (V/V) of different adsorbents at various pressures	398
8.8	Methane adsorption capacity (mol.kg), methane delivery capacity (v/v), and methane retained (cm3) at 500psi for various adsorbents understudy.	399
8.9	Comparison between thermal dispersion (TD) modified zeolite and incipient wetness impregnation (IWI) modified zeolite	401
8.10	Physical properties of metal oxides (Náray-Szabo, 1969)	403
8.11	Methane adsorption capacity per kilogram adsorbent onto modified microporous and mesoporous sample	405
8.12	Constant of Freundlich isotherm model for the adsorption of methane in modified adsorbents (0 – 500 psi)	409
8.13	Methane storage and delivery capacity at 500 psi for modified adsorbents	413

LIST OF FIGURES

FIGURE NO.	TITLE	PAGE
2.1	The framework structural of synthetic zeolites (a) zeolite Linde A (b) zeolite Beta (c) Ferrierite (d) Mordenite (e) Zeolite Y and (f) ZSM-5 (International Zeolite Association, 2000)	13
2.2	Primary building unit of SiO_4 and AlO_4 tetrahedral (Nagy *et al*., 1998)	14
2.3	Secondary building units (SBUs) of zeolite (Meier and Olson, 1992).	15
2.4	New classification of adsorption isotherms for physical adsorption of gases on solids (Donohue and Aranovich, 1998)	38
2.5	Interaction of energy of simple gases adsorption at Low temperature (Llewellyn and Maurin, 2005)	49
2.6	The adsorbed state of pure CH_4 and CO_2 in micropores at 298 K (Zhou *et al*., 2005)	53
2.7	Adsorption vessel of volume V' including porous sorbent mass m^8 (Keller et al., 1998)	56
2.8	Schematic diagrams of the volumetric apparatus 58 (Zhang et al., 2004)	
2.9	General principle of the volumetric apparatus 60 (Belmabkhout et al., 2003)	

2.10	The square root mean deviations of z-values from the equations of state to that from the experimental data (Zhou and Zhou, 2001).	62
2.11	The calculated empty cell volume (Zhang et al., 2004)	63
3.1	A flow diagram of experimental procedures used in the study	69
3.2	The schematic diagram of thermogravimetric adsorption system	85
3.3	A schematic diagram of gas - zeolite interaction adsorption cell	87
3.4	The schematic structure of in situ FTIR cell.	87
3.5	A schematic diagram of ANG pressurized gas vessel	90
3.6	Experimental rig used for the ANG experiment	92
3.7	A Schematic Diagram ANG Experimental Rig (15 ml)	93
	XRD patterns of metal oxides (a) Group IIA (b) Group IIIA and (c) Group IVA metal oxides modified Na-Y zeolite	85
4.1	The XRD patterns of channel type structures: (a) zeolite beta; (b) ferrierite; (c) mordenite; and (d) ZSM-5.	104
4.2	The XRD patterns of cage-type structures: (a) NaY; (b) NaX; (c) Na-SZ18; and (d) zeolite A.	105
4.3	The FTIR spectra of zeolites: (a) ZSM-5, (b) ferrierite, (c) mordenite, and (d) zeolite beta.	107
4.4	The FTIR spectra of zeolites: (a) NaY, (b) NaX (13X), (c) Na-SZ18, and (d) zeolite A.	107
4.5	Nitrogen adsorption isotherm of channel-type zeolites.	110
4.6	Nitrogen adsorption isotherm of cage-type zeolites.	110
4.7	The CH_4 adsorption capacity on different types of zeolites at 323 K and 137 kPa.	115
4.8	The CO_2 adsorption capacity on different types of zeolites at 323 K and 137 kPa.	116
4.9	Zeolite pore system of zig-zag, parallel, and three dimensional pore network systems.	118
4.10	The amount of methane adsorbed as a function of zeolite pore size.	119

4.11	The amount of methane and carbon dioxide adsorbed as a function of zeolite pore size.	120
4.12	A schematic diagram of methane and carbon dioxide diffuse through different zeolite pore openings.	121
6.13	The amount of methane adsorbed on cage and channel zeolites as a function of zeolite surface area.	122
6.14	The amount of carbon dioxide adsorbed on cage and channel zeolites as a function of zeolite surface area	123
6.15	The amount of methane adsorbed on cage and channel zeolites as a function of zeolite pore volume.	124
6.16	The amount of carbon dioxide adsorbed on cage and channel zeolites as a function of zeolite pore volume.	124
6.17	The methane adsorption isotherms on channel and cage type zeolites at 298 K.	130
6.18	The carbon dioxide adsorption isotherms on channel and cage type zeolites at 298 K.	130
6.19	The adsorption isotherm of methane fitted into Henry and Freundlich equations: (a) ZSM-5 and (b) NaX.	133
6.20	The adsorption isotherm of carbon dioxide fitted into Freundlich and Dubinin equations: (a) ZSM-5 and (b) NaX.	134
4.21	The adsorption isotherm of carbon dioxide fitted into Langmuir equation: (a) ZSM-5 and (b) NaX.	135
4.22	The methane fractional uptake curve of channel type structures at 323 K and 137 kPa.	141
4.23	The methane fractional uptake curve of cage type structures at 323 K and 137 kPa.	142
4.24	The carbon dioxide fractional uptake curve of channel type structures at 323 K and 137 kPa.	142
4.25	The carbon dioxide fractional uptake curve of cage type structures at 323 K and 137 kPa.	143
4.26	The effect of surface area on initial adsorption rate: (a) methane and (b) carbon dioxide.	146
4.27	The effect of pore volume on initial adsorption:	147

	(a) methane and (b) carbon dioxide.	
4.28	The effect of average pore diameter on initial adsorption rate: (a) methane and (b) carbon dioxide.	149
4.29	The effect of surface area of channel and cage type zeolites on adsorption equilibrium time: (a) methane and (b) carbon dioxide.	152
4.30	The effect of pore volume of channel and cage type zeolites on adsorption equilibrium time of (a) methane and (b) carbon dioxide.	153
4.31	The effect of average pore diameter of channel and cage type zeolites on adsorption equilibrium time of (a) methane and (b) carbon dioxide.	154
4.32	Effect of pore size on diffusivity.	160
4.33	The FTIR spectra of methane (gas phase) at 293 K and 137 kPa.	165
4.34	The FTIR spectra (v_3) of methane adsorbed on zeolites at 293 K and 137 kPa: (a) zeolite beta; (b) ZSM-5; (c) mordenite; and (d) ferrierite.	166
4.35	The FTIR spectra (v_3) of methane adsorbed on zeolites at 293 K and 137 kPa: (a) NaY; (b) Na-SZ18; and (c) NaX.	167
4.36	The FTIR spectra (v_4) of methane adsorbed on zeolites at 293 K and 137 kPa: (a) zeolite beta; (b) ZSM-5; (c) mordenite; and (d) ferrierite.	168
4.37	The FTIR spectra (v_4) of methane adsorbed on zeolites at 293 K and 137 kPa: (a) NaY; (b) Na-SZ18; and (c) NaX.	168
4.38	The FTIR of carbon dioxide molecules (gas phase) at 293 K and 137 kPa.	171
4.39	The FTIR spectra (v_3 and v_4) of carbon dioxide adsorbed on channel type zeolites at 293 K and 137 kPa: (a) mordenite; (b) ferrierite; (c) zeolite beta; and (d) ZSM-5.	172
4.40	The FTIR spectra (v_3 and v_4) of carbon dioxide adsorbed on channel type zeolites at 293 K and 137 kPa:	172

	(a) Na-SZ18; (b) NaX; and (c) NaY.	
4.41	The effect of pressure on v_3 band of methane adsorbed at different pressures: (a) 5 psi; (b) 10 psi; (c) 20 psi; (c) 30 psi; and (d) 40 psi.	175
4.42	The effect of pressure on v_4 band of methane adsorbed at different pressures: (a) 5 psi; (b) 10 psi; (c) 20 psi; (d) 30 psi; and (e) 40 psi.	175
4.43	A schematic diagram illustrates gas diffusion inside the zeolite structures.	178
4.44	A schematic diagram allustrates gas adsorption on different zeolite adsorbents.	180
4.45	A schematic diagram indicates all possibilities of electrostatic interactions between adsorbate and zeolite adsorbent.	181
5.1	A Periodic Table indicates the groups of the selected metals cations used in the study (marked in black).	189
5.2	The SEM image of the Na-SZ18 crystallites (based zeolite).	190
5.3	The SEM crystallite images of the metal cation exchanged zeolites: (a) LiNa-SZ18; (b) KNa-SZ18; (c) MgNa-SZ18; and (d) BaNa-SZ18.	191
5.4	The XRD patterns of the alkali metal cation exchanged zeolites: (a) Na-SZ18; (b) LiNa-SZ18; (c) KNa-SZ18; and (d) RbNa-SZ18.	192
5.5	The XRD patterns of the alkaline earth metal cation exchanged zeolites: (a) Na-SZ18; (b) MgNa-SZ18; (c) CaNa-SZ18; and (d) BaNa-SZ18.	192
5.6	The XRD patterns of the transition metal cation exchanged zeolites: (a) Na-SZ18; (b) MnNa-SZ18; (c) NiNa-SZ18; and (d) ZnNa-SZ18.	193
5.7	The FTIR spectra of alkali metal cation exchanged zeolites: (a) Na-SZ18; (b) LiNa-SZ18; (c) KNa-SZ18; and (d) RbNa-SZ18.	196
5.8	The FTIR spectra of alkaline earth metal cation	196

	exchanged zeolites: (a) MgNa-SZ18; (b) CaNa-SZ18; (c) BaNa-SZ18; and (d) Na-SZ18.	
5.9	The FTIR spectra of transition metal cation exchanged zeolites: (a) MnNa-SZ18; (b) NiNa-SZ18; (b) ZnNa-SZ18; and (d) Na-SZ18.	197
5.10	The nitrogen adsorption isotherms of alkali metal cation exchanged zeolites.	198
5.11	The nitrogen adsorption isotherms of alkaline earth metal cation exchanged zeolites.	199
5.12	The nitrogen adsorption isotherms of transition metal cation exchanged zeolites.	199
5.13	The hysteresis loops of based zeolite and several metal cation exchanged zeolites: (a) Na-SZ18; (b) LiNa-SZ18; (c) MgNa-SZ18; and (d) NiNa-SZ18.	201
5.14	Location of cations in faujasite structural framework.	202
5.15	The adsorption capacity of methane on metal cation exchanged zeolites at 323 K and 137 kPa.	207
5.16	The adsorption capacity of carbon dioxide on metal cation exchanged zeolites at 323 K and 137 kPa.	207
5.17	The effect of surface area on gas adsorption capacity: (a) methane and (b) carbon dioxide.	210
5.18	The effect of charge/ionic radius on adsorption capacity: (a) methane and (b) carbon dioxide.	212
5.19	The CH_4 adsorption isotherm of alkali metal cation exchanged zeolites.	216
5.20	The CH_4 adsorption isotherm of alkaline earth metal cation exchanged zeolites.	216
5.21	The CH_4 adsorption isotherm of transition metal cation exchanged zeolites.	217
5.22	The CO_2 adsorption isotherm of alkali metal cation exchanged zeolites.	218
5.23	The CO_2 adsorption isotherm of alkaline earth metal cation exchanged zeolites.	218
5.24	The CO_2 adsorption isotherm of transition metal	219

	cation exchanged zeolites.	
5.25	The adsorption isotherm of methane fitted into Henry and Freundlich equations: (a) LiNa-SZ18 and (b) MgNa-SZ18.	220
5.26	The adsorption of carbon dioxide fitted into Freundlich and Dubinin-Polanyi equations: (a) LiNa-SZ18 and (b) MgNa-SZ18.	222
5.27	The adsorption of carbon dioxide fitted into Langmuir equations: (a) LiNa-SZ18 and (b) MgNa-SZ18.	223
5.28	The methane fractional uptake curves of alkali metal cation exchanged zeolites.	228
5.29	The methane fractional uptake curves of alkaline earth metal cation exchanged zeolites.	229
5.30	The methane fractional uptake curves of transition metal cation exchanged zeolites.	232
5.31	The carbon dioxide fractional uptake curve of alkali metal cation exchanged zeolite.	233
5.32	The carbon dioxide fractional uptake curve of alkaline earth metal cation exchanged zeolite.	233
5.33	The carbon dioxide fractional uptake curve of transition metal cation exchanged zeolites.	234
5.34	The effect of cation's properties on initial adsorption rate for different adsorbates: (a) methane and (b) carbon dioxide.	237
5.35	The effect of relative crystallinity on equilibrium time: (a) methane and (b) carbon dioxide.	240
5.36	The effect of surface area on the equilibrium time: (a) methane and (b) carbon dioxide.	242
5.37	The effect of cation on equilibrium time: (a) methane and (b) carbon dioxide.	243
5.38	The electrostatic charge model and adsorption force on zeolite surface.	251
5.39	The FTIR spectra (v_3) of CH_4 adsorbed on alkali metal cation exchanged zeolites: (a) LiNa-SZ18; (b) Na-SZ18	252

	(based zeolite); (c) KNa-SZ18; and (d) RbNa-SZ18.	
5.40	The FTIR spectra (v_3) of CH_4 adsorbed on alkaline earth metal cation exchanged zeolites: (a) MgNa-SZ18; (b) CaNa-SZ18; (c) BaNa-SZ18; and (d) Na-SZ18 (based zeolite).	252
5.41	The FTIR spectra (v_3) of CH_4 adsorbed on transition metal cation exchanged zeolites at 293K and 137 kPa: (a) MnNa-SZ18; (b) NiNa-SZ18; (c) ZnNa-SZ18; and (d) Na-SZ18 (based zeolite)	253
5.42	The FTIR spectra (v_4) of CH_4 adsorbed on alkali metal cation exchanged zeolites at 293K and 137 kPa: (a) LiNa-SZ18; (b) Na-SZ18 (based zeolite); (c) KNa-SZ18, and (d) RbNa-SZ18.	254
5.43	The FTIR spectra (v_4) of CH_4 adsorbed on alkaline earth metal cation exchanged zeolites at 293K and 137 kPa: (a) Na-SZ18 (based zeolite); (b) MgNa-SZ18; (c) CaMg-SZ18; and (d) BaNa-SZ18.	254
5.44	The FTIR spectra (v_4) of CH_4 adsorbed on transition metal cation exchanged zeolites at 293K and 137 kPa: (a) Na-SZ18 (based zeolite); (b) MnNa-SZ18, (c) NiNa-SZ18, and (d) ZnNa-SZ18.	255
5.45	The FTIR spectra (v_3 and v_2) of CO2 adsorbed on alkali metal cation exchanged zeolites at 293K and 137 kPa (a) Na-SZ18 and (b) LiNa-SZ18.	257
5.46	The FTIR spectra (v_3 and v_2) of CO_2 adsorbed on alkaline earth metal cation exchanged zeolites: (a) Na-SZ18; (b) MgNa-SZ18; and (c) CaNa-SZ18.	258
5.47	The FTIR spectra (v_3 and v_2) of CO_2 adsorbed on transition metal cation exchanged zeolites at 293K and 137 kPa: (a) Na-SZ18; (b) MnNa-SZ18 and (c) NiNa-SZ18.	258
5.48	A schematic diagram of adsorbate diffusion in the presence of different size cations.	261
5.49	Electrostatic attractions between adsorbate-zeolite	262

	adsorbent. M1 and M2 represent either Na^+ or exchanged cations respectively.	
5.50	A schematic diagram of adsorbate-adsorbent interaction with different cation exposure.	263
6.1	XRD patterns of metal oxides: (a) Group IIA; (b) Group IIIA; and (c) Group IVA metal oxides modified Na-Y zeolite	270
6.2	XRD patterns of metal oxides (a) Group IB (b) Group IIB and (c) Group IIIB metal oxides modified Na-Y zeolite	271
6.3	XRD patterns of metal oxides (a) Group VB (b) Group VIB and (c) Group VIIIB metal oxides modified Na-Y zeolite	272
6.4	Morphology of surface of the CuO on Cu_2O after oxidation at 873.15K (Zhu *et al.*, 2005)	274
6.5	Nitrogen adsorption and desorption isotherms of metal oxides modified Na-Y zeolite	275
6.6	The correlation between the micropore surface area and the micropore volume of metal oxides modified Na-Y zeolite samples	277
6.7	SEM micrograph of samples (a) Na-Y zeolite (c) 5 CuO/NaY (c) 5 HgO/NaY and (d) 5 V_2O_5/NaY	279
6.8	The EDAX quantification analysis of samples (a) Na-Y zeolite (b) 5 CuO/NaY (c) 5 HgO/NaY and (d) 5 V_2O_5/NaY	280
6.9	FTIR spectra of Group IIA metal oxides modified Na-Y zeolite (a) Na-Y (b) MgO/NaY (c) CaO/NaY and (d) BaO/NaY	282
6.10	Infrared correlation chart for metal oxides (Nyquist and Kagel, 1971)	284
6.11	FTIR spectra of metal oxide (a) Group IIA (b) Group IIIA (c) Group IVA (d) Group IB (e) Group IIB (f) Group IIIB (g) Group VB (h) Group VIB and (i) Group VIIIB modified Na-Y zeolite adsorbents	285

6.12	The possible structure of copper oxide in the micropores of zeolite Y (Huang *et al*., 2004)	287
6.13	XRD patterns of CuO/NaY samples (a) CuO (b) NaY (c) 2.25wt.% of CuO/NaY (d) 5wt.% of CuO/NaY (d) 10wt.% of CuO/NaY and (f) 15wt.% of CuO/NaY	288
6.14	The influence of CuO loading concentration (wt.%) to the structure of modified samples	290
6.15	Effect of CuO loading concentration on Na-Y zeolite physical properties.	290
6.16	FTIR spectra of copper (II) oxide modified Na-Y zeolite (a) CuO (b) Na-Y (c) Physical mixture of 2wt.% CuO/NaY (e) 2wt.% CuO/NaY (e) 5wt.% CuO/NaY (f) 10wt.% CuO/NaY and (g) 15wt.% CuO/NaY	291
6.17	XRD patterns of 5 CuO/NaY samples after heat treatment: (a) CuO (298.15 K) (b) NaY (298.15 K) (c) 5 CuO/NaY (773.15 K) (d) 5 CuO/NaY (873.15 K) (e) 5 CuO/NaY (973.15 K) and (f) 5 CuO/NaY (1073.15 K)	293
6.18	FTIR spectra of copper (II) oxide modified Na-Y zeolites calcined at different temperatures: (a) 773.15 K; (b) 873.15 K; (c) 973.15 K; and (d) 1073.15 K	294
6.19	The influence of calcination time to the structure of modified samples	295
6.20	FTIR spectra of (a) NaY; (b) CuO/NaY calcined for 0 hour; (c) 6 hours; (d) 12 hours; (e) 24 hours; and (f) 48 hours	297
6.21	XRD patterns of CuO/NaY samples: (a) CuO (b) NaY (c) 5 CuO/NaY prepared by thermal dispersion technique and (d) 5 CuO/NaY prepared by incipient wetness impregnation technique	298
6.22	XRD patterns of Ga_2O_3/NaY samples: (a) Ga_2O_3 (b) NaY (b) 5 Ga_2O_3/NaY prepared by thermal dispersion technique (c) and (d) 5 Ga_2O_3/NaY prepared by incipient wetness impregnation technique	299

6.23	Effect of specific surface area and micropore volume on gases adsorption capacity	305
6.24	Effect of copper (II) oxide loading concentration on methane adsorption characteristics	308
6.25	Effect of calcination temperature on methane adsorption characteristics	309
6.26	Effect of duration calcination process on methane adsorption characteristics	310
6.27	Effect of modification techniques on methane adsorption characteristics	311
6.28	Relationship between N_2 adsorption capacity and isosteric heat of adsorption	313
6.29	Relationship between CO_2 adsorption capacity and isosteric heat of adsorption	313
6.30	Relationship between CH_4 adsorption capacity and isosteric heat of adsorption	314
6.31	Gases adsorption characteristics of MoO_3 modified Na-Y adsorbent at 138 kPa and 323.15 K	317
6.32	Kinetics of CO_2 diffusion into Na-Y and metal oxide modified Na-Y adsorbents at 138 kPa and 323.15 K	320
6.33	Kinetics of N_2 diffusion into Na-Y and metal oxide modified Na-Y adsorbents at 138 kPa and 323.15 K	320
6.34	Kinetics of CH_4 diffusion into Na-Y and metal oxide modified Na-Y adsorbents at 138 kPa and 323.15 K	321
6.35	The corresponding areas of the FTIR spectrum peak at (2300 – 2360 cm^{-1} region) versus the amount of N_2 adsorbed on samples	326
6.36	FTIR spectra of (a) activated Na-Y (673.15 K) (b) activated HgO/NaY (673.15 K) (c) N_2 adsorbed at 298 K on Na-Y and (d) N_2 adsorbed on HgO/Na-Y at 298 K and 138 kPa	327
6.37	FTIR spectra of N_2 dosed on (a) Na-Y (b) MgO/NaY (c) CaO/NaY and (d) BaO/NaY at 298 K and equilibrium pressures fixed at 138 kPa	328
6.38	FTIR spectra of N_2 adsorbed on HgO/Na-Y at 298 K	330

	with equilibrium pressure (a) 34 kPa (b) 69 kPa (c) 138 kPa (d) 207 kPa and (e) 276 kPa	
6.39	Effect of equilibrium pressure to the FTIR absorbance areas (2340 – 2352 cm^{-1} region) and gas N_2 adsorption characteristics	330
6.40	FTIR spectra of CO_2 adsorbed on (a) Na-Y (b) MgO/NaY (c) CaO/NaY and (d) BaO/NaY at 298 K and equilibrium pressures fixed at 138 kPa	333
6.41	FTIR spectra of CO_2 adsorbed on (a) Na-Y (b) Ag_2O/NaY (c) Cu_2O/NaY and (d) CuO/NaY at 298 K and equilibrium pressures fixed at 138 kPa	333
6.42	FTIR spectra of CO_2 adsorbed at on MgO modified zeolite Na-Y at 298 K and pressure (a) 34 kPa (b) 69 kPa (c) 138 kPa (d) 207 kPa and (e) 276 kPa	334
6.43	The corresponding areas of the FTIR spectrum peak at (2450 – 2250 cm^{-1} region) versus the amount of CO_2 adsorbed on samples	335
6.44	FTIR spectra of CH_4 adsorbed on (a) Na-Y (b) MgO/NaY (c) CaO/NaY and (d) BaO/NaY at 298 K and equilibrium pressures fixed at 138 kPa	336
6.45	FTIR spectra of CH_4 adsorbed on (a) Na-Y and (d) V_2O_5/NaY at 298 K and equilibrium pressures fixed at 138 kPa	336
6.46	FTIR spectra of CH_4 adsorbed on HgO modified zeolite Na-Y at 298 K with equilibrium pressure (a) 34 kPa (b) 69 kPa (c) 138 kPa (d) 207 kPa and (e) 276 kPa	339
6.47	The corresponding areas of the FTIR spectrum peak at (3030 - 2990 cm^{-1}) and (1315 - 1290 cm^{-1}) regions versus adsorption equilibrium pressures	339
7.1	XRD pattern of a as-synthesized MCM-41	343
	metals cations used in the study (marked in black).	
7.2	XRD patterns of grafted amine-MCM-41. (PEI= polyethylenimine, MDEA= methyl diethanolamine,	343

	TEA= triethanolamine, DEA= diethanolamine, MEA= monoethanolamine)	
7.3	Nitrogen adsorption isotherm of MCM-41 and 20 wt% MEA MCM-41.	345
7.4	FTIR spectra of MCM-41	347
7.5	FTIR spectra of amine modified MCM-41	348
7.6	XRD patterns of different metal loading on MCM-41 (Cu= copper, Ni= nickel, Co= cobalt) exchanged zeolites: (a) Na-SZ18; (b) MnNa-SZ18; (c) NiNa-SZ18; and (d) ZnNa-SZ18.	349
7.7	XRD patterns of MEA grafted on metals modified MCM-41.	351
7.8	XRD patterns of zeolite NaY and MEA modified NaY	353
7.9	XRD patterns of zeolite 13X and MEA modified 13X.	353
7.10	The effect of MEA loadings on the diffraction intensity of the (100) plane of MCM-41	355
7.11	Gas CO_2 adsorption capacity for MCM-41 support and amine modified MCM-41	358
7.12	TGA curves of CO_2 adsorption capacity for MCM-41 support and amine modified MCM-41	360
7.13	Gas CO_2 adsorption capacity for various mesoporous and microporous supports and MEA modified supports	363
7.14	TGA curves of CO_2 adsorption capacity for MEA modified mesoporous and microporous supports	365
7.15	CO_2 adsorption capacity for MEA modified MCM-41 at different concentration	368
7.16	TGA curves of CO_2 adsorption capacity for MEA modified MCM-41 at different concentration	369
7.17	Gas CO_2 adsorption capacity for 20 wt% MEA modified MCM-41 at different adsorption temperatures	371
7.18	TGA curves of CO_2 adsorption capacity for 20 wt% MEA modified MCM-41 at different adsorption temperatures	372
7.19	CO_2 adsorption capacity for 20 wt% MEA modified MCM-41 at different heating temperatures	374

7.20	TGA curves of CO_2 adsorption capacity for 20 wt% MEA modified MCM-41 at different heating temperatures	375
7.21	FTIR spectra of CO_2 adsorbed on: (a) MCM-41; (b) 20 wt% MEA MCM-41; (c) 20 wt% DEA MCM-41; (d) 20 wt% TEA MCM-41; (e) 20 wt% MDEA MCM-41; and (f) 20 wt% PEI MCM-41 at equilibrium pressures of 138 kPa and room temperature 25˚C	377
7.22	FTIR spectra of CO_2 adsorbed on MEA modified MCM-41 at 25˚C and equilibrium pressure: (a) without CO_2; (b) 138 kPa; (c) 276 kPa; (d) 414 kPa and (e) 552 kPa.	379
7.23	Effect of equilibrium CO_2 pressure on the FTIR absorbance areas (2345 – 2335 cm^{-1} region) for the physisorption peak	379
7.24	Effect of equilibrium CO_2 pressure on the FTIR absorbance areas (1450 – 1420 cm^{-1} region) for the chemisorption peak	380
8.1	Methane adsorption capacity at 500 psi versus adsorbents surface area	386
8.2	Methane adsorption isotherm on various zeolite	388
8.3	Methane adsorption isotherms on various zeolite ; solid lines, Freundlich model; dotted symbol, experimental data	390
8.4	Methane adsorption isotherms on MCM-41 and SBA-15 ; solid lines, Freundlich model; dotted symbol, experimental data	391
8.5	Langmuir plots for the adsorption of methane onto various adsorbents	392
8.6	Temperature of the adsorption cell during methane adsorption onto H-Beta zeolite at various pressures	393
8.7	A typical transient pressure of the adsorption cell during discharging process	395
8.8	Temperature of the adsorption cell during methane desorption from the zeolite H-Beta.	396

8.9	Effect of modification techniques on methane adsorption	402
8.10	ZSM-5 type zeolite (Ming and Wu, 2006).	404
8.11	X-type zeolite (Ming and Wu, 2006)	406
8.12	Methane adsorption isotherm for modified H-beta; solid lines, Freundlich model; dotted symbol, experimental data	407
8.13	Methane adsorption isotherm for modified ZSM-5; solid lines, Freundlich model; dotted symbol, experimental data	408
8.14	Methane adsorption isotherm for modified MCM-41; solid lines, Freundlich model; dotted symbol, experimental data	408
8.15	Langmuir plots for the adsorption of methane on modified H-beta	410
8.16	Langmuir plots for the adsorption of methane on modified ZSM-5	411
8.17	The methane release from selected modified adsorbent at different pressure	413

LIST OF SYMBOLS

^0C	-	Degree Celsius
T	-	Temperature (K)
P	-	Pressure (kPa)
ΔH	-	Different enthalpy of adsorption
Q_{st}	-	Isosteric heat of adsorption
R	-	Gas constant
b	-	Linear function of temperature
ΔG	-	Free energy of adsorption
K	-	Surface partition coefficient
ΔH_{st}	-	Isosteric enthalpy of adsorption
ΔS	-	Different entropy of adsorption
V_N	-	Net retention volume
n_s	-	Total amount of solute adsorbed
T_{av}	-	Average temperature
t	-	Time (s)
R	-	Fractional uptake
a_t	-	Amount of gas adsorbed at time t
a_0	-	Amount of gas adsorbed at time t = 0
a_∞	-	Amount of gas adsorbed at equilibrium
S_{ext}	-	External surface area
V	-	Volume of adsorbent
K	-	Ratio of adsorbate in gas to adsorbed phase at equilibrium
D	-	Diffusion coefficient
E_a	-	Energy of gas adsorption

F	-	Fractional uptake
D	-	Fickian diffusivity
R	-	Adsorbent particle radius (cm)
Δv	-	Magnitude of wavenumber shift
E	-	Strength of the electric field
S_1	-	Band intensity
n_1	-	Amount of gas adsorbed at cationic site
N_A	-	Avogrado's number
c	-	Light velocity
d	-	Spacing of indices planes
a_0	-	Unit cell parameter
h	-	Miller indices planes
k	-	Miller indices planes
l	-	Miller indices planes
%	-	Percentage
Σ	-	Sum of the value
t	-	Crystallite size (nm)
B	-	System broadening in radians
θ	-	Angle
λ	-	Wavelength
I_{rel}	-	Relative Intensity
wt.	-	Weight
Å	-	Angstrom (1Å = 10^{-10} m)
A	-	Absorbance
a.u.	-	Arbitrary unit

LIST OF ABBREVIATIONS

PSA	-	Pressure Swing Asorption
VPSA	-	Vacuum Pressure Swing Adsorption
TSA	-	Temperature Swing Adsorption
FTIR	-	Fourier Transform Infrared Spectroscopy
US	-	United State
SBU	-	Secondary Building Unit
GCMC	-	Grand Carnonical Monte Carlo
DR	-	Dubinin Radushkevich
BET	-	Brunauer, Emmett, Teller
XRD	-	X-Ray Diffraction
SEM	-	Scanning Electron Microscope
EDS	-	Electron Dispersive Spectroscopy
TGA	-	Thermogravimetric Analyzer
TD	-	Thermal Dispersion
IWI	-	Incipient Wetness Impregnation
XPS	-	X-Ray Photoelectron Spectroscopy
TPR	-	Temperature Programmed Reduction
TPD	-	Temperature Programmed Desorption

CHAPTER 1

INTRODUCTION

1.1 Background

The study of gas adsorption characteristic on adsorbents is growing awareness in the last two decades for gas separation and purification processes applications (Barrer, 1978; Suzuki, 1990; Yang, 1997). Now, about one-fifth of air separation is carried out using adsorption technologies (Rege and Yang, 1997). The performance of the chosen adsorbent material is the most crucial factor for controlling the efficiency of commercial separation and purification operations in a wide range of industries (Sherman, 1999; Yong *et al*., 2002; Rutherford and Coons, 2005). Pressure swing adsorption (PSA), vacuum pressure swing adsorption (VPSA) and temperature swing adsorption (TSA) technologies are processes of interest in gas separation industry due to their low energy requirements and cost advantages (Baronskaya *et al*., 1996; Ishibashi *et al*., 1996; Boger *et al*., 1997; Dong *et al*., 1999; Warmuziński and Sodzwiczny, 1999; Rege *et al*., 2001; Takamura *et al*., 2001; Gomes and Yee, 2002; Chou and Chen, 2004; Jayaraman and Yang, 2005; Cavenati *et al*., 2006).

CHAPTER 2

LITERATURE REVIEW

2.1 Zeolite Adsorbent

2.1.1 Introduction to zeolite

Zeolite was originally discovered in the 18th century (1756) by a Swedish mineralogist, Cronstedt, who observed the natural zeolite stones began to boil upon rapid heat treatment (Frost and Sullivan, 2001). The word derives from two Greek words *zeo* and *lithos*, which means "stone that boils". Typically, zeolites are hydrated, porous crystalline aluminosilicates. The framework is an assemblage of SiO_4 and AlO_4 tetrahedral joined together by sharing oxygen atoms (Barrer, 1978). Zeolites are commercially attractive materials because of their unusual crystalline structures that give them unique chemical properties. Interest in the field of zeolites has been triggered in a large number of research and development organizations due to the possibility of tailoring specific types of zeolites for specific applications.

Generally, there are about 50 known natural zeolite minerals which have been identified and more than about 150 types synthetic zeolite have been prepared (Frost and Sullivan, 2001). Natural zeolite is a naturally formed mineral when ash from volcanoes was deposited in alkaline or saline lakes millions of years ago. The natural zeolites can be broadly classified into seven families, namely analcime, chabazite, gismondine, harmotome, heulandite, natrolite and stilbite (Sand and Mumpton, 1978). Several types of common commercial natural zeolites products are listed in Table 2.1. Each type of natural zeolites consists of different crystal structures and chemical compositions. Temperature, geographic location, ash or water properties and different ratio of silica to alumina from ash impart the unique properties of natural zeolites. Meanwhile, the particle size, cation selectivity, molecular pore size, and strength are some of the properties that can differentiate them to difference groups of natural zeolite (Sing, 1989; Vaughan, 1978). The major application areas of natural zeolites are as ion exchangers in removing ammonium and heavy metal ions for water purification, radioactive waste treatment, adsorbents for air separation and natural gas purification, pollution control, animal feed supplements, agriculture, horticulture, aquaculture, and thermal storage (Vaughan, 1978; Suzuki, 1990).

Synthetic zeolites were first prepared by the Union Carbide Corporation in 1954 as a new class of adsorbents and as hydrocarbon-conversion catalysts in 1959 (Sherman, 1999). It has been prepared in large industrial quantities due to the great demand of zeolites for commercial applications. All the synthetic zeolites are different from each other on basic chemical composition, crystal structure and sorption properties. Different physicochemical properties of synthetic zeolites allow the selection of a particular zeolite having optimum properties for a particular application as summarized in Table 2.2. Meanwhile, the framework structures of several types of commercial synthetic zeolite are presented in Figure 2.1. The large internal surface area and pore volumes, molecular-size pores, regularity of crystal structures, and the diverse framework chemical compositions allow, “tailoring” of structure and properties. In other words, controlling the zeolite synthesis process optimizes a zeolite for different applications.

Table 2.1: Properties of natural zeolites (Sand and Mumpton, 1978).

Natural Zeolite	Si/Al Range	Structure	Application
Analcime	2.0	The cubic structure consists of 4, 6 and 8 rings linked to give 16 large interconnected cavities, which form non-intersecting channels, and 24 smaller individual cavities.	Ammonia adsorbent, ion exchangers.
Chabazite	1.4 - 2.8	Stacked, double six-member ring prisms, interconnected through 4 rings, in a cubic close packed array	Natural gas purification, rare gas adsorption, drying agents, hydrocarbon cracking catalyst.
Clinoptilolite	2.7 – 5.3	Sheet like structure. Sheet contains open rings of 8 to 10 sides. The rings stack together to form channels.	Gas adsorber, molecular sieve, food additive, odor control agent, and catalyst.
Erionite	3.0 – 4.0	Hexagonal structure with 3.0 × 8.0 Å pore size, wool-like aggregates and crusts.	CO_2 and SO_2 adsorbent, hydrocarbon conversion catalyst.
Ferrierite	3.2 – 6.2	Elliptical 10-ring channels of dimensions 5.4 × 4.2 Å and 8-ring channels (4.7 × 3.4 Å) parallel to the c-axis.	Benzene and CO sorption, ion exchangers, hydrocracking catalyst.
Mordenite	4.4 – 5.5	Orthorhombic blocky crystal system with 6.0 × 7.0 Å pore size, crystal shape tends to be equate, 'kidney-like' in shape.	NH_3 and CO_2 adsorbent, Mineral specimen, hydro-isomerization catalyst, chemical filter.
Phillipsite	1.3 – 2.9	Two 8-ring channels having dimensions of 4.2 × 4.4 Å and 2.8 × 4.8 Å.	Water and CO_2 adsorption, ion exchangers.

Table 2.2: Properties of synthetic zeolites (Frost and Sullivan, 2001).

Synthetic Zeolite	Si/Al Ratio	Structure	Application
Zeolite Y	1.5 - 3.0	Faujasite structure, three-dimensional pore structure formed by 12-member oxygen rings, large cavity of 13Å and surrounded by 10 sodalite cages.	Petroleum cracking catalyst, hydrophobic molecules adsorbent, NO_X reduction and gas separation.
Zeolite X	1.0 – 1.5	Faujasite structure, three-dimensional pore structure formed by 12-member oxygen rings, large cavity of 13Å and surrounded by 10 sodalite cages.	Catalyst, molecular sieve adsorbent and dehydration agent.
ZSM-5	10 - 50	Zig-zag pattern intersecting two-dimensional pore structure formed by 10-membered oxygen rings.	Hydrocarbon conversion catalyst.
Mordenite	5.0 - 100	Orthorhombic crystal structure with straight 12-membered ring channels (6.5 × 7.0 Å) and crossed 8-membered ring channels (2.8 × 5.7 Å).	Paraffin and xylene isomerization, aromatics alkylation, catalytic NO_X reduction, exhaust gas purification.
Linde Type A	1.0 – 1.5	Polyhedral units linked in three-dimensional space through 4 member rings.	Detergent, molecular sieve adsorbent and dehydration agent.
Beta	5.0 - 100	Tetragonal crystal structure with straight 12-membered rings channels (7.6 × 6.4 Å) with crossed 10-membered ring channels (5.5 × 6.5 Å).	Aromatic catalyst, hydrocarbon absorbent, isomerization of waxes, NO_X reduction.

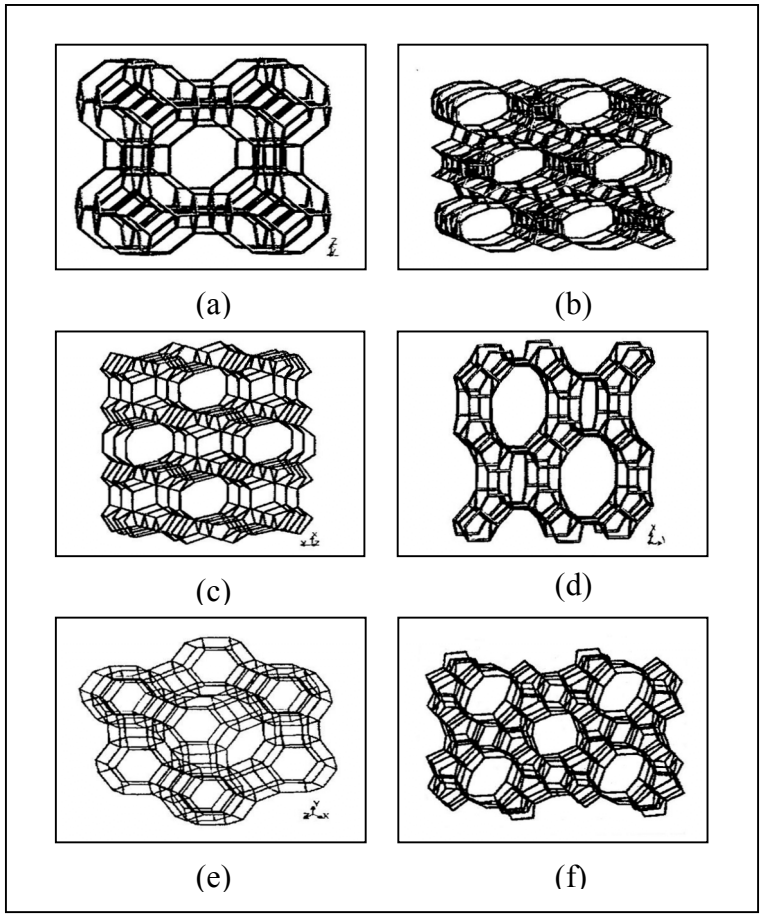

Figure 2.1: The framework structural of synthetic zeolites: a) zeolite Linde A; b) zeolite Beta; c) Ferrierite; d) Mordenite; e) Zeolite Y; and f) ZSM-5 (International Zeolite Association, 2000).

Tables 2.1 and 2.2 summarized the promising properties of natural and synthetic zeolites, respectively in the gas separation and purification processes. Natural zeolites have not had the commercial success, as synthetic zeolites due to the variations of their properties, impurity and limited sources. It still has not been examined in such great detail due to industrial disadvantages such as inconsistency of composition and cost of purifications and modifications. However, where uniformity and purity are not so important in a particular application, the cheapness of a natural zeolite may favor its use. Synthetic zeolites, on the other hand, are more attractive for a specific application when high purity processes are required. Thereinafter, it is well concluded that natural and synthetic zeolites typically do not compete in the same application areas but play their own roles suitably to the demands.

2.1.2 Zeolite structure and properties

Zeolite comprises a significant group of aluminosilicate compounds. Its structure is enclosed with interconnected cavities and is relatively porous. The fundamental building block of the zeolite is a tetrahedron of four oxygen atoms surrounding a silicon or aluminium atom as shown in Figure 2.2 (Sing, 1989). Each tetrahedra was then formed over other tetrahedral structural units, the so called secondary building unit (SBU's) as shown in Figure 2.3 that contains up to 16 T atoms form regular crystalline structures of zeolite (Sing, 1989). Secondary building units are commonly accepted criterion for classification of zeolites into individual structural groups (Mozgawa, 2005).

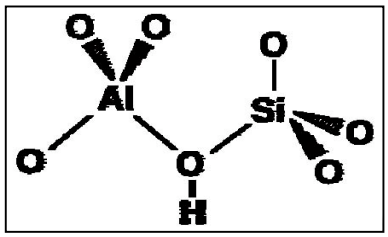

Figure 2.2: Primary building unit of SiO_4 and AlO_4 tetrahedral (Meier and Olson, 1992).

Zeolites have widespread industrial applications such as highly selective adsorbents, ion exchangers and highly activity catalysts due to their open, cage like structures, high cation exchange capacities, high internal surface areas, variable aggregate sizes and high permeability properties (Sand and Mumpton, 1978). Zeolites present strong interactions with adsorbates. Different diffusion and polarity properties of adsorbates have a different interaction with the zeolite framework, and thus are well separated by particular types of zeolite. Apart from that, silica to alumina ratio in zeolite structure, pore volume and size, types of adsorption sites, acidity properties, chemical composition, shape of cages and channels in zeolite structure also are some of the factors, which contribute to the variations of zeolite adsorption properties (Joshi *et al*., 2001).

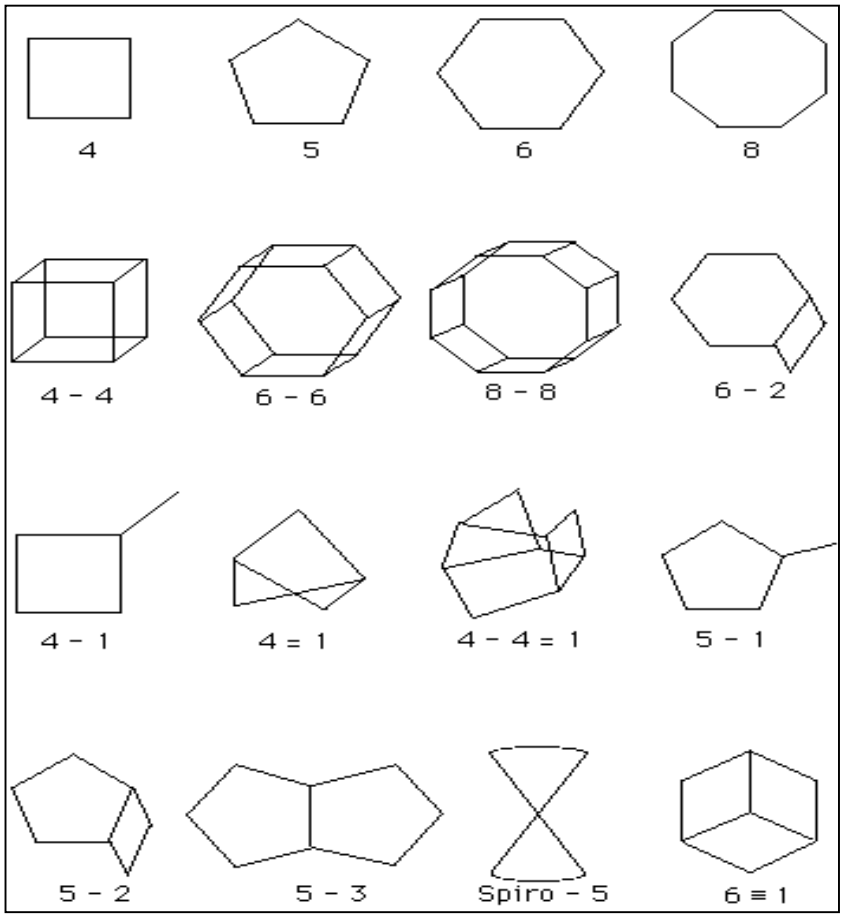

Figure 2.3: Secondary building units (SBUs) of zeolite (Meier and Olson, 1992).

Moreover, the content of aluminium in zeolite regulates the polar properties of zeolite. The polar properties of zeolite surfaces will produce strong interaction with polar molecules. Low silica zeolites such as zeolite A and X consist of hydrophilic surface selectivity. Meanwhile, high silica zeolites, which can be prepared by framework modification of hydrophilic zeolite like zeolite Y and mordenite, present hydrophobic properties. Hydrophobic zeolites normally are very stable and withstand temperatures of up to 873 K or higher. The hydrophilic and hydrophobic character of the zeolite can influence the activity of adsorption and catalytic processes (Ribeiro *et al*., 1995). In addition, zeolites are stable either in acidic media or alkaline environment. High humidity condition shows no effect on their adsorption properties. They also can be used to adsorb radioactive cation in the ionizing process. These stability properties of zeolite are crucial to their applications as ion-exchangers, sorbents and catalysts (Stelzer *et al*., 1998).

From the economic viewpoint, zeolites are reusable nanomaterials. Zeolites can be regenerated by using relatively easy methods such as heating to remove the adsorbed materials, ion exchanging process with sodium to remove cation, or pressure swing to remove adsorbed gases. Meanwhile, in the health and safety aspects of zeolites, it was found to be non-toxic via oral, dermal, ocular, and respiratory routes of exposure; it was also found to be environmental friendly. Zeolites are safe to handle and are easy to use in a variety of reactors like other solid materials. They have wide applications in food, drugs, cosmetic products and detergents (Frost and Sullivan, 2001).

2.1.3 Development of zeolite adsorbent

Serious environmental issue concerning global warming is mainly caused by gases such as carbon dioxide, water, methane and chlorofluorocarbon. Gas adsorption using zeolite as gas adsorbent is an adequate method to reduce these gases directly with advantage concerning energy (Mizukami *et al*., 2001). By studying the adsorption of a wide range of polar and non-polar molecules by zeolites and other well-defined adsorbents, they were able to demonstrate the importance of the adsorbent-adsorbate and adsorbate-adsorbate interactions in zeolite pore structure as high efficiency gas adsorbent. The most significant characteristic of an adsorbent is its high porosity that provides large surface area. Each adsorbent surface contains the particular dispersed attractive sites for the adsorbate molecules. The adsorbed molecules may be mobile or fixed at certain position, depend on the strength of the forces binding them to the sites. The adsorbent must have properties as high adsorption capacity, high selectivity, good mechanical strength, high stability adsorption capacity and adequate adsorption/desorption kinetic (Yong *et al*., 2002).

Basically, all the porous materials like γ-alumina, mesoporous M41S, silica gel, activated carbon, pillared clays, metal oxides and zeolites can be used as adsorbents. Among all these porous materials, zeolites show good physical-chemical properties that are useful for a great number of applications principally because of their sorption capacity and their physicochemical properties. Zeolites have long been established as a better adsorbent for drying and purifying processes and for separating certain components (Barrer, 1978; Vaughan, 1978). The shape selective properties of zeolites are also the basic for their use in molecular adsorption. The ability to adsorb certain molecules, while excluding others, has opened up a wide range of molecular sieving applications. Highly polar cationic zeolites carry strong electric field gradients, thereby improving their status as gas adsorbents. Zeolite are also advantageous as adsorbents in gas purification due to their reusable properties, that can lower material and operating costs, capital investment and eliminate the need for the disposal of large amounts of waste product as well as obtaining higher overall throughput for the adsorption system.

Early in the 1970s where synthetic zeolites are not yet being prepared in large quantity, natural zeolites have been widely investigated as gas adsorbent for purification and separation process (Sand and Mumpton, 1978). A large variety of natural zeolites were investigated on the equilibrium adsorption and diffusion properties. These large variations of sorptive and diffusive properties exist in natural zeolite minerals are due to their diverse origins. Several types of exchange isotherms have been observed to study the characteristics of cation-exchange equilibria in natural zeolites (Barrer, 1978). In addition, sorption and diffusion of C_2H_4, C_2H_6 and n-C_5H_{12} in natural erionite that have been investigated by Ruthven and Derrah (1978) also revealed the unique gas adsorption characteristics of natural zeolites. Ma and Lee (1978) have presented a brief review of some previous works on sorption and diffusion in natural zeolites as shown in Table 2.3.

Table 2.3: Studies on natural zeolites (Ma and Lee, 1978).

Type	Adsorbate	Types of Studies	Reference
Chabazite	CO_2, CH_4, Ar, Freon 21	Rate curves, diffusivities change with concentrations	Brandt and Rudloff, 1968
Chabazite	He, Ar, O_2, N_2, CH_4, C_2H_6, C_3H_8, n-C_4H_{10}	Isotherms, heat, entropy and free energy of adsorption	Barrer and Ibbitson, 1944
Chabazite, Mordenite, Levynite	C_3H_8, n-C_4H_{10}, CH_2Cl_2, $(CH_3)_2NH$	Diffusivities and activation energy for diffusion	Barrer and Brook, 1953
Chabazite, Ca-Chabazite	N_2, CO, CO_2, H_2	Heat of adsorption. Diffusion of surface heterogeneity and the role of quadrupoles	Kington and Macleod, 1959
Chabazite, Clinoptilolite, Erionite, Phillipsite	CH_4	Adsorption capacity, ion exchanged properties and isotherms	Munson, 1973
Clinoptilolite	CO_2, Kr	Effect of framework charges on gas sorption characteristics	Barrer and Coughlan, 1968
Erionite	SO_2	Diffusion coefficients increased with increasing crystal sizes	Gupta *et al*., 1971
Mordenite, Clinoptilolite	SO_2 and CO_2 mixtures	SO_2 and CO_2 separation, sorption rates	Ma and Belmonte, 1974

Apart from that, adsorption of N_2, CO, CO_2 and NO has been studied on various molecular sieves include H-Mordenite, 4A and 5A zeolites, natural clinoptilolite and activated carbon (Triebe and Tezel, 1995). The natural clinoptilolite show most promise for the separation of CO and NO from N_2 at the temperature range of 273-398 K. Mercer and Ames (1978) studied the adsorption

characteristics of natural zeolites for the separation of radioactive cesium from highly radioactive processing wastes. Natural zeolites were also found as good adsorbent in the removal of ammonia-nitrogen in wastes (Hagiwara and Uchida, 1978; Hayhurst, 1978), CO adsorption (Lee *et al*., 1996) and nitrogen-methane separation process (Hernández-Huesca *et al.,* 1999). All the results revealed that zeolites are showing different adsorption characteristics at different adsorption conditions.

As gas adsorbents, synthetic zeolites have found wide use in drying and purifying both gaseous and liquid streams in chemical, petroleum, and natural gas operations. Adsorption of some hydrocarbons on 4A and 13X zeolites by inverse gas chromatography had been carried out to evaluate the adsorption thermodynamic parameters (Ĭnel *et al*., 2002). Interactions of the benzene and n-hexane with 13X were found to be stronger than that on 4A. In addition, measurement of adsorption equilibria and kinetics for argon, oxygen and nitrogen on 3A molecular sieve (Rutherford and Coons, 2005); oxygen and nitrogen adsorption on zeolite 4A, 5A and 13X (Valyon *et al*., 2003); CO_2 adsorption on zeolite 5A (Cheng *et al*., 2005) and nitrosamines on zeolite KA and NaA (Yun *et al*., 2004) have been investigated.

Apart from zeolites type A and faujasite, the adsorption behavior of methane and carbon monoxide in the pore of Ω-zeolite (Yamazaki *et al*., 2000); gas methane, ethane, ethylene, and carbon dioxide adsorption on silicalite-1 (Choudhary and Mayadevi, 1996); adsorption of nitrogen molecules at room temperature on copper-ion exchanged ZSM-5 zeolite (Itadani *et al*., 2004) and alumina as gas adsorbent for SO_2 and CO_2 also being widely investigated (Rao *et al*., 1996; Horiuchi *et al*., 1998). Besides, H-ZSM-5 zeolite modified with zinc ions surprisingly shows improvement in methane adsorption selectivity (Kazansky *et al*., 2004a). Therefore, the structural properties of different types of zeolite give great effects on gas adsorption characteristics. All types of zeolite have their own properties and potential that suited for a particular adsorbate. More adsorbents rather than zeolite type X and A should be advance investigated and well developed.

It has been reported that zeolite NaY is an important synthetic zeolite material as catalyst for petrochemical applications, and furthermore as adsorbent, for example in the separation of C_8 aromatics. Recently, zeolite NaY was found to present some attractive adsorptive and catalytic properties for eliminating NO_x from exhaust gases of diesel and lean burn engines (Sultana *et al*., 2004). A variety of molecules such as oxygen, argon, helium, nitrogen, and xenon can approach the OH-groups in the supercages of zeolite, since it has a 12-oxygen aperture with 0.74 nm in diameter. On the other hand, the open aperture of the small cavities in a 6-oxygen ring is 0.26 nm in diameter, so that most molecules, except water and ammonia, cannot approach the sites in the small cavities (Wakabayashi *et al*., 1997). These molecular sieving properties enabling zeolite Na-Y exploited commercial in the adsorption process.

Harlick and Tezel (2004) studied the adsorbent screening for CO_2 and N_2 gases using thirteen adsorbents and they found out that Faujasites types-13 X and NaY zeolites are the most promising zeolites to be employed in the gas adsorption processes. 13 X zeolite shows the best equilibrium performance at low feed and low regeneration of CO_2 pressures. Meanwhile, NaY adsorbent exhibited higher efficiency for both high feed and high regeneration pressures. The NaY adsorption behavior at high pressure condition as a function of temperature with excellent expected working capacities shows promise for Pressure Swing Adsorption (PSA), Temperature Swing Adsorption (TSA) and Pressure Temperature Swing Adsorption (PTSA) applications (Harlick and Tezel, 2004). Due to these reasons, many research have been carried out using NaY zeolite as the membrane or adsorbent in the gas separation processes which require high temperature and high pressure operating conditions (Kusakabe *et al*., 1998; Hasegawa *et al*., 2001; Mizukami *et al*., 2001). These adsorption characteristics are well suited for the purpose of our study in the adsorption of gas CH_4, N_2 and CO_2 at supercritical conditions.

The use of natural zeolite in adsorption process leads to synthesizing zeolites with different structures and properties. This prompts from the fact that natural zeolite encounter several limitations such as limited resources and variation in properties due to chemical composition. Therefore, research on synthetic zeolites that started in 1950s give a new dimension on gas adsorption and catalytic processes. Since then, many types of zeolite structures have been synthesized using hydrothermal condition method in order to meet various applications for chemical and petrochemical processes (IZA-Structure Commission; Barrer, 1982; Dabrowski, 2001).

Different methods have been established to produce different types of zeolites (van Bekkum *et al*., 1991; Barrer, 1978). The method developed by Milton in the late 1940's involves the hydrothermal crystallization of the reactive alkali metal aluminosilicate gels at low temperature and pressures. Recently, Feijen *et al*. (1994) outlined steps for the synthesis of zeolite. The preparation of an inhomogeneous gel was obtained by combining a silica source and an alumina source in water, under basic condition. The zeolite reaction mixtures are formulated in the molar oxide ratio of the reactants. For example, the reactant formulation for zeolite A is 8.7 Na_2O: Al_2O_3: SiO_2: 560 H_2O (van Bekkum *et al*., 1991). The most simple zeolite composition is given by the overall Si/Al ratio, and the type and quantity of cation. The synthesis mechanism involves crystallization of mediated solution of the amorphous gel at a temperature near 100 °C (van Bekkum *et al*., 1991).

However, the existing synthesized zeolite structures encounters problems such as highly hydrophobic or hydrophilic, thermally unstable at temperature higher than 700 °C, only allow monoatomic or diatomic molecules to pass through the pore, and adsorb at very low capacity (van Bekkum *et al*., 1991; Kucherov *et al*., 1998). These properties limit their applications in many industrial processes. Therefore, modifications or post synthesis treatment are carried out in order to produce modified materials with desired properties (van Bekkum *et al*., 1991; Siantar *et al*., 1995; Rakic *et al*., 1999; Qian and Yan, 2001; Kurama *et al*., 2002; Trigueiro *et al*., 2002; Sato *et al*., 2003).

Generally, there are two major types of treatments that can be applied to zeolites; structural framework modification and surface interaction modification (Vansant, 1987; van Bekkum *et al*., 1991; Impens *et al*., 1999; Bae and Seff**,** 2001**).** Methods such as dealumination, deammoniation and cation exchange caused some changes not only to the physical properties but also the chemical properties of zeolites. Dealumination (Muller *et al*., 2000; Fernandez *et al*., 1986) and desilication (van Mao *et al*., 1997, Cizmek *et al*., 1995; Ogura *et al*., 2001) is the removal of aluminium and silica from the framework respectively. The removal of atoms can cause the enlargement of pore size as it occurs preferentially at lattice defects, thus 'opening' the main channels, or generates secondary micropores by connecting side pockets of adjacent channels. It also promotes the formation of mesoporous system or secondary pore structure. However, cation exchange and metal ion dispersion methods are used for fine tuning the pore opening and the surface properties of zeolites (Vansant, 1987; Kurama *et al*., 2002; Kaushik *et al*., 2002; Sato *et al*., 2003). Table 2.4 shows that structure and framework modification caused some changes in pore size opening, pore size distribution, pore volume or formation of mesoporous structure.

Since modification could lead to structural defects or variant special attention has to be paid to the method of modifications. In this case, cation exchange offers several advantages for modification of zeolites. It has simple procedure and can tailor not only the pore properties of zeolites, but also surface characteristics of adsorbent. The presence of different cation change the physicochemical properties of zeolite, thus may improve gas adsorption characteristics. Since the cations are not covalently bound, it can easily be replaced by other cations (Barrer, 1982; Armor, 1998; Kurama *et al*., 2002). According to Armor (1998), once the cation exchange takes place, zeolite exerts a strong, localized electrostatic field that can alter the chemistry of cations in the exchange site positions. The success however, depends on the interrelation between the zeolite structure and the adsorption characteristics of adsorbates (Ackley and Yang, 1991; Armor, 1998; Kaushik *et al*., 2002). Therefore, in order to control the accessibility of adsorbates, the suitable cation needs to be

identified and the amount of exchanged should be monitored and controlled. Besides all the advantages, structural destruction also occurs due to the acidity of solution or the size of cation exchanged (Sato *et al*., 2003).

Table 2.4: Modification techniques and the effect on zeolite properties.

Modification methods	**Changes in properties**	**References**
Dealumination	• Removal of aluminium from the framework, increased acidity and hydrphobicity. • Enlargement of pores or formation of secondary pores.	Muller *et al.* (2000), Goovaerts *et al*. (1989).
Cation exchange	• "Fine tuning" the pores. • Change thermal stability, acidity and catalytic activity.	Kurama *et al.* (2002) Li *et al.* (2000)
Desilication	• Removal of silica from the framework. Silica precipitates on the surface. • Increase activity. • Mesopore formation.	Van Mao *et al.* (1997) Cizmek *et al.* (1995). Ogura *et al.* (2001)
Silylation	• Surface modification. • Change zeolite porosities and affinities.	Impens *et al*. (1999)
Spontaneous monolayer dispersion	• Surface modification without changing chemical composition of based zeolite. • Pore size changed due to the formation of monolayer.	Qian *et al.* (2001), Xie and Tang (1990)
Silanation	• Pore modification. • Change the acidity.	Klemm *et al.* (1997), Kim *et al.* (1999)

Many studies mainly focused on the physical features of modified zeolites (Carvalho *et al*., 1994; Siantar *et al*., 1995; Oka *et al*., 1997; Huang *et al*., 1998; Triantafillidis *et al*., 2000; Albert and Cheetham, 2000; Qian and Yan, 2001; Trigueiro *et al*., 2002; Sato *et al*., 2003; Nery *et al*., 2003), and only a few reported the effect of modification on gas adsorption capacity (Bellat *et al*., 1995; 1995; Hutson *et al*., 1999; Hajiivanov *et al*., 2003) that involve several types of zeolites such clinoptilolite, zeolite Y (NaY), and zeolite X (NaX). However, thermodynamic and kinetic data are also equally important in determining the adsorption characteristics of the modified adsorbents. In this case, the effect of aluminium or silicon removal, the presence of different cation or metal oxides or metal halides on gas adsorption capacity, gas adsorption isotherm, kinetic of adsorption, and gas-zeolite interaction need to be further studied in order to understand the potential used of this modification methods in tailoring zeolite for specific application.

2.1.4 Natural gas adsorbents

Natural gas is a combustible mixture of hydrocarbon gases. While natural gas is formed primarily of methane, it can also include ethane, propane, butane and pentane. The composition of natural gas can vary widely, below is a chart outlining the typical makeup of natural gas before it is refined. From Table 2.5, it is clearly shows that carbon dioxide is the highest impurities (up to 8%) compare to others. Since the presence of carbon dioxide tend to cause corrosive and inert property problem, therefore it is necessary to remove this unwanted gas. In its purest form, such as the natural gas used in Natural Gas Vehicles (NGV), it is almost pure methane. Methane is a molecule made up of one carbon atom and four hydrogen atoms, and is referred to as CH_4. Ethane, propane, and the other hydrocarbons commonly associated with natural gas have different chemical formulas.

Table 2.5: Typical composition of natural gas (Anon, 2005)

Composition	Molecular Formula	Percentage
Methane	CH_4	70 – 90%
Ethane	C_2H_6	0 – 20%
Propane	C_3H_8	
Butane	C_4H_{10}	
Carbon Dioxide	CO_2	0 – 8%
Oxygen	O_2	0 – 0.2%
Nitrogen	N_2	0 – 5%
Hydrogen Sulphide	H_2S	0 – 5%
Rare Gases	A, He, Ne, Xe	trace

Natural gas is considered 'dry' when it is almost pure methane, having had most of the other commonly associated hydrocarbons removed. When other hydrocarbons are present, the natural gas is considered 'wet' gas. It has many uses, residentially, commercially, and industrially. Natural gas can be found in reservoirs underneath the earth and is commonly associated with oil deposits. Production companies search for evidence of these reservoirs by using sophisticated technology that helps to find the location of the natural gas, and drill wells in the earth where it is likely to be found. Once brought from underground, the natural gas is refined to remove impurities like water, other gases, sand, and other compounds. Some hydrocarbons are removed and sold separately, including propane and butane. Other impurities are also removed, like hydrogen sulfide (the refining of which can produce sulfur, which is then also sold separately). After refining, the clean natural gas is transmitted through a network of pipelines. From these pipelines, natural gas is delivered to its point of use.

2.1.4.1 Carbon Dioxide Removal

Fossil fuels will likely remain the mainstay of energy supply well into the 21st century. Availability of these fuels to provide clean, affordable energy is essential for the prosperity and the security of the world. However, increased CO_2 concentration in the atmosphere due to emissions of CO_2 from fossil fuel combustion has caused concerns about global warming. Improving the efficiency of energy utilization and increasing the use of low-carbon energy sources are considered to be potential ways to reduce CO_2 emissions. Recently, CO_2 capture and sequestration are receiving significant attention and being recognized as a third option for reduction in the global CO_2 emission (Khatri *et al*., 2005; Kaggerud *et al*., 2006). Furthermore, enriched CO_2 streams can be an important starting material for synthetic clean fuels and chemicals. For carbon sequestration, the cost for CO_2 capture is expected to comprise about 75% of the total costs for geological or oceanic sequestration, with the other 25% costs attribute to transportation and injection. Therefore, the development of techniques for the cost-effective separation and capture of CO_2 is considered to be one of the highest priorities in the field of carbon sequestration (Xu *et* al., 2002; Xu *et* al., 2005).

Several techniques to remove CO_2 from gas mixtures have been studied since 1970, but most of them were applied to produce technical CO_2 as process gas, mainly for the food and chemical industry. In the following decade, some of the CO_2 capture systems were considered for application in power plants and separation of natural gas. With the discovery of increased number of natural gas fields, more power plants are converting to the use of natural gas.

Among the alternative for CO_2 capture, chemical absorption with amine aqueous solutions was demonstrated as one of the most mature and less expensive technologies to be applied to power plants. The absorption stripping system is particularly interesting because of its possibility to regenerate the solution

continuously, thereby in an almost closed cycle (Desideri and Paolucci, 1999; Xu *et* al., 2005). The plant for removing CO_2 from flue gases has two main elements, which are the absorption and stripping packed columns. It allows a continuous regeneration of the amine solution, which saves considerable amounts of solvent. Amines in the water solution react with CO_2 in the absorption column, forming chemical compounds that separate CO_2 from the gas mixtures at a higher rate than the natural CO_2 absorption in pure water (Desideri and Paolucci, 1999).

To date, all commercial CO_2 capture plants use processes based on chemical absorption with alkanolamine such as monoethanolamine (MEA) solvent. An example is the Fluor Econamine process. However, the liquid amine-based processes suffer from high regeneration energy, large equipment size, solvent degradation and equipment corrosion. To overcome these disadvantages, several other separation technologies, such as, adsorption, membrane and cryogenic separation have been studied. Because of the low energy requirement, cost advantage, and ease of applicability over a relatively wide range of temperatures and pressures, adsorption separation attracts much interest. The main target for adsorption separation is to develop an adsorbent with high CO_2 adsorption capacity and high CO_2 selectivity (Desideri and Paolucci, 1999; Xu *et* al., 2003; Xu *et* al., 2005).

2.1.4.2 Adsorption as CO_2 removal method

Adsorption is one of the promising methods that could be applicable for separating CO_2 from gas mixtures, and numerous studies have been conducted on separation of CO_2 by adsorption in the last two decades. Various adsorbents, such as activated carbons, pillared clays, metal oxides, and zeolites have been investigated. At lower temperatures (room temperature), the zeolite-based adsorbents have generally been found to show higher adsorption capacity. CO_2 adsorption capacity of zeolite 13X, zeolite 4A, and activated carbon was about 160, 135, and 110 mg/g-

adsorbent, respectively, at 25 °C and 1 atm CO_2 partial pressure. However, their adsorption capacities rapidly decline with increasing temperature (Zheng *et al*., 2005). Moreover, since all the gases are physically adsorbed into/onto these adsorbents, the separation factors (such as CO_2/N_2 ratio) are low. To operate at relatively high temperature and reach a high separation factor, chemical adsorption was adopted. Investigation of the adsorption performance of hydrotalcite showed a CO_2 adsorption capacity of 22 mg/ g-adsorbent at 400 °C and 0.2 atm CO_2 partial pressure. Meanwhile, MgO showed an adsorption capacity of 8.8 mg/g-adsorbent at 400 °C. Both types of adsorbents need high temperature operation and have a low adsorption capacity, thus they are not suitable for practical use for CO_2 separation (Desideri and Paolucci, 1999; Xu *et* al., 2002; Xu *et* al., 2005).

For practical applications, selective adsorbents with high capacity are desired. Many of the separations should preferably be operated at relatively higher temperature, for example, higher than room temperature and up to ~150 °C which is a typical value of power plant stack temperature (Pedersen *et al*., 1995; Kaggerud *et al*., 2006). Developing an adsorbent with high CO_2 selectivity and high CO_2 adsorption capacity, which can also be operated at relatively high temperature, is desired for more efficient CO_2 separation by an adsorption method.

Eventually, a new concept called “molecular basket” has been explored to develop a high capacity, highly selective CO_2 adsorbent. A novel type of solid adsorbent has been discovered, which can serve as a “molecular basket” for “packing” CO_2 in condensed form in the nanoporous channels. To capture a large amount of CO_2 gas, the adsorbent needs to have large pore channels filled with a CO_2 capturing substance as the “basket”. To cause the “basket” to be a CO_2 “molecular basket”, a substance with numerous CO_2 affinity sites should be loaded into the pores of the support to increase the affinity between the adsorbent and CO_2 and as a result, the CO_2 adsorption selectivity and CO_2 adsorption capacity can be increase. In addition, the adsorption affinity to CO_2 by the CO_2 –philic substance increased in the confined mesoporous environment and therefore the mesoporous

molecular sieve can have a synergetic effect on the adsorption of CO_2 by CO_2 –philic substance (Xu *et al*., 2003; Xu *et al*., 2002; Xu *et al*., 2005).

2.1.4.3 Mesoporous silica as CO_2 adsorbents

In addition to zeolites, the applications of mesoporous molecular sieves are as exciting as their discovery. In earlier years, mesoporous materials were examined for applications relating to their large pore volumes. Such applications including the use of mesoporous adsorbents for removal of volatile organic compound (VOC) in the industrial setting. In pursuit of such goals, the behavior of a variety of adsorbates has now been comprehensive. Almost all reported data agree that mesoporous materials have large accessible internal pore volumes which can be filled at pressures appropriate with the pore size (Zhao *et al*., 2001; Beck and Vartuli, 1996).

The sorptive properties of MCM-41, the hexagonal member of the M41S family of mesoporous silicates, have been extensively characterized using a variety of adsorbates. Some recent highlights include careful comparison of adsorption of a series of gases in a single sample of MCM-41. This work showed that the type of isotherm observed is highly dependent upon a number of factors including the material composition, pore size, and nature of the adsorbent. Current study of adsorption isotherms on gases like argon, nitrogen and oxygen using well characterized MCM-41 sample confirm that MCM-41 has a narrow pore size distribution and exhibits extraordinary pore volume compared to classical microporous materials (Zhao *et* al., 1996; Dabrowski, 2001; Barton *et al*., 1999; Beck and Vartuli, 1996).

Despite the impressive adsorption capacities of these materials, their type IV isotherm behavior requires the adsorbate, in the gas phase, to be at high partial

pressure. However, by contrast in most industrial application, for example VOC uptake, where adsorption at low partial pressures (type I isotherms) is required and poses constraint to the mesoporous materials application. Industrial applications which utilize mesoporous materials are catalytic processes, mini-reactors for electron transfer reaction, as a host for quantum confinement, molecular wires and shape-selective polymerization (Beck and Vartuli, 1996).

2.2 Gas Adsorption

2.2.1 Introduction

Adsorption is a phenomenon denotes the taking up of gas, vapor or liquid by a surface on interface. It is a fundamental physicochemical property of solids and liquids to retain one or more components (atom, molecules or ions) from another solid, liquid or gas in contact with the surface. The adsorbing phase is the adsorbent, and the material concentrated or adsorbed at the surface of that phase is the adsorbate. Adsorption is different from absorption; a process in which material transferred from one phase to another interpenetrates the second phase to form a 'solution'. Adsorption is mainly caused by Van der Waals force and electrostatic force between adsorbate molecules and the adsorbent surface. Therefore, surface properties such as surface area, polarity and pore size distribution are important properties for adsorbents characterization (Suzuki, 1990; Yang, 1997).

Generally, gas adsorption in zeolite adsorbents can be classified into two types of phenomena, namely physisorption and chemisorption. Physical force of attraction hold the gas molecule to the adsorbent is known as physisorption. It is a process in which attraction force fields at the solid surfaces pull molecules or ions from the gas phase and bind them reversibly to the surface (Dabrowski, 2001).

Meanwhile, chemisorption is a process where the chemical forces hold the gas molecules to the surface of the adsorbent. It involves a displacement of electrons between the adsorbate and adsorbent. Physisorption is the preferred method used in the gas separation and purification application. This is due to the fact that the adsorbent can be regenerated by heating or flushed to remove the adsorbed gas molecules that attached to the solid. Thereby, the process is more profitable and economical.

Adsorption of gas on microporous zeolite-based adsorbents generally behaves as Type I isotherms in the international (IUPAC) classification. This isotherm is suitable apply for temperature below critical temperature of adsorbate (Aranovich and Donohue, 1995). It does not include the behavior of supercritical adsorbates at high pressures (1 – 200 atm). Several studies have been developed as summarized in Table 2.6 for gas adsorption characteristics on zeolite-based adsorbents that involved discussion on adsorption equilibria study, kinetics study, thermodynamic data (differential heat of adsorption, differential entropy of adsorption, internal energy) and adsorbate-adsorbent interaction.

Each experimental works resulting different opinions in adsorption isotherm selection for equilibrium study. The variant in experimental conditions and parameters such as pressure, temperature, adsorbates and adsorbent is lead to the significance differences in their results and discussions. Only few literatures are available for gas adsorption at supercritical conditions, which means adsorption at both high temperature and high-pressure condition. Furthermore, gas adsorption characteristics study on metal oxide modified zeolite is not comprehensively discussed. Therefore, the adsorption controlling parameters effects on single gas adsorption equilibrium, kinetic transport, thermodynamic properties and gas-zeolite interaction should be well reviewed and understood before predicting any adsorption isotherm and kinetic model of zeolite based adsorbents especially novel metal oxide modified zeolite adsorbent for commercial separation and adsorption applications.

Table 2.6: Studies on zeolite based adsorbents.

Adsorbent	Adsorbate	Adsorption properties	Temperature	Pressure	Reference
Na-Y, K-Y, Ba-Y	Xylene	Isotherms, enthalpies and entropies of adsorption.	423 – 673 K	1.2 kPa	Bellat and Simonot-Grange, 1995.
Natural zeolite	CO	Isotherms and adsorption capacity.	288 K	3.17 kPa	Lee *et al*., 1996.
H-Y	O_2, Ar, He, N_2, Xe	Adsorbate-adsorbent interactions.	150 –182 K	0.4 – 19.7 kPa	Wakabayashi *et al*., 1997.
Ω-zeolite	CH_4, CO	Isotherms, isosteric heat of adsorption and adsorbate-adsorbent interaction.	184 – 323 K	0 – 70 kPa	Yamazaki *et al*., 2000.
H, Li, Na, K-exchanged Ferrierite	H_2, N_2, CO, NO	Adsorbate-adsorbent interaction.	100 K	6.6 kPa	Bordiga *et al*., 2000.
Alkali metal cations-exchanged Y zeolite	CO_2, N_2	Diffusitivities and isotherms.	308 K	0 – 100 kPa	Hasegawa *et al*., 2001.
5 A	CO_2	Isotherms and adsorption capacity.	273 – 523 K	0.00013 – 133.3 kPa	Yong *et al*., 2002.
4 A, 5 A, 13 X	N_2, O_2	Isotherms, heat of adsorption and interaction energy.	298 – 393 K	100 – 700 kPa	Valyon *et al*., 2003.

Table 2.6: Continued

Adsorbent	Adsorbate	Adsorption properties	Temperature	Pressure	Reference
Be^{2+}, Mg^{2+}, Ca^{2+}, Sr^{2+}, Ba^{2+}-exchanged Y zeolite	CO	Adsorbate-adsorbent interaction.	85 – 293 K	1 – 2 kPa	Hadjiivanov *et al*., 2003.
Zn-ZSM-5	CH_4	Adsorbate-adsorbent interaction.	295 K	0.13 – 2 kPa	Kazansky *et al*., 2004a.
Cu-ZSM-5	N_2	Isotherms and differential heat of adsorption.	301 K	0 – 15 kPa	Itadani *et al*., 2004.
5 A, 13 X, NaY, HY, H-ZSM-5 and their ion-exchanged form.	N_2, CO_2	Heat of adsorption and internal energy of adsorption.	295 K	0.13 – 253.3 kPa	Harlick and Tezel, 2004.
Li^+, Na^+, K^+ and Ca^{2+}, Sr^{2+}, Ba^{2+} exchanged X zeolite.	N_2, Ar	Isotherms and differential enthalpies of adsorption.	300 K	50 kPa	Maurin *et al*., 2005.
Na-ZSM-5, K-ZSM-5	H_2	Differential heats of adsorption and differential entropies of adsorption.	89 – 135 K	0.285 – 11.0 kPa	Areán *et al*., 2005
5 A, NaX, H-ZSM-5 and ion-exchanged NaX	N_2, Ar	Isotherms of adsorption, differential enthalpies and differential entropies of adsorption.	77 – 302 K	0 – 4000 kPa	Llewellyn and Maurin, 2005.

2.2.2 Adsorption parameters

The phenomenon of adsorption of gases by solids strongly depends on the nature of adsorbent and adsorbate, surface area of the adsorbent, rate of adsorption, temperature and pressure. Gases like SO_2, NH_3, HCl and CO_2, liquefy more easily, adsorbed more readily than permanent gases like H_2, N_2 and O_2 due to have greater Van der Waals or the molecular forces of attraction or cohesive forces. The amount of gas adsorbed is dependent on the types of adsorbents selected (Chhatwal and Mehra, 1974). For example, the adsorption of same types of adsorbates (CO_2, CH_4 and N_2) in coals (Cui *et al*., 2004) and in natural zeolites (Hernández-Huesca *et al*., 1999) showed totally different equilibrium and kinetic results due to the structural properties and experimental conditions effects.

Instead of nature of adsorbent and adsorbate, high surface area adsorbents are essential for gas adsorption. A large specific surface area is preferable for providing large adsorption capacity; the well-ordered micropore size distribution also determines the accessibility of adsorbate molecules to the internal adsorption surface (Suzuki, 1990). Small pores in the adsorbent materials would increase the force fields and enhances the adsorption in the micropores (Ruthven, 1984). Zeolite framework modification via ion-exchange method for instance, changed the behavior of adsorption phenomena in zeolite (Sousa-Aguiar *et al*., 1998; Bordiga *et al*., 2000).

In addition, gases with higher adsorption rates will adsorb much faster than other gases in the gas adsorption and separation processes. This characteristic is depending on molecular weight, shape, polarity and size of pores in the adsorbent. Chemical attraction between adsorbent and adsorbate is also another major factor that controls the adsorption behavior. The attraction is largely due to polarity and particle size. Adsorbent with small pore sites will not be able to hold large adsorbate particles. Moreover, the variation in zeolite molecular dimension might cause the differences in gas uptake rate and diffusivities in the adsorption process as well (Rutherford and Do, 2000).

The extent of adsorption also depends upon the temperature and pressure of the process. According to the Le Chatelier principle, at constant adsorption pressure, the decrease in temperature will increase the rate of adsorption. This is due to the decrease of gas molecules mobility and enhances the adsorption capability on adsorbent surfaces. Conversely, at constant adsorption temperature, the magnitude of adsorption decreases with the decrease in pressure and vise versa. High pressure caused high force of Van der Waals and electrostatic force between adsorbate and adsorbent (Chhatwal and Mehra, 1974; İnel *et al*., 2002; Ustinov *et al*., 2002; Areán *et al*., 2005). However, at supercritical condition that will be further discussed in Section 2.3.5.2, high temperature give not much effects on the adsorption capacity. Meanwhile, the magnitude of adsorption decreases with the increase in pressure when the adsorption equilibrium reaches the saturation capacity (Aranovich and Donohue, 1995).

2.2.3 Adsorption equilibrium

2.2.3.1 Adsorption equilibrium isotherm

Analysis of adsorption equilibria begins with classification of the isotherms. In gas adsorption, dynamic phase equilibrium is established for the distribution of the solute between the gas and the solid surface. The equilibrium is usually expressed in terms of partial pressure and the solute loading on the adsorbent, expressed as mass, mole or volume of adsorbate per unit mass, mole or volume of the adsorbent (Suzuki, 1990). At a constant temperature, a plot of solute loading on the adsorbent versus partial pressure is called the adsorption isotherm. From the physisorption isotherms, the isotherm type, the nature of the adsorption process and type of pore structure for its quantitative evaluation could be identified (Sing, 1989). The majority of sorption isotherms can be grouped into six types as summarized in Llewellyn and Maurin

(2005). It is based on an earlier classification by Brunauer with five types of isotherm (Donohue and Aranovich, 1998). The hypothetical differential enthalpy of adsorption curves that correspond to the IUPAC also included (Llewellyn and Maurin, 2005). The IUPAC classifications cover the behavior of a great number of adsorption systems. However, there are many systems whose isotherms do not fall into any of the IUPAC classes. These isotherms still lack of data to permit the calculation of contact time or amount of adsorbent required to reduce the concentration of solute below or over the prescribed limits. It is incomplete and it gives the incorrect impression that adsorption isotherms are always monotonic functions of pressure (Donohue and Aranovich, 1998; Sangwichien *et al*., 2002).

Basically, features of physical adsorption of supercritical gases at high pressure are different compared to subcritical fluid adsorption, which presents a challenge for fundamental theoretical researches. Excess adsorption isotherm is very important rather than absolute adsorption alone that counted in the subcritical adsorption process. Recently, two assumptions are mainly used and proposed: the excess adsorption obeys Ono-Kondo equation, while the absolute adsorption followed the Langmuir equation (Ustinov *et al*., 2002). The theory of adsorption of supercritical fluids at high pressure is not complete. Ono-Kondo equation that being widely investigated also involve fitting parameters that do not consider the real pore structure of adsorbents and pore size distribution. Grand canonical Monte Carlo (GCMC) simulations also can obtain adequate description of high-pressure adsorption (Suzuki *et al*., 2000; Do and Do, 2003; Raaen and Ramstad, 2005). However, these methods are time consuming and lead to poor predictions for pure component adsorption. Due to the awareness of incomplete information, a new classification of adsorption isotherms based on Gibbs approach has been introduced by Donohue and Aranovich (1998) in Figure 2.4. This new classification is based on the IUPAC scheme. There are five types of isotherms in this classification based on Gibbs adsorption, which would change dramatically to become non-monotonic when experimental conditions approaching the critical point in the adsorption.

Table 2.7: Six IUPAC classified isotherms and corresponding hypothetical differential enthalpy of adsorption isotherm (Llewellyn and Maurin, 2005).

IUPAC Isotherms	Remarks	Differential Heat of Adsorption	Remarks
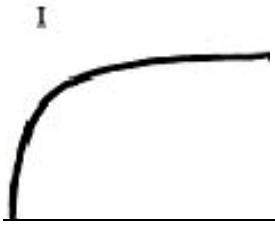	- Microporous. - Monolayer adsorption. - High capacity at low P/P_0.	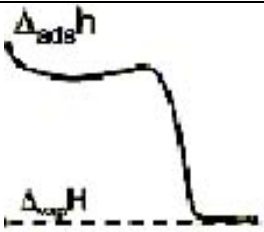	- Strong interactions in the initial uptake for monolayer coverage.
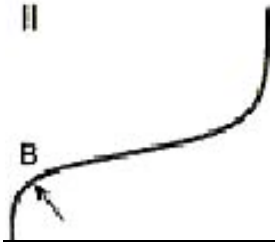	- Non-porous or macroporous. - Monolayer and multilayer adsorption.	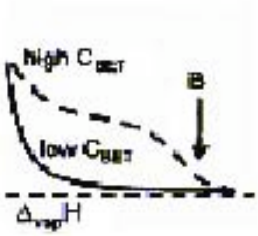	- Decrease rapidly to the enthalpy of $\Delta_{vap}H$. - Varied with C_{BET}, specific sites.
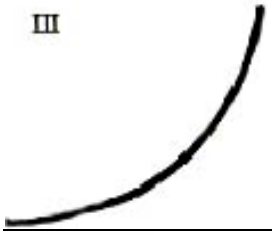	- Weak adsorbent-adsorbate interactions.	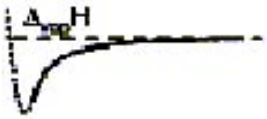	- Initially below the $\Delta_{vap}H$ of gas. - Entropy effect drives the adsorption.
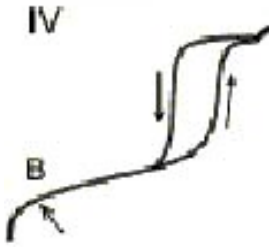	- Mesoporous. - Multilayer adsorption. - Capillary condensation occurs.	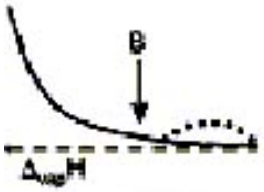	- Decrease to $\Delta_{vap}H$ of the gas. - Slight increase during capillary condensation.
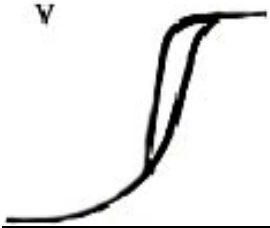	- Weak adsorbent-adsorbate interactions.		- Initially below the $\Delta_{vap}H$ of gas. - Entropy effect drives the adsorption.
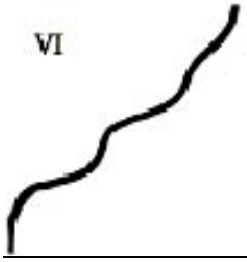	- Uniform non-porous surface. - Multilayer adsorption.	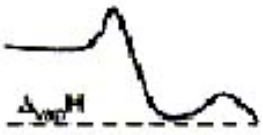	- Constant for initial coverage. - Distinct peak when complete of monolayer.

Type I shows adsorption isotherms on microporous adsorbents for subcritical and supercritical conditions. At supercritical conditions, the isotherm reveals non-monotonic adsorption and shows a maximum peak near the critical density. Types II and Types III are isotherms for macroporous and non-porous adsorbents, respectively. At low temperatures, both isotherms have steps; they transform to smooth monotonic curves with increasing temperature until the stage of critical temperatures for the adsorbate, these isotherms dramatically change to non-monotonic behavior. They show sharp maxima near the critical temperature. Types IV and V characterize mesoporous adsorbents with strong and weak affinities respectively. They show adsorption hysteresis at low temperature. The hysterisis decrease with the increase of adsorption temperature (Sangwichien *et al*., 2002).

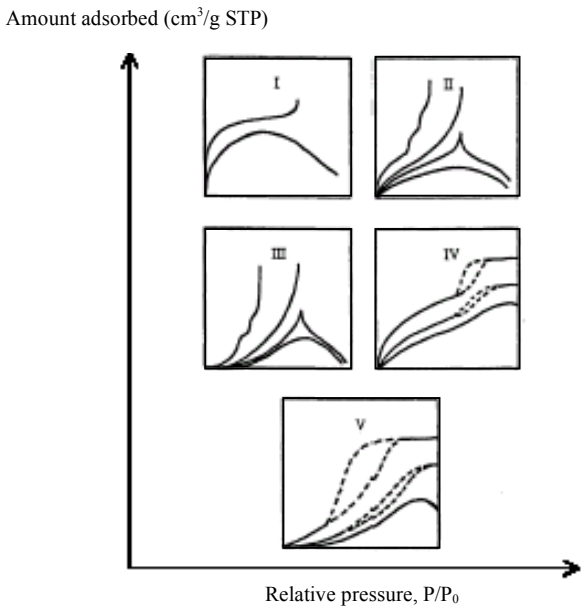

Figure 2.4: New classification of adsorption isotherms for physical adsorption of gases on solids (Donohue and Aranovich, 1998).

It is therefore very important to select the appropriate isotherm equation to describe a measured gas/solid isotherm with physical properties of the adsorbent or adsorbate. Software for gas/solid adsorption measurements even developed for adsorption experiments (Tóth, 2000).

2.2.3.2 Adsorption equilibrium model

In adsorption equilibrium study, many types of equilibrium models have been investigated to predict the experimental works data on gas adsorption and separation processes. Unfortunately, there is always a limitation and some drawbacks for a specific model. First of all, Henry's law constants are used to calculate the initial linear portion of the adsorption isotherms. The temperature and pressure ranges that studied are too limited. The adsorption equilibrium models selected for particular adsorbate are varied depending on the nature of adsorbates and adsorbents, temperature and pressure of adsorption processes (Choudhary and Mayadevi, 1996; Burggraaf *et al*., 1998; Burggraaf, 1999).

In the fundamental view of point, the thermodynamic models Langmuir, Fowler, and Dubinin-Radushkevich (DR model) are those often selected due to their simplicity and frequently used to describe the adsorption of gas on zeolite (Bellat and Simont-Grange, 1995). DR equation and its modification have been used widely for the analysis of adsorption on microporous adsorbents with Type I isotherm. Nevertheless, DR equation does not give correct behavior either for very low pressures or for moderate to high pressures. It contains a parameter, saturated pressure, which cannot be defined in the supercritical region by any physical theorem (Zhou and Zhou, 1998).

In Langmuir theory, the surface area of high porous adsorbent such as zeolite cannot be easily defined (Sing, 1998). The fist two assumptions in Langmuir isotherms, which the gas is assumed to be ideal and monolayer adsorption, are reasonable for zeolite adsorbent but not for metal oxide modified zeolite (heterogeneous surface). Adsorbed molecules may be mobile on the surface, interact with each other, multilayer adsorption and not localized as assume by Langmuir model (Ma and Lee, 1978). In Brunauer, Emmett, Teller (BET) model, each site of adsorbent can accommodate to infinity adsorbate molecules, which are not mobile on the surface (Yang, 1997). However, this model is not applicable to adsorption under

supercritical conditions (Sing, 1998). Freundlich isotherm has the same drawback for supercritical gas adsorption as well. The Freundlich isotherm expressed the amount adsorbed as a function of the equilibrium concentration (Sing, 1998). At high-pressure condition, the tendency of adsorption isotherm is not followed the Freundlich equation in which the amount of gas adsorbed attains a constant values instead of increases in an exponential form (Cordeiro *et al*., 2005). Rege *et al.* (2000) also found that the Polyani potential theory is the suitable model for description of low pressure or low concentration data only.

In the Khelifa *et al*. (2004) model review, the adsorption of CO_2 behavior is contradictory to the fundamental of Fowler-Guggenheim isotherm. Poor agreement was also found with Volmer and Sips equation for there is always an interaction between the adsorbed molecules related to the thermodynamic data as isosteric heat of adsorption. Meanwhile, Hill de Boer equation that takes account the mobility and interactions between the adsorbed molecules is found not suitable to express the adsorption for CO_2 adsorption on hydrophilic zeolite surface at low coverage (Khelifa *et al*., 2004). Moreover, the Ono-Kondo lattice model based on Gibbs adsorption theory was based on the adsorption behavior on slit pore lattice model.

Apart from that, Zhou and Zhou (1998) modified and linearized the Dubinin-Astakhov equation for gas hydrogen adsorption on activated carbon under supercritical conditions. Compared to conventional isotherm equations, the proposed model for linear isotherms avoid the use of any fictitious physical quantity, preserves the temperature invariance characteristic curve, able to identify the effect of adsorbate volume on adsorption isotherms give more precise values of isosteric heats of adsorption (Aranovich and Donohue, 1997). Nevertheless, there is not enough information in literature up to date relating to the linearized isotherms for zeolite adsorption applications. The suitability of this linear isotherm model approach on zeolite-based adsorbents still does not reach the conformity and recognized. Table 2.8 gives a basic review on several empirical and theoretical approaches pursued by many researchers for the gas adsorption processes.

Generally, every equilibrium model was connected with explicit equations in isotherm and, conversely, for every equation could be constructed a model. These models are limited in their scope in trying to understand the fundamental nature of the adsorption process. Despite all the equations and fundamental theory described above, it is also obvious that the adsorption behavior of gases on metal oxides modified zeolites is neither well defined nor been investigated for sub critical and supercritical conditions.

Table 2.8: Summary of existing adsorption models.

Model of adsorption	Remarks	References
Henry	Mobile; two-dimensional gas.	Bellat and Simont-Grange, 1995; Harlick and Tezel, 2004.
Langmuir	Located, homogeneous; no interaction between the molecules.	Bellat and Simont-Grange, 1995; Khelifa *et al*., 2004.
Fowler-Guggenheim	Located, homogeneous; interactions between the molecules.	Bellat and Simont-Grange, 1995; Khelifa *et al*., 2004.
Dubinin-Radushkevich (DR)	Adsorption in micropore volume and large void materials.	Yang, 1997; Roque - Malherbe, 2000.
Volmer	Mobile gas; no interaction between the adsorbates	Khelifa *et al*., 2004.
Hill-De Boer	Mobile gas; interactions between the adsorbates.	Khelifa *et al*., 2004; Tóth, 2004.
Sips	Localized adsorption; no adsorbates interaction.	Pakseresht *et al*., 2002; Khelifa *et al*., 2004.
Ono-Kondo	Lattice model with adsorbate-adsorbent interactions for whole ranges of relative pressures.	Aranovich and Donohue, 1995; 1997).
Freundlich	Heterogeneous surfaces adsorption; no limit of adsorption capacity.	Kanô *et al*., 2000; Cordeiro *et al*., 2005.
Brunauer, Emmett, Teller (BET)	Multilayer adsorption; heat of adsorption constant; adsorption sites are equivalent.	Suzuki, 1990; Yang, 1997.
Gibbs	Absolute adsorption and excess adsorption.	Sanwichien *et al*., 2002; Backhaus-Ricoult, 2003; Tóth, 2004.

2.2.3.3 Heat of adsorption

Gas adsorption process is an exothermic process. Adsorption isotherms are methods for characterizing adsorbents, but characterization is incomplete without information on heat of adsorption (energy). The isosteric heat of adsorption of gases at different surface coverage and constant adsorbate loading was normally calculated from the isotherm data by the Clausius-Clapeyron equation (Choudhary and Mayadevi, 1996; Ĭnel *et al*., 2002).

$$-\Delta H = Q_{st} = R\left[\frac{(T_2 T_1)}{(T_2 - T_1)}\right] In\left(\frac{P_2}{P_1}\right) \qquad (2.1)$$

This equation defined the isosteric heat of adsorption by differentiating a series of adsorption isotherms at constant loading. One common feature is that the isosteric heat of gas adsorption sharp decreases with the increase of adsorbate loading that due to the site heterogeneity (Hernández-Huesca *et al*., 1999; Khelifa *et al*., 2004). Subsequently, a flat heat profile with increasing adsorbate loading indicates a balance between the strength of energetic heterogeneity of adsorbate-zeolite interactions and adsorbate-adsorbate interactions. However, the above equation assumes a perfect state or ideal gas properties for the equilibrium phases. Its connection with the enthalpy of the adsorbed phase and its extension to the case of real gas mixtures had led to the considerable confusion. It could not give precise values of isosteric heat of adsorption for some conventional isotherm models at supercritical conditions (Myers, 2002). Therefore, the linearized isotherm model has been developed by Zhou and Zhou (1998) to satisfy the prerequisite of Clausius-Clapeyron equation where the effect of non-ideal states of the equilibrium phase was eliminated. The final equation used for calculating the isosteric heat of adsorption is given by Equation 2.2:

$$-\Delta H = RT^2\left[\frac{In\,P}{b}(0.009684\,In\,P - 0.10595)\right] \qquad (2.2)$$

Moreover, it is obvious that many studies applied the inverse gas chromatography method to evaluate the gas adsorption characteristics and isosteric heat of adsorption as well (Katsanos *et al*., 1999; İnel *et al*., 2002; Díaz *et al*., 2004a; Díaz *et al*., 2004b). Based on free energy of adsorption (İnel *et al*., 2002):

$$\Delta G = RT\,In\,p = RT\,In(cRT) = RT\,In\left(\frac{qRT}{K}\right) \tag{2.3}$$

where c is the concentration of the adsorbate in the gas phase, q the amount of adsorbate adsorbed per unit area of adsorbent and K the surface partition coefficient between the adsorbed phase and the gaseous state. For gas adsorption at isobar condition using volumetric method with elevated temperatures, the Equation 2.3 can be modified to Equation 2.4.

$$In(RTn_s) = In(V_N) - \frac{\Delta S}{R} + \frac{\Delta H}{R}\frac{1}{T} \tag{2.4}$$

One can calculate ΔH from the slope and ΔS from the intercept of the plot of In (RTn_s) versus 1/T, provided that the range of T is narrow enough for ΔH and ΔS regarded as temperature independent. The first term is negligible and can be ignored. The Equation 2.4 is then simplified to Equation 2.5 and applied to obtain heat of gas adsorption. Meanwhile, the differential enthalpy of adsorption (ΔH) obtained is related to the isosteric enthalpy of adsorption (ΔH_{st}) by the Equation 2.6.

$$In(n_s) = \frac{\Delta H}{R}\frac{1}{T} - \frac{\Delta S}{R} \tag{2.5}$$

$$\left|\Delta H_{st}\right| = \left|\Delta H\right| + RT_{av} \tag{2.6}$$

The Equations 2.3 – 2.4 are mostly applied for inverse gas chromatograph method that assumes the negligible effect of gas adsorption capacity. The Equation 2.4 that being modified for static volumetric method also ignored the flow rates effect on gas adsorption capacity. Thereinafter, the appropriate isotherm model that selected and isosteric heat of adsorption derived from the data obtained are still in a great challenge today especially for supercritical gas adsorption conditions.

2.2.4 Adsorption kinetics

2.2.4.1 Initial gas uptake rate

In engineering practice, adsorption equilibrium relationships are combined with mass transfer and diffusion coefficients to describe the thermodynamic and kinetic model of gas adsorption. The kinetics of gas adsorption over various adsorbents has been studied extensively since the early 1950s as reviewed by Ruthven (2001). Except for a few cases, most studies have been limited to low temperatures and low pressures of operation, and in which only unmodified zeolite, bulk metal oxide and ion-exchange modified zeolite are being discussed rather than metal oxide modified zeolite adsorbent which are of industrial importance (Triebe and Tezel, 1995; Roque-Melherbe, 2000; Ruthven, 2001; Kärger, 2003; Ponce *et al*., 2004; Rutherford and Coons, 2005).

In adsorption system when the equilibrium isotherm is linear, the diffusivity is generally constant. This is true for both micropore and macropore diffusion control. However, when the isotherm is non-linear the diffusivity is generally concentration dependent (Ruthven, 2004). The behavior of such systems has been studied to some extent and general features are well understood but many important details remain unresolved.

Generally, there are four basic mechanisms that described mass transport in porous materials (Mugge *et al*., 2001), namely molecular diffusion, Knudsen diffusion, surface diffusion and viscous flow. Normally, it is assumed that one or two of these four mechanisms influence the rate of gas uptake in the adsorption phenomenon. Hernández-Huesca *et al*. (1999) has carried out the investigation of gas CO_2, CH_4 and N_2 adsorption equilibria and kinetic study in natural zeolites. In the experimental works, adsorbate uptake rates of all gases were measured until equilibrium was reached. During the initial period of adsorption in a constant volume, the fractional uptake can be found from the following equation.

$$R = \frac{a_t - a_0}{a_\infty - a_0} \tag{2.7}$$

where R is the fractional uptake, a_t, a_0 and a_∞ are the amount of gas adsorbed at time t, $t = 0$ and $t = \infty$ (equilibrium), respectively. The kinetic transport behaviors greatly influence the initial uptake rate of gas into the adsorbent. Basically, there are two types of adsorbate molecules kinetics transport in the adsorption process, micropore diffusion and transport through pore mouth barrier. The micropore diffusion obeyed the Fick's law. Meanwhile, when the gas uptake is restricted by the pore mouth barrier, the non-Fickian uptake is described by a Linear Driving Force model (LDF) (Ding and Alpay, 2000). The fractional uptake, F is expressed as:

$$F = 1 - \exp(-kt) \tag{2.8}$$

A plot of In (1-F) versus time will yield a linear line with intercept and a slope of $-k$ (rate constant) for both types of diffusion kinetics. A zero intercept of the asymptote indicates the LDF kinetics and an intercept of -0.5 indicates Fickian micropore diffusion (Carta and Cincotti, 1998; Rutherford and Coons, 2005). However, LDF model fails for the adsorption at short uptakes times and for non-linear isotherms. Pore diffusion was said to be more realistic model to apply for short uptake time adsorption (Mugge *et al*., 2001).

2.2.4.2 Diffusion rate constant

It has long been established that diffusion in commercial zeolite is strongly depends on the physicochemical properties such as pore size and chemical composition. Under severe modifications, the partial collapse of the zeolite structure or addition of guest materials at the surface may lead to a surface barrier, which increases the overall mass transfer resistance. It has reported that, two lumped kinetic models – Pseudo first order and Pseudo second order models are widely used to describe the diffusion of gas or liquid in an adsorption process (Chang and Juang, 2005; Liang *et al*., 2005; Tongpool and Yoriya, 2005). However, these models cannot identify the gas adsorption mechanisms accordingly.

The intraparticle diffusion model and the Elovich equation, hence have been attracted much attentions and be discussed in adsorption process (Hernández-Huesca *et al*., 1999; Chang *et al*., 2004; Tongpool and Yoriya, 2005). Elovich equation is one of the most useful models for describing the activated adsorption which involving reaction of chemisorption of gases on a solid surface without desorption (Zhou and Gould, 1998; Liu and Ren, 2005). The transport of gas species into symmetrical and uniform structure of zeolite micropore are generally obeys a Fickian diffusion process (Marecka and Mianowski, 1998; Webb and Pruess, 2003; Rutherford and Coons, 2005). The intraparticle diffusion model is originates from the Fick's second law and therefore it is usually apply for describing gas diffusion characteristics into microporous materials. According to Barrer (1978) and Ruthven (2001), the plot uptake proportional to square root time in the initial region of an adsorption process is called as diffusion model, while the initial uptake directly proportional to time is so called as surface resistance model. When comprises short time region, the equation of Fick's second law is simplified as:

$$F = 6\sqrt{\frac{D}{\pi R^2}}\, t^{\frac{1}{2}} \qquad (2.9)$$

where the F is the adsorbate fractional uptake, D is the Fickian diffusivity (cm^2s^{-1}), R is the adsorbent particle radius (cm), and t is the time of adsorption. Gas initial gas uptake rate is linearly related to the diffusion rate constant (Hernández-Huesca *et al.*, 1999). The higher the initial gas uptake rate means larger diffusion coefficient of adsorbate to diffuse into the adsorbent. Equation 2.8 can therefore be described as:

$$R = \frac{a_t - a_0}{a_\infty - a_0} = \frac{2S_{ext}}{V}\left(\frac{1+K}{K}\right)\left(\frac{Dt}{\pi}\right)^{\frac{1}{2}} \qquad (2.10)$$

where $K = [(a_0)_g - (a_\infty - a_0)]/a_\infty$ is the ratio of the adsorbate in the gas phase to that in the adsorbed phase at equilibrium; S_{ext} and V are the specific external surface area of the particles (cm^2/g) and the volume (cm^3/g) of the zeolite; $(a_0)_g$ is the amount of gas initially available for adsorption and D is the diffusion coefficient (cm^2/s). The values of the diffusion coefficients at difference temperatures obtained (D_0 = initial diffusion coefficient) can then be represented as Equation 2.11 to interpret the energy of gas adsorption (kJ/mol).

$$D = D_0 \exp\left[-\frac{E_a}{RT}\right] \qquad (2.11)$$

A very small change in the molecule to pore sizes relationships would include very large changes in the diffusion coefficient. This is one of the fundamental effects that give rise to shape selectivity (Ribeiro *et al.*, 1995). The measurement of diffusion in zeolite has become a never-ending challenge to the research development (Kärger, 2003). The diffusion coefficient of zeolites depends on the specific adsorbate and zeolite system, the shape and size of adsorbate, the polarity of adsorbate, the concentration of adsorbate and the structural properties zeolite framework (Ruthven, 2001).

2.2.5 Gas adsorption mechanisms

2.2.5.1 Diffusion effects

In general, adsorption in zeolites occurs as micropore filling process, later at high pressures, surface coverage, consisting of monolayer and multilayer adsorption (Roque-Malherbe, 2000). Diffusion effect of adsorbate into the micropore of zeolite, surface interaction between the adsorbate and adsorbent, and adsorption at supercritical conditions (high pressure and high temperature) are important phenomena to understand the mechanisms of gas-zeolite adsorption.

Most of the adsorbents commercially used are porous particles. Diffusion effects control the mass transport of adsorbate into the adsorbent. Adsorbate molecules come from outside adsorbent particles and diffuse into the particle to fully utilize the adsorption sites. Depending on the structure of the adsorbent, several different types of diffusion mechanisms become dominant and sometimes two to three of them compete or cooperate. The dominant mechanism also depends on a combination of adsorbate and adsorbent and adsorption conditions such as temperature and concentration range. .

When bulk adsorbed molecules are mobile on the surface of the adsorbent, surface diffusion due to migration of the adsorbed molecules may contribute more than pore diffusion. However, when the size of an adsorbate molecule is close or smaller to the size of the micropore, diffusion of the molecule becomes restricted and the rate of transport in the micropore resulted a significant effect in the overall adsorption rate. This phenomenon is called micropore diffusion, which depends heavily on adsorbate properties (Suzuki, 1990). Micropore diffusion is very restricted because of the effect of potential field of the wall atoms. This case is accompanied by relatively large activation energy. Ordinary, diffusion coefficient is defined in terms of amount of gas adsorbed.

2.2.5.2 Surface interaction

Interactions between the adsorbed molecules on a metal oxide modified zeolite surface are of important phenomenon. Adsorbate-adsorbate interactions on the adsorbent surface are often important for the adsorption at high coverage (Mortensen *et al*., 1998). According to Llewellyn and Maurin (2005), an increase amount of gas adsorbed on an adsorbent leads to an increase of the interactions between the adsorbate molecules. The interaction of an adsorbate molecule will give a constant signal with an energetically homogenous surface. Meanwhile, for energetically heterogeneous adsorbent, relatively strong interactions between the adsorbing molecules and the surface happen initially. The strength of these interactions will then decreases as these specific sites are occupied as shown in Figure 2.5.

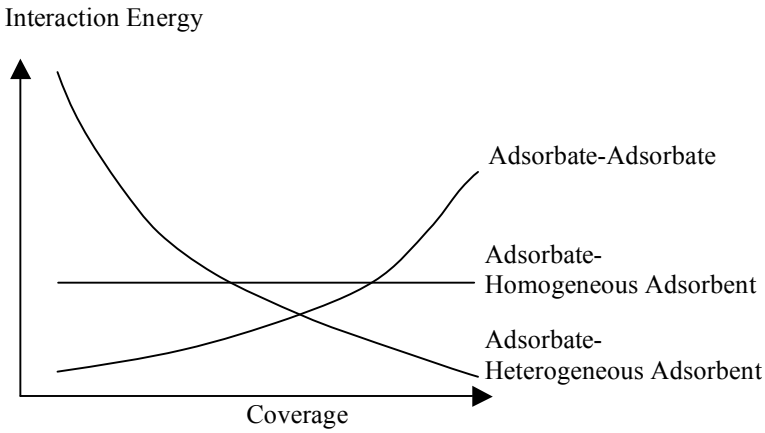

Figure 2.5: Interaction of energy of simple gases adsorption at low temperature (Llewellyn and Maurin, 2005).

Nevertheless, this interaction of energy described the gas adsorption at low temperature condition. The study that involved supercritical adsorption with temperature near or above the critical point is not yet clearly identified. The interaction energy of adsorbate on adsorbent surface is important to investigate for evaluating the gas adsorption characteristics of metal oxide modified zeolite.

Gas-zeolite surface interactions have been widely studied by means of transmission FTIR spectroscopy recently. It is an effective method to study adsorbed species interaction with zeolite directly. Small and non-polar gases such as O_2, N_2 and rare gases present very weak bases properties that they would interact with strong acid sites in zeolite (Ferwerda and Van der Maas, 1995; Sousa-Aguiar *et al*., 1998). Conversely, polar and acid gas as CO_2 will interact strongly with basic active sites of zeolite surface. These surface interaction mechanisms are responsible in the applications of zeolite as catalyst, adsorbent and nanoparticle technology materials. By examining the adsorption bands that attributed to particular gas molecules species and the band shifted energy that indicating the formation of bonding between the adsorbate and adsorbent, the behavior of each adsorbed species and their interaction with zeolite can be well characterized.

From Yamazaki *et al*. (2000) review, it reported the adsorption behavior of CH_4 and CO in the pores of Ω-zeolite at low pressure and low temperature conditions. Using the wave number shift from the gaseous position, the strength of the electric field on the cation site of zeolite can be estimated. The magnitude of the wavenumber shift is correlated with the strength of the electric field in the vicinity of the adsorption sites, E given by:

$$\Delta \nu\ (\mathrm{cm}^{-1}) = -6.14 \times 10^{-19}\ \mathrm{E}\ (\mathrm{Vm}^{-1})^2 \qquad (2.12)$$

It is known that the band intensity is proportional to the amount of adsorption on the cation sites as well as the square of the strength of electric field on the sites as:

$$S_1 = \left(\frac{\pi N_A}{3c^2}\right)\left(\frac{n_1}{2.303}\right)\left(\frac{\partial\alpha}{\partial Q_1}\right)^2 E^2 \qquad (2.13)$$

where N_A, n_1, c and $(\partial\alpha/\partial Q_1)$ are Avogadro's number, the amount of adsorption on the cation site, the velocity of light, and the first derivative of polarizability with the normal coordinate of vibration, respectively. Therefore, the amount of adsorption on the cationic site can be estimated from the strength of the electric field mentioned above and the integrated peak intensity (Yamazaki *et al*., 2000).

As we realized, many studies normally conducted the experimental works at very low temperatures and low pressure conditions (Ferwerda and Van der Maas, 1995; Wakabayashi *et al*., 1997; Sousa-Aguiar *et al*., 1998; Hadjiivanov *et al.* 2003), which the results are hardly represent the adsorption behavior of industrial significance in PSA. Thereinafter, Valyon *et al. (*2003) carried out the investigation on high-pressure gas adsorption at ambient temperatures to understand the zeolite structure and composition influence on the adsorption interaction of N_2 and O_2 with the adsorption sites of different types of zeolite.

On the other hand, for adsorption on metal oxide supports, Šljivančanin and Pasquarello (2004) investigated the adsorption of gas nitrogen on the iron nanocluster supported on magnesium oxide. Scarano *et al*. (2001) studied the adsorption of H_2, CO and gas CH_4 on zinc oxide. From the results obtained, MgO and ZnO support plays an important role in increasing the binding energy of the adsorbed species. The potential energy of adsorbed atoms is stabilized and enhanced by the interactions of adsorbates and between the adsorbates and the metal oxides support. Therefore, all these previous works reviewed that related on gas-zeolite surface interaction through FTIR measurement indicated a great potential to developed a novel good adsorbent by modifying zeolite with metal oxide that have not being investigated so far in detail.

2.2.5.3 Adsorption at supercritical conditions

High-pressure adsorption under equilibrium conditions when both pressure and temperature are higher than the critical is sometimes referred as supercritical condition (Zhou and Zhou, 1998; Fu and Zhu, 2003). Determination of adsorption isotherms behavior over high temperature and high pressure will benefit the development of industrial application of gas adsorption in fuel storage or pressure swing adsorption separation and purification processes. However, the physical picture for such supercritical adsorption mechanisms has not been clearly depicted and, hence, certain theoretical difficulties have not been overcome in modeling the isotherms.

At high pressure, the total amount of gas contained in the micropore tends toward a limit called the saturation capacity, while the density in the gas phase increases without limit. Eventually, when the density in the gas phase increases with pressure at the same rate as the absolute density in the pores, the excess adsorption passes through a maximum and then begins to decline with pressure (Myers, 2002). This unusual behavior can be explained by Ono-Kondo equation. There will be no condensation occurred for any pressure, for example, gas methane adsorption at 293 K on activated carbon since the critical temperature of methane is at 190.6 K. The amount of gas adsorption will decrease after the maximum adsorption is achieved by further pressure increment (Aranovich and Donohue, 1995).

Monolayer adsorption mechanism was assumed for the components at above-critical temperatures, and multilayer adsorption mechanism was assumed for the components at sub-critical temperatures. This assumption was obeyed to a classical law of physics that gas cannot be liquefied at above-critical temperatures no matter how high-pressure applied; the subsequent layers obviously cannot exist at supercritical gas adsorption. Furthermore, the heat of adsorption will drop to the latent heat of condensation in the subsequent layers.

The physical state of the adsorbed phase that showed in Figure 2.6 is based on a simple rule: vapor is adhesive, but supercritical gases are not. Generally, the adsorption mechanisms must experience a transition from multilayer coverage or volume filling at subcritical temperatures to monolayer coverage at above critical temperatures (Zhou *et al*., 2002; Zhou *et al*., 2005). On the other part, the effect of the surface area of adsorbents on adsorption capacity of CO_2 becomes less important when increasing the adsorption temperature. This indicates that adsorption mechanism of CO_2 at high temperature is not completely physical adsorption (Yong *et al*., 2002). Several peaks corresponding to the carbonate species appear in the region of 1200 – 1700 cm^{-1} from FTIR spectra of pure CO_2 adsorption at 295 K as investigated by Rege and Yang (2001).

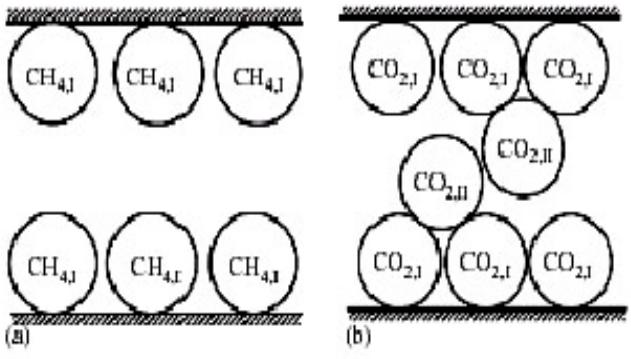

Figure 2.6: The adsorbed state of pure CH_4 and CO_2 in micropores at 298 K (Zhou *et al*., 2005).

Several studies related to supercritical adsorption have been carried out. Ustinov *et al*. (2002) had suggested a new approach for analyzing adsorption of supercritical gases (Ar, N_2, CH_4, C_2H_4, CO_2 and He) at high-pressure range from 0 to 50 MPa on activated carbon at 25 – 70 ^{0}C by gravimetric measurements method. Li *et al*. (2003) proposed an optimization procedure to evaluate the adsorbate density directly from supercritical adsorption isotherms of methane on activated carbon (283 – 323 K) from 0 to 14 MPa. Meanwhile, Li and Gu (2004) applied the adsorption potential theory to predict the adsorption equilibria of supercritical N_2 and CH_4 on activated carbon. High-pressure data on CH_4, N_2, Ar and CO_2 on activated carbon also being investigated by Dreisbach *et al*. (1999) and Herbst and Harting (2002).

Generally, most of the supercritical gas adsorption studies reported so far were conducted on activated carbon. There is not yet any unambiguous way showing the isotherm and supercritical adsorption characteristics of zeolite and metal oxide modified zeolite adsorbent so far. Since we do not know the adsorption behavior of a particular adsorbate on metal oxide modified zeolite under high pressures, neither do we can have any sophisticated theory for their application in high-pressure adsorption conditions.

Thereinafter, by investigating single component gas adsorption on zeolite as well as metal oxide modified zeolite, the fundamental basis and the parameters evaluated from the single component adsorption data were then crucial to use for modeling the new isotherms of single component and multicomponent adsorption model in the gas mixtures separation and purification applications.

2.2.6 High pressure adsorption

High pressure adsorption plays an important role in the industries, application that involve high pressure adsorption are hydrogen storage, separation process, and adsorbed natural gas. Hydrogen storage is a technology for the advancement of fuel cell power systems in transportation, stationary, and portable applications. In absorptive hydrogen storage, hydrogen is absorbed directly into the bulk of the material, these material are adsorbent such as activated carbon and zeolilte. Another technology that has connection with hydrogen storage and high pressure adsorption is adsorbed natural gas. Adsorbed natural gas where methane gas is stored in microporous adsorbent such as activated carbon to pressure 500 psi and discharge when needed to atmospheric pressure is an alternative to compressed natural gas (CNG). This technology that applies high pressure adsorption is much safer and economical compare to CNG.

Other than that, high pressure adsorption also plays a vital role in gas separation processes. Different gases have different molecular weight, and according to Burchell and Rogers (2000), adsorbent prefer to adsorb heavier hydrocarbon. However, according to research done by Busch *et al* (2003), they found that different gases will adsorb more at certain pressure. Pressure swing adsorption (PSA) is a technology that is used to separate some species from a gas, preferentially adsorbing the undesired gases at high pressure. The process then swings to low pressure to desorb the adsorbent material. PSA is used for separation of carbon dioxide from methane, purification of oxygen or nitrogen from air etc.

Gas storage by adsorption is to use the micropores in the adsorbent material to enhance the density of the stored gas. The amount adsorbed increases with increasing storage pressure. If the storage pressure is higher than P_c, then compression is better than adsorption. However, at lower pressures, adsorption is better than compression and the introduction of adsorbent can markedly improve the capacity. The total gas maintained in the container can be classified into free gas and fixed gas. Assume V_t is the total volume of the container, it must be the sum of (Zhou *et al*., 2005):

$$V_t = V_c + V_v \tag{2.14}$$

where V_c is the volume occupied by the skeleton carbon and V_v is the volume of void space. The stored gas in the void space is called free gas and the quantity of free gas per unit mass of adsorbent, n_f can be calculated using the equation 2.3.

$$n_f = PV_v / zRT \tag{2.15}$$

Where z is the compressibility factor and can be determined uses various equations of state such as virial, Redlich-Kwong and Peng-Robinson equation. The void volume, V_v can be known by using helium expansion method (Keller *et al*., 1998).

Other equation that also represent the total volume V_t associated with adsorbent and container is from Vasilliev and co-workers. According to them, the total volume can be split up into its components:

$$V_t = V_c + V_\mu + V_v + V_{void} \qquad (2.16)$$

V_c is the volume of atoms which the adsorbent composed; V_μ micropore volume; V_v meso- and macropore volume; V_{void} the space inside the vessel free from adsorbent bed. V_{void} can be eliminated by making the solid block of adsorbent (compressed with binder) (Vasilliev *et al*., 2000). Figure 2.7 shows the adsorption vessel of volume $V^* = V_t$.

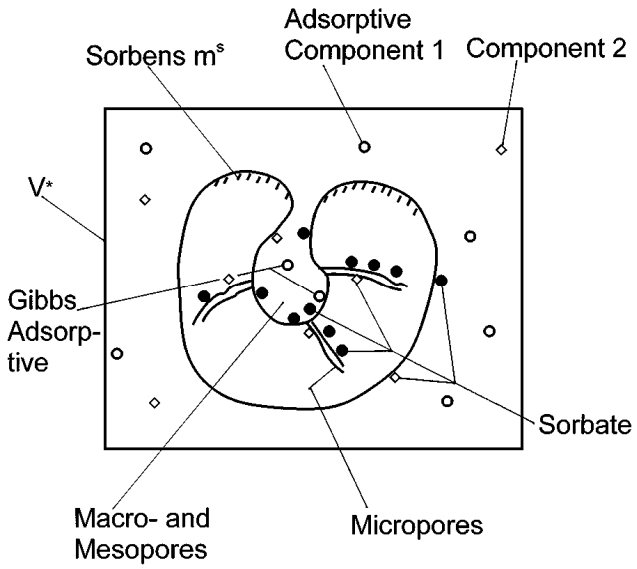

Figure 2.7: Adsorption vessel of volume V^* including porous sorbent mass m^s (Keller *et al*., 1998)

Volumetric and gravimetric capacities are two capacities that are commonly used. Volumetric capacity is defined as the amount of gas adsorbed either in mass or in volume divided by the total volume occupied by the adsorbent and the adsorbed gas, in this case the volume of the container. Because the gas is adsorbed in the solid, the volume of the adsorbent can be regarded as the total volume provide it fill up the entire container. For the ease of comparison, the volume of the adsorbed gas is commonly converted to the volume at a reference point. The standard temperature

and pressure (STP, 1 bar and 15° C) is taken as the reference point. So the volumetric storage capacity is defined as:

V = (volume of adsorbed gas converted to STP) / (volume of solid adsorbent)

A study done by Zhang *et al*. (2004) to determine the uptake of hydrogen in carbonaceous materials using volumetric method had been performed in 2004. The schematic diagram of the volumetric apparatus is shown in Figure 2.8. The principle of the volumetric measurement method could be concisely described as:

$$n(P, T) = n(P_0, T) + n(P_1, T, V_{rc}) + n(P_2, T, V_{sc}) - n(P, T, V_{rc}) - n(P, T, V_{sc}) \quad (2.17)$$

where P is the pressure when adsorption reaches equilibrium after the valve bv6 is opened. P_1 and P_2 are respectively the initial pressures in the reference cell and the sample cell when valve bv6 is closed. V_{re} and V_{se} are respectively the volume of the reference cell and the residual volume of the reference cell.

Zhang and co-workers (2004) applied the step-by-step method to measure adsorption isotherm. The pressure was changed step-by-step and the amount of adsorption was summed up at each step. P_0 is the pressure corresponding to the last adsorption equilibrium and T is the temperature of adsorption. While n (P; T) is the cumulative adsorption amount at pressure P and $n(P_0; T)$ is the cumulative adsorption amount at last equilibration pressure P_0. $n(P_1; T; V_{rc})$ and $n(P_2; T; V_{sc})$ are, the initial bulk gas amount in the referenced cell at pressure P_1 and in the sample cell at pressure P_2 respectively. $n(P; T; V_{rc})$ and $n(P; T; V_{sc})$ are the bulk gas amount in the referenced cell and in the sample cell at the equilibration pressure P, respectively. By using helium, the remaining volume of the sample cell is determined but with one assumption, helium adsorption amount at room temperature is zero (Zhang et al., 2004).

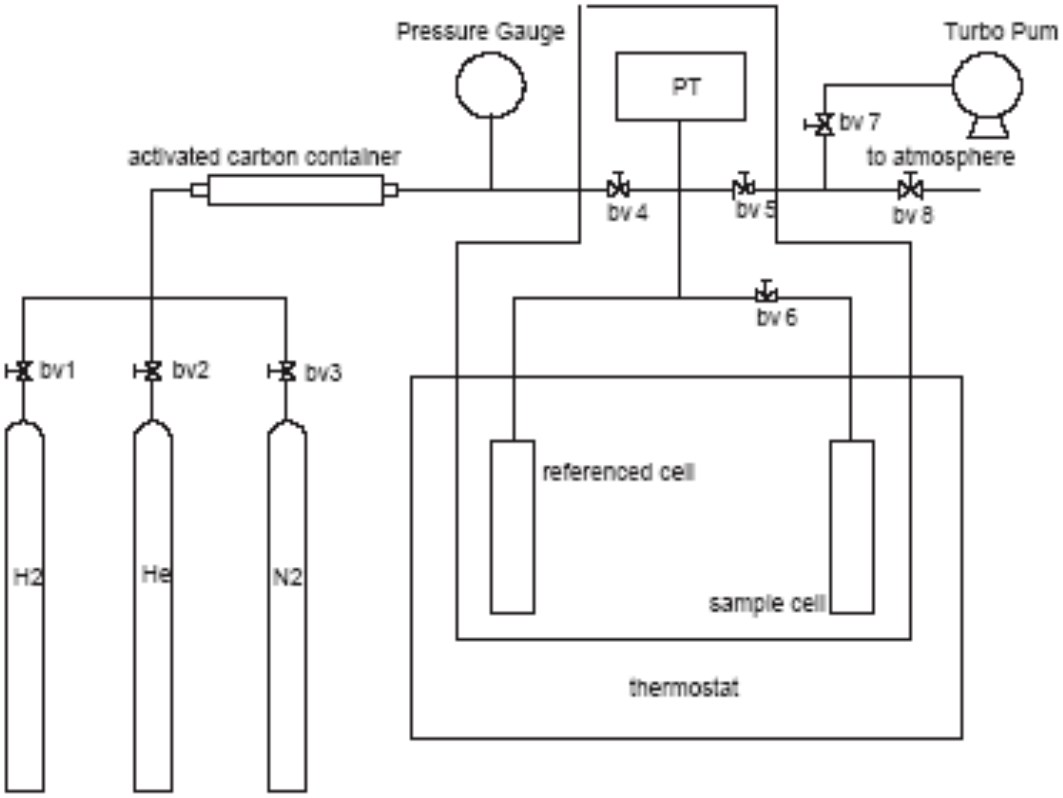

Figure 2.8: Schematic diagrams of the volumetric apparatus (Zhang *et al*., 2004)

Besides Zhang and co-workers (2004), Belmabkhout *et al*. (2003) also performed volumetric experiment to measure high pressure adsorption. Volumetric method consists of expanding a gas from a pressure cell into an evacuated adsorption cell containing a clean adsorbent during an isothermal process (Belmabkhout *et al*., 2003). The volumes of both cells are known (V_{prc} and V_{ads}). Each measurement of the total quantity of gas admitted into the system V_{prc}(n1) and the amount of gas remaining in the gas phase ($V_{prc} + V_{ads}$) at the adsorption equilibrium (n2) was determined by P-V-T measurements before and after adsorption (P1, P2, T1 = T2) using a real gas equation of state. The amount adsorbed is calculated based on mass balance. Equations involve are:

$$n_1 = \frac{V_{prc}}{v_a(T_1, P_1)} \tag{2.18}$$

$$n2 = \frac{V_{prc} + V_{ads}}{v_a(T_2, P_2)} \tag{2.19}$$

$$n_{ads} = \frac{n1 - n2}{m_{sample}} \tag{2.20}$$

where,

n1 = adsorbate mole number in the pressure cell before adsorption

n2 = adsorbate mole number remaining in the gas phase after adsorption

T_1 = T_2, experimental temperature

P_1 = pressure in the pressure cell before adsorption

P_2 = equilibrium pressure in both pressure cell and adsorption cell

V_{prc} = volume of the pressure cell

V_{ads} = volume of the adsorption cell (volume of adsorbent is not included)

v_a = molar volume of the adsorbate in gas phase at T and P

n_{ads} = adsorbed mole number per unit of mass of the adsorbent

m_{sample} = mass of the outgassed adsorbent

The significant disadvantage of the volumetric method is the gas tightness and the inherent errors due to the indirect determination of the adsorbed quantities, which may considerably influence the accuracy of the measurements (Belmabkhout et al., 2003). Figure 2.9 shows the general principle of the volumetric apparatus.

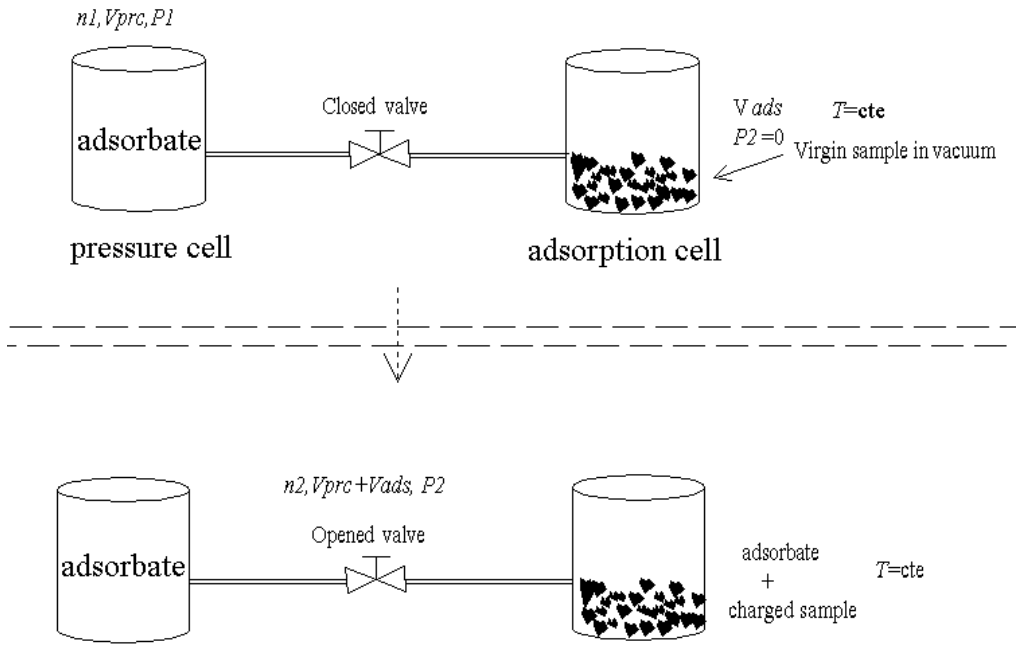

Figure 2.9: General principle of the volumetric apparatus (Belmabkhout *et al.*, 2003)

Alternatively to the volumetric method is the gravimetric method. It mainly consists of a microbalance to see the changes of the mass of the adsorption container. The main advantage of the gravimetric method compared to volumetric method is that it only needs a small amount of sorbent material; a high sensitive microbalance is required (Keller et al., 1999). The gravimetric capacities are often defined as the weight percentage of the adsorbed gas to the total weight of the system, including the weight of the gas:

V = (weight of adsorbed gas) / (weight of solid adsorbent + adsorbed gas) (2.21)

For methane, a variety of equations of state are available describing the volumetric behaviour of this gas with good precision. The most commonly applied EOS are Peng-Robinson and Redlich-Kwong (Krooss *et al*., 2002). Zhou and Zhou (2001) had selected two equations of state, Soave-Redlich Kwong (SRK) and Benenedict-Webb-Rubin (BWR) in the adsorption storage study. SRK is a good

trade-off between precision and tediousness of calculation and is widely applied in petrochemical processing computations. BWR contain eight parameters and is recommended especially for hydrogen (Zhou and Zhou, 2001).

The SRK equation relates the compressibility factor and the fugacity coefficient as follows:

$$\ln\frac{f}{P} = z - 1 - \ln(z - B^*) - \frac{A^*}{B^*}\ln(1 + \frac{B^*}{z}) \qquad (2.22)$$

where,

$\Phi \quad = f / \mathrm{P}$

$A^* \quad = 0.428 \times \alpha \times \frac{P/P_c}{T/T_c}$

$B^* \quad = 0.0867 \times \frac{P/P_c}{T/T_c}$

$\alpha^{0.5} \quad = 1 + \mathrm{m}(1 - \mathrm{T_r}^{0.5})$

$\mathrm{m} \quad = 0.480 + 1.574\mathrm{w} - 0.176\mathrm{w}^2$

The BWR equation contain eight parameters, it is suitable to use at above critical temperatures and not very high pressures.

$$\mathrm{P} \quad = RT\rho + (B_oRT - A_o - \frac{C_o}{T^2})\rho^2 + (bRT - a)\rho^3 + a\alpha\rho^6$$

$$+ \frac{c\rho^3}{T^2}[(1 + \gamma\rho^2)\exp(-\gamma\rho^2)] \qquad (2.23)$$

ρ is the density of gas, which relates to the compressibility factor by

$$\mathrm{z} \quad = 1 + (B_o - \frac{A_o}{RT} - \frac{C_o}{RT^3})\rho + (b - \frac{a}{RT})\rho^2 + \frac{a\alpha}{RT})\rho^2 + \frac{a\alpha}{RT}\rho^5$$

$$+ \frac{c\rho^2}{RT^3}[(1+\gamma\rho^2)\exp(-\gamma\rho^2)] \qquad (2.24)$$

BWR is a dimensional equation where P is in atm, T in K, ρ in mol/l or kmol/m^3, R = 0.08205 atm l/ mol K. The eight parameters are not the same for all type of gases. Comparison between SRK and BWR for the z values calculated with equation of state with those evaluated from the experiment P-V-T data for hydrogen was done. The root mean square of the deviations between the two kinds of z is shown in Figure 2.10. Result shows that BWR seems to be more precise than SRK. However, the BWR are limited to 273K and higher. That is why, value for z at 253K and below is not calculated. The SRK equation only gives a 1% deviation at temperature as low as 113K. This shows that SRK equation can be used in a wider range of temperature.

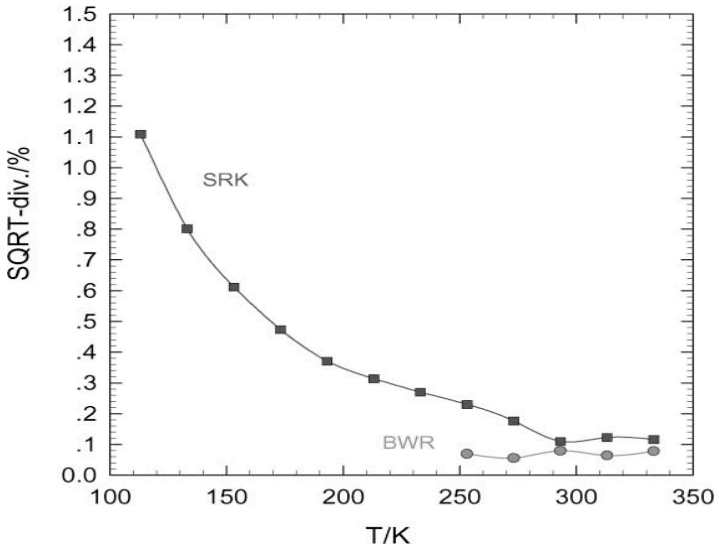

Figure 2.10: The square root mean deviations of z-values from the equations of state to that from the experimental data (Zhou and Zhou, 2001)

Another study to determine which equation of state is better was also performed by Zhang and co-workers (2004). They used three different equations which are SRK, ideal gas equation and Modified-Benedict-Webb-Rubin (MBWR) equation to calculate the volume of a cell (Figure 2.11). This empty cell volume is known which is 25 ml, so the volume of the empty sample cell should be

independent of the pressure and keep unchanged. However, after experiment had been done using helium, result shows that ideal gas equation and SRK equation are dependent on pressure. Only the MBWR equation is independent of the pressure and closes to the real value of the empty sample cell.

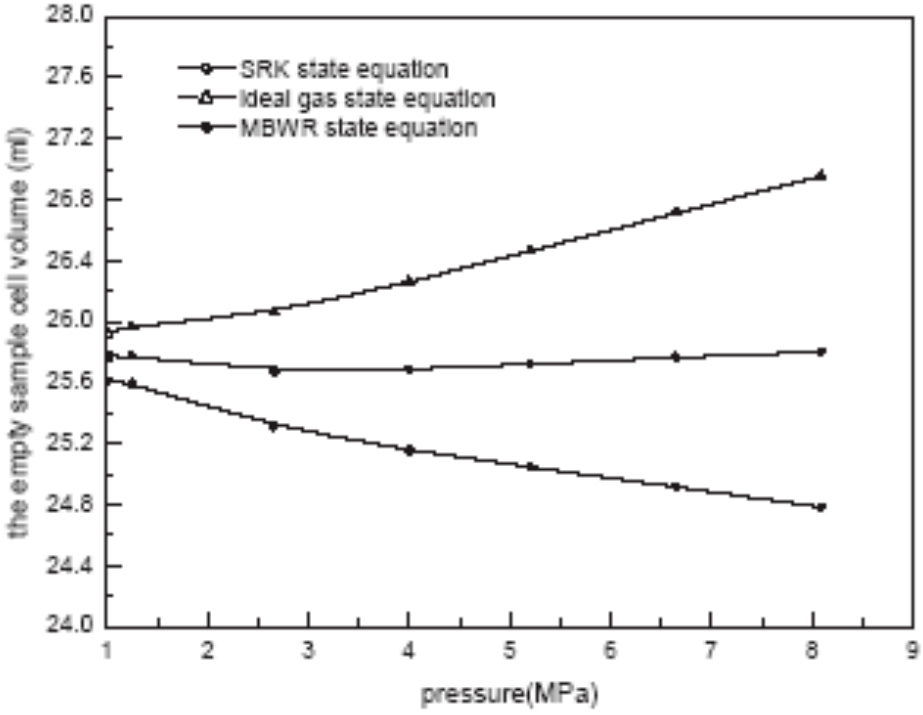

Figure 2.11: The calculated empty cell volume (Zhang *et al*., 2004)

In general, porous adsorbents have different structures and sizes that perform differently to different type of gas. Factors like micropore volume, size distribution, packing density and properties of adsorbent and adsorbate have to be taken into account when selecting adsorbent for adsorption application. Volumetric and gravimetric capacities are two capacities that are commonly used in discussion of adsorption capacity while Benedict-Webb-Rubin and Soave Redlich-Kwong equations of state are commonly used to describe the volumetric behaviors of gas stored.

2.3 Potential Applications of Silica Based Adsorbents

Zeolite microporous adsorbent industry is a mature industry with a wide variety of products satisfying the requirements of well-established applications. The expanded applicability of environmental regulations, along with improving living standards around the world, are stimulating significant increases in demand for these products. The modification of metal oxide-zeolite opens a new route and widens their applications range from high-end catalyst in chemical and petroleum industry, adsorbents to sensor and semiconductor support in nanoparticle technology.

The most important application of zeolite is as catalysts (Kanazirev and Price, 1994; Neyestanaki *et al*., 1995; Alkhawaldeh *et al*., 2003; Gheno *et al*., 2003). Metal oxide modified zeolite will tailor the pore sizes and increase the shape selectivity results from the limited diffusivity of some of the reactants, which cannot effectively diffuse inside the channel system. For those slowly diffusing molecules in the channel cannot rapidly escape from crystal will undergo secondary reactions. Metal oxide modified zeolites were also being applied as inorganic catalysts in the oxidation, reformation, photochemical reaction, reduction and combustion processes (Yoshida *et al*., 2000; Bi and Lu, 2003; Dutta and Vaidyalingam, 2003; Masteri-Farahani *et al*., 2003; Watanabe *et al*., 2003; Liu *et al*., 2004) as well as functioning as biocatalyst for enzymes immobilization reaction (Zhao, 1998; Zhao *et al*., 2003). These modified catalysts improve yield, cost-efficiency and environmental control.

In addition, zeolites are selective, high capacity adsorbents because of their high intracrystalline surface area and strong interactions with adsorbates. Molecules are separated base on the size, diffusivity and structure relative to the size and geometry of the apertures of the sieve. Zeolite mostly adsorbs molecules with a permanent dipole moment. Different polar molecules have a different interaction with the zeolite framework (Ćurković *et al*., 1997). Through metal oxide modification, the hydrophobicity and acidity properties of zeolite framework would

be regulated to suit for a particular adsorbate. Metal oxide modified zeolites also can be used as adsorbents and ion exchangers for environmental demands (Hernández-Huesca *et al*., 1999; Li *et al*., 2000).

Meanwhile, in the gas separation and purification processes, the modified zeolite adsorbents can play a very important role in petroleum refining processes, natural gas treating, industrial gas production and purification through pressure swing adsorption process (Sherman, 1999; Jiang *et al*., 2002). Recently, Polychronopoulos *et al.* (2005) reported the novel ZnO and TiO based mixed metal oxide sample for low temperature adsorption of H_2S from industrial gas streams. Cerium modified ZSM-5 zeolite reported having the good ability as NO gas adsorbent (Salama *et al*., 2005).

Moreover, the high heat of zeolite adsorption and ability to hydrate and dehydrate while maintaining structural stability has been found to be useful in various heat storage and solar refrigeration systems (Frost and Sullivan, 2001). Gas on solid adsorption is an inherently safe and potential high energy density gas storage method that could be more energy efficient than chemical or compressed gas storage. Consequently, as an alternative, encapsulation of gas in microporous media could be envisaged (Nishimiya *et al*., 2001). Reversible occlusion of gases in zeolites is a well-known phenomenon. The working principle is that the guest molecules are forced, under elevated temperatures and pressures, into the cavities of the zeolite host. Upon cooling to room temperature or below, gas is trapped inside the cavities. It can be released again by raising the temperature. Thereinafter, with the increase of zeolite stability by metal oxide dispersion, gas storage capacity or amount of encapsulated gas is further optimized (Weikamp, 1996; Nishimiya *et al*., 2001; Njikamp *et al*., 2001).

In nanoparticle technology, transition metal oxides are well-known base materials that most widely used for nanoparticles sensors due to their electrical conductivity properties (Pohle *et al*., 2001; Ponce *et al*., 2004). They have been

adopted as model systems for fundamental studies and as parent materials for the development of various sensors for the detection of gases such as H_2, CO, NO_x, CO_2, CH_4 and other hydrocarbons (Akbar and Dutta, 1999; Remillard, 1999; Hotovy *et al*., 2002; Wöllenstein *et al*., 2003; Korotcenkov *et al*., 2004). Moreover, some solid oxides were used in the application as material for fuel cells as well (Özkan and Özçelik, 2005). Therefore, the dispersion of these metal oxides onto zeolite system with high gas adsorption capability would enhance both their applications as gas sensor materials (Szabo, 2003). Furthermore, CeO_2 and NiO also were reported as good conductors when coated on the YBCO surface (Kim *et al*., 2003).

In addition, the discovery of the first ordered (where the pores are ordered periodically), mesoporous molecular sieves also have sparked interest throughout the scientific community. These materials have attracted the attention of chemists and materials scientists due to commercial interest in their application in chemical separations and heterogeneous catalysis as well as scientific interest in the challenges posed by their synthesis, processing, and characterization. Application of basic scientific principles to the key technological issues involved has been difficult, however, and much more progress has been achieved in tailoring porous materials through manipulation of processing parameters than through understanding of the chemical and physical mechanisms that influence porosity. As a result, the tailoring of porous materials has proceeded largely in an empirical fashion rather than by design (Barton *et al*., 1999).

As summary, zeolites and other porous materials have a direct impact in many aspects of people's live. The many benefits achieved from the applications of zeolites and other molecular sieves are the fruits of the basic investments made decade ago, and into the present, in many research areas on their structure and property modification, keep on improving zeolite adsorptive characteristics, functionalities and their applications. The basic concepts and understanding from these efforts, coupled with creative considerations of how the properties and functionalities so discovered might be of service to solve the needs of mankind, continue to create new benefits.

2.4 Summary

Zeolite microporous materials are involved in a large domain of chemical science and technology including catalytic and adsorption processes, gas storage, ion exchange and nanoparticles technology. The combination of many properties among different types of zeolite such as microporous molecular dimension and uniform pore system, high internal surface area, the ion exchange properties, high thermal stability and ability to tailor the framework and acidity properties make zeolites special and unique among inorganic oxide materials. Much research efforts performed both experimentally and theoretically have been thus focused on this class of materials. The review has outlined the great possibilities and importance of metal oxide modified zeolite as gas adsorbent in a number of applications. Indeed, the modified zeolite offer great possibilities for investigating their adsorption properties as a function of many parameters such as size and shape of pores, chemical composition of framework, polarity as well as hydrophobicity properties after the modification. Apart from that, the fundamental studies of gas adsorption characteristics on zeolite-based adsorbents also enable researchers to gain a greater understanding of the equilibrium, kinetic transport and mechanisms in play during gas adsorption phenomena at subcritical and supercritical conditions.

CHAPTER 3

MATERIALS AND METHODS

3.1 Introduction

In order to achieve the underlined objectives and scopes of study as presented in Chapter I, the materials used, experimental and analytical procedures for this research are discussed in this Chapter. The materials used including general chemicals; zeolite Na-Y, metal oxides, metal nitrates and gases were presented. The experimental procedures for samples preparation via cation exchange method, thermal dispersion and incipient wetness impregnation method were discussed in detail. Meanwhile, the gases (N_2, CO_2, and CH_4) adsorption characteristics and gas-solid interaction on pure and modified zeolites adsorbents were measured using Thermogravimetric Analyzer (TGA) and Fourier Transform Infrared (FTIR) spectroscopy, respectively. Furthermore, analytical procedures for samples structural characterization were measured using X-Ray Diffractometer (XRD) and Fourier Transform Infrared (FTIR) spectroscopy; physical properties characterization using Micromeritics ASAP 2000 as well as morphological characterization using Scanning Electron Microscope (SEM) were also discussed extensively. The flow of research methodology is summarized in the flowchart as shown in Figure 3.1.

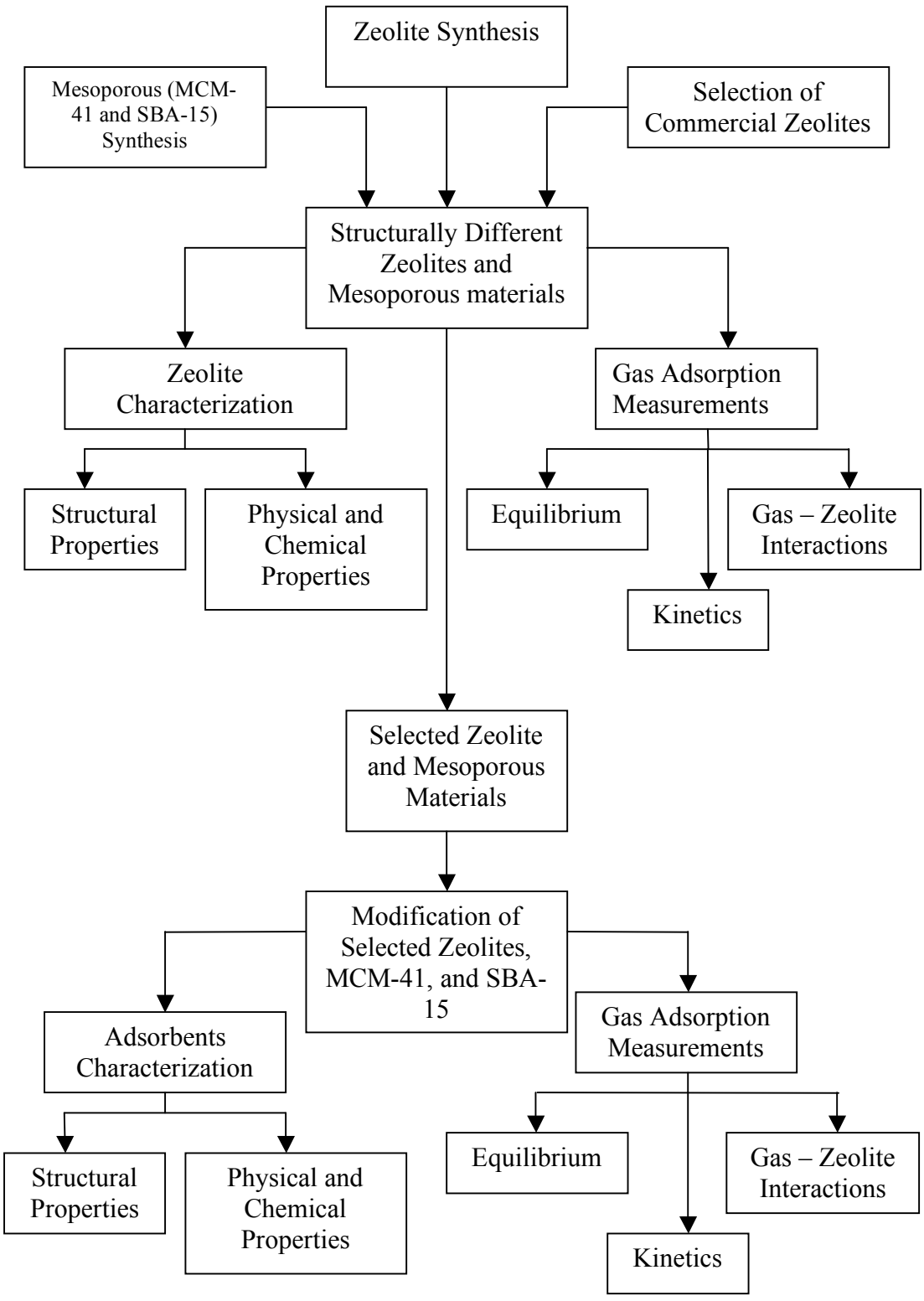

Figure 3.1: A flow diagram of experimental procedures used in the study.

3.2 Materials

3.2.1 General chemicals

Aqueous solution of metal nitrates were prepared using freshly deionised water from Purite Select AN HP40 (Purite Ltd, England) with resistivity ~15 – 16 MΩ cm. All the glassware, mortar and evaporating disks used was thoroughly washed and rinsed with deionised water as well before drying in oven. Meanwhile, the potassium bromide (KBr) used for Fourier Transform Infrared (FTIR) spectroscopy characterization was purchased from Buck Scientific (P/N 5231, CT 06855). Chemicals used for synthesizing and modifying zeolite are NaOH, calcium nitrate tetrahydrate, magnesium nitrate hexahydrate, and zink nitrate tetrahydrate (MERCK), sodium aluminate anhydrous (Riedel-de Haën), colloidal silica-(Aldrich Chemical), and lithium nitrate, rubidium nitrate, barium nitrate and, nickel (II) nitrate hexahydrate (Fluka Chemika) and were used as received.

Other chemicals includes V_2O_5 (99.6+%, Fisher Chemicals), MoO_3 (99.5%, Merck), Co_3O_4 (72.5% Cobalt, Aldrich), WO_3 (99.995%, Acros Organics), PdO (86.8-87.1% Pd, Acros Organics), CuO (99.999%, Acros Organics), Cu_2O (97%, Acros Organics), Ag_2O (99%, Acros Organics), HgO (99%, Acros Organics), GeO_2 (99.999%, Acros Organics), SnO (99%, Acros Organics), PbO (99%, Merck) MgO (99.99%, Acros Organics), CaO (96%, Acros Organics), Y_2O_3 (99.99%, Acros Organics), Fe_2O_3 (99.999%, Acros Organics), NiO (97%, Acros Organics), ZnO (>99.5%, Fisher Chemicals), and Ga_2O_3 (99.99+%, Acros Organics) were tentatively selected as guest materials to modify zeolite NaY in sample preparation via thermal monolayer dispersion method.

For the synthesis of MCM-41 and SBA-15, chemicals used include Cetyltrimethylammonium Bromide (CTAB) and Pluronic P123 ($PEO_{20}PPO_{70}PEO_{20}$)

as surfactants, Tetraethyl Orthosilicate (TEOS) as silica precursor, and NH_4OH and HCl as mineralizing agents. The modifications involves several types of amine; polyethylimine (PEI), methyl diethanolamine (MDEA), triethanolamine (TEA), diethanolamine (DEA), and monoethanolamine (MEA).

3.2.2 Zeolites

In order to examine the potential use of zeolite as gas adsorbent, commercially available synthetic zeolites were purchased from Aldrich Chemical (NaX) and Zeolyst International (NaY, ZSM-5, mordenite, ferrierite, and zeolite beta). In addition, synthetic zeolite belong to faujasite structural framework group was synthesized with different Si/Al ratio. Zeolite Y (Si/Al = 2.88) and zeolite X (Si/Al = 1.0) was selected and used as support or parent material in the modification procedures. These material were chosen by virtue of its importance as adsorbents in the adsorption processes (Huber and Knözinger, 1995; Kusakabe *et al*., 1998; Hasegawa *et al.,* 2001; Mizukami *et al*., 2001; Hadjiivanov *et al*., 2002; Harlick and Tezel, 2004) and catalytic reaction (Dutta and Vaidyalingam, 2003; Gheno *et al*., 2003; Masteri-Farahani, 2003; Liu *et al*., 2004).

3.2.3 Gases

Linde Gas Singapore PTE LTD supplied all gases used in this study. The specifications on the gases were as follow: Carbon dioxide (high purity grade, 99.995%), nitrogen (high purity grade, 99.995%) and methane (high purity grade, 99.995%).

3.3 Synthesis and Modification Procedures

3.3.1 Zeolite synthesis procedures

Zeolites were synthesized from a wide range of batch composition and temperatures from a variety of alumina and silica sources. It involves a few elementary steps, which convert a mixture of Si and Al species, metal cations, and water via an alkaline supersaturated solution into a microporous crystalline aluminosilicate (Barrer, 1982). In this study, sodium form of zeolite (Na-SZ18) was synthesized using reactant mixture with molar composition of $6.4Na_2O$: $1Al_2O_3$: $8SiO_2$: $180H_2O$, at a crystallization temperature of 373 K and crystallization time of 24 hours. In preparing gel composition, sodium aluminate anhydrous was added into sodium hydroxide solution and heated under rigorous stirring until dissolved. Colloidal silica was added into sodium hydroxide solution and heated under rigorous stirring until clear solution appeared. Both solutions were mixed and stirred for 2 hours to obtain a homogeneous mixture. The mixture was then transferred into a polyethylene bottle and heated in an oven at 373K for 24 hours to allow crystallization to occur. The crystallized solids obtained were recovered by filtration, washed with distilled water until pH <10, followed by drying overnight in the oven at 100^oC.

3.3.2 Mesoporous silica synthesis procedures

Many preparation methods have been developed by researchers for the synthesis of mesoporous MCM-41 and SBA-15 (Beck and Vartuli, 1996; Weitkamp, 2000; Bennadja et al., 2001; Fulvio et al., 2005; Katiyar et al., 2006). MCM-41

sample was synthesized by dissolving 2.4 g CTAB in 120 g deionised water and the solution was stirred to form homogeneous and clear solution. Then, 8ml ammonium hydroxide was added into the solution and stirred for 5 min after which 10ml of TEOS was added into the solution. The solution was stirred overnight. Then, the solution was transfer into a container and put in oven at 100ºC for 2 days. After that, pH control is done at 10.2 each day until stable (2-3 days). The final product was filtered and washed with deionised water. Then, the sample was spread onto a plate and dried in oven at 100ºC for 24 hours. Calcination is performed at 550 ^{0}C for 5 hours (Kumar *et al*., 2001; Xu *et al*., 2003; Hadi Nur *et al*., 2004; Vartuli *et al*., 2001; Zhao *et al*., 1996).

Meanwhile, SBA-15 was prepared using 4.0 g of Pluronic P123 dissolved in 30 ml of deionised water. Then, 120ml of 2.0 M HCl was added into the solution and stir at room temperature for 2 hours. The resulting solution was then transfer into a container and stirred at 40ºC. After that, 8.5g of TEOS was added drop by drop into the solution while stirring for 30 minutes. Then, slow down the stirring rate to around 120 rpm and stirred for another 20 hours at the same temperature. After that, ageing of the solution was done in an oven at 100ºC for 48 hours without stirring. The final product was filtered, washed with deionised water and dried for 24 hours at 80ºC. Finally, the calcination was carried at 550ºC for 5 hours under flowing air (Klimova *et al*., 2006; Fulvio *et al*., 2005; Mirji *et al*., 2006; Luan *et al*., 2005; Srivastava *et al*., 2006; Andreza and Edesia, 2005).

3.3.3 Zeolite modification procedures

Modification means that a given material is manipulated by appropriate treatment in order to change its properties. In this study, cation exchange method, thermal dispersion technique, and incipient wetness inpregnation techniques were

performed in order to obtain various form of modified zeolites. According to Kurama *et al*. (2002) the fine tuning of zeolite properties can be achieved by variation of the cation type which is located at preferred sites within the framework of the zeolites. At the same time cation exchange may also produce some remarkable change in zeolite properties, such as thermal stability, pore size and catalytic activity (Li *et al.,* 2000).

3.3.3.1 Cation Exchange technique

Synthesized zeolite (Na-SZ18) is used as a based zeolite for modification of zeolite using cation exchanged method. The process is carried out using batch method. 5 g of finely ground zeolite is dispersed in 250 mL of 0.5 M $LiNO_3$ solution. The suspension is stirred and heated at 80^o C for 5 hours, and the exchanged zeolite is filtered, dried in the oven at 105^o C for 12 hours, kept equilibrated under constant humidity in a desiccator filled with saturated ammonium nitrate. The same procedure is repeated with other cation listed in Table 3.1. Again, characterization is carried out to determine the changes in structural, physical and chemical properties of the exchanged zeolites.

Table 3.1: The cations used and products obtained from metal cation exchange method.

Types of cation	Source of cation	Sample code
Li^+	$LiNO_3$	LiNa-SZ18
K^+	KNO_3	KNa-SZ18
Rb^+	$RbNO_3$	RbNa-SZ18
Mg^{2+}	$Mg(NO_3)_2.6H_2O$	MgNa-SZ18
Ca^{2+}	$Ca(NO_3)_2.4H_2O$	CaNa-SZ18
Ba^{2+}	$Ba(NO_3)_2$	BaNa-SZ18
Mn^{2+}	$Mn(NO_3)_2.4H_2O$	MnNa-SZ18
Ni^{2+}	$Ni(NO_3)_2.6H_2O$	NiNa-SZ18
Zn^{2+}	$Zn(NO_3)_2.4H_2O$	ZnNa-SZ18

3.3.3.2 Thermal dispersion technique

Thermal dispersion involves heating the finely divided powders of metal oxide and zeolite Na-Y at a temperature between the Tammann temperature and melting point of the metal oxide. Zeolite Na-Y (Si/Al = 2.88, surface area of 820 m^2/g) was calcined at 773.15 K for 3 hours before use. Then, calcined zeolite Na-Y was extensively mixed in a mortar with powdered metal oxide for 20 minutes at a predetermined ratio corresponding to up to 5 metal oxides per unit cell zeolite Na-Y (290 μmol metal oxide/g adsorbent). The amount of metal oxide and zeolite Na-Y used were weighed carefully using the Precisa 205 ASCS (Precisa Instruments AG, CH-Dietikon) balance with accuracy ± 0.0001 g. The resulting mixture was sieved to particle sizes of 300 μm and consecutive calcined at elevated temperature with heating rates of 10 ^{0}C/min to the temperature between Tammann temperature and melting point temperature of the metal oxide at 873.15 K (V_2O_5, MoO_3, WO_3, Co_3O_4, PdO, CuO, Cu_2O, GeO_2, SnO and PbO) and 673.15 K (Ag_2O and HgO) in a Carbolite Furnace CWF 1300 for 24 hours.

To study the effects of parameters on the modified samples, the experimental procedures as discussed above were repeated by varying the parameters and experimental conditions using one of the selected sample, copper (II) oxide modified zeolite Na-Y to investigate the effect of calcination temperature (773, 873, 973 and 1073 K), copper oxide loading concentration (2, 2.25, 5, 10 and 15wt.%) and duration of calcination (0, 6, 12, 24 and 48 hours) on the structural and gas methane adsorptive characteristics. Copper (II) oxide modified zeolite Na-Y sample was selected for modification parameters variation due to its well-defined structure and promising physicochemical properties as gas adsorbents after the characterization. The initial adsorption characteristic results also showed that CuO modified Na-Y zeolite is presenting superior methane gas adsorption capacity following after the mercury (II) oxide modified sample as shown in Chapter IV. However, from the economic, safety and environmental effects point of view, copper (II) oxide is preferable over mercury (II) oxide for some of the commercial applications.

3.3.3.3 Incipient wetness impregnation technique

The dispersion of the high melting point metal oxides inside or outside the microporous channels of zeolite Na-Y by incipient wetness impregnation method was carried out at room temperature. The samples were prepared by impregnating commercial zeolite Na-Y with equimolar amounts of metal oxides. For this purpose, 0.1 M aqueous solution of metal nitrates, $Mg(NO_3)_2.6H_2O$, $Ca(NO_3)_2.3H_2O$, $Ba(NO_3)_2$, $Y(NO_3)_2.6H_2O$, $Fe(NO_3)_3.9H_2O$, $Co(NO_3)_2.6H_2O$, $Ni(NO_3)_2.6H_2O$, $Cu(NO_3)_2.3H_2O$, $Zn(NO_3)_2.6H_2O$ and $Ga(NO_3)_3.XH_2O$ (9 ml) was kept under mild stirring for 2 hours with 3 g of zeolite Na-Y. Similarly, the amount of metal nitrate and zeolite Na-Y used were weighed carefully using the Precisa 205 ASCS (Precisa Instruments AG, CH-Dietikon) balance with accuracy ± 0.0001 g.

The resulting mixtures were dryed at room temperature followed by overnight drying at 383.15 K in Memmert convective oven. After that, all the adsorbents were activated by calcination at 823.15 K (heating rates of 2 K/min) in Carbolite Furnace CWF 1300 with air for 5 hours in order to ensure the formation of corresponding metal oxides. The prepared adsorbents were then sieved to particle sizes of 300 μm for the sample characterization purposes. Heating at this temperature (823.15 K) was found enough for the transfer of metal oxide precursor into stable oxide form. It is also prevents the growth of grain size metal oxide clusters in the sample (Arishtirova *et al*., 2003; Huwe and Fröba, 2003; Korotcenkov *et al*., 2004). The amount of metal oxide introduced in each sample was 290 μmol/g adsorbent.

3.3.3.4 Amine wet impregnation procedures

Modification of MCM-41 and SBA-15 using amine as functional groups utilize the same conventional method, which is known as wet impregnation method. For MCM-41, methanol was use as a solvent to allow amine solution dissolves in a mixture before adding to the calcined MCM-41. The resultant slurry was stirred and dried at 70°C for 16 hours under 700 mmHg vacuum (Xu *et al*., 2002; Xu *et al*., 2005). The same method was applied for SBA-15 with the only different is that, the solvent used is toluene solution and the impregnated sample was heated at 150°C for 20 hours in a vacuum oven (Khatri *et al*., 2005; Gray *et al*., 2005). Meanwhile, amine modified zeolites are prepared by reaction of raw zeolite with amine at 200°C in an autoclave for 48 hours and some required calcination at high temperature of up to 500°C for 2 hours (Han *et al*., 2005; Guo *et al*., 2006).

Through literature study, it can be observed that by using wet impregnation and autoclave method, temperature of up to 200°C must be apply. This proves to be inappropriate since the boiling point of most amine solutions are in a range of moderate temperature. Therefore, this study attempts to introduce a new modification method, which is freeze-drying method. In a typical preparation, the desired amount of amines will be mixed together with calculated amount of adsorbent and stir for 2 hours. The mixture is then solidified in a freezer for 24 hours and the crystal ice mixture will finally go through freeze drying process utilizing Freeze Dryer (Heto FD 4.0) to remove water and other impurities as well as to obtain powder form product.

3.4 Zeolite Characterization Procedures

3.4.1 Structural characterization

Powder X-Ray diffraction (XRD) has been in use in two main areas, for the fingerprint characterization of crystalline materials and the determination of their structure. It provides information on types and structural of crystalline phases present, morphology of samples, degrees of crystallinity, phase purity, micro strain, sizes and orientation of crystallites (Cullity, 1978). By applying Bragg's Law, powder XRD pattern is a plot of intensity of the diffracted beams as a function of 2-Theta (2θ).

For structural identification, the observed XRD pattern of the metal oxide modified zeolite is compared with the simulated standard XRD pattern of Na-Y zeolite that used as the reference sample (Szostak, 1992). Any extra or missing peaks observed in the modified zeolite indicate the presence of other crystalline phase (metal oxide) or changes of structure after modification. Many studies have been used X-Ray diffraction data to characterize the dispersion of metal oxide on the surface of zeolite microporous materials. Large crystallite would be obvious by appearance of XRD reflections (Rao *et al*., 1996; Xiao *et al*., 1998; Xu *et al*., 2000; Qian and Yan, 2001; Zheng *et al*., 2003; Liu *et al*., 2004).

In the cubic lattice, the unit cell parameter, a_0 is related to the spacing of Miller indices (*h,k,l*) planes (d_{hkl}) through the relationship (Cullity, 1978):

$$d_{hkl} = \frac{a_0}{\sqrt{h^2 + k^2 + l^2}} \qquad (3.1)$$

The position of the diffraction peaks change with the composition of the lattice. When Al-O bond length is being substituted with shorter Si-O bond length in the framework, the position of the diffracted peaks are shifted towards lower values and the unit cell parameter or lattice constant is decreased. The ratio of Si/Al of the modified zeolite Na-Y can be calculated using the following relation (Breck, 1974):

$$Si/Al = \frac{1.66656}{(a_0 - 24.191)} - 1 \qquad (3.2)$$

Meanwhile, the intensities of the diffraction peaks are used to determine the crystallinity of the samples as given by Equation 3.3. The percentage of crystallinity of zeolite Na-Y was calculated using 6 reflection peaks (ASTM D3906) namely {331}, {511}, {440}, {533}, {642} and {555}.

$$\% \; Crystallinity = \frac{\sum Intensity \; of \; peaks \; hkl \; of \; samples}{\sum Intensity \; of \; peaks \; hkl \; of \; s\tan dard} \times 100 \qquad (3.3)$$

In addition, XRD data was used to determine the crystallite size of the samples as given by Scherrer equation (Cullity, 1978; Liu *et al.*, 2005):

$$t = \frac{0.9\lambda}{B\,Cos\,\theta} \qquad (3.4)$$

where t is the crystallite size (nm), $B^2 = B_m^2 - B_s^2$ where B_m is the broadening measured in radians at the full width at half maximum for the highest peak of sample. B_s is the system broadening which was found to be 5.34×10^{-4} radian as measured by using a polycrystalline silicon standard. λ is 0.15418 nm (CuKα radiation).

In this study, the powder X-Ray Diffraction (XRD) patterns were analyzed using Bruker D8 Advance X-Ray Diffractometer were used for structural and relative crystallinity identification for all the samples. A typical sample holder is a 3 mm thick square plastic plate with a 25 mm diameter hole in the center. About 0.35 g of sample was well ground in a mortar to average particle sizes inferior to 300 μm, and then spread on the plate and smoothed flat. The structural properties before and after modification were characterized using XRD with CuKα radiation (λ = 1.5418 Å) in the range of $2\theta = 2^0 - 50^0$ at scanning speed of 0.05^0 per second for zeolites, and 2θ

= 0.6° - 10° for SBA-15 and 2θ = 1.5° - 10° for MCM-41 with a scan speed of 0.02° per second. (Gaydhankar *et al*., 2005; Klimova *et al*., 2006). The working voltage and current were 40 kV and 40 mA respectively.

Apart from X-Ray Diffractometer, Fourier Transform Infrared Spectrometer (FTIR) Perkin Elmer Model 2000 can be used for identifying types of chemical bonds (functional groups) in the metal oxide modified zeolite Na-Y samples. FTIR is most useful for identifying chemicals that are either organic or inorganic. It can be applied to the analysis of solids, liquids, and gases. Furthermore, FTIR can be used for characterizing in-situ reaction catalysis and gas-solid interaction. The FTIR region can be divided into three sub regions. The near-infrared region extends from 12, 900 to 4000 cm^{-1}, the mid-infrared region from 4000 to 400 cm^{-1} and the far-infrared region from 400 to 10 cm^{-1} (Ingle and Crouch, 1988).

Mid-infrared spectrum is mostly applied in the sample chemical composition identification. It can be approximately divided into the X-H stretching region (4000 – 2500 cm^{-1}), the triple-bond region (2500 – 2000 cm^{-1}) and the fingerprint region (1500 – 600 cm^{-1}). The FTIR spectrum of zeolites contains the fundamental vibrations of tetrahedral units TO_4 (T = Si, Al) that reflects the structural characteristics of the zeolite framework. According to Flanigen *et al*. (1971) and Yong and Wha (1999), the band positions assigned to the vibrations of zeolite structural are as presented in Table 3.2.

After metal oxide-zeolite modification, FTIR absorption bands of all the modified samples were compared to the commercial zeolite Na-Y to characterize the chemical nature and structure effect of the modified samples. The samples were milled with potassium bromide (KBr) in the ratio of 1 mg sample to 100 mg KBr to form a very fine powder (sieved to average particle sizes of 300 μm). This mixture is then compressed into a thin pellet 1.3 cm using hydraulic press (Carver Hydraulic

Unit Model 3912) under 5 metric tons of pressure for 5 minutes. The FTIR vibration spectrum was collected of 10 scans and recorded between 4000 - 370 cm^{-1} with 4 cm^{-1} resolutions.

Table 3.2: The assignment of FTIR bands in zeolites (Flanigen *et al*., 1971).

Structure insensitive vibrations	Band positions (cm^{-1})
Asymmetric stretching of TO_4	950 – 1250
Symmetric stretching of TO_4	650 – 720
T-O bending	420 - 500
Structure sensitive vibrations	**Band position (cm^{-1})**
Asymmetric stretching of TO_4	1054 – 1150
Symmetric stretching of TO_4	750 – 820
Double ring vibrations	500 – 650
Pore opening vibration	300 - 420

Apart from that, the Scanning Electron Microscope (SEM) that equipped with Electron Dispersive Spectroscopy (EDS) was used for detecting the chemical composition of unmodified and metal oxide modified zeolites framework. The EDAX quantification analysis from EDS analyzer was carried out. The fraction of metal element composition in metal oxide compound of the modified sample was apparent in the EDAX data. Five measurements at different spots were scanned to obtain an average value of the data as well as to confirm the homogeneity properties of metal oxide modified Na-Y samples.

3.4.2 Physical properties characterization

The surface area and pore size properties of metal oxide modified Na-Y zeolite prepared in this study were characterized using Micromeritics ASAP 2000

Version 3.00 surface area and pore size analyzer at 77 K (liquid nitrogen temperature) with accompanying software from Micromeritics. It utilizes the principle of physical adsorption to obtain adsorption and desorption isotherms. The single point and multipoint surface area analyses were automatic performed plus pore size and pore volume distributions information. Prior to the actual measurement, it is necessary to remove any adsorbed gases or vapors. For this purpose, the zeolite sample 0.1-0.2 g was grinded in a mortar to particle size of 300 μm before it was placed in the sample bulb, attached to the sample station for outgas and dehydrated at 673 K under vacuum at 1.0 Pa for 2 hours. After sample cooling to room temperature, the sample bulb was immediately moved to the analysis port for gas nitrogen adsorption measurement. Adsorption isotherm was obtained by a volumetric method. Equilibrium time for isotherm measurements was about 5 minutes per equilibration point. The surface areas were calculated by using the conventional Brunauer, Emmett, Teller (BET) method. The pore parameters were calculated from the desorption branches of these isotherms using t-plot and Barrett-Joyner-Halenda (BJH) methods. Meanwhile, the calculation of micropore volume and micropore surface area was using t-plot method.

3.4.3 Morphological characterization

The Scanning Electron Microscope (SEM) and Transmission Electron Microscope (TEM) are microscopes that use electrons rather than light to form an image. They produce images of high resolution, which means that closely spaced features can be examined at a high magnification. The combination of high magnification, larger depth of focus, greater resolution, and ease of sample observation makes the SEM and TEM heavily used instruments in research areas today (Scüth *et al*., 2001; Kosanović *et al*., 2002; Bi and Lu, 2003; Zhang *et al*., 2003; Ponce *et al*., 2004; Zhu *et al*., 2005).

For morphological characterization in this study, Scanning Electron Microscope images were acquired for several samples structural identification using a SEM Philip XL 40 Series equipped with Electron Dispersive Spectroscopy (EDS) system for chemical analysis. Experiments were carried out at 30 kV with a resolution of 5 nanometers to study the fine structure and morphology of the metal oxide species that dispersed on the zeolite Na-Y samples. Before the characterization, the sample is mounted on a specimen stub and sputter with gold at pressure below 10^{-1} mbar for 120 second to prevent surface charging and to protect samples from thermal damage by the electron beam. These thin layer gold coated samples also makes them conductive and ready to be viewed by the SEM. The samples were then placed on the stage, vacuumed and the magnification was manipulated to 5000 times for the characterization. The focus was then adjusted, the contrast and brightness of the image was well controlled.

3.5 Gas Adsorption Measurements

Gas adsorption study involves several types of adsorbates namely methane (CH_4), carbon dioxide (CO_2), nitrogen (N_2) and oxygen (O_2). It involves measurements on gas adsorption capacity, gas adsorption isotherm, uptake rate of the adsorbates, and gas – solid interactions on different zeolites. The experimental data obtained will be used to determine the characteristics of gas adsorption on structurally different zeolites and different metal cation exchanged zeolites.

3.5.1 Gas adsorption isotherm measurements

Since adsorption equilibrium is the most fundamental property, a number of studies have been conducted to determine the amount of species adsorbed under a

given set of conditions (Suzuki, 1990). Adsorption isotherms measurements of methane and carbon dioxide were carried out in a similar manner as nitrogen adsorption isotherm (Section 3.4.2) except that the adsorption was carried out at 298 K. The adsorption was measured using volumetric adsorption analyzer (Micromeritics ASAP 2000). Each sample weight between 10 – 20 mg was activated at 673 K for a minimum of 2 hours. The sample was allowed to cool to 298 K before the adsorption of adsorbate was carried out. The amount adsorbed was expressed as volume adsorbate (cm^3) per unit mass (g) of adsorbent.

3.5.2 Gas adsorption kinetics measurements

Gas adsorption capacity of zeolites was determined using gravimetric method using thermal gravimetric analyzer (Perkin Elmer, TGA 7). Zeolite sample between 5 – 15 mg is spread on a platinum pan (*ca* 5mm in diameter), activated at 673 K for at least 2 hours or until no weight change was observed. The sample was cooled and then held at 323 K for adsorption to occur until it reached equilibrium. Adsorbed amounts were expressed as the amount adsorbed (mmol) per unit mass (g) of an adsorbent. Figure 3.2 shows the schematic diagram of the system used to measure the gas adsorption capacity dan the uptake rate of adsorbate.

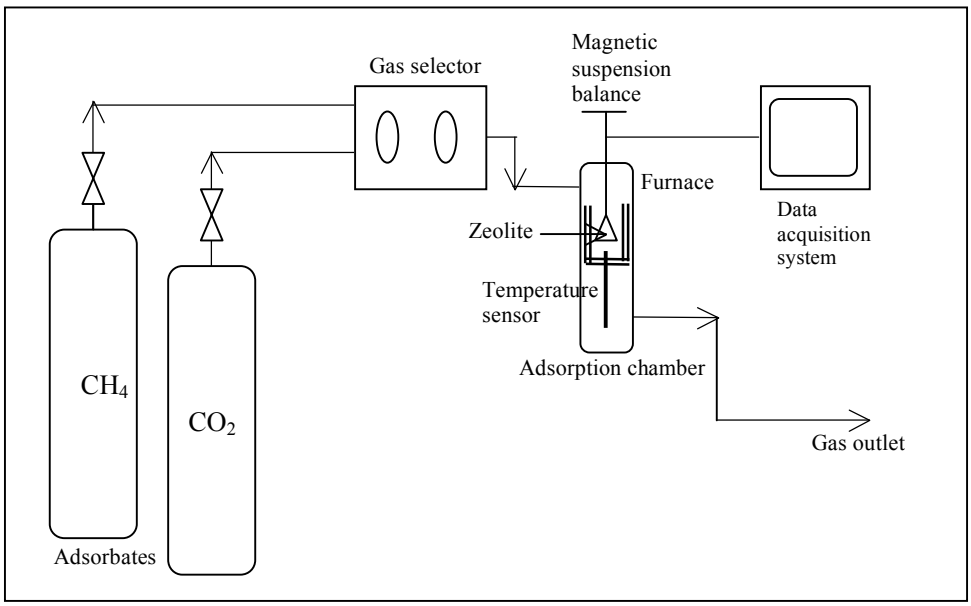

Figure 3.2: A schematic diagram of thermogravimetric adsorption system.

3.5.3 Heat of adsorption measurements

The heat of adsorption for pure and selected modified samples were also measured using Thermogravimetric analyzer by varying the temperature of gas adsorption from 323.15 to 363.15 K at 138 kPa. First, the sample was heated from 303.15 K to 673.15 K at 50 ^{0}C/min and held at 673.15 K for 30 minutes to remove water molecules and impurities. The sample was then cooled down to 323.15 K at 20 ^{0}C/min for gas adsorption until equilibrium (400 minutes). Then, by setting the temperature program, the sample was heated up again to 343.15 K at 50 ^{0}C/min and held at that temperature for around 200 minutes until no weight loss was observed. Lastly, the sample was further heated to 363.15 K and held for 200 minutes until gas adsorption capacity reaches the saturation or equilibrium condition. Amount of gas adsorbed for each sample studied was calculated. The enthalpy of adsorption is interpreted from the slope of the plot of In n_s versus 1/T, while the entropy of gas adsorption is evaluated from the intercept of the plot using Equation 2.6.

3.5.4 Gas-zeolite interaction measurements

Measuring gas-zeolite interaction is not a simple method. A review by Rege (2001) revealed that neither gravimetric nor volumetric method would be well suited in measuring the interaction. Their study showed that FTIR spectroscopy has emerged as a tool to study microscopic behavior of adsorbed molecules. Therefore, in order to study the behavior of the adsorbed molecules, an adsorption cell was fabricated with CaF_2 infrared window that could be integrated with FTIR instrument (Figure 3.3). The cell could stand pressures in the range of 0.001 to 1013.5 kPa. In this study, a thin self-supported wafer of each sample was prepared and outgassed (activated) in a dynamic vacuum (residual pressure < 2 x 10^{-3} kPa) for 2 hours at about 700 K inside an infrared adsorption cell which allowed in-situ high temperature activation, gas dosage, and variable-pressure spectroscopic measurements to be carried out.

A laboratory-made FTIR cell unit used in this study is illustrated in Figure 3.4. The apparatus for FTIR measurement is made up of stainless steel equipped with a CaF_2 window 25 mm in diameter in order to be used at 673.15 K under the pressure up to 276 kPa. CaF_2 with 77, 000 – 900 cm^{-1} useful range has been chosen as window material due to the high resistance to most acids and bases; does not fog; insoluble in water and useful for high pressure work (Stuart, 2004). The diameters of external and internal FTIR cell are 31 mm and 25 mm, respectively.

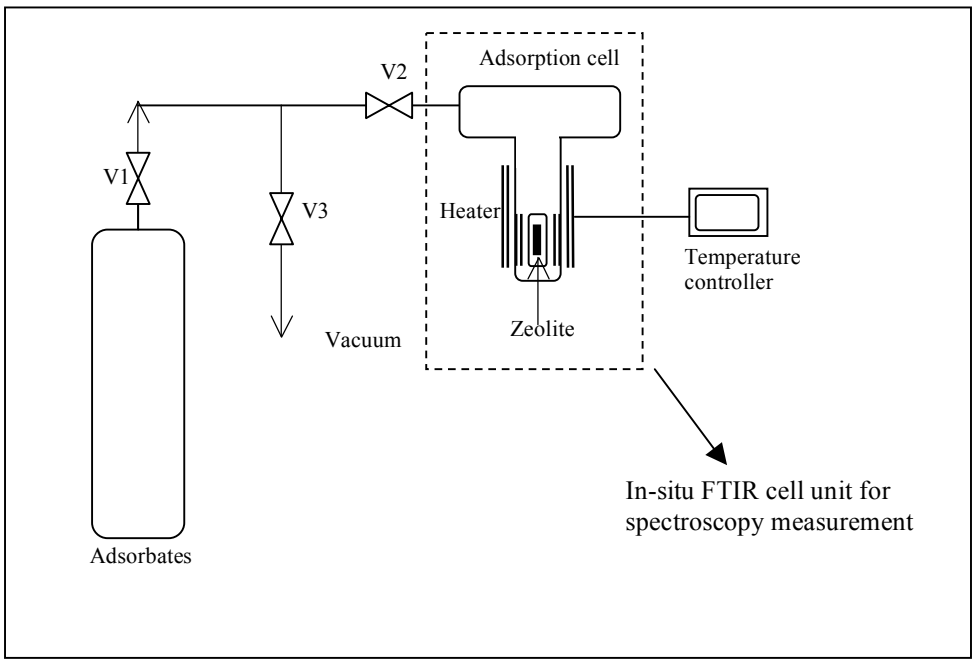

Figure 3.3: A schematic diagram of gas - zeolite interaction adsorption cell.

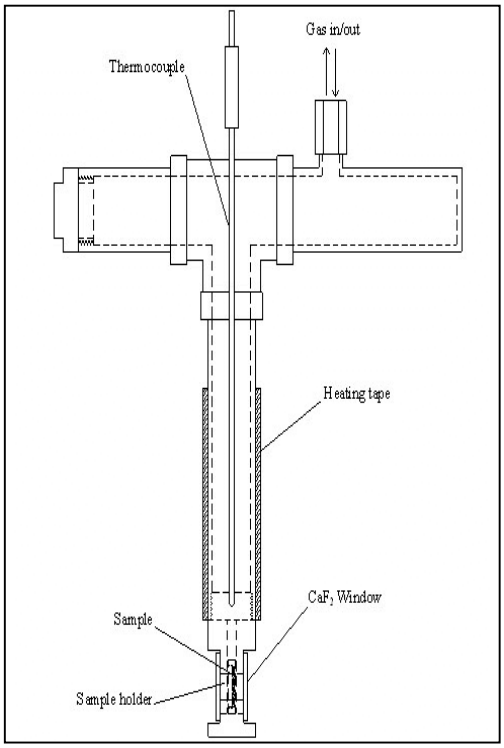

Figure 3.4: The schematic structure of in situ FTIR cell.

The pretreatment was carried out by closing V1 valve and opening V3 and V2 valves to vacuum the adsorption cell. The sample was heated for 2 hours to remove the moisture and other components, if any, adsorbed on the zeolite. The adsorption cell was then isolated by closing V2 and V3 valves and the sample was allowed to cool to room temperature. The recording of the spectrum was carried out using FTIR spectroscopic instrument (Perkin Elmer) at room temperature. The gas adsorbate was introduced at 137 kPa by opening V1 and V2 valves to allow the gas to adsorb on the zeolite sample for 2 hours. V2 valve was then closed and the recording of the adsorbed molecules was carried out using the same FTIR spectroscopy instrument. The spectra obtained were compared against the background spectrum of zeolite wafer.

3.6 Adsorption Isotherm Model Constant Estimation

As discussed in Chapter 2, equation models such as Henry (Equation 2.1), Langmuir (Equation 2.3), Freundlich (Equation 2.5), and Dubinin-Polanyi (Equation 2.10) could be used to describe adsorption of gases at equilibrium. Table 3.3 shows methods of plotting gas adsorption data in order to estimate the respective model parameters

Table 3.3: Methods of plotting gas adsorption data and calculating the constants

Equation	Plotting A vs B	Calculation of constants, C_1 and C_2	
Henry's, $q = kP$	q vs P	Slope, $m = k$	
Langmuir, $\frac{q}{q_m} = \frac{BP}{1+BP}$	$1/q$ vs $1/P$	Slope, $m = 1/Bq_m$ $B = c/m$	Intercept, $c = 1/q_m$ $q_m = 1/c$
Freundlich, $q = KP^{1/n}$	$\ln q$ vs $\ln P$	Slope, $m = 1/n$ $n = 1/m$	Intercept, $c = \ln K$ $K = \exp(c)$
Dubinin-Polanyi $\ln W = C - D\left(\ln \frac{P}{P_o}\right)^2$	Plot $\ln q$ vs $(\log P/P_o)^2$	Slope, $m = C$	Intercept, $c = D$

3.7 High Pressure Adsorption Measurement

3.7.1 Adsorptive gas storage

The vessel used for high pressure adsorption measurement is a 15 cm^3 stainless steel pressurized gas cell. This pressurized cell was specially made from stainless steel type 316L. The head is flanged-type and it is airtight. It can be opened and closed to replace the adsorbent used. The specification and schematic diagram of the cell is shown in Table 3.4 and Figure 3.5, respectively.

Table 3.4: ANG vessel specification

Type	Natural Gas pressurized Vessel	
Material	Stainless Steel Type 316	
Design Pressure	300 MPa	
Design Temperature	Up to 100^0C	
Internal Volume	15 cm^3	
	15 ml	
Dimension	Internal height	4.8 cm
	Internal Diameter	2.0 cm
	Wall Thickness	1.0 cm
Product Storage	Methane	

The ANG cell is installed with a thermocouple and is connected to the methane supply using stainless steel tubing. The thermocouple is installed at the middle of the cell to measure the storage temperature. It has been reported that the central region of the adsorbent bed suffers from the severest temperature fluctuation in a short period during discharge (Zheng *et al*., 2005). Thus, the temperature probe is installed at the middle of the cell in which temperature varies the most. Other than

that, results from Chang and Talu (1996) also find out that in the radial direction of 10 cm distance, the temperature gradient only significantly occurred beyond 4 cm of the cylinder radius after 100 minutes of discharge (about 1^{o}C at 4 cm radius). Since the radius of the vessel is only 1 cm, while the discharging period is below 100 minutes, it is assumed that the radial temperature variation is negligible.

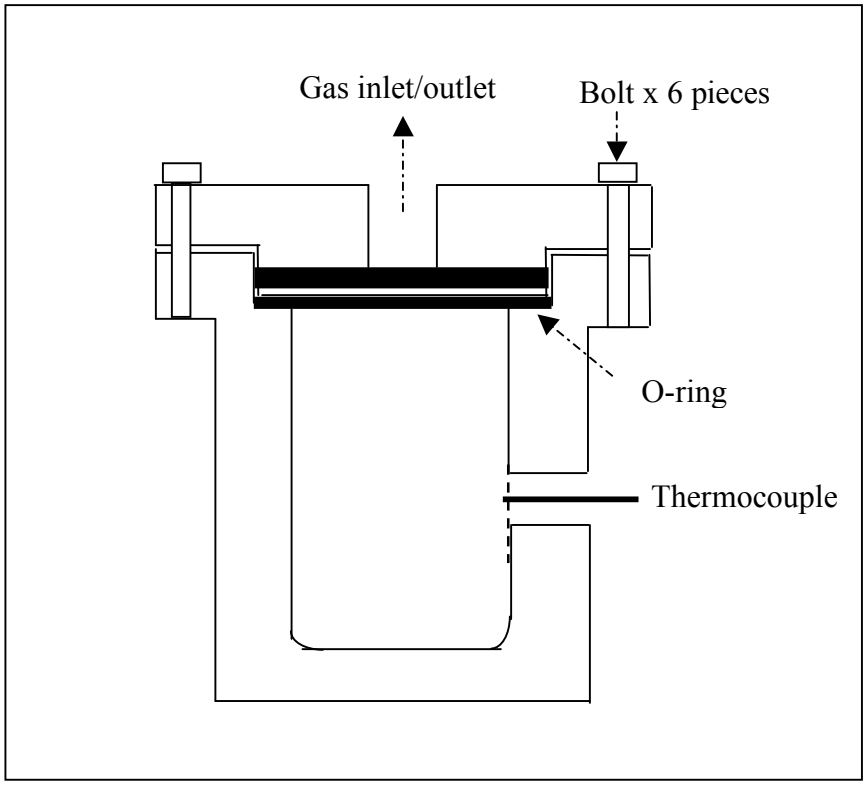

Figure 3.5: A schematic diagram of ANG pressurized gas vessel

The measuring devices used for this experiment are thermocouple, digital pressure gauge and measuring cylinder. Other controlling equipments are ball valves and pressure regulator. Vacuum pump is being used to evacuate the ANG cell before charging process is being done. List of equipment is shown in Table 3.5.

Table 3.5: Measuring and controlling equipment

Item	Operating range	Function
Thermocouple	-60 to 100 ^{o}C	To measure the temperature of the gas inside the cell
Pressure gauges	0 to 1500 psi 0 to 1000 psi	To measure the pressure inside the cell To measure pressure in the tubing
Measuring cylinder	0 to 500ml	To measure the outlet of the gas.
Needle valve	-	To open and close gas flow. To control the flow rate of the gas.
Multi stage regulator	0 to 600 psi	To step down gas supply pressure to operating pressure.
Vacuum pump	-760 to 0 mmHg	To evacuate the test cell before methane charging.

The overall picture for the high pressure adsorption is shown in Figure 3.6 and it is illustrated schematically in Figure 3.7. The union-T fitting connects the test cell, digital pressure gauge and methane supply tubing. The tubing used to connect these equipments is a 2 mm internal diameter stainless steel tubing. Four ball valves are installed at four directions as shown in the diagram and are connected using a union cross. The measuring cylinder is used to measure the total gas discharge and the digital pressure to indicate the pressure inside the cell and tubing.

Figure 3.6: Experimental rig used for the ANG measurement

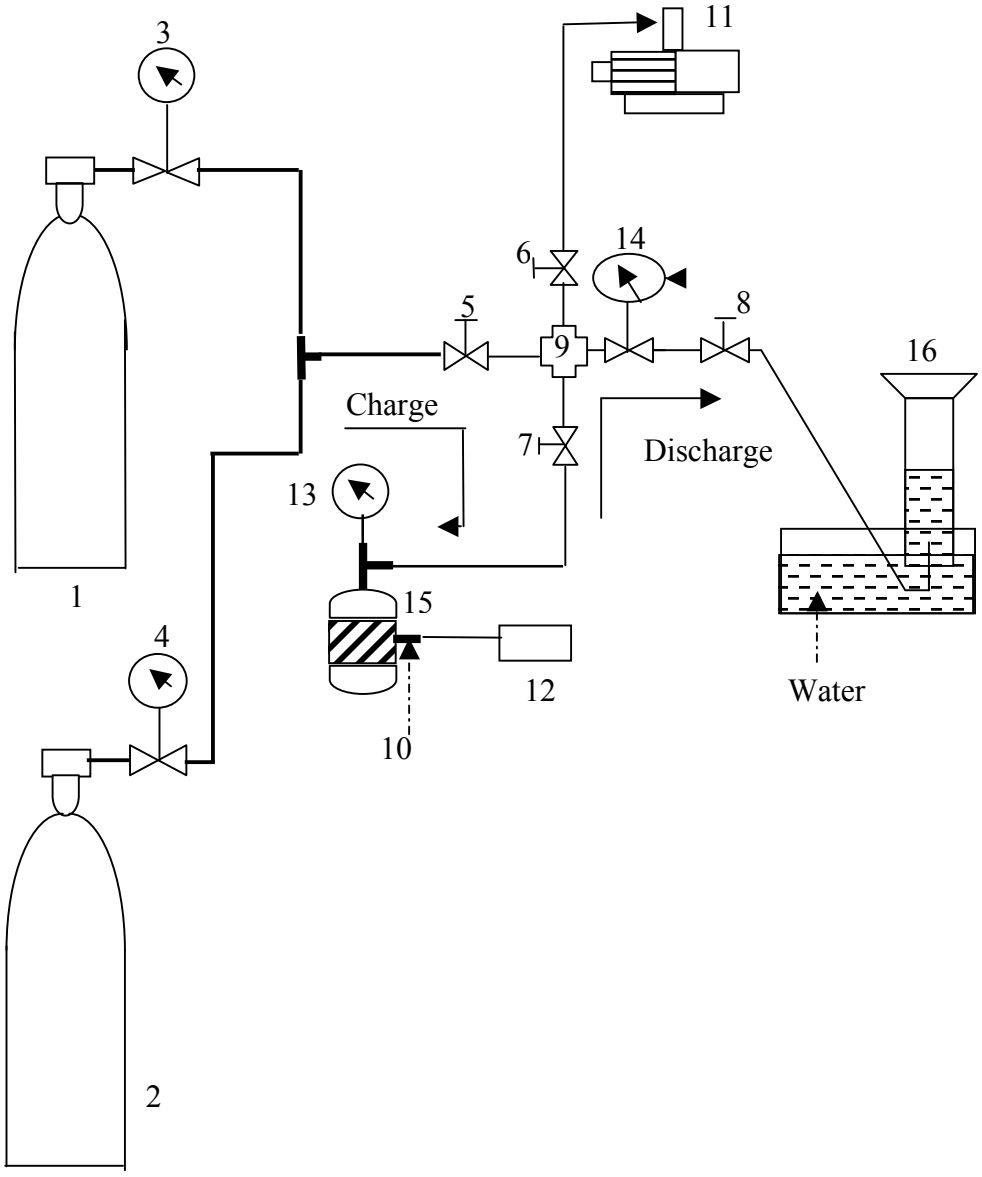

Figure 3.7: A schematic diagram ANG rig (15 ml) (1. Methane gas cylinder; 2. Helium gas cylinder ; 3, 4. Multi-stage pressure regulator; 5,6,7,8. Needle valve; 9. Union cross fitting; 10. Thermocouple; 11. Pump;12. Temperature data control board; 13,14. Digital pressure meter; 15. ANG cell; 16. Measuring cylinder)

3.7.2 Experimental Procedure

The experimental procedures involve empty cell measurement, remaining volume available after the adsorbent loading, pre-adsorption treatment and dynamic adsorption/desorption measurement. Pre-adsorption treatment involves preparation of the adsorbent before loading into the cell. While dynamic adsorption/ desorption procedure is the charge and discharge process under cyclic test at various charging and discharging rates. The amount of methane being charged cannot be determined using the electronic balance because the weight of the methane being charged is difficult to measure since the size of the cell is small and thus, the weight change is not significant. Instead, helium gas will be used to determine the remaining volume available after the adsorbent being loaded into the cell with the assumption that helium is not being adsorbed on the adsorbent.

Using the empty cell without adsorbent, all valves were closed and the pressure regulator output V2 for helium was set to 500 psi. Valve V5 was slowly opened followed by V7 to allow the helium gas to enter the cell. V2 and V5 valves were close when the pressure inside the cell reaches equilibrium (500 psi). V8 was slowly open to allow the gas to flow into the measuring cylinder until the pressure inside the cell reaches atmospheric pressure. Then, volume of the gas, X1 was recorded. This is a volume of the cell at 1 bar. The volume of the gas occupies at charging pressure will be calculated using equation below:

$$(P_1X1) / Z_1\ T1 = (P_2V_2) / T_2Z_2 \qquad (3.1)$$

where,

P_1 = Pressure at atmospheric (1 bar)

X1 = Volume of helium gas release at measuring cylinder

T_1 = Temperature at atmospheric pressure.

P_2 = Charging pressure

V_2 = Volume of gas occupy in the tubing and cell at P_2

T_2 = Temperature at P_2

Z = Compressibility factor

$$V_{tiub} + V_{cell} = V_2 \quad (3.2)$$

Helium gas was also used to determine the remaining volume of the cell after the cell is loaded with the adsorbent. One assumption has been made, the amount of helium adsorbed at room temperature is nil (Zhang et al., 2004). The empty cell testing was repeated for different pressures, 400 psi, 300 psi and 200 psi.

In order to determine the volume of remaining cell after adsorbent loading, adsorbent is heated in oven for approximately 3 to 4 hours at 110 °C to remove the volatile compounds trapped inside the pores. The cell was weighed without the adsorbent and the value was recorded. Adsorbent were then loaded into the cell by adding the adsorbent bit by bit followed by swinging and softly hammering the vessel (Bastos-Neto *et al*., 2005). The intensity of force applied during pressing must be appropriate to avoid the adsorbent particles from being damaged by excessive force. Then, the adsorbent-fill cell was weighed the packing density of the adsorbent bed was calculated. All valves were closed except for V6 and V7. The vacuum pump was switched to ON position in order to remove the remaining residual gas. A very fine stainless steel wire mesh was used to cover the top of the cell to avoid the adsorbent being sucked out of the cell during the vacuuming process.

After that, all valves were closed except for V5 and V7. By controlling V2, the gas regulator was slowly opened to allow gas to flow into the cell. When pressure inside the cell reaches equilibrium at 500 psi, valve V5 was closed and the cell temperature was allowed to reach thermal equilibrium with the surrounding. Then the V8 was slowly opened to release the gas. Amount of gas helium release is recorded as X2, a volume of the helium at 1 bar. The remaining volume inside the cell then can be obtained. This procedure was repeated for pressures 100 psi, 200 psi, 300 psi and 400 psi.

The volume of the gas occupies at charging pressure was calculated using equation below:

$$(P_3X2) / T_3Z_3 = (P_4V_4) / T_4Z_4 \quad (3.3)$$

where,

P_3 = Pressure at atmospheric (1 bar)

X2 = Volume of gas release at measuring cylinder

T_3 = Temperature at atmospheric pressure.

P_4 = Charging pressure

V_4 = Volume of gas occupy in the tubing and cell at P_4

T_4 = Temperature at P_4

Z = Compressibility factor

$$V_{tiub} + V_{available} = V_4 \quad (3.4)$$

From equation 3.2, value of V_2 was obtained. The volume of the adsorbent occupied the cell after loading the adsorbent is:

$$V_{adsorbent} = V_2 - V_4 \quad (3.5)$$

By knowing the volume of the empty cell (15 cm^3), the remaining volume, $V_{available,}$ can be calculated.

$$V_{adsorbent} + V_{available} = 15cm^3$$

$$V_{available} = 15 - V_{adsorbent} \quad (3.6)$$

Calculating $V_{available}$ for each pressure, a graph of $V_{available}$ versus pressure was plotted. To determine the volume of the tubing, let's rearrange the equations.

Using He, $V_{tiub} + V_{cell} = V_2$ (3.2)

Using He, $V_{tiub} + V_{available} = V_4$ (3.4)

Volume of adsorbent only, $V_{adsorbent} = V_2 - V_4$ (3.5)

Volume in cell + adsorbent, $V_{available} = 15 - V_{adsorbent}$ (3.6)

Volume of tubing, $V_{tubing} = V_4 - (15 - V_{adsorbent})$ (3.7)

After obtaining the $V_{remaining}$ for the cell, the helium gas in the system need to be removed. The adsorbent-filled cell was emptied until the pressure reach 0 atm or -14.7 psi using the vacuum pump. The gas regulator was slowly opened and the pressure set around 100 psi. Then, V5 was slowly opened followed by V7 to charge the cell until it reaches 100 psi. The cell was left overnight for the adsorption to achieve equilibrium. Then the gas was released from the cell at the atmospheric

pressure. The time, volume released and temperature were recorded. After that, the remaining gas was removed from the cell using the vacuum pump.

This procedure was repeated for pressure 200 psi, 300 psi, 400 psi and 500 psi. The amount of gas release at the respective pressure need to minus the gas release from the tubing at the respective pressure to get the actual amount of gas release from the adsorbent fill cell. Then, from the data obtain, graph is plotted for amount of methane released versus charging pressure. This experiment was repeated for other adsorbent.

3.7.3 Estimating the amount of methane stored, delivered and adsorbed.

Amount of methane delivered (at specific pressure), $V_{delivered}$:

$V_{delivered}$= Amount of methane release (at specific pressure from graph)

= Amount of methane stored (at specific pressure) –
Amount of methane remain in cell (from graph P = 0 psi) (3.8)

Amount of methane stored (at specific pressure), V_{store} :

V_{store} = Amount of methane release (at specific pressure from graph) +
Amount of methane remaining in cell (from graph P = 0 psi) (3.9)

Amount of Methane Adsorbed (at specific pressure), $n_{adsorbed}$:

$n_{adsorbed}$= Amount of methane store (at specific pressure) –
Amount of methane in remaining volume ($V_{available}$) (3.10)

The amount of gas in $V_{available}$ can be calculated using the equation :

$$PV_{available} = Zn_{adsorbed}RT \quad (3.11)$$

where

P	=	Pressure of cell
$V_{available}$	=	Volume occupy by helium at specific pressure
Z	=	compressibility factor of methane gas at specific pressure and temperature
$n_{adsorbed}$	=	Amount of methane adsorbed at specific pressure
R	=	Gas constant, 83.14 cm^3 bar/ mol K
T	=	Temperature

3.7 Summary

The materials and methods were designed and presented accordingly to fulfill the mentioned objectives and scopes as presented in Chapter I. The experimental procedures involving zeolite and mesoporous synthesis, characterization of parent and modified microporous and mesoporous adsorbents, and gas adsorption measurements were carried out to obtain related data of zeolite properties on gas adsorption of different zeolites and mesoporous materials. The selected analytical procedures with effective instrumentations enable highly accuracy and efficient characterization on the adsorbents physicochemical properties and gases adsorptive characteristics be carried out and investigated. The addition of metal cations, metal oxides, and amines to the selected adsorbent is to study the effect of different substances on gas adsorption characteristics. In general, the study on gas adsorption characteristics of porous adsorbents was achieved by carrying out the above-mentioned procedures.

CHAPTER 4

GAS ADSORPTION CHARACTERISTICS OF STRUCTURALLY DIFFERENT ZEOLITES

4.1 Introduction

Zeolites are potential adsorbent due to the ability of their microporous structures to adsorb molecules at relatively low pressure. They have been used extensively in industries as adsorbent for separating gases such as CH_4, NH_3, H_2S, N_2, O_2, and CO_2. Considering the structural difference, it seems interesting to explore the adsorptive activities of zeolites. Studies on this area might clarify the relationship between gas adsorption and zeolite structure. It is important to realize that different structural framework might produce different adsorption characteristics. Even though many studies have been carried out involving microporous zeolites such as ZSM-5, X and Y zeolites, the relationship between adsorptive characteristics and its structure and physicochemical properties still need to be further clarified especially in the adsorption of gases at room temperature or slightly higher temperature. Properties such as pore size, pore volume, surface area, and unit cell parameter may have greater influence on the characteristics of gas adsorption. Other factors such as Si/Al ratio and crystallinity may also affect gas adsorption characteristics. At the same time, gas molecules (adsorbates) also have an effect on the adsorption characteristics. Kinetic diameter of adsorbates

determines the accessibility and type of diffusion that occur inside the pore, whereas charge and the polarity or dipole/quadrapole moment determines the strength of interaction between adsorbate and zeolite. However, it is still important to understand the way different structures response to different types of adsorbates.

In this study, types of zeolites chosen are ZSM-5, mordenite, ferrierite, zeolite beta, zeolite A, and faujasite (Na-SZ18, NaX, and NaY). As described in Table 4.1, the choice of these zeolites makes it possible to understand the effect of zeolite properties such as pore network system, pore size, surface area, pore volume, and zeolite compositions (Si, Al, and Na) on gas adsorption characteristics. In order to carry out the study, zeolites were divided into two groups, one that provides a uniform channel system either in one, two, or three dimensional channel systems, called channel type zeolite and the other that has internal pore system of interconnected cage-like void called cage type zeolite. ZSM-5, mordenite, ferrierite and zeolite beta belong to channel group whereas zeolites A, NaX, NaY and Na-SZ18 are cage type zeolites having three-dimensional pore system. In order to understand the differences between those zeolites, characterizations were carried out to determine the structure and the physical properties of zeolites. The effects of zeolite structural framework and properties on gas adsorption capacity were studied. Further investigation was carried out to determine gas adsorption characteristics based on gas adsorption capacity, gas adsorption isotherm and gas uptake rate using two types of gases, CH_4 and CO_2. To elucidate the data obtained, model equations were used to determine thermodynamic and kinetic parameters of gas-zeolite adsorption.

Table 4.1: Structural framework and pore network of zeolites.

Framework	Description
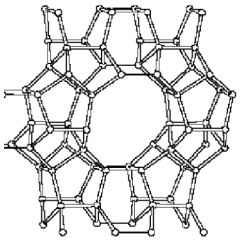 ZSM-5	Three dimensional pore system of straight and zig-zag channels. The straight channels are formed by elliptical 10-membered rings of 0.51 x 0.55 nm. Another channel formed by nearly circular 10 membered rings of 0.54 x 0.56 nm (Wu *et al*., 1983; Zhang *et al*., 2003; Koriabkina *et al*., 2005).
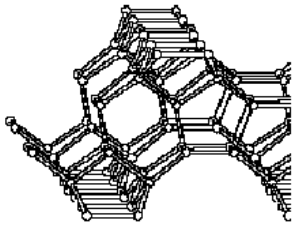 Zeolite beta	Disordered tetrahedral framework structure along [001]. It has perpendicular 12 rings channel systems with pore opening of 0.60 x 0.73 nm and 0.68 x 0.73 nm. The sinusoidal channels have the circular opening of 0.5 nm (Stelzer *et al*., 1998; Barcia *et al*., 2005).
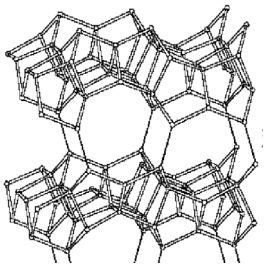 Ferrierite	Composed of four- and five membered rings of tetrahedral. Ten membered ring channels have pore diameter of 0.54 x 0.42 nm and eight membered ring channels formed in this zeolite have pore diameter of 0.48 x 0.35 nm (van Well, 1998).

Table 4.1: Structural framework and pore network of zeolites (continuation).

Framework	Description
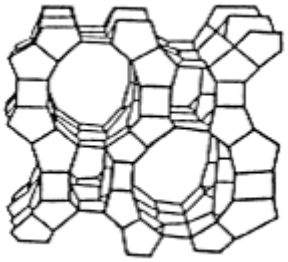 Mordenite	The building unit consists of four and five member rings. It contains a two dimensional channel system, a straight 0.70 x 0.65 nm channels connected by short alternating 8 ring channels (0.26 x 0.57 nm) (Nagy *et al*., 1998; Izumi *et al*., 2002; Hincapie *et al*., 2004)
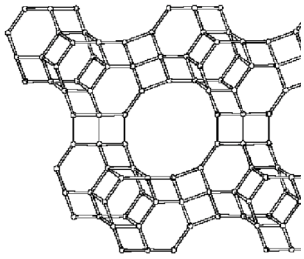 Faujasite	A linkage of TO_4 tetrahedra in a truncated octahedron in a diamond-type structure is referred to as the sodalite unit or sodalite cage. The main cavities are about 0.13 nm and interconnected through 12 membered ring apertures about 0.74 nm in diameter (Takaishi, 1996; Nagy *et al*., 1998; Weitkamp, 2000).
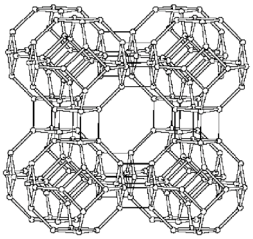 Zeolite A	Truncated octahedral linked to other cavities through 6-membered ring and truncated cubo-octahedra linked together through 8-membered ring. The internal cavity is 0.11 nm in diameter and connected by circular aperture of 0.42 nm. The cavities are connected in three- dimensional system (Nagy *et al*., 1998; Kaushik *et al*., 2002).

Therefore, based on the methodology presented in Chapter 3, this chapter discusses the effect of zeolite structure and physical properties of structurally different zeolites on gas adsorption behavior at controlled temperature and pressure. Commercial and synthesized zeolites were used in identifying important attributes affecting gas adsorption characteristics, followed by discussion on the adsorption equilibrium and adsorption kinetics of the zeolites. The gas interactions were investigated using FTIR spectroscopy method and finally, gas adsorption mechanism describing the adsorption in zeolite pore system was proposed.

4.2 Properties of Zeolites

4.2.1 Structural determination

Since the development of zeolite science, determination of zeolite structure has involved a number of techniques such as x-ray diffraction (XRD), Fourier transform infrared (FTIR) spectroscopy, and nuclear magnetic resonance (NMR) spetroscopy (Flanigen and Khatami, 1971; Nagy *et al*., 1998; van Bekkum *et a*l., 1991). Structural characterizations are important to provide direct information of structure, identification of crystal phase with the known structure, investigation of framework properties, the silicon-aluminium ordering, and the states of various elements incorporated in zeolite structure (Nagy *et al*., 1998). However, in this study, the characterization of zeolites structural framework using XRD and FTIR techniques is carried out in order to gather more insight into structural properties of these materials.

Determination of zeolite structure in gas adsorption study is very important in order to gain comprehensive understanding on factors that influence the adsorption phenomena. The difference in structural framework arrangement and

pore network system would produce different gas adsorption characteristics. XRD patterns of zeolite samples were obtained using x-ray diffractometer (Bruker) by $CuK\alpha_1$ radiation. This method was used based on the fact that every crystalline material has its own characteristic XRD pattern (van Bekkum *et al*., 1991). In order to verify types of structural framework used, the XRD pattern of each sample was compared with the simulated patterns collected by International Zeolite Association Structure Commission (IZA-SC). The XRD measurements showed that crystallites of ZSM-5, mordenite, ferrierite, and beta exist in the respective sample (Figure 4.1). The intensity of peaks indicates that the formation of crystallite phase for ZSM-5, mordenite and ferrierite zeolites are relatively high. However, XRD pattern of zeolite beta has a combination of sharp and broad reflection that indicates a partial structural disorder of the framework and even some peaks were not observed in the diffraction patterns.

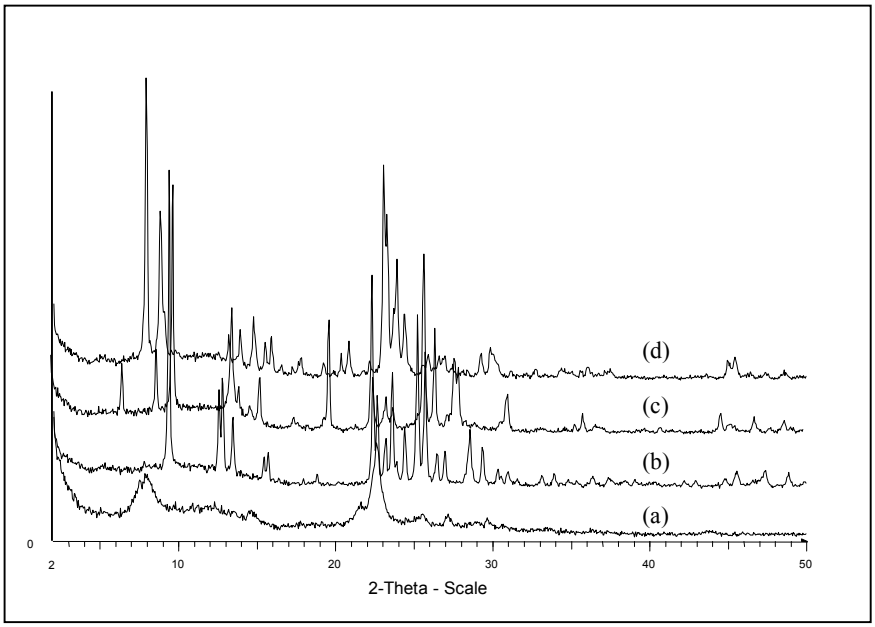

Figure 4.1: The XRD patterns of channel type structures: (a) beta; (b) ferrierite; (c) mordenite; and (d) ZSM-5.

The XRD patterns of cage structures are shown in Figure 4.2. Diffraction patterns of NaX and NaY zeolites are found to be similar to faujasite structure.

Another typical faujasite XRD pattern belongs to Na-SZ18, a zeolite that was synthesized under hydrothermal condition at 373 K. The peak positions of the faujasite group zeolites are in good agreement with those reported in IZA-Structure Commission (Table 4.2). Except for the minor change in peak positions, this sample exhibits a low background signal and sharp reflection, indicating excellent crystallinity of the sample. The XRD pattern of zeolite A, another cage type zeolite is also shown in Figure 4.2.

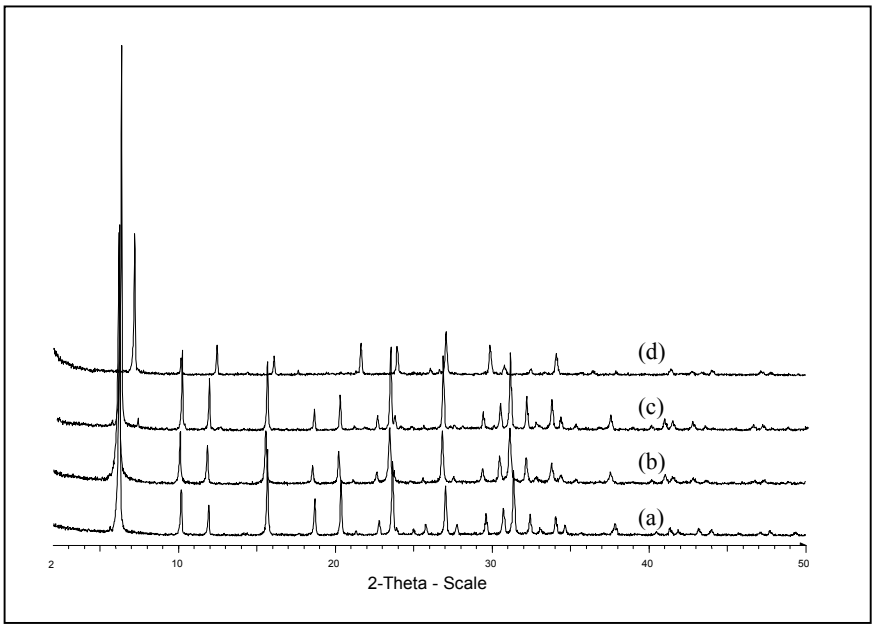

Figure 4.2: The XRD patterns of cage type structures: (a) NaY; (b) NaX; (c) Na-SZ18; and (d) zeolite A.

Table 4.2: The peaks position and intensities of cage type zeolites obtained from XRD data.

hkl	Hydrated FAU (IZA-SC)*	NaY		NaX		Na-SZ18	
	2θ	*2θ*	*I(cps)*	*2θ*	*I(cps)*	*2θ*	*I(cps)*
331	15.419	15.647	855	15.527	605	15.523	474
551	18.405	18.688	341	18.436	198	18.533	175
440	20.053	20.362	556	20.085	320	20.199	296
533	23.286	23.650	712	23.321	735	23.449	501
642	26.631	25.787	548	26.660	654	26.832	474
555	30.916	30.748	615	30.975	682	31.134	499

*(IZA-SC) International Zeolite Association – Structure Commission

Another method to characterize the framework structure is by infrared spectroscopy (Flanigen *et al*., 1971). IR spectroscopy was applied to detect the presence of polyhedral building unit presence in zeolite frameworks. The infra- red region of the spectrum used is between 1400 to 370 cm^{-1} since that region contains the fundamental vibration of aluminosilicate framework and should reflects the framework structure. Each zeolite species has a typical infrared pattern which is generally similar to zeolites from the same structural type and group. As shown in Figures 4.3 and 4.4, the infrared spectra of zeolites in this region that consist of 2 classes of vibrations: Internal vibrations which is insensitive to variations in framework and vibrations related to external linkages between tetrahedra which are sensitive to the framework structure. The spectra could also indicate the presence of some secondary building unit (SBU) and building block polyhedral such as double rings and large pore openings (Flanigen *et al*., 1971).

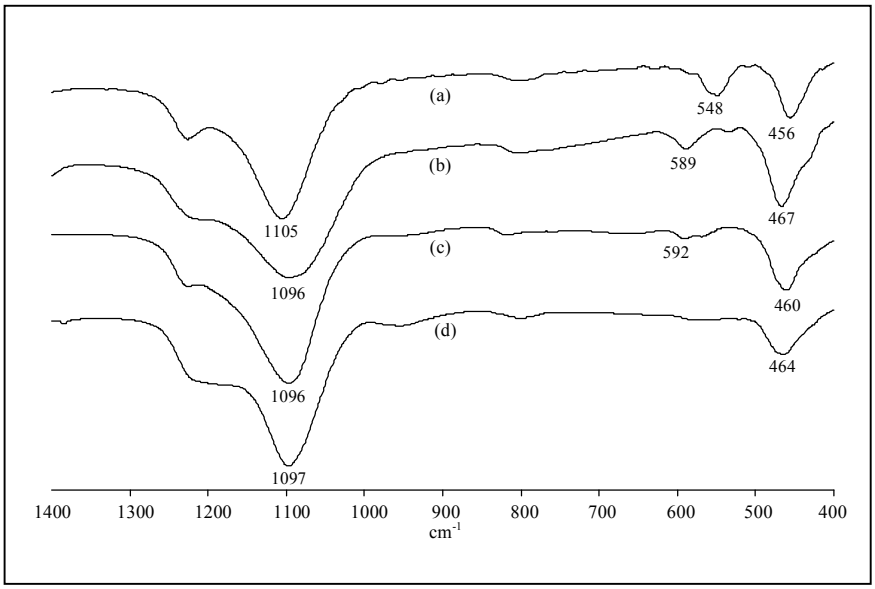

Figure 4.3: The FTIR spectra of zeolite: (a) ZSM-5; (b) ferrierite; (c) mordenite; and (d) zeolite beta.

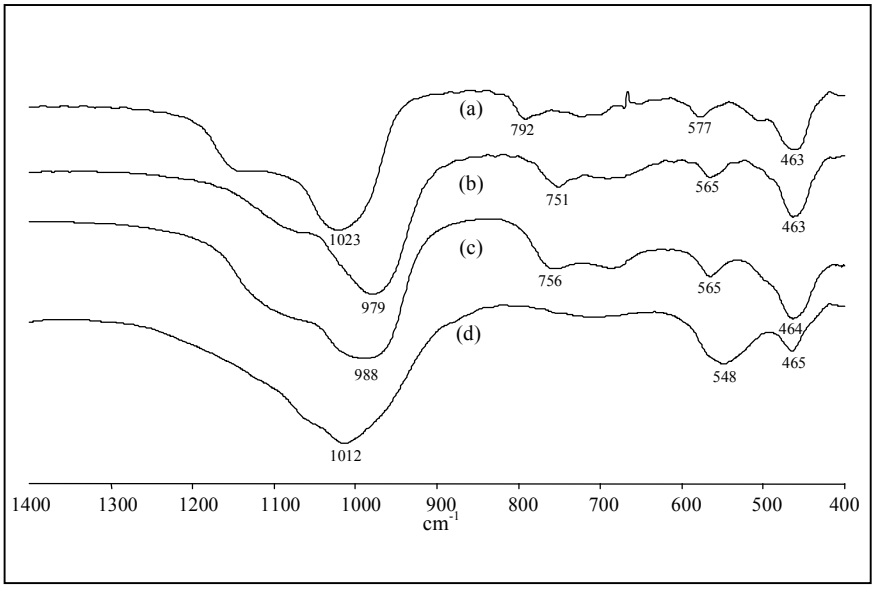

Figure 4.4: The FTIR spectra of zeolite: (a) NaY; (b) NaX (13X); (c) Na-SZ18; and (d) zeolite A.

As reported by Flanigen *et al*. (1971), the strongest vibration in the range of 950-1250 cm^{-1} is assigned to a T-O stretch involving motion primarily associated with oxygen atoms, or alternately described as an asymmetric stretching mode ← OT →← O. The next strongest band (except for zeolite A) in the region of 420 – 500 cm^{-1} is assigned to a T – O bending mode. Stretching modes involving motions primarily associated with the T atoms, or alternately described as symmetric stretching modes ← OTO →, are assigned in the region of 650-820 cm^{-1}. The symmetric modes are further classified into an internal tetrahedron stretch in the lower spectral region of 650 – 720 cm^{-1} and an external linkage symmetric stretch reflecting structure-sensitive external linkages in the higher region of 750 – 820 cm^{-1}.

The stretching modes (950 – 1250 cm^{-1}) are sensitive to framework Si/Al composition and are shifted to lower frequency with increasing Al content (Flanigen *et al*., 1971). This is shown in Figure 4.4 where the stretching modes with highest wavenumber is assigned to $NaY_{Si/Al = 2.5}$ (1023 cm^{-1}), followed by SZ-18 $_{Si/Al = 1.53}$ (988 cm^{-1}) and the lowest wavenumber (979 cm^{-1}) assigned to $NaX_{Si/Al= 1.06}$. However, the framework Si/Al does not substantially affect T-O bending mode. The results as presented in Figures 4.3 and 4.4 also show that FTIR spectra for channel and cage zeolite are in good agreement with typical zeolite structures (Flanigen *et al.,* 1971; Chen *et al*., 1999; Hincapie *et al*., 2004). The presence of double ring is shown in the region of 540 – 585 cm^{-1} irrespective of Si/Al ratio. Other infrared bands showing characteristics related to framework topology and assigned to external linkages modes appeared as shoulder near 1050 – 1150 cm^{-1} in the asymmetric stretch region.

4.2.2 Physicochemical properties of zeolite

The IUPAC classification of gas-solid adsorption isotherms covers the behavior of adsorption systems. As accordingly recommended by IUPAC, the first step is to identify the isotherm type and hence the nature of the adsorption process (Sing, 1984). Nitrogen adsorption was carried out using volumetric method as described in Section 3.4.2. The experimental isotherm obtained for channel structures as presented in Figure 4.5 follow type I isotherm except for zeolite beta where the shape of the initial part of isotherm is rather similar to type I but as it reaches saturation, the adsorption rapidly increases to a higher value (Type II). This indicates a shift of micropore-size distribution with formation of larger micropores progressively filled at higher pressure. A slope at the end of the isotherm signify the presence of mesoporous or external surface area (Carvalho *et al*.,1994). Adsorption isotherms of cage structures show a rapid increase in the amount adsorbed followed by a long nearly flat region at higher pressures (Figure 4.6). As reported by Khelifa *et al*. (2004), the volume of the adsorbed phase is limited by the volume of the microporosity at which the adsorption occurred. However, close examination on adsorption isotherm of cage type structure revealed that synthesized zeolite (Na-SZ18) possesses slightly more mesopores than other cage structures. Similar pattern appears for nitrogen adsorption isotherm of 5A zeolite.

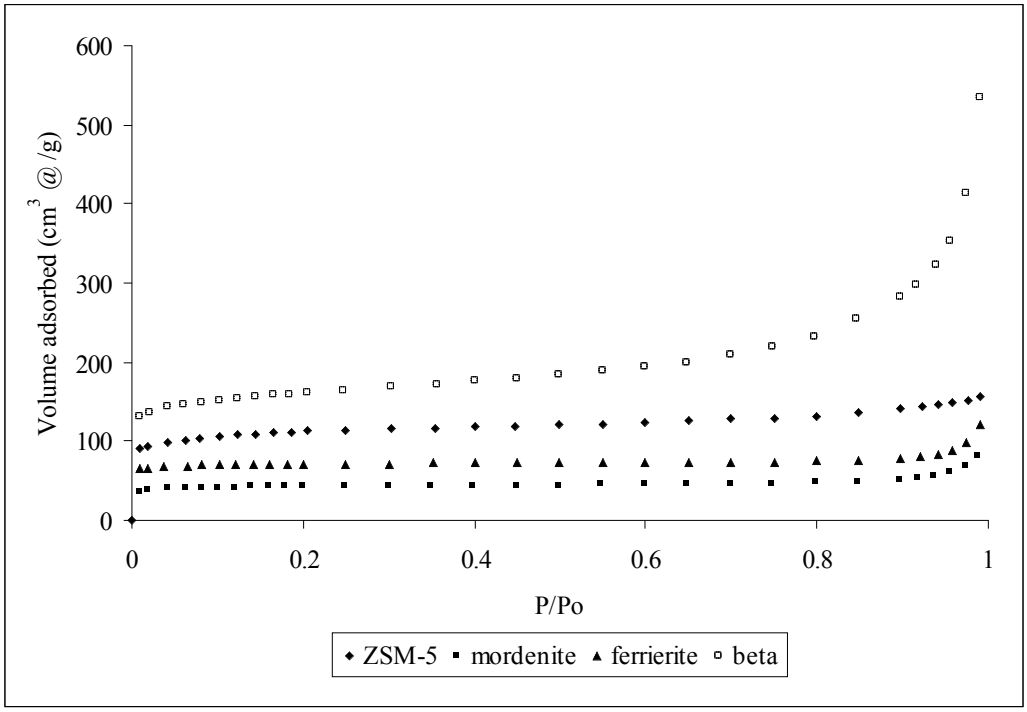

Figure 4.5: Nitrogen adsorption isotherms of channel-type zeolites.

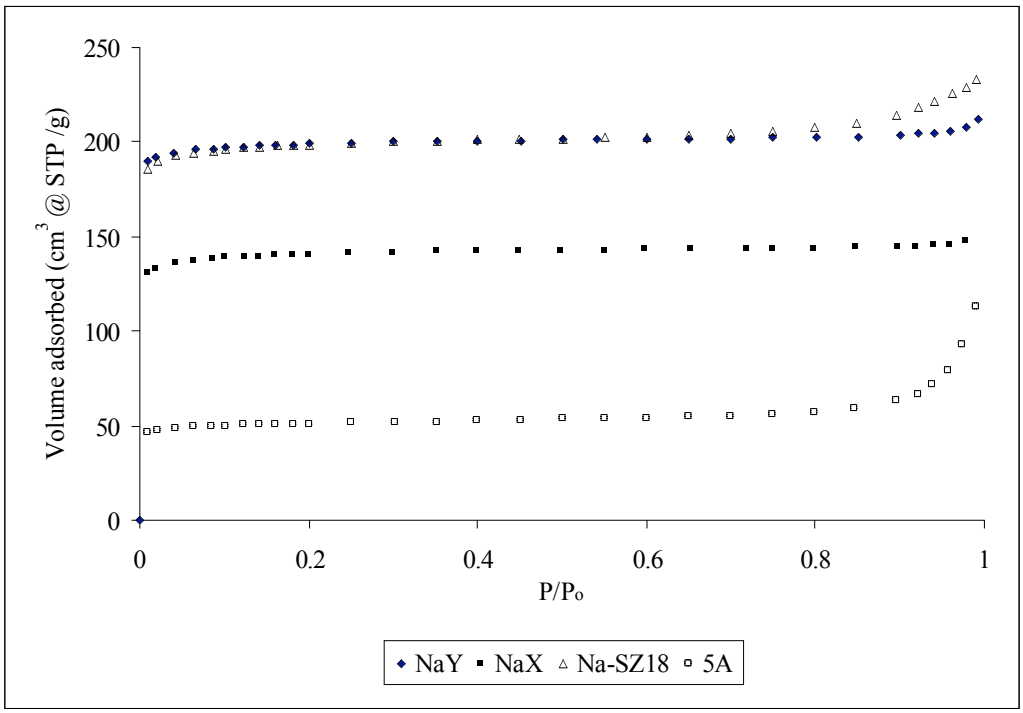

Figure 4.6: Nitrogen adsorption isotherms of cage-type zeolites.

Other properties determined from the adsorption isotherm data are micropore area, pore volume, and average pore diameter. Table 4.3 shows that for channel type zeolites, mordenite has the highest surface area followed by ZSM-5, beta, and ferrierite. The area calculated consists of micropore area and external surface area that provide space for gas molecules to adsorb. These values are in accordance with data provided by Zeolyst International. However, some variation are also reported by Triantafillidis *et al*. (2000) and Sato *et al*. (2003) that the BET surface area of NaY zeolite is 879 m^2/g and 718 m2/g respectively. As discussed in Chapter 2, the differences are due to the complexity of accessing the surface area, which is due to pore blocking that leads to low amount of nitrogen adsorbed on the zeolite. One dimensional pore network or zig-zag channel (ZSM-5) also encounter more blockage inside the pore than three dimensional open framework structures such as zeolite NaY.

In general, faujasite structures offers some advantages in term of surface area and pore volume since it provides more space for adsorbates to accumulate and adsorb inside the cage. These structures also have relatively lower average pore diameter than channel type zeolites which indicate the capability of faujasite structures retaining its microporosity (Table 4.4). As reported by Triantafillidis et al. (2000), large average pore diameter is due to the presence of meso- and macropore that also contribute to the total pore volume. The average pore diameter takes into account the size of micropore and meso-macropore size that was calculated using Equation 3.4.

Table 4. 3: The physical properties of channel-type zeolites calculated from nitrogen adsorption data.

Zeolite	Surface area (m^2/g)		Pore volume (cm^3/g)		Ave. pore diameter (nm)
	BET	Micropore	Micropore	Mesopore /Macropore	
ZSM-5	428.7	357.7	0.145	0.096	2.25
Zeolite beta	494.0	325.7	0.131	0.730	6.97
Mordenite	520.4	461.1	0.180	0.064	3.04
Ferrierite	290.7	275.4	0.106	0.122	2.31

Table 4.4: The physical properties of cage-type zeolite calculated from nitrogen adsorption data.

Zeolite	Surface area (m^2/g)		Pore volume (cm^3/g)		Ave. pore diameter (nm)
	BET	Micropore	Micropore	Mesopore /Macropore	
NaY	820.0	809.5	0.304	0.024	1.60
NaX	567.4	557.7	0.214	0.017	1.63
Na-SZ18	813.6	793.8	0.299	0.061	1.78
5A	204.4	187.2	0.072	0.103	3.42

In addition, for further comparison, calculation based on faujasite group of zeolites was carried out to determine relative crystallinity, unit cell parameter, and Si/Al of zeolites. The XRD data presented in Section 4.2.1 were used to calculate relative crystallinity (Equation 3.1), unit cell parameter (Equation 3.2), and Si/Al ratio of zeolites (Equation 3.4). The zeolites was chosen since it possess cubic symmetry and could easily be determined by the lattice constant along the *a* direction. In order to calculate the total intensities of the samples, six peaks at *hkl* positions of 331, 551, 440, 533, 642, and 555 are chosen (ASTM D3906). The peaks intensities are shown in Table 4.2. The total intensities are compared with the total intensities of the selected reference sample (NaY is assigned as reference sample with relative intensities 100 %). The results show that relative crystallinity of NaX and Na-SZ18 is 88 % and 66 % respectively. The values give some indications of the amount crystallite formation in the sample. The unit cell parameter and Si/Al ratio were calculated using Equations 3.2 and 3.4 respectively. The unit cell dimensions decrease upon increase of the Si/Al ratio which is due to the bond length of Si-O (0.162 nm) that is shorter than Al-O (0.172 nm), thus leads to smaller dimensions of the unit cell (Bae and Seff, 2001).

Table 4.5: The physical properties and Si/Al ratio of faujasite type zeolites calculated from XRD data.

Zeolite	Rel. crystallinity (%)	Unit cell parameter (Å)	Si/Al ratio
NaX	88	25.00	1.06
Na-SZ18	66	24.85	1.53
NaY	100	24.67	1.60

4.3 Adsorption Equilibrium

Adsorption of gases on different adsorbents and comparison on the adsorption properties are of great importance in the development of adsorption process especially in the area of gas separation and purification and adsorptive gas storage. As discussed in Chapter 2, it can be anticipated that several factors affect the adsorption of gases particularly on microporous zeolite. Therefore, using methane (CH_4) and carbon dioxide (CO_2) adsorption as adsorbates, gas adsorption measurements were carried out to determine gas adsorption capacity, gas adsorption isotherm, and the uptake rate of the adsorbents.

4.3.1 Gas adsorption capacity

4.3.1.1 Effect of different types of structures

Zeolite frameworks contain pores, channels and cages of different dimensions and shapes. These properties may influence the amount of methane and carbon dioxide adsorb on zeolites. In this study, adsorption capacity of samples at 137 kPa and 323 K was measured according to procedures described in Section 3.5.2. The amount of the gas adsorbed is the difference between the initial weight (solid adsorbent) and final weight (adsorbent + gas adsorbed) that was expressed as mol of adsorbed gas per gram of solid adsorbent (mmol/g). Therefore, using different zeolite structures, properties that affect the performance adsorption were evaluated.

Firstly, comparison was made between channel and cage type zeolite to determine the most effective structure for adsorption. Based on physical and

chemical properties of zeolite, factor(s) that influence the adsorption characteristics of adsorbates will then be identified. Nevertheless, other aspects such as properties of gases and the gas operating condition that might influence the adsorptive characteristic of gases will be discussed in other sections. The adsorption capacity of structurally different zeolites is shown in Figures 4.7 and 4.8. The amount of adsorbed adsorbates increase according to the following order,

CH_4: SZ-18 > NaX > NaY > zeolite A > FER > ZSM-5 > zeolite beta > MOR

CO_2: SZ-18 > NaY > NaX > zeolite A > FER > ZSM-5 > MOR > zeolite beta

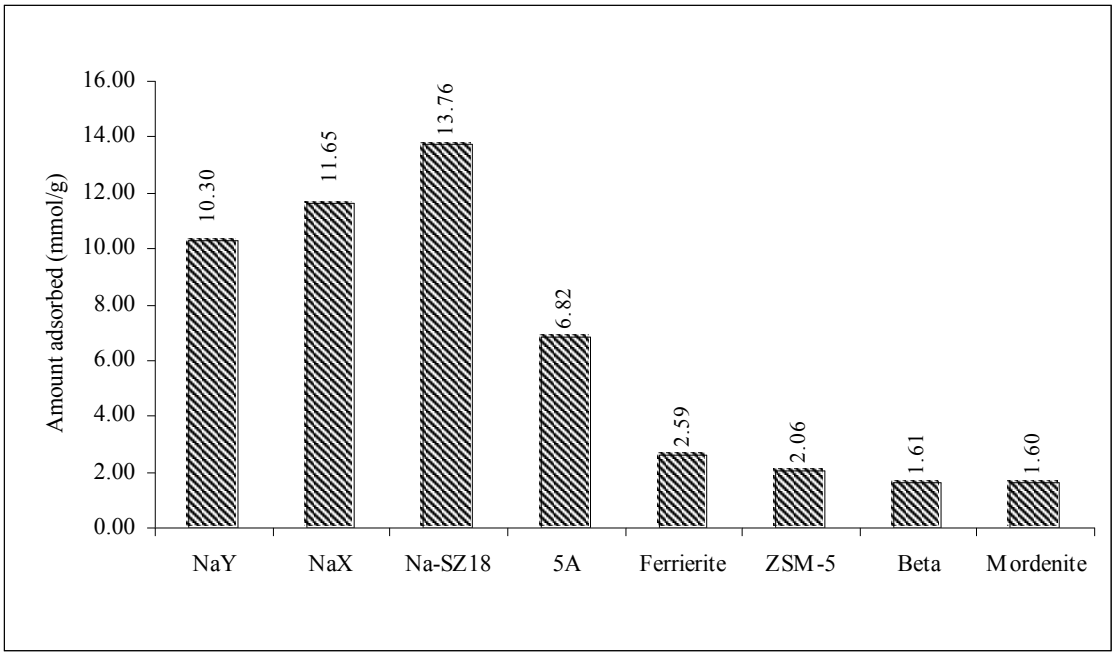

Figure 4.7: The methane adsorption capacity on different types of zeolites at 323K and 137 kPa.

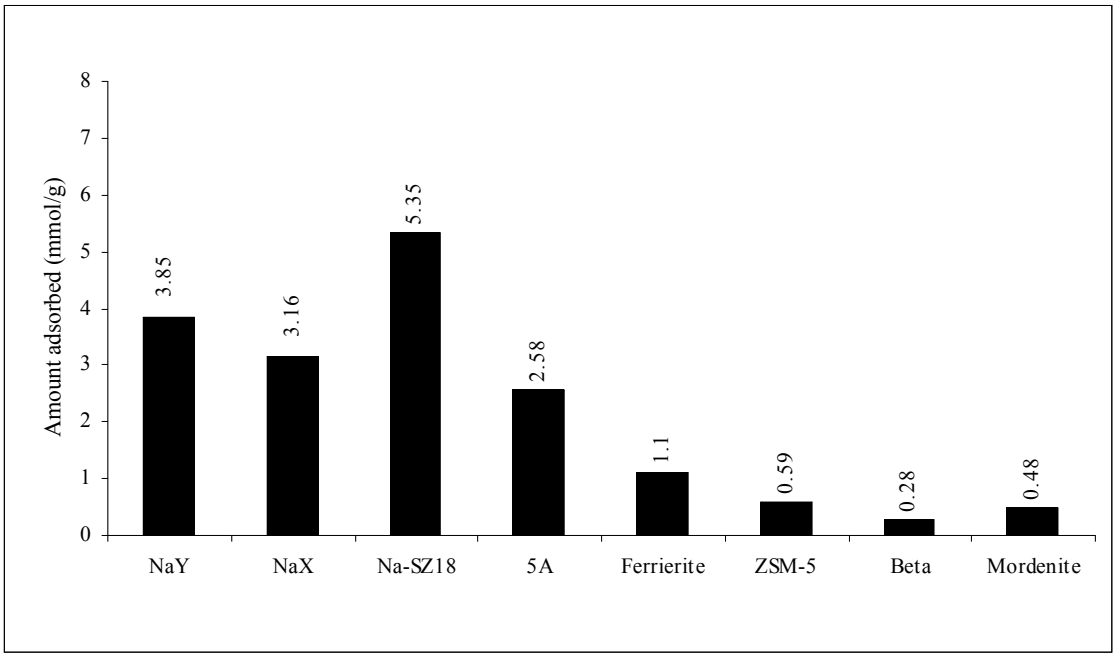

Figure 4.8: The carbon dioxide adsorption capacity on different types of zeolites at 323K and 137 kPa.

Several important findings were observed on the adsorption capacity of zeolites. First, adsorption at 323 K and 137 kPa shows that cage type structures are capable to adsorb more gases than channel type zeolites. Second, in cage type structure, synthesized faujasite structure (Na-SZ18) is a better adsorbent than commercial samples (NaX and NaY). The third observation shows that there are differences on the sequence of CH_4 and CO_2 adsorption capacity in which indicate that there were no common factors controlling the adsorption of these adsorbates. Finally, the amount of CH_4 adsorbed is relatively higher than CO_2. Therefore, in the following sections, the effect of structural and physicochemical properties of zeolite on gas adsorption will be discussed in order to highlight the behavior of CH_4 and CO_2 adsorption on zeolites.

4.3.1.2 Effect of pore system

Adsorption on a series of materials classified as channel and cage type zeolites demonstrates the effect of structural framework on gas adsorption. As presented in Section 4.3.1.1, cage-type structures demonstrate better performance than channel-type structure. High adsorption capacity could be associated with the presence of supercages and sodalite cages that encapsulated adsorbates inside the structure. Channel type structures provide the channel itself for the molecules to adsorb. However, according to van Well (1998), ferrierite pore structure not only consists of intersecting channel but also cages-like structures with diameter of about 0.7 nm. This explains the reason why ferrierite demonstrated better adsorption than ZSM-5, beta and mordenite. It also suggests that the formation of cages contribute to high adsorption capacity.

In addition, pore network that connected the channels and cages might affect the diffusivity of adsorbates. Any deposition inside the channel can affect the diffusivity and adsorptivity of gas molecules. Adsorption in parallel channel (mordenite) is considered faster than the zig-zag channel, however once the channel is blocked, the adsorbate could not diffuse further to the adsorption sites. As for ZSM-5, zig-zag channels may encounter some problems at the intersection since any deposition could either partially or fully obstruct the diffusion and thus, affect the adsorption of adsorbates even though the zeolite has three dimensional pore system (Figure 4.9). At 323 K and 137 kPa, cage structures shows better adsorptive characteristic than the channel structures. At this pressure, more gas molecules can enter the cage that results in high adsorption capacity of adsorbates. This results are in agreement with earlier findings reported by Cook (1961), and Breck (1964) that cage structures (zeolites A and X) act as storage container for monoatomic molecules such as argon and krypton.

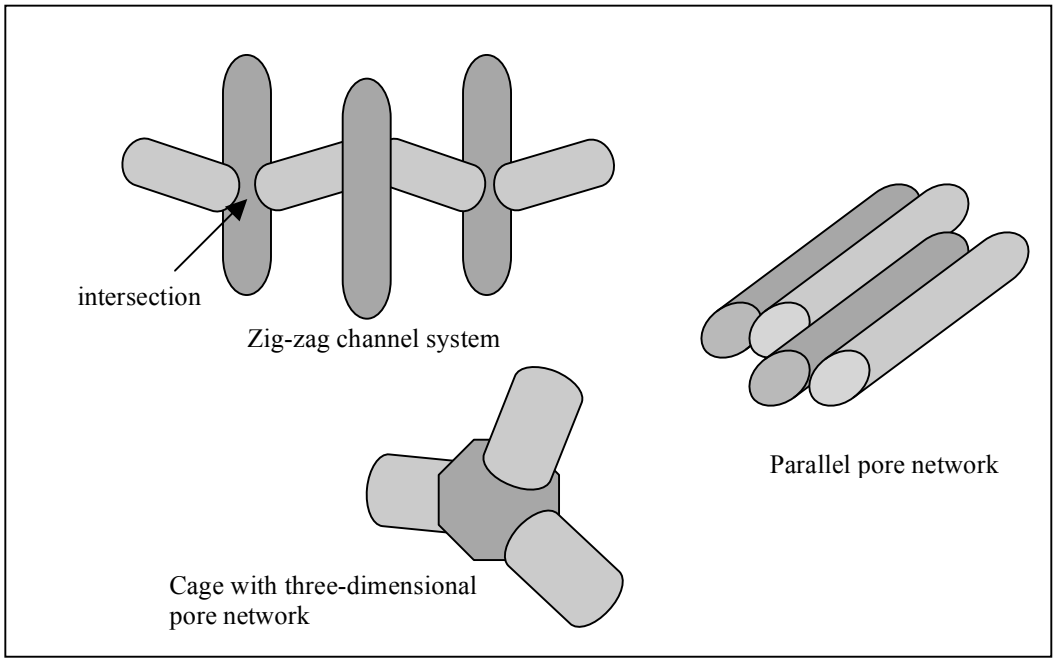

Figure 4.9: Zeolite pore system of zig-zag, parallel, and three dimensional pore network systems.

The difference in the amount of CH_4 and CO_2 on zeolite is also attributed to the properties of adsorbates. However, it is important to note that the study on cage structures shows that synthesized faujasite-like zeolite (Na-SZ18) has better adsorption capacity than other types of adsorbents. Hence, by understanding the factors that influence the adsorption on the zeolite, selected structures could be engineered to obtain a good and an effective adsorbent for specific applications.

4.3.1.3 Effect of pore size

As presented in Table 4.1, the pore opening of faujasite structures (cage type zeolites) is larger than channel type zeolites. However, it is also important to note that other types of zeolites used in this study have at least two channel systems with different pore dimensions that are large enough for adsorbates to diffuse into the

pore system (Table 4.1**).** The presence of smaller pore dimensions (for example, 0.26 x 0.57 nm for mordenite) also affects the diffusivity thus the adsorption capacity of the adsorbates. As reported by Bae and Lee (2005), the kinetic diameter of the CH_4 and CO_2 is 3.8 Å and 3.3 Å respectively. It is expected that the molecules can only enter porous network through selected channels. In addition, the presence of zig-zag or sinusoidal channel may also affect the diffusivity of gases in ZSM-5. Moreover, the accessibility is also refused if the pore blockage occurred due to the collapse of the lattice structure. These explained the reasons of low adsorption for several types of zeolite. The effect of zeolite pore size on the adsorption capacity of methane and carbon dioxide are shown in Figures 4.10 and 4.11.

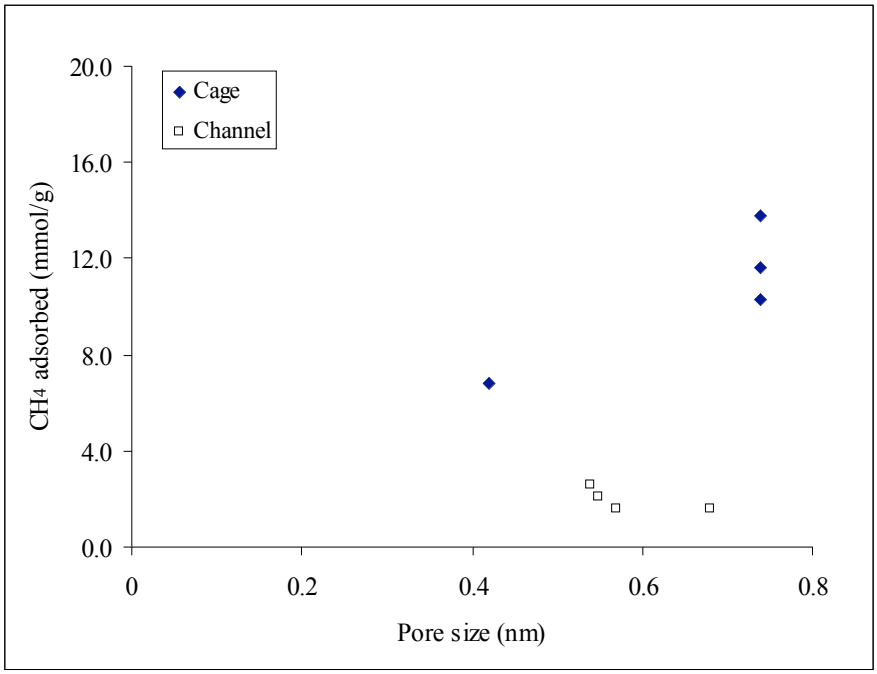

Figure 4.10: The amount of methane adsorbed on different zeolites as function of pore size.

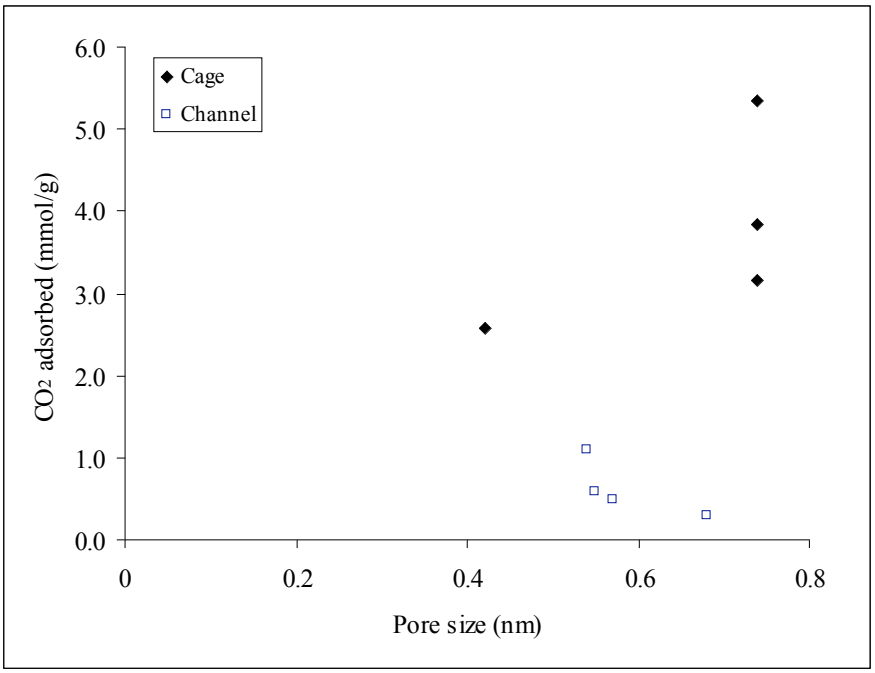

Figure 4.11: The amount of carbon dioxide adsorbed on different zeolites as function of pore size.

This study shows that faujasite structures have higher adsorption capacity than zeolite A and channel type zeolites (ZSM-5, mordenite, ferrierite, and beta). Since the pore opening of faujasite structure is twice the size of gas molecules, problem due to pore blockage is not significant. Even if the gas molecules adsorbed at the pore opening, other gas molecules can still diffuse through the pore window and adsorb onto the inner side of the cage. In addition, the presence cage structures also contribute to higher methane and carbon dioxide adsorptions. As the pore and cage size of zeolite A (0.42 nm and 1.10 nm respectively) are smaller than faujasite structures (0.74 nm and 1.30 nm respectively), this explained the reason of lower adsorption for zeolite A than other types of cage zeolites.

As discussed in previous section, the presence of cages in ferrierite contributes to slightly higher adsorption capacity than other zeolites of the same group (ZSM-5, beta and mordenite). As the smallest dimension for ferrierite is 0.48 x 0.35 nm, it is assumed the molecules can still pass the pore aperture at the right

orientation. In addition, Coker *et al*. (1998) have reported that zeolite frameworks are inherently flexible and readily to change symmetry or undergo distortions in response to changes in temperature or adsorbed species. Silicon and oxygen atoms that formed the zeolite framework are thermally in motion and this will allow a slightly bigger molecule to pass through the pore opening. Figure 4.12 shows the pore opening of 8 and 10-membered rings that exist in zeolite structural framework. CH_4 and CO_2 molecules could easily diffuse through the pore with 10-membered ring or even bigger pore (Barrer, 1982; van Bekkum et al., 1991; Nagy et al., 1998). However, for 8-membered ring or less, some molecules (in this case is CO_2 molecules) could only diffuse at certain molecules orientation. The adsorption at the pore opening could hinder other molecules to diffuse and adsorb through the channel and cages.

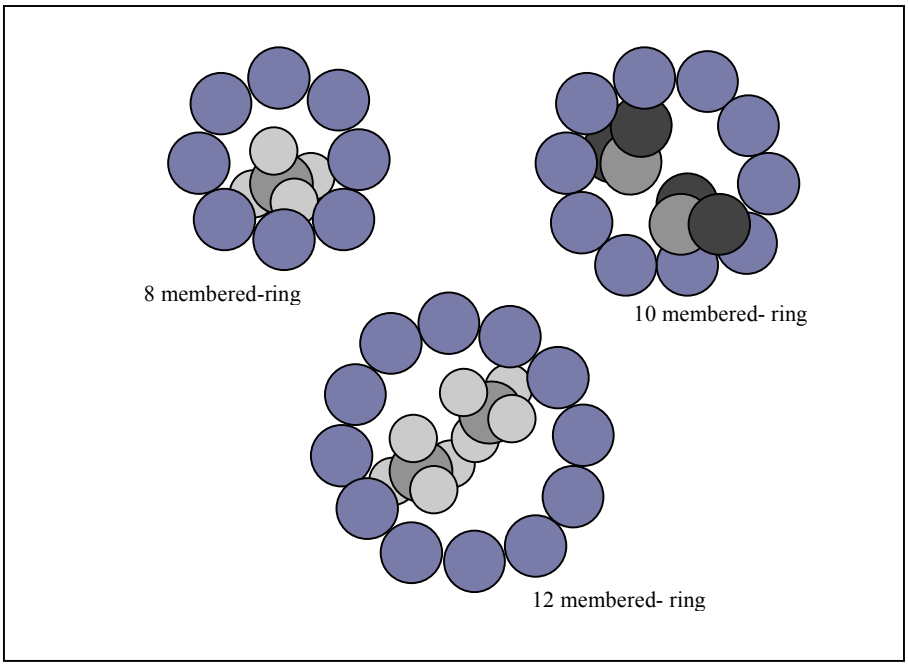

Figure 4.12: A schematic diagram of methane and carbon dioxide diffuse through different zeolite pore openings.

4.3.1.4 Effect of surface area and pore volume

Generally, high surface area and pore volume leads to high adsorption capacity. Evidently, this general statement could not be easily applied since at the same time other factors may also influence the amount of gas adsorbed on zeolite. Even though it is clearly shown that the surface area (~ 800 m^2/g) and pore volume (0.214 cm^3/g) of faujasite structures lead to high adsorption capacity, the adsorption of mordenite with relatively high surface area (520 m^2/g) and pore volume (0.180 cm^3/g) does not follow the theoretical sequence. In fact, zeolite A with lower surface area (~ 200 cm^2/g) and pore volume (0.072 cm^3/g) has higher adsorption capacity than mordenite. Similarly, ZSM-5 and zeolite beta did not perform as a potential adsorbent for CH_4 and CO_2. The relationship between surface area and pore volume are shown in Figures 4.13 and 4.14 respectively.

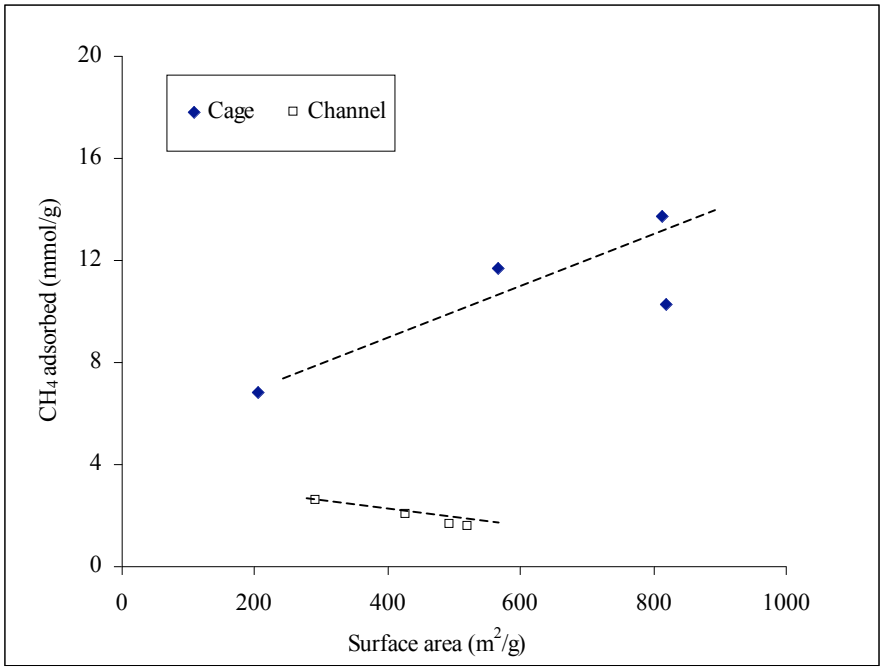

Figure 4.13: The amount of methane adsorbed on cage and channel zeolites as a function of zeolite surface area.

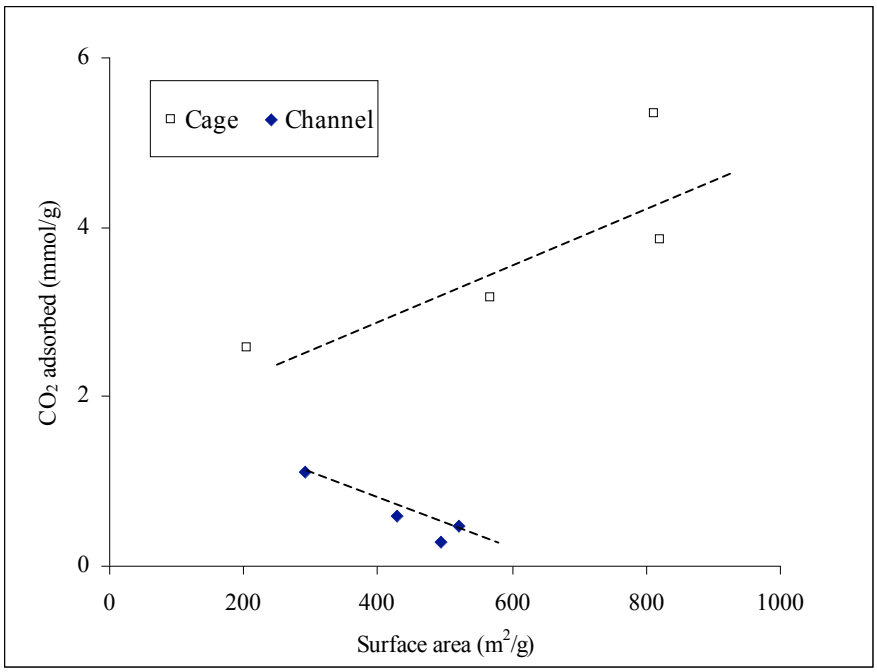

Figure 4.14: The amount of carbon dioxide adsorbed on cage and channel zeolites as a function of zeolite surface area.

Even though a fundamental understanding on adsorbent indicate that high surface area and large pore volume lead to high adsorption capacity, this study shows that adsorption of CH_4 and CO_2 does not exactly follow this general assumption on adsorption. For cage type zeolites, high surface area leads to high adsorption capacity which indicates by the confinement effect of zeolites structures (Chmelka *et al*., 1991 and Jameson *et al*., 1992). However, channel type zeolite does not follow the theoretical sequence, in fact, opposite relationship could be observed as methane and carbon dioxide were adsorbed on zeolites. Similar relationships are also observed in pore volume-adsorption capacity of methane and carbon dioxide (Figures 4.15 and 4.16). The results suggest that pore diameter have more influence on adsorption characteristics of methane and carbon dioxide. For example, inside the narrow channel of ferrierite, the adsorbate cannot pass each other, thus the mobility is greatly reduced. In addition, the presence of zig-zag channel in the pore network system of ZSM-5 can also caused blockage that hinder the adsorbate to reach the adsorption sites (Barrer, 1982, Wu *et al*., 1983; Kurama *et al.*, 2002; Schuring, 2002).

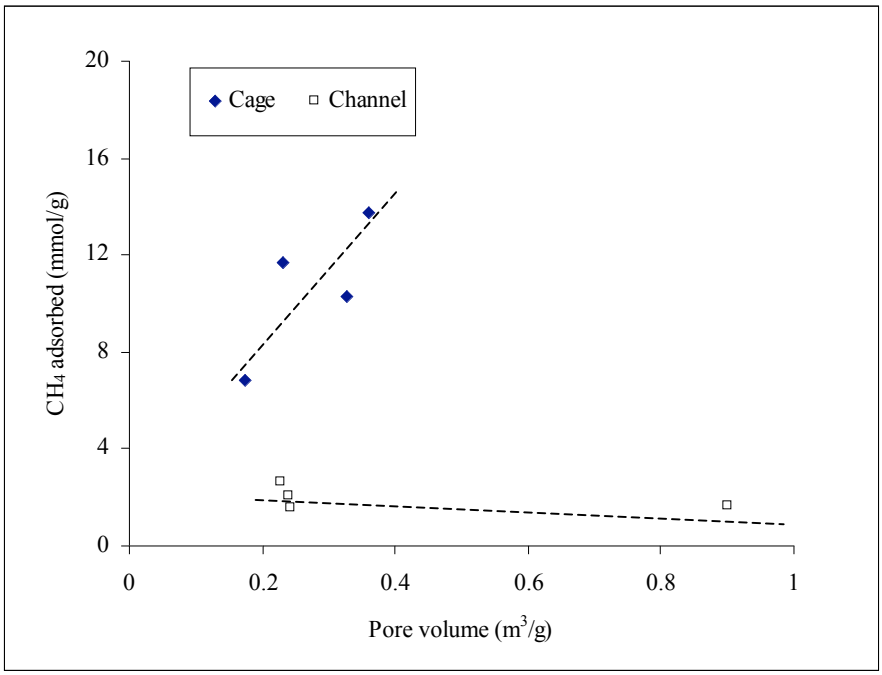

Figure 4.15: The amount of methane adsorbed on cage and channel type zeolites as a function of average pore volume.

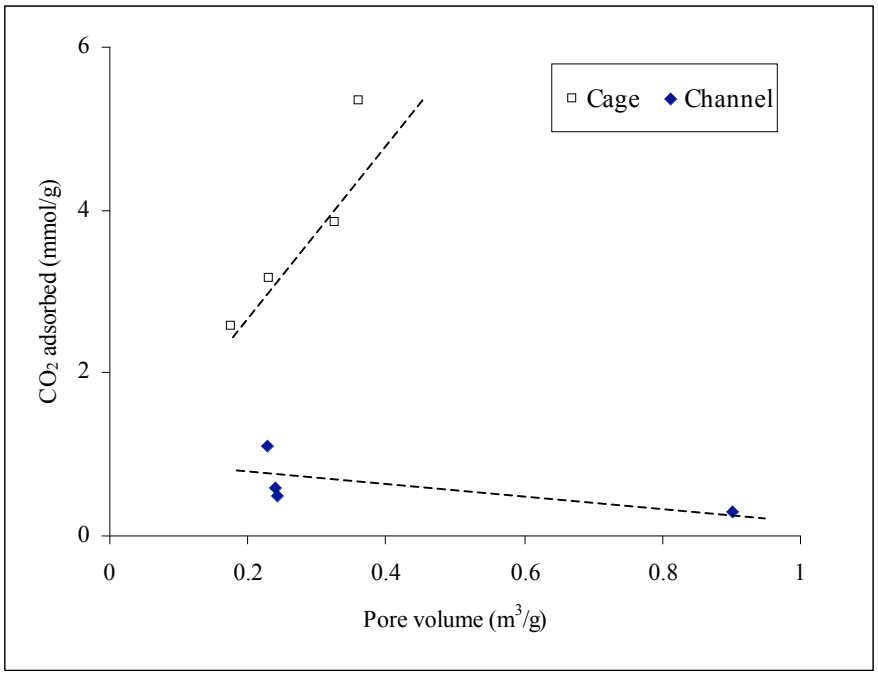

Figure 4.16: Amount of carbon dioxide adsorbed on cage and channel type zeolites as a function of zeolite pore volume.

As previously mentioned, Chmelka *et al*. (1991), Jameson *et al*. (1992) and Schuring (2002) have elucidated the presence of confinement effect in various zeolite materials. It is also possible to gain insight into the confinement effect of cage structures from the evaluation on fractional surface coverage (Table 4.6). In this study similar effect could be observed, in which surface coverage ratios for CH_4 on cage structures are greater than 1. Zeolite A has the highest ratio ($\theta_R = 2.09$), followed by NaX ($\theta_R = 1.78$), Na-SZ18 ($\theta_R = 1.47$), and NaY ($\theta_R = 1.09$). As a result of confinement effect, the molecules were highly packed inside the cage structures. On the other hand, the results on channel type zeolites show that the adsorbed molecules (CH_4) covered only 77 % of ferrierite surface. Other types of zeolites have even lesser values ($\theta_{RZSM-5} = 0.42$, $\theta_{Rbeta} = 0.28$, and $\theta_{Rmor} = 0.27$) which indicate that only part of the adsorbent surface was covered by the adsorbates.

Table 4.6: The fraction of surface coverage for methane (CH_4) and carbon dioxide (CO_2) for different zeolites.

Zeolite	Fraction of surface coverage, θ_R	
	CH_4	CO_2
Channel:		
ZSM-5	0.42	0.09
Beta	0.28	0.04
Mordenite	0.27	0.06
Ferrierite	0.77	0.25
Cage:		
NaY	1.09	0.31
NaX	1.78	0.36
Na-SZ18	1.47	0.43
5A	2.09	0.83

However, the confinement effects were not evident in the adsorption of CO_2 even though the surface coverage values for cage type zeolites are higher than channel type zeolites. The difference could be attributed to the properties of adsorbates, strong interaction between the active site (adsorption site) and quadrapole moment of carbon dioxide could possibly result in pore blockage. This phenomenon might hinder further diffusion to occur.

In general, porosity of zeolites does not directly influence gas adsorption characteristics but as mentioned in many literatures, large surface area is preferable, since the creation on internal surface area in a limited volume inevitably gives rise to large numbers of small sized pores that allow adsorption to take place. The presence of large cavities allows more molecules to be confined inside the cages, thus increase the amount of adsorbate adsorbed. However, there are other factors such as pore opening, and structure of the pore wall, the interaction between the surface atoms and the diffusing molecules, and the way the channels are connected (Schuring, 2002) that also influence the adsorption of methane and carbon dioxide.

4.3.1.5 Effect of crystallinity

Besides the pore system, pore size, micropore area, and micropore volume, the crystalline phase formation could also play a role in determining the adsorption capacity of zeolites. By comparing the XRD patterns of channel and cage type zeolites (Figures 4.1 and 4.2), it is clearly shown that the crystallite formation of cage type zeolite is more evident than channel type zeolite. The presence of amorphous phase could be clearly observed by the broad reflection of zeolite beta diffractogram. Even though XRD patterns do not give any indication on the extent of pore formation, relative crystallinity might give some indication on structural defects that occurred within the structure. Relatively, the values indicate the extent

of destruction on structural framework or part of the structure. Depending on the type of crystal imperfection, the adsorption process might be affected.

In the case of zeolite beta, low crystalline phase also contributes to low adsorption of CH_4 and CO_2 since the surface area available is mainly external surface area. However, crystallinity is not the only factor that determines the adsorptivity of gas molecules. Table 4.7 shows that high relative crystallinity does not ensure high adsorptive capacity. It was also found that zeolite with slightly lower crystallinity (Na-SZ18) adsorbed more than the other faujasite samples. It is also important to note that surface area were determined based on the adsorption of nitrogen at very low temperature (77 K) where condensation might occur. Since this study involves adsorption at higher temperature (323 K), condensation is not possible for both adsorbates.

Apart from the entrapment inside the cage, structural defects and extra-framework species also function as additional adsorption sites (Murphy, 1996). This explain the reason why the adsorption capacity of Na-SZ18 higher than NaY. However, this result does not conclusively indicate that crystallinity has no influence on gas adsorption, but rather shows that other factors are more dominant than crystallinity in determining the amount of gas adsorbed on zeolites understudied.

Table 4.7: The relative crystallinity and the amount of CH_4 and CO_2 adsorbed on faujasite structures.

Zeolite	Relative crystallinity (%)	Amount adsorbed (mmol/g)	
		CH_4	CO_2
NaY	100	10.30	3.85
NaX	90	11.65	3.16
Na-SZ18	76	13.76	5.35

4.3.1.6 Effect of Si/Al ratio

As mentioned earlier, Si/Al ratio affect the unit cell parameters since the length of Si—O is shorter than Al—O. Thus, the unit cell parameters decreases as the ratio increases. However, since the changes are relatively small, Table 4.8 shows that adsorption capacity was not affected by Si/Al ratio and unit cell parameters. However, the amount of aluminium in the zeolite framework determines the number of charge balancing cation which in turn would probably affect gas adsorption characteristics. Discussion on the effect of cation's size and charge will be discussed in Chapter 5.

In general, the structural and physical properties, and zeolite chemical composition might influence the adsorptivity of the gases. This phenomenon has important implications for the use of zeolites for separation and purification, and adsorptive gas storage. The selection of suitable adsorbent is the determining factor for the successfulness of the adsorption process. Mismatching between the adsorbate size and the pore size of adsorbent for example, could result in low performance of the adsorption process.

Table 4.8: The Si/Al ratio and unit cell parameter of faujasite structures.

Zeolite	Si/Al ratio	Unit cell parameter, a_o (Å)	Amount adsorbed (mmol/g)	
			CH_4	CO_2
NaX	1.06	25.00	11.65	3.16
Na-SZ18	1.53	24.85	13.76	5.35
NaY	1.60	24.67	10.30	3.85

4.3.2 Gas adsorption isotherms

Adsorption system is usually characterized at equilibrium by the adsorption isotherm, a plot of the adsorbed phase concentration against the gas phase concentration or partial pressure at equilibrium. As discussed by Seidel-Morgenstern (2004), there are several methods capable of measuring adsorption isotherms, but the most common method is either gravimetric or volumetric method. In this study adsorption isotherms of CH_4 and CO_2 were determined at 298 K in a volumetric apparatus as described in Section 3.5.1. Samples selected to represent the channel type zeolites are ZSM-5, and ferrierite, and for cage type structures are NaY, NaX and Na-SZ18. Contrary to nitrogen adsorption isotherm, the shape of the curves is now dependent on type of adsorbates and the adsorbents.

The adsorption isotherms of CH_4 and CO_2 are shown in Figures 4.17 and 4.18 respectively. The adsorption isotherms show a linear increase of CH_4 adsorption but an abrupt increase of CO_2 adsorption over pressure ranges understudy. Similar phenomena were also reported by Khelifa *et al*. (1999). At this temperature, CO_2 adsorption is markedly greater than CH_4 adsorption. As expected, adsorption isotherm of CH_4 is far from saturation.

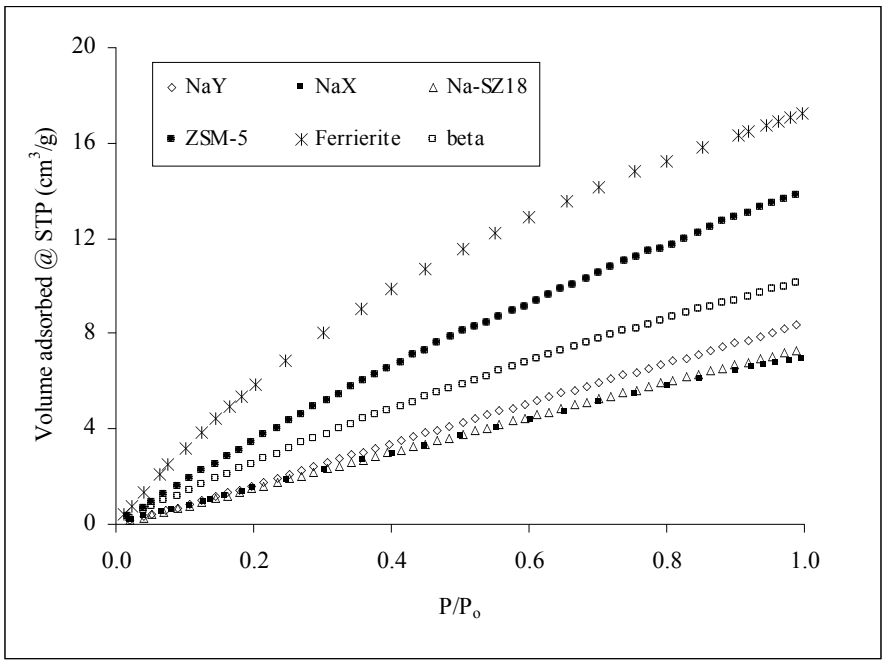

Figure 4.17: The methane adsorption isotherms on channel and cage type zeolites at 298 K.

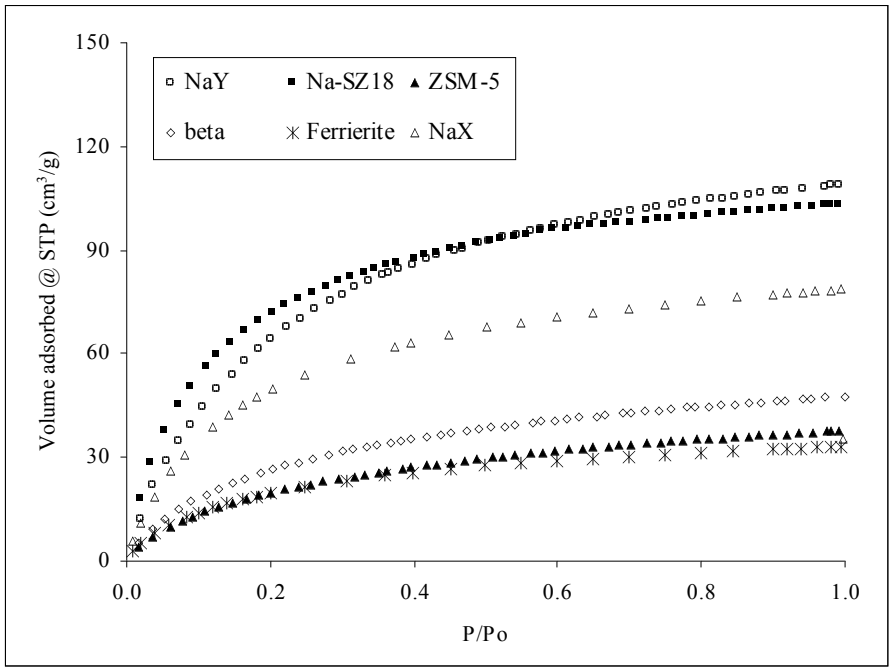

Figure 4.18: The carbon dioxide adsorption isotherms for channel and cage type zeolites at 298 K.

The adsorption isotherm curves obtained reveal that CO_2 has greater affinity to adsorb than CH_4 even though the kinetic diameter of CH_4 (3.8 Å) and CO_2 (3.3 Å) are comparable and small enough to pass through the pore opening of zeolites. The adsorption isotherms show that CO_2 adsorbs at least 10 times greater than CH_4. The specific interaction of quadrapole of CO_2 molecule with electric field created by cation is likely the reason for higher adsorption of CO_2. These results also suggest that non-polar molecules such as CH_4 have low adsorption affinity towards zeolites. These results are in accordance with previous observation by Hernández-Huesca *et al*. (1999) and Maurin *et al*. (2005c) in which high adsorption is probably due to the specific interaction of the quadrapole of CO_2 molecules with zeolite structure.

The adsorption isotherms of CH_4 reveal interesting phenomena in which channel type zeolite adsorbed more than cage type zeolites. However this could be due to the diffusivity of CH_4 molecules through the pore of zeolites. Since the average pore diameter of channel type zeolites are relatively larger than the cage type zeolites, as non-polar molecules, CH_4 are more easily diffused through the larger pore network system. However, this circumstance is not applicable for CO_2 since it has the quadrapole moment that specifically determine at which site it would be attached to. Moreover, rapid increase also indicates that there are strong interactions between the adsorbate and the adsorbents.

It has been realized that the presence of sodium cations could improve the surface properties of zeolites since the ratio of Si/Al for cage type zeolites is much lower than channel type zeolites. As mentioned earlier, Si/Al for NaY and Na-SZ18 is 1.60 and 1.53 respectively. Hence, in every unit of NaY structural framework, there are 16 silicon atoms (Si) and 10 aluminium atoms (Al) arranged together to form AlO_4^- or SiO_4 tetrahedra. Sodium ions or other cations are required to balance the negative charge in the framework and at the same time produce strong electrostatic field within the structural that could specifically interact with the adsorbates such as CO_2.

In order to elucidate further the adsorption characterictics of gas adsorption on zeolite, the experimental adsorption isotherm data were fitted into several well-known adsorption model equations. Parameters of the equation model were estimated using methods described in Section 3.6. The adsorption isotherm data involve the volume of methane and carbon dioxide adsorbed at standard temperature and pressure (STP). As discussed in Chapter 2, Henry, Langmuir, Freundlich and Dubinin-Polanyi equations have long been used to describe the adsorption of gas on adsorbent mostly on activated carbon and to lesser extent on zeolite. In this study, the applicability of the model equations was examined for the adsorption of methane and carbon dioxide at room temperature. Figures 4.19(a) and (b) show that the methane adsorption data fits very well with Henry's equation indicates that adsorption occurs in a dilute form. The Freundlich equation, further verifies this condition (dilute form) where α values are close to unity and the equation reduces to a linear equation (Henry's type of equation). Similar trend was also observed by Maurin *et al*. (2005b).

However, Henry's equation could only be applied at extremely low concentration of CO_2, in which occurs at very low adsorption pressure. Hence, as the pressure increases up to 1 bar, CO_2 adsorption could be better described either by Langmuir or Freundlich models (Figures 4.20 and 4.21). According to Yang (1997), Langmuir equation is clearly a model for localized adsorption. However, even when the adsorbed molecules are mobile, the isotherm could be determined by the above equation. The Langmuir parameters of CO_2 adsorption on NaX is in accordance with reported values (Ahn *et al*., 2004). So, Langmuir equation could be used as a correlating equation even when the above assumptions are not completely fulfilled. Furthermore, using Langmuir model, it is possible to determine and to compare the maximum loading of gases on selected zeolite based on the assumption that monolayer adsorption occurred. Using this model, the maximum adsorption, q_m and B, Langmuir constant could be determined. The constant is temperature dependence and its value decreases rapidly with increasing temperature (Yang, 1997). The values obtained are in close agreement with Freundlich and Langmuir parameters for methane and carbon dioxide adsorption on zeolite reported by Choudhary and Mayadevi (1996).

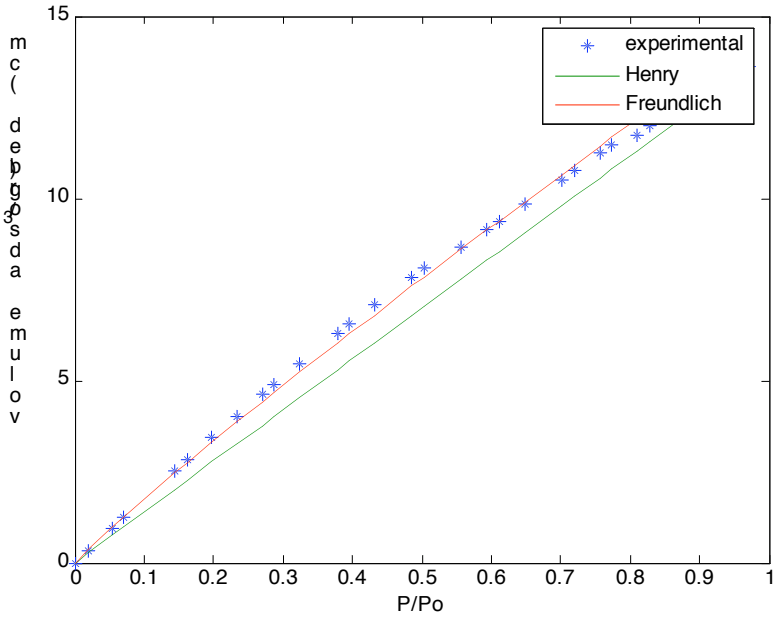

(a)

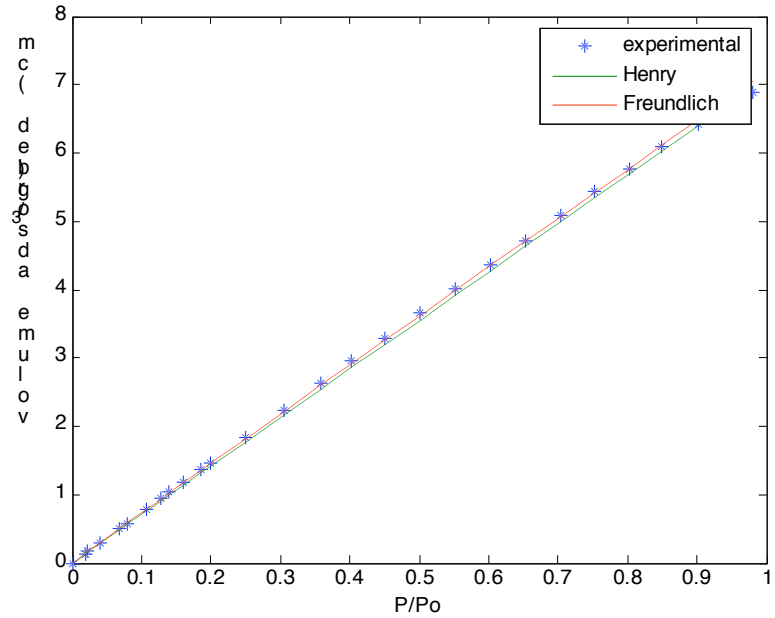

(b)

Figure 4.19: The adsorption isotherm of methane fitted into Henry and Freundlich equations: (a) ZSM-5 and (b) NaX.

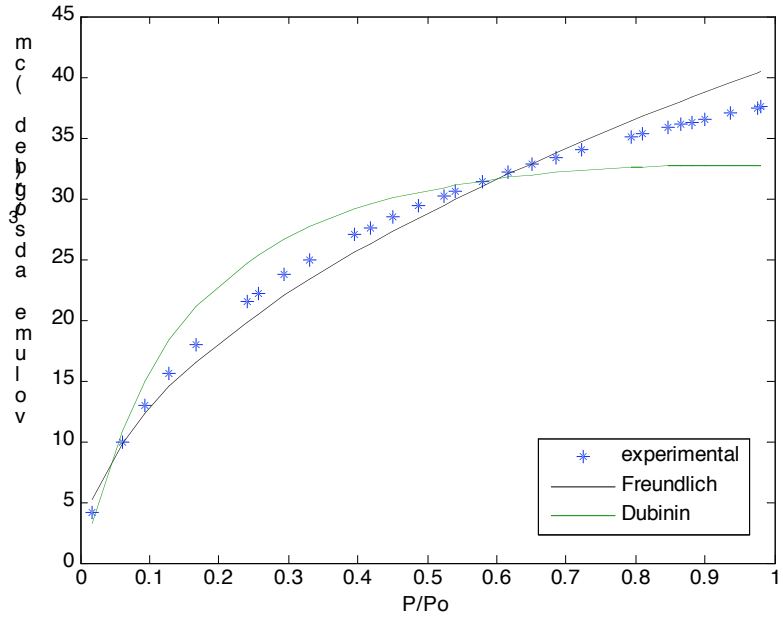

(a)

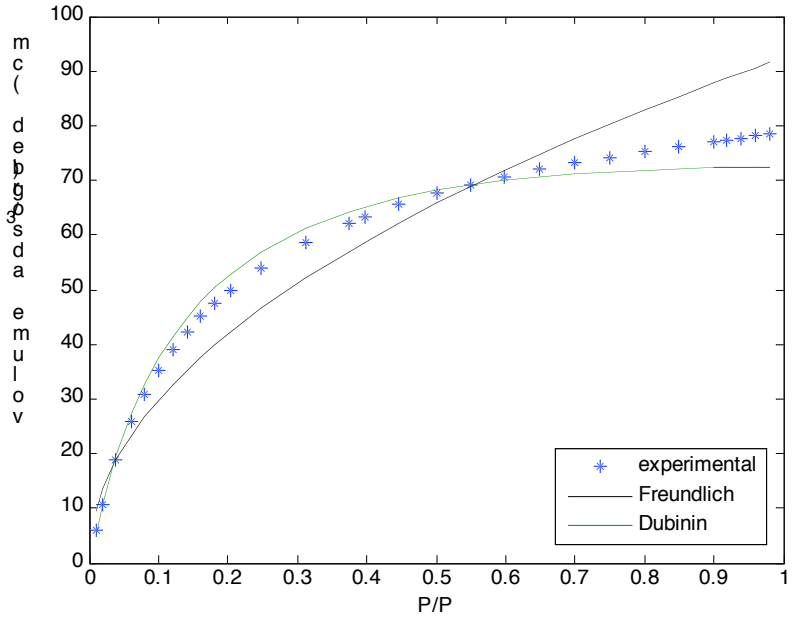

(b)

Figure 4.20: The adsorption isotherm of carbon dioxide fitted into Freundlich and Dubinin equations: (a) ZSM-5 and (b) NaX.

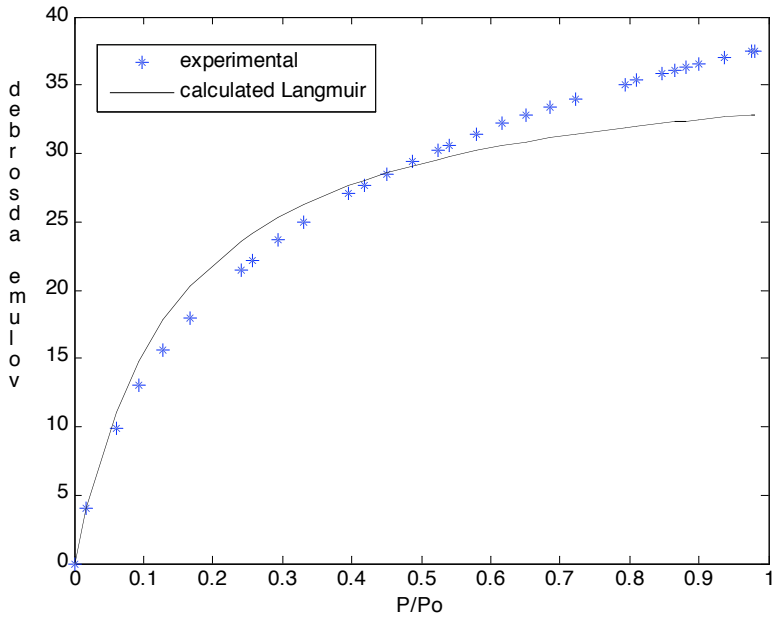

(a)

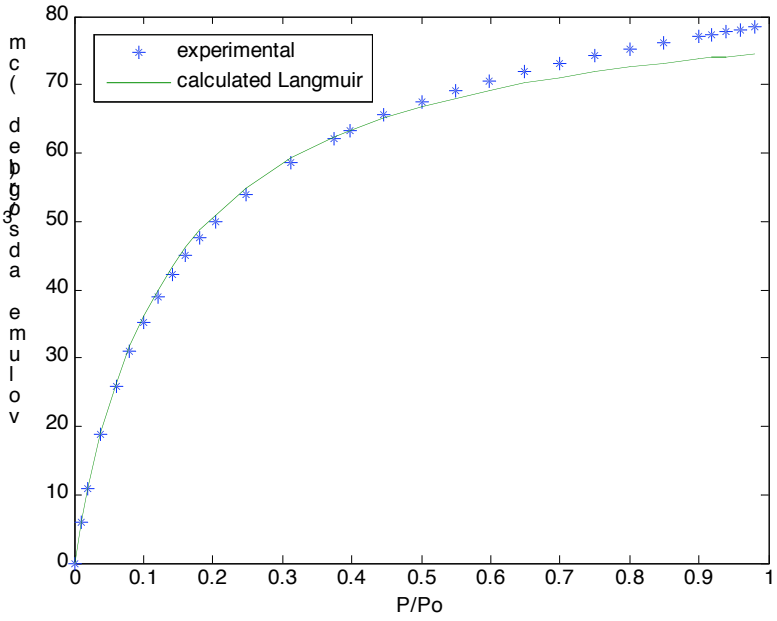

(b)

Figure 4.21: The adsorption isotherm of carbon dioxide fitted into Langmuir equation: (a) ZSM-5 and (b) NaX.

In describing gas adsorption, Polanyi viewed the process as a gradual concentration of gas molecules toward the solid surface according to potential theory, resembling the atmosphere of a planet (Yang, 1997). As reported by Sievers and Mersmann (1994) characteristic curves would be useful to extrapolate any equilibrium from one reference state. The characteristics curves should be independent of temperature. However, since the adsorption of methane involves a very dilute concentration, Dubinin-Polanyi equation only best fitted into carbon dioxide adsorption data (Figure 4.20) and at lesser extent to methane adsorption data. Conversely, the model constants (*C* and *D*) could be used to obtain a characteristic curve describing carbon dioxide adsorption. The results also show that for each adsorbate, the constants are limited to a rather narrow range of values, thus agree with the Dubinin's characteristic curves given by Yang (1997) and Choudhary and Mayadevi (1996). The estimated values of the model constants of the best fitting adsorption isotherm for CH_4 and CO_2 are presented in Tables 4.9 and 4.10. The values are found to be in accordance to results reported by Triebe *et a*l. (1996) on channel type.

Table 4.9: The model constants calculated from the fitting of CH_4 adsorption isotherm data of different zeolites.

Zeolite	Henry's	Freundlich		Dubinin-Polanyi	
	k	*K*	*1/n*	*C*	*D*
Channel:					
ZSM-5	13.96	14.78	0.92	2.25	0.25
Ferrierite	16.95	19.37	0.81	2.53	0.20
Cage:					
NaY	8.48	8.59	1.03	1.47	0.26
NaX	7.10	7.19	0.99	1.65	0.28
Na-SZ18	7.44	7.50	1.00	1.52	0.27

Table 4.10: The model constants calculated from the fitting of CO_2 adsorption isotherm data for different zeolites.

Zeolite	Freundlich		Langmuir		Dubinin- Polanyi	
	1/n	*K*	*B*	q_m	*C*	*D*
Channel:						
ZSM-5	0.51	40.85	6.95	120.79	3.49	0.14
Ferrierite	0.49	37.71	9.45	31.28	3.38	0.12
Cage:						
NaY	0.49	123.96	6.16	120.79	4.61	0.14
NaX	0.49	92.76	7.43	84.76	4.28	0.12
Na-SZ18	0.38	115.58	10.60	108.78	4.59	0.11

In many cases, equilibrium data are very useful and a reliable correlation to be used to interpolate or extrapolate data to a pressure or temperature not measured. The coefficients obtained show that zeolite of different structural properties have different adsorptive characteristics. Close agreement between the experimental and Langmuir isotherms for the faujasite group of zeolites were also reported by Khelifa *et al.* (1999). The structural regularity of lattices and the existence of well defined cavities of faujasite group of zeolites could be the reason of good correlation with the model equations.

It has been realized that several mismatches between the experimental data and other model equations are likely due to assumptions associated with the model in which uniform particle sizes and spherical shape of all macro and micro particles, whereas in actual cases the size of particles are not uniform and not all in spherical shapes. Generally, smaller particles have faster adsorption than larger particles and the particles are actually having different geometries in nature. It is always assumed that the adsorbent has constant porosity and void volume. However, during adsorption processes, with increase of gas loading, the porosity and void volume of the system might change due to adsorption swelling and adding of adsorbed gases.

These factors explained the reason why the experimental data produced several percent of errors (Appendix D3).

4.3.3 Heat of adsorption

As discussed in Chapter 2, heat of adsorption could be determined using Equation 2.16. As described in Section 3.5.3, ΔH was obtained from the slope and ΔS from the intercept of the plot of ln $1/V_N$ versus $1/T$ provided that the range of T is narrow enough for ΔH and ΔS to be regarded as temperature independent (Inel *et al*., 2002). Depending on the experimental method and type of adsorbent used, the enthalpy change (ΔH) of methane and carbon dioxide varies in the range of 20 – 26 kJ/mol (Sun, 1997; Yoshida *et al*., 2000; Mugge *et al*., 2001; Yang *et al*., 2001). However, Maurin *et al*. (2005b) also have reported that ΔH of CH_4 and CO_2 on siliceous faujasite is 14 kJ/mol and 16 kJ/mol respectively.

The study also shows that cage type zeolite where the adsorption occurs mainly within the cage has higher heat of adsorption than channel zeolites (Table 4.11). It agrees with Derouane *et al.* (1987) that heat of adsorption in zeolite cavity were enhanced by the increased contact between sorbed molecules and a wall with high curvature. Thus, the confinement effect could also be the reason for higher ΔH values for methane adsorption on cage type zeolite. This phenomenon also indicates that intermolecular interactions exist between sorbed molecules. Adsorption in wider channel or in large cage not only leads to a smaller gain in enthalpy but also to a smaller loss of entropy (Eder and Lercher, 1997). The ΔS values obtained indicate that the degree of ramdomness of adsorbed molecules inside the zeolite channels or cages are almost the same.

Table 4.11: The enthalpy and entropy change in the adsorption of methane and carbon dioxide.

Zeolite	Methane (CH_4)		Carbon dioxide (CO_2)	
	ΔH (kJ/mol)	ΔS (J/mol.K)	ΔH (kJ/mol)	ΔS (J/mol.K)
Channel:				
ZSM-5	12.43	44.10	13.2	57.50
Ferrierite	10.01	57.71	9.70	69.32
Cage:				
NaY	23.89	29.39	16.9	58.87
Na-SZ18	13.38	58.32	6.01	95.20

The results also indicate that the present of cage structures give advantages to non-polar molecules since it might not experience any blockage due to strongly bonded molecule at any particular site. The calculated values (ΔH) suggest that the adsorption is mainly physical type of adsorption (physisorption). Lower values also indicate that chemical bond hardly exists between the adsorbate and the adsorbent. However, the heats of adsorption obtained in this study are generally lower than the reported values. This could be due to the surface coverage of the zeolite in which the value would decrease as the surface coverage increases(Exter *et al*., 1997; Savitz *et al*., 2000; Yang *et al*., 2001; Maurin *et al*., 2005a).

Results presented in Section 4.3.1.4 showed that the surface coverage for ferrierite is higher than ZSM-5. Similarly, the surface coverage of Na-SZ18 is also higher than NaY. Thus, it explains the reason for lower heat of adsorption of ferrierite and Na-SZ18 than ZSM-5 and NaY respectively. The heat of adsorption of carbon dioxide also supports the fact that the amount of carbon dioxide adsorbed is lower than methane at temperature 323 K. This is due to the properties of carbon dioxide itself, in which the molecules exist as supercritical component at temperature above 304 K (critical temperature). Comparatively, these findings suggest that at supercritical conditions, the adsorption of methane is higher than carbon dioxide. As reported in the literatures, the adsorption of carbon dioxide

would be higher at temperature below critical temperature (Hernandez-Huesca *et al*., 1999; Khelifa *et al*., 1999; Armenta *et al*., 2001).

4.4 Gas Adsorption Kinetics

Adsorption kinetics of any adsorbate depends on factors such as adsorbent structural arrangement, physical and chemical properties, adsorbate physical and chemical properties, and the operating conditions involves,which is important in the design of industrial adsorption process. Generally, adsorption process involves adsorbate which diffusing from the bulk fluid phase to external surface of the particle, diffusing into macro-micropore filling, and adsorbate interaction with the surface of the solid particles. So far, several studies have been carried out using silicalite as an adsorbent (Wu *et al*., 1983; Choudhary and Mayadevi, 1996; Krishna *et al*., 1999; Song and Rees, 2000; Chong *et al*., 2005). However, there are still few studies on kinetics of adsorption for adsorbates such as CH_4 and CO_2 on zeolites beta, ferrierite, mordenite, NaX, or NaY. In this section, gas uptake data will be used to determine diffusional constant, initial adsorption rate, and equilibrium time of CH_4 and CO_2. Diffusion characteristics of different pore network system were determined based on the properties of adsorbate and adsorbent. These results would provide an insight on gas adsorption activities of CH_4 and CO_2 in zeolite structural framework.

4.4.1 Gas adsorption uptake curve

In this study, CH_4 and CO_2 exhibit different behavior of gas uptake as a function of time. Adsorption of CH_4 on zeolite involves unspecific interactions

between the solid surface and the adsorbate. The only relationship exist is between the pore window of zeolite and the molecular dimension of adsorbates. Figures 4.22 and 4.23 show the uptake curves of CH_4 on channel and cage type zeolites**.** In the adsorption of CH_4 on cage type zeolites, gradual increase was observed with almost linear relationship. Similar phenomenon for ferrierite also suggests the existence of cage-like structure in ferrierite structural framework. Yang *et al*. (2001) reported that the interaction between CH_4 and the wall of zeolite structure is not based on the acid sites but more likely due to the confinement effect. However, adsorption of CO_2 shows slightly different pattern, in which convex curves were observed for both channel and cage groups of zeolites (Figures 4.24 and 4.25).

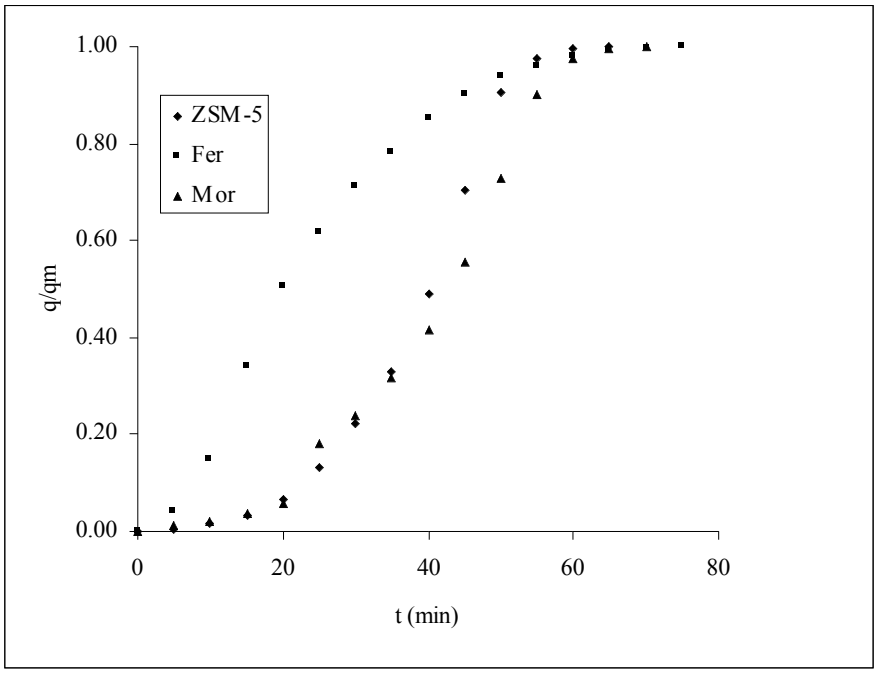

Figure 4.22: The methane fractional uptake curves of channel type structures at 323 K and 137 kPa.

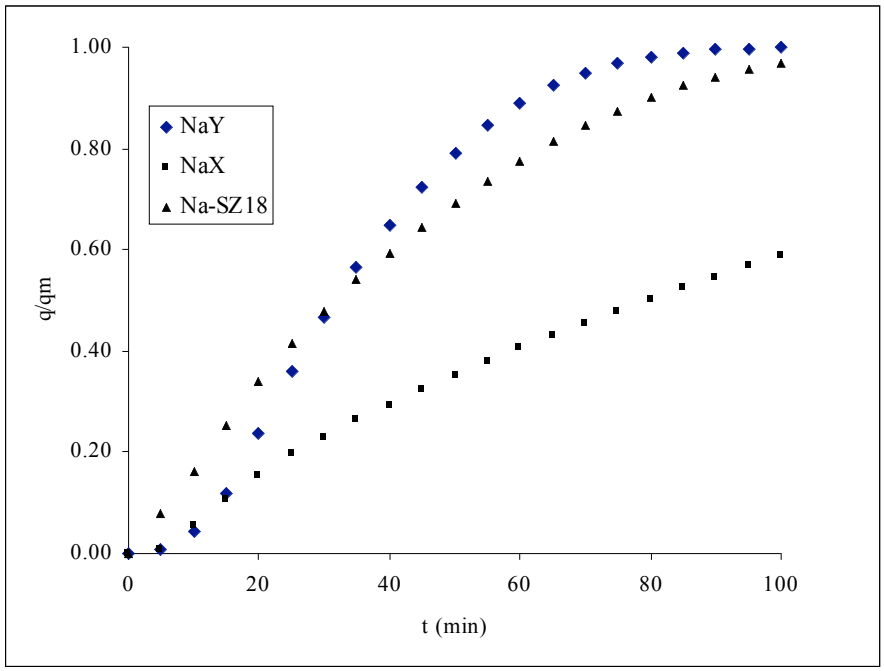

Figure 4.23: The methane fractional uptake curve of cage type structures at 323 K and 137 kPa.

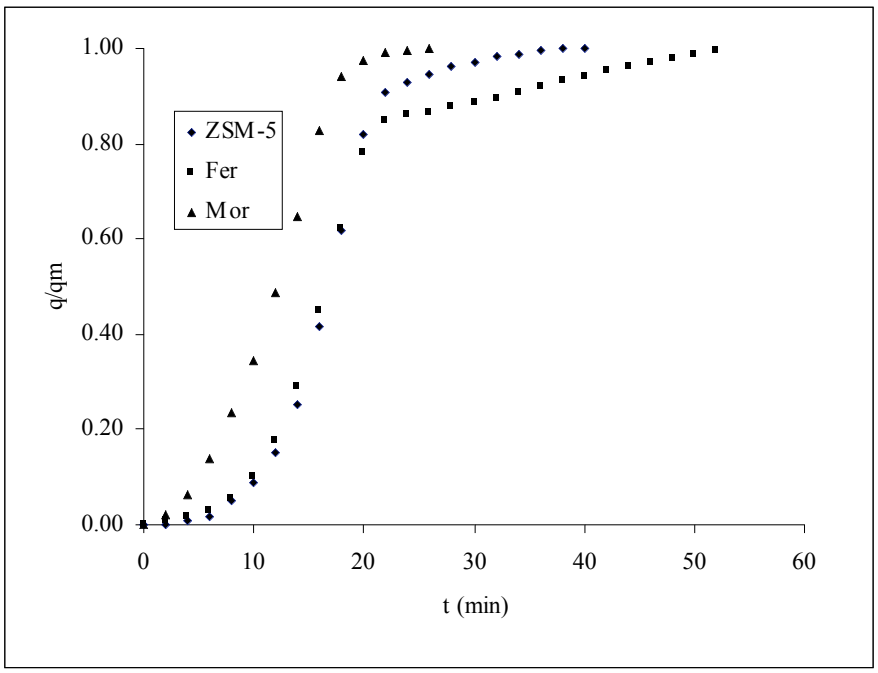

Figure 4.24: The carbon dioxide fractional uptake curves of channel type structures at 323 K and 137 kPa.

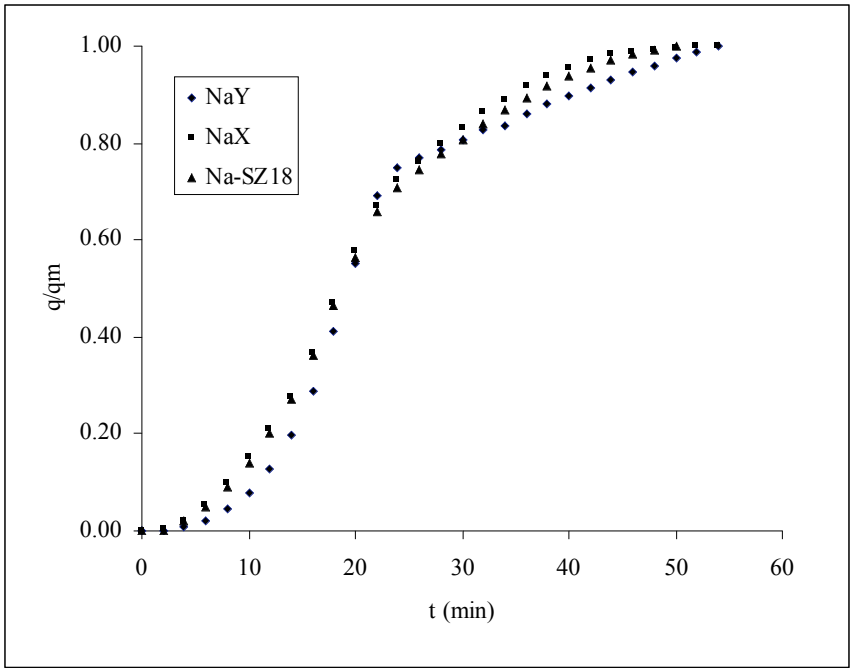

Figure 4.25: The carbon dioxide fractional uptake curves of cage type structures at 323 K and 137 kPa.

At a very early stage, the adsorption rate is relatively slow, then it adsorbed at high rate until it reached a point where the adsorption slowly increased until it reached the plateau. This corresponds to the adsorption on the strongest sites by quadrapole moment of CO_2 and later followed by the adsorption on the outer layer. Hence, the fractional uptake curves give some indication that adsorption characteristics were influenced by structural framework and properties of adsorbates. In order to elucidate further, diffusional constant, initial rate of adsorption, and equilibrium time were determined from the gas uptake data. The initial uptake rate and equilibrium time physically describes the adsorption phenomena of the adsorption.

4.4.2 Initial adsorption rate

In this study, initial adsorption rate of gases was determined from the experimental data points in order to observe how the molecules act initially toward the microporous materials of different structural framework with different physical and chemical properties. Table 4.12 shows that at initial stage, adsorption rate for cage type zeolite is higher than channel type zeolites for both gases. Again, for channel group of zeolite, ferrierite could adsorb faster than ZSM-5 and mordenite. As discussed in Section 4.3.1.1, the presence of cage-like structure in ferrierite could be the reason for higher adsorption capacity than other channel type zeolites. However, as comparisons are made on cage type structures, it is found that the initial adsorption rate of Na-SZ18 is higher than NaY and NaX for both adsorbates. Since the surface area and crystallinity could not be the reasons for high adsorption rate, then it could probably due to the presence of adsorption sites on zeolite surface.

Table 4.12: The initial adsorption rate of methane and carbon dioxide on different types of zeolites.

Sample	Initial adsorption rate (mol/sec) x 10^6		Adsorption capacity (q_e) (mol/g) x 10^3	
	CH_4	CO_2	CH_4	CO_2
Cage:				
NaY	3.45	3.00	10.30	3.85
NaX	1.54	2.91	11.65	3.16
SZ-18	3.57	3.53	13.76	5.35
Channel:				
ZSM-5	0.75	0.85	2.06	0.59
Ferrierite	0.99	1.33	2.59	1.11
Mordenite	0.76	0.62	1.60	0.48

Apart from the cation sites, any defects could act as adsorption sites. This could be explained from lower crystallinity of Na-SZ18 than NaY and NaX. Thus, the results show that high adsorption rate does not result in high adsorption capacity since there are factors that significantly affect the adsorption characteristics of cage and channel type zeolites. In addition, the properties of adsorption could also affect the adsorption characteristics of zeolite adsorbents. When the size of an adsorbate molecule is close to the size of the micropore, the penetration of the molecules into the micropore becomes restricted and the rate of transport might have significant effect on the overall adsorption rate (Bae and Lee, 2005).

In general, large diffusion resistance and a long pathway could affect the uptake rate of gases. Further investigation on the relationnship between initial adsorption rate and the physical properties of zeolites shows that for non-polar molecules (CH_4), surface area and pore volume might influence the initial adsorption rates of zeolites (Figures 4.26 and 4.27). Generally, higher surface area and pore volume lead to high high adsorption rate. This is especially true for cage type zeolites since the adsorbates could easily diffuse into the inner part of the cage and adsorb on the zeolite surface.

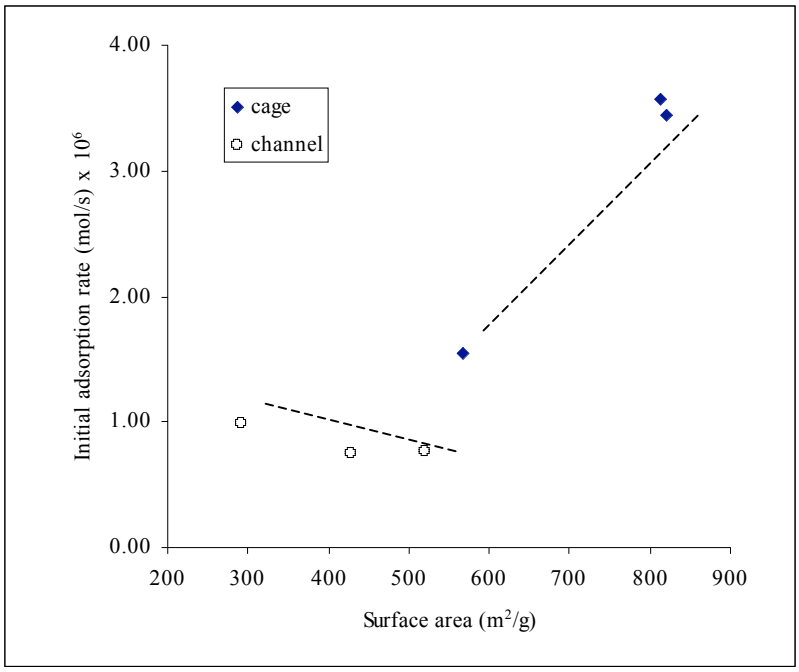

(a)

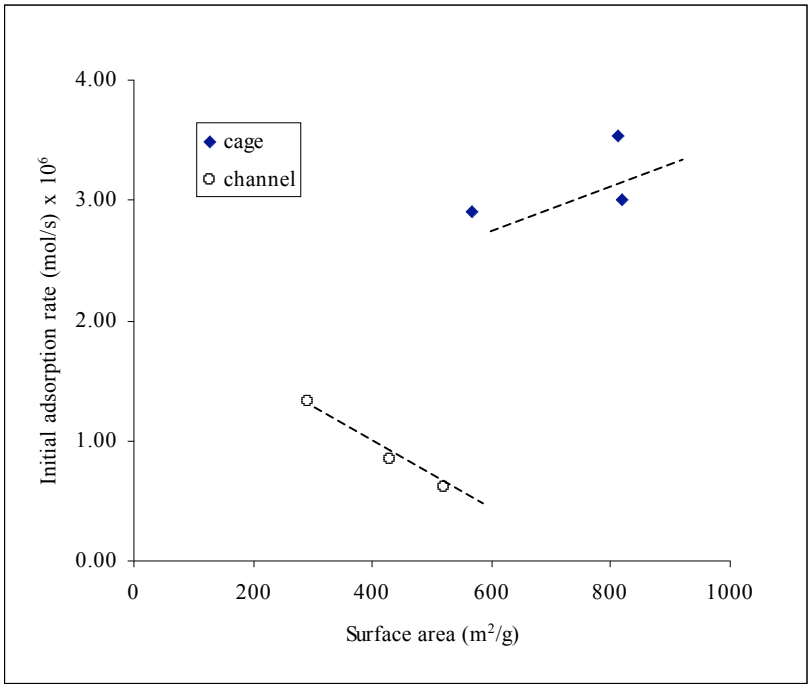

(b)

Figure 4.26: The effect of surface area on initial adsorption rate of channel and cage type zeolites: (a) methane and (b) carbon dioxide.

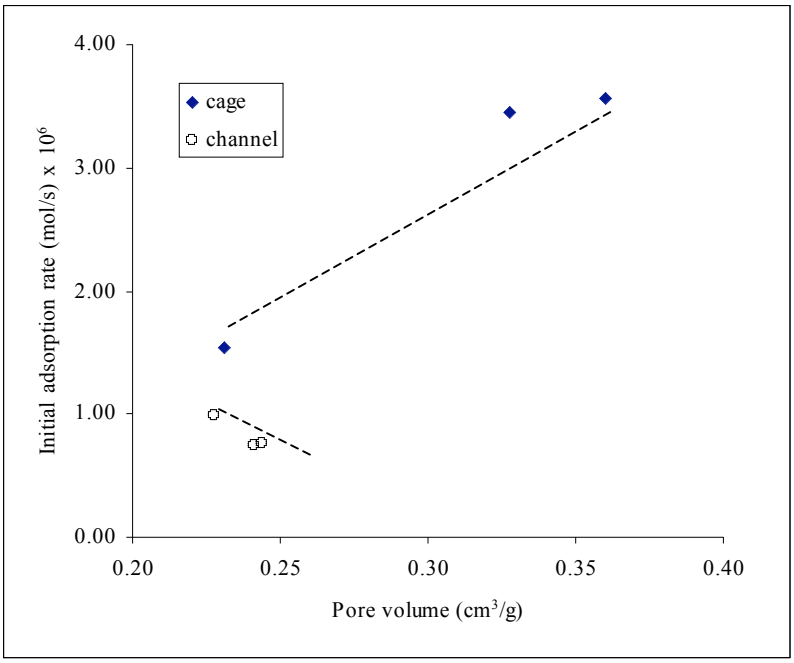

(a)

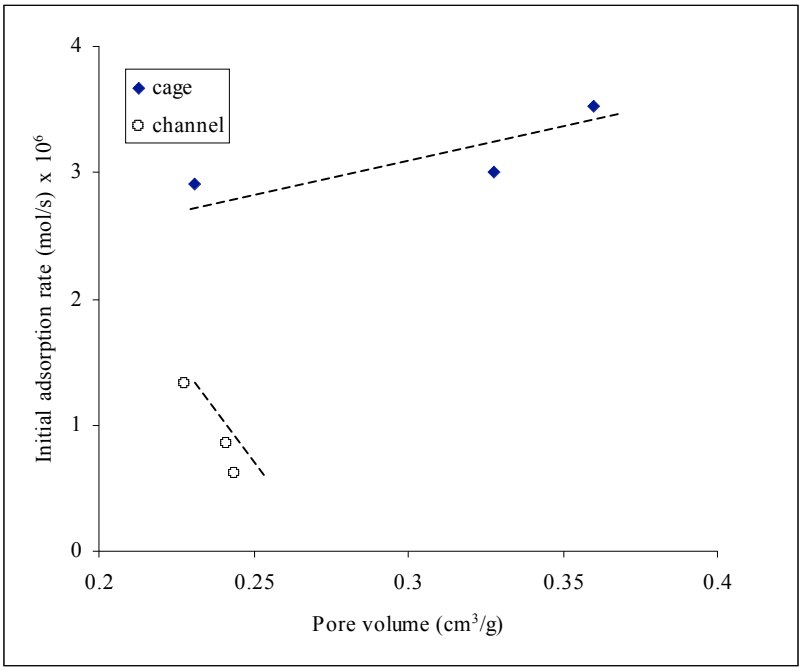

(b)

Figure 4.27: The effect of pore volume on initial adsorption rate of channel and cage type zeolites: (a) methane and (b) carbon dioxide.

However, for molecule such as CO_2, a combination between the surface properties and the physical properties of the zeolites might influence the initial adsorption rate. This study reveals that the relationship between physical properties and initial adsorption rates of carbon dioxide is oppposite to methane adsorption. Since CO_2 molecules are having quadrapole moment, we could assume that specific interaction between the adsorbate and the wall of adsorbent might dominate the initial adsorption rate of CO_2, and hence the adsorption characteristics in zeolite. If the molecules get into contact with any active specific site, the adsorption might occur. As reported by Choudhary and Mayadevi (1996), the specific interactions could occur particularly between the adsorbates (CO_2) and the metal balancing cation, in this case the cation is Na^+.

The relationship between the average pore diameter of zeolites and the initial adsorption rate are shown in Figures 4.28 (a) and (b). Generally, smaller pore diameter would increase the adsorption rate since the interactions between adsorbate and zeolite adsorbent are more frequent in small pore channel. In addition, the molecular structure might affect the diffusivity of adsorbate to pass through a pore opening. The slower adsorption of CH_4 compares with CO_2 might be due to structural orientationof the molecules in which CH_4 is tetrahedral but CO_2 is linear (Bae and Lee, 2005). Thus, in this case, the molecular structure also contributes in determining the adsorption rate of methane and carbon dioxide.

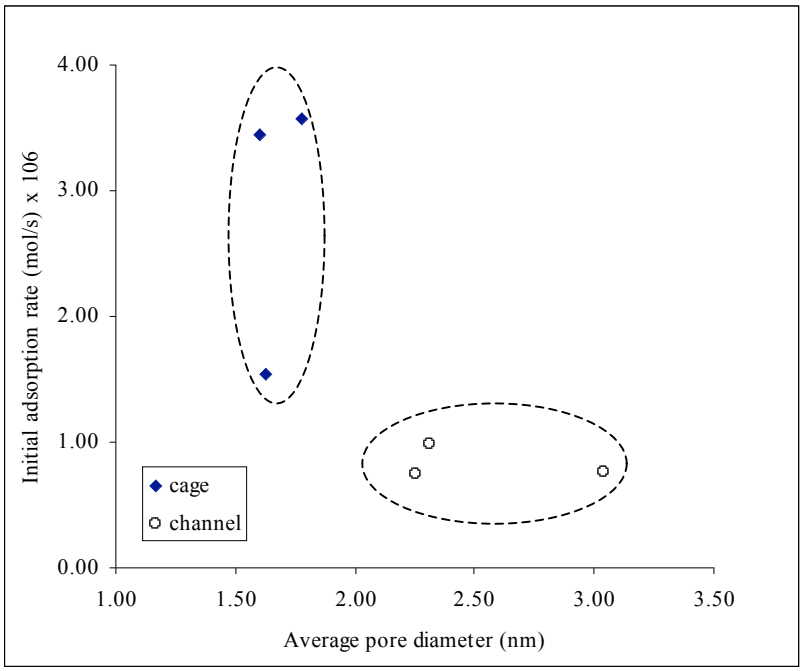

(a)

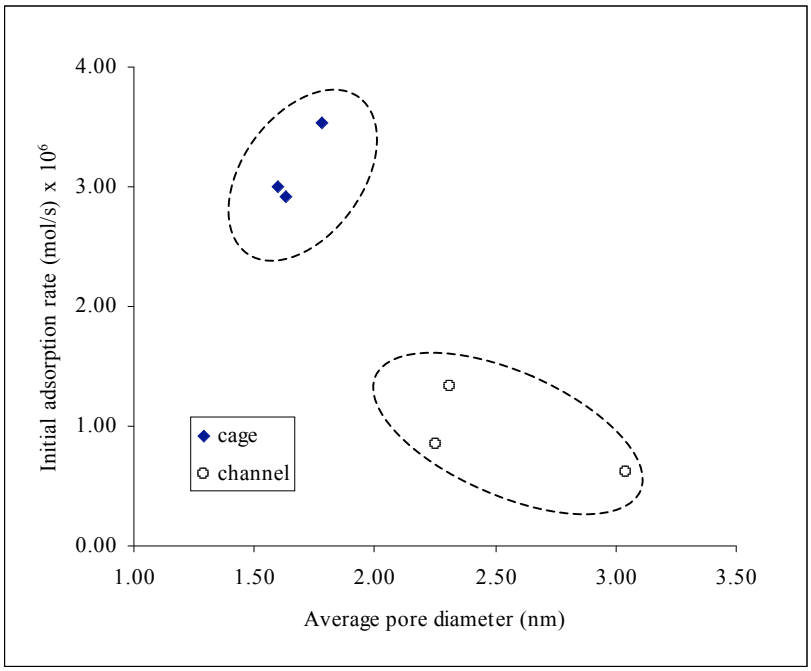

(b)

Figure 4.28: The effect of average pore diameter of channel and cage type zeolites on initial adsorption rate of: (a) methane and (b) carbon dioxide.

4.4.3 Adsorption equilbrium time

Adsorption equilibrium time is also crucial because it will determine the efficiency of the adsorption process. There are also several factors determined the time taken for the adsoprtion to reach equilibrium. In general, CO_2 adsorption takes shorter time to reach equilibrium than CH_4 adsorption. It supports the fact that there are some interactions between sodium cations and CO_2 molecules. Taking faujasite structure as examples, it is commonly known that Si/Al ratio of NaX is > 1 but < 1.5, the ratio of Na-SZ18 is 1.53 and followed by NaY (Si/Al = 1.60). Lower ratio indicates more sodium (Na) present as charge balancing cation.

This study shows that as surface area and pore volume increases, the time taken for CO_2 to reach equilibrium also increases. It is assumed that for larger surface area and bigger pore volume, the adsorbates 'jump' from one site to another before it adsorbed on the surface. However, opposite relationships are observed in which the time taken to reach equilibrium increases as the surface area decreases. Since the pores might experience some defects, it might affect the overall adsorption process. Larger pore size indicates the presence of defect on the zeolites. Thus, it explained reason for longer adsorption equilibrium time for zeolites with larger average pore diameter. Except for ferrierite, channel type structure reach equilibrium less than 35 minutes, shorter time with low adsorption capacity (Table 4.13).

Table 4.13: The adsorption equilibrium time and adsorption capacity of methane (CH_4) and carbon dioxide (CO_2) on different zeolites.

Sample	Equilibrium time (min)		Adsorption capacity x 10^3 (mol/g)	
	CH_4	CO_2	CH_4	CO_2
Cage:				
NaY	84	81	10.30	3.85
NaX	263	49	11.65	3.16
Na-SZ18	125	56	13.76	5.35
Channel:				
ZSM-5	21	34	2.06	0.59
Ferrierite	64	13	2.59	1.11
Mordenite	15	18	1.60	0.48

Since the adsorption equilibrium time of NaX is shorter than NaY and Na-SZ18, it suggests that charge balancing cation has greater influence on zeolite adsorbent especially for adsorbate that potentially interacts with the surface due to the presence of quadrapole moment of the molecules. As the effect of physical properties was investigated, it is also found that at certain extent, physical properties influence the adsorption equilibrium time of CH_4 and CO_2 (Figures 4.29, 4.30, and 4.31). Even though adsorption capacity is among the main criteria for selection of adsorbent, adsorption equilibrium time is also important since it is not economically feasible if longer time is required for adsorption to complete. Diffusion study and the adsorption rate provide some insight on the gas adsorption phenomena on different types of zeolites using two different adsorbates (CH_4 and CO_2). Schuring *et al.* (2000) supported the fact that diffusion and adsorption in zeolites greatly depends on structures of the pore network system and adsorbates. The large interactions between molecules and zeolite lattice also results in molecules strongly adsorbed inside the channels.

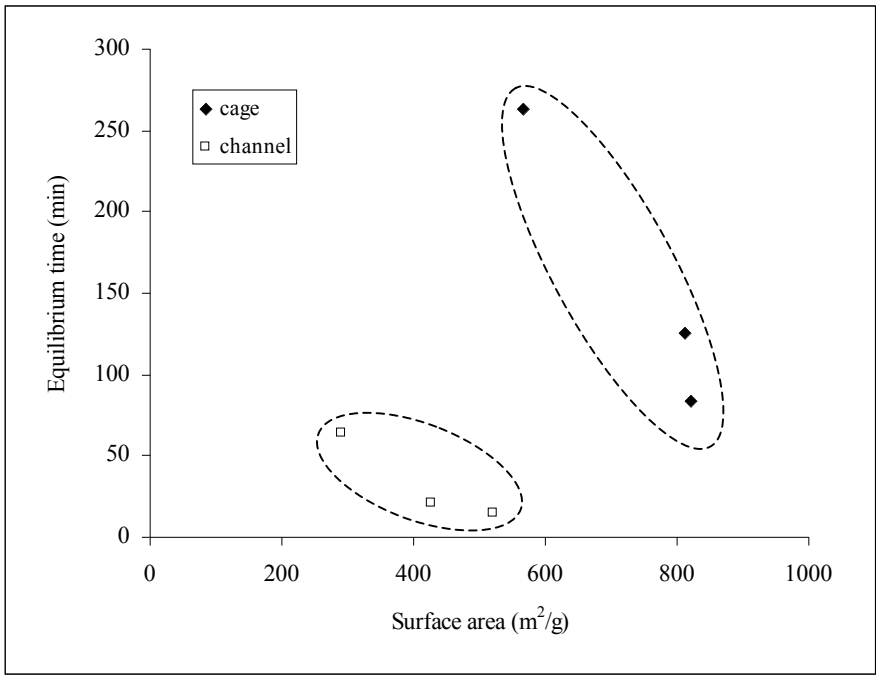

(a)

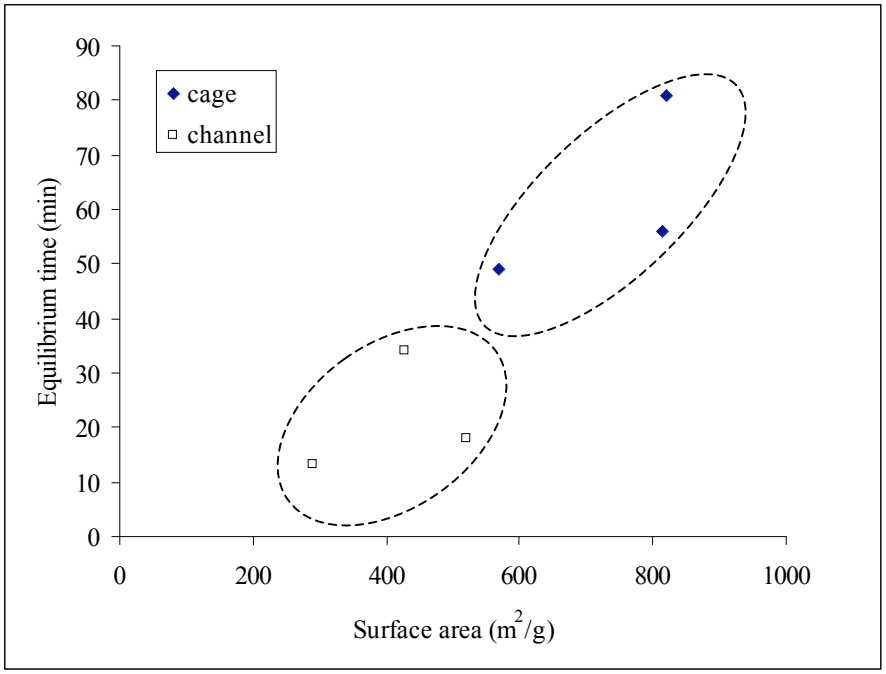

(b)

Figure 4.29: The effect of surface area of channel and cage type zeolites on adsorption equilibrium time: (a) methane and (b) carbon dioxide.

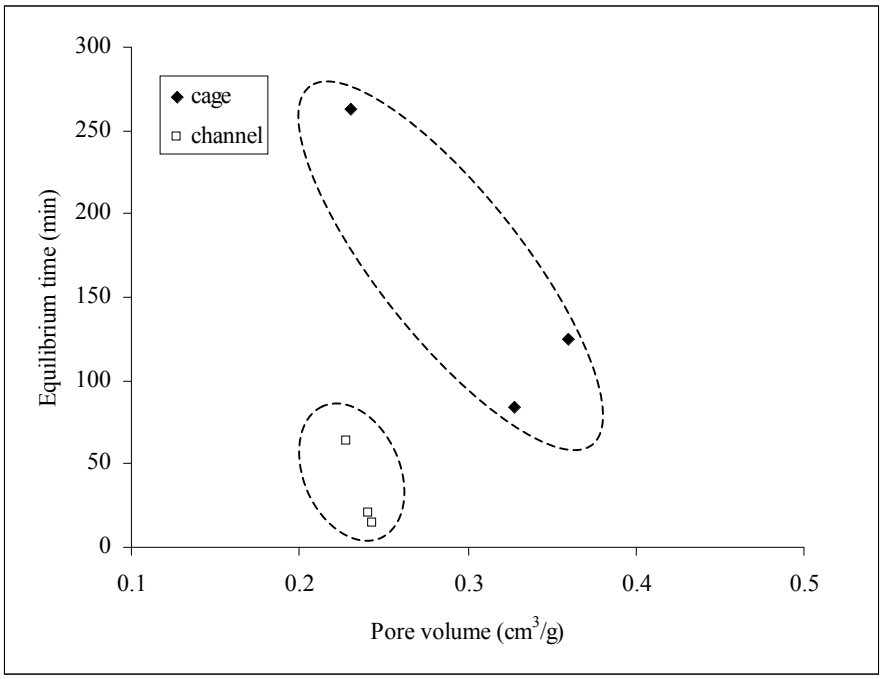

(a)

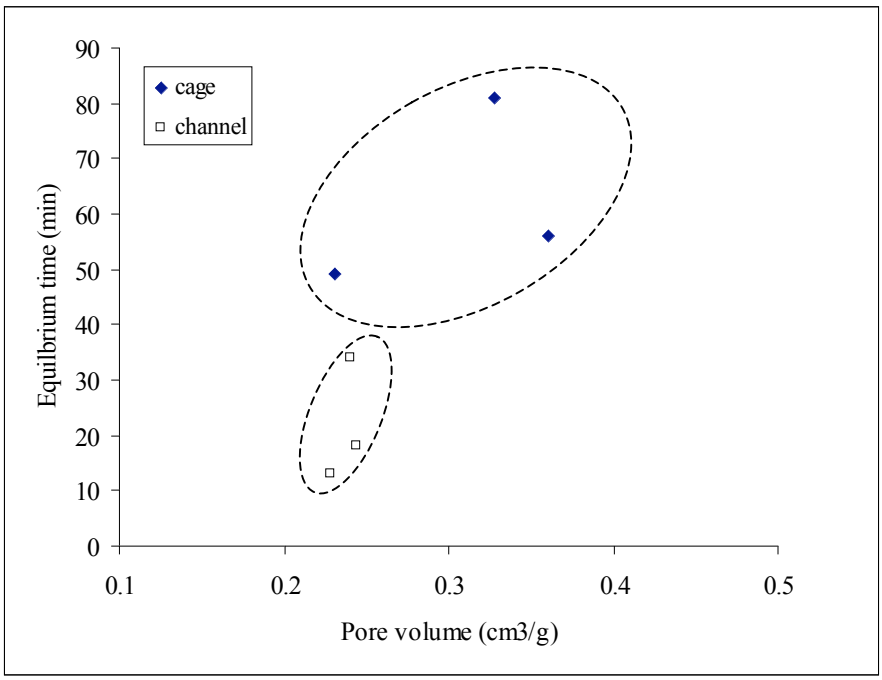

(b)

Figure 4.30: The effect of pore volume of channel and cage type zeolites on adsorption equilibrium time: (a) methane and (b) carbon dioxide.

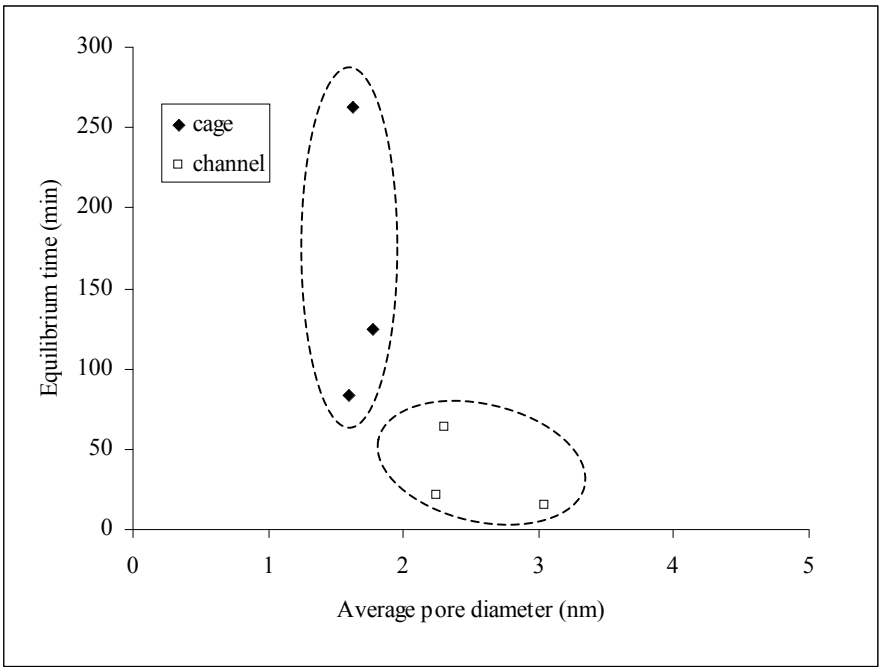

(a)

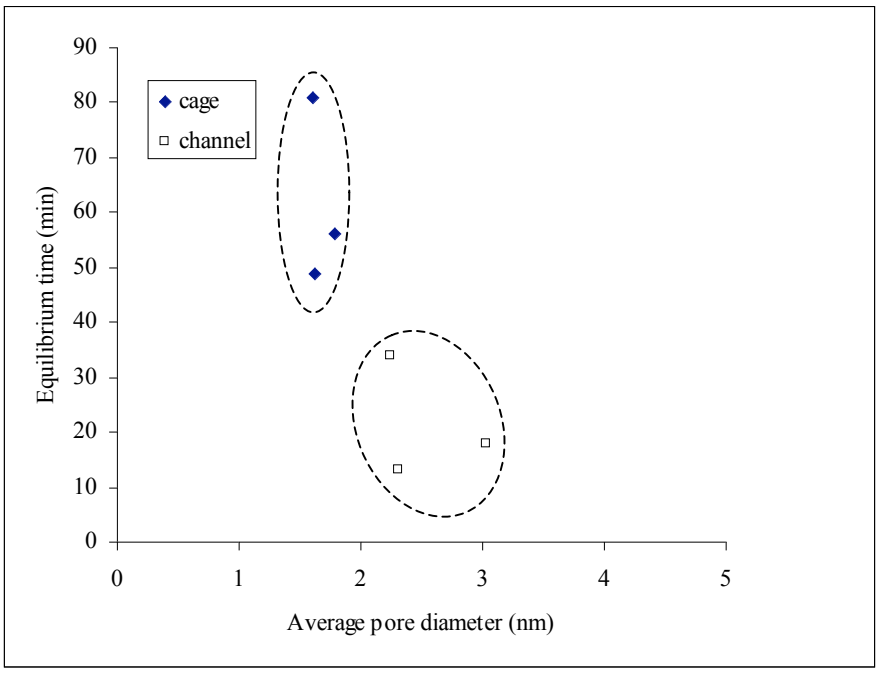

(b)

Figure 4.31: The effect of average pore diameter of channel and cage type on adsorption equilibrium time of (a) methane and (b) carbon dioxide.

4.4.4 Gas diffusivity

In general, diffusions in porous solid are governed by the structural and physical properties of adsorbent and adsorbate (Mugge *et al*., 2001; Ruthven, 2004; Delgado *et al*., 2004). According to Geankoplis (1993), diffusion in porous solid and capillaries can be either Fick's diffusion (molecular diffusion) or Knudsen diffusion. For large pore diameters (macropores), molecular diffusion involves frequent collision between the molecules. As the size of the pore decreases, the number of collision with the wall increases. In some cases, the pore size (d) is smaller than the mean free path (λ). Thus, Knudsen diffusion takes place and the mobility now depends on the dimension of the pore (Schuring *et al*., 2002).

4.4.4.1 Bulk phase gas diffusivity

In any process, mass transfer occurs when there is a driving force (e.g. concentration gradient) exists between two points. The mass transfer process could be either controlled by the molecular diffusion or bulk diffusion (convective process). The molecular diffusion (Fick's diffusion) involves the diffusion of adsorbate molecules from the bulk gas phase to external zeolite surface, which is generally controlled by molecular collisions. The diffusion through large pore size (intra-particle diffusion) could also be considered to be molecular diffusion. Molecular diffusivity in bulk gas phase may be estimated by Chapman-Enskog equation (Suzuki, 1990; Geankoplis, 1993);

$$D_m = \frac{1.8583\times10^{-7}T^{3/2}}{P\sigma_{AB}^2\Omega_{D,AB}}\left(\frac{1}{M_A}+\frac{1}{M_B}\right)^{1/2} \qquad (4.\ 1)$$

where D_m is the diffusivity (m^2/s), T is the temperature in K, M_A and M_B are molecular weight of the molecules, and P is the absolute pressure in atm. The term σ_{AB} is the average collision diameter and $\Omega_{D,AB}$ is the collision integral based on the Lennard-Jones potentials (Geankoplis, 1993). Using Equation 4.1, it is found that the diffusivity of methane and carbon dioxide is 4.87×10^{-5} and 2.40×10^{-5} m^2/s respectively. It is the diffusion of adsorbate from the bulk phase to the external surface of zeolite.

4.4.4.2 Internal zeolite pore diffusivity

Inside the microporous adsorbent, as the adsorbed molecules are mobile on the surface of the adsorbent, diffusion due to migration of the adsorbed molecules may have greater influence than the bulk diffusion. This type of diffusion is called surface diffusion. As the size of an adsorbate molecule is close to the size of the micropore, diffusion of the adsorbate molecule becomes restricted and the rate of transport in the micropore may have a significant effect on the overall adsorption rate. This type of micropore diffusion is an activated process which depends heavily on adsorbate properties. Diffusion in molecular sieve materials is often of this type. Diffusion in this case is accompanied by relatively large activation energy and can be correlated by assuming that the driving force of diffusion is the chemical potential gradient (Suzuki, 1990).

Therefore, depending on Knudsen number (N_{Kn}), the ratio of molecule mean free path (λ) and the pore diameter (d), it is possible to determine the type of diffusion occurred inside the zeolite pores by using the following criteria (Geankoplis, 1993):

$\lambda/d \geq 10$ Knudsen diffusion;

$\lambda/d \leq 0.01$ Fickian (molecular) diffusion;

$0.01 < \lambda/d < 10$ Transition.

The mean free path or average distance between collisions for an adsorbate molecule may be estimated from kinetic theory. The mean free path could then be taken as the length of the path divided by the number of collisions. The resulting mean free path is

$$\lambda = \frac{1}{\sqrt{2}\pi(2r)^2 n_V} \tag{4.2}$$

where n_V is number of molecules per unit volume and r is the radius of the adsorbate molecule. Since n_V can be determined from Avogadro's number (N_A) and the ideal gas law, leading to

$$n_V = \frac{nN_A}{V} = \frac{nN_A}{\frac{nRT}{P}} = \frac{N_A P}{RT} \tag{4.3}$$

and when substituted into Equation 4.2, we will obtain Equation 4.4.

$$\lambda = \frac{RT}{\sqrt{2}\pi(2r)^2 N_A P} \tag{4.4}$$

where R is the universal gas constant, N_A is the Avogadro number, and $2r$ is gas molecule diameter. Hence, using Equation 4.4, it is found that the mean free path for CH_4 (λ_{CH4}) and CO_2 (λ_{CO2}) is 5.08 x 10^{-8} m and 6.70 x 10^{-8} m respectively. It was found that the diffusion inside different types of zeolite pores is either Knudsen diffusion or transition between molecular diffusion and Knudsen diffusion (Table 4.14). Except for zeolite beta, the diffusion inside the pore network systems is Knudsen diffusion. The mobility of adsorbate is restricted by the size of the pores. However, more collisions allow interaction with the surface and hence, more possible interaction and adsorption occurs inside the zeolite pore.

Table 4.14: The Knudsen number (N_{Kn}) and type of diffusion in zeolite pore systems based on average channel diameter.

Zeolite	Methane (CH_4)		Carbon dioxide (CO_2)	
	$\lambda / 2r$	Types of diffusion	$\lambda / 2r$	Types of diffusion
Channel:				
ZSM-5	22.5	Knudsen	29.9	Knudsen
Beta	7.3	Transition	9.6	Transition
Mordenite	16.7	Knudsen	22.1	Knudsen
Ferrierite	22.0	Knudsen	29.1	Knudsen
Cage:				
NaY	31.7	Knudsen	42.1	Knudsen
NaX	31.1	Knudsen	41.3	Knudsen
Na-SZ18	28.5	Knudsen	37.8	Knudsen

The results also show that cage-type zeolites are also categorized into the Knudsen diffusion region having lower Knudsen number than the channel-type zeolites. Therefore, the collision between the adsorbate molecules and the wall of zeolite is less, but the presence of supercage allows more entrapment of gases that leads to high adsorption capacity of faujasite type zeolites (NaX, NaY and NaSZ-18). In addition, intercage hopping is unlikely to occur because it is also a slow process involving high activation barrier (Barzykin *et al*., 2001). The Knudsen diffusivity was estimated using Equation 4.5 and values for CH_4 and CO_2 are shown in Table 4.15.

$$D_K = 9700(d/2)\sqrt{\frac{T}{M}} \tag{4.5}$$

where *d/2* is the pore radius in cm, *T* is the temperature in K, *M* is the molecular weight of the gas and D_K is the Knudsen diffusivity (cm^2/s). Basically, diffusivity (Knudsen) is depending on the pore diameter, molecular weight of adsorbate and temperature. For the same molecule, the diffusivity is influenced by the pore

diameter of the adsorbent. This is clearly shown in Table 4.15 that the diffusivities of channel type zeolite are subsequently larger than cage type zeolites.

This is due to bigger average pore diameter of channel type zeolites calculated from the adsorption data of nitrogen measured at 77 K. In addition, diffusion in zeolite beta is affected by structural disorder of the framework that results in formation of mesopores and macropores. However, when determining types of diffusion occurred specifically inside the pore network of zeolites, Post (1991), Xiao and Wei (2001), and Schuring *et al*. (2002) classified diffusion either Knudsen diffusion or configurational diffusion depending on the size of the pores and the gas molecules (Figure 4.32). According to Xiao and Wei (2001), configurational regime takes place when the ratio of molecular diameter (*2r*) to channel diameter (*d*) is greater than 0.8.

Table 4.15: The Knudsen diffusivity of methane and carbon dioxide inside the zeolite pores.

Zeolite	Knudsen diffusivity, D_K x 10^7 (m^2/s)	
	Methane (CH_4)	Carbon dioxide (CO_2)
Channel:		
ZSM-5	9.81	5.91
Mordenite	13.25	7.98
Ferrierite	10.07	6.07
Cage:		
NaY	6.97	4.20
NaX	7.10	4.28
Na-SZ18	7.76	4.67

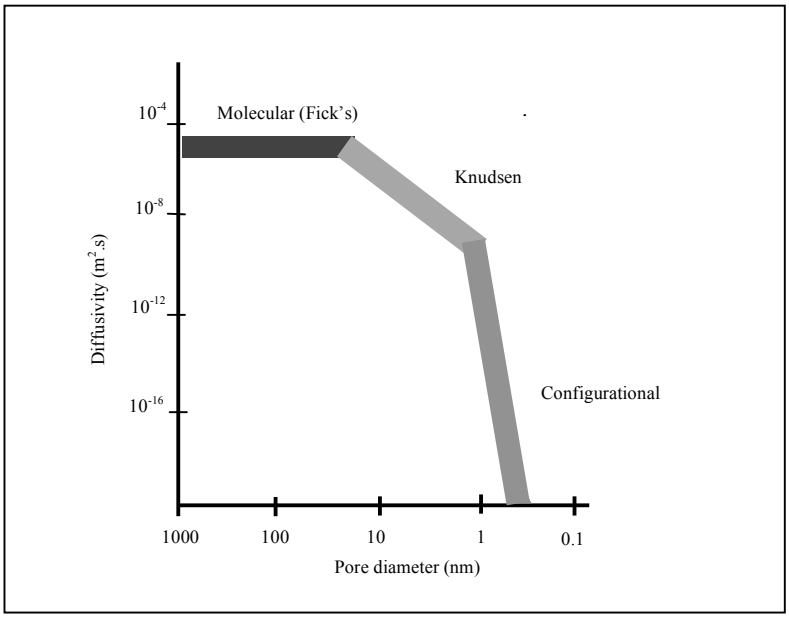

Figure 4.32: Effect of pore size on diffusivity (Post, 1991).

Therefore, based on the pore diameter presented in Table 4.1, it can be assumed that the configurational diffusion start to take place in several zeolite structures (Table 4.16). However, it is also important to realize that the structural frameworks of zeolites used in this study are in not in their perfect form. This is clearly shown in Tables 4.4 and 4.5 in which the average pore diameters (d_{ave}) are much greater than the pore diameters (d) reported in literatures (Barrer, 1982; Szostak, 1992; Nagy *et al*., 1998). Using pore diameters reported in the literatures, it is found that the configurational regime only exist in zeolites when CH_4 molecules diffuse inside ZSM-5, beta and ferrierite structures, and CO_2 molecules diffuse inside ZSM-5 and ferrierite structures (Tables 4.16 and 4.17).

Table 4.16: The diffusional characteristics of methane for different zeolite structures.

Zeolite	*d* (nm)	*2r/d*	Type of diffusion	d_{ave} (nm)	*2r/d*	Type of diffusion
Channel:						
ZSM-5	0.52	0.73	Configurational	2.25	0.17	Knudsen
Mordenite	0.65	0.58	Knudsen	3.04	0.12	Knudsen
Ferrierite	0.35	1.08	Configurational	2.31	0.16	Knudsen
Cage:						
NaY	0.72	0.53	Knudsen	1.60	0.24	Knudsen
NaX				1.63	0.23	Knudsen
Na-SZ18				1.78	0.21	Knudsen

Table 4.17: The diffusional characteristics of carbon dioxide for different zeolite structures.

Zeolite	*d* (nm)	*2r/d*	Type of diffusion	d_{ave} (nm)	*2r/d*	Type of diffusion
Channel:						
ZSM-5	0.52	0.63	Configurational	2.25	0.15	Knudsen
Mordenite	0.65	0.51	Knudsen	3.04	0.11	Knudsen
Ferrierite	0.35	0.94	Configurational	2.31	0.14	Knudsen
Cage:						
NaY	0.72	0.46	Knudsen	1.60	0.20	Knudsen
NaX				1.63	0.20	Knudsen
Na-SZ18				1.78	0.18	Knudsen

In actual cases where meso or macropores are also formed due to structural imperfection, average pore diameter should be used to determine the type of diffusion in zeolite structures. Therefore, it is found that Knudsen regime would be more dominant than configurational regime since the average pore diameters are considerably larger than pore diameter of perfect structure. Thus, one could assume that Knudsen diffusion occurrs inside zeolite structures even though configurational regime might also exist. Hence, our study on diffusion inside zeolite pore structure indicates that diffusion of adsorbates strongly depend on structural framework, pore size, and type and molecular size of the diffusing molecules. The extents of interaction between adsorbates and adsorbent affect the mobility and finally, the amount adsorbs onto the zeolite surface.

4.4.4.3 Diffusional time constant

According to Yang (1997), adsorption of gases by commercial zeolite pellets occurs almost entirely within the zeolite crystals. Based on the data obtained from fractional uptake curve and the assumption that adsorption occurred on isothermal single-component and controlled by micropore diffusion, the diffusional time constant could be determined. For a single spherical zeolite crystal of radius r, the total amount of diffusing substance entering or leaving the sphere is given by Equation 2.24. However, for small value of t, the equation reduces to the simple root – t law (Equation 2.28) in which fractional uptake is proportional to $t^{1/2}$. For large value of t, the diffusional time constant ($\boldsymbol{D}/r^2$) could be calculated by plotting the fractional uptake (γ) versus t (Table 4.18). The diffusional time constant obtained are in accordance with the reported values, vary for more than three order of magnitude (Ackley and Yang, 1991; Olson *et al*. (2004). Jayaraman *et al*. (2004) reported that for methane diffusional time constant are in the range of 10^{-3} to 10^{-5} sec^{-1} and Mohr *et al*., 1999 also reported that methane diffusional time constant of 3.8×10^{-4} sec^{-1}. However Wang *et al*., 2001, Ahn *et al*. (2004) and Bae and Lee

(2005) reported the carbon dioxide diffusional time constant in the range $10^{-2} – 10^{-4}$ sec^{-1}. The values show that zeolites act differently towards different types of adsorbate.

Table 4.18: The diffusional time constants of methane and carbon dioxide at 323 K and 137 kPa.

	$D/r^2 \times 10^4$ (sec^{-1})	
Zeolites	Methane (CH_4)	Carbon dioxide (CO_2)
Channel:		
ZSM-5	1.50	1.03
Ferrierite	3.54	2.61
Mordenite	2.99	8.74
Cage:		
NaY	3.14	1.90
NaX	1.75	2.71
Na-SZ18	2.42	2.33

However, diffusional time constant could not solely be used to evaluate the performance of the adsorbent. This is shown by the diffusional time constant of NaX- methane in which is relatively lower than cage type zeolites, it does not necessarily indicate low amount of methane adsorbed. In this case, even though the diffusional time constant is high, limitation due the inappropriate pore network system (zig-zag channel or one dimensional network system) and pore blockage could result in low adsorption capacity. The adsorption capacity would not reach the optimum capacity even though the space is still available for further adsorption. This condition is shown by mordenite in which the surface coverage of this sample was found to be extremely low (6 % surface coverage). This finding is supported by Olson *et al*. (2004) in which the diffusional time constant depends on physical and chemical properties of adsorbates. In addition, since this study was carried out at constant temperature and pressure, the values do not represent the effect of single

parameter but they are rather a combination of parameters that include structural, physical and chemical properties of adsorbents and adsorbates.

4.5 Gas - Zeolite Interaction

In adsorption of gases, the number of molecules attracted to a solid surface depends on the experimental conditions and types of gas and the surface properties of adsorbent. The monolayer, multilayer, or volume filling in micropore space is possible for microporous material such as zeolites. In monolayer adsorption which relatively few molecules are adsorbed at very low pressure, only a fraction of the solid surface is covered. As the gas pressure increases at a given temperature, the surface coverage also increases. When all sites become occupied, the adsorbed molecules are said to form a monolayer. Further increase in pressure promotes multiplayer adsorption. However, it is also possible for multilayer adsorption to occur on one part of a porous surface while other sites remain vacant.

According to Nicholson and Pellenq (1998), in large pores, the adsorbate-adsorbate interactions are dominant. However, in micropores, the adsorbent-adsorbate interaction would be more important. This phenomenon is supported by Knudsen number (N_{Kn}) calculated in Section 4.4.2.2, in which Knudsen diffusion takes place in the micropore channel. In general, there are several possible interactions between methane and zeolite structures. The electrostatic forces might exist between C -- Na, H -- O, and Si -- C. Similarly, the interactions between carbon dioxide molecules and zeolite could be due to the electrostatic forces of O -- Na, O -- Si, and C -- O. The results of these interactions could be indicated in the FTIR spectra of asymmetric and symmetric bands of the adsorbates.

As described in Section 3.5.3, the study of adsorbate-adsorbent interaction was carried using FTIR spectroscopy method. FTIR spectra of adsorbed molecules could be observed in the region between 3200 – 1200 cm^{-1} and 2800 – 1400 cm^{-1} for CH_4 and CO_2 respectively. FTIR spectra of methane molecules are shown in Figures 4.33. Although unique identification of the adsorption spectra is difficult to performed, some peaks that attribute to specific interactions of the adsorbate on the adsorbent could be observed. Two peaks appeared in the region around 3020 cm^{-1} and 1306 cm^{-1} are assigned to asymmetric band (v_3) and symmetric band (v_4) respectively (Yoshida *et al*., 2000). Symmetric band (v_1) was not detected because it is not sensitive in the infra-red region.

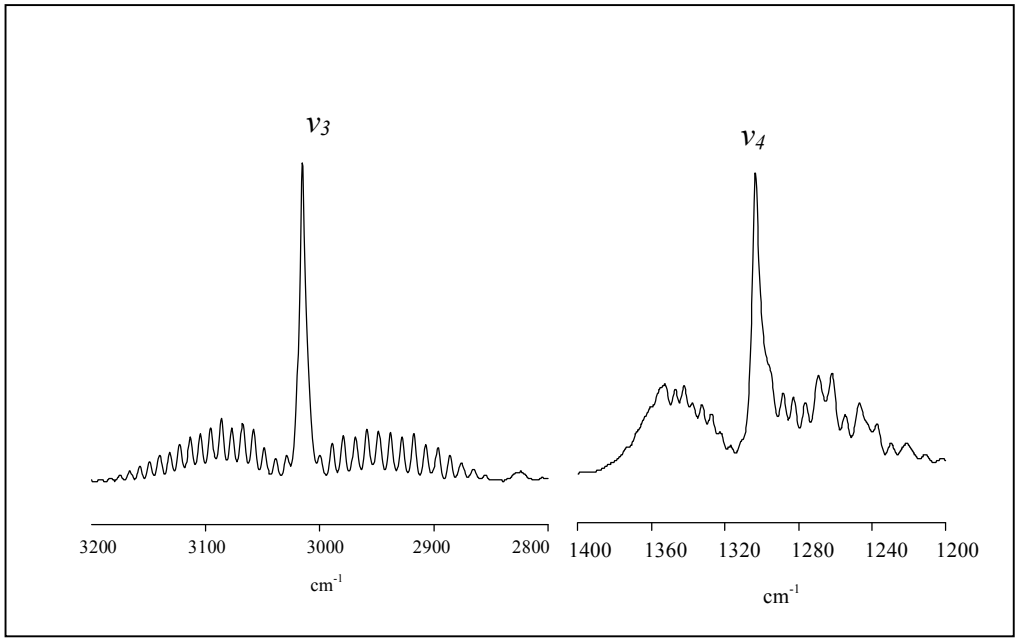

Figure 4.33: FTIR spectra of CH_4 (gas phase) at 293 K and 137 kPa .

Figures 4.34 and 4.35 show the FTIR spectra of methane adsorbed on channel and cage-type zeolites. Peak around 3015 cm^{-1} is assigned to the v_3 (antisymmetric) of adsorbed CH_4. It is a result of free rotation of the adsorbed molecules around a single axis normal to the adsorbent surface (Yamazaki *et al.*, 2000). Except zeolite beta, peaks in this region are relatively weak and v_3-vibration band of methane splitted at pressure 137 kPa. This finding suggests that the methane molecules experience non-symmetrical field from the pore wall of the zeolites.

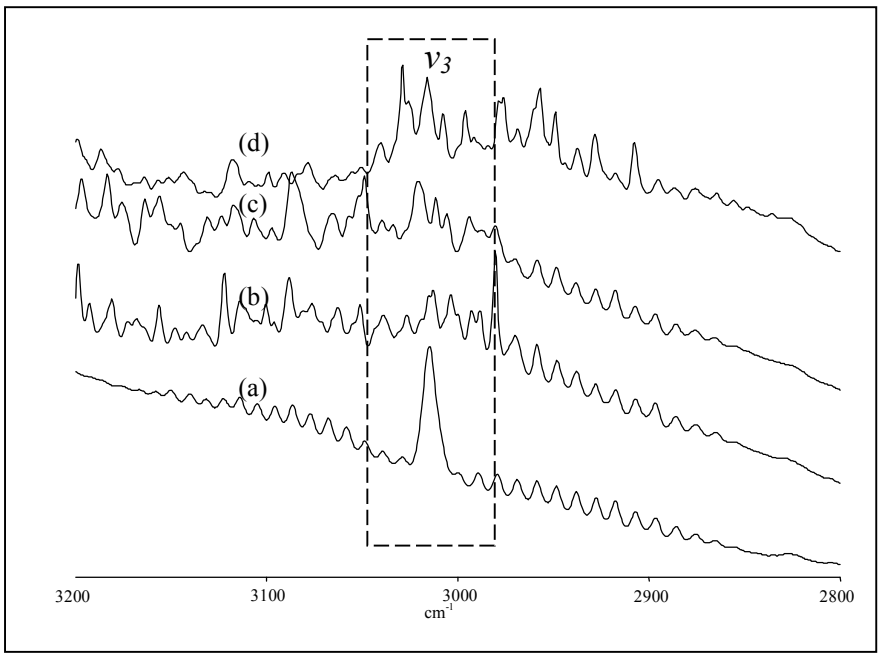

Figure 4.34: The FTIR spectra (v_3) of methane adsorbed on zeolites at 293K and 137 kPa: (a) zeolite beta; (b) ZSM-5; (c) mordenite; and (d) ferrierite.

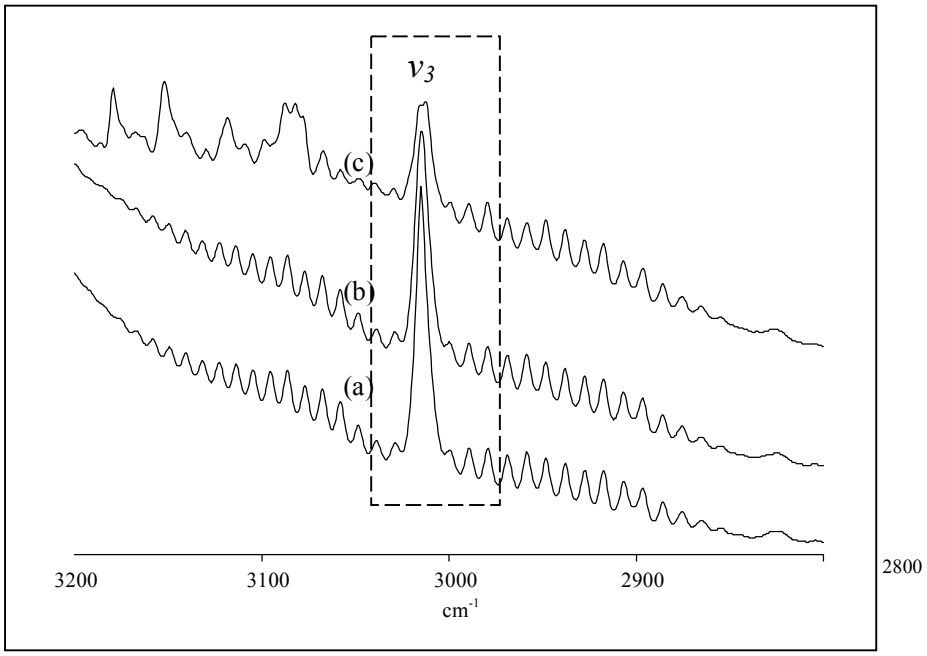

Figure 4.35: The FTIR spectra (v_3) of methane adsorbed on zeolites at 293K and 137 kPa: (a) NaY; (b) Na-SZ18; and (c) NaX.

In contrast to that, zeolite beta having larger pore size (based on the average pore diameter) and the adsorbed molecules in the pore have large freedom of rotation and would experience symmetrical field from the pore wall of the zeolites. The spectra also show that the peak intensities for cage type zeolites are higher and sharper than channel type zeolites. The peak positions also shift to the low-frequency side of methane gas, in which indicate that the adsorbed molecules experience some perturbation. The presence of supercages within faujasite structures (NaX, NaY, and Na-SZ18) would allow the larger freedom for the adsorbed molecules to rotate and experience a symmetrical field from the pore wall of the zeolites.

A weaker band in the spectra around 2900 cm^{-1} assigned to v_1 (symmetric) band is induced by adsorbate interaction with the adsorption site which could only be observed at temperature lower than 273K (Yamazaki *et al*., 2000). According to Yoshida *et al*. (2000), the band is very weak, and the integrated intensity ratio of v_1 band to v_3 is about 1/40. The band (v_1) actually represents the effect of the electrical

field on the adsorption sites rather than a strong dispersion force at the surface of the zeolite (Yoshida *et al*., 2000). This peak could not be detected in all samples and as reported by Yamazaki *et al*. (2000), it is only clearly visible in the adsorption of CH_4 on Ω-zeolite at lower temperature (196 K).

There is another band in the region around 1300 cm^{-1} that is assigned to v_4 band. The appearance of v_4 band is induced by the interaction of adsorbed molecules with the sites creating an electrical field at the surface. Figure 4.36 shows the FTIR spectra of the channel type zeolites. However, except for zeolite beta, the peaks could not be clearly distinguished from other peaks. This indicates that only weak interaction exists between the adsorbate and the channel type zeolite adsorbents. Stronger peak appeared in zeolite beta spectrum could be due to the unspecific interaction between methane and the pore, which has larger average pore diameter. In contrast to channel type zeolites, FTIR spectra of v_4 band for methane adsorbed in cage type zeolites are clearly shown in Figure 4.37.

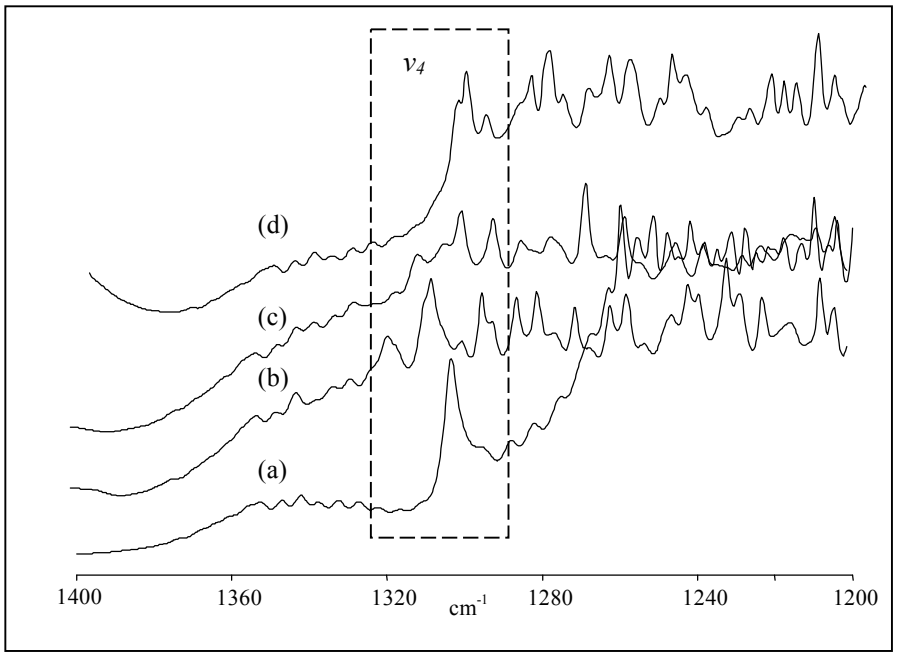

Figure 4.36: The FTIR spectra (v_4) of methane adsorbed on zeolites at 293K and 137 kPa: (a) zeolite beta; (b) ZSM-5; (c) mordenite; and (d) ferrierite.

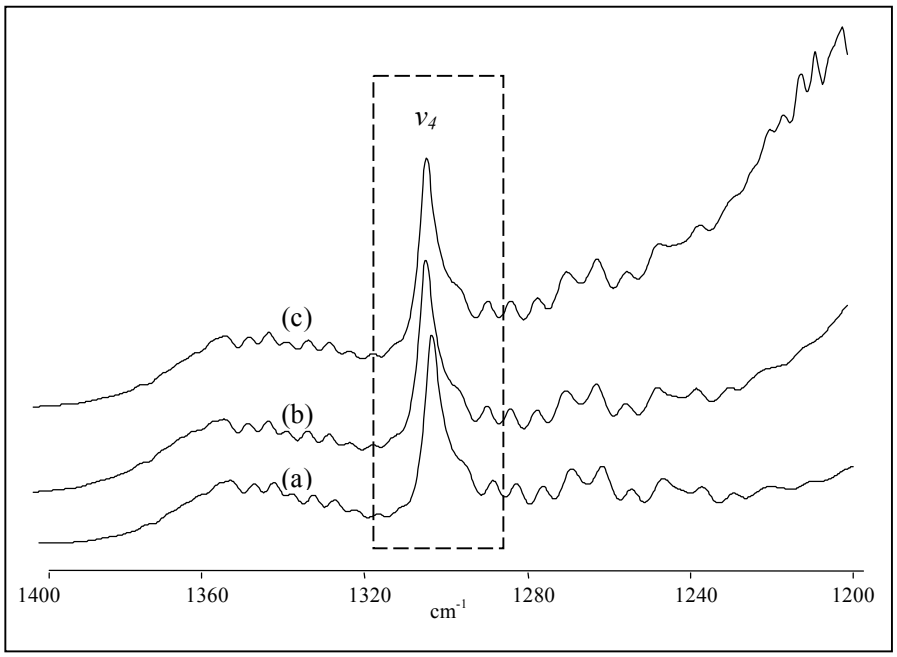

Figure 4.37: The FTIR spectra (v_4) of methane adsorbed on zeolites at 293K and 137 kPa: (a) NaY; (b) Na-SZ18; and (c) NaX.

As discussed in the earlier section, the interaction between CH_4 and the wall of zeolite structure is not based on the active sites but it is more likely due to the confinement effect (Yang *et al.*, 2001). This explains the reason why peaks that assigned to v_3 and v_4 are clearly shown in FTIR spectrum of NaX, NaY, and Na-SZ18 zeolites (cage-type structure). The FTIR spectra were further examined in order to understand the interaction between the adsorbed molecules and the zeolites. The magnitude of the *v*-peak shift is correlated with the strength of the interaction at the adsorption site. It is also known that the band intensity relatively represents the strength and the amount of molecules adsorbed on zeolites. Table 4.19 shows that at 298 K and 137 kPa, the peaks are shifted to lower wavelength values. These phenomena indicate that there are some interactions between methane and zeolite even though they are only a weak interactions.

It suggests that desorption could be easily achieved either by increasing the temperature or reducing the pressure of the adsorption system. As reported by Yamazaki *et al*. (2000), peak area does not actually represent total the amount of

methane adsorbed, but it relatively indicates the extent of adsorption in each zeolites. From the peak area of other samples, it is evident that cage type zeolite gives better adsorption than channel type zeolites.

Table 4.19: The peak position of v_3 and v_4 bands and area of the adsorbed methane.

Zeolite	v_3 band		v_4 band	
	Peak position (cm^{-1})	Area (cm^2)	Peak position (cm^{-1})	Area (cm^2)
CH_4	3020		1306	
Channel:				
Beta	3015 (-5)	14.80	1303 (-3)	9.12
ZSM-5	3013 (-7)	3.23	1307 (+1)	4.56
Mordenite	3011 (-9)	0.95	1303 (-3)	0.13
Ferrierite	3016 (-4)	4.04	1303 (-3)	4.50
Cage:				
NaY	3015 (-5)	18.52	1303 (-3)	11.35
NaX	3012 (-8)	9.67	1303(-3)	10.81
Na-SZ18	3015 (-5)	15.66	1303 (-3)	11.90

The FTIR spectra of carbon dioxide are shown in Figure 4.38. The asymmetric stretching is predicted at 2640 cm^{-1} but it could only be observed at 2345 cm^{-1}. Another symmetric stretching is predicted at 1537 cm^{-1} which is not IR active. In the case of adsorbed CO_2 on zeolites, two well defined peaks appear in two regions, 2300 cm^{-1} and 1600 cm^{-1}. Peak in the first region is likely belong to v_3 band, which represents the physisorbed undissociated molecular CO_2 species (Rege and Yang, 2001). Another peak corresponding to chemisorbed species that appears in the second region (~1600 cm^{-1}). This typically corresponds to CO_2 molecules adsorbed either in linear configuration on cations (v_2 band), or in non-linear (bent) manner in the form of carbonate or bicarbonate ions.

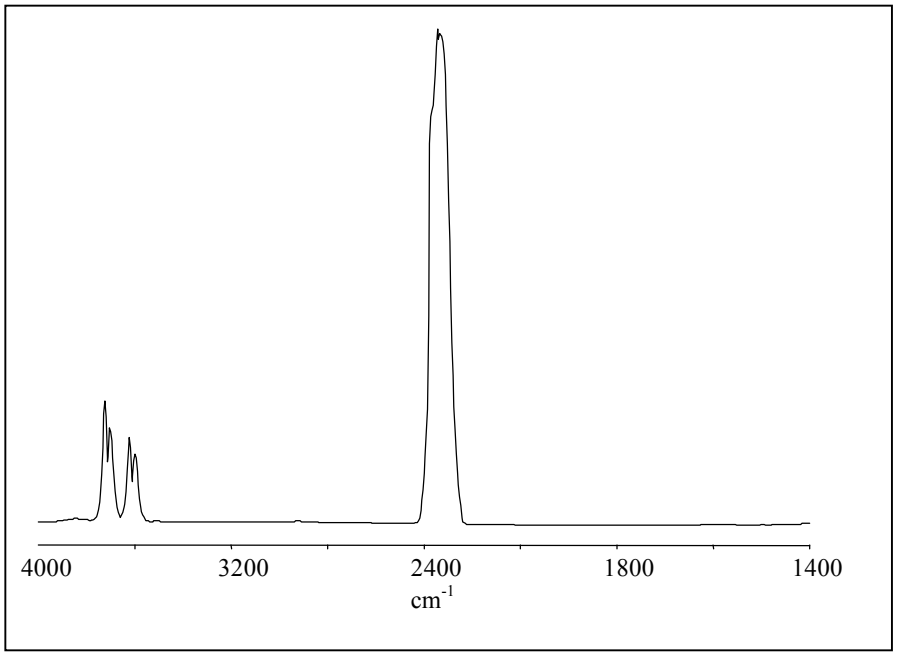

Figure 4.38: The FTIR of carbon dioxide molecules (gas phase) at 293K and 137 kPa.

The analysis of adsorbed spectra on different types of zeolites indicates the presence of adsorption band in the region of the 2350 – 2370 cm^{-1} and 1500 – 1700 cm^{-1} that assigned to v_3 and v_2 respectively (Figures 4.39 and 4.40). General observation shows that the v_3 and v_2 bands of cage type zeolite have higher intensity than the channel type zeolites. It was also observed that the v_3 peaks broadens and resolved into several peaks. This fine structure of the CO_2 bands probably reflects CO_2 adsorption at different sites. These peaks are in accordance with previous observation by Rege and Yang (2001). Thus, it is important to note that quadrapole moment could cause a strong interaction between CO_2 molecules and zeolite surfaces especially in the v_3 band region. Similarly, v_2 bands for Na-SZ18, NaX and NaY are also broadened and resolved into several peaks. However, a weak v_2 bands are visible in the region of 1500 – 1700 cm^{-1} for mordenite, ferrierite, beta and ZSM-5 zeolites. This indicates that more molecules are physically adsorbed on the surface.

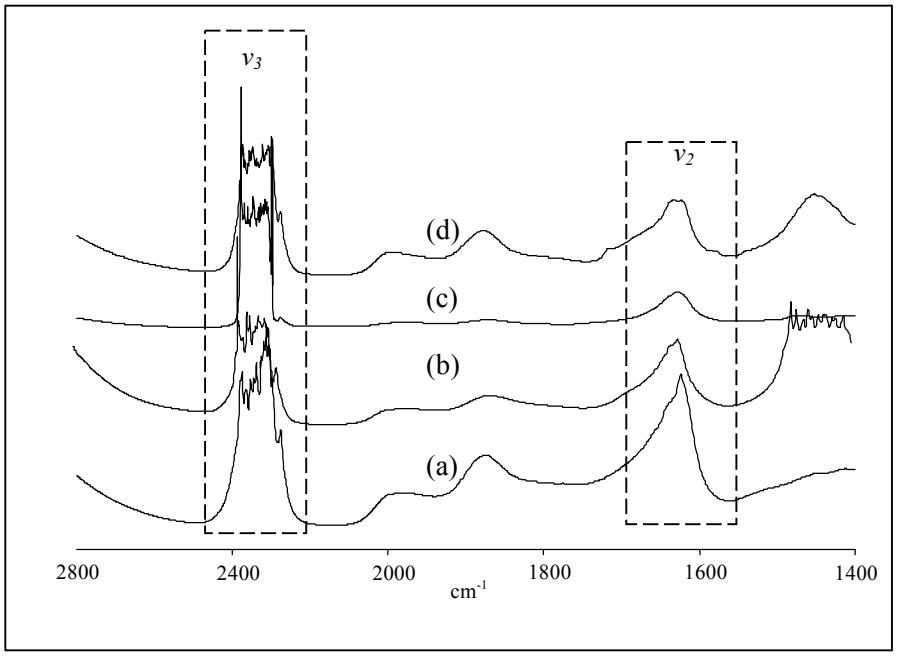

Figure 4.39: The FTIR spectra (v_3 and v_2) of carbon dioxide adsorbed on channel type zeolites at 293K and 137 kPa: (a) mordenite; (b) ferrierite; (c) beta; and (d) ZSM-5.

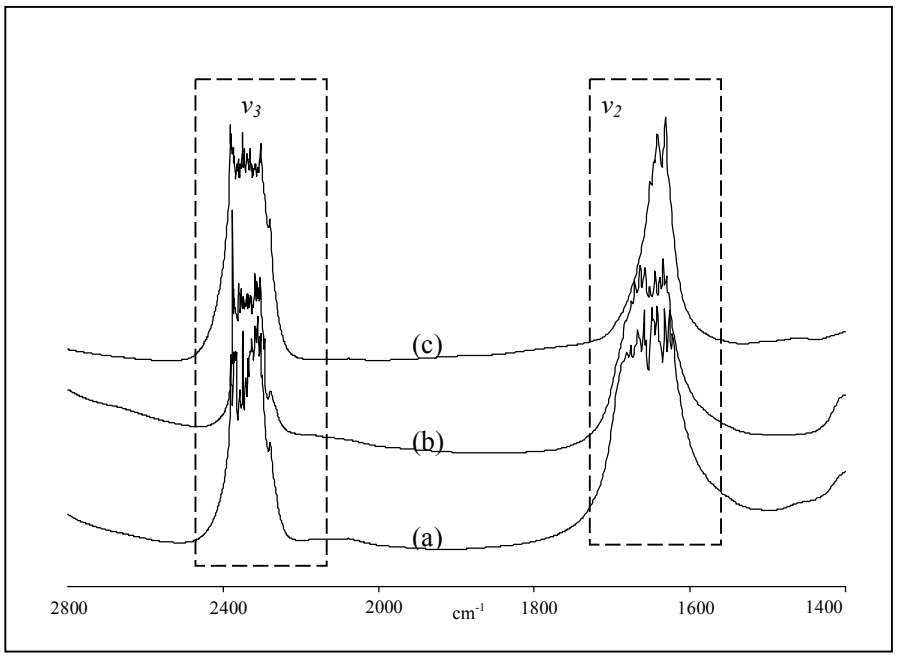

Figure 4.40: The FTIR spectra (v_3 and v_2) of carbon dioxide adsorbed on cage type zeolites at 293K and 137 kPa: (a) Na-SZ18; (b) NaX; and (c) NaY.

As mentioned previously, the magnitude of *v* peak shifting indicates the strength of the interaction between the adsorbed molecules and the adsorption sites. Table 4.20 shows that the magnitude of peak shifting for chemisorbed species (v_2) is greater than the physisorbed species (v_3), which is more obvious in channel type zeolites and NaY zeolite. However, results for NaX and Na-SZ18 zeolites show an equal strength of physisorption and chemisorption interactions between CO_2 and zeolite. The calculated area also gives some insight on the adsorption phenomena of CO_2. The results show the amount of molecules physically and chemically adsorbed on the sites. As shown in the XRD patterns, zeolite beta used in this study has low crystallinity as compared to other channel type zeolites. This might explain the reason why the peak area is small. Hence, the collapse of structural framework resulting in the formation of mesopore and macropore reduces the active sites for adsorption.

Table 4.20: Peak position of v_3 and v_2 band and area of the adsorbed carbon dioxide.

Zeolite	v_3 band		v_2 band	
	Peak position (cm^{-1})	Area (cm^2)	Peak position (cm^{-1})	Area (cm^2)
CO2	2359	-	1687	-
Channel:				
Beta	2339 (-20)	155.35	1628 (-59)	58.89
ZSM-5	2329 (-30)	347.70	1629 (-58)	108.48
Mordenite	2319 (-40)	263.65	1624 (-63)	107.01
Ferrierite	2329 (-30)	243.57	1624 (-63)	102.69
Cage:				
NaY	2339 (-20)	433.69	1635 (-52)	160.57
NaX	2329 (-30)	193.68	1655 (-32)	293.56
Na-SZ18	2317 (-42)	303.11	1649 (-38)	297.65

In this study, both adsorbates have kinetic diameter smaller than pore diameter of zeolites. It is assumed that the diffusions of these molecules are not affected by the pore size of the zeolites. However, the adsorption on different structural framework shows that each adsorbate does not have similar adsorption characteristics. This study clearly shows that adsorption of CO_2 was affected by the interaction between the quadrapole moment of gas molecules and the electrical field created by the structural cations in zeolites. Strong interactions between CO_2 and zeolites are clearly shown in the FTIR spectra especially in the region of 1500 – 1700 cm^{-1}. However, CH_4 is a non-polar molecule which has no specific interaction with zeolite surfaces. The adsorption mechanism of CH_4 follows micropore filling theory which the adsorption increases gradually until it reaches saturation. The FTIR study also shows that adsorbate properties influence the adsorption characteristics of zeolites.

It is important to realize that apart from the properties of adsorbate and adsorbent, other experimental parameter such as temperature and pressure could affect the interaction of the adsorbate and adsorbent. As described in Section 3.5.4, adsorption at different pressures was carried out by introducing the gas at the respective pressures after outgassing (vacuum pressure < 2 x 10^{-3} kPa) the adsorption cell for 2 hours. The FTIR spectra show that as the pressure increases, the peak assigned to v_3 band resolves into two peaks, but v_4 band retains as single peak (Figures 4.41 and 4.42). Hence, this explained the disappearance of sharp peaks in the region of 3015 cm^{-1} for samples such as ZSM-5, mordenite, and zeolite beta. The splitting of peaks might indicate the effect of high adsorbate concentration. As the concentration at particular site increases, the adsorbate molecule might lost a certain degree of rotational freedom (Yamazaki *et al*., 2000; Scarano *et al*., 2001).

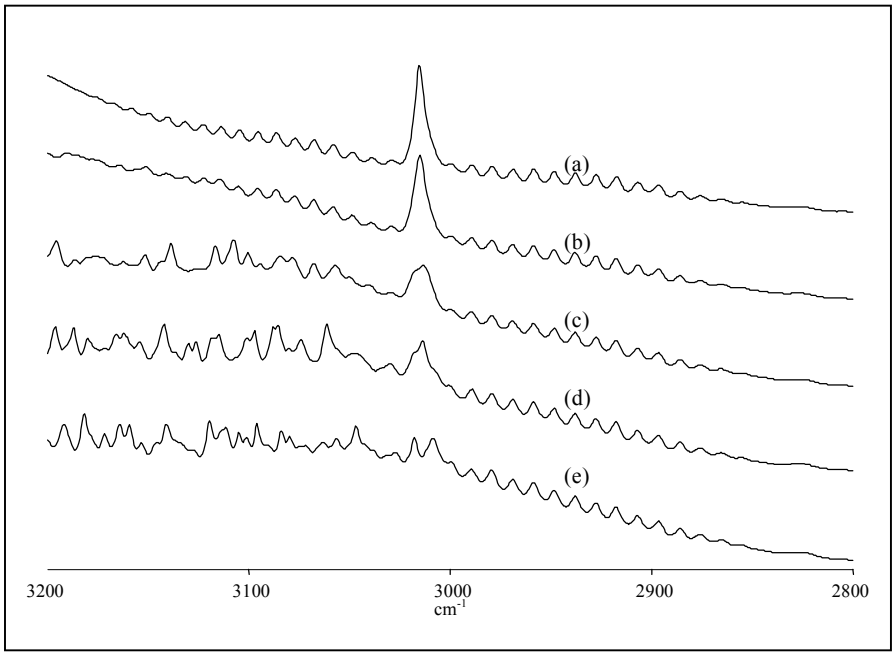

Figure 4.41: The effect of pressure on v_3 band of methane adsorbed at different pressures: (a) 5 psi; (b) 10 psi; (c) 20 psi; (d) 30 psi; and (e) 40 psi.

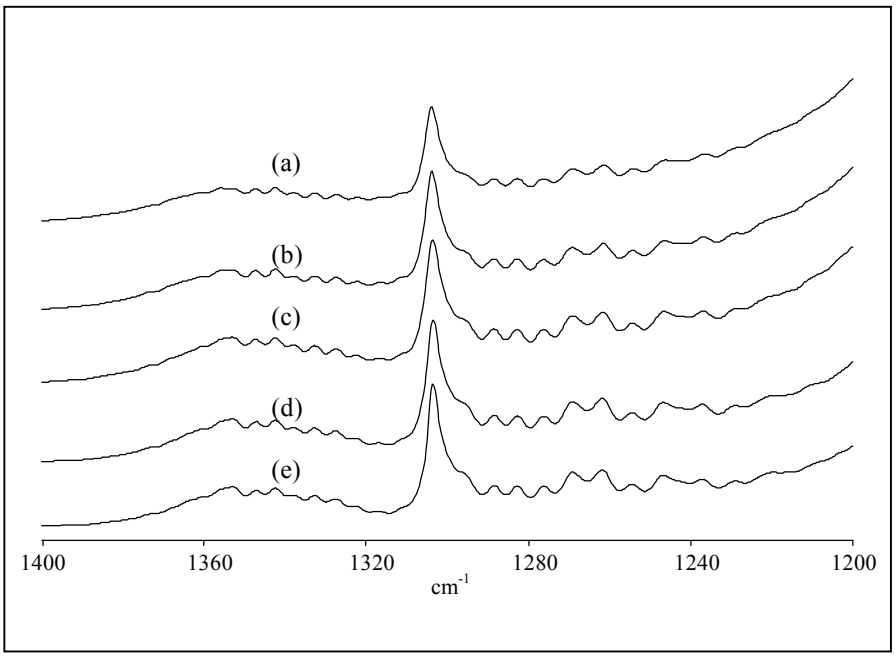

Figure 4.42: The effect of pressure on v_4 band of methane adsorption: (a) 5 psi; (b) 10 psi; (c) 20 psi; (d) 30 psi; and (e) 40 psi.

4.6 Gas Adsorption Mechanism of Different Zeolite Structural Frameworks

According to Suzuki (1990), depending on the structure of the adsorbent, several types of diffusion mechanisms become dominant and sometimes two or three of them compete or cooperate. The dominant mechanism also depends on a combination of adsorbate and adsorbent, and adsorption conditions used such as pressure, temperature, and concentration range. In microporous adsorbent such as zeolite and activated carbon, macropores usually act as a path for the adsorbate molecules to reach the interior part of the particle.

Based on results presented on previous sections, this section will summarise and propose the mechanistic model of gas adsorption process with special emphasize on the influence of structurally different zeolites. It has well established that the adsorption process involves several mechanisms namely bulk phase diffusion, macropore diffusion, micropore diffusion, and finally adsorption on the surface of the pore adsorbents. As presented in Section 4.4.3.1, the bulk phase diffusion (molecular or Fick's diffusion) is in the order of 10^{-5} for both types of adsorbate. Similarly, as the size of the macropore is larger than the molecular size of the adsorbates, it is assumed that the diffusion inside the macropore channel is also molecular (Fick's) diffusion. However, based on the average pore diameter of the zeolites and the kinetic diameters of methane and carbon dioxide, diffusion inside zeolite's microchannel is Knudsen-type diffusion. The interaction between gas molecule and the wall of the micro-channel becomes more dominant. The diffusion of gas molecules inside the pores is slower than bulk phase diffusion, in which Knudsen diffusivity (D_{Kn}) is in the order of 10^{-7}(Table 4.15). Except for zeolite beta, the results presented in Section 4.4.2.2 suggest that, in general, the diffusion in the microstructure of zeolite is much slower than the bulk phase diffusion.

Since the properties of adsorbates used in this study are different, thus the adsorption mechanisms are expected to be different. Figure 4.43 illustrates the

adsorption phenomena that occurred inside the zeolite structures. As discussed in Section 4.3.1, the adsorbates are more easily diffuse through a straight channel than the zig-zag channel. The blockage either at the pore opening of cage structure or at the zig-zag channel is more likely to occur during CO_2 adsorption. This is because the quadrapole moment of CO_2 strongly interacts with the active adsorption sites (cation sites) and the migration of molecules from one site to another is restricted by the microchannel diameters through which the migration takes place. In this case, any channel with diameter that is approximately of the same magnitude of the diameter of adsorbates might experience 'trapping' condition. This is especially true for CO_2 molecules in which the strong interaction with the adsorption sites would prevent further diffusion of molecules.

In the case of CH_4, the forces between the molecules and the wall of adsorbent are likely the most important interactions for stabilizing adsorption in the cavities. Even though the affinity of CH_4 on zeolite is low and in most cases was neglected, the adsorption isotherm proved that adsorption occurs inside the micropore. In addition, since the adsorbates (methane) are not strongly bonded, the molecules could easily diffuse to low concentration site according to the pore filling theory.

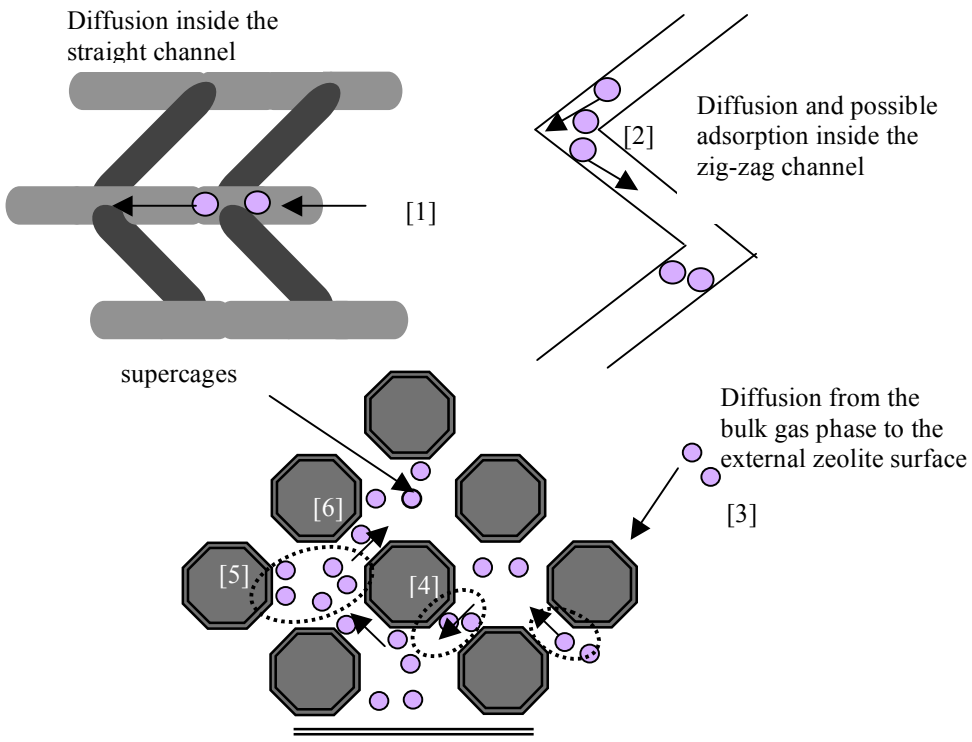

[1] Adsorbates could easily diffuse inside the straight channel.

[2] There is possible blockage inside the zig-zag channel especially when the adsorbate strongly adsorbed (e.g carbon dioxide) at the adsorption site. The flexibility of the framework structure would allow the adsorbate to diffuse.

[3] Molecules could easily diffuse due to large pore diameter - Fick's or molecular diffusion.

[4] The flexibility of pore diameter would allow the molecules diffuse through the micro-channel.

[5] Molecules could easily 'jump' one adsorption site to another site – pore filling.

[6] Strongly bonded adsorbate at the pore opening could possibly become a hindrace for other molecules to diffuse - Knudsen diffusion.

Figure 4.43: A schematic diagram illustrates gas diffusion inside the zeolite structures.

According to Guo (1998), when a porous solid contains pores of molecular dimension like zeolites pores, it is more realistic to consider that there is only adsorption phase instead of co-existing gas phase and adsorption phase. In addition, as this study was carried out at between 298 to 323 K and pressure up to 137 kPa, the calculated compressibility factor of adsorbates lies between 0.99 – 0.96 indicates that the molecules behaves like ideal gas. If the gas adsorption follows BET theory, the first layer of adsorbate is fixed on the solid surface due to interaction between the gas and solid.

When the surface is fully covered with a layer of adsorbate, other gas molecules will adsorbed above the first layer, due to interaction between the same species and so on. The ratio of surface coverage > 1 indicates that multilayer adsorption might occur. However, for surface coverage < 1, the multilayer adsorption could also possibly occur at selected active sites. Figure 4.44 illustrates the phenomena monolayer and multi-layer adsorption that occurred inside the channel and cage type zeolites. It is also important to note that interaction between the first layer and the adsorbent is not the same as the interaction between the first and the second layer of adsorbates, the second and the third layer of adsorbates, and so on. Similarly, the effect of electrostatic field from the solid surface decreases as the distance between adsorbate-adsorbent increases.

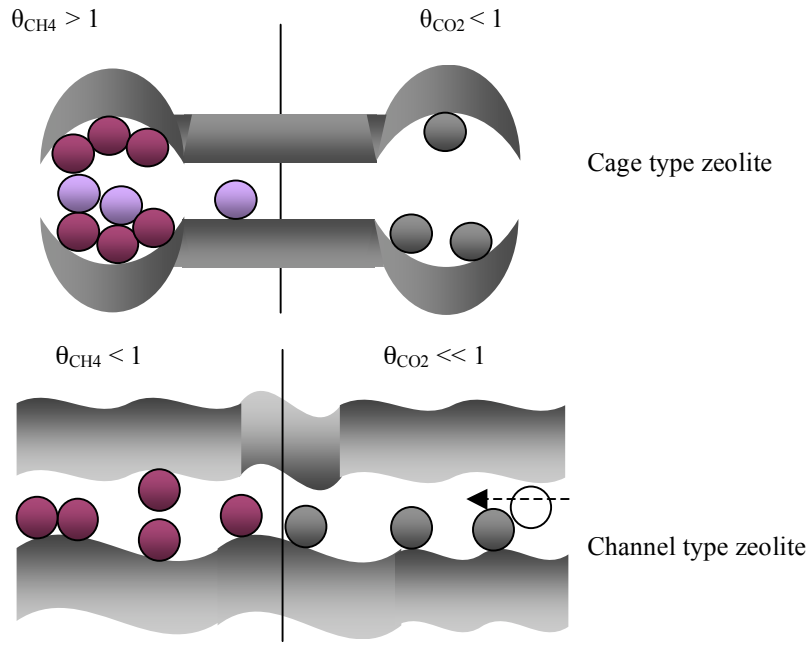

[1] Surface coverage (θ) greater than 1 indicates the formation of multilayer adsorption inside the cage type zeolite. Small pore diameter reduces the possibility of multilayer adsorption.

[2] It is also possible for multilayer adsorption to occur even though the surface coverage (θ) is less than 1. The adsorption of carbon dioxide most likely occurs on selected adsorption site, whenever the diffusion is possible.

[3] Methane easily diffuses through the pore due to less specific interaction,

- longer equilibrium time,
- low initial adsorption rate.

[4] The amount of carbon dioxide adsorbed is significantly reduced as the adsorbate could not further diffuse to other adsorption sites due to blockage from the strongly bonded adsorbate,

- low heat adsorption ,
- shorter equilibrium time.

Figure 4.44: A schematic diagram illustrates gas adsorption on different zeolite adsorbents.

As discussed in Section 4.4, there are several possible adsorption sites for methane and carbon dioxide adsorption. The electrostatic attractions between the adsorbate and zeolite adsorbent are illustrated in Figure 4.45. The carbon atom of adsorbed methane may interact with silicon and sodium atom of zeolite adsorbent while hydrogen may interact with oxygen and aluminium atoms. Similarly, carbon atom of adsorbed carbon dioxide may interact with oxygen while oxygen atom of the adsorbed carbon dioxide may interact with sodium, silicon, and aluminium of the adsorbent.

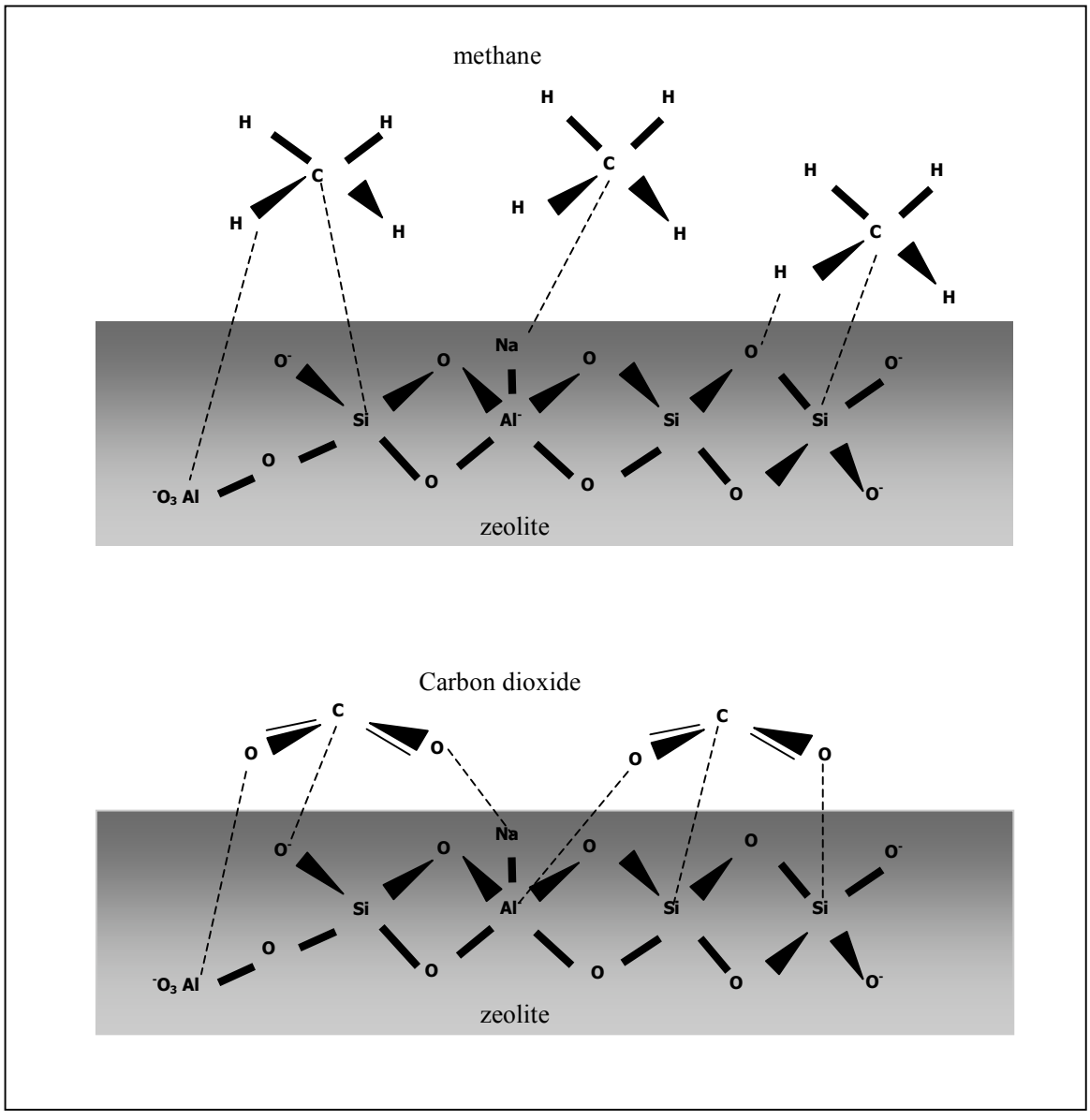

Figure 4.45: A schematic diagram indicates all possibilities of electrostatic interactions between adsorbate and zeolite adsorbent.

4.6 Summary

A large numbers of different zeolite structures offer many possibilities for specific application. In order to choose suitable adsorbent, adsorption characteristics of adsorbate-adsorbent need to be well understood. Proper understanding of zeolite structure and its characteristics may improve many existing process economically and many new chemical processes are possible. Since there are several zeolitic materials available in the market, it is important to know the potential use of different structures by investigating the effect of zeolites physical and chemical properties on adsorption as well as the interaction between gas molecules and zeolites. This knowledge will enable us to evaluate the performance of structurally different zeolite as an adsorbent.

The study based on structurally different zeolites has found that cage type of zeolites (NaY, NaX, and Na-SZ18) adsorbed more than channel type zeolites. The cages provide space for the adsorbate to reside inside the structure. It suggests that type of structural framework is important factor in selecting type of adsorbent used especially when high adsorption capacity is required. In addition, the accessibility is also important in determining adsorption capacity. Three dimensional pore system and large pore opening would reduce the possibility of pore blocking problem. However, the physical properties such as surface area and pore volume are still important in gas adsorption.

Gas adsorption using synthesized zeolite (Na-SZ18) as adsorbent proved that achieving 100 % crystalline phase should not be the ultimate goal in zeolite adsorbent production. This study shows that that the presence of structural defects increase the active sites, thus increase the amount of methane and carbon dioxide adsorbed. However, too much amorphous phase as shown in the adsorption of methane and carbon dioxide on zeolite beta is not also recommended. Therefore,

using zeolite characterization technique such as XRD and nitrogen adsorption, the properties of suitable adsorbent can be determined.

In addition, the thermodynamic data have shown that properties of adsorbate, (methane - non-polar molecule and carbon dioxide - quadrapole moment) affect the characteristics of adsorption. However, the fractional uptake curve of methane shows the effect of cage-like structure on methane adsorption. The result indicates properties of adsorbent (type of structure and pore diameter). There that the kinetic of methane adsorption is strongly influence by the is no clear evidence on the adsorption of carbon dioxide, which suggests that the quadrapole moment (adsorbate property) has greater influence on the kinetic of carbon dioxide adsorption the structural framework of zeolites. Furthermore, the study on gas-zeolite interaction also indicates that there is strong interaction between carbon dioxide and the adsorption site (cation) of zeolite.

Therefore, based on the gas adsorption characteristic of structurally different zeolites, cage type zeolite shows a promising performance as methane and carbon dioxide adsorbents. Na-SZ18 was selected for modification by metal cation exchange method. The effect of different metal cations on zeolite structural framework, zeolite physical properties, and gas adsorption characteristics will be discussed in Chapter 5.

CHAPTER 5

GAS ADSORPTION CHARACTERISTICS OF METAL ION EXCHANGED ZEOLITES

5.1 Introduction

As discussed in Chapter 2, crystalline zeolite consists of silicon and aluminium atoms, which are tetrahedrally coordinated by oxygen atoms. For every aluminium atom that is incorporated into the framework, one excess negative charge results, which needs to be balanced by an equivalent amount of extra-framework cation, in order to maintain neutrality of the framework. These cations exist inside the cages and channels together with intra-zeolitic water. Since the cations are not covalently bound, it can easily be replaced by other cations. The exchange of sodium ion in zeolite structural framework with other cation of different charges and molecular sizes, and with different quantity influences the physical and chemical properties of the zeolite. According to Hernandez-Huesca *et al*. (1999), different cationic forms may lead to differences in the adsorption of a given gas, due to the properties and location of the cations in the structure. Cation also affects the local electrostatic field and polarization of adsorbates (Bellat *et al*., 1995; Choudhary and Mayadevi, 1996; Hernandez-Huesca *et al*., 1999; Hutson *et al*., 1999, Walton *et al*., 2006).

One of the modification methods that could be used to investigate the effect of different cation on gas adsorption is cation exchange. Using this method, modification of zeolite properties at the molecular level takes place in which the extra-framework sodium is replaced by other metal cations. Ma (1984) has reported that the effect of cation on adsorption depends primarily on the size and shape of the guest molecule, the size of the cation and its location in the channel, and the interaction between cation and the guest molecule. It was also reported that the adsorption capacity of several hydrocarbons on ZSM-5 modified with Li, Na, K, Rb, and Cs decreases as the radius of the cation increases (Wu and Ma, 1983). This is due to the fact that cation exchange treatments cause some changes in structural properties and physicochemical properties of zeolites, thus affect the amount adsorbed and adsorption behavior of the gases.

According to Öhman *et al*. (2002), the strength of cation bind to the exchange sites depends on the type of cation. Di- and trivalent ions frequently bound stronger than monovalent ions. However, the latter may act as site blocker for the former. In addition, changing the cations in a zeolite may effectively enlarge or narrow the pore openings by diminishing or adding the cation population and/or resiting of cation, which are normally located near these openings. Typically, the presence of a divalent cation opens the aperture to full diameter, whereas exchanging it with a larger univalent ion diminishes the aperture size. It has been reported that using both cavities of faujasite group of zeolite could be utilized as a nano-container (Heo and Lim, 1996).

However, the presence of different cations might change the adsorptive characteristics of zeolite adsorbents. Thus, in order to control the accessibility of gas molecules, suitable types of cation need to be initially identified and the amount of exchanged cations should to be monitored and controlled. Besides all the advantages of using cation exchanged as modification method, structural destruction might occur which is due to the acidity of the solution or size of cation. The damage may have occurred during the exchange or during the dehydration. Thus, before

investigating the characteristics of gas adsorption on metal exchanged zeolites, it is also important to determine the structural, physical and chemical properties of the adsorbent and the changes due to cation exchange treatment.

Therefore, this chapter will discuss the effect of exchanging sodium ions with several types of cations (alkali metals, alkaline earth metals, and transition metal) on gas adsorption characteristics. The materials and method used in the cation exchange procedures have been previously described in Chapter 3. The study on structurally different zeolites (Chapter 4) has shown that cage type zeolites (NaX, NaY and Na-SZ18) are better adsorbent than channel type zeolites. It was based on the results of adsorption capacity, the initial adsorption rate, and adsorbate-zeolite interaction study. Since the adsorption capacity of Na-SZ18 is higher than NaX and NaY zeolites, Na-SZ18 was selected for further gas adsorption study by modifying the zeolite using cation exchange method.

As discussed in Chapter 4, faujasite structure (eg. NaX and NaY) consists of large and small cavities namely supercages and sodalite respectively. The Si/Al ratio indicates that the zeolite has high aluminium content. It is important to note that by using zeolite with high aluminium content, the possibility of having sodium being exchanged with other cation is high, thus allowing investigation on the adsorption characteristics as a function of pore size, micropore area, and pore volume in the presence of different cation. Again, based on methodology presented in Chapter 3, this chapter will discuss the effect of metal cations in zeolites on gas adsorption isotherm of methane and carbon dioxide, the uptake rate, heat of adsorption, and gas-zeolite interaction. Finally, the mechanism of gas adsorption on metal exchanged zeolites is proposed.

5.2 Properties of Cation Exchanged Zeolites

5.2.1 Introduction to metal cations

This study involved exchange of extra-framework sodium with metal cation that belongs to Group IA, IIA, and transition metals (IIB, VIIB, and VIIIB) in the Periodic Table (Figure 5.1). The metal cations were selected to represent three different groups of metal that listed in the Periodic Table. Study on these groups of metal cations is important in order to understand their effect on adsorption characteristics of methane and carbon dioxide. Consequently, the potential metal or groups of metal would be identified for future research in gas adsorption applications. Group IA metals are known as alkali metal. Each element in Group IA has single valence electron. It consists of lithium (Li), sodium (Na), potassium (K), rubidium (Rb), cesium (Cs) and francium (Fr). The last element (Fr) is a radioactive element. These elements are highly reactive and their reactivity increases on decending the group from lithium to cesium.

Group IIA consists of beryllium (Be), magnesium (Mg), calcium (Ca), strontium (Sr), barium (Ba) and radium (Ra). Similarly, the last element is radioactive element. Group IIA is also known as alkaline earth metal with high in reactivity, but it is not as high as the alkali metal group. These metals do not exist in nature as free atoms. Atomic and ionic radii of the metals increased smoothly down the group. The ionic radii are all much smaller than the corresponding atomic radii. Transition metal is defined as an element which forms at least one cation with a partially filled sub-shell of *d* electrons. It consists of 40 elements which represent the successive addition of electrons to the *d* atomic orbitals of the atoms as one progresses through each of the three periods. The transition element form cation with a wide variety of oxidation states. Based on the methodology presented in Section 3.3.2, the sodium cations (Na^+) present in the based zeolite (Na-SZ18) was exchanged with the selected metals as shown in Table 5.1.

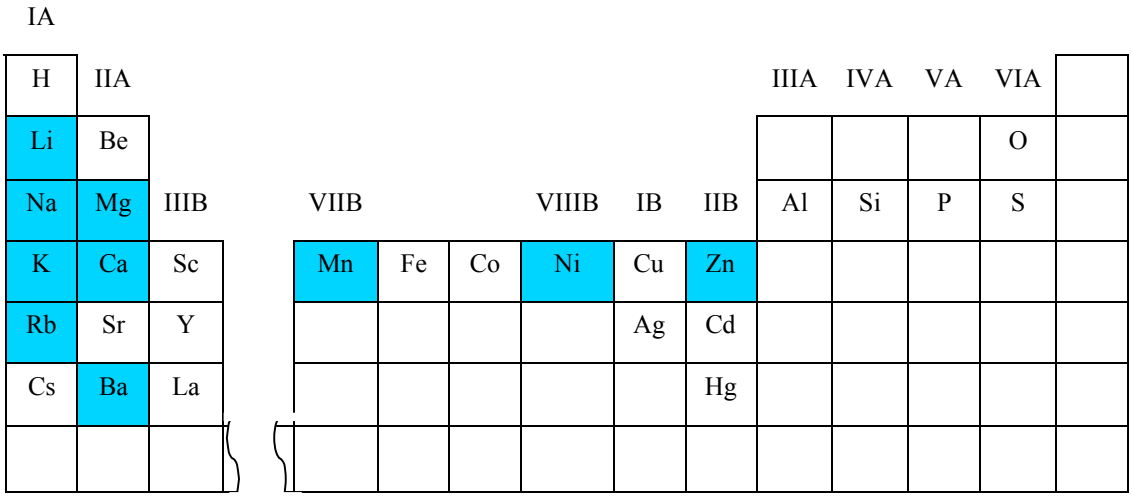

Figure 5 1: A Periodic Table indicates the groups of the selected metals cations used in the study (marked in black).

Table 5.1: The properties of cations used in this study for the cation exchanged treatment.

Cations	Atomic radius (nm)	Ionic radius (nm)	Electronegativity (Pauling)
Alkali metal:			
Lithium (Li^{+})	0.124	0.076	0.98
Sodium (Na^{+})	0.185	0.098	0.93
Potassium (K^{+})	0.227	0.138	0.82
Rubidium (Rb^{+})	0.248	0.152	0.82
Alkaline earth metal:			
Magnesium (Mg^{2+})	0.160	0.072	1.31
Calcium (Ca^{2+})	0.197	0.099	1.00
Barium (Ba^{2+})	0.217	0.135	0.89
Transition metal:			
Manganese (Mn^{2+})	0.136	0.046	1.55
Níkel (Ni^{2+})	0.125	0.069	1.91
Zink (Zn^{2+})	0.133	0.074	1.65

5.2.2 Structural determination of metal cation exchanged zeolites

As reported in the literatures, the cation exchange treatments could cause some changes in the structure and properties of zeolites (Shibata and Seff, 1997; Armor, 1998; Albert and Cheetham, 2000; Nery *et al*., 2003; Khelifa *et al*., 2004). Thus, an attempt was made to clarify the changes due to cation exchange since it may also affect the adsorption characteristics of zeolites. Scanning electron microscopy (SEM) was used to observe any changes on the morphology of cation exchanged zeolites. In this study, SEM images provide evident of almost similar size before and after the exchange treatment. Figures 5.2 and 5.3 show SEM images of the based material (Na-SZ18) and the cation exchanged zeolites respectively.

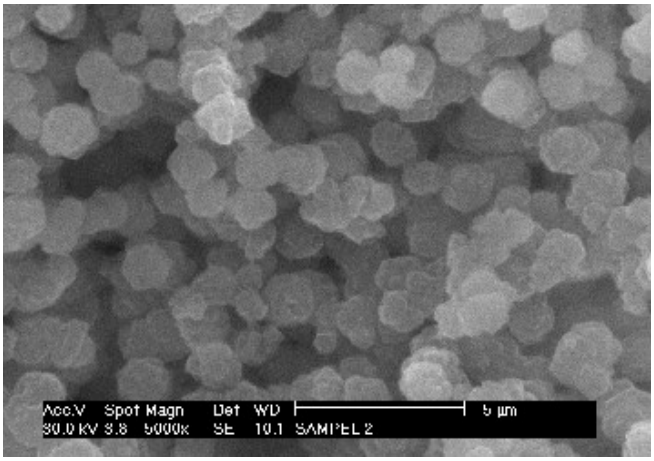

Figure 5.2: The SEM image of the Na-SZ18 crystallites (based zeolite).

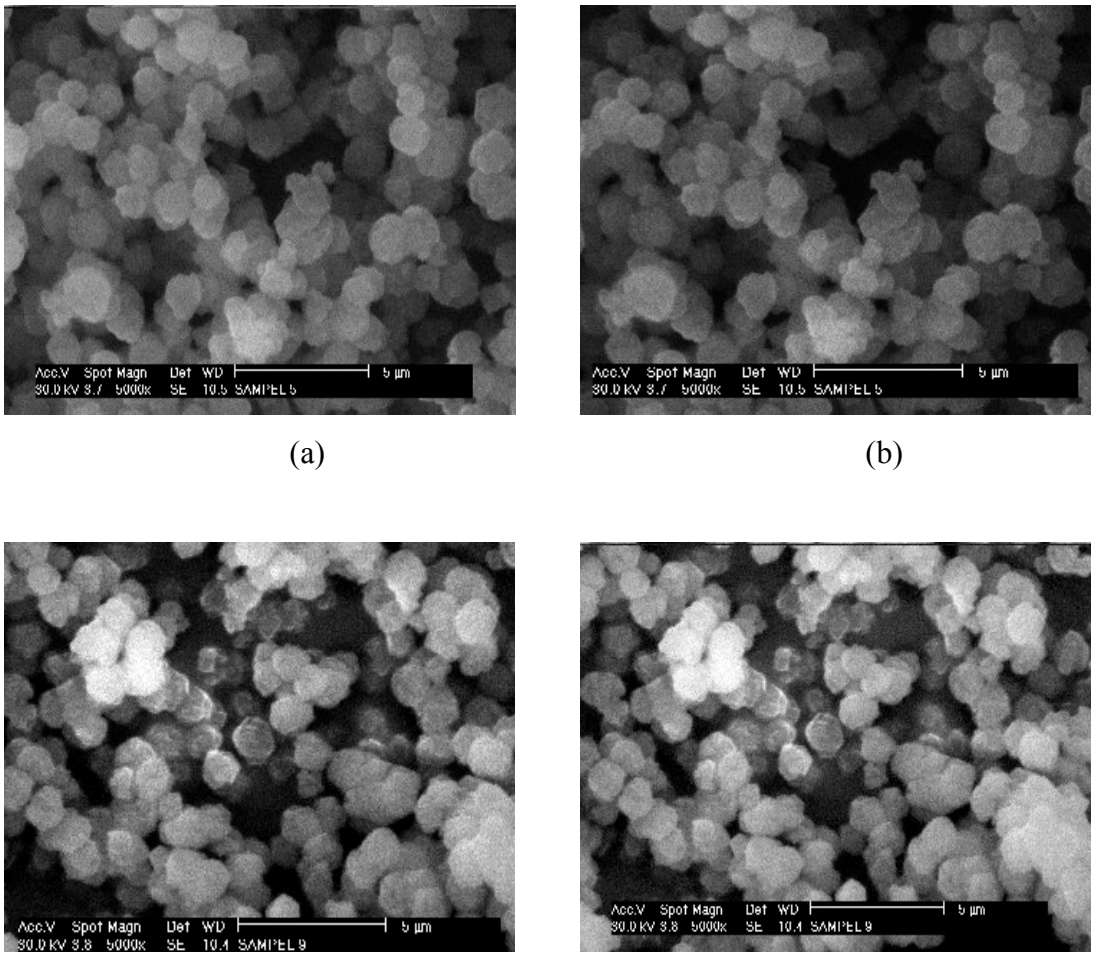

(a) (b)

(c) (d)

Figure 5.3: The SEM crystallite images of metal cation exchanged zeolites: (a) LiNa-SZ18; (b) KNa-SZ18; (c) MgNa-SZ18; and (d) BaNa-SZ18.

In general, the crystallites have nearly spherical shapes with particles diameter remains in the range of 1.0 to 1.5 µm. The particles are either in the form of single crystallites or stacked-together in small crystallites. It has irregular polyhedron, and after exchanging sodium with other cation, the particle size shows no significant changes in term of particle size. In addition, in order to elucidate the effect of cation exchange treatment on structural arrangement of the faujasite type structure, XRD spectra of metal exchanged zeolites were measured and analyzed. Again, the XRD spectra demonstrate that after cation exchange treatment, samples still retain the faujasite structural framework (Figures 5.4, 5.5, and 5.6). The crystalline phases are still visible but their intensities vary.

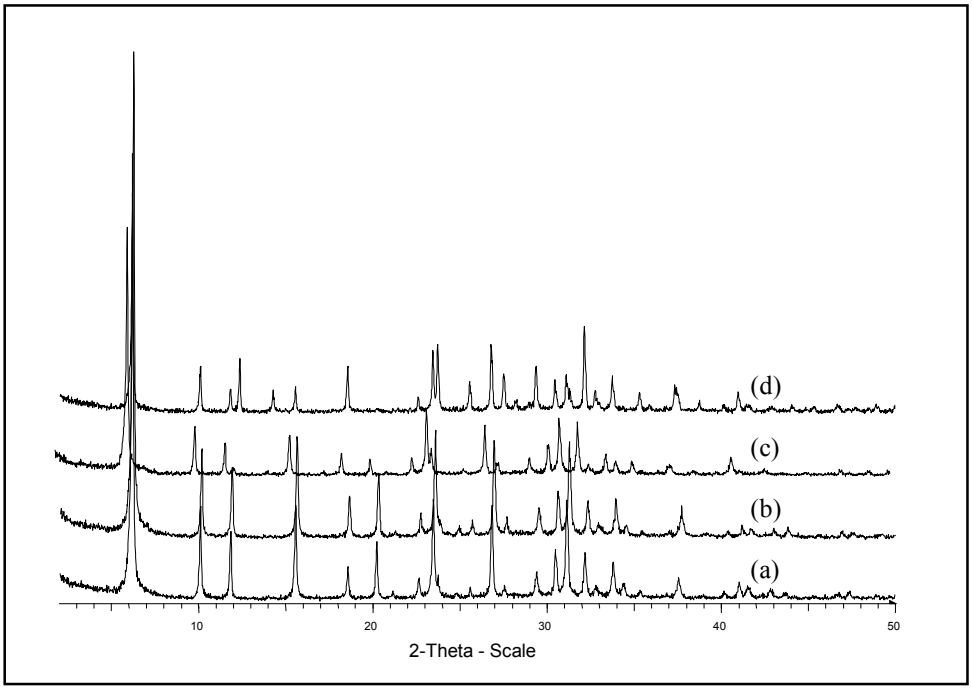

Figure 5.4: The XRD patterns of the alkali metal cation exchanged zeolites: (a) Na-SZ18; (b) LiNa-SZ18; (c) KNa-SZ18; and (d) RbNa-SZ18.

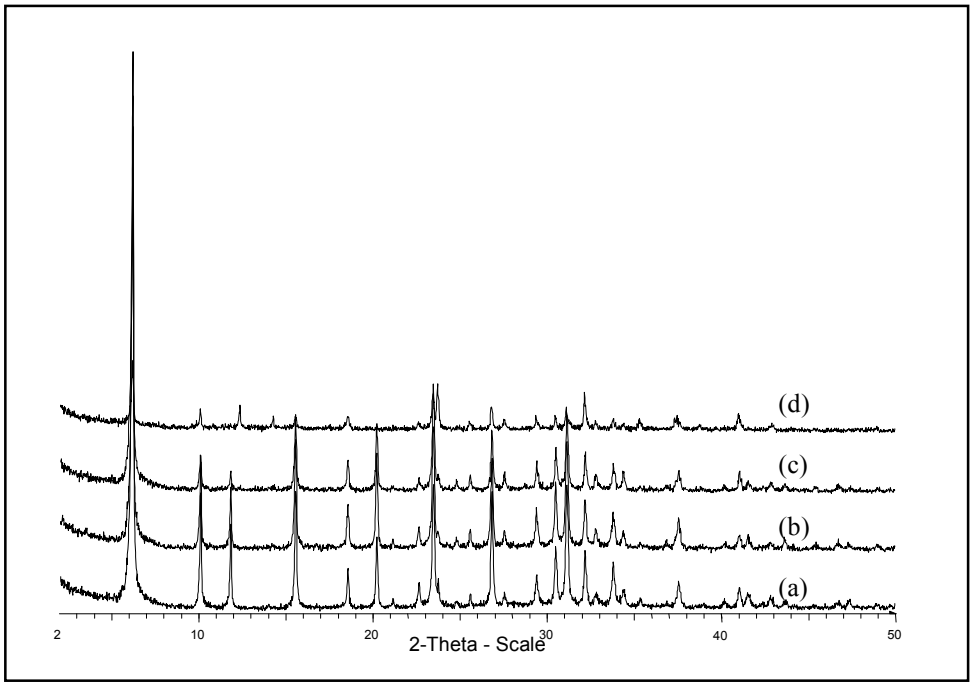

Figure 5.5: The XRD patterns of the alkaline earth metal cation exchanged zeolites: (a) Na-SZ18; (b) MgNa-SZ18; (c) CaNa-SZ18; and (d) BaNa-SZ18.

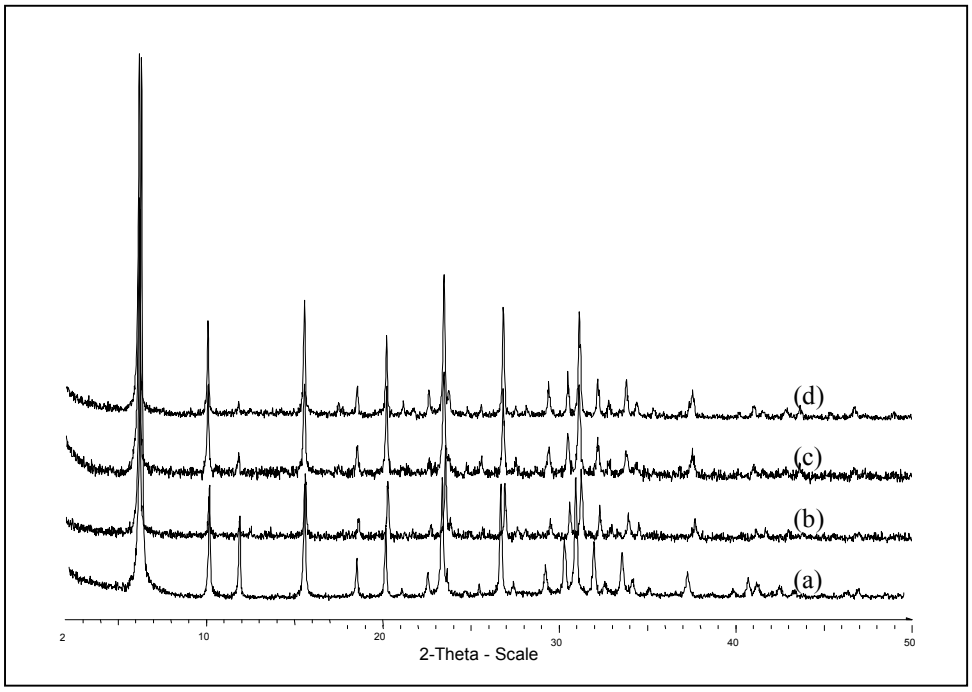

Figure 5.6: The XRD patterns of the transition metal cation exchanged zeolites: (a) Na-SZ18; (b) MnNa-SZ18; (c) NiNa-SZ18; and (d) ZnNa-SZ18.

The cation exchange process leads to rearrangement of other ions in zeolite structure. When one cation (for example Mg^{2+}) replaces two sodium cations, it causes changes in local distributions and the electrostatic fields. The changes may cause an alteration of the framework, leading to shifting of the diffraction peaks (Tables 5.2, 5.3, and 5.4). The exchange of sodium cation with other metal cations of larger ionic size (Rb^{+} and Ba^{2+}) results in some peaks either disappeared or lowered intensities, and shift to a lower angle of XRD diffractogram. On contrary, exchanging sodium with lithium and other transition metal ions having cationic size smaller than sodium ion result increasing the intensities of the respective peaks. Most of the peaks were shifted towards high angle indicates the shrinkages of the unit cell. Hence, we could assume that the extent of changes depend the size of the cation. The bigger size cation results in more changes to the zeolites.

Table 5.2:The peak positions of the alkali metal cation exchanged zeolites obtained from XRD data.

Na-SZ18		LiNa-SZ18		KNa-SZ18		RbNa-SZ18	
2θ	*I(cps)*	*2θ*	*I(cps)*	*2θ*	*I(cps)*	*2θ*	*I(cps)*
15.523	474	15.596	509	15.468	198	15.520	144
18.533	175	18.603	218	18. 467	120	18.528	242
20.199	296	20.290	330	20.134	88	-	-
23.449	501	23.558	539	23.362	327	23.697	348
26.832	474	26.925	489	26.713	256	26.793	348
31.134	499	31.265	483	31.004	292	31.099	203

Table 5.3: The peak position of the alkaline earth metal cation exchanged zeolites obtained from XRD data.

Na-SZ18		MgNa-SZ18		CaNa-SZ18		BaNa-SZ18	
2θ	*I(cps)*	*2θ*	*I(cps)*	*2θ*	*I(cps)*	*2θ*	*I(cps)*
15.523	474	15.521	446	15.517	314	15.509	70
18.533	175	18.521	195	18.526	137	18.535	70
20.199	296	20.184	394	20.190	278	-	-
23.449	501	23.454	496	23.447	433	23.694	198
26.832	474	26.821	375	26.830	249	26.796	109
31.134	499	31.135	438	31.141	326	31.109	109

Table 5.4: The peak positions of the transition metal cation exchanged zeolites obtained from XRD data.

Na-SZ18		NiNa-SZ18		MnNa-SZ18		ZnNa-SZ18	
2θ	*I(cps)*	*2θ*	*I(cps)*	*2θ*	*I(cps)*	*2θ*	*I(cps)*
15.523	474	15.529	435	15.592	297	15.534	471
18.533	175	18.529	205	18.608	127	18.537	147
20.199	296	20.199	430	20.274	268	20.182	338
23.449	501	23.453	483	23.538	402	23.466	566
26.832	474	26.822	420	26.933	261	26.834	444
31.134	499	31.134	434	31.254	312	31.147	426

FTIR spectroscopy method has also been used to characterize the structural properties of zeolites. The FTIR spectra of metal cation exchanged zeolites are shown in Figures 5.7, 5.8, and 5.9. In general, the spectra of the modified samples are found to be very similar to the based zeolite (Na-SZ18). The strongest vibration assigned to T – O stretch in the range of 950 – 1250 cm^{-1} are observed in the FTIR spectra of all metal exchanged zeolites understudied. Similarly, T – O bending modes around 420 – 500 cm^{-1} region were also appeared in the FTIR spectra.

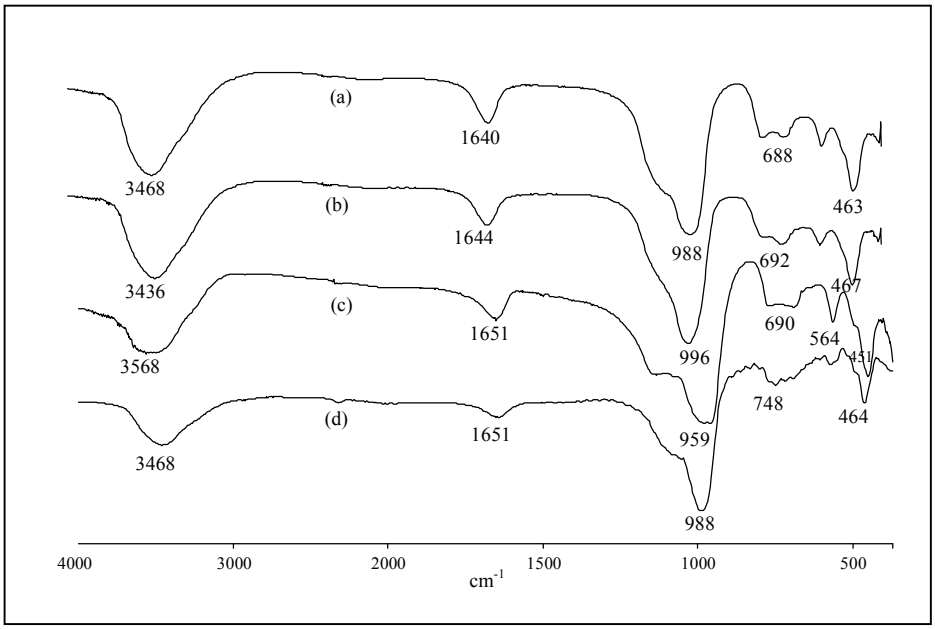

Figure 5.7: The FTIR spectra of alkali metal cation exchanged zeolites: (a) Na-SZ18; (b) LiNa-SZ18; (c) KNa-SZ18; and (d) RbNa-SZ18.

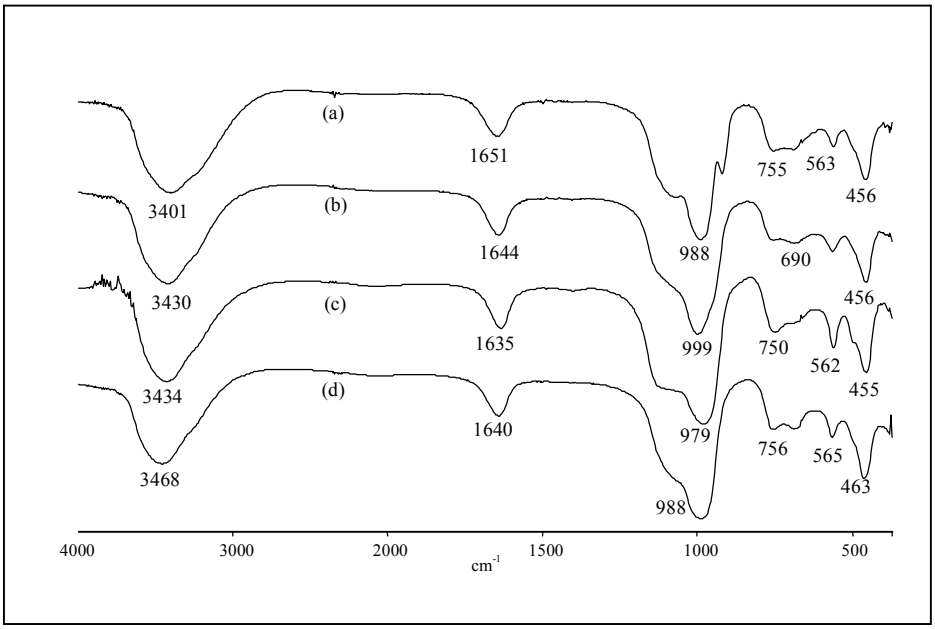

Figure 5.8: The FTIR spectra of the alkaline earth metal cation exchanged zeolites: (a) MgNa-SZ18; (b) CaNa-SZ18; (c) BaNa-SZ18; and (d) Na-SZ18.

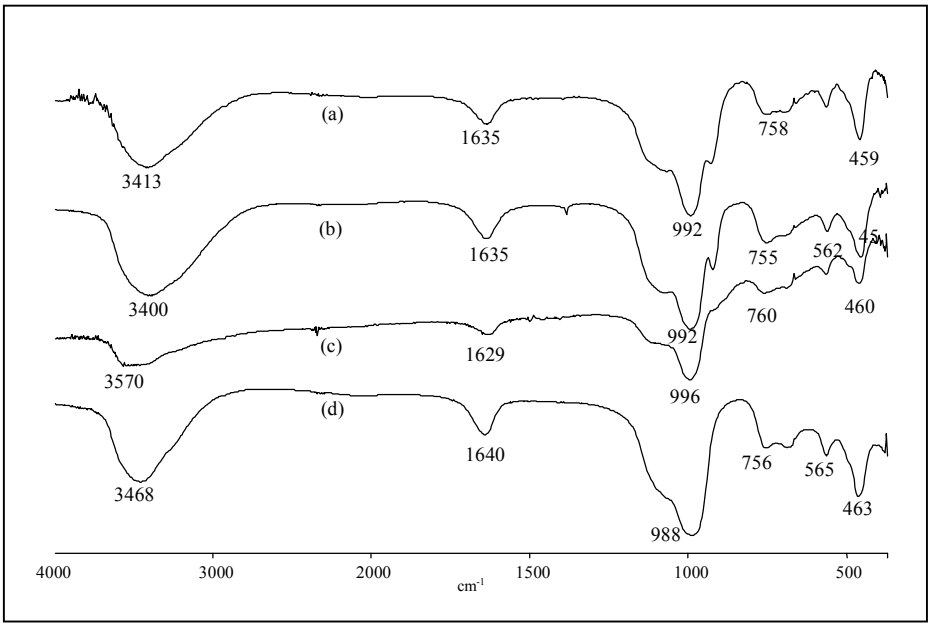

Figure 5.9: The FTIR spectra of the transition metal cation exchanged zeolites: (a) NiNa-SZ18; (b) MnNa-SZ18; (c) ZnNa-SZ18; and (d) Na-SZ18.

However, according to Maxwell and Baks (1973), cations could exert a remarkable influence on the frequency of the adsorption bands in the ranges of 440 – 490 cm^{-1} and 540 – 590 cm^{-1}. The former is attributed to T – O bending and the latter arises from the double ring vibration. In this case**,** the vibration at 556 cm^{-1} for the double ring spectrum of Na-SZ18 shifts within the region of 560 - 570 cm^{-1} after cation exchanged treatment. According to Ward (1970), the presence of alkali metals and transition metal cations could be determined from the hydroxyl group of the exchanged zeolite. The band frequencies near 3640 and 3540 cm^{-1} are a function of the electron affinity of the cations (Ward, 1970). The frequencies increased with increasing electrostatic field of the cations in exchanged zeolites. The presence of the peak for Na-SZ18 at 3468 cm^{-1} is shown in Figure 5.7. The peak was shifted as Na^{+} was exchanged with other cations. However, it is important to realize that Na^{+} ions in the based zeolite are not fully exchanged with other cations. This explained the reason why the frequencies of divalent cation exchanged zeolites do not increase even though the electrostatic field of the cations is high.

5.2.3 Physicochemical properties of metal cation exchanged zeolites

In order to determine the porosity of the exchanged zeolites, nitrogen adsorption was measured at 77 K. As discussed in Section 4.2.2, nitrogen adsorption isotherm of Na-SZ18 (based zeolite) follows Type I classification, a typical crystalline microporous material isotherm. The nitrogen adsorption isotherms of the zeolites after cation exchange were also measured. It was found also that the isotherm curves of cation exchanged zeolites follow IUPAC classification of type I, in which a steep rise was observed but the samples reached equilibrium at different adsorption capacity (Figures 5.10, 5.11, and 5.12**)**. The isotherms are also reversible and the shapes of initial part of isotherms are rather similar to the based zeolite, which indicates that the microporous character is largely preserved.

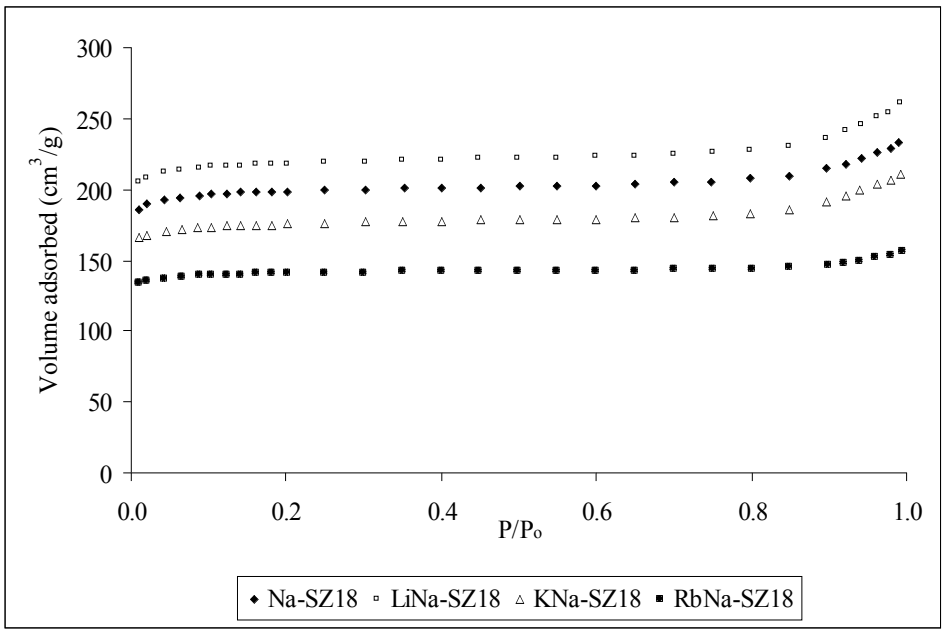

Figure 5.10: The nitrogen adsorption isotherms of the alkali metal cation exchanged zeolites.

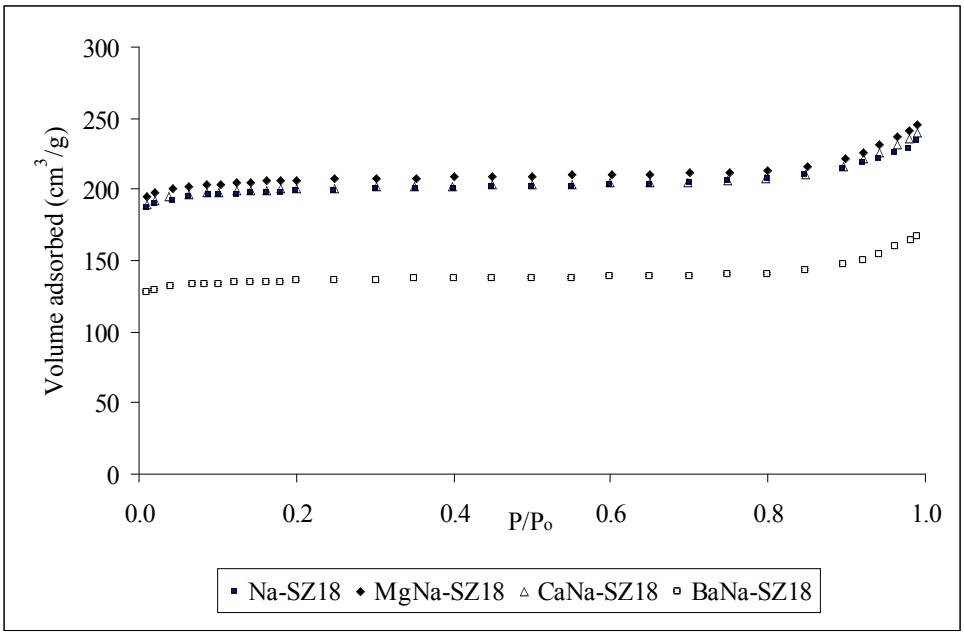

Figure 5.11: The nitrogen adsorption isotherms of the alkaline earth metal cation exchanged zeolites.

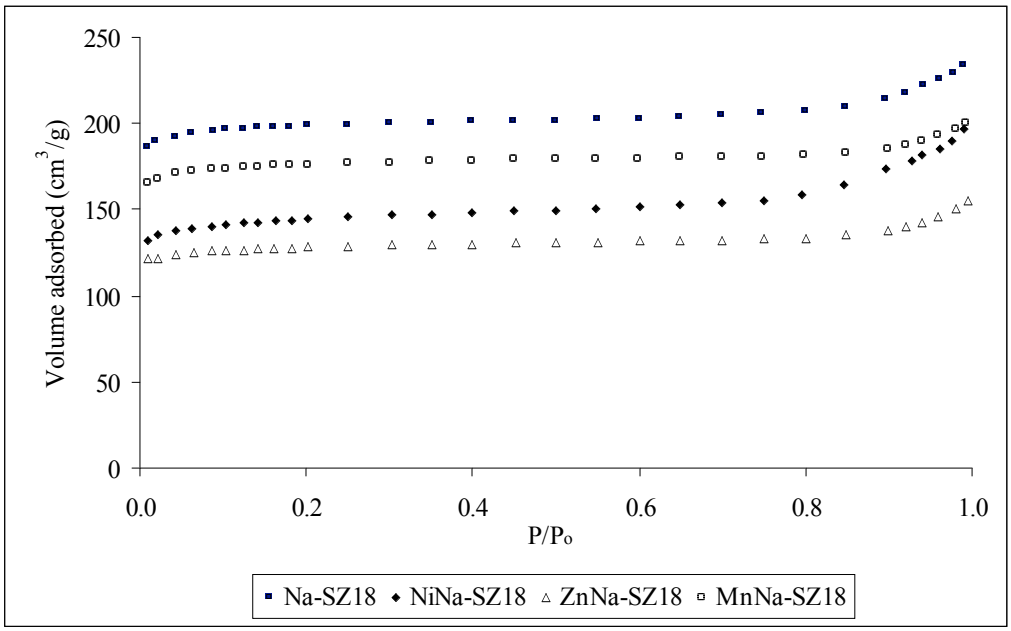

Figure 5.12: The nitrogen adsorption isotherms of the transition metal cation exchanged zeolites.

The nitrogen adsorption isotherms show that the presence of lithium (Li^{+}), magnesium (Mg^{2+}) or manganese (Mn^{2+}) ions results in several improvements as the plateau rises to a higher value which will be discussed in later sections. However, the presence of cations such as potassium (K^{+}), rubidium (Rb^{+}), calcium (Ca^{2+}), barium (Ba^{2+}), and zink (Zn^{2+}) caused a drop of the plateau to a level lower than the based zeolite. The results also show that the nitrogen adsorption behaviors of alkali and alkaline earth metals are similar, decrease from the top to the bottom of the groups (Group IA and IIA).

Similar adsorption behavior was observed as the transition metals from left to the right of the periods replacing the sodium cation in the based zeolite (Na-SZ18). The changes are associated with the size and charge of cations that determining the properties of the zeolites. In addition, after cation exchange, the loss of microporosity is anticipated, accompanied by the formation of secondary pores. The loss of microporosities is verified by the presence of hysteresis loop, which is clearly shown in the transition metal exchanged zeolite (NiNa-SZ18). However, the hysteresis loops appear in alkali metal exchanged zeolite (LiNa-SZ18) and alkaline earth metal (MgNa-SZ18) appear relatively insignificant (Figure 5.13). The difference might correspond to larger micropores or formation of mesopores that gave rise to typical adsorption-desorption hysteresis loops.

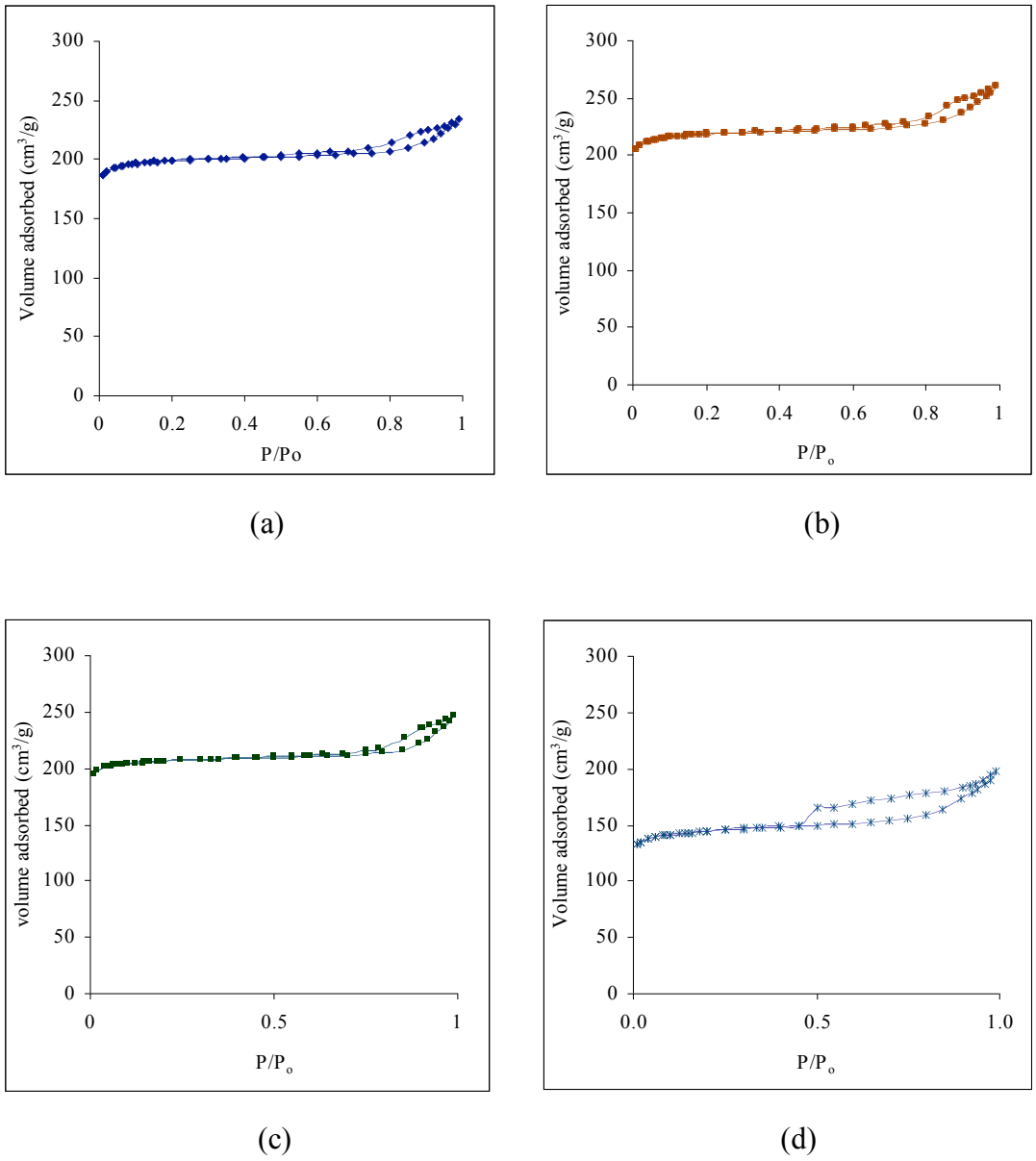

Figure 5.13: The hysteresis loops of based and several metal cation exchanged zeolites: (a) Na-SZ18; (b) LiNa-SZ18; (c) MgNa-SZ18; and (d) NiNa-SZ18.

As reported by Cen (1990), there are some limitations in the ion exchange equilibrium that resulting only part of Na^+ in the zeolite lattice could be exchanged by other cations. Hence, the presence of secondary pores depends on the cation exchange capacity of the zeolites. Meanwhile, the nitrogen adsorption isotherm data were used to determine physical properties of exchanged zeolites namely surface

area, pore volume and average pore diameter. In order to obtained quantitative assessment of porosity, surface area was calculated using conventional BET method. The calculation of micropore volume and micropore surface area was conducted using *t*-plot. The values calculated show some changes, a decrease in term of surface area and pore volume as the ionic radius of the cation increases. This effect may be attributed to the presence of the cation itself or extra-framework aluminium species in the interior of zeolite pores and channels, causing a decrease on the micropore area.

In addition, cations in zeolite cavities are located on specific sites, the exchange of sodium cation at site II with cation of bigger size may partially block the aperture or pore window (Figure 5.14). It hinders the diffusion of probe molecules (nitrogen) from entering the inner side of the cages, thus reduces the amount of nitrogen adsorbed. Besides the cationic size, structural defect during cation exchange treatment is also a reason for formation of secondary pores, either super-micropores or mesopores. These phenomena led to reduction of micropore area and micropore volume of samples such as RbNa-SZ18, BaNa-SZ18, and the transition metals used in this study.

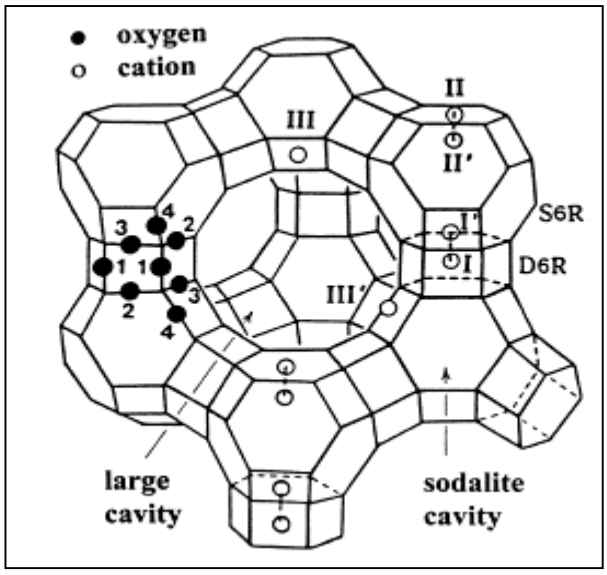

Figure 5.14: Location of cations in faujasite structural framework (Haniffa *et al*., 1998).

This study also reveals that the physical properties of the metal cation exchanged zeolites such as surface area and pore volume decrease moving down in the group (Groups IA and IIA)le. Similarly, these properties also decrease as the sodium in based zeolites are exchanged by other metal cations (Ca^{2+}, Mn^{2+}, Ni^{2+}, and Zn^{2+}) moving from the left to the right of the periods. The surface area and pore volume of the exchanged zeolites show a common behavior (Group IA: LiNa-SZ18 > KNa-SZ18 > RbNa-SZ18; Group IIA: MgNa-SZ18 > CaNa-SZ18 > BaNa-SZ18; Group IIA to transition metal groups: CaNa-SZ18 > MnNa-SZ18 > NiNa-SZ18 > ZnNa-SZ18).

Table 5.5: The physical properties of the metal cation exchanged zeolites calculated from nitrogen adsorption data.

Zeolite	Surface area (m^2/g)		Pore volume (cm^3/g)		Average pore diameter (nm)
	BET	Micropore	Micropore	Mesopore /Macropore	
Alkali:					
LiNa-SZ18	894.8	874.4	0.300	0.074	1.80
Na-SZ18*	813.6	793.8	0.299	0.062	1.78
KNa-SZ18	719.4	702.1	0.265	0.062	1.82
RbNa-SZ18	569.8	561.6	0.215	0.027	1.51
Alkaline:					
MgNa-SZ18	845.9	828.8	0.313	0.068	1.80
CaNa-SZ18	821.5	804.0	0.303	0.067	1.80
BaNa-SZ18	553.8	542.2	0.206	0.052	1.86
Transition:					
MnNa-SZ18	710.0	694.5	0.2671	0.0428	1.86
NiNa-SZ18	574.9	540.9	0.2097	0.0951	2.12
ZnNa-SZ18	514.8	499.9	0.1927	0.0466	1.76

*Based zeolite

However, the average pore diameters of the metal cation exchanged zeolites do not show any common behavior. This is probably due to fact that average pore diameter is not only affected by the presence of cations but it is also the experimental condition used during cation exchange treatment. Hence, with appropriate selection of cations and experimental conditions used, the properties of adsorbent could be improved. This indicates that the physical changes in zeolites during cation exchange process are quite complex. Although sodium can be easily replaced from zeolite framework by cation exchange method, the results shows that as the size and charge of cation differ, it affects the properties of the zeolite. Further evaluation on XRD data revealed that there are also some changes to chemical composition (in this case the Si/Al ratio), the unit cell parameter and relative crystallinity of the exchanged zeolites (Table 5.6).

Table 5.6: The physical properties and chemical composition of the metal cation exchanged zeolites calculated from XRD data.

Zeolite	Unit cell parameter (Å)	Framework Si/Al ratio	Relative crystallinity (%)
Alkali:			
LiNa-SZ18	24.75	2.0	106
Na-SZ18*	24.85	1.5	100
KNa-SZ18	24.95	1.6	52
RbNa-SZ18	24.88	1.4	58
Alkaline:			
MgNa-SZ18	24.85	1.5	100
CaNa-SZ18	24.85	1.5	72
BaNa- SZ18	24.88	1.4	20
Transition:			
MnNa-SZ18	24.75	2.0	71
NiNa-SZ18	24.85	1.5	101
ZnNa-SZ18	24.85	1.5	99

* Based zeolite

In general, the Si/Al ratio of each metal group decreases as the atomic number of the cation increases. The increase indicates the release of Al from zeolite framework during cation exchange treatment. Based on total peak intensities, it was also found that the relative crystallinity of metal exchanged zeolites experiences some changes. The intensities of LiNa-SZ18 and NiNa-SZ18 increase exceeding the based zeolite. However, exchanging Na^{+} with bigger size cation such K^{+} and Rb^{+} (Group IA) or Ca^{2+} and Ba^{2+} (Group IIA) reduces the crystallinity of zeolites. The same result occurs for Mn^{2+} (Group VIIB) exchanged zeolite. However, the presence of either Ni^{2+} (VIIIB) or Zn^{2+} (IIB) in the extra-framework of zeolite only results in small changes to the relative crystallinity of the respective zeolites.

5.3 Gas Adsorption Equilibrium

Many adsorption processes carried out in microporous and nanoporous material benefits from the small pore sizes. As the area per unit weight increases, the contact between the surface and the adsorbates also increases. There are, however, several factors that influence the adsorption capacity. Factors such as geometrical constraints, adsorbates properties, and surface characteristics affect the gas adsorption characteristics of zeolites. The presence of different cations also changes the nature of interaction between adsorbate and adsorbent. Even though it is difficult to assess the effects, this study would give an insight on the effect of different cations on gas adsorption characteristics. Thus, the gas adsorption capacity, gas adsorption isotherm, heat of adsorption, and the uptake rate of the adsorbents using methane and carbon dioxide as adsorbates were used to elucidate the relative effect of the cations on gas adsorption characteristics.

5.3.1 Gas adsorption capacity

As discussed in Section 5.2, the presence of cation by means of cation exchange method causes some changes to the structure and physicochemical properties of the zeolites. When Na^+ was exchanged with other cations, new physical and chemical environment within the structural framework such as electrostatic potentials, and electrical field within the cage as well as the vacant space available for the guest within the supercage were altered accordingly depending on the exchanged cations. Based on methodology presented in Chapter 3, this section will examine the effect of cations in extra-framework zeolites on gas adsorption capacity. As previously discussed in Chapter 4, Na-SZ18 belongs to faujasite group of zeolites. It consists of primary and secondary cages that can act as nano-container for the adsorbates. Interestingly, the presence of several cations improves the performance of metal exchanged zeolite either as methane or carbon dioxide adsorbent (Figures 5.15 and 5.16). Apart from LiNa-SZ18, transition metal cation exchanged zeolites may be the choices for methane adsorbent, and MgNa-SZ18 and CaNa-SZ18 for carbon dioxide adsorbent. Thus, the following section will discuss several aspects that affect the adsorption of methane and carbon dioxide in the presence of different cations in zeolites.

In the presence of mixed cation in zeolites, the adsorbents react differently towards methane and carbon dioxide adsorption. Results presented in Section 5.2 show that after cation exchange treatment, the structural, physical and chemical composition of the exchanged zeolites experience some changes. However, the XRD spectra showed that the structural framework of metal cation exchanged zeolites was retained and this could be the basis for reasonably high adsorption capacity of the metal exchanged zeolites.

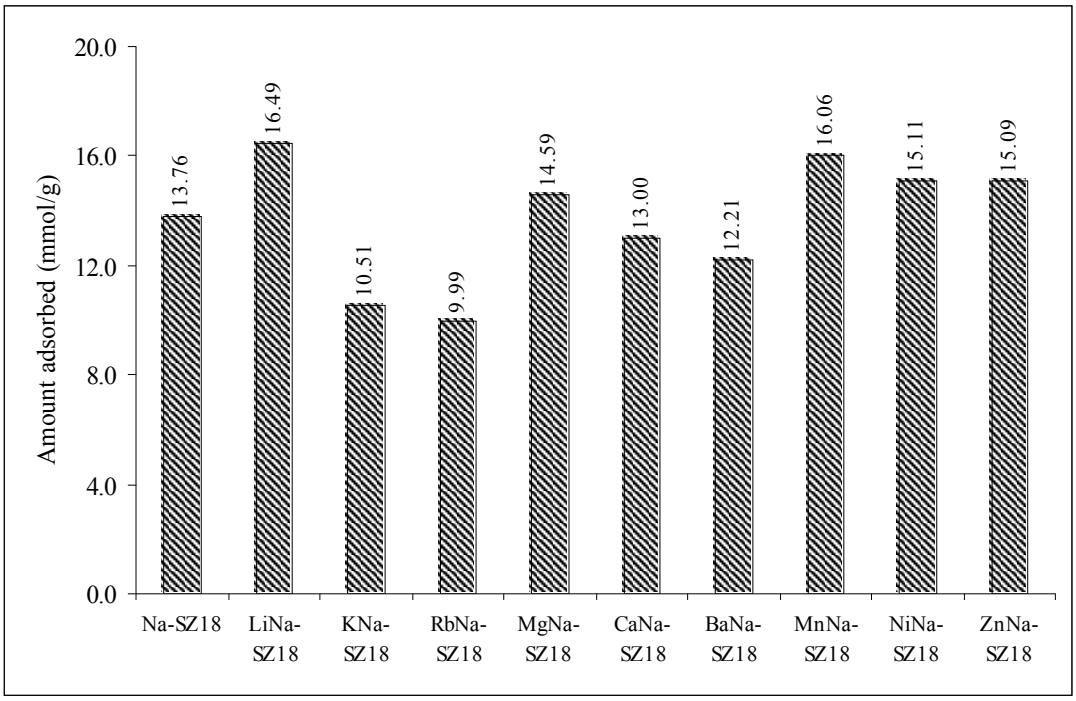

Figure 5.15: The adsorption capacity of methane on the metal cation exchanged zeolites at 323K and 137 kPa.

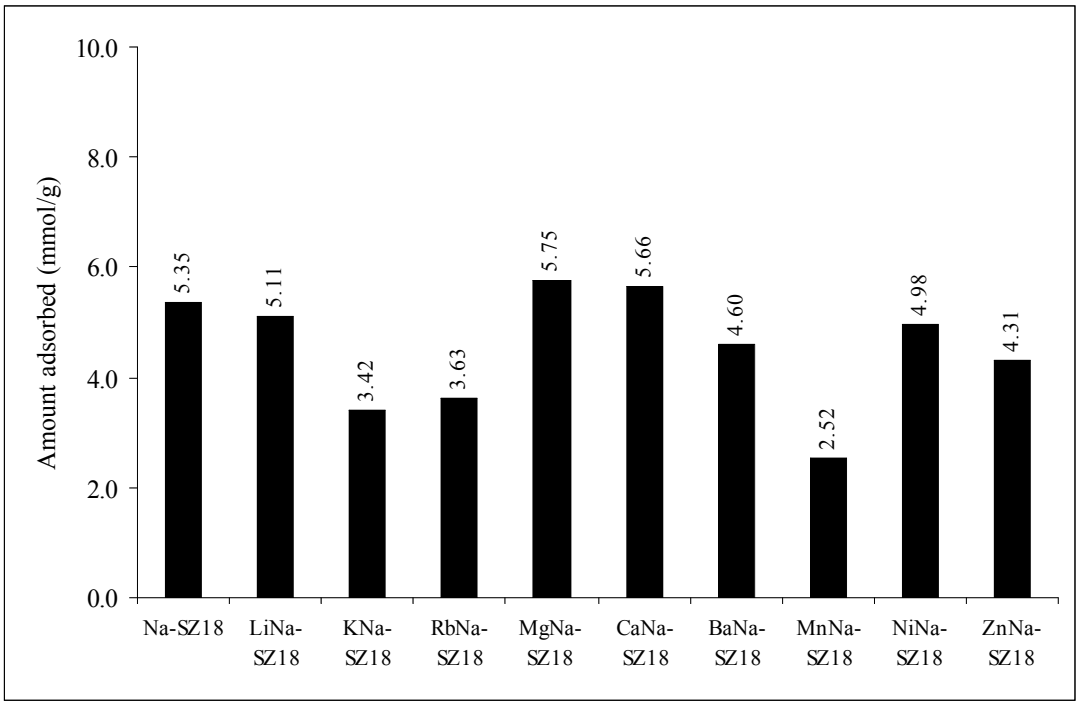

Figure 5.16: The adsorption capacity of carbon dioxide on the metal cation exchanged zeolites at 323K and 137 kPa.

This study shows that exchanging sodium with lithium cation (Li^+) increases the methane adsorption capacity (20 % higher than Na-SZ18), however the adsorption capacity of other metal cation exchanged zeolites (KNa-SZ18 and RbNa-SZ18) are lower than the based zeolite (Na-SZ18). The results indicate that the size of cation influence the adsorption. This due to the size of lithium cation (Li^+) is smaller than the size of Na^+ in the based zeolite. Thus, the pore opening of the modified zeolite becomes larger than the based zeolite. The finding also supported the fact that the large pore opening reduces the possibility of pore blockage, thus as discussed in Section 4.3.1.3, the adsorbates can easily diffuse through the pore opening and adsorb onto the inner side of the cage. Higher adsorption capacity was also obtained after exchanging Na^+ with Mg^{2+} , Mn^{2+}, Ni^{2+}, and Zn^{2+} which also proved that the pore opening influence adsorption characteristics of CH_4 on zeolite. In both cases, exchanging Na^+ with the smaller size cation from Group IA, Group IIA and transition metal group improves the adsorption capacity of CH_4.

Higher CH_4 adsorption capacity of transition metal cation exchanged zeolites (Figure 5.15) also proved the previous finding (Chapter 4) that surface area and pore volume are not the main factor in determining adsorption capacity. It is shown in Table 5.5 that the surface area and pore volume of NiNa-SZ18 and ZnNa-SZ18 are relatively lower than Na-SZ18 (based zeolite). However, the adsorption capacities of the modified adsorbents (NiNa-SZ18 and ZnNa-SZ18) are higher than the based zeolite (Na-SZ18). The results also show that crystalline phase also does not directly affect the adsorption characteristics of zeolites. This is shown by the adsorption capacity of MnNa-SZ18 in which has lower relative crystallinity than based zeolite. In addition, the relative crystallinity of BaNa-SZ18 is very much lower than the based zeolite (20 % vs 100 %), the adsorption capacity of BaNa-SZ18 is only 11 % less tha the based zeolite. The results indicate that the encouraging performance of CH_4 adsorption is due to the presence of Ba^{2+} cation in the extra-framework of zeolite.

Meanwhile, the amount of carbon dioxide adsorbed on LiNa-SZ18 was found to be slightly less than the based zeolite. A lesser amount of carbon dioxide was also

observed on the other metal cation exchanged zeolite of Group IA. However, after exchanging with Group IIA cations, it was found that MgNa-SZ18 and CaNa-SZ18 adsorbed more carbon dioxide than the based zeolite. However, BaNa-SZ18 and the transition metal cation exchanged zeolites adsorb less than the based zeolite with the percentage of reduction of 14 % and 7 % for BaNa-SZ18 and NiNa-SZ18 respectively. As reported in literatures, the results indicate that the charge play important role in the adsorption of quadrapolar molecule such as CO_2 (Bulow, 2002; Hadjiivanov *et al*., 2003; Khelifa *et al*., 2004). Divalent cation could be a choice as charge balancing cation in zeolites and the alkaline earth metal (IIA) proved to be better than the transition metal.

Generally, adsorbents having high surface area would adsorb more gases. However, there is no apparent relationship between surface area and the adsorption capacity of adsorbates on metal cation exchanged zeolites (Figure 5.17). The results show that even though the surface areas of transition metal exchanged zeolites are lower than the based zeolite (Na-SZ18), the adsorption capacity of methane are relatively high. The results suggest that besides the surface area, pore volume, and pore diameter of zeolite adsorbent, the properties of cation play important role in the adsorption of CH_4 on the adsorbents. Similarly, adsorption capacity of carbon dioxide is not directly proportional to the surface area. Transition metal cation exchanged zeolite with low surface area (NiNa-SZ18) adsorb at relatively high adsorption capacity. The results also support the assumption that the surface area is not the only determining factor in the adsorption of gases.

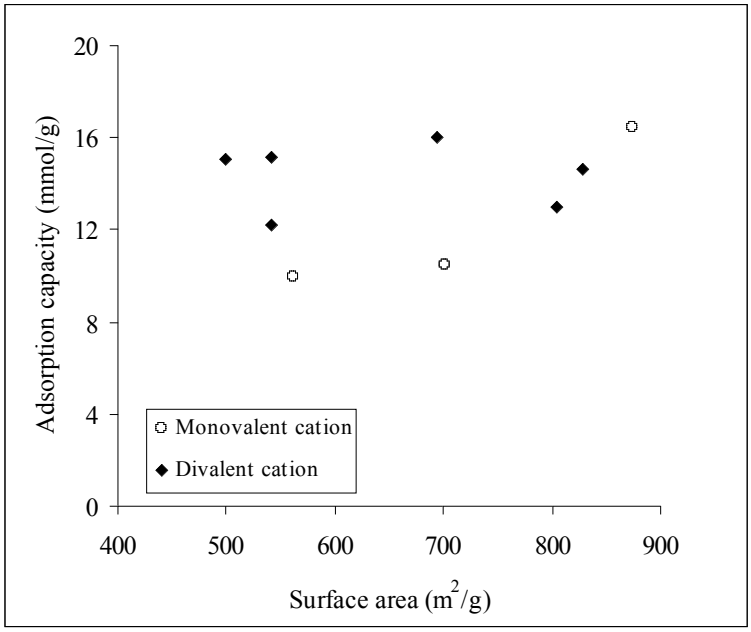

(a)

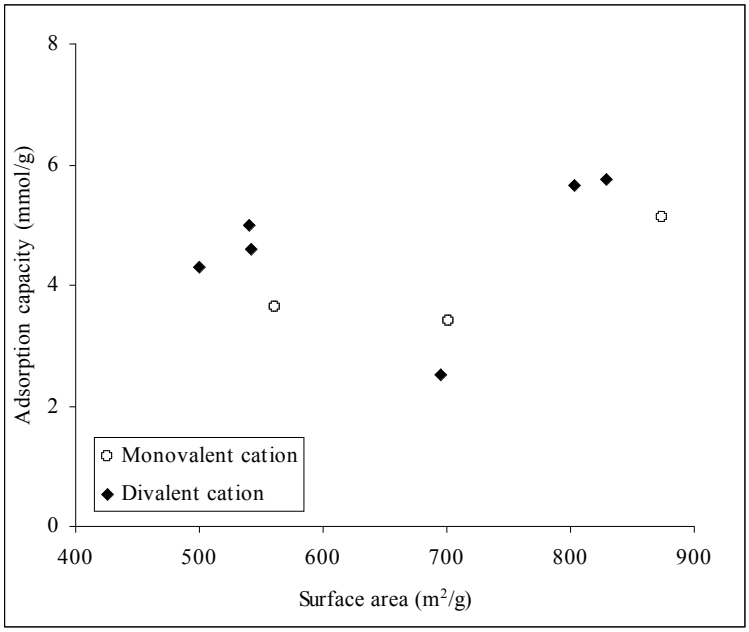

(b)

Figure 5.17: The effect of surface area on gas adsorption capacity of the metal cation exchanged zeolites: (a) Methane and (b) carbon dioxide.

In order to investigate the effect of cation properties on the adsorption characteristics of CH_4 and CO_2, the relationship between charge/ionic radius of cation and adsorption capacity of CH_4 and CO_2 was observed (Figure 5.18). Generally, it was found that the adsorption capacity increases as the charge/ionic radius increases. Even though it has been mentioned before that there is no specific interaction between methane molecules and the zeolite surface, at certain extent, non-specific interactions with electrostatic field created by cations might influence the adsorption on zeolites. Again, Figure 5.18(b) shows the effect of charge/ionic radius on carbon dioxide adsorption capacity. Moreover, the presence of cations affects gas adsorption capacity of carbon dioxide**.** It is an acceptable fact that surface area and pore volume provide space for the encapsulation of adsorbates inside the pore, the presence of cation becomes an additional factor for high adsorption capacity of gases.

The results also reveal that the electrostatic field created in the presence of cations might influence the adsorptivity of methane. There is linear relationship between charge/ionic radius of cation and the adsorption capacity of methane that verifies the role of cation in the adsorption methane. In the case of carbon dioxide adsorption, the interactions between carbon dioxide and the metal cation are still exist, however there are also other factors that affect the adsorption of carbon dioxide. The strength of the dipole moment interacts with the adsorption sites other than the cation might be the reason for non-linear relationship between the adsorption capacity and the cations. Moreover, it is also important to realize that the actual pore diameters in zeolite structures depends on the type of cation present because cations could occupy certain position, in which it might block the pore opening. However, in most cases, the molecules could adapt the aperture upon adsorption because of the flexibility of the framework. The degree of flexibility is a function of the framework structures in the presence of extra-framework cations and molecules (Coker *et al*., 1998). This explains why cation such as K^+ would allow methane and carbon dioxide to penetrate through the pore window into the cage of the zeolites.

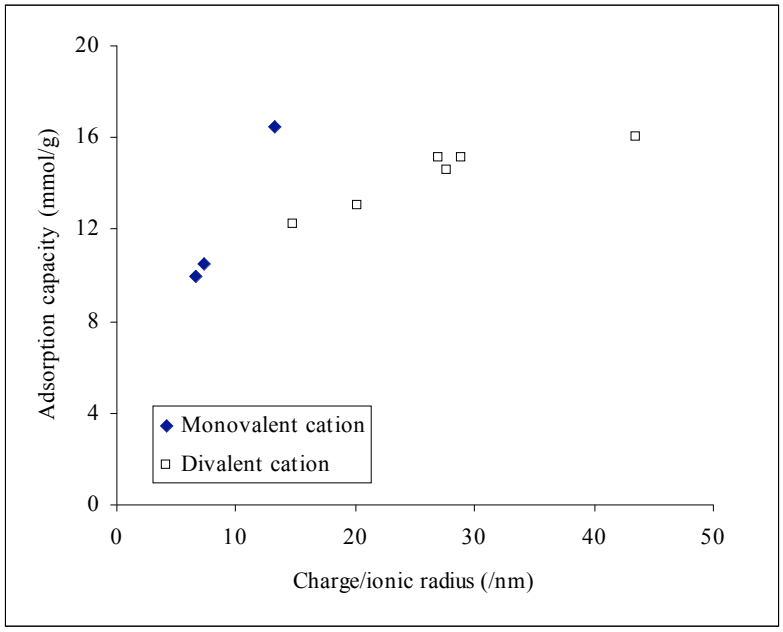

(a)

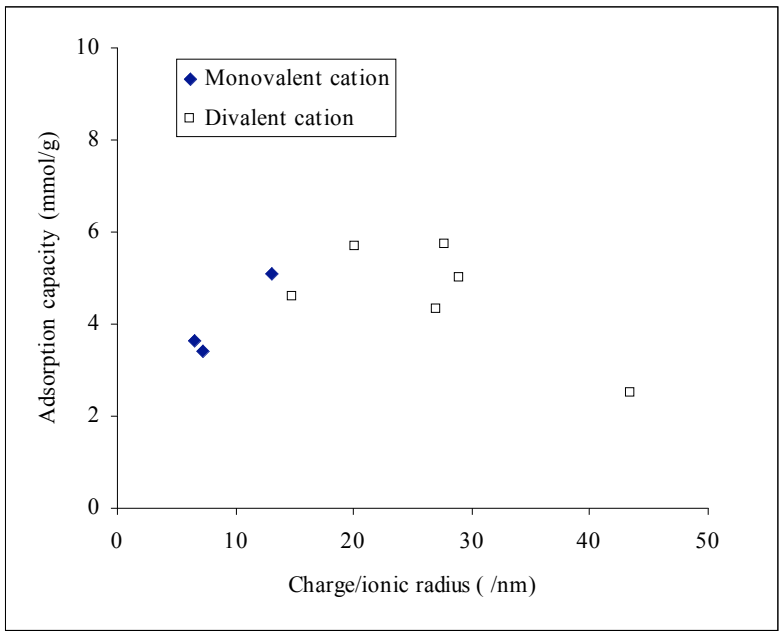

(b)

Figure 5.18: The effect of charge/ionic radius on adsorption capacity of the metal cation exchanged zeolites: (a) methane and (b) carbon dioxide.

Similarly, the presence of a divalent cation replacing two sodium ions would enlarge the window aperture, thus allowing the adsorbates to diffuse easily into the inner side of the cage (Kurama et al., 2002; Kaushik et al., 2002; Sato et al., 2003). However, as the diameter of cation increases, the molecules could only adsorbed in the supercages. Khelifa *et al*. (1999) have reported that exchanging sodium with divalent cation results in two consequences, total number of cation in the supercages decreases and carbon dioxide could not adsorb in the sodalite cages for larger size cation. This indicates that cation could play a major role in controlling access to the sodalite cages and supercages. As discussed in Section 5.2.3, the surface area was affected by cation exchange treatment. Samples such as RbNa-SZ18 and BaNa-SZ18 were obviously affected as the surface area were reduced from 793.8 m^2/g to 569.8 m^2/g and 553.8 m^2/g respectively. Consequently, the adsorption capacity of the sample was also reduced. However, further evaluation on the effect of cation was carried out by determining the surface coverage of the adsorbents (Table 5.7).

This study shows that the surface coverage increases as methane was adsorbed on several types of zeolites such as LiNa-SZ18, RbNa-SZ18, MgNa-SZ18, and BaNa-SZ18. Similarly, the surface coverage of transition metal cation exchanged zeolites was also increased. These results suggest that the charge and size of cation have greater influence on adsorption characteristics of methane. As the size of cation might affect the cation exchange capacity (CEC), thus limits the amount of other metals present as extra-framework cation. However, at the same time, the charge density might influence the amount of adsorbate adsorbed which explain reason for higher surface coverage of transition metal cation exchanged zeolites.

Table 5.7: The surface coverage of methane and carbon dioxide for the metal cation exchanged zeolite adsorbents.

Zeolite	Fraction of surface coverage, (θ_R)	
	CH_4	CO_2
Alkali:		
LiNa-SZ18	1.60	0.37
Na-SZ18*	1.47	0.43
KNa-SZ18	1.27	0.31
RbNa-SZ18	1.52	0.42
Alkaline:		
MgNa-SZ18	1.50	0.44
CaNa-SZ18	1.37	0.45
BaNa-SZ18	1.92	0.54
Transition:		
MnNa-SZ18	1.97	0.23
NiNa-SZ18	2.55	0.63
ZnNa-18	2.28	0.49

* Based zeolite

As presented in Table 5.1, the ionic radius of transition metal cation (divalent cation) is much smaller than sodium cation that results in larger pore opening. Thus, it will allow more adsorbate molecules gain access to the inner cavity of the zeolite. This fact is also supported by the surface coverage of carbon dioxide on alkaline earth metal cation exchanged zeolites (MgNa-SZ18, CaNa-SZ18, and BaNa-SZ18) and transition metal exchanged zeolites (NiNa-SZ18 and ZnNa-SZ18). Similar findings were also reported by Qian and Yan (2001) and Kaushik *et al*. (2002) in which the cations influence the adsorption capacity of gases. Hence, these results suggest that by introducing selected cations, the performance of zeolite adsorbent for methane and carbon dioxide could be improved.

5.3.2 Gas adsorption isotherms

In order to understand the methane and carbon dioxide adsorption phenomena on different types of cation exchanged zeolites, the adsorption isotherms were measured by varying the pressure at 298 K. The changes on the adsorption isotherms of methane on metal cation exchanged zeolites are shown in Figures 5.19, 5.20, and 5.21. As discussed in Chapter 4, the adsorption isotherms of methane show linear relation between the amount adsorbed and the pressures in which indicating the adsorption is far from saturation. The isotherms also indicate the slowness of methane adsorption that needs longer time to reach equilibrium. The effects of different cations are depicted in the adsorption isotherms. As the atomic number of alkali metals increase, the slopes of adsorption isotherm curves increase. Similarly, the slope of alkaline earth metal adsorption isotherm curves are also increase as the atomic number and the size of metal cations increase down the group (Group IIA). In most cases where a small amount of sodium cations are still present in the zeolite extra-framework, the presence of larger size cations improves the adsorption characteristics of methane. These phenomena are supported by the adsorption isotherm of transition metals exchanged zeolites, in which smaller size cations could be the reason for lower adsorption isotherms.

The results also show that after cation exchange treatment, the presence of cations such as Rb^{+} and Ba^{2+} resulting more methane being adsorbed on the exchanged zeolites. These cations act as strong adsorptive centers that attract the methane molecules to the respective site, thus lead to high adsorption capacity. In the case of carbon dioxide, the adsorption increases rapidly particularly at relative pressure (P/P_o) less than 0.1. However, this study shows that as the adsorbed gas concentration increases, the influence of cation gradually reduces, and the effect of pore volume becomes more profound. This is clearly shown as the pressures reaching 1 bar.

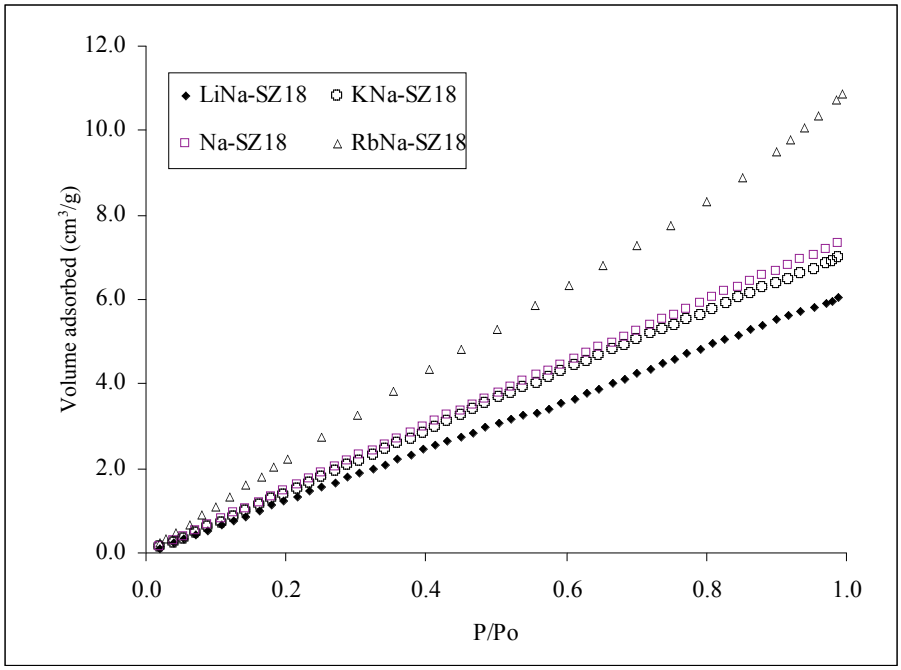

Figure 5.19: The CH_4 adsorption isotherm of the alkali metal cation exchanged zeolites.

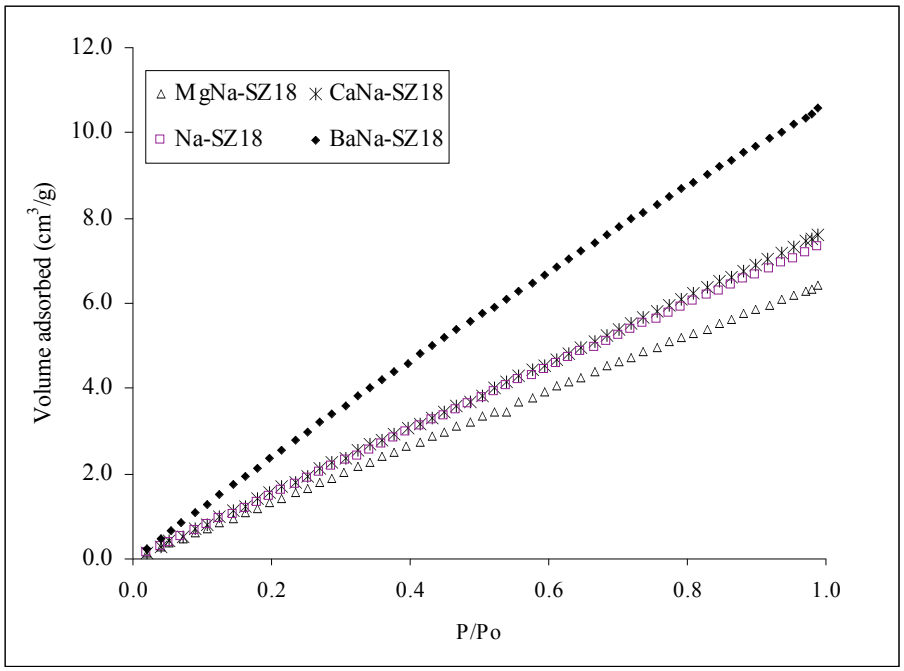

Figure 5.20: The CH_4 adsorption isotherms of the alkaline earth metal cation exchanged zeolites.

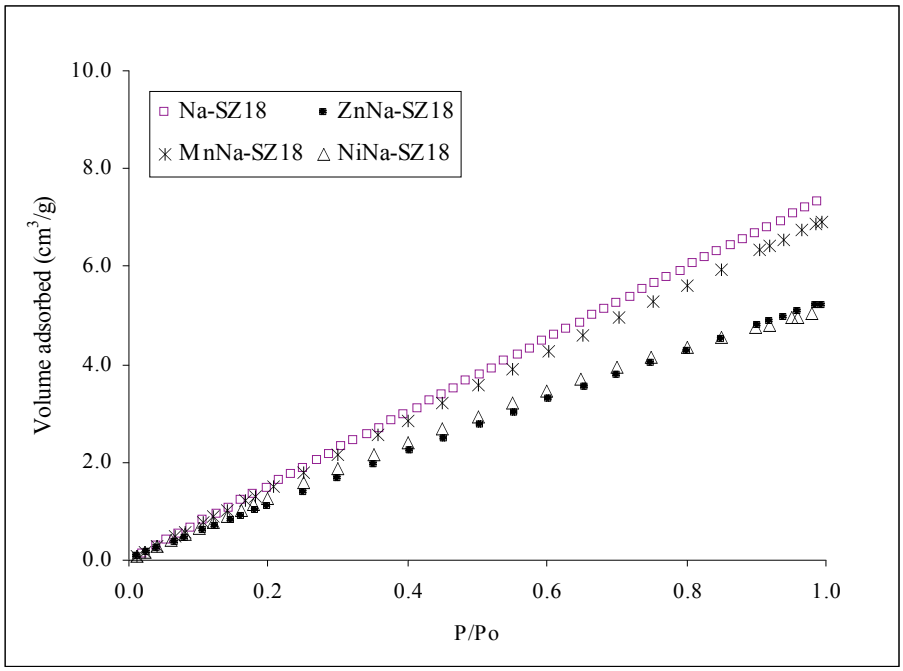

Figure 5.21: The CH_4 adsorption isotherms of the transition metal cation exchanged zeolites.

In contrast to methane adsorption, the adsorption isotherms of carbon dioxide show that the effect of different metal cation is more pronounced than methane (Figures 5.22, 5.23, and 5.24). It was shown by the adsorption isotherm curves of carbon dioxide show a gradual increase leading to saturation suggesting possible monolayer coverage of gas on the surface of the adsorbent (Malik, 2004), whereas the adsorption isotherm of methane is rather a straight curve (Figures 5.19, 5.20, and 5.21). The differences on adsorption isotherm curves of carbon dioxide proved that the metal cations affect the physical and chemical properties of zeolites, and thus affecting the adsorption characteristics of the gases (Bellat *et al*., 1995; Hutson *et al*., 1999; Trigueiro *et al*., 2002; Khelifa *et al*., 2004).

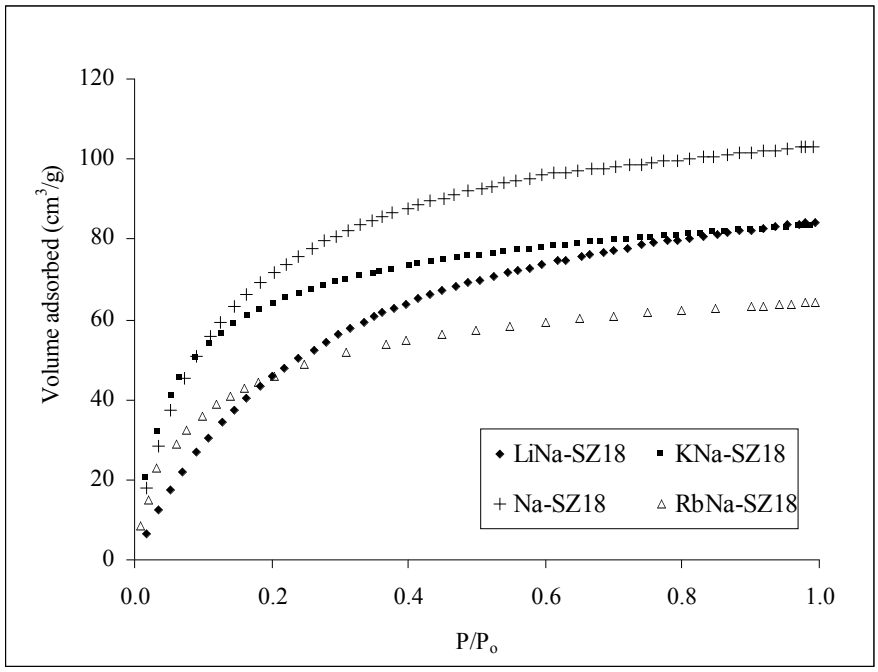

Figure 5.22: The CO_2 adsorption isotherms of the alkali metal cation exchanged zeolites.

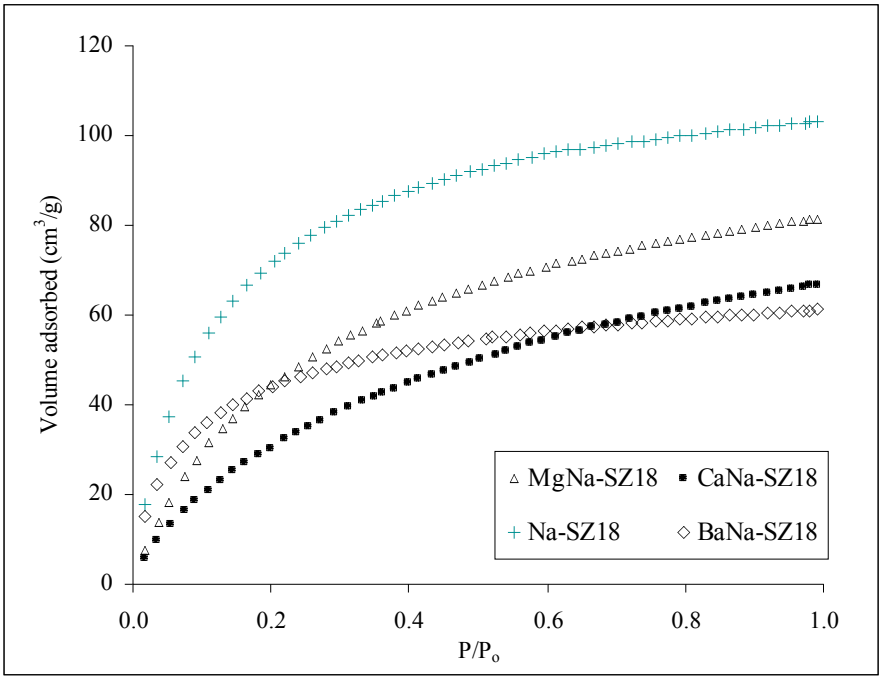

Figure 5.23: The CO_2 adsorption isotherms of the alkaline earth metal cation exchanged zeolites.

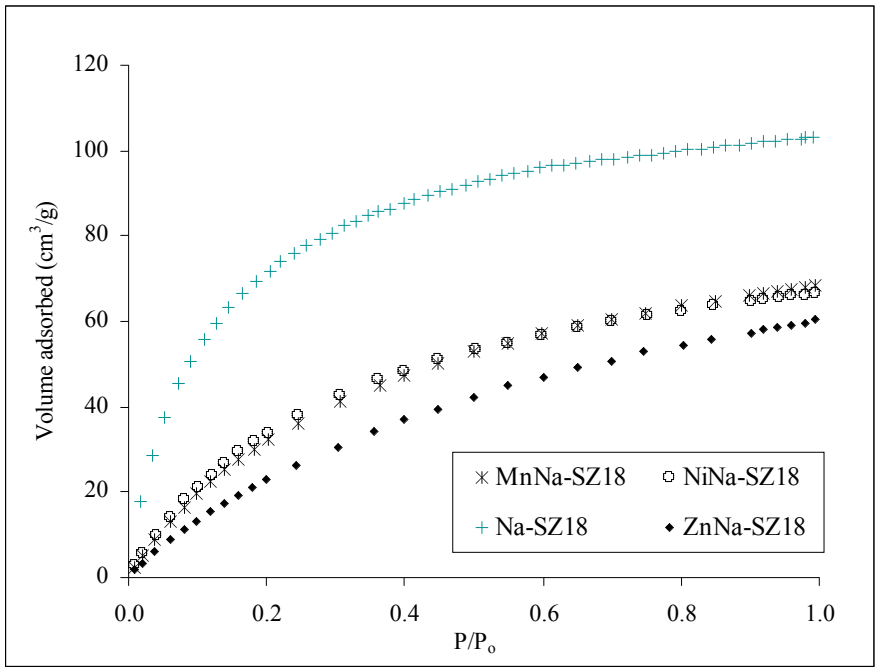

Figure 5.24: The CO_2 adsorption isotherms of the transition metal cation exchanged zeolites.

In general, the cation alters the electrostatic field within the zeolite cavities and hence, it influences the amount of methane and carbon dioxide adsorbed on zeolite surface. Due to different adsorbate properties, methane and carbon dioxide adsorptions show different patterns toward different group of cations. Similar observation was also reported by Maurin *et al*. (2005c). The amount of gas adsorbed increases as the atomic number of cations increased even though the surface area and pore volume decrease. As shown by the slope of the curves, at pressure below 1 bar, the charge and size of cations have stronger influence on gas adsorption than the surface area and micropore volume of the metal cation exchanged zeolites. In order to elucidate further, the experimental data obtained from different metal cation exchanged zeolites are fitted into the adsorption isotherm model equations. The model equations are also used to determine the model constants that could demonstrate the effect of metal cation in extra-framework zeolites on methane and carbon dioxide adsorption (Tables 5.8 and 5.9). The experimental data of methane adsorption isotherm of cation exchanged zeolites and the predicted adsorption isotherm based on calculated parameters of Henry's and Freundlich equations are shown in Figure 5.25.

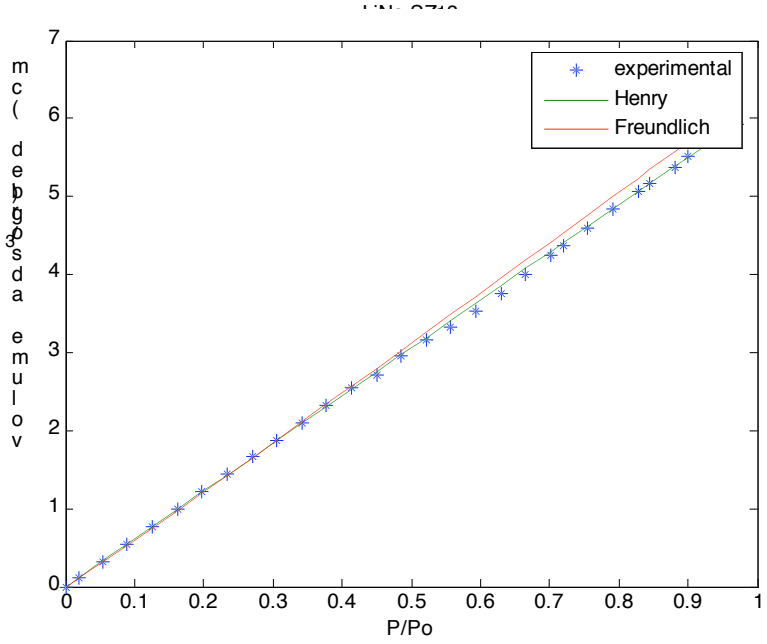

(a)

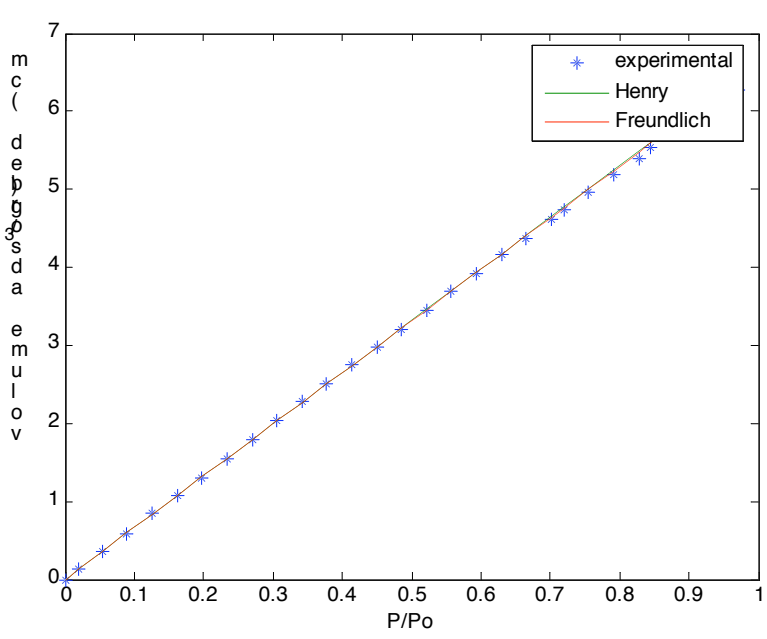

(b)

Figure 5.25: The adsorption isotherm of methane fitted into Henry and Freundlich equations: (a) LiNa-SZ18 and (b) MgNa-SZ18.

The result shows that Henry's equation could describe well the adsorption of methane. This indicates that adsorption occurs in a dilute form. The validity of this model is further verified on Freundlich plot in which the values of *n* are close to unity. However, for carbon dioxide adsorption, the linear region appears at extremely low pressure. In this case, Henry's equation is not a suitable model equation for carbon dioxide adsorption since the adsorption does not occur in dilute form. Thus, based on volumetric adsorption, the experimental data were fitted into Freundlich (Eq. 2.5), Langmuir (Eq. 2.3) and Dubinin-Polanyi (Eq. 2.10) equations and the model parameters were determined. The experimental data of adsorption isotherm of metal cation exchanged zeolites and the predicted adsorption isotherms based on Freundlich (Eq. 2.5), Dubinin-Polanyi (Eq. 2.3), and Langmuir (Eq. 2.10) equations are presented in Figures 5.26 and 5.27.

It is found that Dubinin-Polanyi equation (Eq. 2.10) is better than Freundlich equation in describing carbon dioxide adsorption. In addition, this study also shows that the adsorption data could nicely fit into Langmuir equation (Eq. 2.3). Since Langmuir equation based on monolayer adsorption, adsorbents with high surface area would adsorb more gases. In relation to Freundlich equation (Eq. 2.5), the adsorption capacity of carbon dioxide shows no limit, it would increase leading to infinity (Figure 5.26). This is due to the fact that Freundlich equation is only applicable at below saturation level (Yang, 1997).

As discussed in Chapter 2, studies on metal cation exchanged zeolite were mainly focused on the physical changes (Shibata and Seff, 1997; Armor, 1998; Choi *et al*., 2000; Trigueiro *et al*., 2002; Ohman *et al*., 2002; Kaushik *et al*., 2002; Kurama *et al*., 2002; Sato *et al*., 2003; Nery *et al*., 2003; Barros *et al*., 2004; Velu *et al*., 2005). Thermodynamic study on metal cation exchanged zeolites was limited to adsorption isotherm curves and adsorption capacity of the adsorbates (Bellat *et al*., 1995; Hutson *et al*., 1999; Kazansky *et al*., 2001).

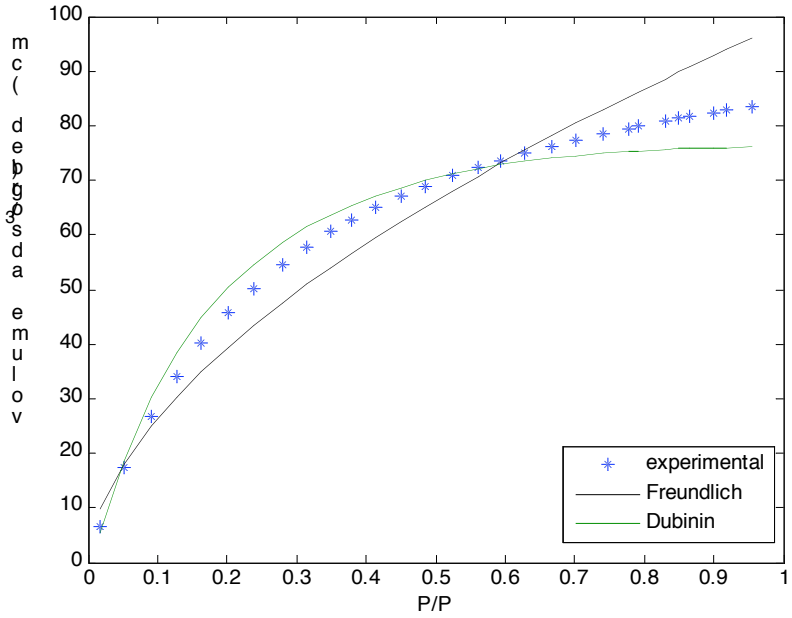

(a)

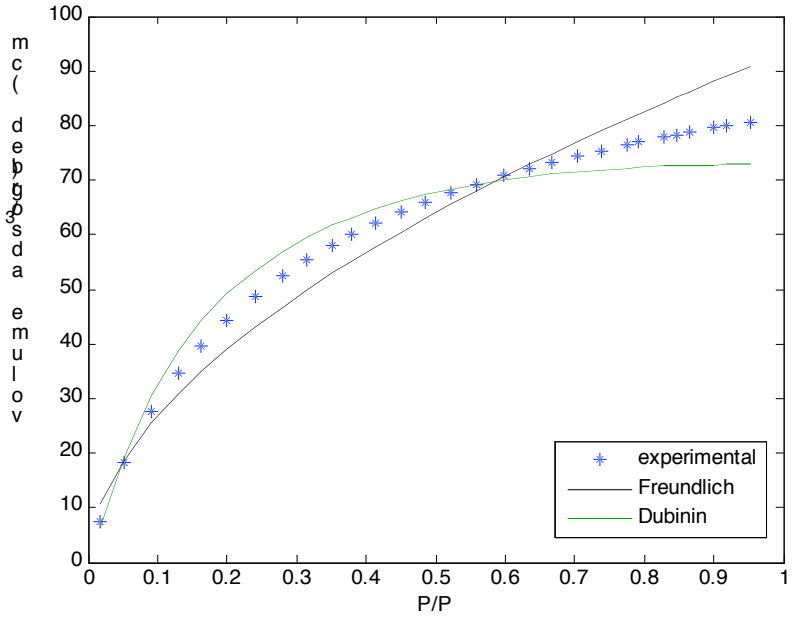

(b)

Figure 5.26: The adsorption isotherm of carbon dioxide fitted into Freundlich and Dubinin-Polanyi equations: (a) LiNa-SZ18 and (b) MgNa-SZ18.

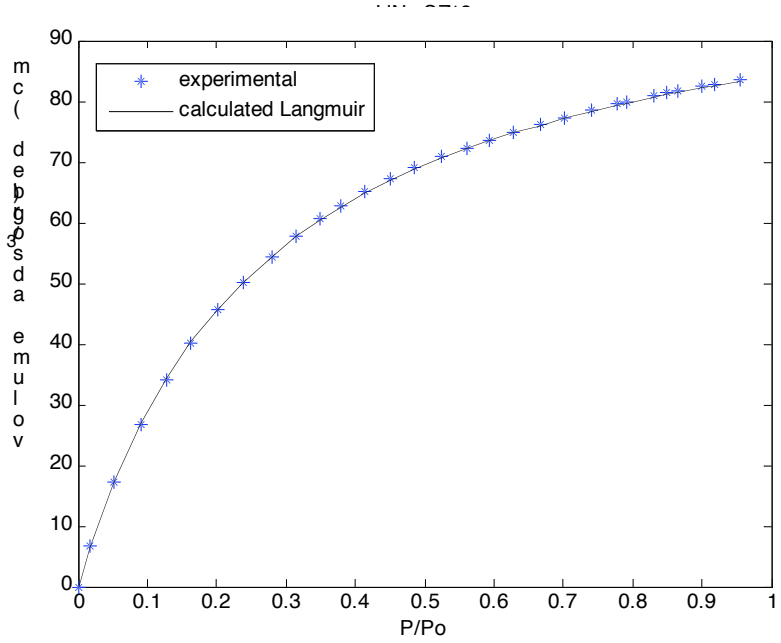

(a)

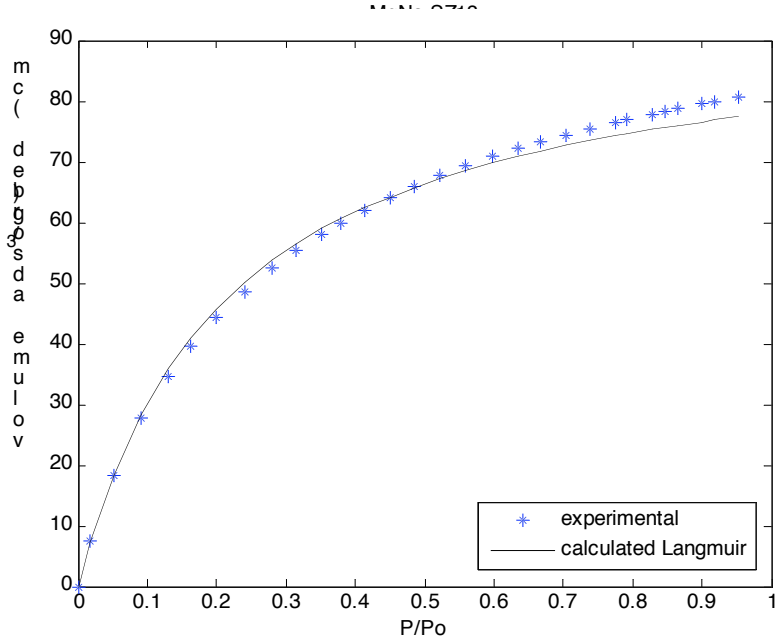

(b)

Figure 5.27: The adsorption isotherm of carbon dioxide fitted into Langmuir equation: (a) LiNa-SZ18 and (b) MgNa-SZ18.

The difference in Henry's (k) and Freundlich (K) constants could be associated to the presence of different extra-framework cations that influence the behavior the zeolites (Choudhary and Mayadevi, 1996; Kazansky *et al*., 2001; Barros *et al*., 2004). During the adsorption, the adsorbates would occupy the active sites belonging to the extra-framework cations. The amount of adsorbates adsorb on the adsorption sites is dependent on the quantity of the cation present and their location in the cavities. It is found that, except for transition metal groups, the model constant values increase as the atomic number increases. As discussed in Chapter 4, the porosity and void volume of the zeolites used in this study could also experience some changes due to adsorption swelling or structural defects. Thus, as shown in Appendix D3, it would result in several percent of errors.

Table 5.8: The model constants calculated from the best fitting of methane adsorption isotherm for metal exchanged zeolites.

Zeolite	Henry's (Eq. 2.1)	Freundlich (Eq. 2.5)		Dubinin-Polanyi (Eq. 2.10)	
	k	K	α	C	D
Alkali:					
LiNa-SZ18	6.12	6.36	1.03	1.33	0.27
NaSZ-18*	7.44	7.50	1.00	1.52	0.27
KNa-SZ18	7.31	7.51	1.04	1.49	0.27
RbNa-SZ18	10.84	10.77	0.99	1.87	0.26
Alkaline:					
MgNa-SZ18	6.63	6.61	1.00	1.40	0. 27
CaNa-SZ18	7.70	7.75	1. 00	1.56	0. 27
BaNa-SZ18	11.51	11.70	1.00	1.94	0. 26
Transition:					
MnNa-SZ18	6.96	7.05	0.99	1.41	0.24
NiNa-SZ18	5.18	5.51	0.94	1.20	0.23
ZnNa-SZ18	5.28	5.36	0.98	1.14	0.24

* Based zeolite

Another evident on the role of cation is the presence of Rb^{+} and Ba^{2+} in zeolites that lead to increase the Henry's and Freundlich constants for methane. After metal cation exchange treatment, both zeolites (RbNa-SZ18 and BaNa-SZ18) have lower crystallinity, surface area and pore volume than the based zeolite (Na-SZ18). However, in the presence of these cations, the adsorption sites and the electrostatic field might increase, thus increase the adsorption of methane. Hence, it could be assumed that at extremely low concentration, cations could play important role in gas adsorption since the adsorbates could adsorb at any adsorption sites which have larger electrostatic fields. In this case, surface area and pore volume would not significantly influence the adsorption of methane.

Again, the constants obtained were used to examine the effect of cations on carbon dioxide adsorption (Table 5.9). From the Freundlich model constant (α), it is proved that carbon dioxide adsorptions are no longer in dilute condition ($\alpha \neq 1$), in fact, it almost reaches the saturation point (plateau). The presence of Li^{+} increases the value of α from 0.38 to 0.57. With other monovalent cations of higher atomic number, the value decreases. The values indicate that the properties of cation (the size of the cation) influence the adsorption characteristics of the adsorbent. The effect would be on the diffusivity and the interaction between adsorbate and the adsorbent. Similarly, the constant (n) decreases in the presence of divalent cations (Group IIA and transition metal) after metal cation exchange treatment. In the presence of Group IA and IIA cations, another constant (K) value decreases as the atomic number increases. Likewise, as the atomic number of the transition metal cations increases, the K values are also decreases. In this case, the size of cation might strongly influence the K values of the metal cation exchanged zeolite. The limitation of this equation lies on the fact that it would reach infinity as the pressure increases.

Table 5.9: The model constants calculated from the best fitting of carbon dioxide adsorption isotherm for metal cation exchanged zeolites.

Zeolite	Freundlich		Langmuir		Dubinin- Polanyi	
	α	K	k	q_m	C	D
Na-SZ18	0.38	115.58	10.60	108.78	4.59	0.11
Alkali:						
LiNa-SZ18	0.57	90.92	3.73	106.62	4.33	0.16
KNa-SZ18	0.28	90.02	18.21	84.07	4.38	0.83
RbNa-SZ18	0.36	72.24	16.09	63.27	4.10	0.09
Alkaline:						
MgNa-SZ18	0.15	92.76	4.67	94.78	4.29	0.15
CaNa-SZ18	0.16	72.97	5.10	67.63	4.01	0.16
BaNa-SZ18	0.08	66.69	18.64	59.24	4.05	0.09
Transition:						
MnNa-SZ18	0.16	79.84	3.17	83.66	4.03	0.16
NiNa-SZ18	0.16	79.04	3.69	80.24	4.04	0.16
ZnNa-SZ18	0.18	68.03	2.39	73.18	3.82	0.11

On the other hand, the maximum amount of carbon dioxide adsorbed (q_m) could be determined using Langmuir equation. As mentioned earlier, Langmuir equation is based on monolayer adsorption. This might explain the reason for high q_m value for LiNa-SZ18 sample as the surface area of LiNa-SZ18 is relatively higher than the based zeolite. However, this study also revealed that the high surface area is not the only factor determining the amount of carbon dioxide adsorbed. Even though the surface area of MgNa-SZ18 and CaNa-SZ18 are higher than the based zeolite, the q_m values are still lower than the Na-SZ18. This phenomenon also indicates the possible influence of cation on gas adsorption.

As reported by Li and Gu (2004), the potential theory based on Dubinin-Polanyi equation could be used to describe the adsorption of pure component. The

characteristic curve obtained, assumed to be temperature invariant could be used to predict the adsorption equilibrium at other temperatures and determine the characteristic energy by the slope of linearized Dubinin-Polanyi equation since $D = (RT/E)^2$. Consequently, the constants (C and D) could be obtained by fitting the experimental data into Dubinin-Polanyi equation (Yang, 1987), in which the characteristic curves could be plotted for particular adsorption system. The results obtained indicate that the characteristic curves are more likely influenced by the properties of the adsorbates with minimum effect by the cations. This is due to the fact that the constants C is in the range of 1.00-2.00 for methane and 3.00 -4.50 for carbon dioxide, and constant D is in the range of 0.20 – 0.30 for methane and 0.10 – 0.90 for carbon dioxide. It was found that the correlation between the experimental data obtained and Langmuir equation is better than the Dubinin-Polanyi equation. The finding is in good agreement with Choudhary *et al*. (1995) in which reported that Langmuir could be used to describe adsorption on faujasite type zeolites (NaX and NaY).

5.3.3 Heat of adsorption

According to Hutson *et al*. (1999), heterogeneity in zeolites results from a number of causes including mixed population of charge compensating cations. In the modification procedures, the sodium cation is not completely exchanged. Therefore, the adsorbents used in this study consist of two types of metal cations. Hence, the adsorption sites would differ depending on type of cation present. Furthermore, the proportion of cation may vary from one cavity to another, thus the behavior would become more complex. The heterogeneity could be determined by isosteric heat of adsorption (ΔH_{ST}). The isosteric heat of adsorption is evaluated at constant loading that result in a positive quantity. However, only differential heat of adsorption (ΔH) could be determined using the gravimetric method. Differential heat of adsorption, however, is calculated by isothermal condition of differential amount of adsorbates. The observed small difference in ΔH suggests the extent of

interactions between the adsorbate and the adsorbent. However, according to Heo and Lim (1996), high densities of molecules crowded in a zeolite cavity within limited volume may enhance induced dipoles, thus the interaction energies among molecules might be greater than physisorbed molecules.

This study shows that the presence of other cations as charge balancing cation alters the adsorption characteristics (Table 5.10). However, the adsorption still remains as physical adsorption (physisorption). As for methane adsorption, the presence of smaller cation such as Li^+ leads to higher ΔH. This value suggests that for non-polar molecules with non-specific interaction between adsorbate and adsorbent, the pore size might play a role in determining the adsorption of the molecules. This is reflected by ΔH values of the metal cation exchanged zeolites (LiNa-SZ18 and RbNa-SZ18). In addition, Zhao *et al*. (2001) suggested that for non-polar molecules, the decrease in the heat of adsorption caused by energetic heterogeneity of the surface.

The simulated values obtained are in the range of 14 – 19 kJ/mol (Maurin *et al*., 2005c). As suggested by Maurin *et al*. (2005c), the differences in the enthalpies are due to the combination of two effects, the variation of the number of cations which give rise to a different magnitude of electric field and the enhancement of adsorbate-adsorbent interactions due to high accessibility of cation sites in NaY compared to Na-SZ18.

Table 5.10: The enthalpy and entropy change in the adsorption of methane and carbon dioxide.

Zeolite	Methane		Carbon dioxide	
	ΔH (kJ/mol)	ΔS (J/mol.K)	ΔH (kJ/mol)	ΔS (J/mol.K)
Na-SZ18	13.38	58.32	6.01	66.64
LiNa-SZ18	15.50	60.58	3.08	53.51
RbNa-SZ18	10.55	71.45	4.60	59.92

However, for molecules such as carbon dioxide, the presence of quadrapole moment requires specific adsorption sites for adsorption to occur. Even though after the metal cation exchanged treatment, the porosity of the metal cation exchanged zeolites increases (e.g. LiNa-SZ18), the number of adsorption sites might be decreases thus affect the adsorptivity of carbon dioxide. In addition, strong interaction between adsorbate and adsorbent that restricting the mobility of the molecules could be the reason for low adsorption capacity. As reported by Choudhary and Mayadevi (1996), ΔS values indicate the extent of mobility of the adsorbed molecules in the respective pores. In this case where both molecules present as supercritical fluids, ΔS values appears to be insignificant difference between methane and carbon dioxide.

5.4 Gas Adsorption Kinetics

The adsorption kinetics of metal cation exchanged zeolites was investigated using the gravimetric dynamic adsorption method. In principle, the adsorption process of adsorbates in porous materials such as zeolites involves molecular diffusion in which molecules collides in large pores, then diffusion into meso- or micropores, pore filling, and finally adsorbate interaction with zeolite surface.

According to Cui *et al*. (2004), gas transport is mainly influence by the adsorbate molecular geometry and the pore structure. However, this section would examine the characteristics of diffusion in zeolite pore network, the uptake rate, and the equilibrium time in the presence of mixed cations in the zeolite structural framework.

5.4.1 Gas adsorption uptake curve

As discussed in Chapter 2, root t-law (Eq. 2.28) could be applied for a short time region in which the fractional uptake curve of metal exchanged zeolite adsorbents could be plotted against t. Figures 5.28 - 5.30 show that as different cation replacing sodium, different adsorption uptake curves were obtained. As reported by Hutson *et al*. (1999) the cation exchange capacity (CEC) of lithium is higher than the other alkali metal cations (K^+ and Rb^+). As the size of lithium cation smaller than sodium, it is assumed that the adsorbate molecules could easily diffuse into the network pore system. In addition, the presence of lithium increases the surface area and crystallinity of could be the reason why LiNa-SZ18 reaches the maximum capacity faster than the other adsorbents (Figure 5.28). Different phenomena were observed for divalent metal cations exchanged zeolites. The charge and the size of cation such as Ba^{2+} affect the adsorption characteristics of adsorption. The uptake rate of alkaline earth metal zeolite is in the order of BaNa-SZ18 > CaNa-SZ18 > MgNa-SZ18, indicates that metal cation will influence the adsorption characteristics of methane on zeolites (Figure 5.29). However, the presence of transition metal in zeolite gives less effect to the adsorption of methane (5.30).

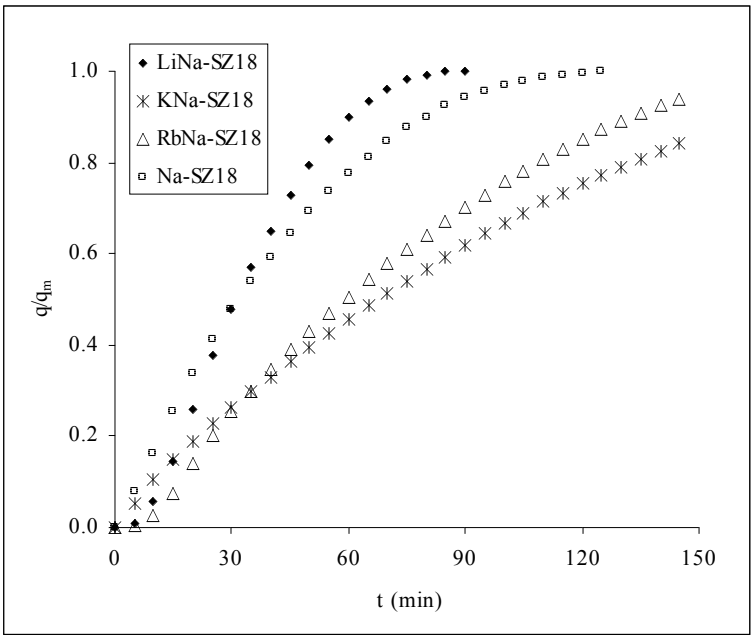

Figure 5.28: The methane fractional uptake curves of the alkali metal cation exchanged zeolites.

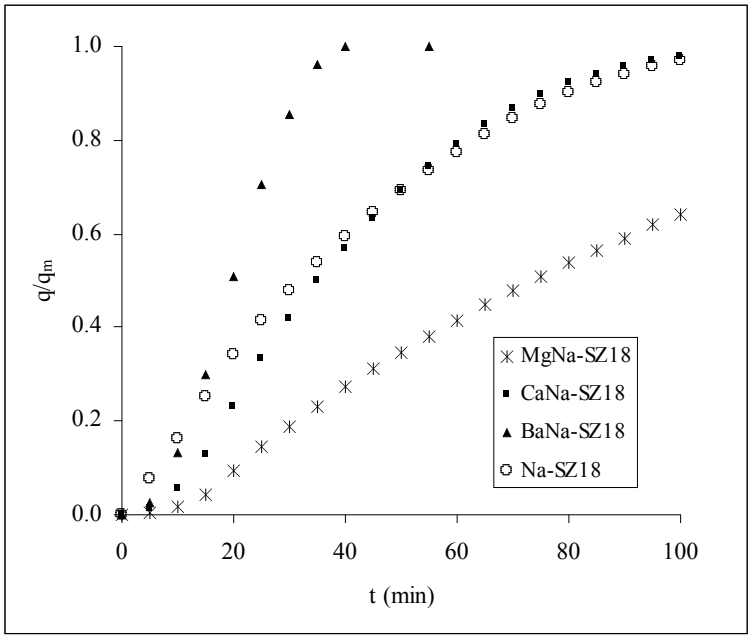

Figure 5.29: The methane fractional uptake curves of the alkaline earth metal cation exchanged zeolites.

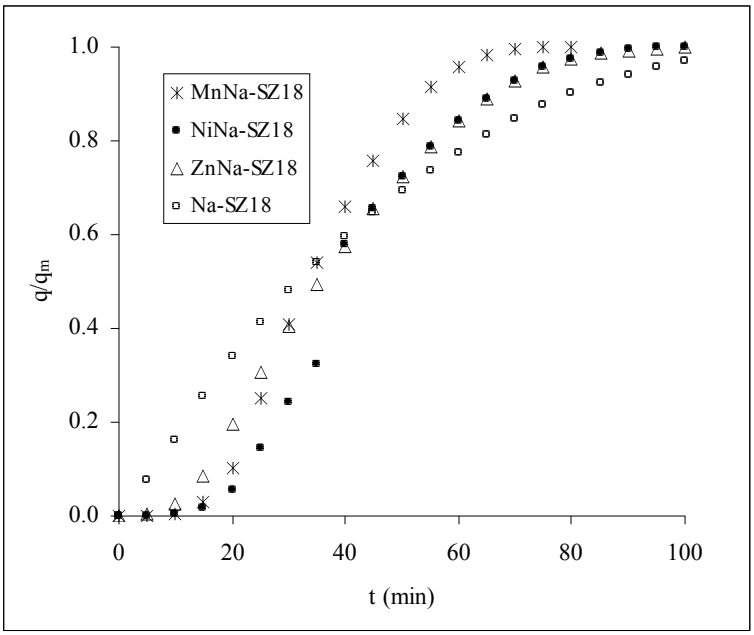

Figure 5.30: The methane fractional uptake curves of transition metal exchanged zeolites.

The presence of larger cation size such as Ba^{2+} induces more electrostatic field that could attract molecules to the adsorption sites. Hence, in alkaline earth metal exchanged zeolites, it is found that BaNa-SZ18 reaches the maximum capacity faster than MgNa-SZ18 and CaNa-SZ18. These phenomena support the fact that the cation has a certain degree of influence on gas adsorption process. The effects of different cations are also shown in carbon dioxide adsorption. The carbon dioxide adsorption behavior of monovalent metal cation exchanged zeolites is presented in Figure 5.31. The curves are convex in nature but each sample would achieve maximum capacity at different time. It was also found that the presence of divalent metal cations in zeolite changes the adsorption characteristics of carbon dioxide. Figures 5.32 and 5.33 show the presence of two stages of adsorption. Since the quadrapole moment of carbon dioxide interacts strongly with cation, the presence of mixed cations in the zeolite adsorbents could be the reason for the observed phenomena.

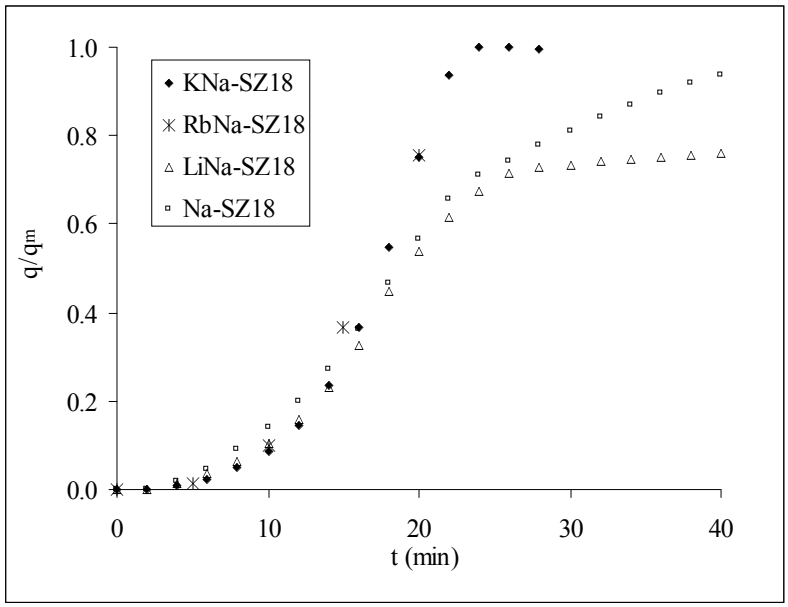

Figure 5.31: The carbon dioxide fractional uptake curve of alkali metal cation exchanged zeolite.

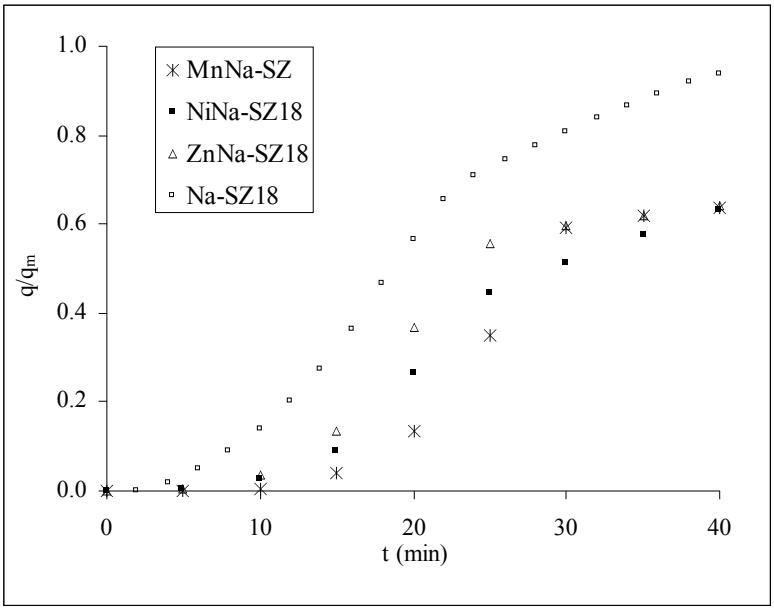

Figure 5.32: The carbon dioxide fractional uptake curve of alkaline earth metal cation exchanged zeolite.

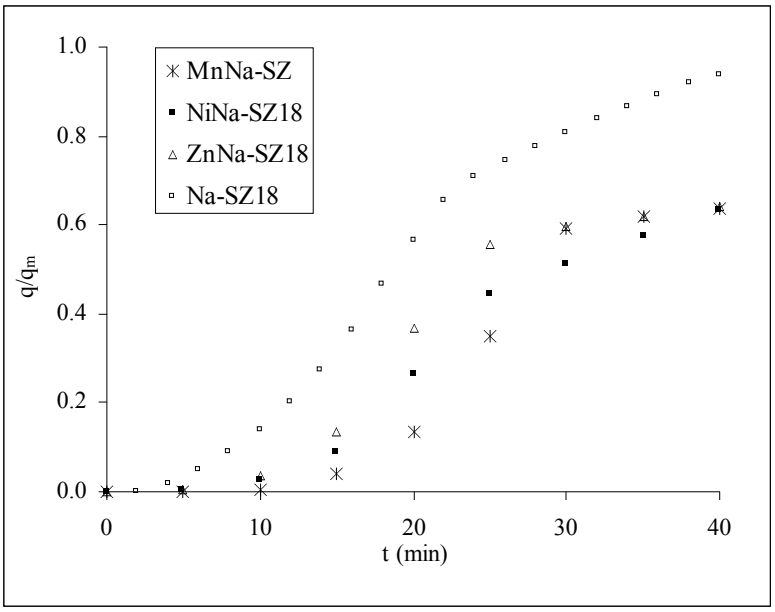

Figure 5.33: The carbon dioxide fractional uptake curve of transition metal cation exchanged zeolites.

5.4.2 Initial adsorption rate

As previously discussed in Chapter 4, the cations could be one of the sites for adsorption to occur. Therefore, further investigation was carried out to study the influence of different cations on the adsorption inside the pore network. In this section, the initial adsorption rate was calculated based on dynamic adsorption data of methane and carbon dioxide (Table 5.11).

Table 5.11: The initial adsorption rate and equilibrium time of metal cation exchanged zeolites.

Sample	Initial adsorption rate (mol/sec) x 10^6	
	CH_4	CO_2
Alkali:		
LiNa-SZ18	5.35	5.25
Na-SZ18*	3.57	3.53
KNa-SZ18	1.24	5.11
RbNa-SZ18	1.48	9.64
Alkaline:		
MgNa-SZ18	1.93	5.01
CaNa-SZ18	3.31	3.80
BaNa-SZ18	6.81	6.15
Transition:		
MnNa-SZ18	5.86	0.59
NiNa-SZ18	4.40	2.48
ZnNa-SZ18	5.18	0.95

* Based zeolite

The introduction of metal cation into zeolite structures affects relative crystallinity of the metal cation exchange zeolites ranging from 20 % to 106 %. Until now, there is no concrete evident that the relative crystallinity has much influence on the initial adsorption rate of methane and carbon dioxide. As a matter of fact, RbNa-SZ18 in Group IA metal cation with relative crystallinity of 58 % has higher carbon dioxide adsorption rate (9.64 mol/s) than LiNa-SZ18 (5.25 mol/s), and even BaNa-SZ18 (RC = 20 %) has relatively high initial adsorption rate (6.15 mol/s). However, the presence of transition metal does not improve the initial adsorption rate of the respective zeolites. The same observation was reported by Khelifa *et al*. (1999) in which the introduction of transition metal into zeolite by cation exchange

method leads to decrease the adsorption affinity of carbon dioxide but this does not the case for divalent cation of alkaline earth metals. This could be due to the depopulation of cationic sites distributed within the supercages. This is also another evident that cation plays an important role in the adsorption of gases.

Conversely, for methane adsorption, large pore opening and large pore volume could also be the reason for high initial adsorption rate. This is clearly indicated by examining the effect of cation on methane initial adsorption rate of BaNa-SZ18 and transition metal cation exchanged zeolites (MnSZ-18, NiNa-SZ18, and ZnNa-SZ18). None of these samples have higher crystallinity and surface area than the based zeolite. However, the results show that the initial adsorption rates of those metal cation exchanged zeolites are relatively higher than the based zeolite. Thus, the presence of cation could enhance the adsorptive properties of the adsorbents even though the structural properties of the adsorbent itself decrease. This result is in good agreement with a study by Ackley and Yang (1991) in which the uptake was strongly influenced by the type, number and location of the cation. In relation to the effect of cation on the adsorption rate of methane and carbon dioxide, the initial adsorption of the metal cation exchanged zeolites were plotted against charge/radius of cations (Figure 5.34).

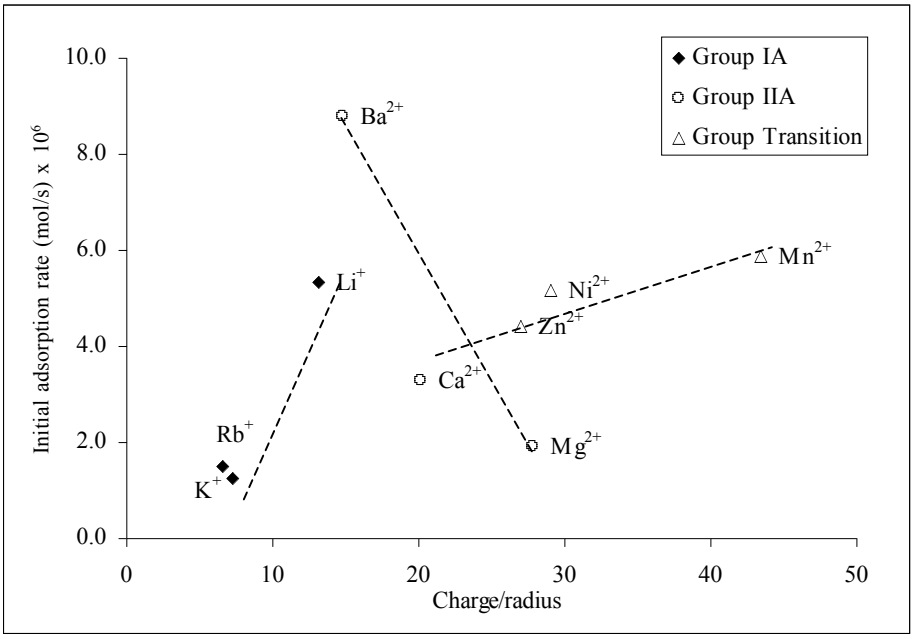

(a)

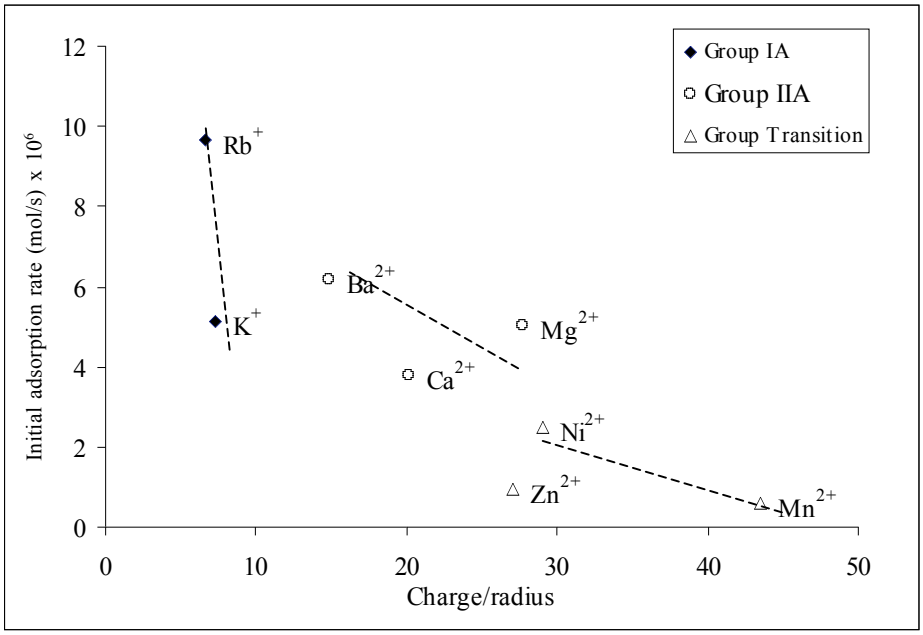

(b)

Figure 5.34: The effect of cation's properties on initial adsorption rate for different adsorbates: (a) methane and (b) carbon dioxide.

The results obtained show that as charge/ionic radius of alkali metal increases, the initial adsorption rate increases. The presence of transition metal cations in zeolites gives similar affects on the adsorption rate of methane the metal cation exchanged zeolites. In contrast, when the sodium cation was exchanged with alkaline earth metal cations, the initial adsorption rate decreases as the ionic radius increases as going down the group in the Periodic Table. This finding suggests that the initial adsorption rates are not only affected by electrostatic charge but also the size of the cations.

5.4.3 Adsorption equilbrium time

As mentioned in Section 4.4.2.2, adsorption equilibrium time is important in the adsorbent selection that needs to be used in any adsorption process. There are many factors that attribute to the time taken for adsorption to complete. After the cation exchanged treatment, the structural and physical properties of zeolite adsorbents were altered. Table 5.12 shows that the several zeolites need longer time to reach equilibrium after the metal cation exchange treatment.

Table 5.12: The adsorption equilibrium time of methane and carbon dioxide adsorbed on metal cation exchanged zeolites.

Zeolite	Adsorption equilibrium time (min)	
	CH_4	CO_2
Alkali:		
LiNa-SZ18	155	180
Na- SZ18*	125	56
KNa-SZ18	290	70
RbNa-SZ18	180	45
Alkaline:		
MgNa-SZ18	205	90
CaNa-SZ18	125	150
BaNa-SZ18	55	150
Transition:		
MnNa-SZ18	80	140
NiNa-SZ18	105	135
ZnNa-SZ18	120	190

* Based zeolite

However, the changes are also followed by some improvement particularly in the adsorption capacity of several types of zeolites. The extent of relationships between structural, physical and chemical properties of zeolites, and the equilibrium time of methane and carbon dioxide are presented in Figures 5.35, 5.36, and 5.37. It is quite difficult to determine factor(s) that influence the equilibrium time of the adsorption, in fact the complexity arises as a combination between these properties might influence the adsorption characteristics of the gases. However, the monovalent cation exchanged zeolites behave differently from divalent cation exchanged zeolites.

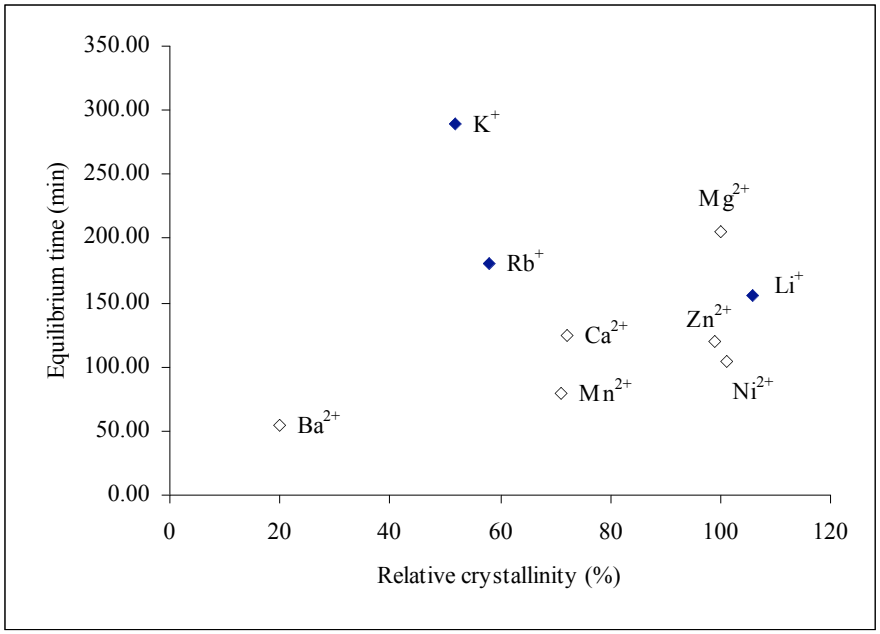

(a)

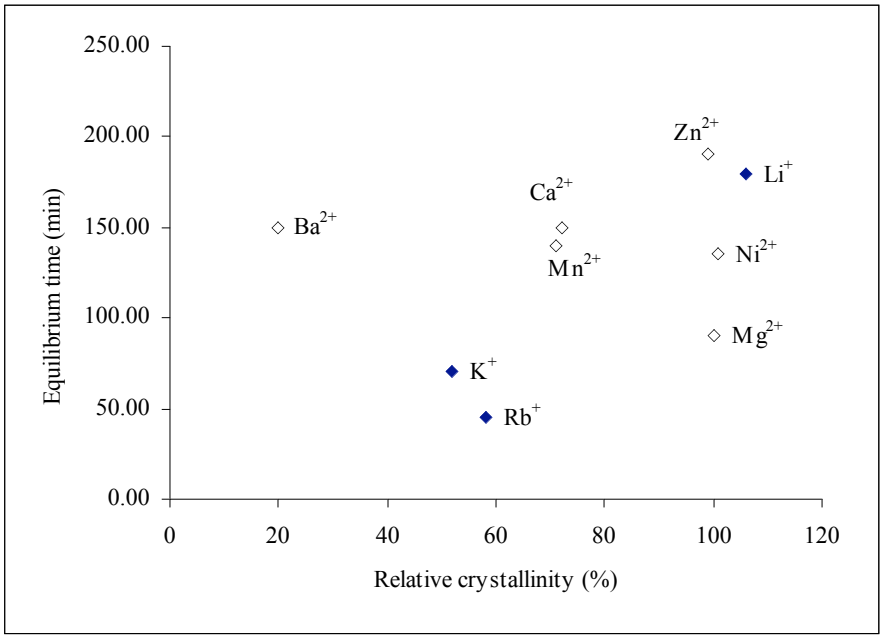

(b)

Figure 5.35: The effect of relative crystallinities on adsorption equilibrium time: (a) methane and (b) carbon dioxide.

Figure 5.36 also shows that the surface area affects the adsorption equilibrium time of methane adsorption particularly for the divalent metal cation exchanged zeolites. On contrary, the adsorption equilibrium time for carbon dioxide adsorption is affected by the surface area of monovalent metal cation exchanged zeolites. The relationships between of cation properties (charge/radius) and the adsorption equilibrium time are shown in Figure 5.37. In the adsorption of methane, the equilibrium time increases as the charge/ionic radius of alkaline earth metal cation increases.

However, opposite relationships were obtained for alkali and transition metal groups. For carbon dioxide adsorption, the adsorption equilibrium time of alkali metal increases as the charge/ionic radius increases, but alkaline earth metal and transition metal groups experience the opposite effect. Thus, these findings show that it is difficult to determine factors that influencing the adsorption equilibrium time of methane and carbon dioxide. The results also show that some variations occurred to the gas adsorption characteristics in the presence of different groups of cations.

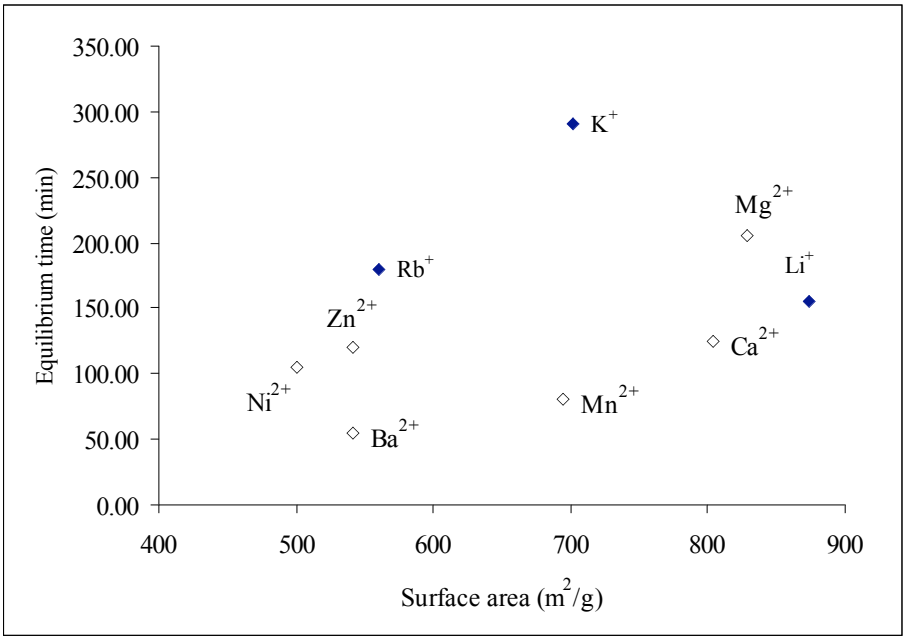

(a)

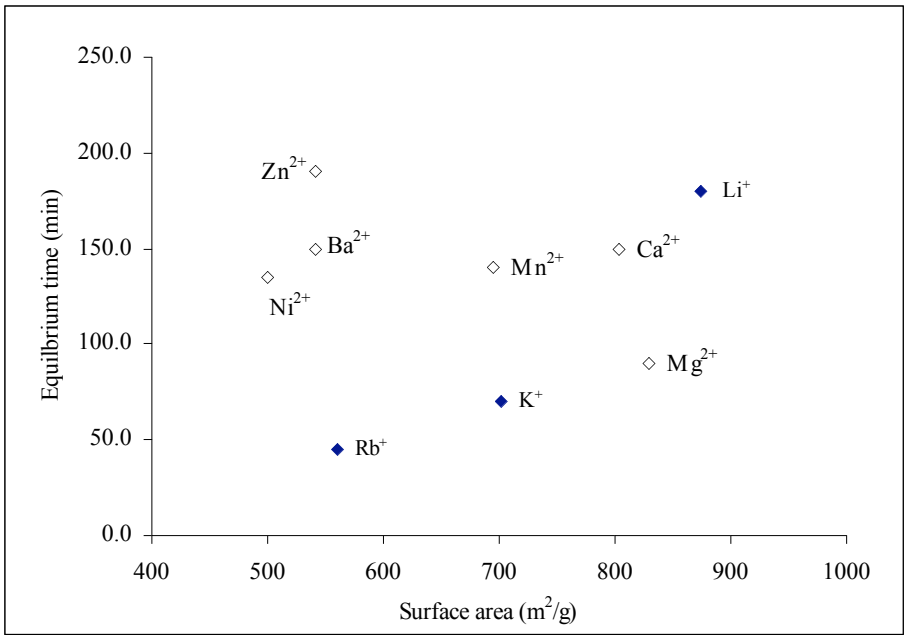

(b)

Figure 5.36: The effect of zeolites surface area on the adsorption equilibrium time: (a) methane and (b) carbon dioxide.

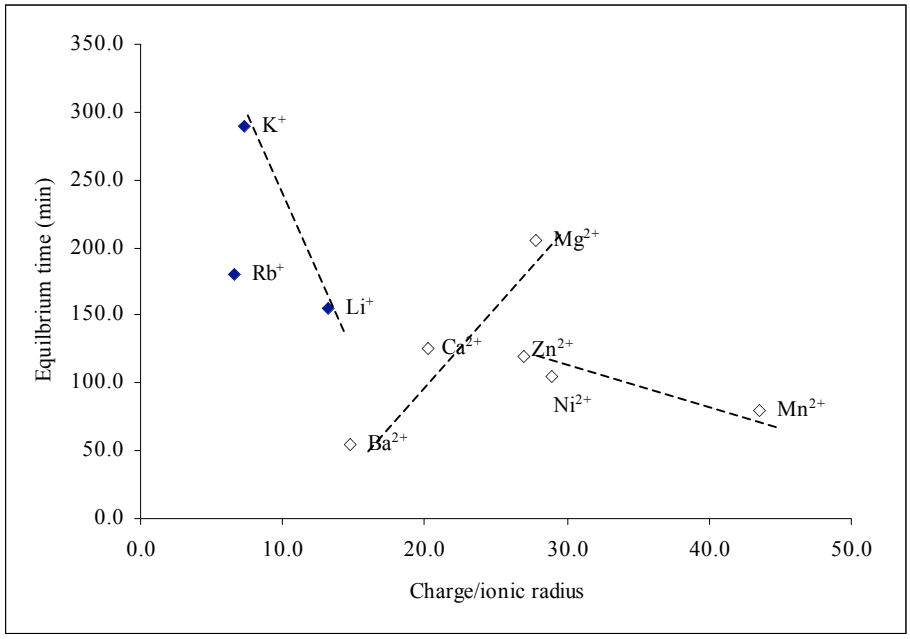

(a)

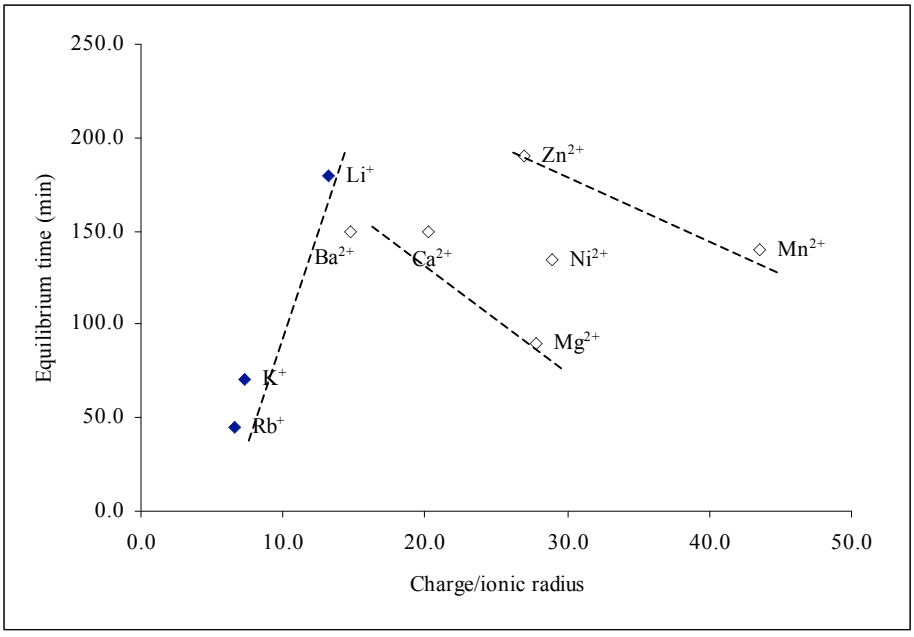

(b)

Figure 5.37: The effect of cations properties on adsorption equilibrium time: (a) methane and (b) carbon dioxide.

5.4.4 Gas diffusivity

5.4.4.1 Bulk phase gas diffusivity

As reported by Yeh and Yang (1990), diffusion in metal cation exchanged zeolites has been the subject of many discussions since it might involves blocked micropores and covered adsorption sites. However, the used of faujasite type zeolite (Na-SZ18) would reduce the possibility of blocked micropores since the pore opening is large enough to avoid any blockage to occur. As presented in Chapter 4, the molecular diffusions of methane and carbon dioxide in bulk phase and macropores are relatively faster than micropore diffusion. Therefore, rather than focusing on the molecular diffusion, this section will focus on gas diffusion inside the micropore structures and the effect of different cations on gas diffusivity.

5.4.4.2 Internal pore diffusivity

The presence of larger cations such as Rb^{2+}, K^{+}, and Ba^{2+} would not significantly affect the micropore diffusivities of the adsorbates (methane and carbon dioxide) since the kinetic diameters of the adsorbates are smaller than the typical pore opening of faujasite type zeolites. It is further proved by the Knudsen numbers in which the changes are relatively small after the metal cation exchange treatment (Table 5.13). It is also shown that the average pore diameter of the zeolites does not significantly change after metal cation exchanged treatment.

In addition, as previously discussed in Section 4.4.3.2, diffusion in microporous zeolite could also be classified either Knudsen or configurational diffusion. Based on average pore diameter of the metal cation exchanged zeolites

and molecular diameter of the adsorbate , it was found that methane and carbon dioxide diffusions also fall into Knudsen diffusion (Table 5.14). The values obtained indicate that except for transition metal cation exchanged zeolites, the ratios between adsorbate molecular diameter and the pore diameter are in the range of 0.21to 0.25 for methane and 0.16 to 0.18 for carbon dioxide. In this study, the presence of Mn^{2+} increases the ratio whereas the presence of Ni^{2+} causes the ratio to drop, relatively lower than the other metal cation exchanged zeolites.

Table 5.13: The Knudsen number (N_{Kn}) and diffusional characteristics of metal cation exchanged zeolites.

Zeolites	CH_4		CO_2	
	N_{Kn}	Types of diffusion	N_{Kn}	Types of diffusion
Alkali:				
LiNa-SZ18	28.5	Knudsen	37.4	Knudsen
KNa-SZ18	27.9	Knudsen	37.0	Knudsen
RbNa-SZ18	33.6	Knudsen	44.6	Knudsen
Alkaline:				
MgNa-SZ18	28.2	Knudsen	37.4	Knudsen
CaNa-SZ18	28.2	Knudsen	37.4	Knudsen
BaNa-SZ18	27.3	Knudsen	36.2	Knudsen
Transition:				
MnNa-SZ18	30. 8	Knudsen	40.8	Knudsen
ZnNa-SZ18	28.8	Knudsen	38.2	Knudsen
NiNa-SZ18	23.9	Knudsen	31.7	Knudsen

Table 5.14: The diffusional characteristics of metal cation exchanged zeolites.

Zeolites	d_{ave} (nm)	Methane		Carbon dioxide	
		$2r/d_{ave}$	Types of diffusion	$2r/d_{ave}$	Types of diffusion
Group IA:					
LiNa-SZ18	1.80	0.21	Knudsen	0.18	Knudsen
KNa-SZ18	1.82	0.21	Knudsen	0.18	Knudsen
RbNa-SZ18	1.51	0.25	Knudsen	0.22	Knudsen
Group IIA:					
MgNa-SZ18	1.80	0.21	Knudsen	0.18	Knudsen
CaNa-SZ18	1.80	0.21	Knudsen	0.18	Knudsen
BaNa-SZ18	1.86	0.20	Knudsen	0.18	Knudsen
Transition:					
MnNa-SZ18	1.65	0.21	Knudsen	0.20	Knudsen
NiNa-SZ18	2.12	0.21	Knudsen	0.16	Knudsen
ZnNa-SZ18	1.76	0.20	Knudsen	0.19	Knudsen

As the diffusion inside the micropore involves Knudsen diffusion, the diffusivities (D_K) calculated using Equation 4.5 are shown in Table 5.15. Knudsen diffusivity takes into account the properties of the adsorbates and the adsorbent. The results show that Knudsen diffusivities of methane are higher than carbon dioxide. As the diffusivities of methane are relatively higher than carbon dioxide, the molecules could diffuse faster into the inner side of the structure than carbon dioxide. This explained the reason why the adsorption capacity of carbon dioxide is lower than methane.

Table 5.15: Knudsen diffusivity of CH_4 and CO_2 inside metal cation exchanged zeolite pores.

Zeolites	Knudsen diffusivity, D_K (m^2/s) x 10^7	
	CH_4	CO_2
Alkali:		
LiNa-SZ18	7.84	4.73
Na-SZ18*	7.76	4.67
KNa-SZ18	7.93	4.78
RbNa-SZ18	6.58	3.97
Alkaline:		
MgNa-SZ18	7.84	4.73
CaNa-SZ18	7.84	4.73
BaNa-SZ18	8.10	4.89
Transition:		
MnNa-SZ18	7.19	4.34
NiNa-SZ18	9.24	5.57
ZnNa-SZ18	7.67	4.63

* Based zeolite

The interaction between the adsorbates and the wall of zeolite adsorbent is higher than the adsorbate-adsorbate interaction, thus allows more interaction with the solid surface. The presence of metal cations other than sodium cations changes the Knudsen diffusivity of the exchanged zeolites. The diffusivity of methane and carbon dioxide increases as the sodium cations were exchanged with alkaline earth metals cations (Mg^{2+}, Ca^{2+}, and Ba^{2+}). Similarly, the presence of Li^+ and K^+ increase the diffusivity of methane and carbon dioxide in LiNa-SZ18 and KNa-SZ18 respectively. However, exchanging sodium cation with larger size molecule (Rb^+) reduces the Knudsen diffusivity of the exchanged zeolite. This is due to the fact that the Knudsen diffusivity depends on the pore size and molecular dimension of the adsorbates. Thus, after cation exchange treatment, the size of the cation and its

location within the pore structure would affect the diffiusivity of the adsorbates. However, it is rather difficult to predict the effect of transition metal cations (Mn^{2+}, Ni^{2+}, and Zn^{2+}) on the Knudsen diffusivities of the metal cation exchanged zeolites.

In general, the differences in Knudsen diffusivities are relatively small and it is rather difficult to predict the changes in the presence of different groups of cation. However, the results show that zeolite such as NiNa-SZ18 demonstrates a promising performance as potential adsorbent. Accordingly, based on the results obtained, detailed study should be carried out in identifying potential adsorbent especially for methane/carbon dioxide separation process.

5.4.4.3 Diffusional time constant

Diffusional time constants ($\boldsymbol{D}/r^2$) of methane and carbon dioxide at 137 kPa and 323K are shown in Table 5.16. Despite the fact that there were only relatively small differences in the size of adsorbate molecule used, a large changes in the magnitude of diffusional time constants were observed. The effect were be attributed to the size, the charge and the quantities as well as types of cation in the metal cation exchanged zeolites. As reported by Bae *et al*. (2005), high apparent time constants are due to the strong adsorption affinity between adsorbate and adsorbent. The results show that the presence of cation affects the diffusional time constant ($\boldsymbol{D}/r^2$), and in several metal cation exchanged zeolites, the values are higher than the based zeolite. However, the results are also affected by cation exchange capacity (CEC). This explained the reason why several types of metal cation exchanged zeolites have low diffusional constant values.

Table 5.16: The diffusional time constants of methane and carbon dioxide adsorption at 323K and 137 kPa.

Zeolites	Diffusional time constant ($\boldsymbol{D}/r^2$) x 10^5 (sec^{-1})	
	CH_4	CO_2
Alkali:		
LiNa-SZ18	6.80	3.04
Na-SZ18	4.01	9.79
KNa-SZ18	1.64	4.81
RbNa-SZ18	23.10	176.03
Group IIA:		
MgNa-SZ18	1.84	18.3
CaNa-SZ18	5.27	6.48
BaNa-SZ18	22.58	27.04
Transition:		
MnNa-SZ18	13.52	4.52
NiNa-SZ18	6.31	4.40
ZnNa-SZ18	9.33	9.02

The results show that for methane, the diffusional time constant of BaNa-SZ18 is relatively higher than the other adsorbents, and for carbon dioxide, RbNa-SZ18 has the highest value. These values indicate how fast the adsorbent reach the maximum adsorption capacity. It is obvious that different adsorbates would react differently towards different metal cation exchanged zeolites. Low diffusional time constants indicate greater diffusion resistance as well as high energy barrier for molecules to diffuse (Ahn *et al.*, 2004). It also indicates that the charge of cation and the total amount of cation present as the extra-framework cations would determine the characteristics of adsorption.

5.5 Gas-Zeolite Interaction

The effect of structural properties on adsorbate-adsorbent interaction was discussed in Section 4.5. In this section the effect of metal cations on gas-solid interaction will be discussed. Using Na-SZ18 as a based zeolite, the adsorbate-adsorbent interaction study focuses on the effect of cations on methane and carbon dioxide adsorption. Apart from the gas adsorption capacity, the effect of different cations was observed from the FTIR spectra of the adsorbates. As previously discussed in Section 4.5, peaks were detected in the region between 3200 – 1200 cm^{-1} and 2800 – 1400 cm^{-1} for methane and carbon dioxide respectively. A study by Eder and Lercher (1997) has showed that sorbate-sorbate interactions influence the uptake curves. Another study by Barbosa *et al*. (2000) also showed that the electrostatic and van der Waal interactions dominate the interaction between adsorbate and adsorbent in which adsorbate molecules interact simultaneously with cationic sites and the oxygen atoms. In addition, according to Izumi *et a*l. (2002), the adsorbate molecules proximity to zeolite surface is influenced by strong electrostatic field of zeolite to polarize and produce a Coulomb force (Figure 5.38). The possible interactions between adsorbate and zeolite have been discussed in Section 4.5. The difference could be due to the presence of other cations after cation exchange treatment that create different electrostatic force between the adsorbate and the metal cations (e.g. Na^{+} and Mg^{2+}).

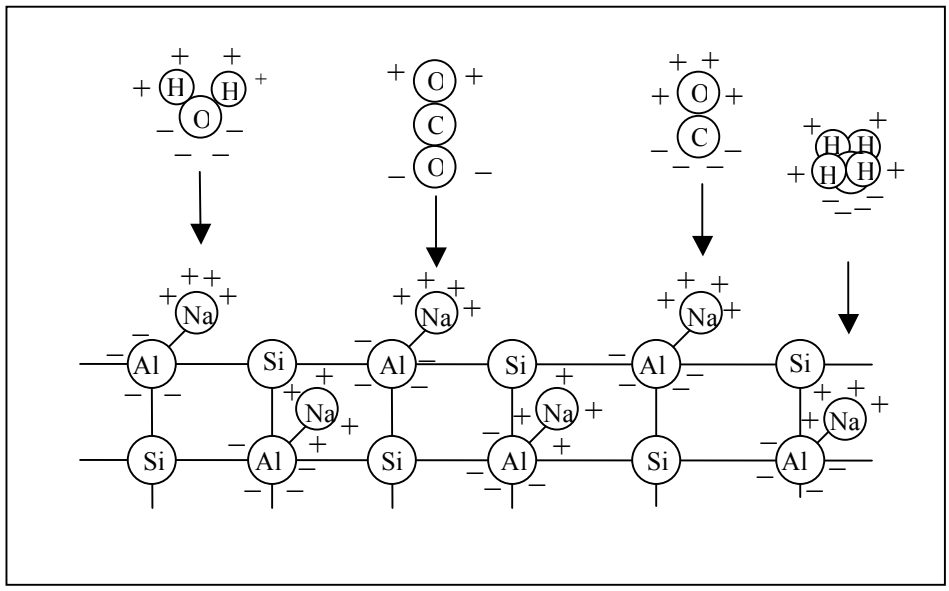

Figure 5.38: The electrostatic charge model and adsorption force on zeolite surface (Izumi *et al*., 2002)

However, it is rather difficult to verify the observed FTIR spectra with those published in literature since most of the previous studies were carried out at low temperature (77 K – 273 K) and low pressure (1 – 10 psi). At relatively low temperature, the spectra were more noticeable even at low pressure. As the pressure increases, the peak intensities increase which indicate the quantity of adsorbate increases. In contrast, this study involves adsorption at relatively high temperature (298 K). Hence, some peaks could not be clearly identified. Figures 5.39, 5.40 and 5.41 show the IR spectra methane adsorbed on different zeolites. A sharp peak assigned to v_3 band is visible as methane interacts with LiNa-SZ18 and BaNa-SZ18 zeolites. The existence of peak around this region is a result of free rotation of the adsorbed molecules around a single axis. However, in other zeolite samples, as the peak assigned to v_3 band shifted, intensity was decreased and other peaks with lower intensities also appear on the both sides of the v_3 band. This is probably due the presence of more than one cation in zeolites after the cation exchange treatment that results in the existence of non-symmetrical field of different strengths.

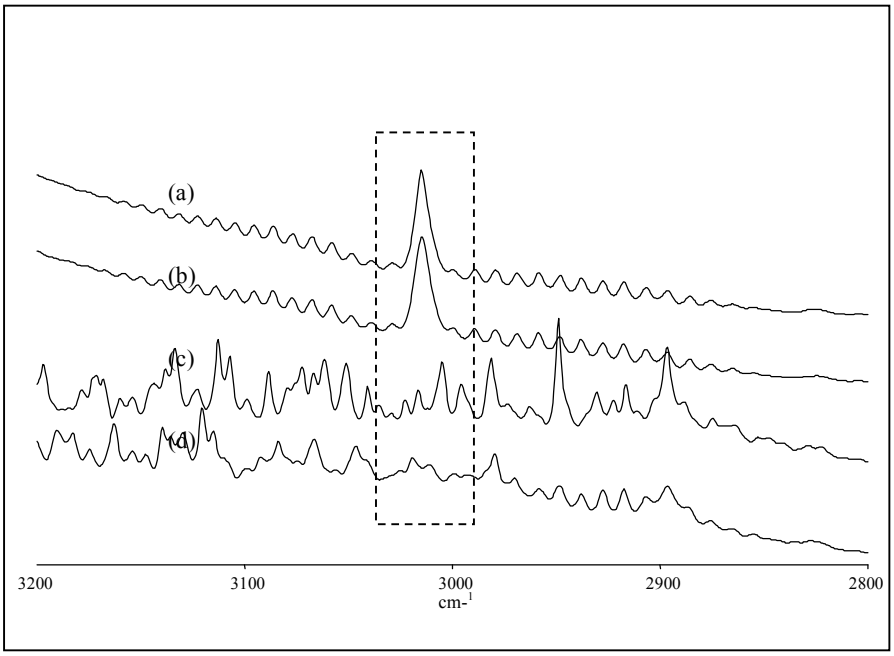

Figure 5.39: The FTIR spectra (v_3) of CH_4 adsorbed on alkali metal cation exchanged zeolites: (a) LiNa-SZ18; (b) Na-SZ18 (based zeolite); (c) KNa-SZ18; and (d) RbNa-SZ18.

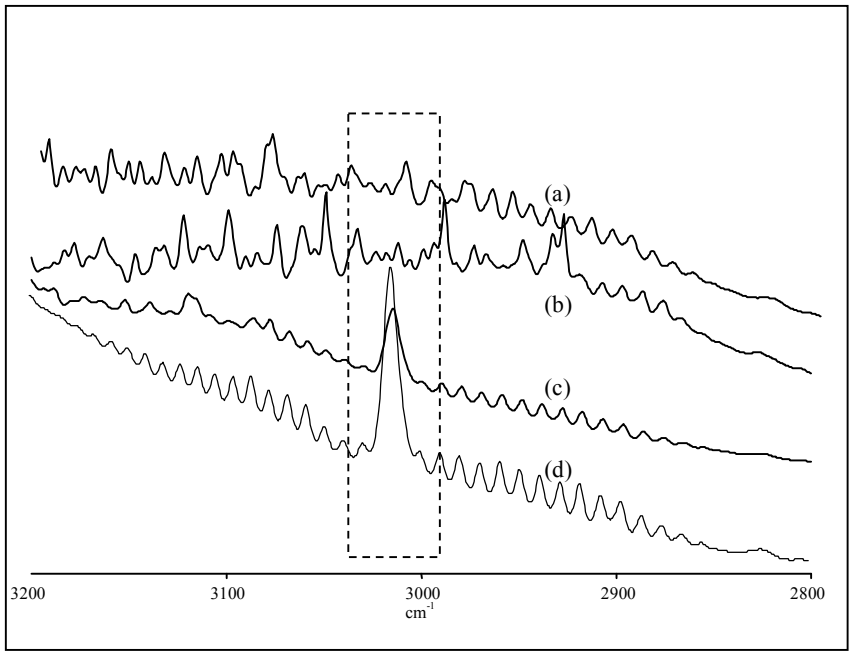

Figure 5.40: The FTIR spectra (v_3) of CH_4 adsorbed on alkaline earth metal cation exchanged zeolites: (a) MgNa-SZ18; (b) CaNa-SZ18; (c) BaNa-SZ18; and (d) Na-SZ18 (based zeolite).

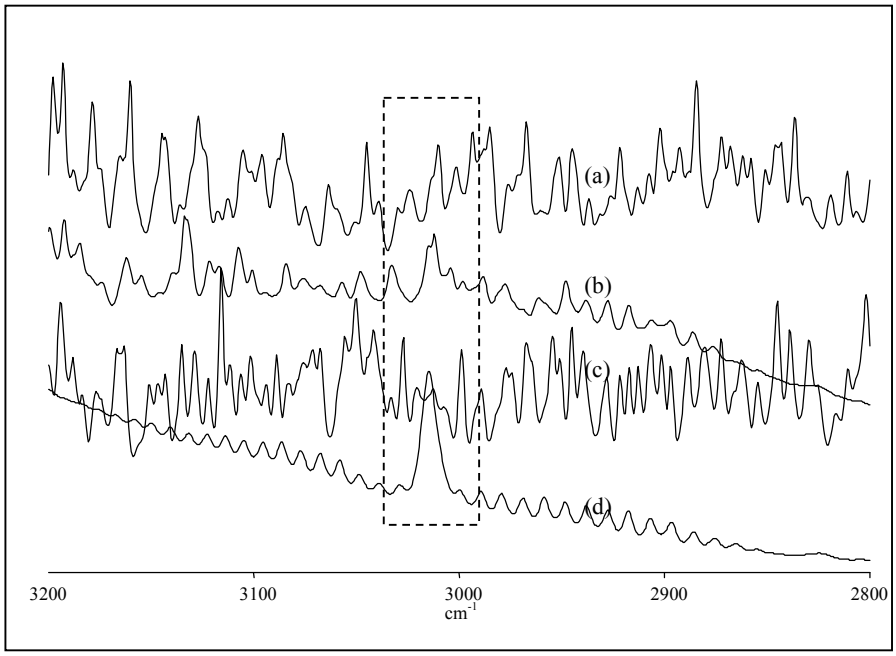

Figure 5.41: The FTIR spectra (v_3) of CH_4 adsorbed on transition metal cation exchanged zeolites at 293K and 137 kPa: (a) MnNa-SZ18; (b) NiNa-SZ18; (c) ZnNa-SZ18; and (d) Na-SZ18 (based zeolite).

These findings also suggest that surface heterogeneity could be the reason for the presence of several peaks in the region of around 3020 cm^{-1}. The appearance of single peak (in the case of LiNa-SZ18) might be due to the interaction between methane and extra-framework lithium. As mentioned in Section 5.4.2, the cation exchange capacity (CEC) of lithium is high, thus the effect of non-symmetrical field would be very minimum. In the case of BaNa-SZ18, it is assumed that the CEC is relatively low, thus the interaction is mainly due to interaction between methane and the extra-framework sodium. Another peak around 1300 cm^{-1} assigned to v_4 band is clearly visible in all metal exchanged zeolites (Figures 5.42, 5.43, 5.44). From the spectra, it was found that the presence of larger cation size results in broader peak with relatively less intensity. In addition, the presence of Mn^{2+} ions results the peak to splitting into two. This might be due to the fact that as the cation exchange takes place, the electrostatic field of the zeolite surface changes according to the properties of the cation involved.

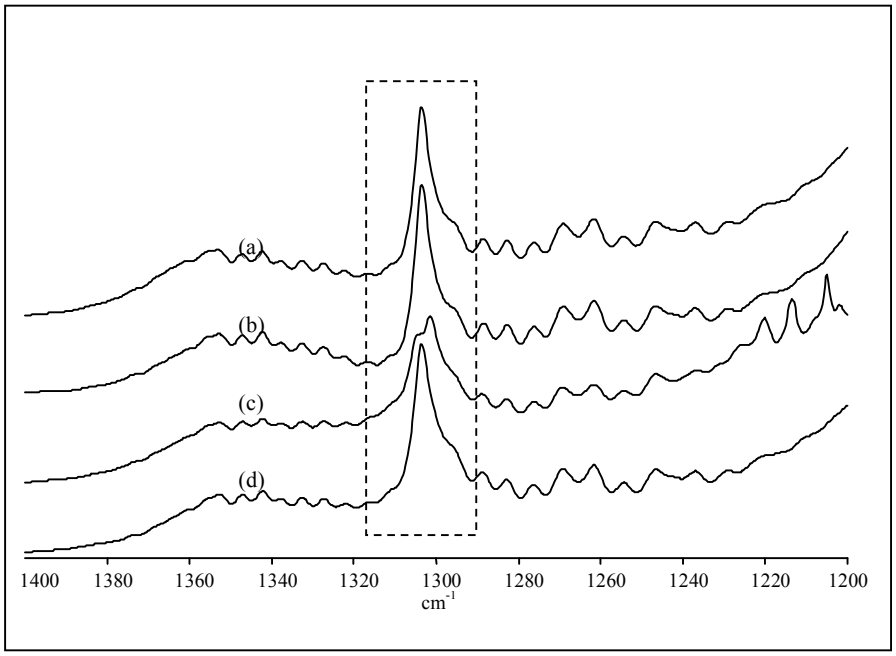

Figure 5.42: The FTIR spectra (v_4) of CH_4 adsorbed on alkali metal cation exchanged zeolites at 293K and 137 kPa: (a) LiNa-SZ18; (b) Na-SZ18 (based zeolite); (c) KNa-SZ18, and (d) RbNa-SZ18.

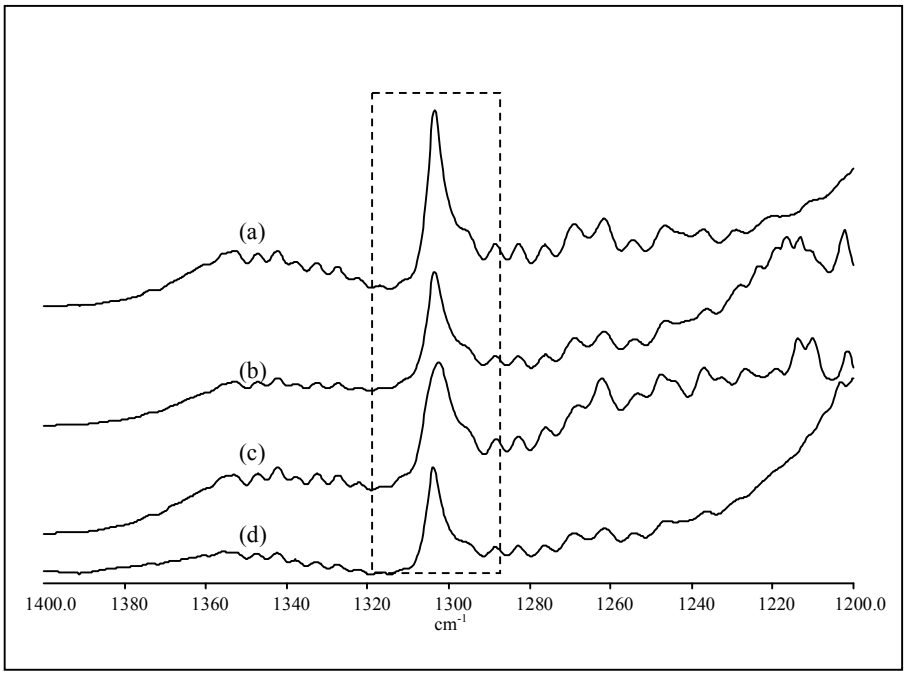

Figure 5.43: The FTIR spectra (v_4) of CH_4 adsorbed on alkaline earth metal cation exchanged zeolites at 293K and 137 kPa: (a) Na-SZ18 (based zeolite); (b) MgNa-SZ18; (c) CaMg-SZ18; and (d) BaNa-SZ18.

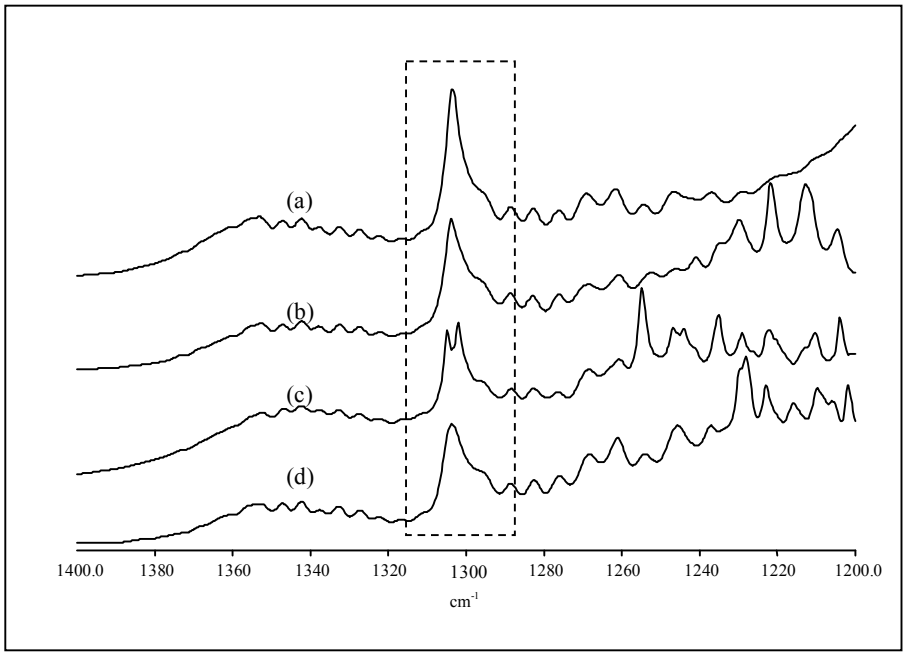

Figure 5.44: The FTIR spectra (v_4) of CH_4 adsorbed on transition metal cation exchanged zeolites at 293K and 137 kPa: (a) Na-SZ18 (based zeolite); (b) MnNa-SZ18; (c) NiNa-SZ18; and (d) ZnNa-SZ18.

However, as reported by Barbosa *et al*. (2000), the difference in structural position could also affect on the nature of interaction between metal cation present and the adsorbate. The location of cation in the extra-framework of zeolite would determine the extent of exposure of the cation to adsorbates. Thus, it explains the reason of different intensities and peak areas observed for different types of cation exchanged zeolites. The FTIR frequencies and peak areas for methane adsorption on different zeolites are shown in Table 5.17. According to Triebe *et al*. (1996), divalent cations in zeolites are also known to be strong adsorptive centres. In this study, the frequencies of the bands shift to lower frequency as a result of methane interaction with the cations.

Table 5.17: The peak position and the area of the peaks for adsorbed methane.

Zeolite	v_3 band		v_4 band	
	Peak position (cm^{-1})	Area (cm^2)	Peak position (cm^{-1})	Area (cm^2)
CH_4	3020		1306	
Group IA:				
LiNa-SZ18	3015 (-5)	15.97	1303 (-3)	11.14
KNa-SZ18	3016 (-4)	1.13	1301 (-5)	14.60
RbNa-SZ18	3019 (-1)	4.38	1303 (-3)	12.77
Group IIA:				
MgNa-SZ18	3013 (-7)	3.19	1303 (-3)	12.86
CaNa-SZ18	3012 (-8)	0.94	1302 (-4)	9.90
BaNa-SZ18	3015 (-5)	11.13	1304 (-2)	8.87
Transition:				
MnNa-SZ18	3011 (-9)	3.53	1303 (-3)	12.43
NiNa-SZ18	3012 (-8)	2.14	1302 (-4)	
			1305 (-1)	9.31
ZnNa-SZ18	3012 (-8)	0.47	1304 (-2)	9.87

It is also found that the peaks of divalent metal cation exchanged zeolites were shifted more than the monovalent metal cation exchanged zeolites. This is due to stronger interaction between the cation and the adsorbate. However, the peak areas represent relatively the amount of adsorbate adsorbed to the adsorption sites. A large quantity of Li^+ cations that act as adsorption sites might be the reason for the large peak area obtained around v_3 band. However, even though the quantity of Ba^{2+} cations might be low, but it could attract more adsorbates than the monovalent metal cations. Thus, the concentration of adsorbates would be higher at the adsorption sites. Hence, both conditions would result in larger peak areas.

It is also important to realize that molecules within the channels and cavities of metal cation exchanged zeolites are exposed to strong electrostatic fields created

by extra-framework cations and neighbouring framework anions. These electric fields bring about polarization of the adsorbed molecule, significantly altered the electron distribution, and its reactivity. Thus, using carbon dioxide as an adsorbate, the effect of different cations in zeolites was further examined. Figures 5.45, 5.46, and 5.47 show FTIR spectra of CO_2 adsorbed on metal exchanged zeolites. Peaks appeared in two regions are assigned to v_3 and v_2 bands, the physisorbed of undissociated CO_2 species and CO_2 molecules adsorbed in the form of carbonate or bicarbonate ions, respectively. Earlier discussion in Chapter 4 stated that the peaks around these regions broaden and resolved into several peaks. Since the adsorption takes place at relatively high pressure, the existence of peaks reflects the adsorbate interactions on different sites, probably close to cation sites. The quantity and the charge of cations would determine the strength and the amount of adsorbate adsorbed on the zeolite surface.

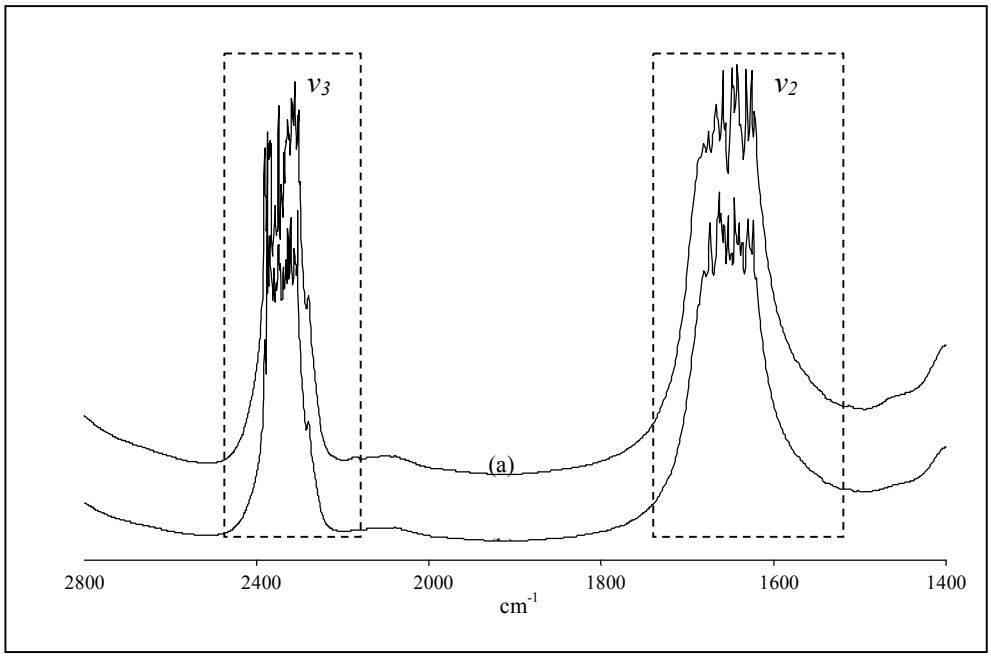

Figure 5.45: The FTIR spectra (v_3 and v_2) of CO_2 adsorbed on alkali metal cation exchanged zeolites at 293K and 137 kPa (a) Na-SZ-18 and (b) LiNa-SZ18.

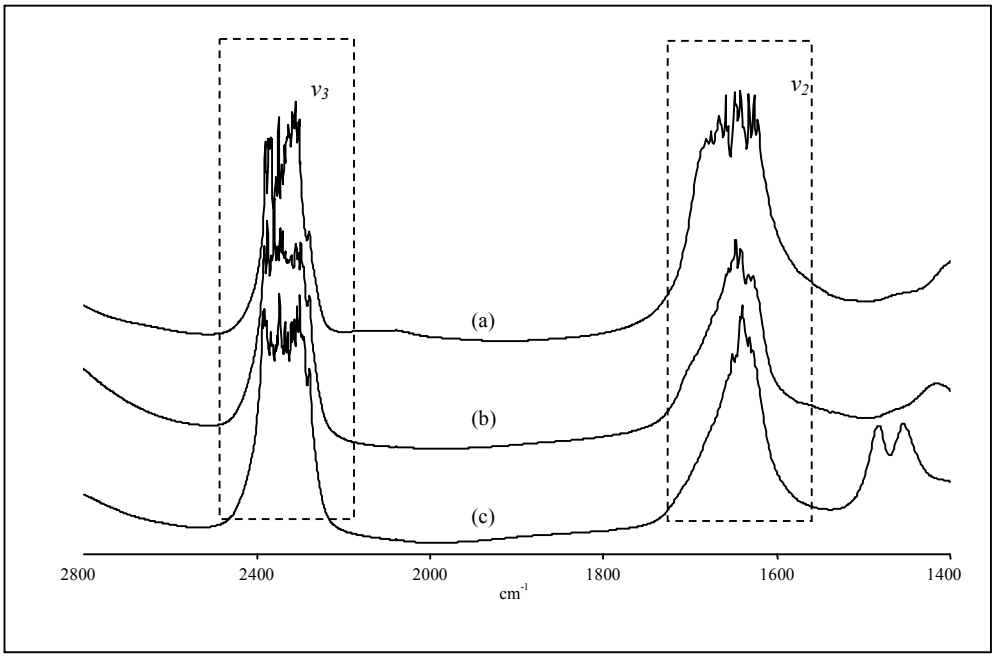

Figure 5.46: The FTIR spectra (v_3 and v_2) of CO_2 adsorbed on alkaline earth metal cation exchanged zeolites: (a) Na-SZ18; (b) MgNa-SZ18; and (c) CaNa-SZ18.

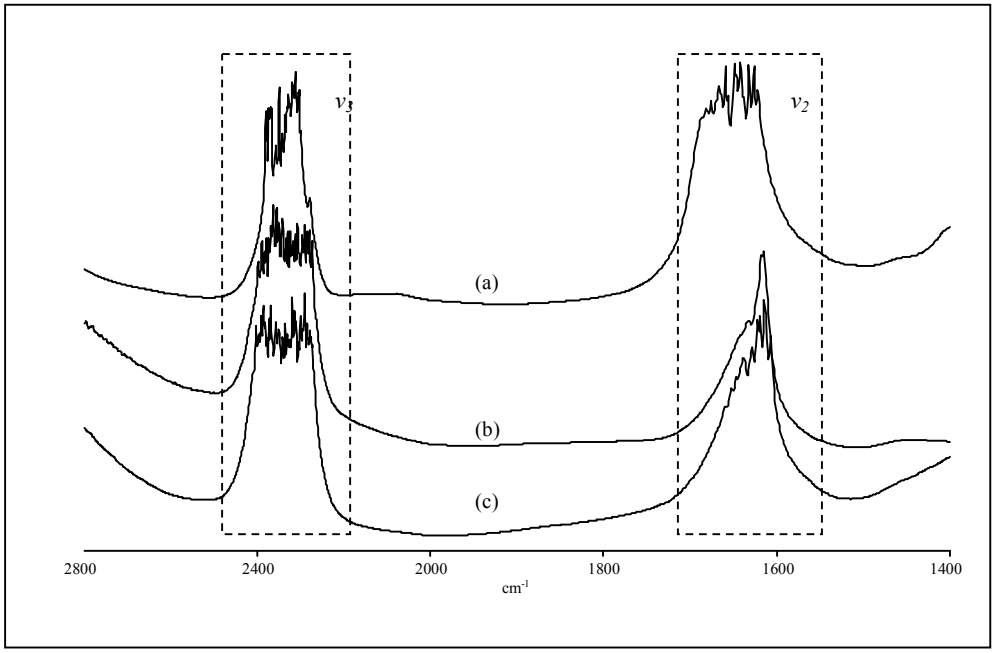

Figure 5.47: FTIR spectra (v_3 and v_2) of CO_2 adsorbed on transition metal cation exchanged zeolites at 293K and 137 kPa: (a) Na-SZ18; (b) MnNa-SZ18; and (c) NiNa-SZ18.

As reported by Triebe *et al*. (1996), divalent cations in zeolite could cause strong interaction between the adsorbates and the adsorbents especially for carbon dioxide which possess the quadrapole moment. As reported by Hadjiivanov *et al*. (2003), there is the possibility of coordination of more than one small molecule to one cation in zeolites. This phenomenon is related to low coordination of cation in zeolites as compared to the same cations incorporated in oxide surfaces. It is also suggested that coordination of two molecules to one cation requires a sufficiently large ionic radius. Table 5.18 shows that v_3 bands shift and the value increases after cation exchanged treatment. However, v_2 bands shift less than the based zeolite (Na-SZ18). The shifted values indicate the strength of interaction of the adsorbed molecules to the adsorption sites.

Table 5.18: The peak position and the area of the peaks for the adsorbed carbon dioxide.

Zeolite	v_3 band		v_2 band	
	Peak position (cm^{-1})	Area (cm^2)	Peak position (cm^{-1})	Area (cm^2)
CO2	2359	-	1687	-
Group IA:				
Na-SZ18	2317 (-42)	303.11	1649 (-38)	297.65
LiNa-SZ18	2350 (-9)	386.74	1637 (-50)	363.61
Group IIA:				
MgNa-SZ18	2347 (-12)	368.08	1646 (-41)	130.74
CaNa-SZ18	2322 (-37)	381.92	1637 (-50)	223.98
Transition:				
MnNa-SZ18	2334 (-22)	369.00	1614 (-73)	148.72
NiNa-SZ18	2334 (-22)	488.67	(1620 (-67)	206.75

As discussed earlier, the peak areas represent the amount of adsorbates adsorbed on the adsorption sites. The results indicate that there are relatively more molecules physically adsorbed (v_3 band) to the metal cation exchanged zeolites than molecules adsorbed as carbonate or bicarbonate ions. Except for LiNa-SZ18, the presence of mixed cation (Na^+ and other metal cation) increased the amount of carbon dioxide physically adsorbed on the zeolite surfaces. The physically adsorbed phenomenon could give advantage to the process in which each process requires maximum desorption capacity. According to Exter *et al*. (1997), aluminosilicate walls can induce an extra non-permanent dipole in carbon dioxide (next to the present linear quadrapole), whereas each adsorbed molecule could induce an extra non-permanent dipole in other carbon dioxide molecules leading to high amounts of carbon dioxide adsorbed. Thus, this phenomena could also be the reason for large surface area of the adsorbed carbon dioxide (Table 5.18).

5.6 Gas Adsorption Mechanism of Metal Cation Exchanged Zeolites

Results in previous sections show that the presence of cation in the extra-framework of zeolites does not only influence the structural and physicochemical properties of zeolite adsorbent, but also the adsorption characteristics of methane and carbon dioxide. However, the bulk fluid diffusion was not affected by the cation exchange treatment and it is therefore, greater than micropore diffusion. Thus, this section will only discuss and propose the mechanistic model of adsorption process in particular, the dependency of gas adsorption on metal cation exchange zeolites.

Nitrogen adsorption isotherm proved that the exchanged zeolites are microporous adsorbent (Type I). The results indicate that the cation exchange treatment results in the formation of mesopore or macropore, which in turn would affect the adsorption of methane and carbon dioxide. In principle, the sodium cation located at the pore opening (SII) of the structure would easily exchange with other

cations. Therefore, depending on the size of the cation, it would affect the adsorbate diffusivity inside the microchannel, and thus the adsorption of the adsorbates. This is clearly shown by the adsorption capacity of methane and carbon dioxide on metal cation exchanged zeolites. However, the Knudsen diffusivities do not clearly shown this effect because the calculated values are based on the average pore diameter (not the pore opening) of the zeolites. Figure 5.48 shows the effect of cation (size and location) on the diffusion and adsorption of adsorbates.

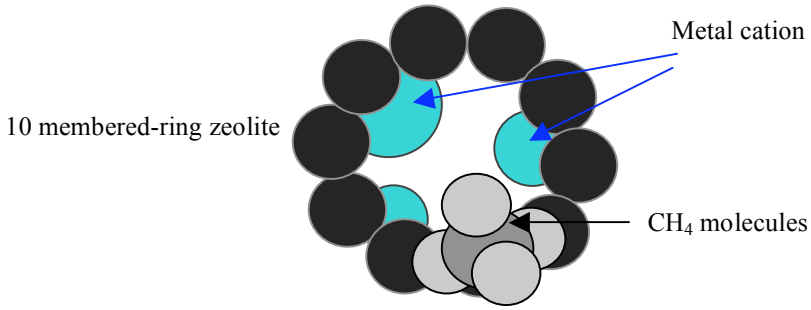

At the pore opening, size of cation would determine the accessibility of the adsorbates in such that:

[1] Smaller cation such as Li^+, it would not cause any blockage for diffusion of methane and carbon dioxide;

[2] Bigger size cation such as Rb^+ would significantly hinder the accessibility especially if more than one cations present at the entrance or pore opening of the zeolite.

Figure 5.48: A schematic diagram of adsorbate diffusion in the presence of different size of metal cations.

Meanwhile, as the sodium cations are not fully exchanged, the presence of different cations (e.g. Li^+ and Na^+ or Mg^{2+} and Na^+) creates different localized electrostatic field within the zeolite pores. Hence, the difference in the adsorption characteristics would be due to the interaction between the adsorbates and different metal cations (Figure 5.49). These phenomena were observed in the FTIR spectra of

adsorbed molecules on metal cation exchanged zeolites. However, cation exchanged treatment might also cause structural defects in the silica-alumina structural framework, thus create adsorption sites for the adsorbates. A schematic diagram indicates all the possibilities of electrostatic interaction between adsorbate molecules and zeolite (Figure 5.49). In this case, the carbon atom of adsorbed methane may interact with different metal cations (M1 and M2). Similarly, the oxygen atom of adsorbed carbon dioxide may interact with different metal cations.

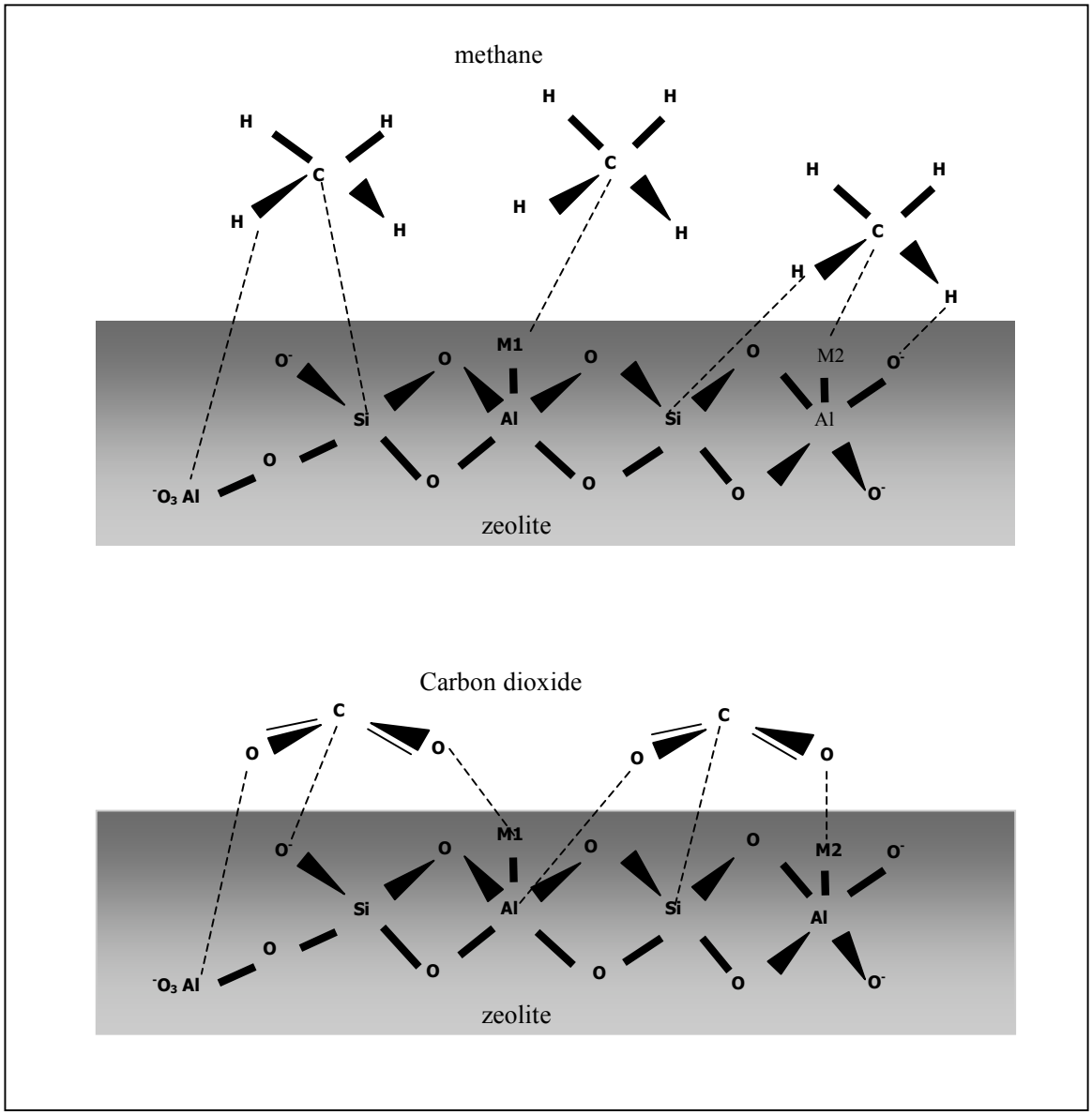

Figure 5.49: Electrostatic attractions between adsorbate-zeolite adsorbent. M1 and M2 represent either Na^+ or exchanged cations respectively.

In addition, the size of cation and its location in zeolite framework could influence the extent of interaction between the adsorbate and the metal cation. Furthermore, larger size cation having high coordination number is capable of interacting with more than one cation which leads to higher surface coverage. The interaction between ***C*** of the adsorbed methane and metal cation (***M***) might cause a certain degree of perturbation (Figure 5.50) as indicated by the FTIR spectra as presented in Section 5.5. The adsorbed carbon dioxide might also experience similar condition as the ***O*** interacts with the ***M*** (metal cation).

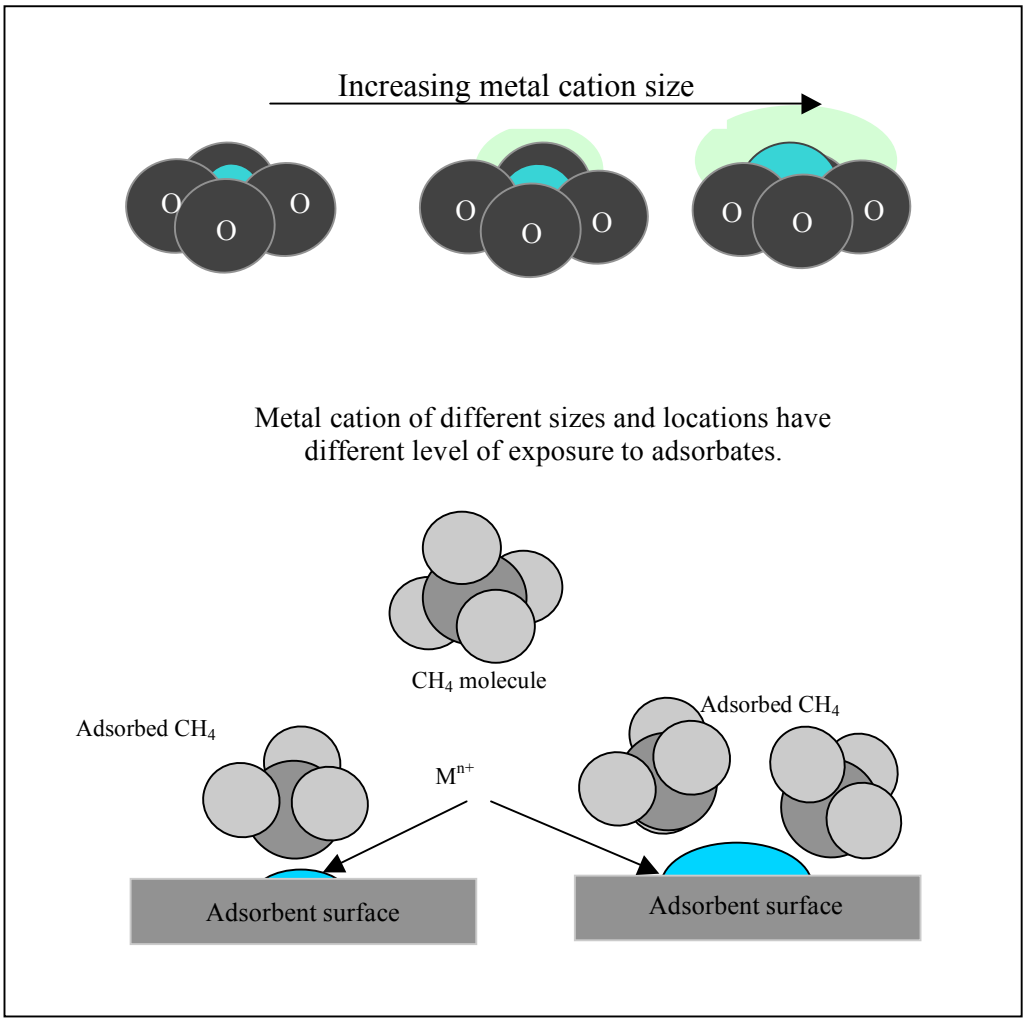

Figure 5.50: A schematic diagram of adsorbate-adsorbent interaction with different cations.

5.7 Summary

The information on gas adsorption characteristics of metal cation exchanged zeolite provides a basis for several technical applications of zeolites, such as drying, air separation (oxygen from nitrogen) and the removal of contaminants from the atmosphere or from natural gas, to name only a few examples. The adsorption study of metal cation exchange zeolite shows that the adsorption of methane and carbon dioxide was affected by the cation in the adsorbent, which lead to various degrees of interactions between the adsorbate and adsorbent. In most of the samples, the presence of different metal cations after cation exchange treatment does not significantly affect zeolite structure. The XRD spectra prove that the zeolites retain its faujasite-type structures. However, the physicochemical properties such as surface area, pore volume, and crystallinity of the zeolites changed after the cation exchange treatment. The release of Al or Si from zeolite framework occurred during the treatment also caused some changes to the Si/Al ratio and the unit cell parameter of the modified zeolite.

Nevertheless, the important aspect in this study is the adsorption characteristics of metal cation exchange zeolite. The study revealed that metals in the Periodic Table not only affect physicochemical properties of zeolites but also the adsorption characteristic of methane and carbon . For non-polar molecule such as methane, the size of cation in the extra-framework of zeolites affects the adsorption characteristics. This is due to the fact that methane could easily diffuse through large pore and adsorbed onto the inner part of the cages.

Conversely, different characteristic of adsorption was observed for carbon dioxide molecules. The quadrapolar molecule caused strong interaction with the adsorption site (especially the cation). In this case, divalent metal cation located at the pore opening would create strong specific interactions with the molecule, thus resulting blockage at the pore opening of the cages. However, the adsorption

isotherms and the fractional uptake curves showed that as the concentration (the amount of adsorbate adsorbed) increases, the surface area and pore volume influence the adsorption of carbon dioxide. It indicates that as the concentration of gases increases, the effect of cation becomes less significant. The equation model parameters also support the fact that the presence of cation affects the adsorption characteristics of methane and carbon dioxide on zeolites. Differences in the parameters of the equation models in the faujasite-type zeolites would be due to the presence of different metal cations. The FTIR spectra also show that the adsorbate-adsorbent interaction was affected by types of cation present in zeolites. Therefore, the study on the adsorption characteristics of metal cation exchanged zeolite has found that smaller metal cation such as Li^{+}, Mn^{2+}, Ni^{2+}, and Zn^{2+} enhanced the adsorption of methane (between 9.7 % and 19.8 %) while divalent metal cations such as Mg^{2+} and Ca^{2+} carbon dioxide enhanced the adsorption of carbon dioxide to 5.8 % and 7.5 % respectively.

CHAPTER 6

GAS ADSORPTION CHARACTERISTICS OF METAL OXIDE BASED ZEOLITES

6.1 Introduction

Zeolites and metal oxides are highly valued for their wide applications as catalysts, adsorbents and nanotechnology materials. The promising dispersion capabilities of metal oxide on zeolite, together with the fact that metal oxide modified zeolites have recently attracted a great interest in variety of application; have encouraged the emerging of this study. Modifications of zeolite with metal oxide will greatly influences the physicochemical properties of zeolite and gases adsorption characteristics. The zeolite structure and surface properties after the modification, the number, types and location of metal oxides are important for the adsorption of gas. In this regard, this chapter will discuss the characterization of metal oxide modified Na-Y adsorbents and their gases adsorption properties – equilibrium and kinetics. In order to understand the adsorbate-adsorbent interaction mechanisms underlying such phenomena, gas-zeolite interaction using FTIR spectroscopy has also been included in the discussion.

6.2 Structural Characteristics and Properties

6.2.1 Effect of various metal oxides

A process that disperses substances in a crystalline state as a monolayer or sub-monolayer into/onto the surfaces of zeolites would gain in entropy. From the first and second laws of thermodynamics, the dispersion of metal oxide on zeolites could occur spontaneously (Xie & Tang, 1990). Twenty types of metal oxides were used to disperse onto zeolite Na-Y host matrix system. These 5 metal oxides/unit cell Na-Y (290 μmol metal oxides/g Na-Y) samples were thermal dispersion (metal oxide Tammann temperature < 873.15 K) and incipient wetness impregnation (metal oxide Tammann temperature > 873.15 K) prepared as discussed in Chapter 3.

Powder X-Ray Diffraction has been used to characterize the crystallinity, particle size and structure of the materials. It was observed that the peak intensities of the X-Ray Diffraction (XRD) reflections decreased as compared to unload commercial Na-Y which are due to the increase contact matching between the Na-Y zeolite framework and the present of some metal oxide nanoparticles within the pore of zeolites (Table 6.1). The increases in the unit cell parameter also give explanation for the introduction of some metal oxide into zeolite framework. Meanwhile, the slightly decrease of the silica to alumina ratio indicated that solid-state ion exchange replacing cation aluminium in small part of the samples as a minority process has been occurred during the modification.

In Na-Y zeolite, there are 8 supercages, 8 sodalite cages and 16 hexagonal prism cages per unit cell (Zhu *et al*., 2004). Since the aperture diameter of hexagonal prism cages and sodalite cages is only 0.26 nm, which is much smaller that the diameter of metal oxide diameter, so the metal oxides would be difficult to go into these sodalite cages during the treatment dispersion. The void volume of these cages of the zeolite is also not large enough to accommodate the dispersed metal oxide.

Therefore, it is reasonable to confer that metal oxide dispersion is mainly occurred at the supercages of Na-Y zeolite.

Table 6.1: Structural characterization of metal oxide modified Na-Y zeolites.

Group of Elements (Periodic Table)	Samples	a_0 (Å)	Si/Al ratio	Relative Intensity (I_{rel})
-	NaY	24.61	2.88	100.00
IIA	MgO/NaY	24.63	2.81	94.14
	CaO/NaY	24.69	2.34	85.95
	BaO/NaY	24.68	2.41	63.88
IIIA	Ga_2O_3/NaY	24.64	2.72	79.62
IVA	GeO_2/NaY	24.63	2.76	90.97
	SnO/NaY	24.63	2.80	83.16
	PbO/NaY	24.62	2.88	45.44
IB	Cu_2O/NaY	24.63	2.85	91.82
	CuO/NaY	24.63	2.88	96.43
	Ag_2O/NaY	24.66	2.86	71.21
IIB	ZnO/NaY	24.69	2.37	86.30
	HgO/NaY	24.69	2.34	86.55
IIIB	Y_2O_3/NaY	24.63	2.80	80.87
VB	V_2O_5/NaY	24.63	2.82	41.93
VIB	MoO_3/NaY	24.63	2.82	62.78
	WO_3/NaY	24.63	2.88	73.22
VIIIB	Fe_2O_3/NaY	24.68	2.41	68.30
	Co_3O_4/NaY	24.66	2.55	84.00
	NiO/NaY	24.62	2.88	91.19
	PdO/NaY	24.63	2.82	86.67

Different types of metal oxides from different groups could be dispersed spontaneously onto the surfaces of support Na-Y with formation of a monolayer or sub-monolayer. In the calcination process, three-dimensional bulk metal oxides are suggested to transform into two-dimensional species on the inner or outer surfaces of zeolite Na-Y. That is the reason showing why no additional peaks are observed corresponding to the crystalline phase of bulk metal oxides has been formed outside the pore structure as shown in the XRD patterns (Figures 6.1 - 6.3). Metal oxide exists as dispersed species on the surfaces of supports after the calcination when the loading is less than the critical dispersion capacity. The residual crystalline phase of

metal oxide peaks will be observed in the XRD patterns after the calcination, when the content of metal oxide in the mixtures exceeds the critical amount.

Apart from that, the crystallinity of samples, which were denoted as relative intensity (I_{rel}) is determined by comparing the sum of the six reflection peaks (ASTM D3906) namely {331}, {511}, {440}, {533}, {642} and {555} of the treated samples with those of the Na-Y zeolite taken as reference (100% crystalline at ambient temperature). The crystalline phase of modified samples decreased as revealed in Table 6.1 but the support has remained unchanged. At the same loading concentration in molecule ratio of metal oxides and the same treatment process, the dispersion of variety types of metal oxides represents different dispersion capacity.

It is suggested that factors such as the pore size of zeolite, the dynamic diameter of the metal oxides - particle size, and their physicochemical properties play important roles for the dispersion of metal oxides into zeolites. The particle size of metal oxides that calculated using Scherrer equation (Cullity, 1978) and their bond length between metal cation and oxygen molecule are listed in Table 6.2. It is reasonable that the dispersion of metal oxides into zeolites only occurs under the condition, when the dynamic diameter of metal oxides is smaller or similar to the pore size of zeolites.

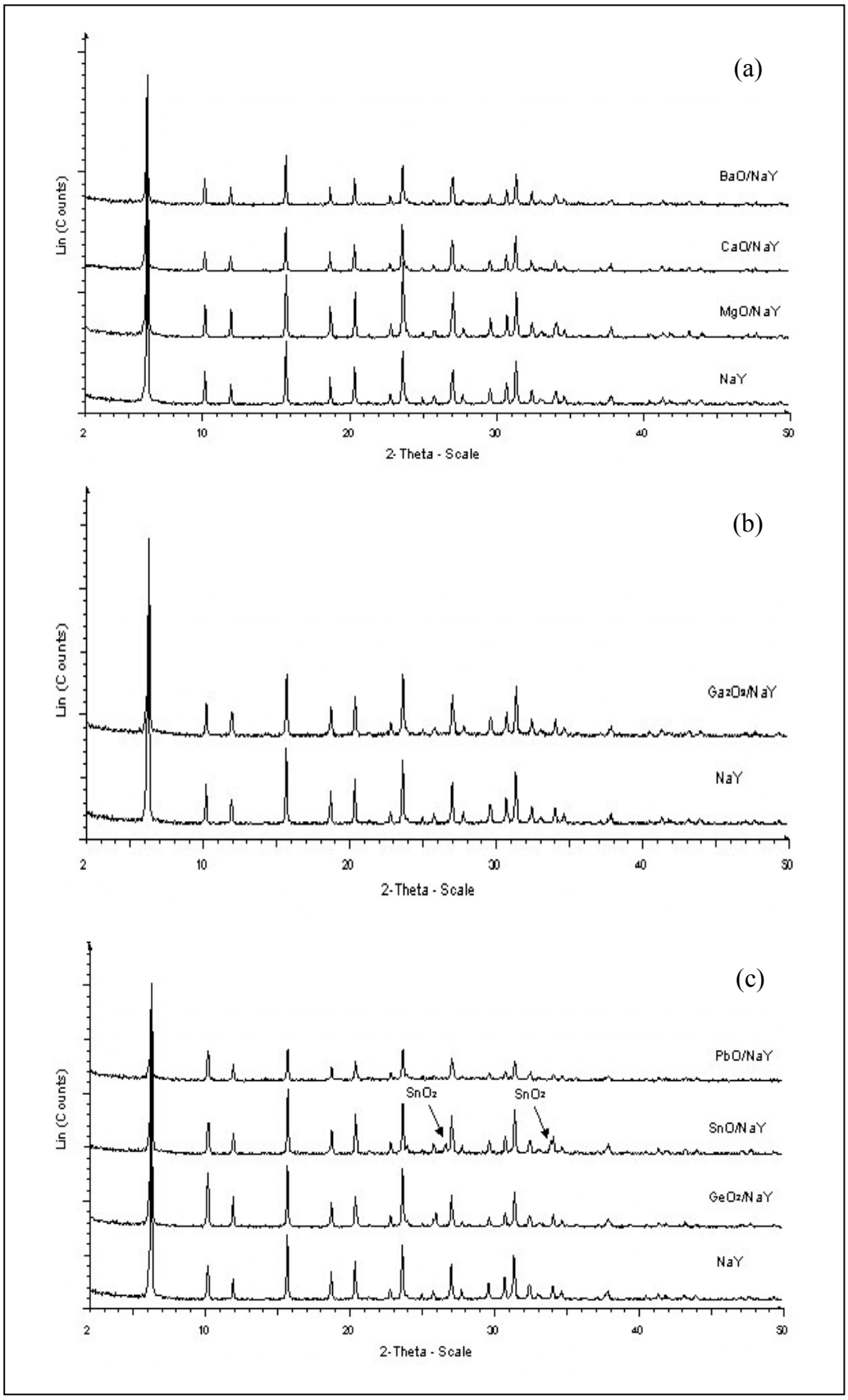

Figure 6.1: XRD patterns of metal oxides: (a) Group IIA; (b) Group IIIA; and (c) Group IVA metal oxides modified Na-Y zeolite.

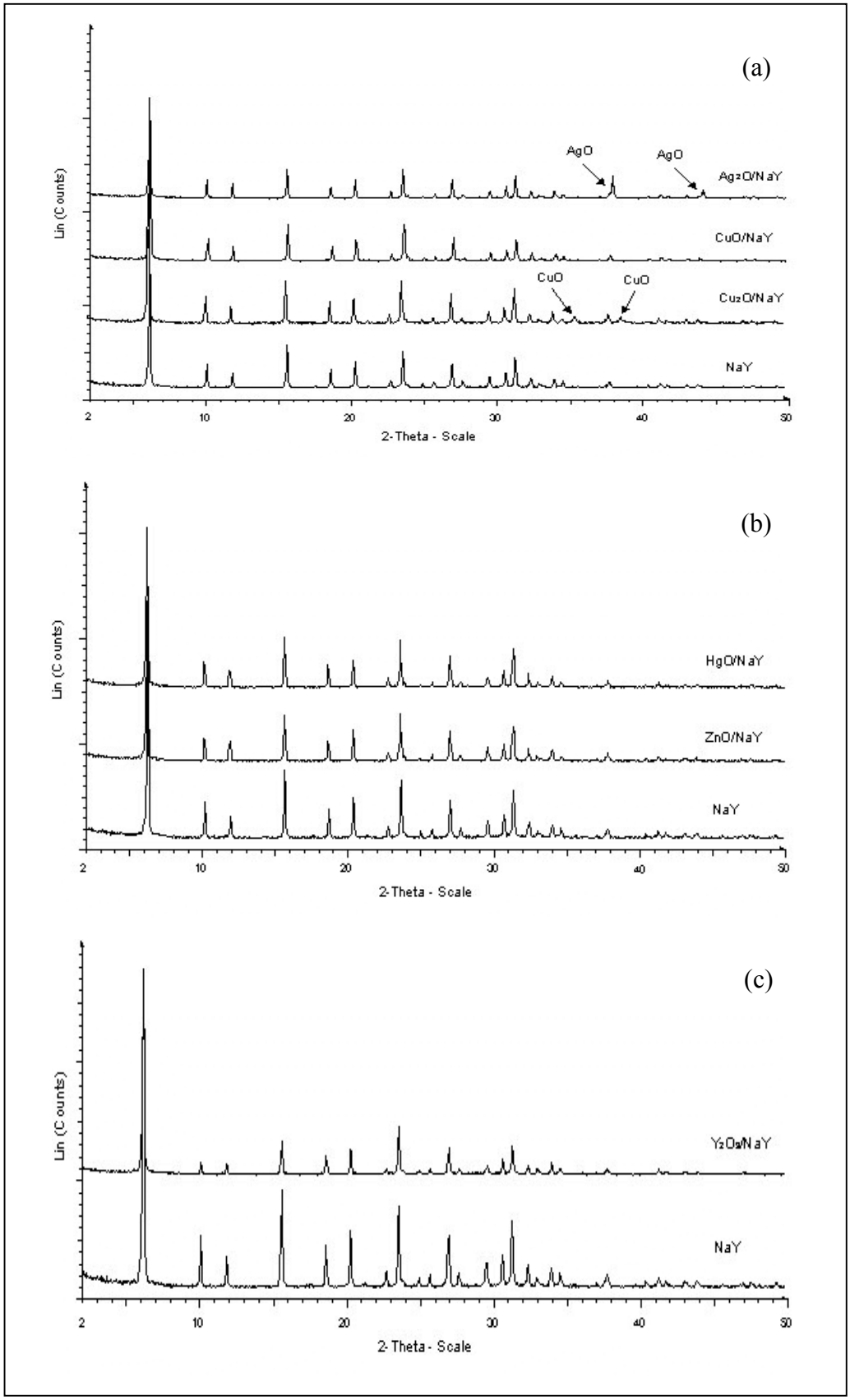

Figure 6.2: XRD patterns of metal oxides: (a) Group IB; (b) Group IIB; and (c) Group IIIB metal oxides modified Na-Y zeolite.

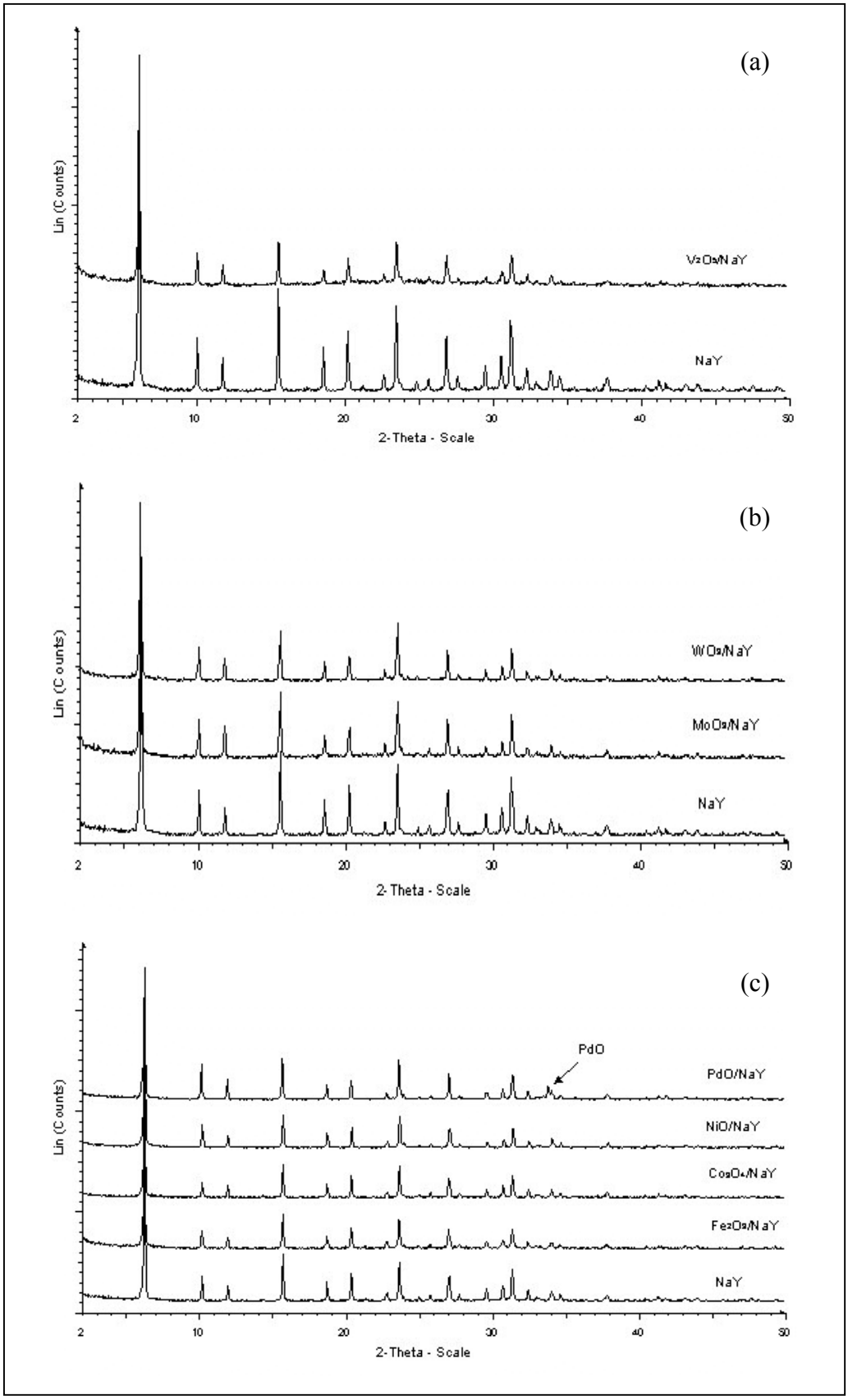

Figure 6.3: XRD patterns of metal oxides: (a) Group VB; (b) Group VIB; and (c) Group VIIIB metal oxides modified Na-Y zeolite.

Table 6.2: Physical properties of metal oxides (Náray-Szabo, 1969).

Group of Elements (Periodic Table)	Samples	Particle Size (nm)*	Bond Length (Å)
IIA	MgO	39.23	2.10
	CaO	92.16	2.40
	BaO	95.00	2.76
IIIA	Ga_2O_3	68.83	1.83
IVA	GeO_2	70.24	1.86
	SnO	46.35	1.84
	PbO	70.72	2.30
IB	Cu_2O	47.14	1.84
	CuO	25.51	1.84
	Ag_2O	71.35	2.04
IIB	ZnO	83.22	1.95
	HgO	75.40	2.03
IIIB	Y_2O_3	46.27	2.00
VB	V_2O_5	80.32	1.83
VIB	MoO_3	81.11	2.08
	WO_3	80.71	2.00
VIIIB	Fe_2O_3	98.53	1.96
	Co_3O_4	99.13	2.10
	NiO	69.91	2.03
	PdO	71.56	2.01

* Calculated based on Scherrer equation (Cullity, 1978).

The XRD patterns show that Cu_2O (Figure 4.2a) and SnO (Figure 4.1c) was oxidized to some extent to form bulk CuO ($2\theta = 35.54^0$ and 38.73^0) and SnO_2 ($2\theta = 26.60^0$ and 33.10^0) respectively, after heat treatment at high dispersive temperature (873.15 K). Meanwhile, Ag_2O was oxidized to form bulk AgO ($2\theta = 37.85^0$ and 44.31^0) when the mixture is heated at calcination temperature 673.15 K (Figure 6.2a). The calcination process at high temperature may result in the transport of some metal oxide species out of pore the system and their subsequent deposition at the external surface, where they agglomerate finally to form larger size crystallites. When all the useable vacant sites are occupied, a close-packed capping O^{2-} layer is formed and transformed them into the most stable form of oxide. This is in confirming with the XRD data where the reflections of crystalline AgO, CuO and SnO_2 can be seen clearly from XRD patterns.

Apart from that, this result is consistent with the research finding reported by Zhu *et al.* (2005). After the heat treatment at 873.15K, the fine CuO grains (a thin CuO layer), including some amounts of whiskers, is formed over the Cu_2O layer as shown in Figure 4.4 (Zhu *et al*., 2005).

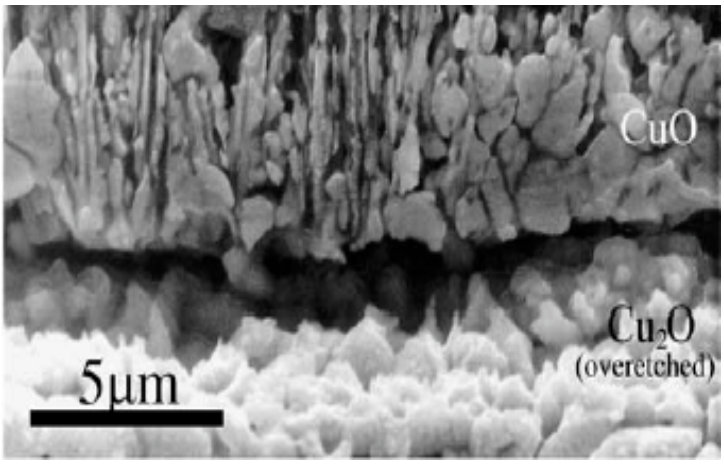

Figure 6.4: Morphology of surface of the CuO on Cu_2O after oxidation at 873.15K (Zhu *et al*., 2005).

In the physical properties characterization, the surface area and pore structure of Na-Y zeolite before and after modification by metal oxides were characterized using N_2 adsorption at 77 K. The nitrogen adsorption isotherms over the whole relative pressure range for four types of metal oxides modified Na-Y zeolites are shown in Figure 6.5. Generally, the adsorption isotherm before and after the metal oxides modification are of type I in the Brunauer, Deming, Deming and Teller (BDDT) classification indicating that they are microporous solids. The abrupt increase of N_2 adsorption at very low relative pressure ($P/P_0 < 0.1$) occurs because N_2 molecules are able to penetrate freely into the micropores of these modified zeolites without steric factor. The second increment for $P/P_0 > 0.8$ was due to multilayer adsorption and capillary condensation of N_2 molecules into zeolite pore system.

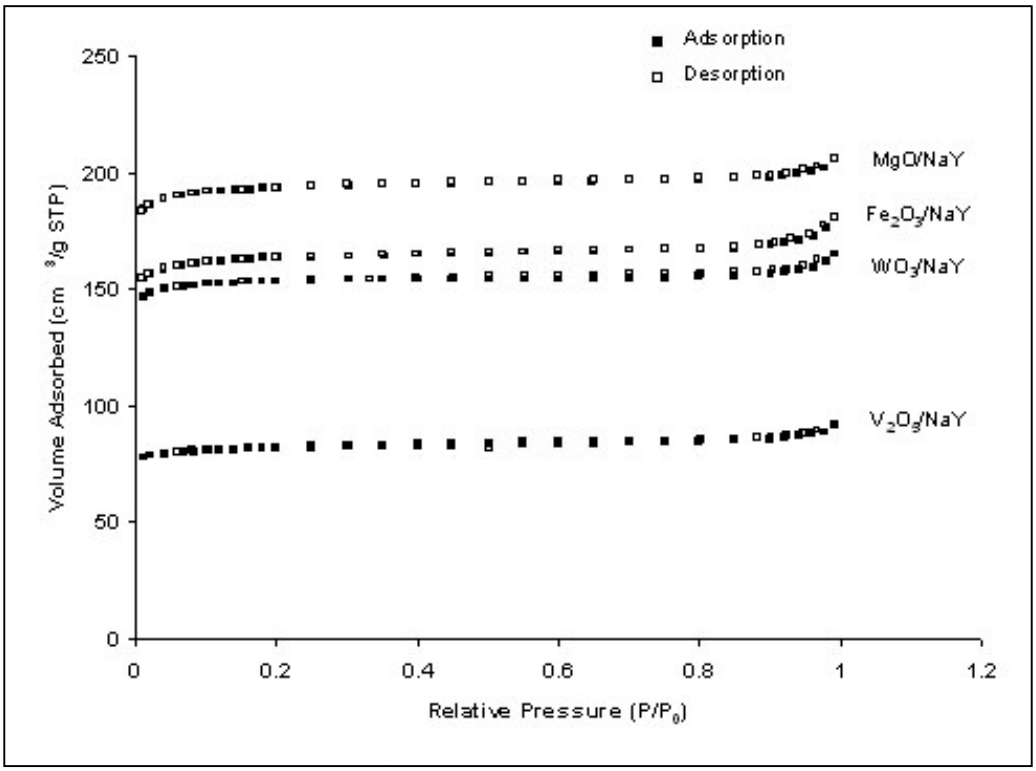

Figure 6.5: Nitrogen adsorption and desorption isotherms of metal oxides modified Na-Y zeolite.

The relative adsorption capacities over the entire equilibrium pressure range are related to two factors: the number of cations available per unit mass of the dehydrated zeolites and the limiting volume of the micropore (Hernández-Huesca *et al*., 1999). The amount of gas adsorbed at low pressures (low degrees of coverage) is directly proportional to the first factor, whereas the micropore volume plays a decisive role at high pressures (high degrees of coverage). At low pressure, the adsorption is greater, because there is a greater cationic density. These isotherms indicate that the main difference between the samples is the adsorption ability at low relative pressures. The adsorption and desorption isotherms almost overlap; indicating that the modified samples posses open and uniform cages system. The structure of Na-Y zeolites is stable toward metal oxide dispersion modification. Table 6.3 lists the data of micropore surface area, external surface area, micropore volume and average pore diameter for the investigated samples.

Table 6.3: Surface area and pore size characterization of metal oxide modified NaY.

Group of elements (Periodic Table)	Samples	Micropore surface area (m^2/g)	External surface area (m^2/g)	Micropore volume ($\times 10^7$ m^3/g)	Average pore diameter (Å)
-	NaY	809.50	10.50	3.04	16.00
IIA	MgO/NaY	776.27	21.16	2.90	15.99
	CaO/NaY	806.33	21.63	3.01	16.00
	BaO/NaY	758.15	12.38	2.82	15.29
IIIA	Ga_2O_3/NaY	772.40	18.61	2.88	15.92
IVA	GeO_2/NaY	779.58	12.97	2.90	15.76
	SnO/NaY	715.87	18.30	2.67	16.26
	PbO/NaY	412.91	6.21	2.41	16.23
IB	Cu_2O/NaY	784.73	13.05	2.93	15.75
	CuO/NaY	773.69	20.94	2.88	16.11
	Ag_2O/NaY	744.08	15.44	2.78	16.02
IIB	ZnO/NaY	762.91	20.78	2.85	16.05
	HgO/NaY	762.41	18.02	2.85	16.02
IIIB	Y_2O_3/NaY	767.21	23.18	2.87	16.03
VB	V_2O_5/NaY	324.31	12.95	1.21	16.91
VIB	MoO_3/NaY	536.90	23.22	2.00	17.53
	WO_3/NaY	622.32	12.32	2.32	16.14
VIIIB	Fe_2O_3/NaY	649.66	21.69	2.43	16.73
	Co_3O_4/NaY	777.35	17.26	2.90	15.82
	NiO/NaY	821.27	16.98	3.06	15.78
	PdO/NaY	756.05	9.27	2.82	15.74

The micropore surface area and micropore volume of Na-Y zeolite are generally decreased after the modification. Figure 6.6 presents the linear relationship between both of the parameters. It is suggested that the metal oxides dispersed might be loaded into the Na-Y cages and on the external surface of zeolite after the heat treatment. The external surface areas are increased markedly, which certainly resulted from the dispersion of metal oxides on the external surface, except for samples PbO and PdO modified Na-Y zeolites. The increase in external surface area for most samples indicated that the dispersion of metal oxides was excellent. Zhang *et al*. (1991) proved that the addition of 4 wt.% of PdO (3.5 wt% PdO in this study) into Na-Y zeolite would show weak diffraction peak as revealed in Figure 6.3c. The surface area properties of 4wt.% PdO modified Na-Y sample had nearly the same structure as unmodified Na-Y suggest that no blocking took place through the modification (Nishimiya *et al*., 2001). Apart from that, Palladium supported on zeolite were found can be extremely active for reaction. PdO dispersed will initially

present on the external surface of zeolite and gradually diffuse into the zeolite pores during heat treatment, which resulted slightly decrease of external surface areas (Correa *et al*., 2000; López-Fonseca *et al*., 2004; Okumura *et al*., 2005; Pröckl *et al*., 2005).

Meanwhile, the addition of PbO probably has destroyed substantial proportion of the internal and external surface areas of Na-Y zeolite during the modification. This can be well explained by the mark decrease of sample relative crystallinity after modification as revealed in Table 6.1. The PbO species in Na-Y zeolite are reactive and easily undergo oxidation process by the trapped oxygen in zeolite. The coordination numbers of PbO modified Na-Y zeolite that measured using X-ray absorption fine structure (EXAFS) techniques shown that PbO species are likely to be deeply trapped inside the Na-Y and hence decrease the micropore volume (Huang *et al*., 2004).

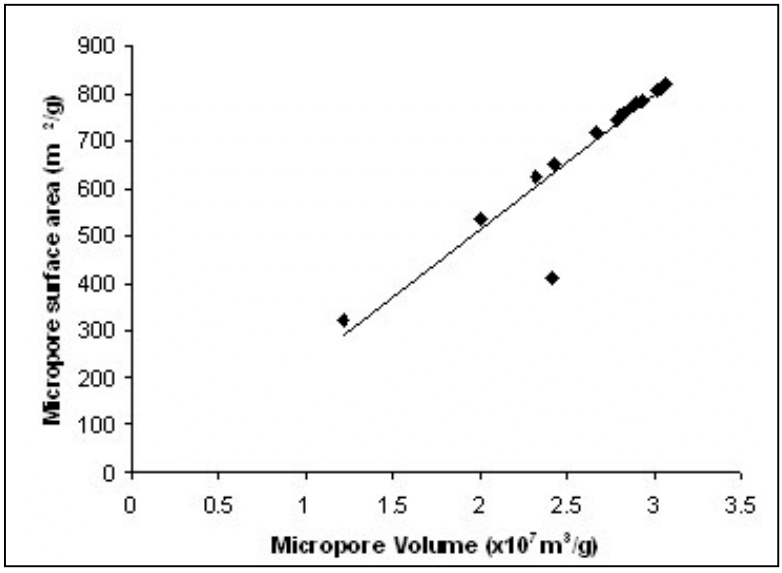

Figure 6.6: The correlation between the micropore surface area and the micropore volume of metal oxides modified Na-Y zeolite samples.

It was interesting to find out that the average pore diameter for some metal oxides modified sample is slightly enlarged. This shows a partial structural collapse

of the support in the corresponding treated samples. Somehow, it might due to the imbedding of some metal oxides into the skeleton of Na-Y zeolite instead of incorporating into the pores system. As it has mentioned that a small part of solid-solid ion exchange process will take place during the dispersion phenomena. These embedded metal cations might substitute the skeletal aluminium and make the pore diameter larger due to the bond length of metal-O is shorter than Al-O.

Generally, the results of surface area and pore size characterization suggested that the dispersion capacity of metal oxides on zeolite supports is mainly related to the internal surface area and pore size of zeolites. Zeolites with larger pore size exhibit higher dispersion capacity. The surface area and pore size of the zeolites, and the dynamic diameter of metal oxides are two factors controlling the dispersion of oxide materials into/onto zeolite surfaces. No matter where the dispersion of metal oxides take places, these exposed metal oxides on the external surfaces as well as in the cavities provide the active adsorption sites for adsorbate that will give influences on the gas adsorption characteristics of zeolite as gas adsorbents.

Apart from that, Scanning Microscope Electron (SEM) has been applied for adsorbent morphological characterization. The SEM photographs of three selected metal oxide modified zeolites are shown in Figure 6.7. After the modification, the SEM micrograph of the calcined samples show almost like zeolite Na-Y particles, the metal oxide particles disappeared completely in the field of vision. The surfaces of the modified zeolite Na-Y look smoother than those in Figure 6.7a (unmodified zeolite Na-Y). Therefore, the results indicate that surface melting of HgO, CuO and V_2O_5 at temperature above Tammann Temperature have occurred on Na-Y particles during the calcination, though the calcined temperature is below their melting points. The disappearance of metal oxides particles can be explained by the assumption of forming a thin oxide films on the surface of Na-Y particles surfaces.

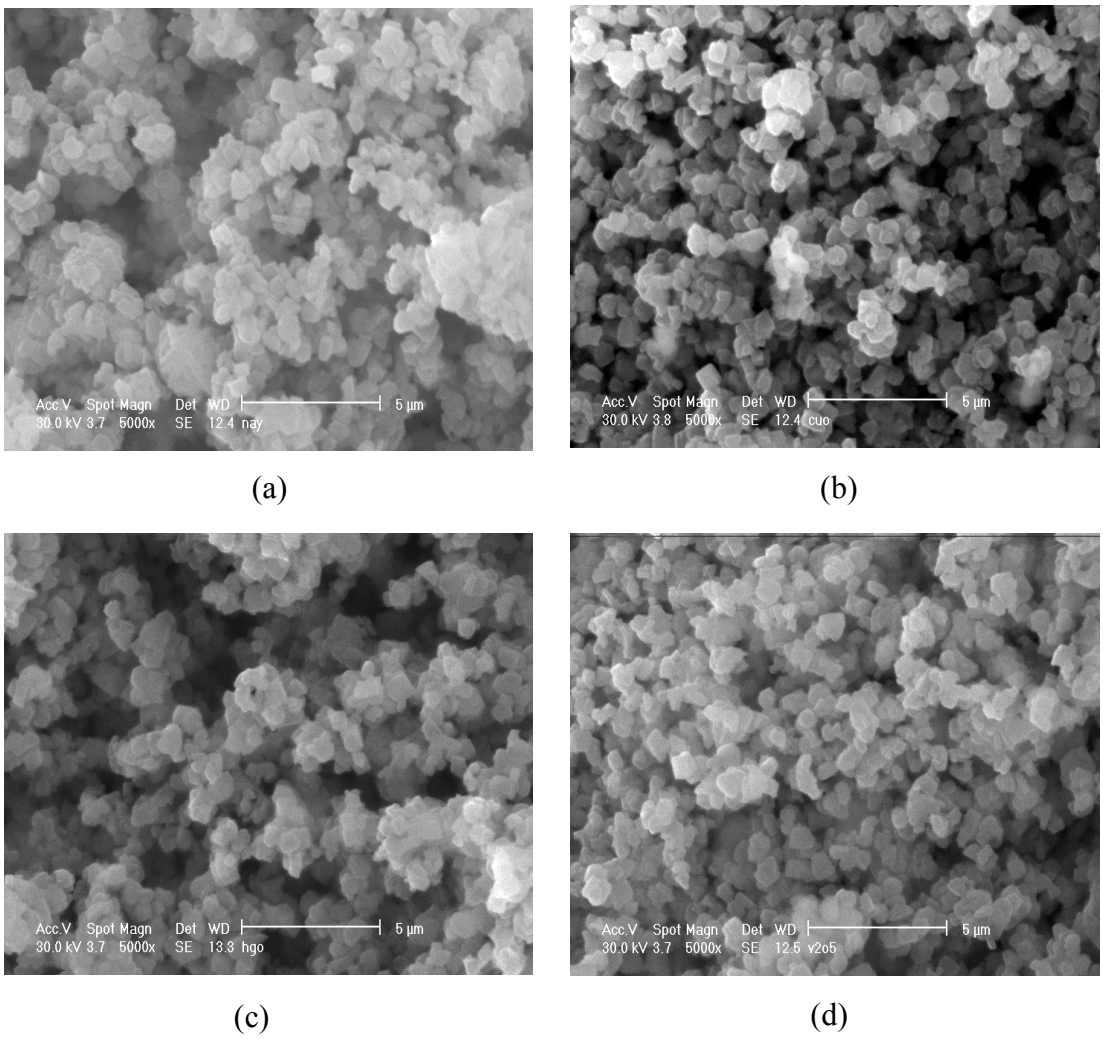

Figure 6.7: SEM micrograph of samples: (a) Na-Y zeolite; (b) 5 CuO/NaY; (c) 5 HgO/NaY; and (d) 5 V_2O_5/NaY.

Meanwhile, the EDAX chemical analysis using Scanning Electron Microscope as well have been used for the chemical composition characterization. The extra components Cu, Hg and V as shown in Figure 6.8 were apparent from EDAX data, these being supported by the dispersion of CuO, HgO and V_2O_5 compounds on the surfaces and zeolite frameworks. After the thermal treatment and metal oxide dispersion processes, the chemical composition of zeolite Na-Y exhibited no differences, as the sample is stable in the calcinations temperature range and modification.

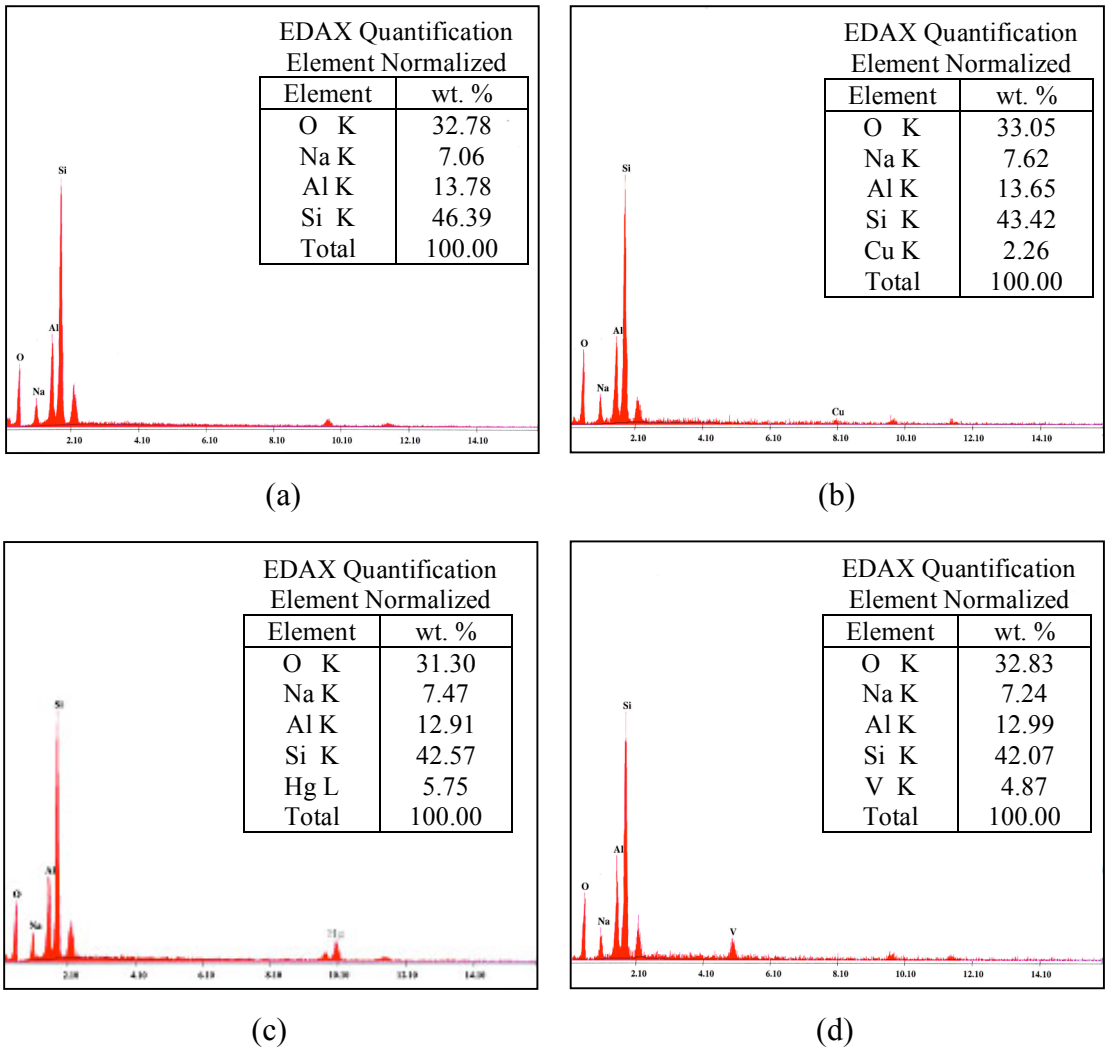

Figure 6.8: The EDAX quantification analysis of samples: (a) Na-Y zeolite; (b) 5 CuO/NaY; (c) 5 HgO/NaY; and (d) 5 V_2O_5/NaY.

Morphological and chemical analysis characterization revealed that metal oxide has spread and dispersed across the surfaces of Na-Y, including the inner and outer surface, since they have similar property. The zeolite loaded with metal oxide particles were scanned with minimum of five measurements at different spots on specimen stubs. As shown in the Electron Dispersive Spectroscopy (EDS) analysis of a set of isolated zeolite and modified samples, the data (average values) indicated that the chemical compositions of the various measurements at different spots are close together, suggesting a homogenous distribution of the metal oxide atoms from one side on zeolite particle to another.

In order to obtain a more understanding features on metal oxide modified Na-Y adsorbents, Fourier Transform Infrared (FTIR) spectroscopy spectra also have been carried out for chemical characterization, which can provide the fundamental molecular level information about the physicochemical and surface properties of modified samples. There are two important regions of FTIR spectra in Na-Y zeolite which are at 1200 - 800 cm^{-1} and 4000 - 3000 cm^{-1} as shown in Figure 6.9a (Stuart, 2004). The region between 1200-800 cm^{-1} is responsible for the vibrations of T-O-T unit (where T is SiO_4 or AlO_4 tetrahedron), whereas the vibrations 4000-3000 cm^{-1} attributable to structural hydroxyl groups.

According to Rodriguez (1995), a bending mode bands at 1638 cm^{-1} present the water molecule in the zeolite system. The strongest vibration at 1022 cm^{-1} is assigned to a T-O asymmetric stretch involving motion primarily associated with oxygen atoms. Symmetric stretch modes involving motions primarily associated with the T atoms are assigned in the region of 720 - 790 cm^{-1}. The external linkage frequencies, which are sensitive to topology and building units in the zeolite frameworks, occur principally at 576 cm^{-1}. Apart from that, the band at 505 cm^{-1} has been attributed to Si-O-Si out of plane bending mode, which only present in Na-Y but absent in Na-X (Sousa-Aguiar *et al*., 1998). The next strongest band 464 cm^{-1} is assigned to a T-O bending mode.

Figure 6.9 presents the FTIR spectra for Group IIA metal oxides modified zeolites. The FTIR spectra of zeolite Na-Y that modified by all twenty types of metal oxides illustrated no marked structure change as Group IIA metal oxides before and after modification. The spectra of metal oxide modified zeolite are found very similar, for example MgO, CaO and BaO modified Na-Y (Figure 6.9), minority of dealumination process or ion exchanged occurred during oxide dispersion, and so the position of the strong framework vibration band 1022 cm^{-1} almost remain unchanged but with increasingly the intensity of Lewis acid sites at bands 1145 cm^{-1}.

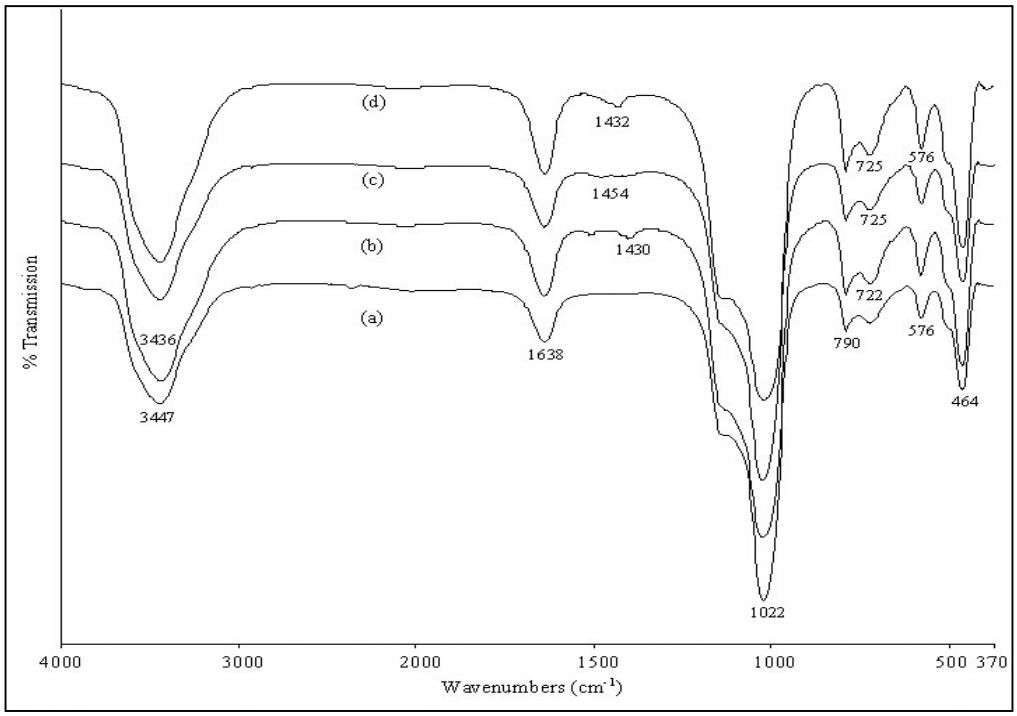

Figure 6.9: FTIR spectra of Group IIA metal oxides modified Na-Y zeolite: (a) Na-Y; (b) MgO/NaY; (c) CaO/NaY; and (d) BaO/NaY.

The silica to alumina ratio that determined from XRD as well as FTIR spectra, indicate the degree of framework aluminium slightly decrease that due to the solid-state ion exchange process. The modification generally does not bring about significant changes in the band frequencies and functional groups of large pore zeolite Na-Y, since interactions between the metal oxide dispersed and the framework are generally weak. Nevertheless, some small differences in the spectra may be observed, mainly in the band symmetry. The band at 576 cm^{-1}, assigned to external bonds of the double six rings, becomes more intense as metal oxide dispersed as two-dimensional species on the surfaces. The changes observed in the 576 cm^{-1} bands seem to be a consequence of the metal oxides coverage dispersion and the thermal treatment effect.

For Group IIA metal oxide-modified zeolites, one may observe small bands at 1430 cm^{-1}, 1454 cm^{-1} and 1432 cm^{-1}, indicating the improvement of Lewis acid sites on the Na-Y zeolite surfaces. Meanwhile, the band at 3447 cm^{-1} attributed to

silanol groups, is intense and rather asymmetrical towards lower wavenumbers (3436 cm^{-1}). Despite of that, the peak at 1638 cm^{-1}, resulting from the structure of water, was strengthened slightly, which indicated that more water was adsorbed on the zeolite because of the existence of metal oxides, in which the results are consistent with Hu *et al.* (1999).

In order to understand the structural characteristics of metal oxide modified Na-Y zeolite well, the infrared correlation chart for metal oxides and FTIR spectra of bulk metal oxides were determined as shown in Figure 6.10 (Nyquist and Kagel, 1971). Metal oxides will show significant structural effects on Na-Y zeolite in the region 1000 - 400 cm^{-1}. By comparing these regions that represent the bulk crystalline metal oxides and the samples after the modification, the small alteration of band symmetry and the incremental of band intensity will be observed which indicated the presence of metal oxide as dispersed species on the inner or outer surfaces of Na-Y zeolite. For different types of metal oxide from different groups of element in Periodic Table, they showed the similarity by increasing the band intensity within 900 – 400 cm^{-1}. The physicochemical properties of Na-Y zeolite were retained after the modification without showing any structure defect.

There are scarce research reports related on MoO_3 modified porous materials sample (Dong *et al*., 1997; Braun *et al*., 2000; Li *et al*., 2003; Zhu *et al*., 2005). The FTIR bands corresponding to the stretching vibrations of Mo-O-Mo and Mo=O in bulk crystalline MoO_3 can be found at 818 and 993 cm^{-1}. After calcination, the absorption band becomes more distinguished and the intensity increases slighter. This indicates that interaction existed between MoO_3 and the support materials. After the dispersion of MoO_3 on Na-Y zeolite and calcination treatment, a FTIR band at 890 cm^{-1} could be found in the profile of Figure 6.11h, which should be the signal of a surface molybdena species.

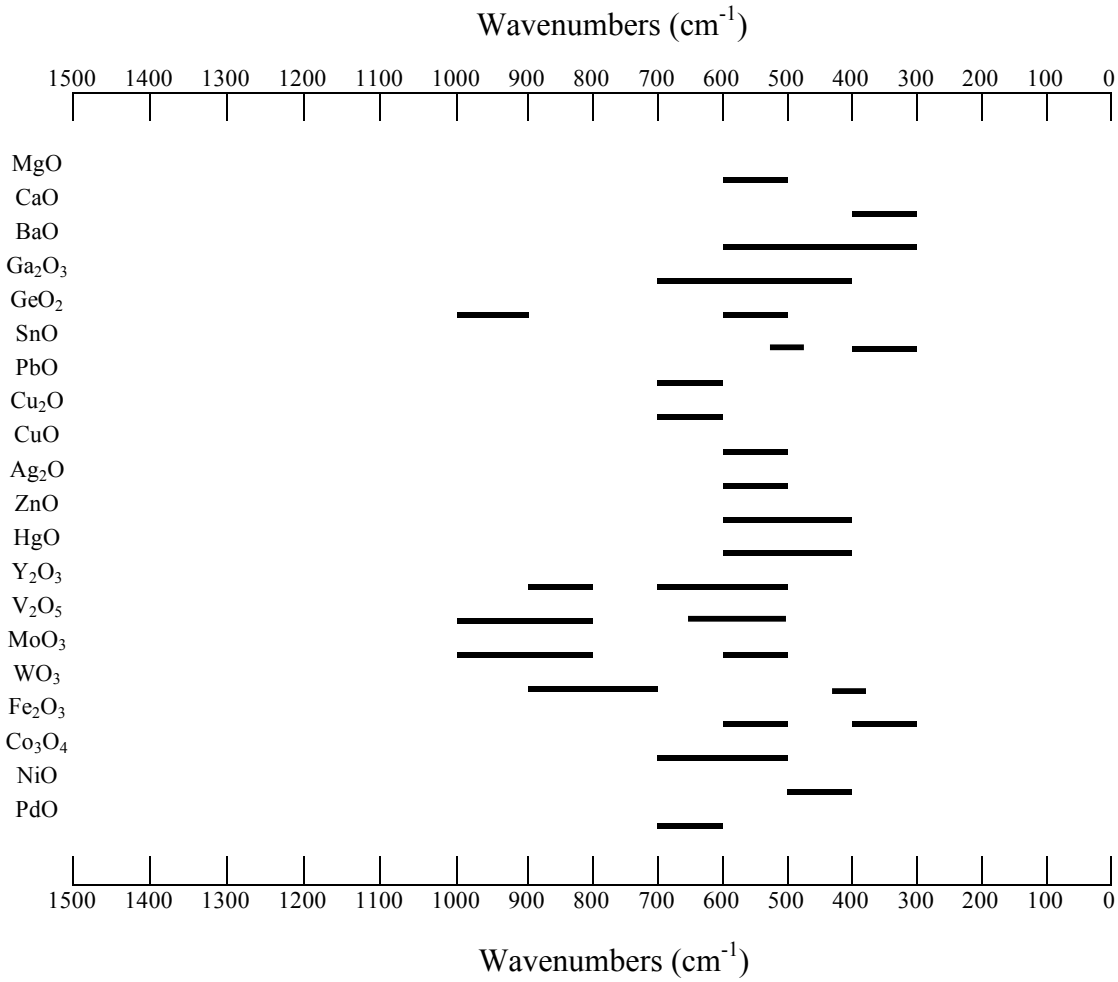

Figure 6.10: Infrared correlation chart for metal oxides (Nyquist and Kagel, 1971).

For WO_3 modified support, peak at 808 and 719 cm^{-1} are attributed to the existence of WO_3 species (Xu *et al*., 2000). In our cases, the FTIR band at both peaks cannot be detected clearly, as a very intensive FTIR band of Na-Y zeolite overlaps it. Same conditions were found for most types of metal oxides in this study; only the increasing bands intensity at region 600 - 400 cm^{-1} can infer and show the existence of metal oxides as a thin dispersion film on the zeolite surfaces after the modification. The FTIR bands at this region for metal oxide species cannot be clearly distinguished, as the bands are overlapped by FTIR band of Na-Y zeolite at region 800 - 400 cm^{-1}. Meanwhile, the appearance of asymmetry broad bending band at 828 cm^{-1} for vanadium (V) oxide modified Na-Y zeolite, which is higher than region 800-400 cm^{-1}, verified the presence of species V_2O_5 interact on the Na-Y zeolite surfaces (Figure 6.11g).

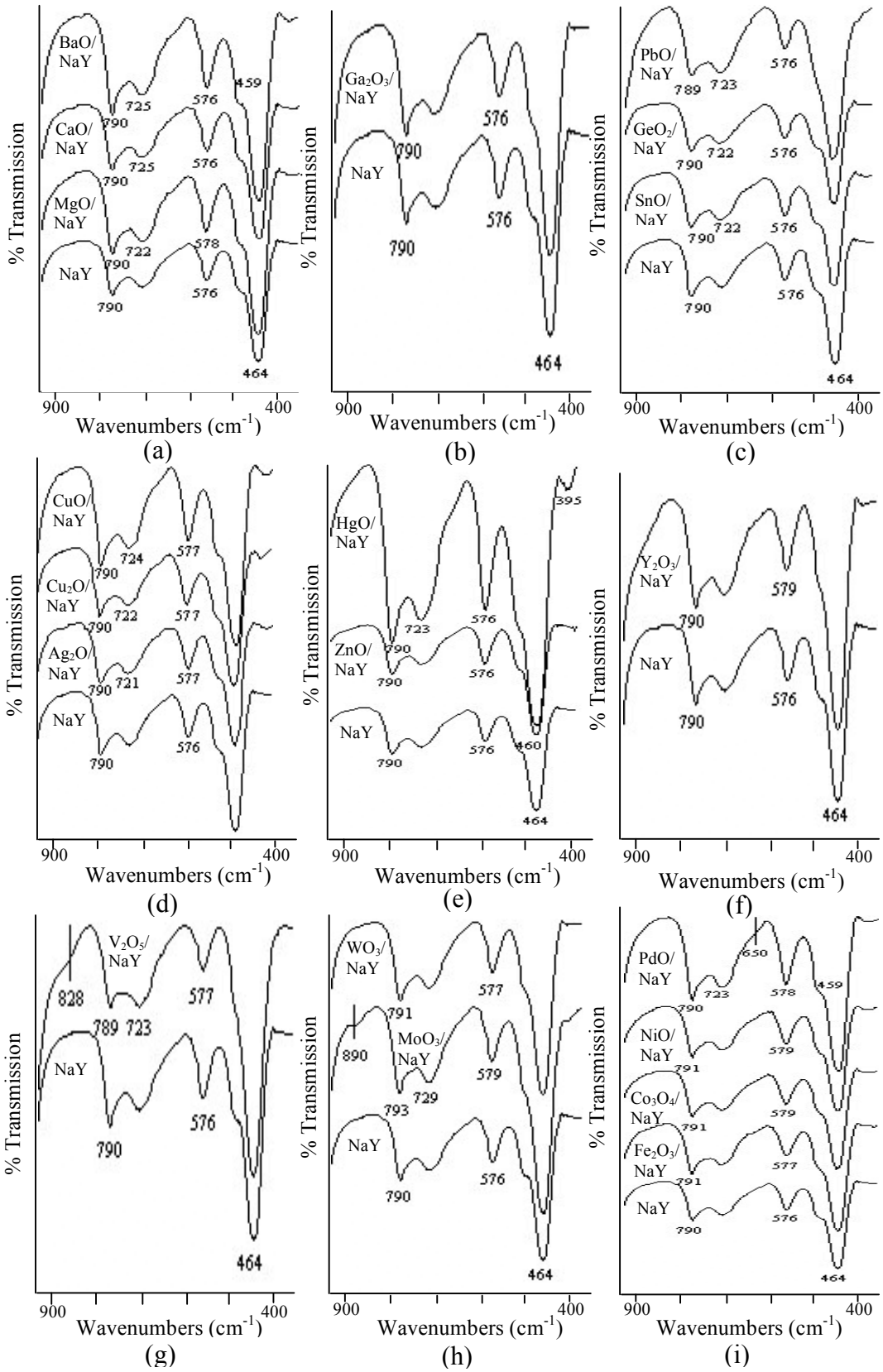

Figure 6.11: FTIR spectra of metal oxide: (a) Group IIA; (b) Group IIIA; (c) Group IVA; (d) Group IB; (e) Group IIB; (f) Group IIIB; (g) Group VB; (h) Group VIB; and (i) Group VIIIB modified Na-Y zeolite adsorbents.

All the results indicate that, various types of metal oxides show great effect to modified samples phyisicochemical properties. The thermal spreading of metal oxides onto Na-Y zeolite provide evidences that after the heat treatment the oxide crystals were either transformed into very small grain crystals, dispersed two-dimensional oxide species over Na-Y zeolite, or both. Different types of metal oxide dispersed Na-Y zeolite showed different physical features after the modification. The physical properties such as the melting point, solid-state structure and the particle sizes of the metal oxides probably play a very important role in the dispersion phenomenon. The dissimilar chemical properties of the metal oxides are responsible as well for the differences in their behavior with the Na-Y zeolite. Despite of that, the modification parameters such as metal oxide loading concentration, calcination temperature, duration of calcination process and modification techniques greatly affect the structural characteristic and properties of metal oxide modified Na-Y zeolite adsorbents.

6.2.2 Effect of copper oxide loading concentration

As described in Chapter III, Copper (II) oxide modified Na-Y zeolite sample has been selected for varying its other modification parameters due to its promising initial results and vast potential applications. To study the effect of metal oxide loading concentration on zeolite structural and physicochemical properties, a series of CuO modified Na-Y zeolite samples were prepared by the mechanical mixing of Na-Y zeolite with various CuO loadings (2.00, 2.25, 5.00, 10.00, 15.00 wt. %) followed by heating at 873.15 K for 24 hours.

For copper (II) oxide modified zeolite Y, the bond distances of Cu-O and Cu-(O)-Cu in zeolites were 1.84 -1.95 and 2.93-2.97 Å, respectively (Náray-szabó, 1969). According to the report of Huang *et al.* (2004), the bond distance of CuO in zeolite Y was 1.93 Å, suggesting that CuO might have a three-dimensional structure

in the supercages or channels of zeolite Y as shown in Figure 6.12. The diameter of the copper oxide in the channels of zeolite Y might be about 5.9 Å. The coordination number of CuO in zeolite Y was approximately 3.5, suggesting an existence of a three dimensional CuO structure in zeolite Y (Huang *et al*., 2004).

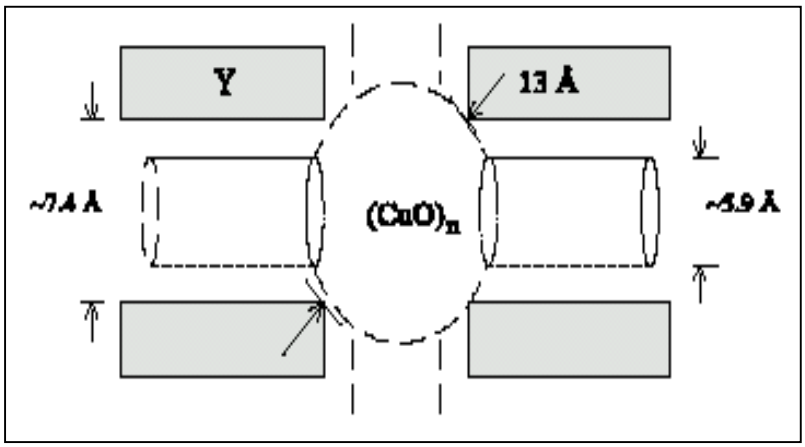

Figure 6.12: The possible structure of copper oxide in the micropores of zeolite Y (Huang *et al*., 2004).

It was observed that the diffraction intensities decreased after CuO-NaY modification (Figure 6.13). The peaks in each pattern observed at 2θ values of 35.4 ^{0} and 38.6 ^{0} correspond to CuO. No peaks corresponding to the crystalline phase of CuO were observed in modified samples with low CuO loadings (<5 wt.% CuO/NaY). The peaks assigned to CuO treated samples disappear completely after the heat treatment. CuO is not known to undergo a reaction with Na-Y support and the transformation of CuO into amorphous phases is really impossible at the temperature of thermal treatment 873.15 K. The disappearance of the XRD peaks assigned to metal oxides can be interpreted from literatures, as CuO exist as dispersed species onto the surface of the support with the formation of a monolayer or sub-monolayer after heat treatment (Thoret *et al*., 1997; Braun *et al*., 2000; Li *et al*., 2003; Zhu *et al*., 2005).

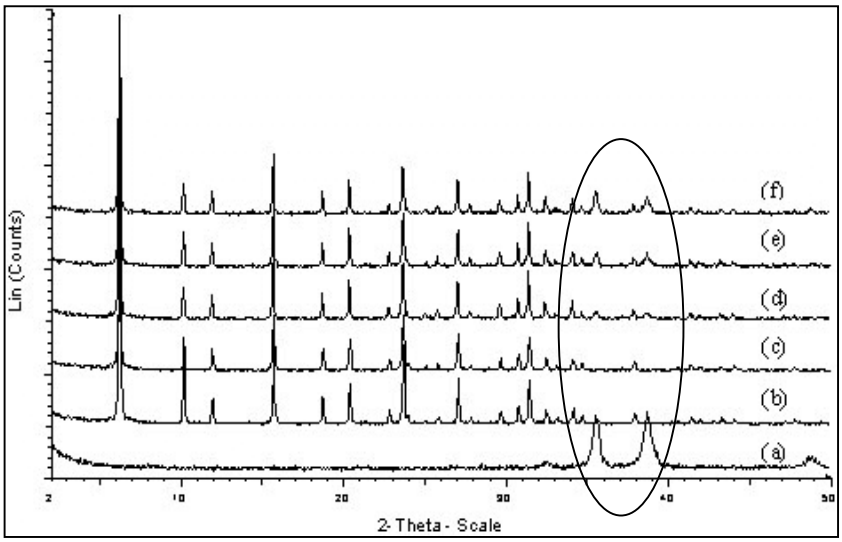

Figure 6.13: XRD patterns of CuO/NaY samples: (a) CuO; (b) NaY; (c) 2.25wt.% of CuO/NaY; (d) 5wt.% of CuO/NaY; (e) 10wt.% of CuO/NaY; and (f) 15wt.% of CuO/NaY.

However, when the CuO loading is increased above its dispersion capacity, the characteristics of crystalline CuO show clearly in XRD diagrams. As the copper oxide loading concentration is increased, the XRD peaks intensities decreased regularly with lower crystallinity quality. The large fraction of CuO were located on the external surface of the zeolite crystals and led to a narrowing of the pore openings on the zeolite, which suppressed the further penetration of CuO into the pores of the zeolite.

The average crystallite sizes estimated for CuO modified zeolite Na-Y particles by the Scherrer equation are presented in Table 6.4. As can be seen, the average crystallite sizes of the copper oxide particles below the dispersion capacity reacted with Na-Y zeolite after the heat treatment, thus decreased the particle sizes after the modification. Meanwhile, the particle size of the modified samples that above 5 wt.% CuO increased with increasing copper oxide weight loadings.

Table 6.4: Effect of loading concentration on the structure characteristics of CuO modified Na-Y zeolite samples.

Samples	Loading (wt.%)	a_0 (Å)	Relative Intensity (I_{rel})	Particle Size (nm)*
NaY	-	24.61	100.00	68.69
CuO/NaY	2.00	24.62	96.02	53.13
CuO/NaY	2.25	24.62	96.43	54.27
CuO/NaY	5.00	24.68	86.45	68.68
CuO/NaY	10.00	24.68	84.32	68.69
CuO/NaY	15.00	24.68	70.15	79.35

* Calculated based on Scherrer equation (Cullity, 1978).

Figure 6.14 shows the relationship of crystallinity and residual crystalline CuO versus loading concentration of CuO in CuO/NaY system. The amount of residual crystalline CuO can be determined by XRD quantitative phase analysis. When the CuO loading exceeds the dispersion threshold value, the residual CuO increased linearly with the total amount of CuO in the samples. However, the peaks of crystalline CuO showed up in XRD patterns were reduced markedly after the heat treatment compared to the origin bulk copper (II) oxide. The intercept of the straight line plotted was assigned to the maximum dispersion capacity of metal oxide that spread on zeolite surfaces (Gao *et al*., 2000; Xu *et al*., 2000; Wang *et al*., 2003; Zhu *et al*., 2004). Therefore, the amount of CuO in the adsorbent corresponding to 2.25 – 5 wt.% CuO loading is approximately equivalent to complete the dispersion on a surface area of the zeolite Na-Y support.

The dispersion of metal oxide onto zeolite surfaces could disperse either as a monolayer or sub-monolayer form depending on types of metal oxide and support matrix used (Xie and Tang, 1990; Zhu *et al*., 2004). The theoretical critical dispersion capacity of CuO dispersed as a monolayer or sub-monolayer could be determined according to the method reported by Xiao *et al*. (1998) and He *et al*. (2001). Notably, the calculated theoretical value (0.078 g CuO) is larger than the critical dispersion capacity obtained from the XRD results. It is concluded that CuO does not disperse on the surface of Na-Y as a close-packed monolayer. It is the structure of Na-Y zeolite with partly ionic bonds between the cations and the Si-O-Al-O surface of the Na-Y lead to the inability to form monolayer dispersion of CuO on the zeolite surfaces (Xu *et al*., 2005).

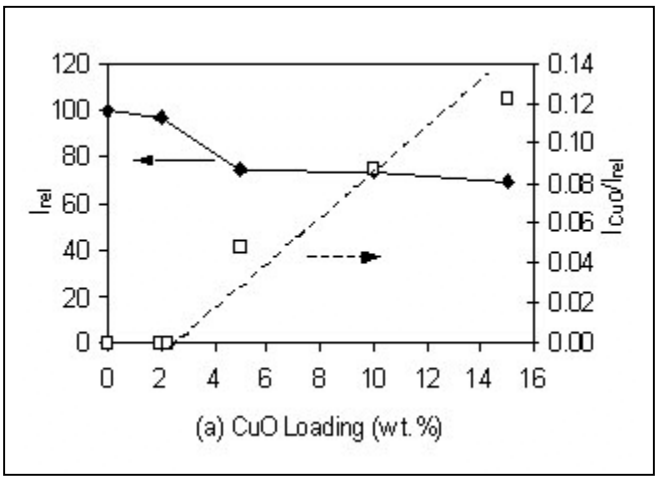

Figure 6.14: The influence of CuO loading concentration (wt.%) to the structure of modified samples.

The loading concentration of metal oxide easily influences the pore sizes of zeolite systems. Physical properties characterization results indicated that the BET specific surface area and micropore volume of CuO modified Na-Y zeolite samples were decreased with the increase of copper oxide loading concentration (Figure 6.15). Therefore, it is suggested that the pore size of zeolites can be designed to various degrees by dispersing various concentration loadings of metal oxide into zeolites, which is very important for the application on adsorbents by zeolites because different types of adsorbate required specific suitable pores of zeolites.

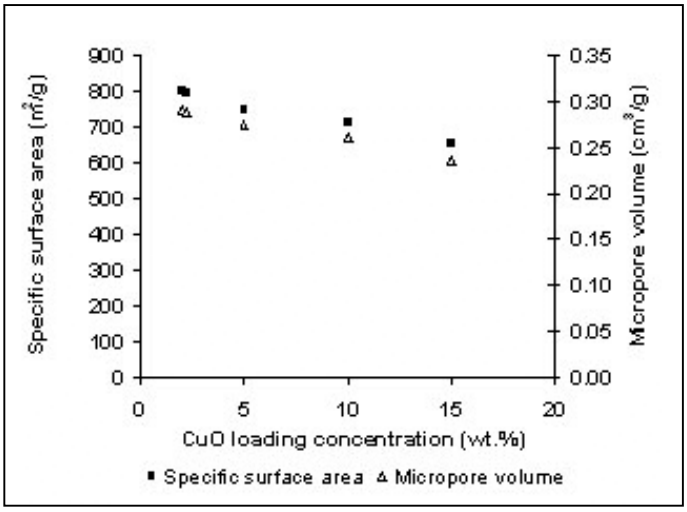

Figure 6.15: Effect of CuO loading on Na-Y zeolite physical properties.

Moreover, copper (II) oxide loading concentration also gives significant effects on the chemical characteristics of Na-Y zeolite as illustrated in Figure 4.16. The structure sensitive Na-Y bands related to external linkages between tetrahedral at about 1145, 790, 725 and 576 cm^{-1} increase significantly in intensity with the increase of CuO loading concentration. Since the heat treatment and other modification conditions remain the same for all samples, the changes of bands intensity might due to the characteristic of CuO species on the surfaces. The bands are therefore assigning to a copper-oxygen vibration, which is formed by CuO coordinating with oxygen from the zeolite lattice. Several works on metal oxide modified support with different loading concentration verified the changes in bands intensity from FTIR characterization are due to the dispersion effect of metal oxide on support surfaces (Chen *et al*., 1999; Xu *et al*., 2000; Zhu *et al*., 2005).

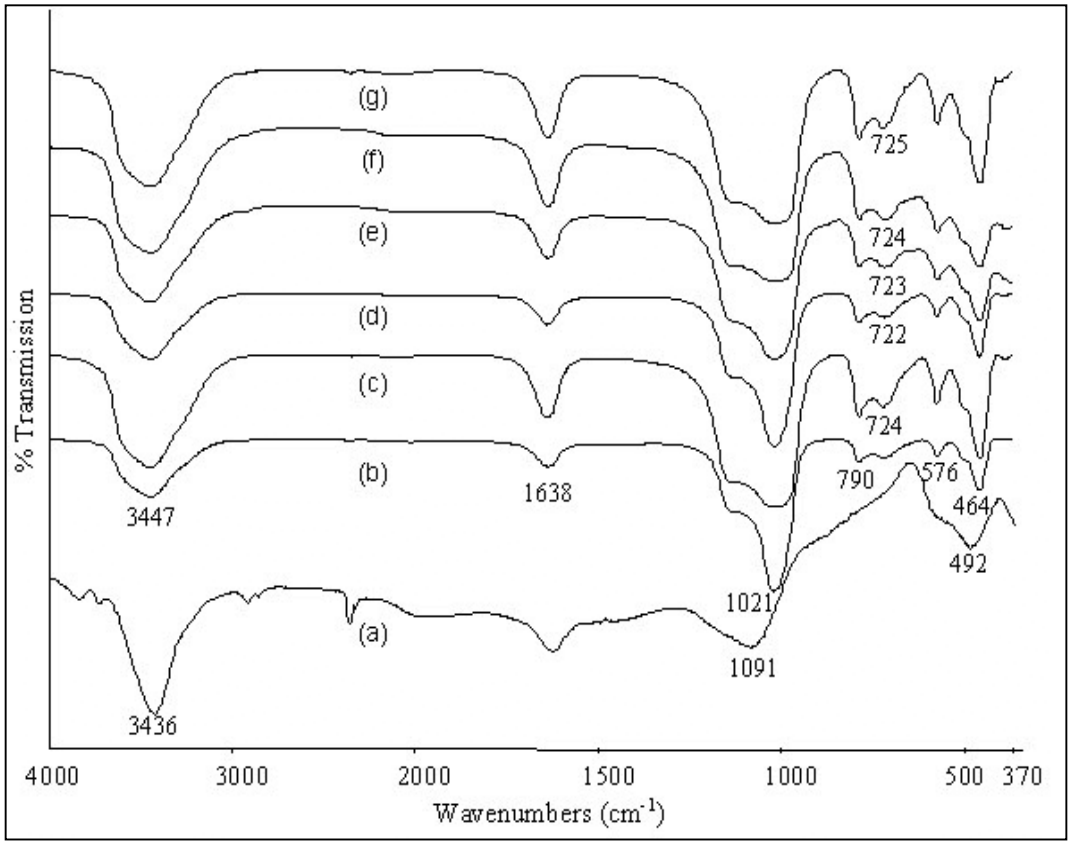

Figure 6.16: FTIR spectra of copper (II) oxide modified Na-Y zeolite: (a) CuO; (b) Na-Y; (c) Physical mixture of 2wt.% CuO/NaY; (d) 2wt.% CuO/NaY; (e) 5wt.% CuO/NaY; (f) 10wt.% CuO/NaY; and (g) 15wt.% CuO/NaY.

Besides that, the addition of copper oxide loading concentration also strengthens the affinity of samples to adsorb water molecules at ambient as can be seen from band intensity increment at 1638 cm^{-1} and 3447 cm^{-1} that assigned to water molecule structure and hydroxyls group, respectively. However, the hydroxyls group at around 3447 cm^{-1} decreased with the CuO dispersion on the calcined samples if compared with the physical mixture sample before the calcination process (Figure 6.16c). The dispersion of metal oxide was accompanied by a gradual consumption of free OH groups at the surface support. Therefore, the results indicated consumption of hydroxyls groups by Cu species in the system, which confirmed a solid-solid reaction between CuO and the Na-Y supports and thus formation of Cu species at the surface after the heat treatment.

6.2.3 Effect of calcination temperature

Calcination temperature is one of the most important parameters that give effects on metal oxide modified zeolite physicochemical and gas adsorptive characteristics. XRD has been used to study the effect of calcination temperature on the interaction between CuO and Na-Y as shown in Figure 6.17. By varying the calcination temperature as variable, in the CuO/NaY system, when the heat treatment temperature is 773.15 K, the relative intensity of the modified sample increased as compared to the physical mixture of copper (II) oxide and Na-Y zeolite at ambient temperature. Na-Y zeolite is thermally stable at 873.15K for 2.25 wt.% copper (II) oxide loading concentration with increasing crystallinity up to 96 %. The structure of CuO-NaY zeolite remains unchanged and thermally stable up to 973.15 K with a lower crystallinity as shown in the XRD diagrams (Figure 6.17) and the relative intensity data (Table 6.5).

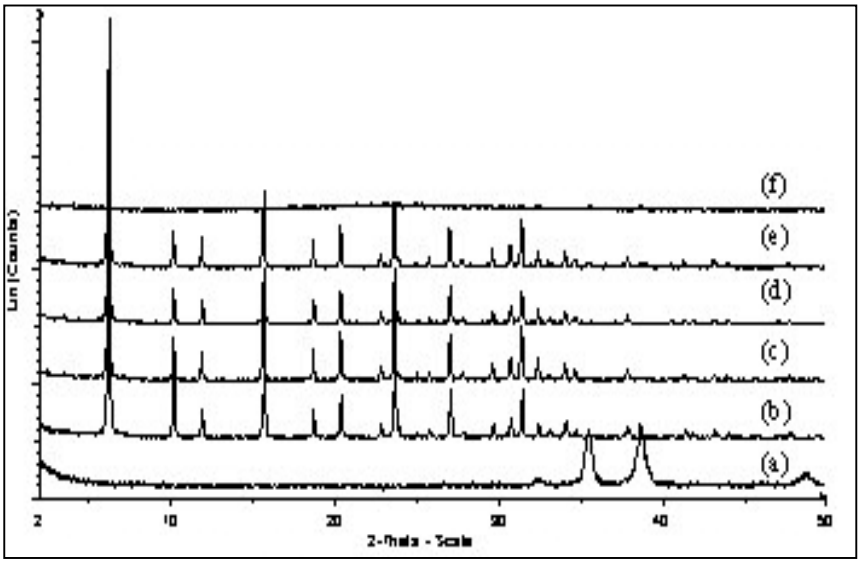

Figure 6.17: XRD patterns of 5 CuO/NaY samples after heat treatment: (a) CuO (298.15 K); (b) NaY (298.15 K); (c) 5 CuO/NaY (773.15 K); (d) 5 CuO/NaY (873.15 K); (e) 5 CuO/NaY (973.15 K); and (f) 5 CuO/NaY (1073.15 K).

Table 6.5: Effect of calcination temperature on the structure characteristics of CuO modified Na-Y zeolite samples at 2.25 wt% loading.

Samples	T (K)	a_0 (Å)	Relative Intensity (I_{rel})	Particle Size (nm)*
NaY	298.15	24.61	100.00	68.69
CuO/NaY	298.15	24.64	91.00	79.35
CuO/NaY	773.15	24.67	92.35	54.27
CuO/NaY	873.15	24.62	96.43	54.27
CuO/NaY	973.15	24.68	84.91	68.68
CuO/NaY	1073.15		Structure collapse	

* Calculated based on Scherrer equation (Cullity, 1978).

For samples calcined at temperature 773.15 K and below, the peaks of crystalline CuO are present, but with reduced intensity. It revealed that heating at this temperature only causes CuO to disperse onto the surface of Na-Y as small grain particles distribution. The relative intensity of the modified sample increases significantly when the sample is heated at 873.15K; CuO can disperse well at this calcine temperature and transformed into two-dimensional copper oxide dispersion species without showing any residual bulk crystalline CuO remains. By further

increasing the calcination temperature, the agglomeration of copper (II) oxide was occurred thus decrease the crystallinity of the samples at 973.15 K. The structure of the modified sample collapsed when the heat treatment temperature is increased to 1073.15 K. These phenomena could be recognized from the physical properties characterization as well, in which the specific surface area decreased dramatically from 794.63 m^2/g at 873.15 K heat treatment to 2.41 m^2/g at 1073.15 K. Meanwhile, the micropore volume of the modified samples also following the same order, decreasing from 2.88×10^{-7} m^3/g at 873.15 K to 5.89×10^{-10} m^3/g at 1073.15 K calcination temperature. High calcination temperature caused zeolite structural defect and lost of its properties. The chemical characterization revealed that the structural and chemical composition bonding of copper oxide modified Na-Y zeolite remained stable for calcination temperature from 873.15 to 973.15 K. The modified zeolite structure is collapsed and the symmetric stretching of TO_4 transformed into Si-O-Si functional group that is evidenced in Figure 6.18d.

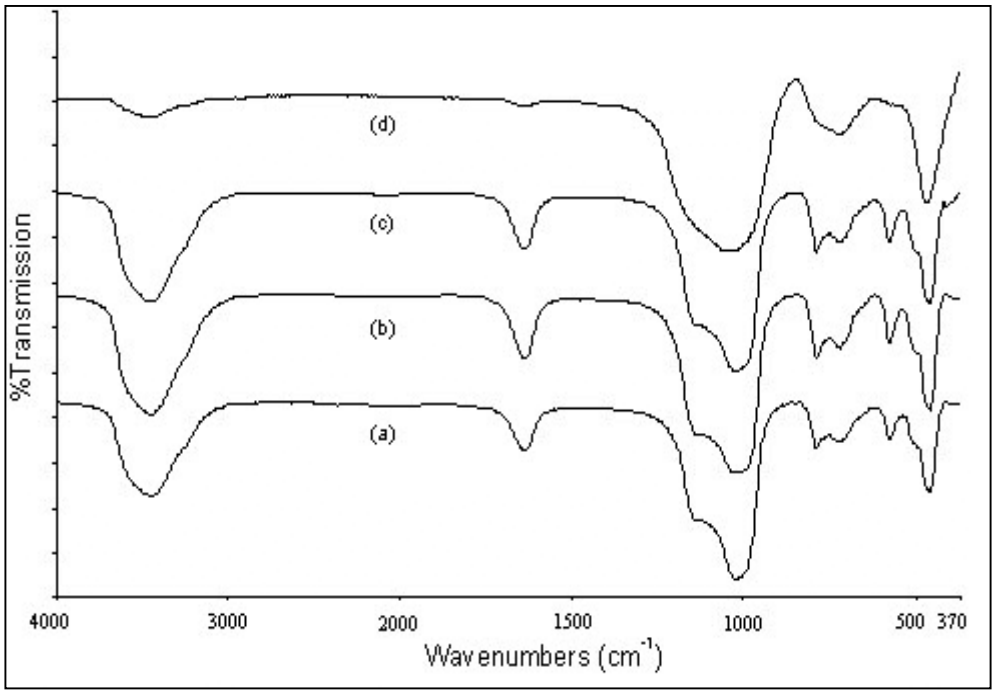

Figure 6.18: FTIR spectra of copper (II) oxide modified Na-Y zeolites calcined at different temperatures: (a) 773.15 K; (b) 873.15 K; (c) 973.15 K; and (d) 1073.15 K.

6.2.4 Effect of duration of calcination process

By varying the duration for calcination process as shown in Figure 6.19, after the mixture has been heated at 873.15K for 12 hours, the peaks of crystalline CuO are still present, but with reduced bulk CuO intensity, indicating that some residual crystalline CuO still remain. These residual CuO totally vanished after the samples were calcined up to 24 hours and above. The crystallinity of the CuO modified Na-Y zeolite samples increases with the increase of calcination duration (Table 6.6).

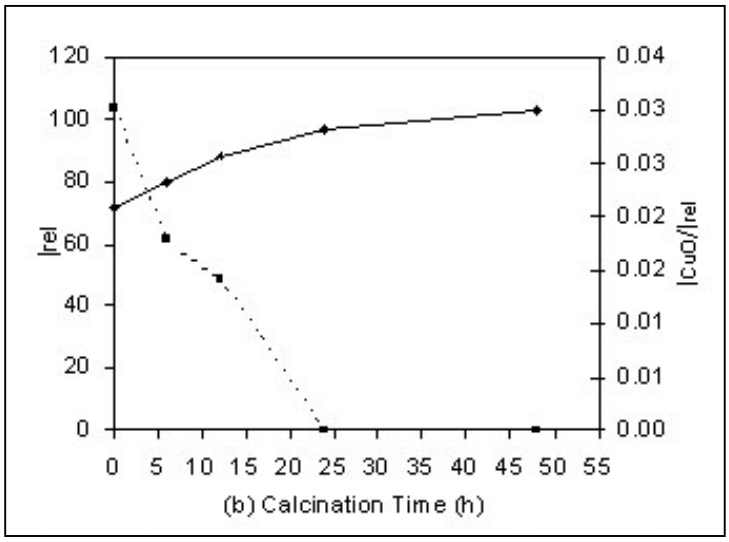

Figure 6.19: The influence of calcination time to the structure of modified samples.

Table 6.6: Effect of calcination time on the structure characteristics of CuO modified Na-Y zeolite samples at 2.25 wt% loading.

Samples	Time (h)	a_0 (Å)	Relative Intensity (I_{rel})	Particle Size (nm)*
NaY	0	24.61	100.00	68.69
CuO/NaY	0	24.64	91.00	79.35
CuO/NaY	6	24.65	92.00	68.69
CuO/NaY	12	24.64	93.16	68.69
CuO/NaY	24	24.62	96.43	54.27
CuO/NaY	48	24.62	103.26	65.20

* Calculated based on Scherrer equation (Cullity, 1978).

The result indicates that at temperature 873.15 K, the dispersion process completes in about 24 hours and for which heat treatment less than 24 hours, the bulk phase of CuO transform into CuO surface dispersed species, CuO (bulk phase) $\longrightarrow$ CuO (surface species). After the heat treatment for 24 hours and above, the formation of bulk phase CuO and surface species CuO occur simultaneous and reversibility, CuO (bulk phase) $\rightleftharpoons$ CuO (surface species) thus further enhancing the dispersion of copper oxide into the zeolite surfaces. However, it was observed that the longer the duration of calcination (48 hours) after the dispersion process completed, the larger the particle size of the adsorbent formed. The effect of duration of calcination to the physical properties is listed in Table 6.7.

Table 6.7: Effect of duration calcination to physical properties characteristics of CuO modified Na-Y zeolite samples at 2.25 wt% loading.

Samples	Time (h)	BET surface area (m^2/g)	Micropore volume ($\times 10^7$ m^3/g)	Average pore diameter (Å)
CuO/NaY	0	744.51	2.71	16.23
CuO/NaY	6	790.23	2.87	16.02
CuO/NaY	24	794.63	2.88	16.11
CuO/NaY	48	813.55	2.97	15.87

The BET specific surface area and micropore volume increase simultaneously with increasing of duration for calcination process. Meanwhile, the average pore diameter generally represents a decline trend. The increase in sample surface area and the decrease in pore size diameter perhaps are due to the well dispersion of CuO into the internal surface of zeolite matrix system. Apart from that, the effect of the duration of calcination to the samples chemical properties and the bonding are identified through FTIR chemical characterization. According to Nyquist and Kagel (1971), the bulk copper (II) oxide is in the region of 600 - 500 cm^{-1}. As revealed in Figure 6.20b, the band intensity of this region was found to increase after non heat treatment CuO dispersion (physical mixtures) compared to commercial zeolite Na-Y.

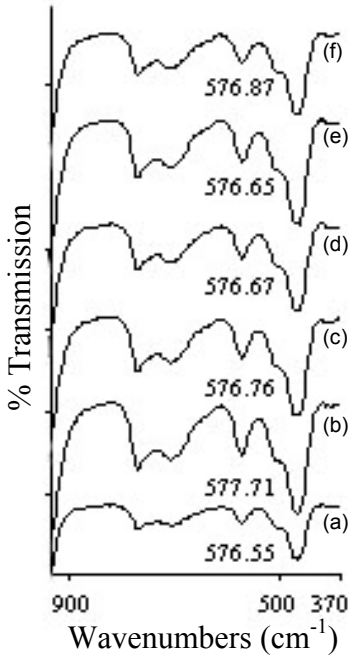

Figure 6.20: FTIR spectra of: (a) NaY; (b) CuO/NaY calcined for 0 hour; (c) 6 hours; (d) 12 hours; (e) 24 hours; and (f) 48 hours.

The intensity of bands (Figure 6.20 b – f) decreases with increasing of duration in calcination process. In addition, the bands were found shifted to lower wavenumbers as the period of calcination process rose. After the heat treatment for 48 hours, the particle size of adsorbent increased, which might due to the addition of bulk phase CuO agglomeration, thus shifted back the wavelength to higher value at band frequency of 576.87 cm^{-1} (Figure 6.20 f). As reported by Dong *et al*. (1997), regarding the relationship between the dispersed metal oxide species and the heat treatment time, the result indicates that at a temperature, which the dispersion process has been completed, more heat treatment would cause the formation of a close-packed capping O^{2-} layer and the formation of bulk phase metal oxide on zeolite surface. Hence, satisfactory heat treatment duration is very important for the well dispersion of metal oxide on the zeolite surfaces. It is another crucial factor that determined the structural and physicochemical properties of metal oxide modified zeolite adsorbents.

4.2.5 Effect of modification techniques

There are several types of modification techniques can be used to disperse metal oxides onto/into zeolite Na-Y host matrix system. Copper (II) oxide and gallium (III) oxide modified zeolite Na-Y adsorbents prepared by thermal dispersion method (TD) and incipient wetness impregnation method (IWI) are compared in this work at the same loading concentration of five metal oxide/Na-Y (290 μmol/g adsorbent).

From the results presented in XRD pattern as shown in Figure 6.21, none of the crystalline CuO modified zeolite Na-Y is detected on both samples that prepared via different techniques. These data suggested that the copper (II) oxide is probably dispersed as sub-monolayer in or on the surface of the Na-Y support. The sample prepared by thermal dispersion shows slightly higher crystallinity compared with incipient wetness impregnation technique.

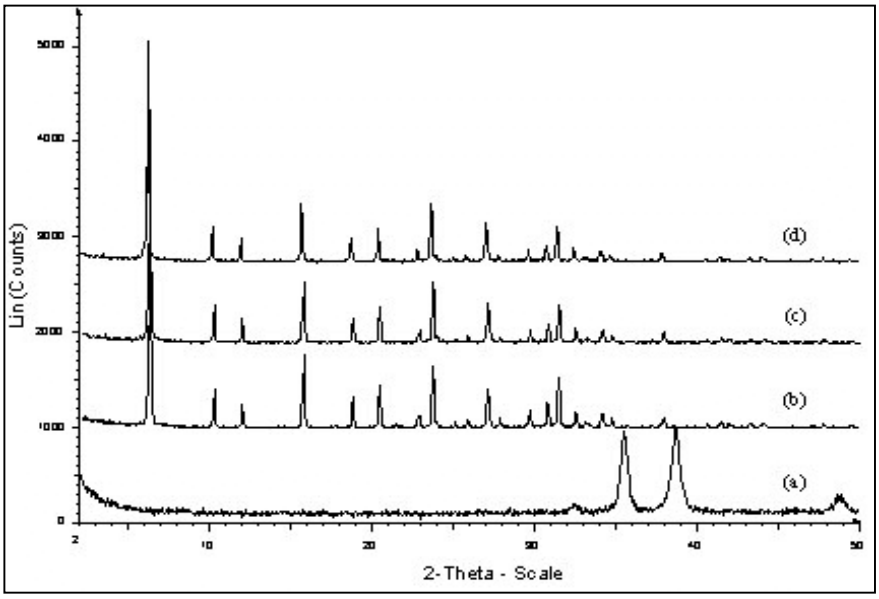

Figure 6.21: XRD patterns of CuO/NaY samples: (a) CuO; (b) NaY; (c) 5 CuO/NaY prepared by thermal dispersion technique; and (d) 5 CuO/NaY prepared by incipient wetness impregnation technique.

On the other hand, as expected, high melting point compound for example, gallium (III) oxide crystallites peaks showed slightly in the thermal dispersed sample but none of the sharp peaks characteristic of Ga_2O_3 crystallites is detected on the impregnated sample (Figure 6.22). The heat treatment at 873.15 K, which is below than Ga_2O_3 Tammann temperature (1007.15 K) is not enough to disperse oxide well as monolayer or sub-monolayer coverage on the zeolite surfaces using thermal dispersion method. In addition, higher temperatures than 973.15 K will cause the structure of zeolite totally collapse as discussed above. Thereinafter, incipient wetness impregnation techniques is utmost important to be applied in the preparation of high melting point metal oxides into zeolite Na-Y system.

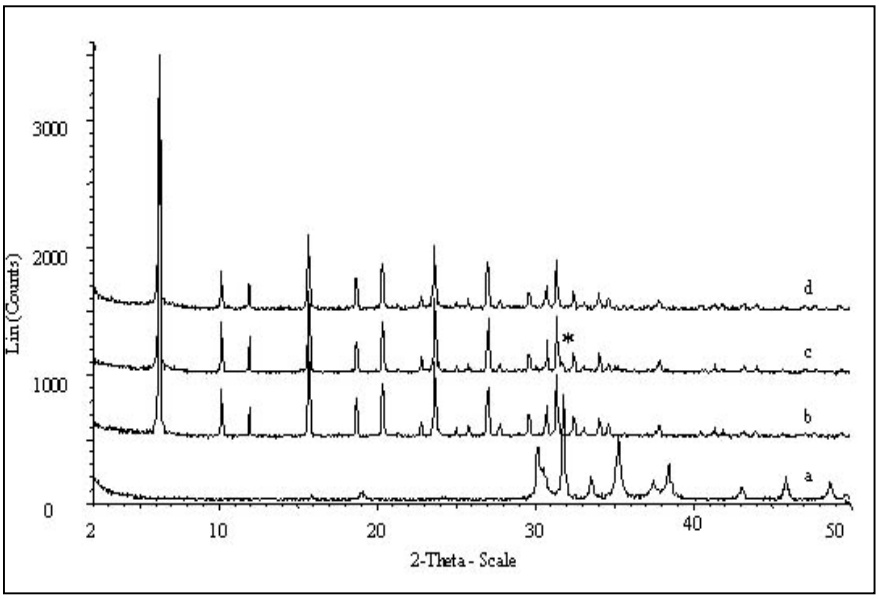

Figure 6.22: XRD patterns of Ga_2O_3/NaY samples: (a) Ga_2O_3; (b) NaY; (c) 5 Ga_2O_3/NaY prepared by thermal dispersion technique (∗ - Ga_2O_3); and (d) 5 Ga_2O_3/NaY prepared by incipient wetness impregnation technique.

However, physical properties characterization found out that the samples prepared by incipient wetness impregnation techniques always have higher specific surface area and micropore volume than the samples modified using thermal spreading technique for both types of metal oxides (Table 6.8). In contrast, thermal

dispersion technique produced metal oxide modified zeolite samples with bigger average pore diameter. Even though incipient wetness impregnation method is perhaps more preferable for preparing high surface area gas adsorbent, it does not mean that this method would in certainty presents higher gas adsorption capacity. This is because the gas adsorption process is not only governed by the surface area but also the pore size of the sample as well as the adsorbate properties.

Table 6.8: Surface area and pore size characterization of CuO/NaY and Ga_2O_3/NaY.

Samples	Micropore surface area (m^2/g)	External surface area (m^2/g)	Micropore volume ($\times 10^7$ m^3/g)	Average pore diameter (Å)
CuO/NaY (TMD)	773.69	20.94	2.88	16.11
CuO/NaY (IWI)	841.68	16.99	3.14	15.79
Ga_2O_3/NaY (TMD)	693.15	18.05	2.59	16.39
Ga_2O_3/NaY (IWI)	772.40	18.61	2.88	15.92

* TMD = thermal monolayer dispersion; IWI = incipient wetness impregnation.

Thereinafter, from the structural and physicochemical characterization on metal oxide modified Na-Y zeolite adsorbents, it is inferred that types of metal oxide, metal oxide loading concentration, calcination temperature, duration of calcination treatment parameters and modification techniques easily influence the physical and chemical properties of zeolite systems. Thus, the understanding and well controlled of these modification parameters are very important to manipulate the adsorptive properties of adsorbents to suit for a specific application.

6.3 Gas Adsorption Characteristics

6.3.1 Adsorption equilibrium

A study of the adsorption capacity of metal oxide modified zeolite Na-Y will be presented for the adsorption of CO_2, N_2 and CH_4. Based upon the results obtained from the equilibrium adsorption capacity and the corresponding heat of adsorption that measured, the effect of the metal oxide modification in the adsorption of each type of gases could be evaluated. The influences of metal oxides modified zeolite system on gas carbon dioxide (3.3 Å), gas nitrogen (3.64 Å) and gas methane (3.8 Å) were investigated in single adsorbate adsorption atmosphere at 323.15 K and equilibrium pressure of 138 kPa. Adsorbate uptake capacity was measured until equilibrium reached.

6.3.1.1 Effect of various metal oxides

Twenty types of metal oxides that have been dispersed on the surfaces of Na-Y zeolite were investigated into their gas adsorptive characteristics. Different types of metal oxides from various groups of elements in the Periodic Table would cause different gases adsorption characteristics as shown in Table 6.9. For gas carbon dioxide adsorption equilibrium study, all samples showed great adsorption rates and capacity at initial adsorption state, which is achieved around 70 % of total adsorption capacity within 30 minutes adsorption time. It is probably due to the specific interactions of the quadrupole of the CO_2 molecule with the basicity properties or electric field created by the cations from metal oxide compound that existing in the structure of the zeolites. Apart from that, the kinetic diameter of CO_2 is the smallest among three gases that enable gas molecules to diffuse more easily into zeolite micropore system at initial adsorption condition. From the results obtained (Table

6.9), it is observed that many types of metal oxide modified Na-Y have enhanced the CO_2 adsorption capacity. Group II A metal oxides with high basicity properties showed great CO_2 adsorption capacity following the sequences: MgO > BaO > CaO. As expected, Vanadium (V) oxide with the lowest specific surface area and high acidity properties presenting the lowest gas CO_2 adsorption capacity.

Table 6.9: Gas adsorption capacity of adsorbents studied at 323.15 K and 138 kPa.

Group of Elements (Periodic Table)	Samples	CO_2 Adsorption Capacity ($\times 10^3$ mol/g)	N_2 Adsorption Capacity ($\times 10^3$ mol/g)	CH_4 Adsorption Capacity ($\times 10^3$ mol/g)
-	NaY	3.83	4.56	10.21
IIA	MgO/NaY	4.97	4.43	9.14
	CaO/NaY	4.59	5.26	11.46
	BaO/NaY	4.74	4.53	12.84
IIIA	Ga_2O_3/NaY	3.13	4.37	6.58
IVA	GeO_2/NaY	3.44	4.25	6.89
	SnO/NaY	4.36	4.20	9.12
	PbO/NaY	3.04	2.18	4.68
IB	Cu_2O/NaY	3.24	4.11	8.56
	CuO/NaY	4.24	4.82	13.44
	Ag_2O/NaY	4.10	3.98	7.40
IIB	ZnO/NaY	3.32	4.63	9.45
	HgO/NaY	4.70	5.70	14.24
IIIB	Y_2O_3/NaY	4.17	3.66	8.85
VB	V_2O_5/NaY	1.77	1.96	4.10
VIB	MoO_3/NaY	3.28	3.08	4.76
	WO_3/NaY	3.67	3.62	6.89
VIIIB	Fe_2O_3/NaY	3.84	4.14	8.18
	Co_3O_4/NaY	4.20	4.80	7.60
	NiO/NaY	3.72	3.43	8.33
	PdO/NaY	4.75	4.09	6.94

As for gas nitrogen adsorption equilibrium, the results found out that five types of metal oxide demonstrate a marked increase in the N_2 adsorption capacity. The increase in the gas nitrogen adsorption capacity among oxides dispersed was in the following sequences: HgO > CaO > CuO > Co_3O_4 > ZnO. Mercury (II) oxide modified zeolite Na-Y exhibited the most pronounced effect for increasing the capacity up to 5.7 mmol/g adsorbent which is 25 % higher compare to unloaded Na-Y zeolite. This capacity value is far higher than the results reported for ion-

exchanged modified zeolite adsorbents (Chao, 1989; Coe *et al*., 1993; Fitch *et al*., 1995). Meanwhile, V_2O_5/NaY greatly diminished the surface areas and showed the least pronounced effect by decreasing the N_2 adsorption capacity.

On the other hand, the dispersion of HgO, CuO, BaO and CaO modified Na-Y demonstrate the increment characteristics of gas methane adsorption capacity compared with unmodified Na-Y zeolite, in which the HgO added Na-Y increased the methane adsorption capacity up to 39.5 %, followed by CuO/Na-Y (31.6 %), BaO/Na-Y (25.8 %) and CaO modified Na-Y (12.24 %). As for vanadium (V) oxide modified sample, it shows the same adsorption behavior with gas CO_2 and N_2, which shows the lowest adsorption capacity toward gas methane. This might due to its inherent physicochemical properties since the same amounts of metal oxides were added for each sample.

Despite of that, it was interesting to found out that the adsorption affinity and saturation volume of CH_4 for all samples are larger than those of CO_2 and N_2 when the adsorption process reached the equilibrium state at this experimental adsorption conditions (Table 6.9). This distinct behavior of CH_4 adsorption equilibrium observed is coincides with the results obtained by Hernández-Huesca *et al.* (1999), in which when the temperature is increased from 273.15 to 313.15 K, the amount of adsorbed CH_4 would increase with temperature.

It was inferred from the experimental screening results that Group II B transition metal oxides (ZnO, HgO) modified zeolite Na-Y represent a great potential as gas methane and nitrogen adsorbent compared with other types and groups of metal oxides. Mercury (II) oxide probably improves the affinity of Na-Y toward those adsorbates with quadrupole moment properties. Meanwhile, Group II A metal oxides modified Na-Y revealed promising results to be applied as excellent gas CO_2 adsorbents. As realized, carbon dioxide is an acid gas. The carbon atom of a CO_2 molecule would exhibit electrophilicity, the electron density is deviated and enriched in the oxygen side (Horiuchi *et al*., 1998). Oxygen anions of the metal oxide that

dispersed into/onto Na-Y surfaces would provide the basic sites to interact with gas CO_2. Therefore, the low electronegativity of Group II A metal cations (high basicity) added would increased the acid CO_2 adsorption capacity compared with other groups of metal oxide.

Accordingly, high surface area adsorbents are essential for gas adsorption (Suzuki, 1990). A large specific surface area is needed to provide more active adsorption sites for large adsorption capacity. Meanwhile, the micropore volume determines the accessibility and amount of adsorbate molecules that can be adsorbed in the internal zeolite surfaces. Figure 6.23 shows the effect of specific surface area and micropore volume on the gases adsorption capacity. It was observed that the amount of gases adsorbed do not posses a linear relationship with the specific surface area and micropore volume of adsorbents, even though the incremental of gases adsorption on the adsorbents are seem to be proportional to both of the parameters. It appeared that the regression of error is rather significant, especially for gas methane adsorption. Therefore, it can be conferred that specific surface area and micropore volume are not the only main determining factor in gas adsorption characteristics of metal oxide modified Na-Y zeolite adsorbents.

Generally, from the surface area and pore size characterization, it is obvious that the adsorption of CO_2, N_2 and CH_4 with unmodified and metal oxide modified Na-Y adsorbents are not limited by the steric factor; the gases molecules could freely penetrate into the cages towards the micropore. The accessibility of gas molecule is restricted only if the pore blockage occurred due to the collapse of the Na-Y structure after the modification or the agglomeration of bulk metal oxide on the zeolite surface.

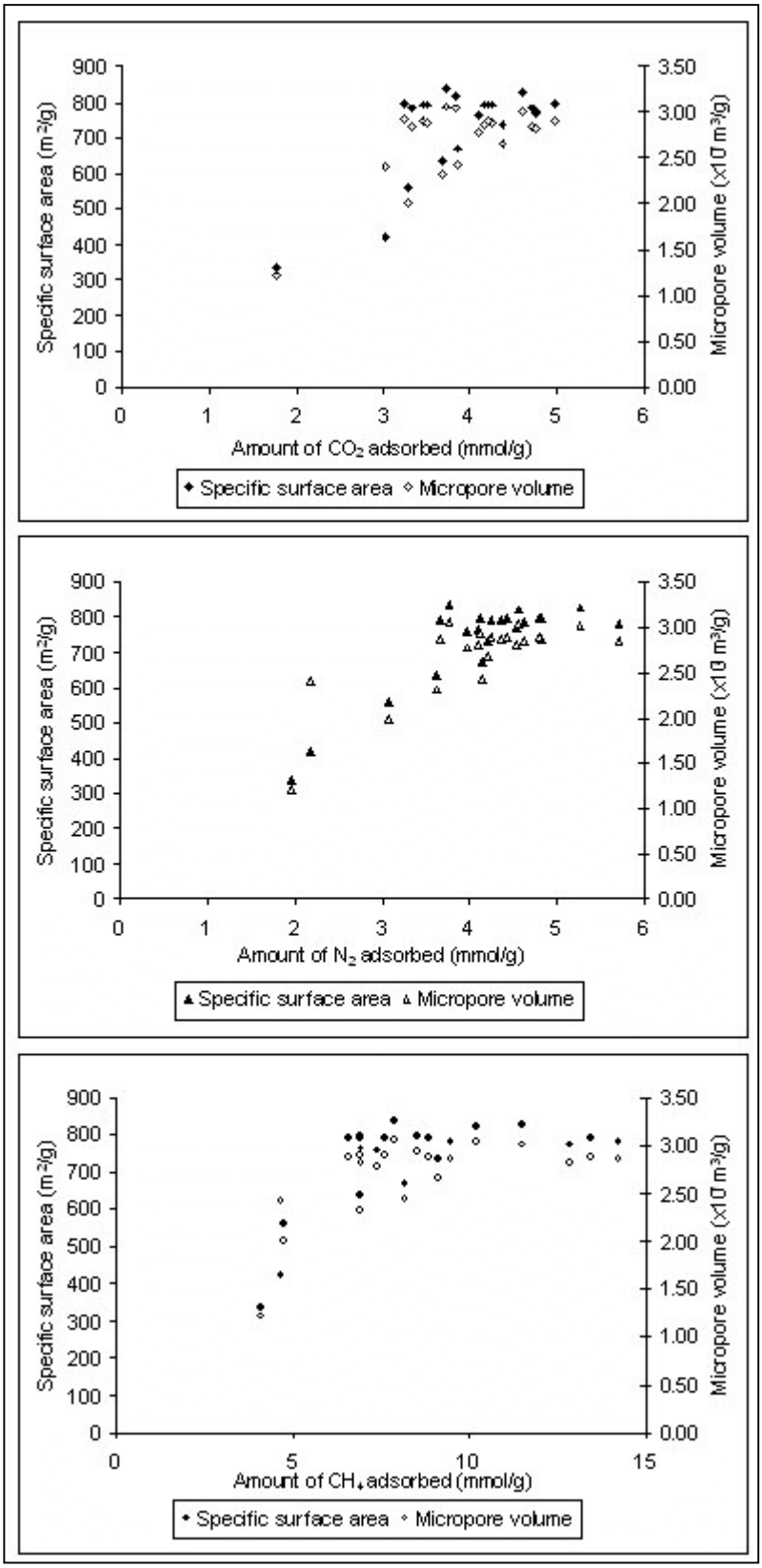

Figure 6.23: Effect of specific surface area and micropore volume on gases adsorption capacity.

The bulk diffusion transport is expected to be fast. The overall transport of gas in Na-Y is influenced by both adsorbate-adsorbent interaction and diffusion characteristics in micropores (Gardner *et al*., 2002; Weh *et al*., 2002). However, the relative pore structure or pore space that modified by metal oxides dispersion and adsorbate molecular geometries likely play the most important role than adsorption equilibrium. This is supported by the fact the adsorption capacity of gas CH_4 in saturation condition are larger than CO_2 and N_2 even though the apparent kinetic diameter of CH_4 is slightly larger than N_2 and CO_2. The support relative molecular size and pore structure after the modification have very strong effects on selective gas adsorption and permeation (Cui *et al*., 2004). Therefore, results infer the relative adsorption capacity over the equilibrium pressure does not solely depend on the surface area and pore volume, but strongly rely on the numbers of cations available per unit mass of zeolite and the limiting volume of the micropores after the metal oxide modification. The structure and physicochemical properties of zeolite Na-Y modified with various types of metal oxides that change accordingly are responsible for the improvement in shape-selective properties as gas adsorbent.

6.3.1.2 Effect of loading concentration

Copper oxide itself with relatively low melting point, easily undergo crystalline growth and thermal sintering, and as a result the adsorbent capacity decreases rapidly. In order to increase the surface area and stability of copper oxide-based adsorbent, copper oxides have been supported on an inactive and porous support, such as aluminium oxide, silicon dioxide and activated carbon (Tseng and Wey, 2004). Zeolites Na-Y can meet most of the desirable properties required for a suitable support. It is well known that the dispersion of an active metallic phase on a support depends not only on the surface area and porosity, but also on the chemistry of the support surface. As a consequence of this, the recently study is carried out used zeolite Na-Y as copper oxide-based adsorbent supports for investigating CH_4 adsorption characteristics.

The influence of CuO loading concentration on the CH_4 adsorption performance of CuO/Na-Y was investigated in pure CH_4 atmosphere at 323.15 K and the results are shown in Figure 4.24. Before the adsorption process was carried out, blank Na-Y support was calcined at 873.15 K for 24 hours using as a standard reference sample. The Na-Y zeolite without CuO dispersion showed a CH_4 adsorption capacity of 8.4 mmol/g-adsorbent. When the CuO loading was 2.0 wt.%, the CH_4 adsorption capacity was only increased to 9.8 mmol/g-adsorbent. When the CuO loading further increased, the adsorption capacity increased. The adsorption capacities were extremely increased up to 13.4 mmol/g-adsorbent for the CuO loading of 2.25 wt.%, which is 60 % higher than that of blank Na-Y.

If the assumption that the CuO and the Na-Y were simply mechanically mixed in the modified sample is true, the adsorption capacity of CuO/NaY should be the linear sum of the adsorption capacity contributed from Na-Y and pure bulk CuO, and was calculated to be around 8.43 mmol/g-adsorbent. This result is nearly identified with the sample (physical mixing) without heat treatment (T = 298.15 K) as shown in Figure 6.25, with methane adsorption capacity of 8.9 mmol/g-adsorbent. However, the adsorption capacities of the modified samples obtained in this study were far higher than that value. The results once again proved that CuO are loaded into the Na-Y cages or be coated on the external surface of the Na-Y after the thermal treatment. For 2.25 wt.% of CuO loading concentration, there is not simply a physical mixture between copper oxide and Na-Y adsorbent that caused the significant improvement in methane adsorption capacity. By increasing the CuO loading concentration above its critical dispersion capacity (> 2.25 wt.%), the CH_4 adsorption capacity decreased from 5 wt.% to 15 wt.%. The CuO loading concentration at 10 wt.% or above probably formed agglomeration of bulk CuO on the zeolite surfaces and block the pore windows, which restricts the further diffusion of gas CH_4 to adsorb on the active adsorption sites on the zeolite internal surfaces.

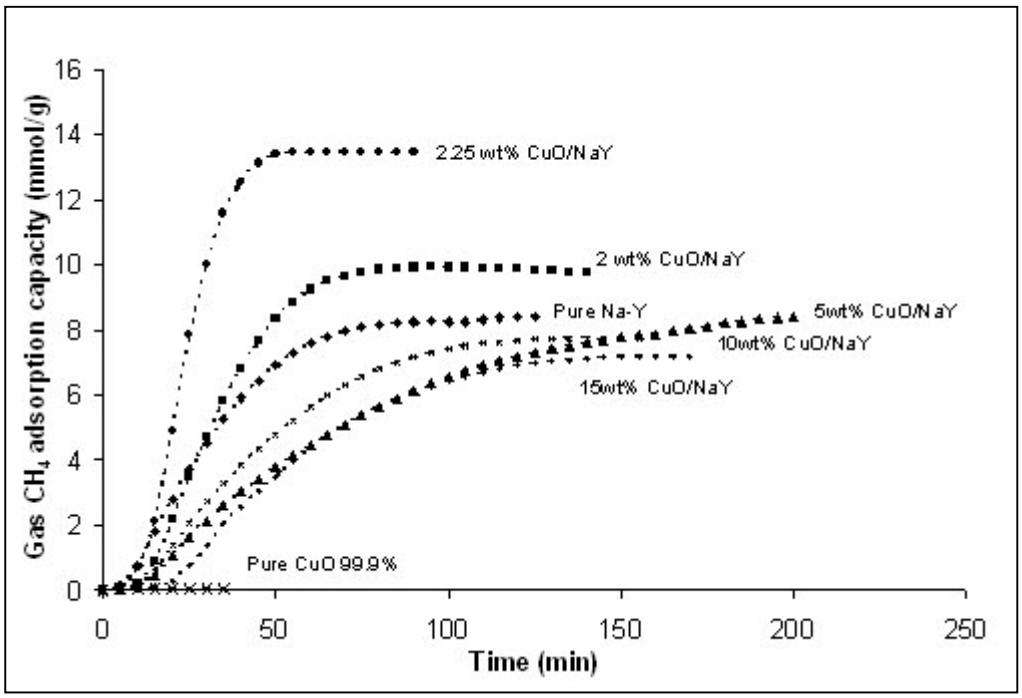

Figure 6.24: Effect of copper (II) oxide loading concentration on methane adsorption characteristics.

6.3.1.3 Effect of calcination temperature

Calcination temperature plays an important role that determining the well dispersion of CuO into/onto the Na-Y zeolite surfaces. From the results obtained as revealed in Figure 4.25, it is observed that the sample prepared at room temperature by physically mixing of CuO and Na-Y zeolite gives CH_4 adsorption capacity up to 8.9 mmol/g-adsorbent. Thermal treatment at 773.15 K had increased the adsorption capacity to 11.3 mmol/g-adsorbent. Further increasing the calcination temperature to 873.15 K presenting a maximum adsorption affinity up to 13.4 mmol/g-adsorbent. This results indicated that a suitable calcination temperature (873.15 K) is utmost critical to ensure the transformation of all three-dimensional bulk CuO to two-dimensional dispersed species. However, the calcination temperature higher than the critical value at 973.15 K caused the CuO dispersed species migrate out to the external surfaces as has been explained in the structural characterization section,

forming agglomeration of bulk CuO that significantly decrease the adsorption capacity to 8.8 mmol/g-adsorbent. The structure of modified sample collapsed for heat treatment at 1073.15 K with only 0.06 mmol CH_4 adsorbed per gram adsorbent.

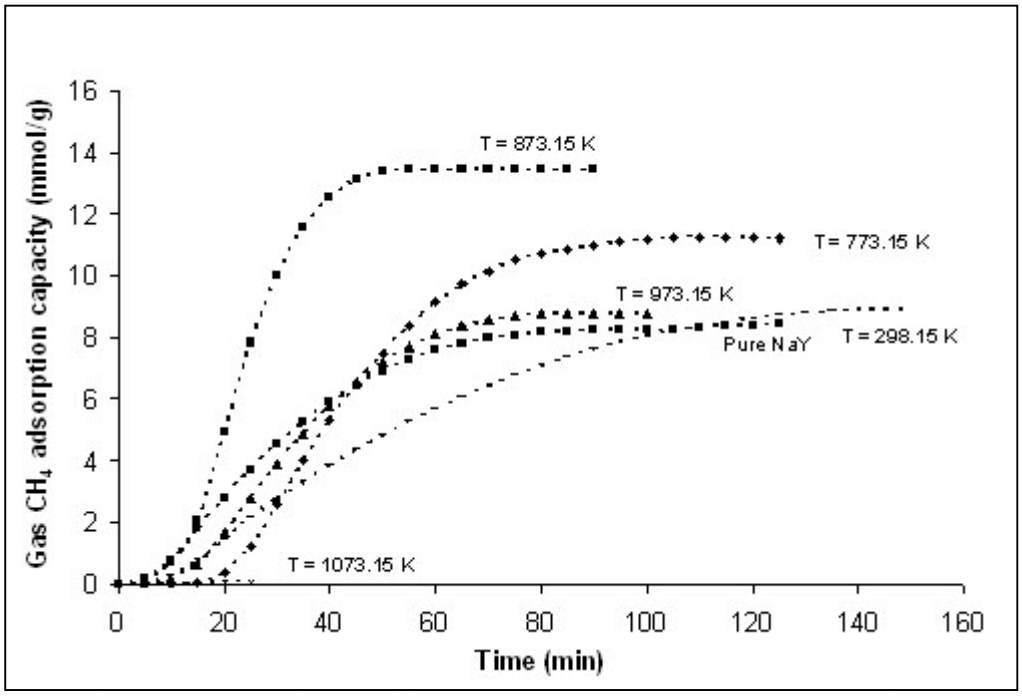

Figure 6.25: Effect of calcination temperature on methane adsorption characteristics.

6.3.1.4 Effect of calcination time

By varying the duration of calcination process at 873.15 K, 6 hours of calcination duration improved CH_4 adsorption capacity to 10.1 mmol/g-adsorbent. Meanwhile, 12 hours and 24 hours of calcination at this dispersive temperature significantly keep enhancing the CH_4 adsorption performances up to 12.9 mmol/g-adsorbent and 13.4 mmol/g-adsorbent, respectively (Figure 6.26). As stated in previous sample characterization section, for heat treatment duration more than 24 hours, the mechanism of CuO that dispersed onto the zeolite surfaces are in

reversible form between bulk CuO phase and dispersed species. Therefore, 48 hours of calcination process not just only increased the particle sizes and agglomeration of bulk CuO of the modified samples, but also brings to the decrement of CH_4 adsorption capacity.

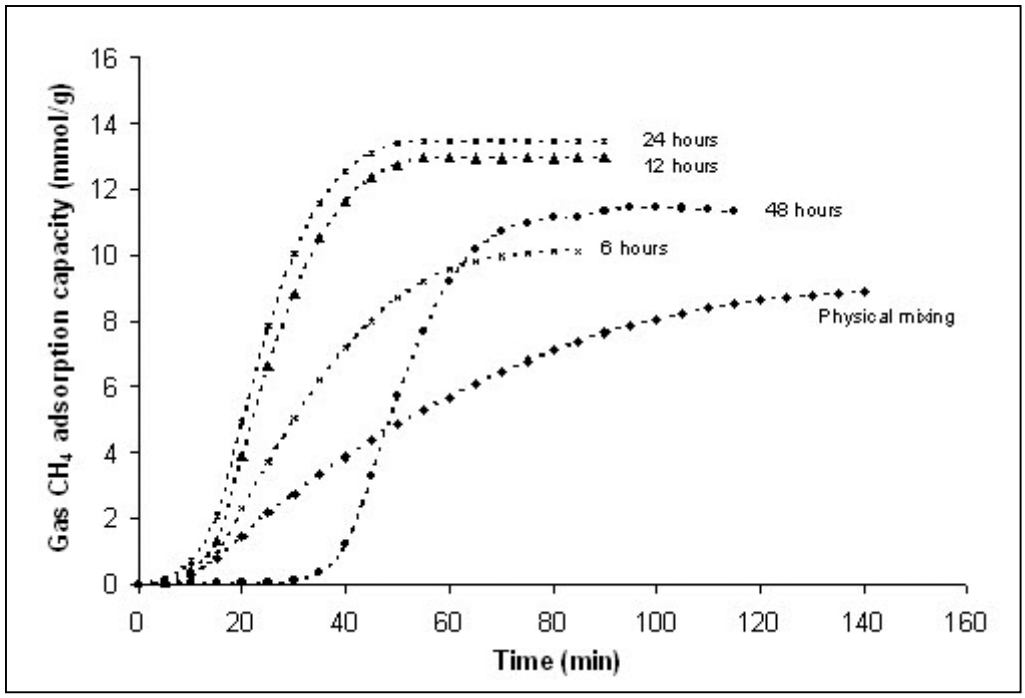

Figure 6.26: Effect of duration calcination process on methane adsorption characteristics.

6.3.1.5 Effect of modification techniques

Thermal dispersion (TD) and incipient wetness impregnation (IWI) were employed for the preparation of 5 CuO/Na-Y. For the thermal dispersion method, CuO was grinded into powder and mixed uniformly with Na-Y support at room temperature. The powder mixture was heated up to 873.15 K and held at that temperature for 24 hours. The adsorption performance of this absorbent was

compared with that of the adsorbent prepared by the wet impregnation method using $Cu(NO_3)_2$ as copper oxide precursor at the same loading concentration (Figure 6.27). At 138 kPa and 873.15 K, on thermally dispersed 5 CuO/NaY, the amount adsorbed of CH_4 was 13.4 mmol/g. The capacity of this sample is 3.9 % slightly greater than of the same adsorbent prepared by impregnation method. However, when the surface areas were compared, the micropore surface area of sample prepared by incipient wetness impregnation method (850 m^2/g) is higher than the one modified via thermal dispersion method (774 m^2/g). Meanwhile, the external surface area of 5 CuO/Na-Y (TD) sample - 21 m^2/g is higher than 5 CuO/Na-Y (IWI) - 17 m^2/g. Therefore, the micropore surface area is not a determining factor that gives the enhancement to the gas CH_4 adsorption capacity. The higher adsorption capacity for the thermal dispersion method was possibly caused by the uniform dispersion of CuO into the Na-Y channels, the pore sizes that being modified after the dispersion and adding by the moltening effect on the external surfaces, which provides more copper active sites for CH_4 adsorption.

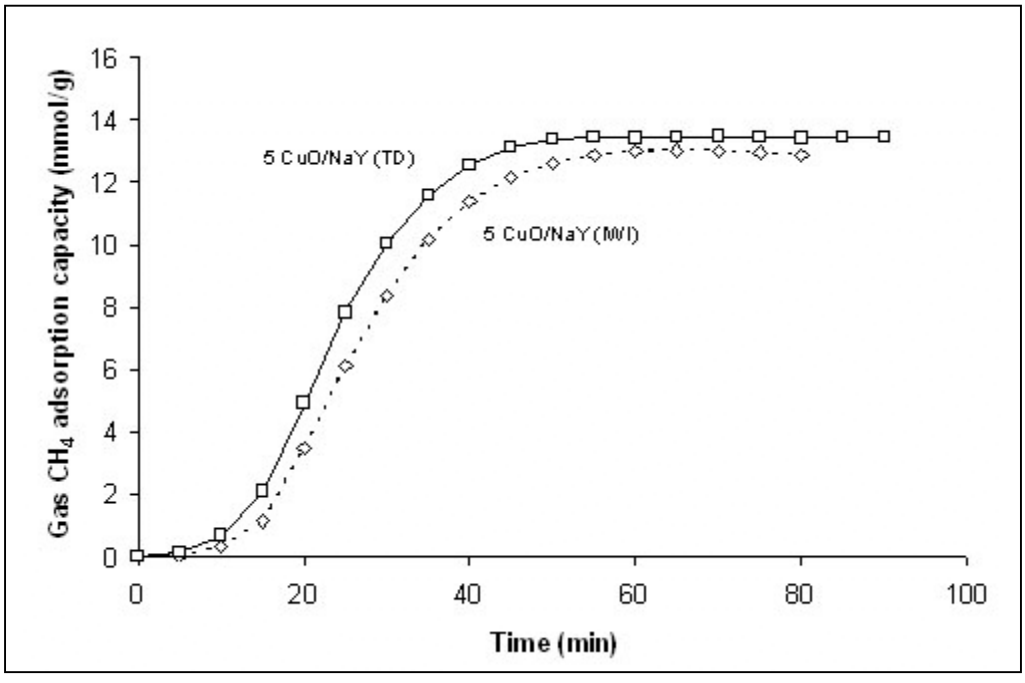

Figure 6.27: Effect of modification techniques on methane adsorption characteristics.

6.3.2 Heat of adsorption

6.3.2.1 Effect of different adsorbate

Gas adsorption is an exothermic process. The correlation between isosteric heat of adsorption and amount of gases adsorbed is important for characterizing the metal oxides modified Na-Y adsorbents. The isosteric heats of gas adsorption were calculated from the equilibrium data at different temperatures. The amount of gases adsorbed were calculated only when the adsorption equilibrium (saturation volume) were reached. At constant adsorbate loading, the isosteric heat of gases adsorption decrease with the increase of the amount of adsorption due to adsorbate-adsorbent interactions, through the interactions of gases with the most active adsorption sites. Subsequently, the isosteric heat of adsorption was found to increase with the increase amount of gas adsorbed, caused by the presence of adsorbate-adsorbate interactions (Hernández-Huesca *et al*., 1999). In other words, heat of adsorption is linearly related to the gas adsorption capacity.

It has been reported that the heat of adsorption for carbon dioxide, nitrogen and methane various significantly. The value is much depending on the nature of the adsorbate and adsorbent. The heat of adsorption for N_2 has been reported in the literatures at around 17 - 28 kJ/mol (Savitz *et al*., 2000; Yoshida *et al*., 2001; Bülow *et al*., 2002; Maurin *et al*., 2005), 20 – 25 kJ/mol for CO_2 (Choudhary and Mayadevi, 1996; Shen and Bülow, 1998; Bülow *et al*., 2002) and 16 – 21 kJ/mol for CH_4 (Choudhary and Mayadevi, 1996), which are more or less consistent with the results obtained in this study.

The isosteric heat of adsorption and entropy of adsorption obtained in this study were calculated based on Equations 2.6 and 2.7. The isosteric heat of CO_2 adsorption, N_2 adsorption, and CH_4 adsorption (Figures 6.28-6.30) of some selected samples are found to increase linearly with the increase of gases adsorption capacity.

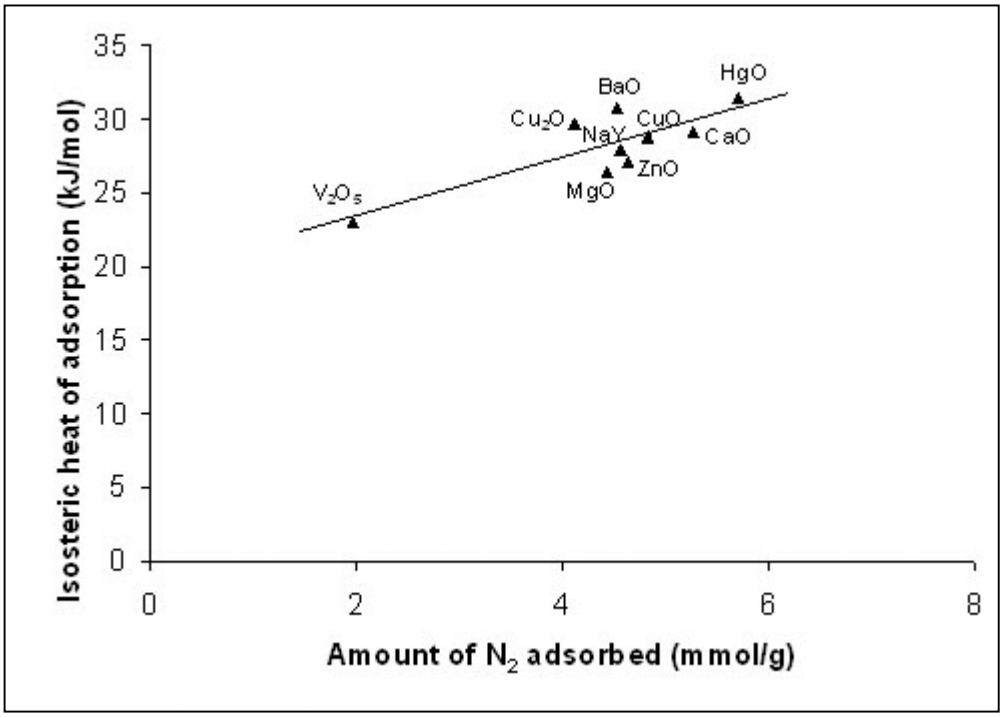

Figure 6.28: Relationship between N_2 adsorption capacity and isosteric heat of adsorption.

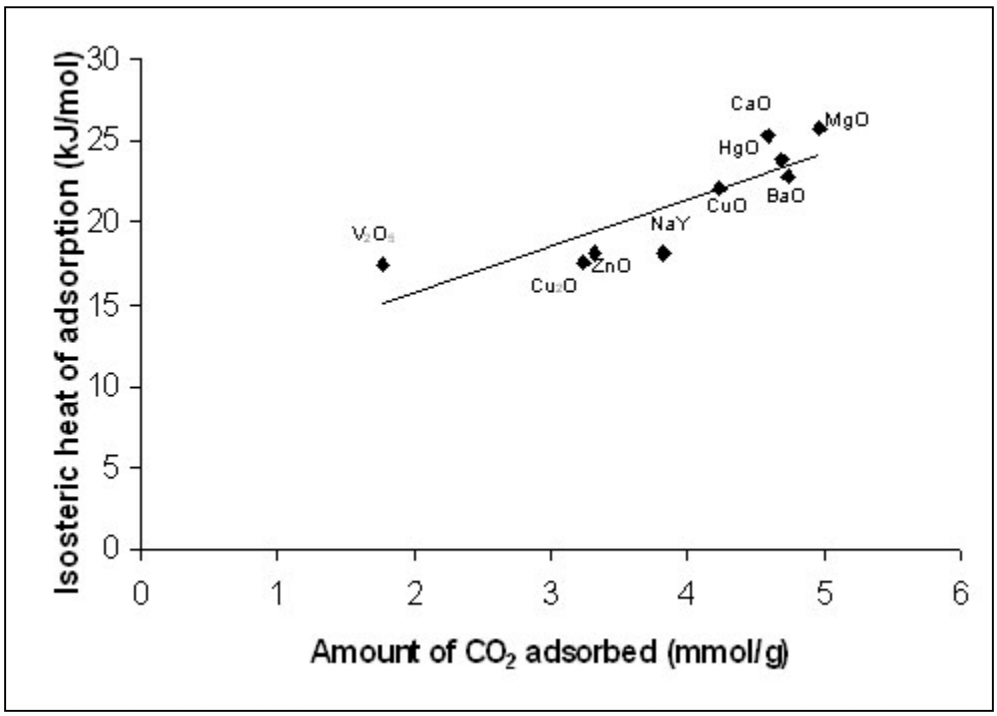

Figure 6.29: Relationship between CO_2 adsorption capacity and isosteric heat of adsorption.

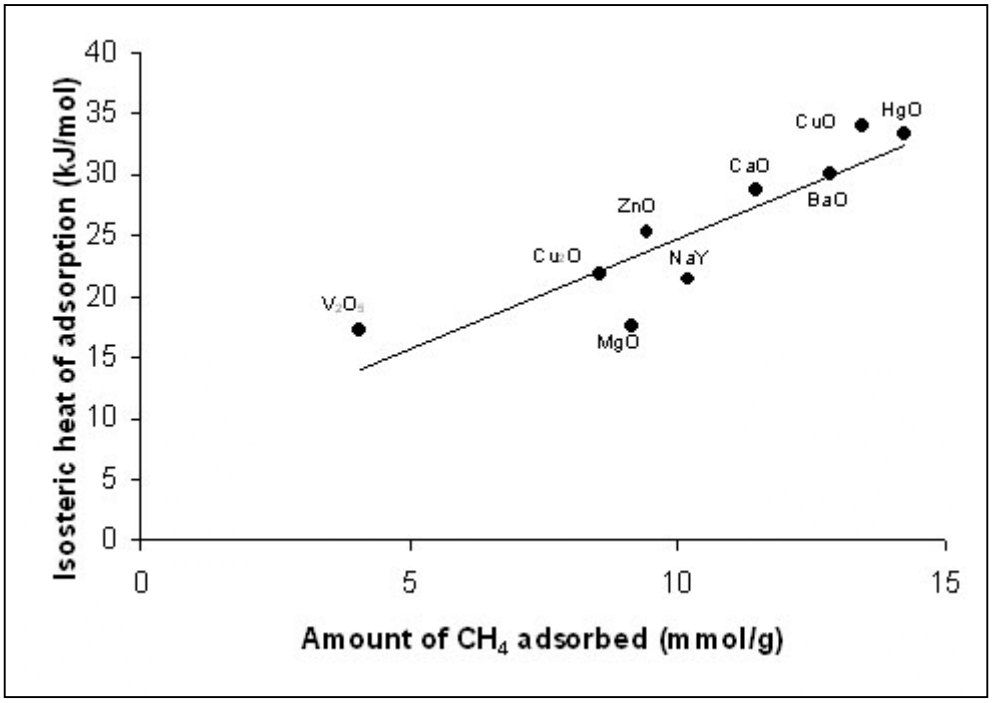

Figure 6.30: Relationship between CH_4 adsorption capacity and isosteric heat of adsorption.

For instance, the value of N_2 isosteric heat of adsorption and entropy are 27.9 kJ/mol and 121.8 J/mol.K (Table 4.10) for the starting Na-Y and increased by adding several types of metal oxides (CaO, BaO, CuO, HgO). Different types of adsorbates were presenting different isosteric heat of adsorption behaviour. It was observed that the isosteric heat of N_2 adsorption for different types of modified samples were closed together and indicated the highest heat of adsorption, compared to gas CO_2 and CH_4. These probably are due to the adsorption characteristics of gas nitrogen that mainly controlled by the micropore of adsorbents. Meanwhile, gas methane poses intermediate heat of adsorption value is because of the effect of micropore adding by active adsorption sites on the adsorbent surfaces. Gas carbon dioxide on the other hands give less interaction with the adsorbents, high mobility on active adsorption sites on the surfaces, thus less isosteric heat of adsorption and entropy properties were obtained.

Table 6.10: Enthalpy and entropy of gaseous adsorption.

Sample	Gas carbon dioxide		Gas nitrogen		Gas methane	
	ΔH_{st} (kJ/mol)	ΔS (J/mol.K)	ΔH_{st} (kJ/mol)	ΔS (J/mol.K)	ΔH_{st} (kJ/mol)	ΔS (J/mol.K)
NaY	18.1	92.7	27.9	121.8	21.4	95.5
MgO/NaY	25.7	115.2	26.4	118.3	17.6	78.7
CaO/NaY	25.3	114.3	29.1	124.3	28.7	117.3
BaO/NaY	22.8	106.2	30.6	130.9	30.0	120.5
Cu_2O/NaY	17.6	92.4	29.6	128.4	21.8	97.8
CuO/NaY	22.0	104.7	28.8	124.3	34.1	133.1
ZnO/NaY	18.1	94.3	27.1	119.8	25.4	108.1
HgO/NaY	23.8	109.6	31.3	130.7	33.2	129.7
V_2O_5/NaY	17.5	98.5	23.1	114.9	17.3	92.0

6.3.2.2 Effect of different metal oxide

Different types of metal oxides modified Na-Y also give significant variety in their isosteric heat of adsorption as well as entropy properties. The largest increase in the nitrogen enthalpy and entropy among the oxides was obtained for HgO modified Na-Y which are 31.3 kJ/mol and 130.7 J/mol.K, respectively. As for carbon dioxide, MgO/NaY give the most pronounce effect for increasing the Na-Y isosteric heat of adsorption from 18.1 to 25.7 kJ/mol. CuO/NaY on the other hands enhances the methane and adsorbents interaction with the increase of isosteric heat of adsorption up to 59 %. Meanwhile, V_2O_5 modified Na-Y showed the least heat of adsorption as well as entropy compared to unmodified Na-Y for all three types of adsorbate. Hence, the physicochemical properties of metal oxides that dispersed on the zeolite surfaces would alter the properties of adsorbent and give influences to the adsorbate adsorption characteristics.

According to Savitz *et al.* (2000), one can make a reasonable assumptions that the van der Waals and electrostatic components are additive. By taking this peculiarity, the adsorbate interactions with metal oxides particularly and effect of metal oxides added to Na-Y zeolite can be determined from the difference between the isosteric heats on the metal oxide modified Na-Y samples and unmodified zeolite Na-Y. From the results obtained, the heat of adsorptions for gas CO_2, N_2 and CH_4 that are less to unmodified zeolite Na-Y will indicate less gas interaction with adsorbents. For example, Cu_2O/NaY, ZnO/NaY and V_2O_5/NaY samples indicated lower isosteric heat of carbon dioxide adsorption and entropy properties compared to unmodified Na-Y zeolite. Meanwhile, MgO/NaY and V_2O_5/NaY show less isosteric heat of nitrogen and methane adsorption released during the adsorption process compared to unmodified Na-Y. As a consequence, less gas adsorption capacity was obtained.

6.3.3 Adsorption kinetics

6.3.3.1 Initial gas uptake rate

In adsorption kinetics study, the initial uptake rate was measured during the initial period of adsorption at constant volume, pressure and temperature condition using Equation 2.8. Generally, initial gas uptake rate constants are linearly related to the diffusion coefficient as well as energy of activation for diffusion as given by Equation 2.11 (Hernández-Huesca *et al.*, 1999). There are many factors governing the peculiarity of gases diffusion for metal oxide modified Na-Y. These include the structure changes (pore sizes) associated with physical treatment; metal oxide distribution; particle size and temperature of adsorption.

Gas carbon dioxide uptake rates for the first 20 minutes of adsorption is found to be always faster than gas methane and followed by gas nitrogen. On this basis, it can be assumed that if the gaseous mixture is put into contact with zeolite as adsorbent in a short time adsorption process, gas CO_2 would be adsorbed preferentially. The adsorption of gases by Na-Y and metal oxide modified Na-Y adsorbents have rapid uptake in the early period, while it slows down at latter periods of the adsorption process. For an example, these adsorption equilibrium and kinetics characteristics were illustrated in Figure 4.31 for MoO_3 modified Na-Y zeolite. The amount of gas adsorbed has been normalized in order to compare the initial gas uptake rates for different types of adsorbate. Gas carbon dioxide adsorbed rapidly to around 0.76 fractional uptake of CO_2 in 20 minutes. Gas methane with a slower uptake rate, achieved the same amount of adsorbate in 35 minutes time. Meanwhile, gas N_2 only obtained 0.06 fractional uptake of nitrogen for the initial 20 minutes of adsorption.

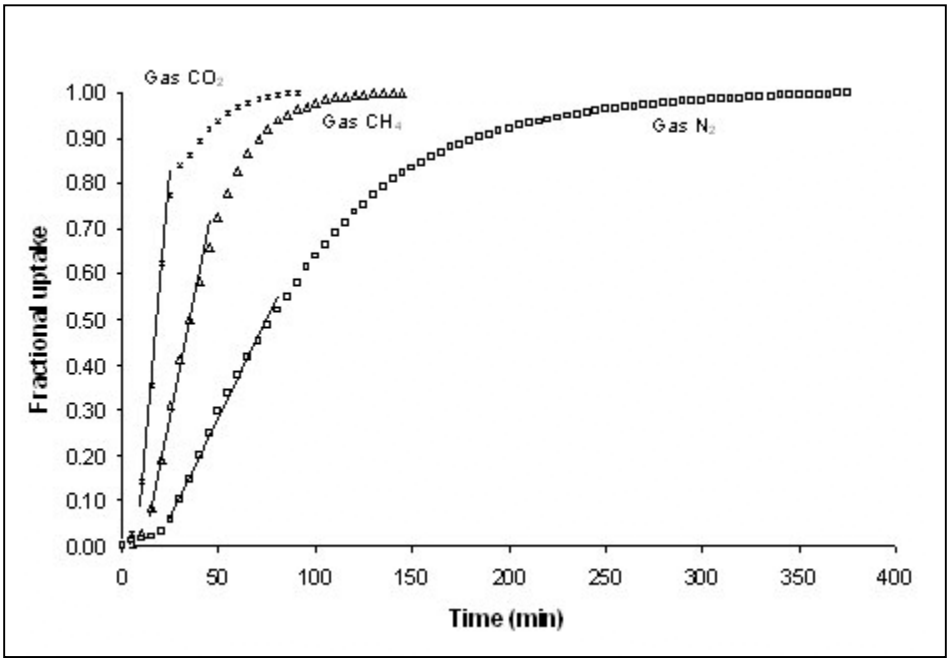

Figure 6.31: Gases adsorption characteristics of MoO_3 modified Na-Y adsorbent at 138 kPa and 323.15 K.

Different types of adsorbate and metal oxide strongly influence the equilibrium adsorption time requirement as well as its gas adsorption kinetic characteristics. The adsorption time that required for an adsorbate to reach equilibrium was shown in Appendix B. In average, the time to reach equilibrium is 120 minutes for CO_2, 120 minutes for CH_4 and 300 minutes for N_2. As in Table 6.11, generally gas nitrogen would take longer time to reach equilibrium compared to gas carbon dioxide and gas methane. However, it was found out that even though the CO_2 adsorption process for several types of samples studied reached the saturation condition faster than methane adsorption process, the adsorption capacity is still lower compared with methane. These results touted that the adsorption processes that reach equilibrium state faster would not necessary result in higher adsorption capacities. It depends on the structure and physical properties of adsorbate and adsorbent as well as the extent of interaction of adsorbate with adsorbent surfaces (Hassan *et al*., 1995; Massman, 1998; Marecka and Mianowski, 1998; Steel and Koros, 2003; Ahn *et al*., 2004; Luca *et al*., 2004).

Table 6.11: Equilibrium adsorption time requirement for adsorbents studied.

Group of Elements (Periodic Table)	Samples	Gas CO_2 (min)	Gas N_2 (min)	Gas CH_4 (min)
-	NaY	90	275	105
IIA	MgO/NaY	125	330	65
	CaO/NaY	180	230	65
	BaO/NaY	170	245	60
IIIA	Ga_2O_3/NaY	180	305	200
IVA	GeO_2/NaY	110	300	305
	SnO/NaY	60	350	145
	PbO/NaY	75	245	65
IB	Cu_2O/NaY	160	350	125
	CuO/NaY	70	260	55
	Ag_2O/NaY	95	290	130
IIB	ZnO/NaY	155	280	95
	HgO/NaY	135	160	60
IIIB	Y_2O_3/NaY	110	290	80
VB	V_2O_5/NaY	140	330	60
VIB	MoO_3/NaY	90	390	145
	WO_3/NaY	100	375	130
VIIIB	Fe_2O_3/NaY	135	390	85
	Co_3O_4/NaY	115	345	190
	NiO/NaY	90	245	145
	PdO/NaY	140	350	200

6.3.3.2 Diffusion rate constant

By employing the metal oxides-Na-Y zeolite modification, the gas adsorption kinetics is improved significantly. Adsorption kinetics was measured from the adsorbate uptake curves versus time of the three gases until equilibrium was reached. Based on Equation 2.10, the linear parts of the initial adsorption curves were selected to calculate the gas diffusion parameter, D/R^2 in unit s^{-1}. The slopes of the curves (diffusion parameter, D/R^2) can be used to characterize the system towards equilibrium. Figures 6.32 to 6.34 illustrate the kinetics of diffusion of gas CO_2, N_2 and CH_4 into unmodified Na-Y and some representative metal oxide modified Na-Y adsorbents at 138 kPa and 323.15 K. As shown in Figure 6.32, gas CO_2 adsorb rapidly early in the adsorption period, while it slows down tentatively when the adsorption reached about 0.60 fractional uptake. The slopes of the initial uptake for metal oxide modified Na-Y zeolite samples obtained seem to have no significant difference with unmodified Na-Y zeolite. Meanwhile, gas nitrogen diffusivities show a stable gas uptake until the adsorption process reached the equilibrium (Figure 6.33). For gas methane diffusion characteristics, the differences of diffusion uptake rate of studied samples are rather significance as illustrated in Figure 6.34.

The adsorption kinetics of three gases behaves differently. However, the similar trends were observed from the slopes of the curves plotted suggest that the faster adsorption kinetic rates are, resulted in the significant improvement on the gases adsorption capacities. The gas diffusion parameters (D/R^2) of studied adsorbents are summarized in Table 6.12. As is presented by the results, the adsorption kinetics behavior of metal oxide modified Na-Y zeolite obeys the Fick's second diffusion law. All the correlation coefficients for linear regression using least squares method analysis are larger than 0.99, except for some samples of gas CO_2 adsorption. Furthermore, the diffusion parameters have clear trends, the higher adsorption rate at initial stage resulted in higher adsorption capacity because of the higher driving force in the adsorption process.

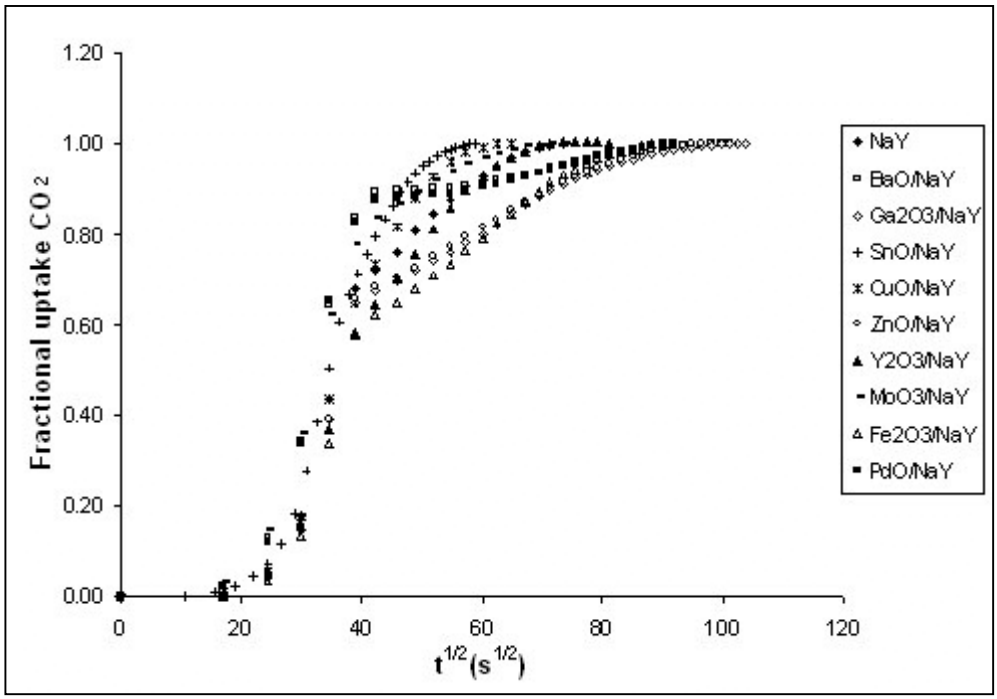

Figure 6.32: Kinetics of CO_2 diffusion into Na-Y and metal oxide modified Na-Y adsorbents at 138 kPa and 323.15 K.

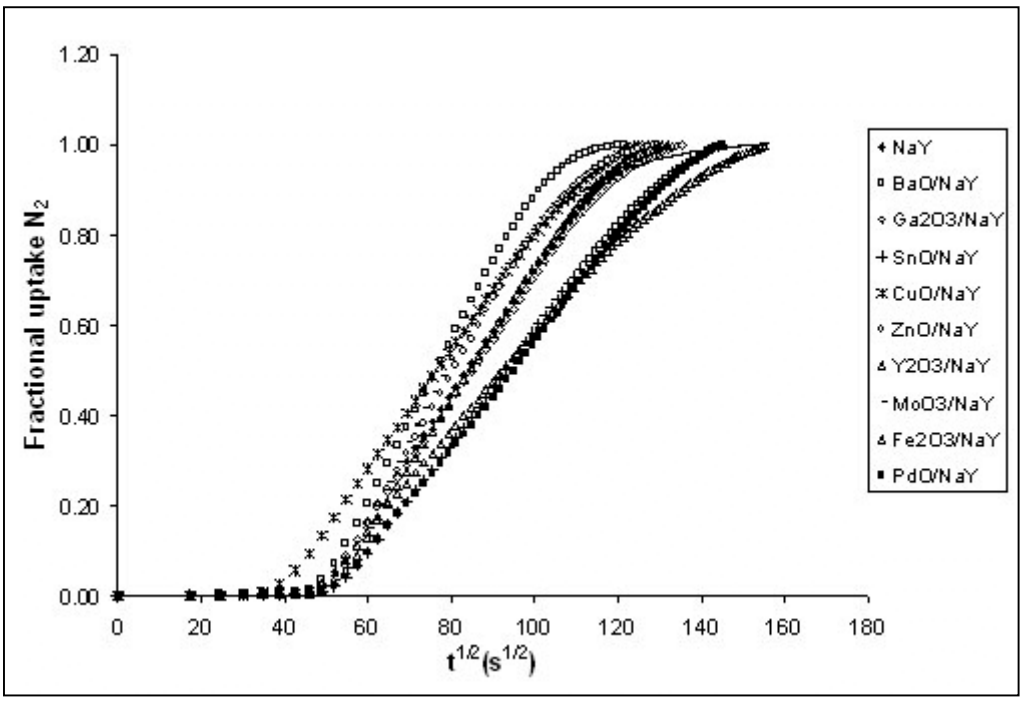

Figure 6.33: Kinetics of N_2 diffusion into Na-Y and metal oxide modified Na-Y adsorbents at 138 kPa and 323.15 K.

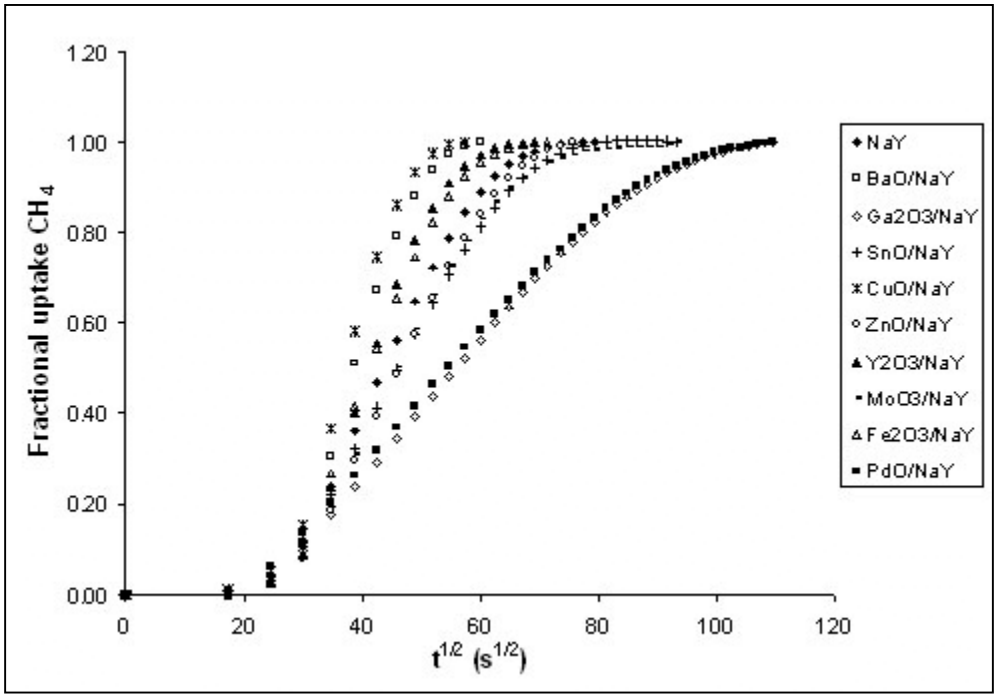

Figure 6.34: Kinetics of CH_4 diffusion into Na-Y and metal oxide modified Na-Y adsorbents at 138 kPa and 323.15 K.

According to Hasegawa *et al*. (2001), the N_2 diffusivities were not strongly affected by the adsorption but might be related to the size of micropores. Therefore, N_2 molecules slowly diffuse through the macropores, transport through pore mouth barrier and diffuse into the micropore system. That is the reason showing the stable gas uptake rate of samples as obtained in this study. Metal oxide dispersed mostly stay on the external surface and in the pore mouth region of the zeolite, in which give influences to the nitrogen diffusivity. For gas CH_4, the adsorption is somehow related to the size of micropores adding by the interaction with adsorbent surfaces. Hence, the rate constants for some metal oxides modified Na-Y are significantly higher compared to unload Na-Y. In the case of CO_2, the interaction between carbon dioxide and adsorbent could affect the diffusivity of CO_2. The transport of gas CO_2 on the surfaces has been described as molecules jumping from one adsorption site to another (Hasegawa *et al*., 2001).

The diffusion parameters as observed from Table 4.12 to achieve equilibrium status are following the sequences of $CO_2 > CH_4 > N_2$. This is due to the smallest

kinetic diameter of gas CO_2 molecule to diffuse easily into zeolite micropore system. Adsorption energy of CO_2 is also found to be always larger than that of methane and much larger than that of nitrogen for the adsorption into pores at all size ranges (Hassan *et al*., 1995; Charmette *et al*., 2004; Cui *et al*., 2004; Luca *et al*., 2004). It is suggested that CO_2 diffuses easily into the micropore system at the initial stage, the strong quadrupole and dipole interaction of the CO_2 molecules and the adsorbents at longer time adsorption would reduce the probability of a jump and as a result suppress the CO_2 diffusion significantly at higher coverage as revealed in Figure 6.32. Results also found out that metal oxide modified Na-Y zeolite samples do not significantly increase the CO_2 diffusion parameters even though they slightly enhance the CO_2 adsorption capacity. In other words, metal oxide dispersion play the main role to the change of Na-Y zeolite pore mouth barrier as well as micropore size and shape, rather than act as active adsorption site on the zeolite surfaces.

Based on the gas characterization data – adsorption equilibrium and adsorption kinetics presented, it is believed that dispersion of metal oxide onto Na-Y greatly influence the surface reactivity of metal oxide with gases and produce high adsorption capacity. The pore structure and pore sizes that changed after the modification do responsible as well for the improvement of adsorption properties of zeolite.

Table 6.12: Gases adsorption kinetics for various adsorbents.

Group of Elements (Periodic Table)	Samples	Gas CO_2 D/R^2 ($\times 10^{-4}$ s^{-1})	R^2	Gas N_2 D/R^2 ($\times 10^{-5}$ s^{-1})	R^2	Gas CH_4 D/R^2 ($\times 10^{-4}$ s^{-1})	R^2
-	NaY	2.89	1.000	1.76	1.000	0.69	0.999
IIA	MgO/NaY	3.38	0.991	2.48	0.999	0.28	1.000
	CaO/NaY	3.27	0.995	3.99	0.999	1.84	0.999
	BaO/NaY	2.90	0.991	2.81	0.999	1.78	0.999
IIIA	Ga_2O_3/NaY	1.91	0.998	1.74	1.000	0.22	1.000
IVA	GeO_2/NaY	2.32	0.982	1.46	1.000	0.17	1.000
	SnO/NaY	2.95	0.996	1.23	1.000	0.51	1.000
	PbO/NaY	1.94	0.982	0.69	1.000	1.58	0.997
IB	Cu_2O/NaY	2.16	0.997	1.34	1.000	0.41	1.000
	CuO/NaY	2.91	1.000	1.58	0.999	2.07	0.998
	Ag_2O/NaY	2.05	0.981	2.16	1.000	0.52	0.999
IIB	ZnO/NaY	2.82	0.996	2.62	0.999	0.56	0.999
	HgO/NaY	2.82	0.990	3.02	0.999	1.95	0.999
IIIB	Y_2O_3/NaY	2.08	0.999	1.76	0.999	1.25	0.996
VB	V_2O_5/NaY	0.14	0.987	0.65	0.999	0.33	0.998
VIB	MoO_3/NaY	2.03	0.986	1.70	0.999	0.61	0.998
	WO_3/NaY	2.68	0.982	1.63	1.000	0.56	1.000
VIIIB	Fe_2O_3/NaY	2.28	0.994	1.26	0.999	1.05	1.000
	Co_3O_4/NaY	2.34	0.994	1.26	1.000	0.27	1.000
	NiO/NaY	2.85	0.989	1.76	0.999	0.38	1.000
	PdO/NaY	2.75	0.986	1.15	1.000	0.18	1.000

6.3.4 Gas – zeolite interactions

The understanding of interaction between the adsorbed molecules on a metal oxide modified Na-Y zeolite surface is of important phenomenon. In situ FTIR spectroscopy is a powerful tool for studying the adsorbed species interaction with zeolite surface directly and the transport of interacting molecules in micropores of zeolites and modified zeolite systems (Bludau *et al*., 1998). In this study, adsorptions of N_2, CO_2 and CH_4 on Na-Y zeolite at room temperatures were studied by transmission FTIR spectroscopy. These gases have different polarity, electrostatic multi-pole moments and molecular sizes (Arcoya *et al*., 1996). The background spectrum, obtained after activation of the zeolite at 673.15 K for 2 hours but before adsorption of gas, was subtracted in each case. Thus, all of the FTIR spectra obtained are the result of the interaction of gas with the zeolite surface only.

6.3.4.1 Interaction of N_2 on metal oxide modified Na-Y zeolite

Non-polar gas N_2 that presents very weak base property would interact with strong acid sites in zeolite. Vibration of homomolecular diatomic nitrogen are infrared inactive in the gas phase (Ingle and Crouch, 1988). However, adsorption in zeolite cavities would reduce the molecular symmetry of these molecules and results in the appearance of interaction in IR spectra (Wakabayashi *et al*., 1997; Valyon *et al*., 2003; Coluccia *et al*., 1999; Šljivančanin and Pasquarello, 2004). One can obtain the frequency of N-N vibrations of nitrogen in gas phase at 2330 cm^{-1} from Raman spectra.

In the present study, N_2 adsorption (equilibrium pressure was fixed at 138 kPa) was carried out at 298.15 K of some selected samples (NaY, Ag_2O/NaY, Cu_2O/NaY, MgO/NaY, CaO/NaY, BaO/NaY, CuO/NaY, ZnO/NaY, HgO/NaY, V_2O_5/NaY) for the sake of brevity. The N≡N stretching vibrations of the molecules adsorbed on Lewis acid centers fall in the region of 2360 – 2300 cm^{-1}. For all samples, a main absorption band is observed at 2340 - 2350 cm^{-1}, which can be assigned to N≡N stretching vibration in the N_2 molecule adsorbed on the metal cation species that existed on the zeolite surface. The appearance of such a FTIR band indicates a strong interaction between the N_2 molecule and metal cation species. Figure 4.35 reveals the areas under the peak corresponding to the physically adsorbed nitrogen species (2360 – 2300 cm^{-1}) increased roughly linear with the corresponding adsorbed amounts which were measured earlier through Thermogravimetric Analyzer. The difference should be caused by the fact that the adsorption temperature used here (298.15 K), which was restricted by the apparatus condition, was lower than the adsorption temperature using gravimetric method in this study.

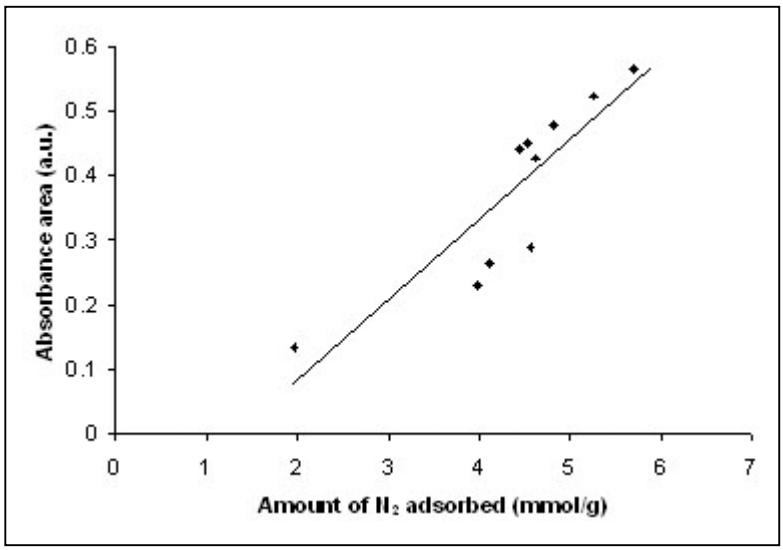

Figure 6.35: The corresponding areas of the FTIR spectrum peak at (2300 – 2360 cm^{-1} region) versus the amount of N_2 adsorbed on samples.

It has been also shown that nitrogen interacts with surface Si-OH groups to forms H-complexes when it is adsorbed on zeolite Na-Y. Figures 6.36 (a) and (b) show the FTIR spectrum of the original OH groups in the samples that being calcined at 673.15 K. A narrow absorption band with a maximum at 3695 cm^{-1} is observed, which is typical of silica and is assigned to vibrations of the Si-OH groups. Nitrogen also interacts with Si-OH groups upon absorption on SiO_2 to form H-complexes. For convenience, it is obvious that the intensity of the absorption band at 3200 – 3800 cm^{-1} region is enlarged in spectra (c) and (d) after N_2 adsorption. When N_2 interact with the Me-O-OH groups, H-complexes are formed, the band due to the original OH groups weakens, and bands due to the hydrogen bonded Me-O-OH groups at 3346 cm^{-1} (Na-Y) and 3358 cm^{-1} (HgO/Na-Y) appear. The extra absorption peaking at 3245, 3513 and 3543 cm^{-1} bands observed on HgO/Na-Y sample after N_2 adsorption may assigned to the strong interaction of N_2 molecule to the hydrogen bonded Hg-O-OH groups.

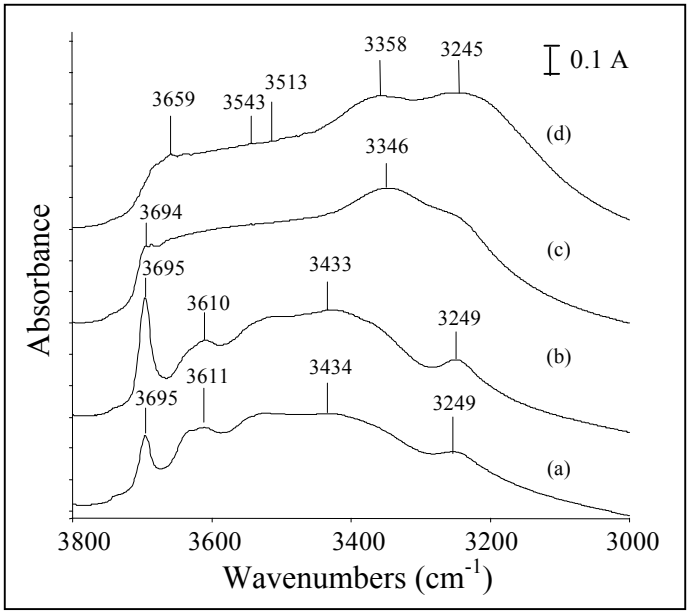

Figure 6.36: FTIR spectra of: (a) activated Na-Y (673.15 K); (b) activated HgO/NaY (673.15 K); (c) N_2 adsorbed at 298 K on Na-Y (135 kPa); and (d) N_2 adsorbed on HgO/Na-Y at 298 K and 138 kPa.

On the other side, the FTIR spectra of N_2 adsorbed on Na-Y and group IIA metal oxides modified samples (in the region 2320 –2360 cm^{-1}) are shown in Figure 4.37. The spectrum of Na-Y (a) shows absorption bands with maximum at 2332 and 2347 cm^{-1}, respectively. The appearance of weak band at 2332 cm^{-1} was assigned to polarization of N_2 molecules adsorbed on Na^+ site, while strong band observed at 2347 cm^{-1} was assigned to the vibrations of nitrogen bound to aluminum cation Lewis site (Malyshev *et al*., 2005b). It was noted that the ν(NN) is shifted upward with respect to the gas phase (blue shift 2 cm^{-1}). The positive shift of the ν(NN) was always observed when these molecules are axially perturbed by an electric field generated by a sodium or hydrogen site with positive character.

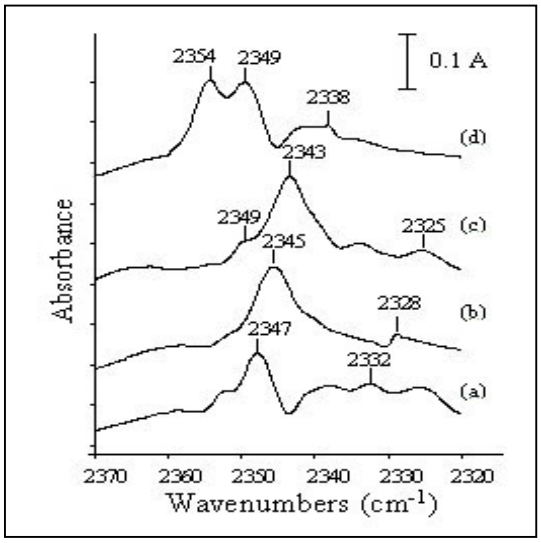

Figure 6.37: FTIR spectra of N_2 dosed on: (a) Na-Y; (b) MgO/NaY; (c) CaO/NaY; and (d) BaO/NaY at 298 K and equilibrium pressures fixed at 138 kPa.

For metal oxide modified zeolite NaY (spectra b to d), an asymmetrical contour with a peak at 2340 - 2360 cm^{-1} is observed in the region of N-N vibrations. This band can be assigned to N-N vibrations in the complexes with Lewis sites (Mg^{2+}, Ca^{2+}, Ba^{2+}) of samples. In general, the N-N stretching mode can be blue or red shift up to 30 cm^{-1} towards higher frequencies (reaching the value of 2360 cm^{-1}) that due to σ-donation of electrons from N_2 to the surface of acid site. The stronger the adsorption, the larger is the frequency shift. These spectrums reveal the adsorptions of nitrogen on metal oxides (Lewis sites) are differing in nature and

strength from the acid sites of zeolites. Different types of metal oxides even in the same Group II A caused different orientation of N≡N interaction with metal species. For BaO modified Na-Y sample, the band of 2345 cm^{-1} become weaken, while the shoulder band of 2349 cm^{-1} increased with two intense satellites at 2338 and 2354 cm^{-1} that become clearly visible.

It was inferred that the size of metal cations dispersed on the surface give great effect to the changes of zeolite structural properties as well as differ the gas adsorption characteristics. The larger shift of the N≡N stretching vibrations for modified zeolite samples indicated that dispersed metal oxides increased the strong Lewis sites in Na-Y zeolite; further by strengthen the adsorbate-adsorbent interaction which plays the main role in the enhancement of nitrogen adsorption capacity and selectivity.

Apart from that, the band shift relative to the frequency of the N_2 Raman band (2330 cm^{-1}) can provide the orientation of adsorbed species with respect to the zeolite surfaces. The *v*NN band appears at higher frequency, when the molecular axis of the adsorbed N_2 is oriented parallel with the active adsorption site (end-on adsorption) and at lower frequency, when the molecule is oriented perpendicular (side-on adsorption) or inclined to the direction of the sites (Lónyi *et al*., 2003). Thereinafter, most of the *v*NN component bands in this study at higher frequency after metal oxide modification are attributed to N_2 molecules in end-on position on the adsorption sites.

In order to investigate the effect of equilibrium pressure to the mechanism of gas interaction with zeolite surfaces, the adsorption of nitrogen molecules at room temperature (298 K) with increasing pressure on HgO modified zeolite Na-Y was carried out as shown in Figure 4.38. The integrated absorbance of the stretching bands changed with the pressure, but the band frequencies almost unchanged. The FTIR spectra show, at the lowest pressure 34 kPa, only one symmetric band at 2348 cm^{-1} was detected and attributed to linear Hg^{2+}- N_2 species. An increase of the

equilibrium pressure resulted in an increase of the intensity and development of a new band at 2343 cm^{-1} which assigned to $Hg^{2+}(N_2)_2$ germinal complexes. At the highest pressure (spectra e), the two bands intend to form a nearly symmetric envelope, accompanied by broadening and intensity decrement that evident in Figure 6.39. The peak area in the 2340 – 2352 cm^{-1} region decreases as nitrogen adsorption achieved the saturation condition (Figure 6.39).

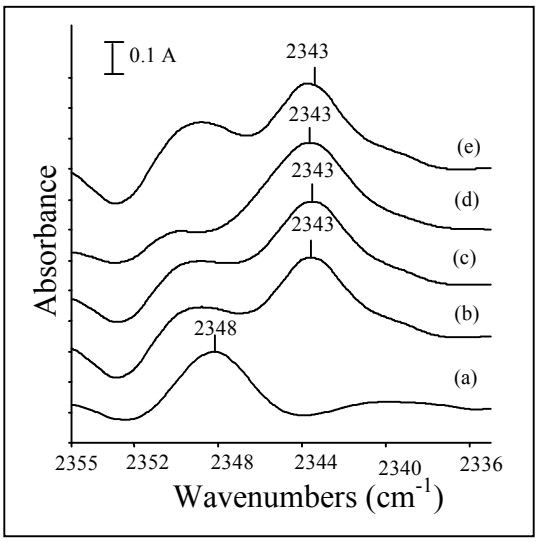

Figure 6.38: FTIR spectra of N_2 adsorbed on HgO/Na-Y at 298 K and equilibrium pressure: (a) 34 kPa; (b) 69 kPa; (c) 138 kPa; (d) 207 kPa; and (e) 276 kPa.

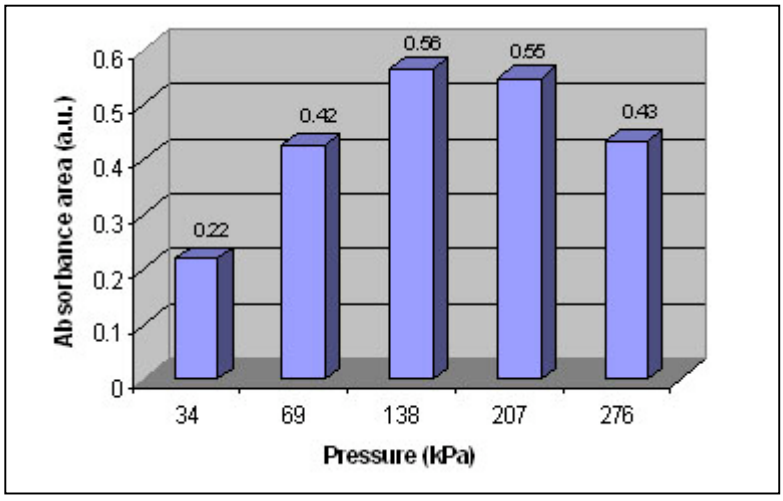

Figure 6.39: Effect of equilibrium pressure on the FTIR absorbance areas (2340 – 2352 cm^{-1} region) and gas N_2 adsorption characteristics.

This result is consistent and well proven by Llewellyn and Maurin (2005) regarding on adsorbate-adsorbent interaction discussion. Accordingly, the interaction of an adsorbate molecule for energetically heterogeneous adsorbent such as modified zeolite, which their pore size distribution and surface chemistry have been varied by metal oxide dispersion, relatively strong interaction between the adsorbing molecules and the surface happens initially. The strength of these interactions will then decreases (absorbance areas) as these specific sites are occupied or reached saturation capacity.

6.3.4.2 Interaction of CO_2 on metal oxide modified Na-Y zeolite

Carbon dioxide gas adsorption has been widely studied on zeolite. CO_2 is frequently employed to probe the Lewis acid sites of both metal oxides and zeolites, as it can interact with cations in low coordination. It can also monitor the properties of the basic surface centers (Coluccia *et al*., 1999). As being reported, the experiments that performed at room temperature do not allow one to obtain significant coverage of hydroxyl groups and Brønsted hydroxyl groups' interaction with the adsorbed molecules (Coluccia *et al*., 1999). In addition, no modification have been done to substitute the cation Si or Al. Since the study focuses on the effect of Lewis acid sites (metal oxide) on Na-Y adsorption characteristics, the interaction with hydroxyl groups (3700 –3000 cm^{-1}) and Brønsted acid group will not be discussed.

Carbon dioxide is a linear molecule and has four fundamental vibration modes: v_1 1340 cm^{-1}, v_3 2350 cm^{-1} and two bending modes at 666 cm^{-1}, only v_3 and one of the v_2 bending modes that in the plane position are infrared active (Ingle and Crouch, 1988). Due to the limitation of CaF_2 window in the range of 77,000 – 900 cm^{-1}, the vibration of CO_2 molecules will be only detected at 2350 cm^{-1}. FTIR results as presented in Figure 6.40 shows that the bands with the frequencies near

2350 cm^{-1} have been attributed to the v_3 vibration of physisorbed CO_2, which is linearly bound to the cation by ion-induced dipole interaction. It was noted that the FTIR spectra of adsorbed CO_2 in metal oxide modified Na-Y is expected to be similar in some respects to that observed for Na-Y zeolite. The observed peaks in the spectra CO_2 appeared at the same location for the gas phase and adsorbed physisorbed phase.

Meanwhile, a broad band in the 1800–1500 cm^{-1} region were obtained during the adsorption of CO_2 on Na-Y zeolite and metal oxide modified zeolite at room temperature. A band near 1650 cm^{-1} was found in the unmodified Na-Y zeolite, as well as for the MgO, CaO and BaO modified Na-Y adsorbents as shown in Figure 4.40. According to Rakić *et al.* (1999), all the bands found in the 1800 –1200 cm^{-1} region were attributed to CO_2 entrapped in the structure. On the other hands, Rege and Yang (2001) describe these bands as carbonate compound. When the temperature of activation of the sample is below 773.15 K, a relatively large hydroxyl concentration is believed to exist on the surface. CO_2 molecule will react with the hydroxyl groups forming bicarbonates on the surface, characterized by adsorption bands at 1650 cm^{-1}. The formation of these carbonate compounds is expected to be rather slow adsorption at room temperature.

It must be clarified that the so-called carbonate formed in this study were due to the reaction within CO_2 molecule and hydroxyl groups on the surface but not because of the chemisorption process. At high temperature, it is realized that chemical adsorption of CO_2 on zeolite would formed a carbonate structures at 1450 – 1300 cm^{-1} (Lavalley, 1996). Due to no significant bands in this spectral region were observed in the experiments, the chemisorption of carbonate structures on the cations are thus confirmed not occurred. In fact, the heat of carbon dioxide adsorption (17 – 25 kJ/mol) calculated from the adsorption equilibrium falls into the region of physical adsorption.

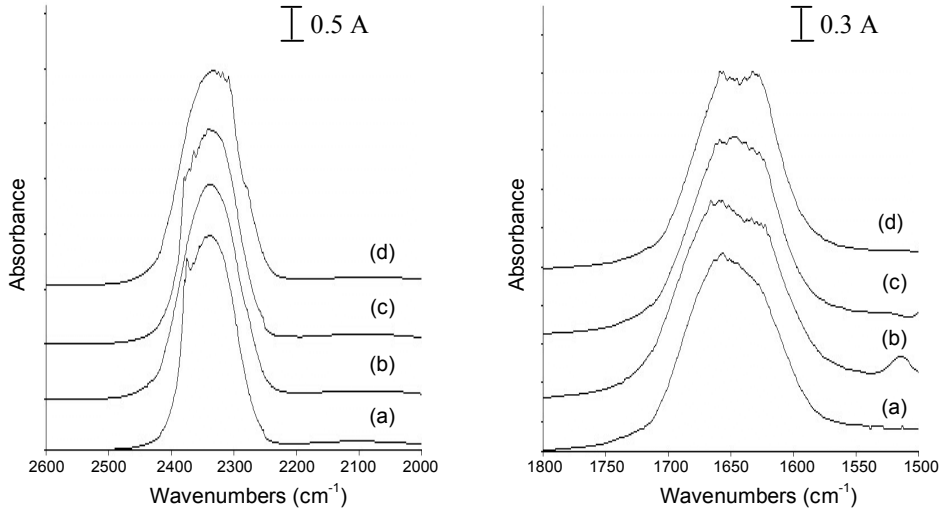

Figure 6.40: FTIR spectra of CO_2 adsorbed on: (a) Na-Y; (b) MgO/NaY; (c) CaO/NaY; and (d) BaO/NaY at 298 K and equilibrium pressures fixed at 138 kPa.

Moreover, as illustrated in Figure 4.41, it was interesting to found that Ag_2O and Cu_2O modified Na-Y consists of shaper band shape and lower peak area compared to CuO/NaY in the region of 1800 –1500 cm^{-1}. Hence, slightly different structural properties of metal oxide as modifiers in the same group would result significant deviation in the surface modification on Na-Y as gas adsorbent.

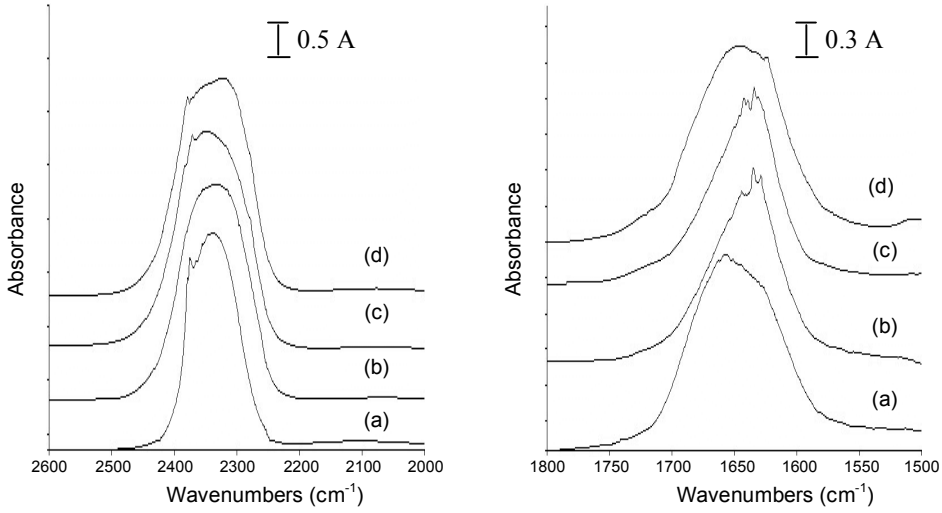

Figure 6.41: FTIR spectra of CO_2 adsorbed on: (a) Na-Y; (b) Ag_2O/NaY; (c) Cu_2O/NaY; and (d) CuO/NaY at 298 K and equilibrium pressures fixed at 138 kPa.

Figure 6.42 shows the FTIR spectra of CO_2 adsorbed, at room temperature and increasing equilibrium pressure, on MgO modified Na-Y zeolite. The peak positions were not shifted by increasing the equilibrium pressure, which is in contradict to the adsorption of gas N_2. However, the peak areas corresponding to the amount of gas adsorbed slightly increased from 350 to 361 arbitrary units for the adsorption equilibrium pressure at 34 kPa to 138 kPa with decreasing intensity. This has been due to increasing dipole-dipole interaction at higher coverage (Scarano *et al*., 2001). Hence, the different arrangements of adsorbed CO_2 on adsorption sites were resulting the lateral interaction effects of different magnitude related to the adsorbent surface coverage.

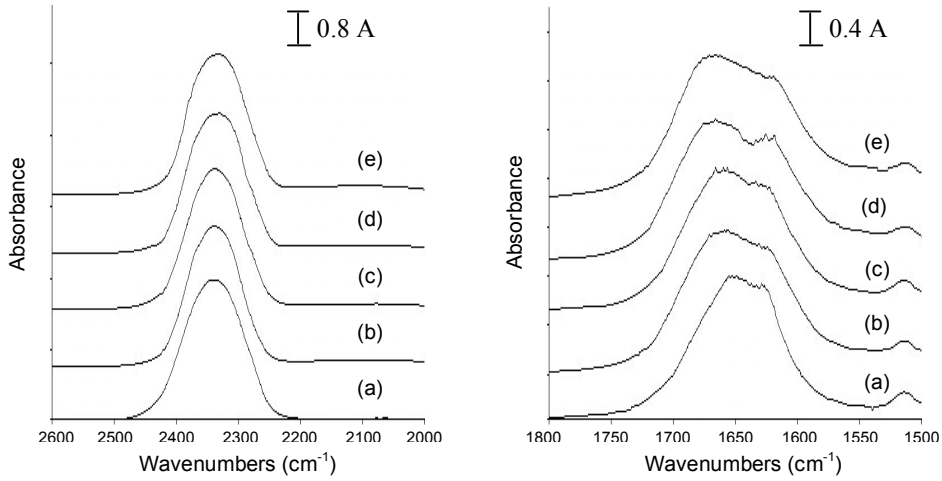

Figure 6.42: FTIR spectra of CO_2 adsorbed on MgO modified Na-Y zeolite at 298 K and pressure: (a) 34 kPa; (b) 69 kPa; (c) 138 kPa; (d) 207 kPa and (e) 276 kPa.

Generally, the main difference of CO_2 absorption bands for different types of metal oxides modified Na-Y is the peak areas corresponding to the physically adsorbed species. As mentioned earlier, the areas of the FTIR absorption peaks are proportional to molar adsorbed amounts. The amount of gas adsorbed for these adsorbate–adsorbent systems were measured using gravimetric experimental technique. Only a few of the sample curves will be shown as revealed in Figure 6.43. Results show the adsorbed amount of CO_2 on Na-Y zeolite and some metal oxide modified Na-Y samples versus the area of the absorbance peak from 2450–2250 cm^{-1} region. It can be seen that the curves were of fairly linear in nature.

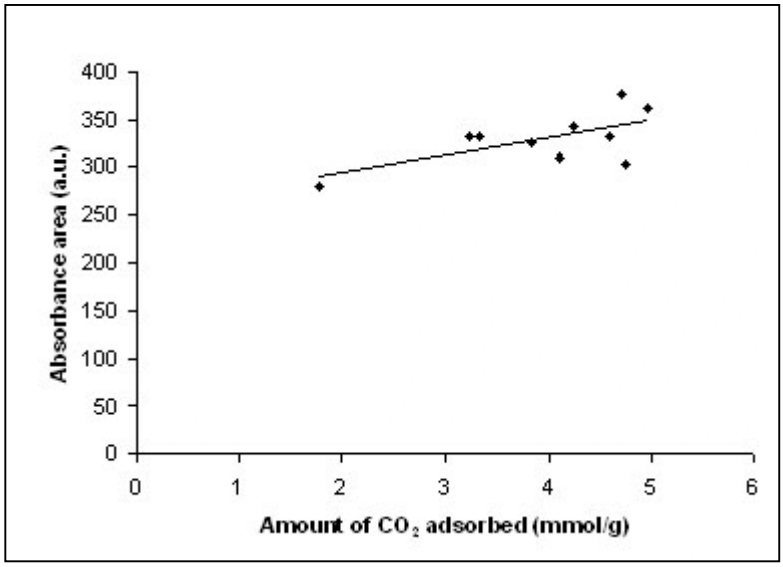

Figure 6.43: The corresponding areas of the FTIR spectrum peak at (2450 – 2250 cm^{-1} region) versus the amount of CO_2 adsorbed on samples.

6.3.4.3 Interaction of CH_4 on metal oxide modified Na-Y zeolite

Gas methane has four fundamental vibrations in the gaseous phase: v_3 (3020 cm^{-1}) and v_4 (1306 cm^{-1}) are infrared active, while v_1 (2914 cm^{-1}) and v_2 (1526 cm^{-1}) are infrared inactive. The gas phase spectrum exhibits the characteristic shape of a rotation-vibration spectrum in the adsorbed samples. The gas phase methane as adsorbed species on zeolite surfaces was found at 3017 ± 1 cm^{-1} (Seidel *et al.*, 2000).

The FTIR spectra of the adsorbed methane on Na-Y and Group IIA metal oxide modified Na-Y at 298.15 K are shown in Figure 6.44 (a). A sharp band around 3015 cm^{-1} and a broad band around 1303 cm^{-1} were assigned to v_3 and v_4 vibrations of adsorbed methane, respectively. The band at 1303 cm^{-1} is assigned to the n bending mode, which has a free molecule value of 1306 cm^{-1}. It is suggested that methane is molecularly adsorbed, forming H_3CH-Me (Me = metal cation) adducts with coordinatively unsaturated metal cations on adsorbent surface. The vibration of

molecular adsorbed methane of MgO/NaY, CaO/NaY and BaO/NaY looked very similar to each other as observed in the spectra. The frequency of adsorbed modified samples with unload Na-Y seem do not cause any significant changes. However, for V_2O_5 modified Na-Y sample (Figure 6.45), the low interaction of CH_4 on modified adsorbent surfaces resulted in the decrease of the absorbance intensity as well as the corresponding peak areas (3035 – 2995 cm^{-1}). This adsorption mechanism brings to the low adsorption capacity of V_2O_5/Na-Y in the equlibrium adsorption process.

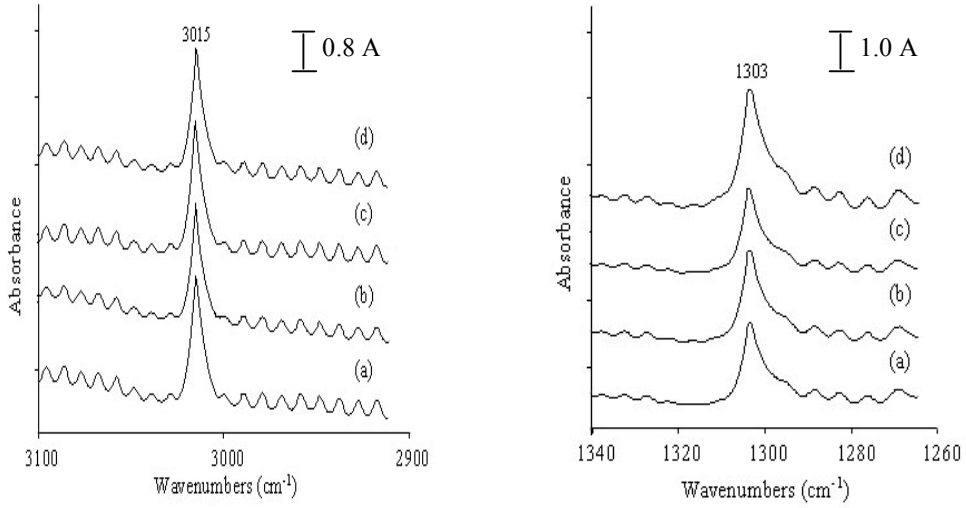

Figure 6.44: FTIR spectra of CH_4 adsorbed on: (a) Na-Y; (b) MgO/NaY; (c) CaO/NaY; and (d) BaO/NaY at 298 K and equilibrium pressures fixed at 138 kPa.

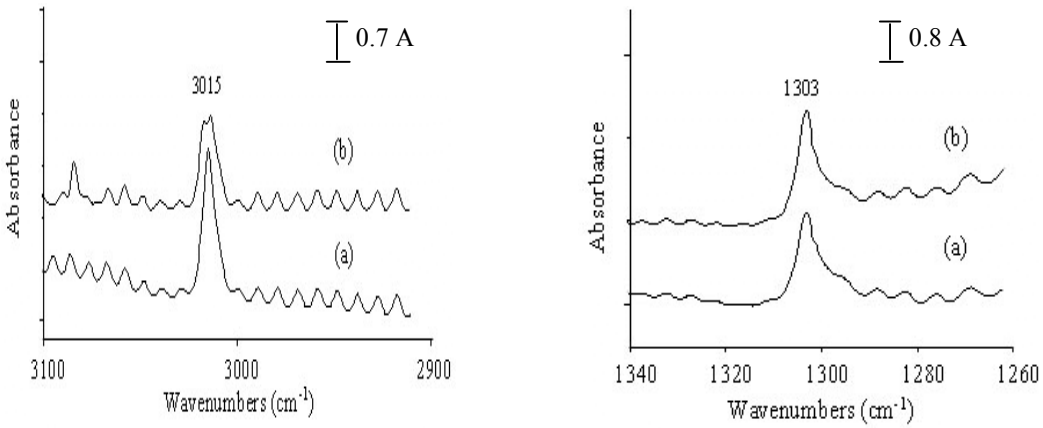

Figure 6.45: FTIR spectra of CH_4 adsorbed on: (a) Na-Y and (b) V_2O_5/NaY at 298 K and equilibrium pressures fixed at 138 kPa.

The salient point in the results obtained are the disappearance of v_1 vibration band, inherently FTIR inactive for gaseous methane. As reported in many literatures for CH_4 adsorption in low temperature and low-pressure conditions, there would be a significantly shifting of spectrum vibration down to a lower frequency as effects of the electric field caused by metal cations on the surfaces (Siedel *et al*., 2000; Yoshida *et al*., 2000; Scarano *et al*., 2001). Therefore, frequency that remain the same before and after the modifications suggested the absent of electric field on the adsorption sites of adsorbents studied. This is impossible as metal oxide dispersion on Na-Y in the previous discussions show significant effect to the gases adsorption capacity as well as adsorption kinetics.

It was very surprising to notice that at room temperature and 39.9 kPa, methane will diffuses into the smaller pores of zeolite system as reported by Yamazaki *et al.* (2000). The above procedures were conducted to compare the adsorption mechanism of CH_4 into the larger pores and smaller pores of zeolite system. The v_3 band (around 3013 cm^{-1}) of methane adsorbed in the smaller pore will always sharper than that on the larger pore surfaces (2914 cm^{-1}). Apart from that, the results from Yamazaki *et al.* (2000) confirmed that an electric field does not exist on the surface of the smaller pores, and the adsorption at these sites are mainly caused by the dispersion force of the pore wall. This is in aggreement with previous discussion that metal oxide would disperse on the larger pores of Na-Y supercages.

It is not suprising that, the kinetic diameter of CO_2, N_2 and CH_4 are larger than the smaller pore of Na-Y zeolite (0.26 nm). Adsorbate molecules are too large to pentrate into small cages windows. However, from the literature, the participation of the sodalite cage protons and OH-group of zeolite Y in the N_2 adsorption process occured at temperature above 298 K (Lónyi *et al*., 2003). Obviously, the interaction of adsorbate with adsorbents is depends both by the strength of the adsorptive site and also on the temperature of adsorption. Therefore, the interaction between adsorbates and zeolite surfaces was found to be favored by the presence of structural defects. Adsorption process at higher temperature (298.15 K) produced higher proton mobility, kinetic energy of adsorbate molecules and flexibility of zeolite framework

(Lónyi *et al*., 2003). This finding is highly supporting the results observed in this study, making the mechanisms of adsorbate-adsorbent interaction completely elucidated. In spite of that, the observed methane spectrum in which the adsorption process carried out at 138 kPa equilibrium pressure and room temperature (298.15 K) are in supercritical adsorption condition. The adsorption mechanisms formed a monolayer coverage as physically adsorbed molecules on the adsorbent surfaces at above methane critical temperature (190.6 K). Therefore, the result shows the nearly similarity of adsorbed methane molecules spectrum with the free gas phase spectrum at wavelength 3015 cm^{-1}.

The results imply that methane adsorbed in the supercages of Na-Y zeolite as well as in the smaller pores as physically adsorbed molecules. Both active adsorption sites contribute to the high methane adsorption capacity. In addition, from the shape of the v_3 band observed, the rotational wings of *P* and *R* branches of the main FTIR peak grow show rotational freedoms of an adsorbed methane molecule on the active adsorption sites is adequately remain. It is therefore suggested that the methane molecule in the pores underwent a symmetrical field from the pore wall.

Moreover, the effect of equilibrium pressure to the mechanism of CH_4 interaction with HgO modified zeolite surfaces were studied at room temperature (298.15 K) with increasing pressure as shown in Figure 6.46. The integrated absorbance areas of the stretching bands and broadening effects were tentatively changed with the pressure, but the band frequencies almost unchanged. It was realized that most of the difference of wavenumbers shifting would be clearly observed with the variation of adsorption temperature. The absorbance areas are subsequently increased with the increase of adsorption equilibrium pressure both in the region of (2990 – 3030 cm^{-1}) and (1315 – 1290 cm^{-1}) as shown in Figure 6.47.

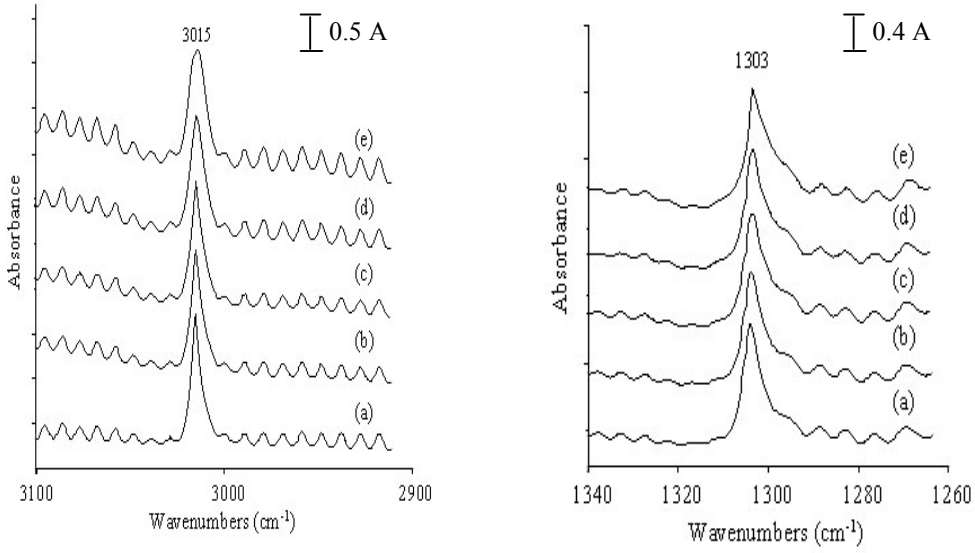

Figure 6.46: FTIR spectra of CH_4 adsorbed on HgO modified zeolite Na-Y at 298 K and equilibrium pressure: (a) 34 kPa; (b) 69 kPa; (c) 138 kPa; (d) 207 kPa; and (e) 276 kPa.

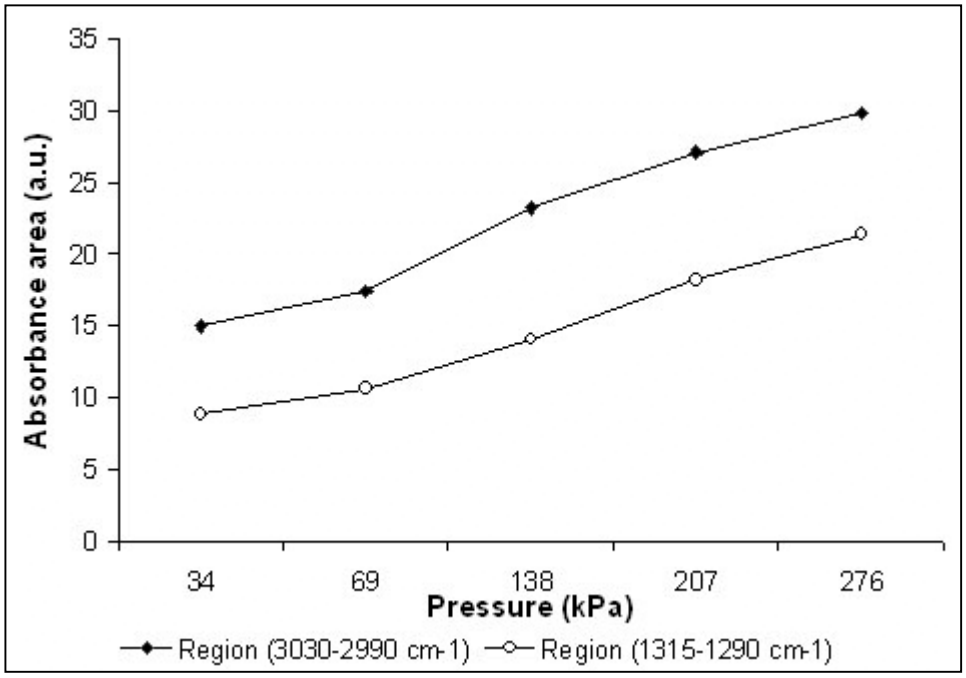

Figure 6.47: The corresponding areas of the FTIR spectrum peak at (3030 - 2990 cm^{-1}) and (1315 - 1290 cm^{-1}) regions versus adsorption equilibrium pressures.

The observed v_3 band and v_4 areas were roughly proportional to the amount of methane adsorption obtained separately by a gravimetric measurement as well. The larger interaction of CH_4 on some metal oxides modified Na-Y adsorbents is surely attributable to the micropore size changes and surface polarity being enhanced by metal oxide dispersion. Apart from that, the availability of active adsorption sites, the pressure and temperature of adsorption are key factors that determined the mechanisms of gases adsorption on the metal oxide modified Na-Y adsorbents.

6.4 Summary

The spontaneous dispersion of metal oxides on Na-Y zeolite adsorbents has been extensively studied for several parametric effects. The adsorption process of zeolites is governed by the pore size and surface properties as well as the strength of adsorbate-adsorbent interactions. The introduction of Group II A metal oxides with high basicity properties on Na-Y greatly improve the CO_2 adsorption performance. Meanwhile, Group II B metal oxides show the great potential as N_2 and CH_4 adsorbents. In adsorption kinetics, the transport of gas molecules into the modified micropore system is obeying the Fick's second diffusion law. The kinetics diameter of adsorbates and their adsorption behaviors on metal oxide modified zeolite play a very important role in determining their adsorption capacity. In addition, the isosteric heat of adsorption and gas-zeolite interaction results also reveals that CO_2, N_2 and CH_4 interact strongly with metal oxides modified Na-Y zeolite.

CHAPTER 7

AMINE-MODIFIED POROUS SILICA AS CO_2 ADSORBENTS

7.1 Introduction

Adsorption is one of the promising methods that is applicable for separating CO_2 from gas mixtures, and numerous studies have been conducted on separation of CO_2 by adsorption using porous materials in the last two decades (Pohorecki and Mozenski, 1998; Baciocchi et al., 2006; Harlick and Tezel, 2004; Song, 2006; Yong et al., 2002). Various adsorbents consist of porous materials, such as MCM-41, activated carbons, zeolites, pillared clays and metal oxides have been investigated (Liu et al., 2007; Sun et al., 2007; Knofel et al., 2007; Siriwardane et al., 2001; Liu et al., 2001; Yang and Liu, 2006; Freitas and Figueiredo, 2001; Matot-Valer et al., 2005; Valente Nabais et al., 2006). Amine functional groups are useful for CO_2 removal because of their ability to form ammonium carbamates and carbonates reversibly at moderate temperature. The incorporation of organic amines into a porous support is another promising approach for CO_2 adsorption combining good capacity and selectivity at moderate temperature. Modifications of porous materials using amines will greatly influence the physicochemical properties of the porous materials and directly affects gases adsorption characteristics of the modified adsorbents. The understanding of structural characteristics and properties before and after the modification, as well as the function of various amines incorporated on the

adsorbents play a vital part in CO_2 adsorption performance. In this regard, this chapter will discuss the characterization of amine modified adsorbents in conjunction to their CO_2 adsorption properties. In order to further understand the adsorbate-adsorbent interaction between CO_2 and modified adsorbents, gas-solid interaction using FTIR spectroscopy has also been included in the discussions.

7.2 Structural Characteristics and Properties

7.2.1 Effects of Various Amines

Powder X-Ray Diffraction has been used to characterize the structure of the materials used in this study. The X-Ray Diffraction (XRD) patterns of synthesized MCM-41 and amine modified MCM-41 are shown in Figures 7.1 and 7.2. As can be seen, XRD pattern exhibit one intense diffraction peak (100) at about 2˚ and three minor peaks indexed as 110, 200 and 210 in the region of 4˚ - 6˚, which are typical of MCM-41 mesoporous phase. From Figure 7.1, 4 peaks were observed, one main peak at 2θ= 2.176˚ corresponding to the 100 plane of MCM-41 which give a value of d_{100} of 4.05nm and 3 smaller peaks at 2θ= 3.747˚, 4.324˚ and 5.708˚ which correspond to the 110, 200 and 210 planes of MCM-41 respectively. The presence of these smaller peaks confirms that long range order was present in the samples (Xu *et al.*, 2002; Zhao *et al.*, 2000; Xu *et al.*, 2003; Kumar *et al.*, 2001).

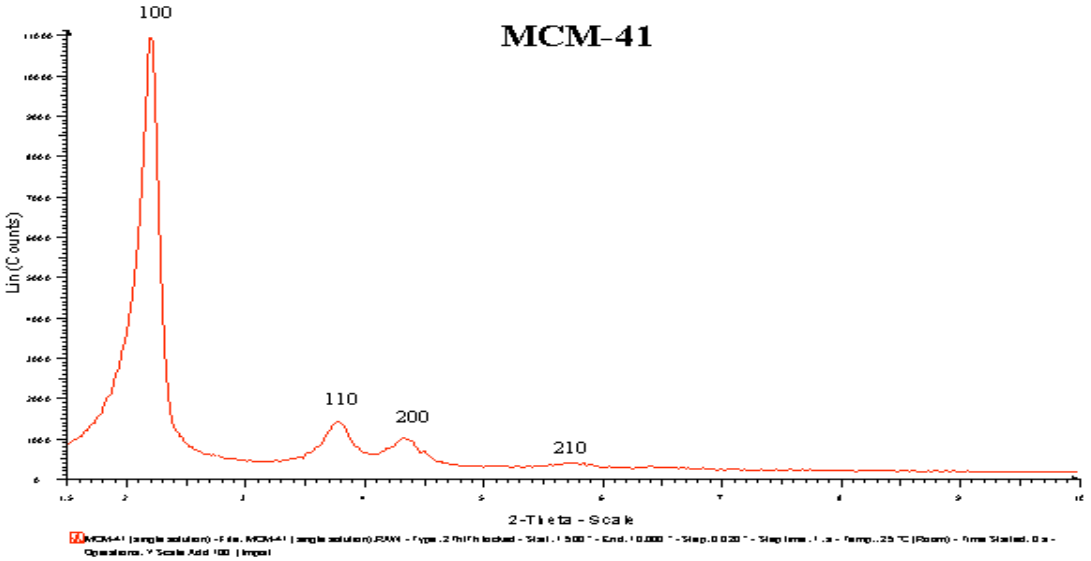

Figure 7.1: XRD pattern of as-synthesized MCM-41.

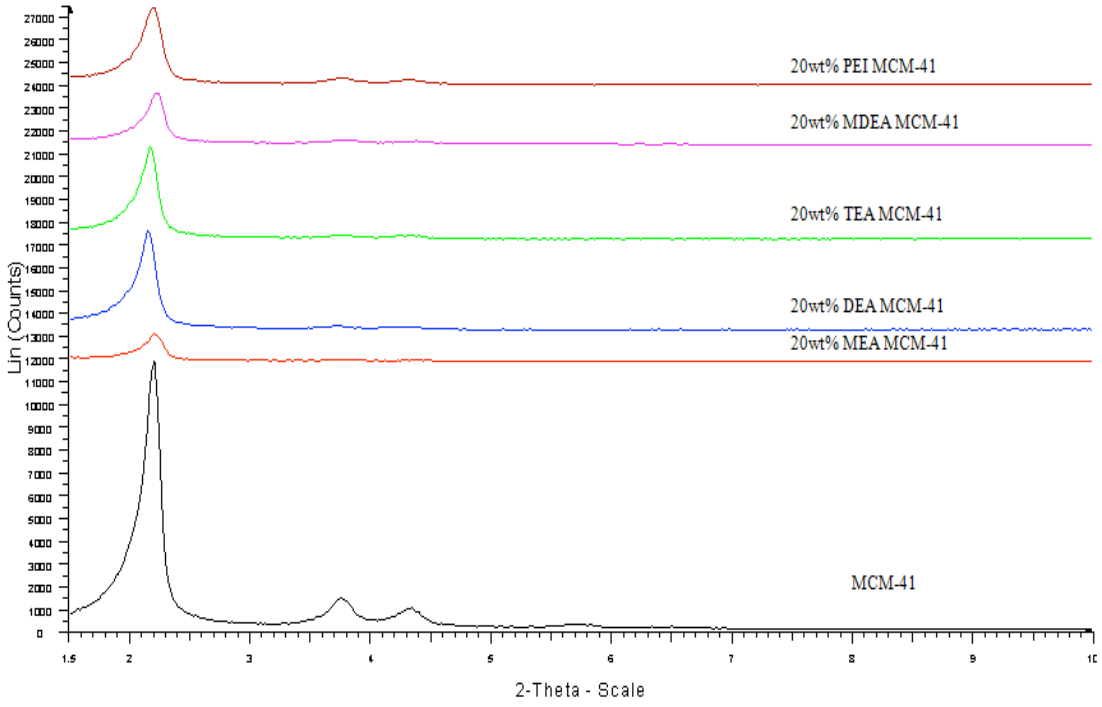

Figure 7.2: XRD patterns of grafted amine-MCM-41. (PEI= polyethylenimine, MDEA= methyl diethanolamine, TEA= triethanolamine, DEA= diethanolamine, MEA= monoethanolamine)

XRD patterns of MCM-41 before and after loading of various types of amines are compared in Figure 7.2. The diffraction patterns of MCM-41 did not change much after different amines were loaded. However, the intensity of the diffraction patterns of MCM-41 changed. Through this study, the diffraction intensity of MCM-41 decreased substantially after modification using different amines. The decreased intensity was caused by pore filling effect and indicated that amine was loaded into the pores of MCM-41.

Furthermore, the degrees of Bragg diffraction angles were nearly identical indicating that the structure of MCM-41 was preserved after loading of various amines. The degree of Bragg diffraction angle of the (100) plane slightly increased from 2.176˚ for MCM-41 to 2.185˚ - 2.212˚ for various amines modified MCM-41. These changes were caused by pore filling effect of MCM-41 channels and amines coating on the outer surface of MCM-41 crystals (Xu *et al.*, 2002; Xu *et al.*, 2005).

From Figure 7.2, the diffraction intensity of 20 wt% MEA MCM-41 is especially low compare to others. There can be two possibilities that caused the lower intensity which are the effect of pore filling and the coating of outer surface of MCM-41 crystals. Xu et al. (2002) reported that amine coated on the outer surface of MCM-41 crystals hardly influenced the diffraction intensity of MCM-41 support. Therefore, the low diffraction intensity of 20 wt% MEA MCM-41 is mainly caused by pore filling effect. Moreover, the size of MEA molecule is smaller than other amines molecule which further verifies that it is easier for MEA molecules to fill the pores of MCM-41 compare to other amines and resulted in lower diffraction intensity. This result will significantly affects carbon dioxide adsorption performance of 20 wt% MEA MCM-41 sample which will be discussed later in the report.

The nitrogen adsorption isotherms of MCM-41 and 20 wt% MEA MCM-41 are shown in Figure 7.3, which further confirm the MEA was loaded into the pore channels of the MCM-41 support. Completely degassed MCM-41 shows type IV

isotherm (Figure 7.3). The surface area, pore volume and average pore diameter were 1035 m^2/g, 0.93 cm^3/g and 2.73 nm respectively. After loading of 20 wt% MEA, the mesoporous pores were partially filled with MEA, resulting in a type II isotherm (Figure 4.3), further restricting the access of nitrogen into the pores at liquid nitrogen temperature. The residual pore volume of 20 wt% MEA MCM-41 is only 0.21 cm^3/g, the surface area is estimated to be 49.98 m^2/g and the average pore diameter was smaller than 1.69 nm. These results correlate with the pore filling effect of MEA as well as other amines which was also reflected by XRD characterization (Burleigh *et al.*, 2001; Murcia *et al.*, 2003; Xu *et al.*, 2002; Zhao *et al.*, 2000).

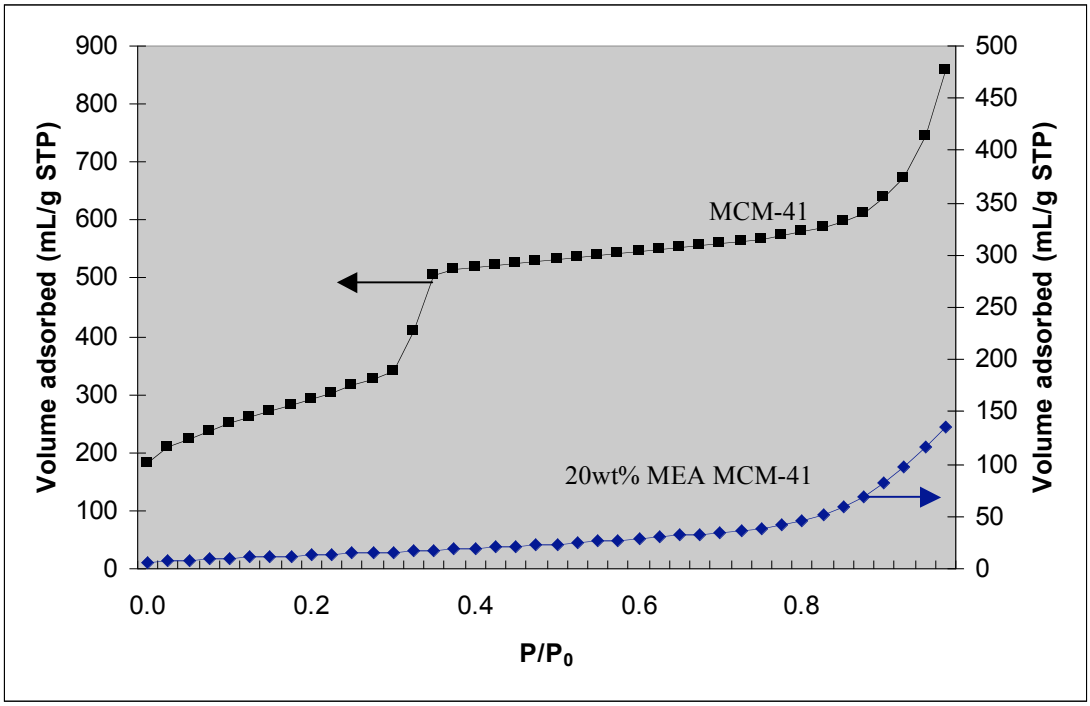

Figure 7.3: Nitrogen adsorption isotherm of MCM-41 and 20 wt% MEA MCM-41.

In the physical properties characterization, the surface area and pore structure of MCM-41 before and after modification by amines were characterized using N_2 adsorption at 77 K. The nitrogen adsorption isotherms over the whole relative pressure range for MCM-41 and 20 wt% MEA MCM-41 are shown in Figure 7.3. Generally, the adsorption isotherm before amine modification are of type IV in the Brunauer, Deming, Deming and Teller (BDDT) classification indicating that they are mesoporous solids. The abrupt increase of N_2 adsorption at relative pressure ($P/P_0 \sim$

0.3) occurs because N_2 molecules are able to penetrate freely into the pores of MCM-41 without steric factor which capillary condensation and multilayer adsorption starting to occurs. As for 20 wt% MEA MCM-41, the low adsorption was due to primary micropore filling effect since the amine modified MCM-41 had reduced pore diameter (1.69 nm) which fall into the region of micropore (< 2 nm). However, since the fluid-solid interaction of nitrogen and 20 wt% MEA MCM-41 is strong, the adsorption isotherm tends to be type II rather than type I of microporous (Xu *et al.*, 2002; Xu *et al.*, 2003).

Figure 7.4 presents the FTIR spectra for the as-synthesized MCM-41. The pure silica shows bands at around 3400, 1640, 1100, 962, 800 and 464 cm^{-1} region. The peak at 3447 cm^{-1} represents stretching vibrations of adsorbed water or structural –OH groups. Another peak at 1637 cm^{-1} is assigned to OH bending vibrations of the adsorbed water molecules. Typical antisymmetric and symmetric Si-O-Si stretching vibrations are centered at 1087 and 798 cm^{-1}, respectively. The band at 968 cm^{-1} corresponds to Si-OH vibrations of the surface silanols, which is characteristic of mesoporous silica (Cheng *et al*., 2006a; Luan *et al*., 2005; Rege and Yang, 2001)

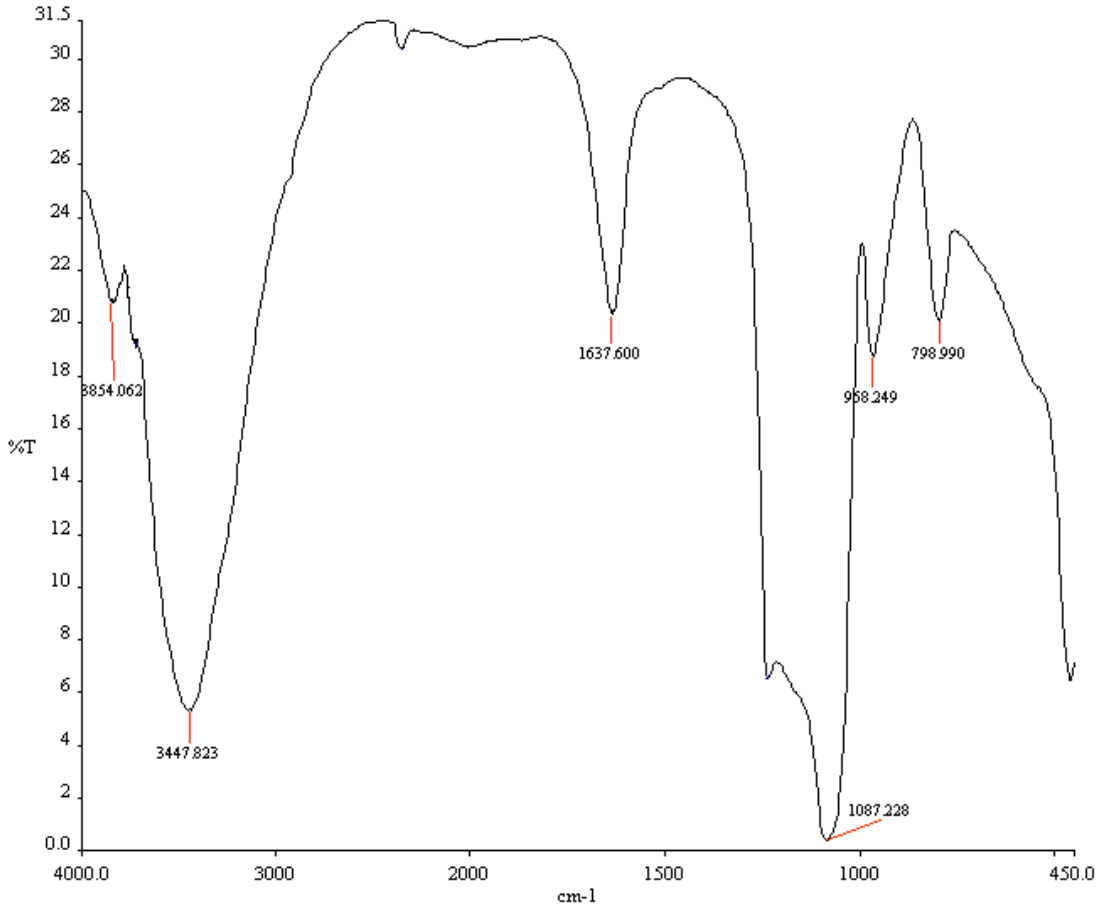

Figure 7.4: FTIR spectra of MCM-41.

The amine modified MCM-41 differs from the pure MCM-41 in several ways. Beside the peaks characteristic of MCM-41, amines molecules vibrations also reflect on the trace as shown in Figure 7.5. The intensity of the peak at 3440 cm^{-1} region is smaller than that of MCM-41 due to the formation of amine in the channels. The weak absorption band at 1550 cm^{-1} region is associated with C-C stretching vibrations, the peak at 1455 cm^{-1} region represents C-N stretching vibrations, while the absorption bands at 785 and 672 cm^{-1} correspond to C-H outerbending vibrations. All these adsorption bands are clearly visible as shown in Figure 4.5 with slightly shifted adsorption band for different type of amines. Absorption bands at 3430, 3280 and 1592 cm^{-1} region are assigned to asymmetric NH_2 stretch (ν_{as} NH_2), symmetric NH_2 stretch (ν_s NH_2) and NH_2 deformation (δNH_2) of hydrogen bonded amino group, respectively (Cheng *et al.*, 2006a; Zhao *et al.*, 1996; Wakabayashi *et al.*, 1997; Hiyoshi *et al.*, 2005). Besides these, absorption bands due to (Si-)OH stretch is visible at 3400 cm^{-1} region, overtone of Si-O-Si lattice weak vibration at 1980 and

1850 cm^{-1} region, CH_2 stretch at 2850 and 2930 cm^{-1} region and CH_2 deformation at 1460 cm^{-1} region were also observed in the spectrum which overlaps with C-N stretching vibrations. In addition, the peak at 1090 cm^{-1} region is assigned to the in-plane deformation vibrations of N^+H_2 formed on the amine chains by protonation, which is overlapped by the peak of the antisymmetric Si-O-Si stretching vibrations of MCM-41 (Zheng *et al.*, 2005; Cheng *et al.*, 2006a; Hiyoshi *et al.*, 2005). As for secondary amine (DEA), the absorption peak of NH stretch (ν NH) would overlap with symmetric NH_2 stretch (ν_s NH_2) at around 3300 cm^{-1}. Meanwhile, as for tertiary amine (TEA) the peak at 1456 cm^{-1} will be the dominant absorption band represents C-N stretching vibrations as can be seen in Figure 4.5 for the spectrum of 20 wt% TEA MCM-41.

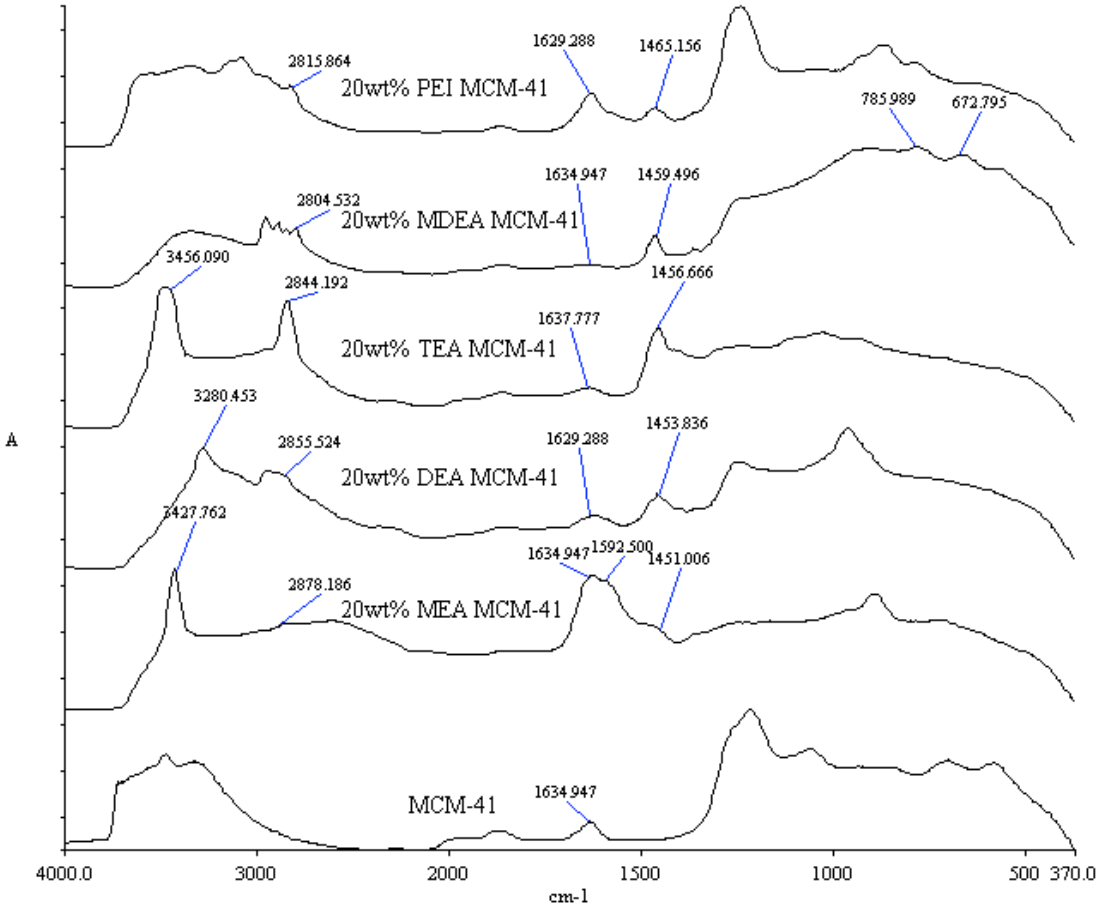

Figure 7.5: FTIR spectra of amines modified MCM-41.

Thus, the FTIR spectra of amine modified MCM-41 confirm the incorporation of amine inside the pore channels of MCM-41. Small shifts between the absorption peaks of amine molecules in the nanocomposite and bulk amine suggest that chain growth of amine in the mesopores is limited by diffusional restriction (Cheng *et al*., 2006a; Cheng *et al*., 2006b; Luan and Fournier, 2005).

7.2.2 Effects of metal loading

XRD patterns of different metals loading on MCM-41 are shown in Figure 4.6. There is no obvious decrease in peak intensity observed which indicates that ordered hexagonal mesoporous structure is well developed for each metal modified MCM-41. Furthermore, the presence of 3 smaller peaks (d_{110}, d_{200} and d_{210} peaks) confirms that long range order was present in the samples.

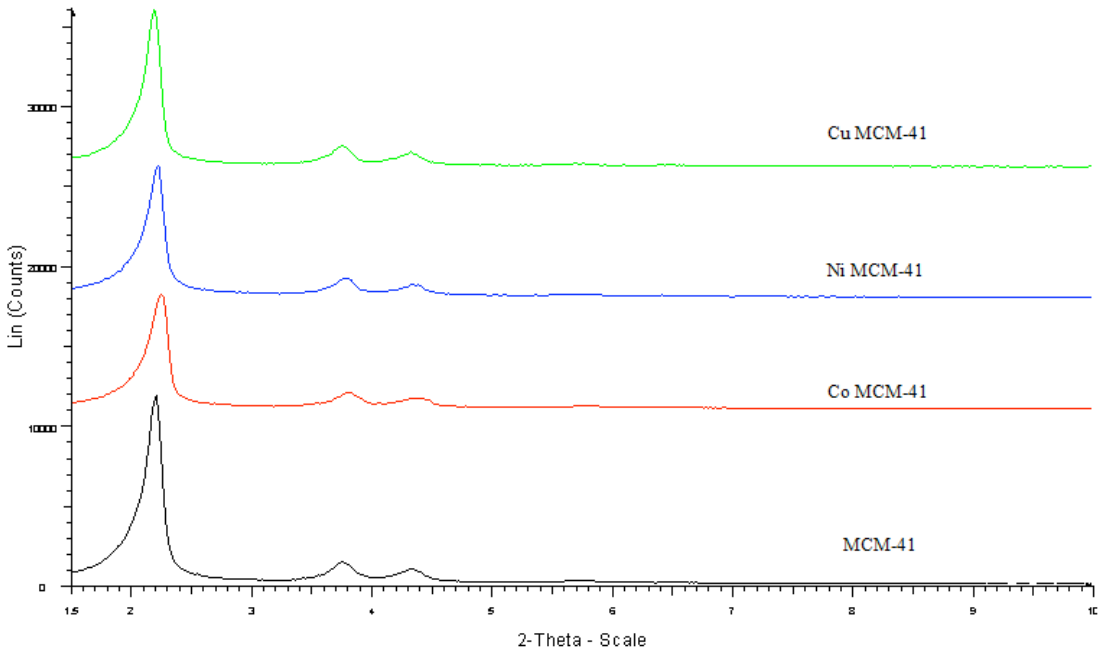

Figure 7.6: XRD patterns of different metals loading on MCM-41. (Cu= copper, Ni= nickel, Co= cobalt)

The calcination process in the direct synthesis of metal modified MCM-41 method used high temperature at 550˚C. This may results in oxidation of metal nitrate which is used in the synthesis to form bulk metal oxide ($CuNO_3 \rightarrow CuO$, $NiNO_3 \rightarrow NiO$ and $CoNO_3 \rightarrow Co_3O_4$). Moreover, the high calcination temperature may also transport some of metal oxide species out of the pore system and remove some of their deposition at the external surface of MCM-41, to form larger size crystallites. When all the useable vacant sites are occupied, a close-packed capping O^{2-} layer is formed and transformed them into the most stable form of oxide (Evans *et al.*, 2000; Xu *et al*., 2003).

The factors such as the pore size of MCM-41, the dynamic diameter of the metal oxides (particle size) and their physicochemical properties highly influence the incorporation of metal on MCM-41 either into the pore channel or onto the external surface of MCM-41. The particle size of metal oxides and their bond length between metal cation and oxygen molecule are listed in Table 7.1. It is reasonable that the incorporation of metal oxides into MCM-41 only occurs under the condition, when the dynamic diameter of metal oxides is smaller or similar to the pore size of MCM-41.

Table 7.1: Physical properties of metal oxides (Náray-Szabo, 1969).

Samples	Particle Size (nm)	Bond Length (Å)
CuO	25.51	1.84
Co_3O_4	99.13	2.10
NiO	69.91	2.03

Figure 7.7 shows the XRD patterns of MEA grafted on metals modified MCM-41. The decrease of the corresponding first peak (d_{100} peak) intensity (especially for MEA CuMCM-41 and MEA CoMCM-41) and the lack of the fourth peak (d_{210} peak) compared to parent MCM-41, reflects a less ordered hexagonal

mesoporous structure for the amine grafted metal modified MCM-41. However, the metal modified MCM-41, after calcination, maintained its typical hexagonal structure, with no obvious decrease in peak intensity is observed as shown in Figure 7.6. This indicates that the decrease in the peak intensity is mainly related to the introduction of amine species instead of the thermal instability of the support (Xu *et al.*, 2002; Evans *et al.*, 2000; Xu *et al.*, 2003). Thus, it is confirm that the decreased intensity was caused by the amine coating on the outer surface of metal modified MCM-41 crystals as well as pore filling effect which further indicates that amine was loaded into the pores of metal modified MCM-41.

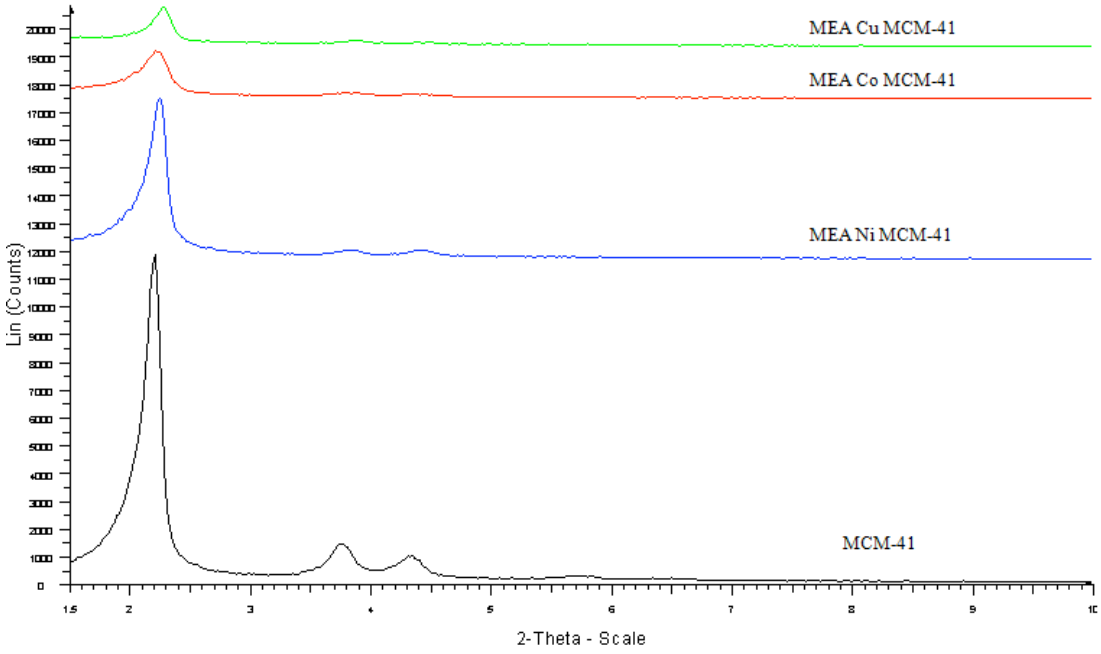

Figure 7.7: XRD patterns of MEA grafted on metals modified MCM-41.

7.2.3 Effects of amine on microporous materials

Powder X-Ray Diffraction has also been used to characterize the crystallinity and structure of microporous materials used in this study which are NaY and 13X.

The flat baselines of the X-ray diffraction pattern as shown in Figures 7.8 and 7.9 indicated a good crystallinity of all the samples. It was observed that the peak intensities of the XRD reflections for MEA modified NaY and 13X decreased as compared to unmodified commercial NaY and 13X. This is due to the presence of MEA particles within the framework of the zeolite NaY and 13X.

The crystallinity of samples, which were denoted as relative intensity (I_{rel}) is determined by comparing the sum of the six reflection peaks (ASTM D3906) namely {331}, {511}, {440}, {533}, {642} and {555} of the modified samples with those of the NaY and 13X zeolite taken as reference (100% crystalline at ambient temperature) respectively. The relative crystallinity was calculated to determine the effects of MEA modification procedure employed on phase crystallinity of the parent zeolite. The crystalline phase of MEA modified samples decreased moderately for MEA NaY sample while MEA 13X crystalline phase decrease further more as calculated in Table 4.2 but the support has remained unchanged. The relative intensity for MEA NaY sample is 78.74 which is about 10% higher than MEA 13X sample at 68.93. The higher relative intensity for MEA NaY indicated that the sample has better crystalline phase than MEA 13X. These results give further explanation for the introduction of MEA into zeolites framework and the phase crystallinity itself proves no significant alteration of the zeolites framework even after MEA modification procedure.

Table 7.2: Structural characterization of metal oxide modified Na-Y zeolites.

Samples	Relative Intensity (I_{rel})
NaY	100.00
MEA NaY	78.74
13X	100.00
MEA 13X	68.93

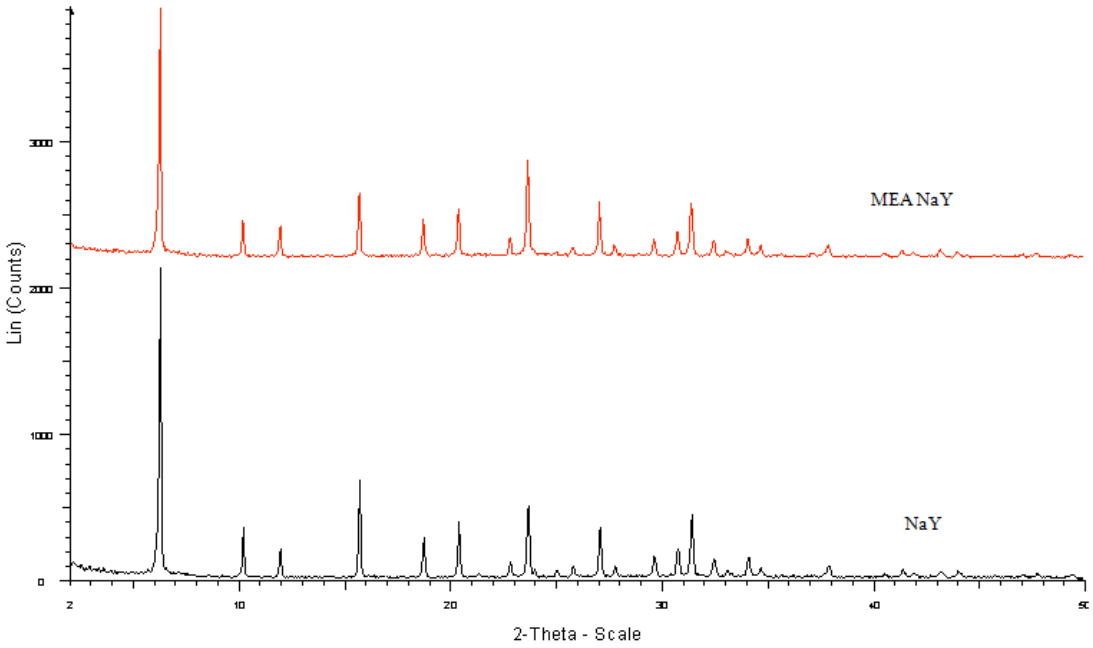

Figure 7.8: XRD patterns of zeolite NaY and MEA modified NaY.

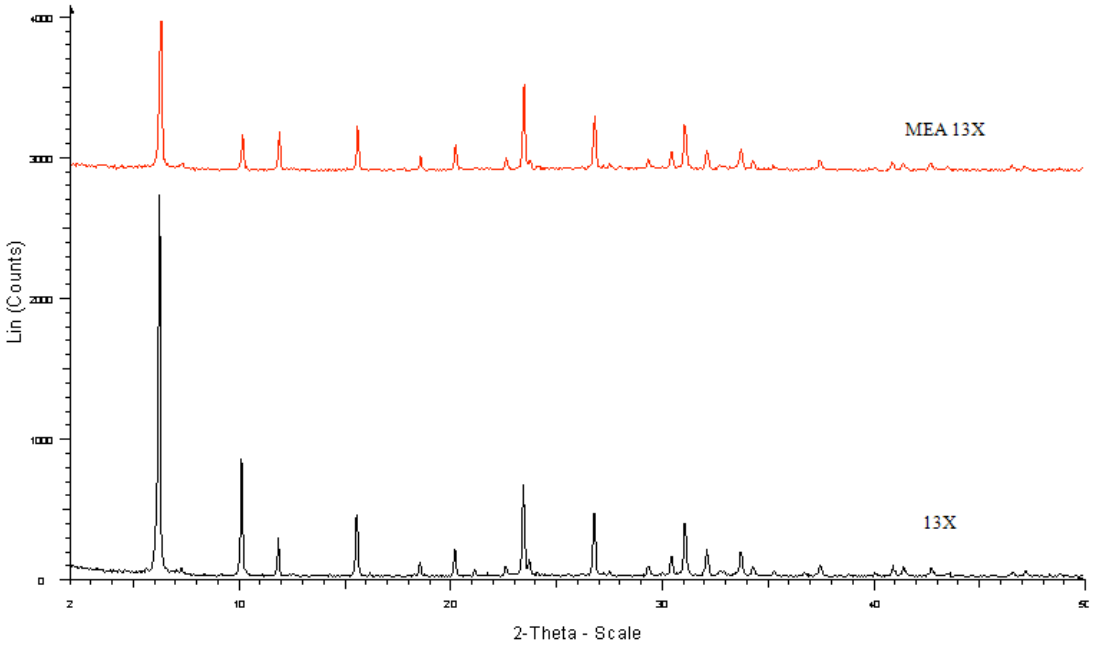

Figure 7.9: XRD patterns of zeolite 13X and MEA modified 13X.

7.2.4 Effects of amine concentration

MEA/MCM-41 samples with different MEA loadings were prepared and characterized by XRD and TGA. From XRD results, comparing the diffraction patterns of MCM-41 with those of MEA MCM-41 modified samples with different MEA loadings, shows that the degree of Bragg diffraction angles were nearly identical, indicating that the structure of MCM-41 was preserved after loading of MEA. However, the intensity of the diffraction patterns of MCM-41 decreased significantly after the MEA was loaded as shown in Figure 7.10.

By using MEA to modified the parent MCM-41, it is expected that the diffraction intensity of the (100) plane of MCM-41 will decreased because of pore filling effect since amine was loaded into the pores of MCM-41. However, when the concentration of MEA is increased it seems that the diffraction intensity of the (100) plane of MCM-41 is decreased as well until certain limit that further concentration increment would not affect the diffraction intensity anymore.

Figure 7.10 shows the diffraction intensity of (100) plane MEA MCM-41 samples with different MEA loadings (0 wt%, 10 wt%, 20 wt%, 50 wt% and 75wt %). By increasing the MEA concentrations, the intensity of the diffraction peaks will decrease as well. The intensity of the diffraction peak of 50 wt% MEA MCM-41 and 75 wt% MEA MCM-41 was reduced to about 10.8% of the original intensity of MCM-41 support.

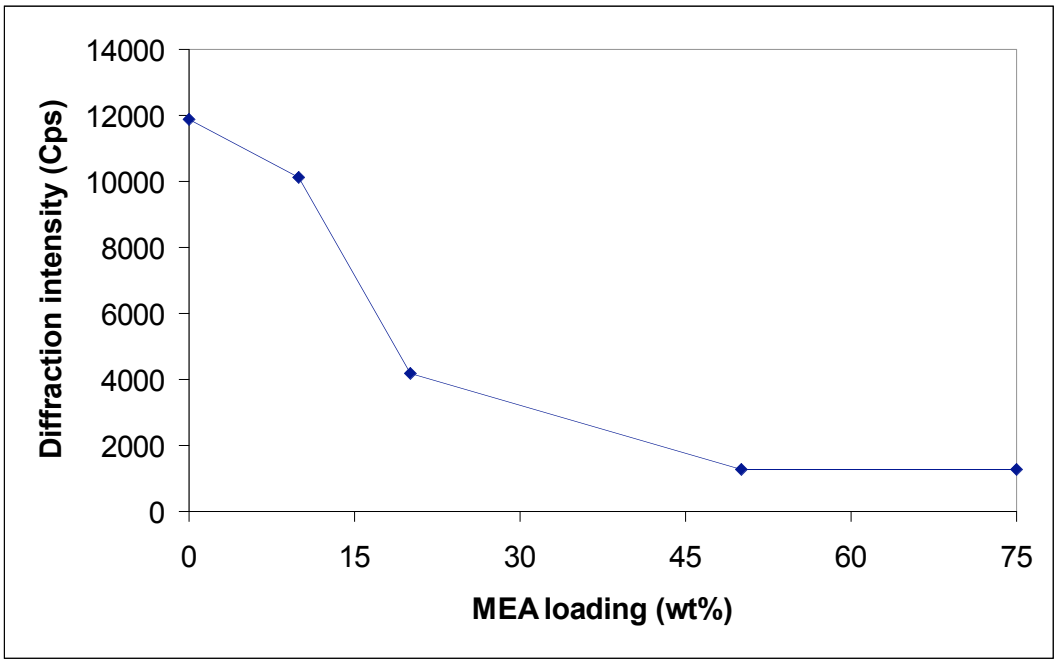

Figure 7.10: The effect of MEA loadings on the diffraction intensity of the (100) plane of MCM-41.

Since the pore volume of MCM-41 support is 0.93 cm^3/g and the density of MEA is about 1.0 g/cm^3, the maximum MEA loading in the pores of MCM-41 is 46.5 wt%. The rest of the MEA should be coated on the outer surface of MCM-41 crystals. As for 75 wt% MEA/MCM-41, there should be more MEA coated on the outer surface of MCM-41 support compare to 50 wt% MEA/MCM-41 since the MEA concentration used is 50% more. However, the diffraction intensity of the (100) plane for 50 wt% MEA/MCM-41 and 75 wt% MEA/MCM-41 was nearly the same. The result indicated that the MEA coating on the outer surface of the crystals hardly influenced the diffraction intensity of the MCM-41 support. Therefore, the decrease in the diffraction intensity of the (100) plane can be ascribed mainly to the loading of MEA into the MCM-41's pore channels (Xu *et al*., 2003; Xu *et al*., 2002).

7.3 Carbon Dioxide Adsorption Characteristics

Gas CO_2 adsorption capacity of amine modified mesoporous and microporous materials were studied and presented in the following section. Based upon the results obtained from the equilibrium adsorption capacity, the effects of amine modification on the CO_2 adsorption could be evaluated and characterized. The procedures for evaluation of gas CO_2 adsorption capacity by amine modified mesoporous and microporous materials were investigated in single adsorbate adsorption atmosphere at equilibrium pressure of 138 kPa and adsorption temperatures at 50˚C as standard. Adsorbate uptake capacity was measured until equilibrium reached.

7.3.1 Effects of various amines

Before amine was loaded, MCM-41 support alone shows CO_2 adsorption capacity of 18.58 mg/g sorbent. The low adsorption capacity was due to weak interaction between CO_2 and MCM-41 at relatively high temperature. In order to strengthen the interaction between CO_2 and MCM-41, different types of amines with numerous CO_2-capturing sites were loaded into MCM-41 pore channels.

CO_2 adsorption capacity increased considerably after modification of MCM-41 using different types of alkanoamines. Delaney et al. reported that the ratio of CO_2 molecular per available N atom in the presence of hydroxyl group is approximately twice that without hydroxyl group. It is suggested that the CO_2 chemical adsorption mechanism of amine changed in the presence of hydroxyl group. Without the hydroxyl group, the formation of carbamate is favored in the manner of following Equation (7.1)-(7.3):

$$CO_2 + 2RNH_2 \Leftrightarrow NH_4^+ + R_2NCOO^- \quad 7.1$$

$$CO_2 + 2R_2NH \Leftrightarrow R_2NH_2^+ + R_2NCOO^- \quad 7.2$$

$$CO_2 + 2R_3N \Leftrightarrow R_4N^+ + R_2NCOO^- \quad 7.3$$

With the absence of hydroxyl group, 2 moles of amine groups are required to react with 1 mole of CO_2 molecule. However, when hydroxyl groups are present, the reaction is two times as much leading to the formation of another type of carbamate. The formation of carbamate type zwitterions is stabilized in a manner depicted in Equation 7.4. In the presence of hydroxyl groups, 1 mole of amine groups react with 1 mole of CO_2 molecule. Therefore, the adsorption capacity of alkanoamine modified MCM-41 increased since the hydroxyl groups of the amines able to promote the formation of carbamate type zwitterions and more CO_2 molecules can be adsorbed (Xu *et al.*, 2002; Zhang *et al.*, 2005; Xu *et al.*, 2003; Evans *et al.*, 2000).

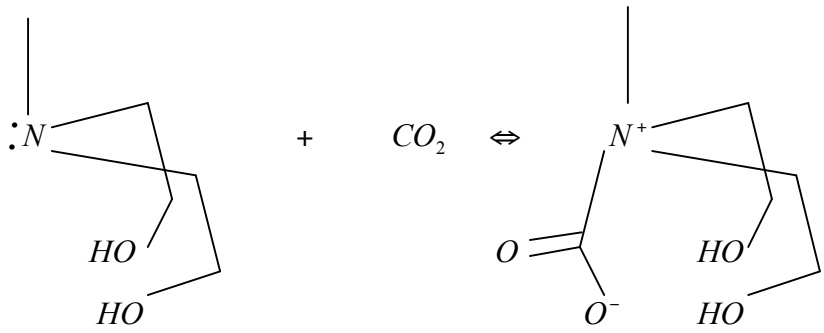

7.4

Figure 7.11 shows gas CO_2 adsorption capacity for MCM-41 support and amine modified MCM-41. MEA modified MCM-41 indicated the highest CO_2 adsorption capacity at 40.91 mg/g sorbent which is 2.2 times higher than MCM-41 support itself. As for tertiary amine modified MCM-41 such as TEA MCM-41 and MDEA MCM-41, the CO_2 adsorption capacity is rather low at 12.04 and 17.26 mg/g

sorbent respectively which is lower than MCM-41 support. Meanwhile, DEA modified MCM-41 also shows high adsorption capacity at 38.18 mg/g sorbent. Although PEI is considered as tertiary amine, the adsorption capacity is quite high at 27.55 mg/g sorbent. This is due to the long chain of numerous alkyl chains within PEI structure (Xu *et al.*, 2002; Zhang *et al.*, 2005; Xu *et al.*, 2003).

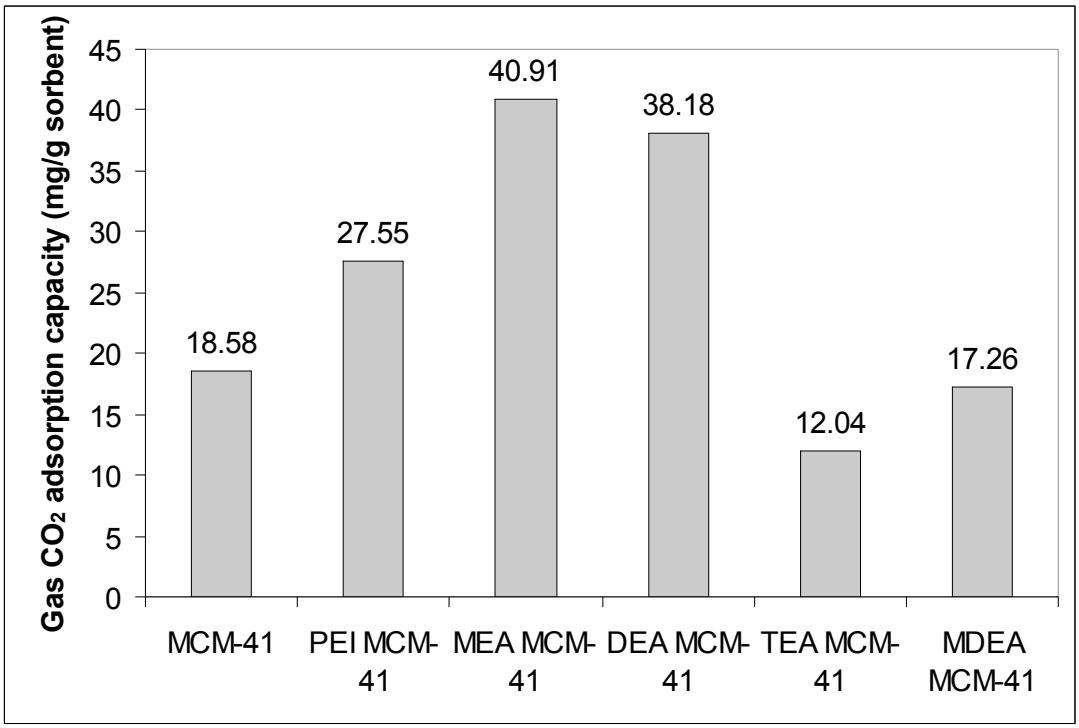

Figure 7.11: Gas CO_2 adsorption capacity for MCM-41 support and amine modified MCM-41.

There are two possible reasons for synergetic effect of MCM-41, one is the high surface area of MCM-41 and another is the uniform mesoporous channel of MCM-41. When amine was loaded onto the materials with high surface area, there will be more CO_2 affinity sites exposed to the adsorbate and thus increasing the adsorption capacity. When the channels of MCM-41 are filled with amine, the apparent pore size of the parent MCM-41 will be decreased as discuss before. However, at the same time more CO_2 affinity sites are introduced into the pore

channel of MCM-41. Both these contradicting effects happen simultaneously and directly affected the adsorption capacity.

The amount of CO_2 adsorbed increases with increasing of the straight alkyl chain in the amines. PEI is one example of this case which consists of numerous long alkyl chains which explain the higher CO_2 adsorption capacity compare to the parent MCM-41. However, amines with larger molecular size will results in lower adsorption due to steric hindrance which explain the low adsorption capacity of TEA MCM-41 and MDEA MCM-41 as both are tertiary amine with large molecular size. Furthermore, this also explains why the adsorption capacity of PEI MCM-41 did not exceed the adsorption capacity of MEA MCM-41 since PEI consists of longer alkyl chains but with larger molecular size.

TGA curves of CO_2 adsorption capacity for MCM-41 support and amine modified MCM-41 are presented in Figure 7.12. The adsorption of CO_2 gas by MCM-41 and amine modified MCM-41 adsorbents have rapid uptake in the early period, but slows down at latter periods of the adsorption process. As illustrated in Figure 7.12, CO_2 gas adsorbed rapidly to around 70% - 85% of total CO_2 uptake in the first 50 minutes. This is true for MCM-41 support and all amine modified MCM-41 except for TEA MCM-41 and MDEA MCM-41. The larger molecular size of TEA and MDEA had resulted not only in lower adsorption capacity but also slower adsorption rate due to steric hindrance. TEA and MDEA modified MCM-41 achieved the same amount of adsorbate (80% of total CO_2 uptake) in more than 100 minutes time. Meanwhile, DEA modified MCM-41 CO_2 gas uptake seem to be the slowest. For the initial 50 minutes of adsorption, only 53% of total CO_2 uptake was obtained. Furthermore, the DEA MCM-41 sample require a staggering more than 900 minutes of adsorption time to reach equilibrium compare to 250 minutes for MCM-41 sample.

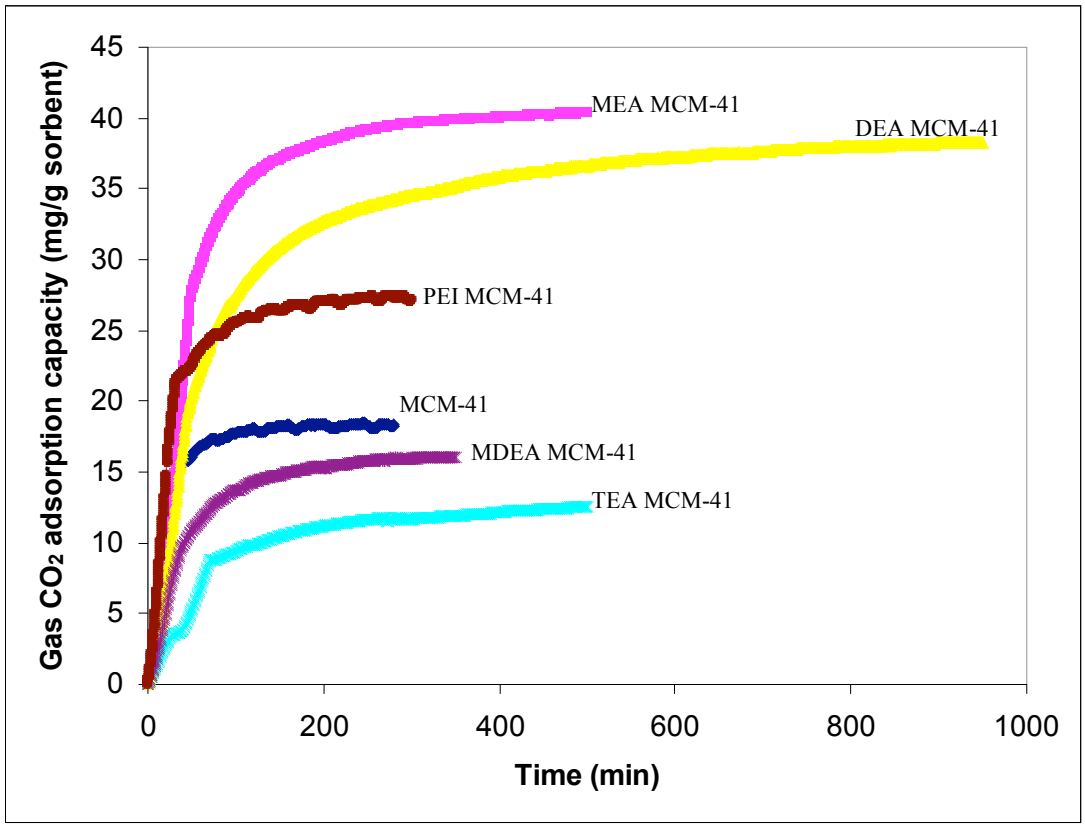

Figure 7.12: TGA curves of CO_2 adsorption capacity for MCM-41 support and amine modified MCM-41.

Different types of amine exhibited different equilibrium adsorption time requirement as well as adsorption capacity. The adsorption time that required for CO_2 adsorbate to reach equilibrium was shown in Table 7.3. Generally DEA MCM-41 sample would take longer time to reach equilibrium compared to other samples. The fastest to reach equilibrium adsorption time would be the parent MCM-41 itself with just 250 minutes. However, the adsorption characteristic results shows that even though the CO_2 adsorption process for several types of samples studied reached the saturation condition faster than others, does not mean that the adsorption capacity is higher as well. Lets observed MEA MCM-41 sample as an example. The equilibrium adsorption time requirement for MEA MCM-41 is 500 minutes which is less than the equilibrium adsorption time requirement for DEA MCM-41 (975 minutes). However, the adsorption capacity of MEA MCM-41 is 40.91 mg/g sorbent which is higher than that of DEA MCM-41(38.18 mg/g sorbent). These results clearly proved that the adsorption processes that reach equilibrium state faster would not necessary result in

higher adsorption capacities. It depends on the structure and physical properties of adsorbate and adsorbent as well as the extent of interaction of adsorbate with adsorbent surfaces

Table 7.3: Equilibrium adsorption time requirement for different amines modified MCM-41.

Samples	CO_2 adsorption time required (min)
MCM-41	250
MEA MCM-41	500
DEA MCM-41	975
TEA MCM-41	505
MDEA MCM-41	585
PEI MCM-41	485

7.3.2 Effects of support materials

In order to investigate the effects of different support materials towards the CO_2 adsorption characteristics, mesoporous and microporous supports will be utilized in the study as well as amine and metal nitrates as the modify agents. Mesoporous supports synthesized in the study are MCM-41 and SBA-15, meanwhile microporous supports of NaY and 13X are obtained commercially. Three Metal nitrates have been chosen which are copper nitrate, cobalt nitrate and nickel nitrate were incorporated into MCM-41 support during direct synthesis. Then, MEA will be use as the standard modify agent for each of the supports. The CO_2 adsorption characterization of the adsorbents produced is done by thermal gravimetric analyzer at standard condition of 138 kPa CO_2 gas pressure and 50˚C of adsorption temperature.

At low loadings, materials with the strongest enthalpic interactions with sorbed molecules will show the highest level of adsorption. These tend to be materials with narrow pores, because small pores increase the interaction between gas and the framework. However, materials with narrow pores also have the highest framework densities and thus the lowest amount of free void space per gram of material. Therefore, at the highest pressure when the pores are nearly filled, the materials with the largest free volumes have more room for quest molecules and consequently show the highest uptake (Frost *et al*., 2006).

Three different adsorption regimes can be identified. At low pressure, the amount adsorbed correlates with the heat of adsorption. At intermediate pressure, the amount adsorbed correlates with the surface area. And at the highest pressure, the amount adsorbed correlates with the free volume. According to Frost *et al*. (2006) hydrogen molecules adsorbed less for zeolite Y than for zeolite X. As zeolite Y has fewer exchangeable cations (and consequently more void space) than zeolite X, these results indicate that interaction of hydrogen molecules with exchangeable cations is important to adsorption process. For zeolite X and Y, hydrogen uptake relates closely to the BET surface area.

Figure 4.13 shows gas CO_2 adsorption capacity for various mesoporous and microporous supports as well as the MEA modified of each supports. From the figure, the adsorption capacity of microporous supports (NaY and 13X) shows significantly high level of CO_2 adsorption compare to mesoporous support. The highest adsorption is achieved by NaY support at 183.57 mg/g sorbent which is about 9.9 times higher than MCM-41 support. This is due to the high level of interaction between CO_2 gas and the framework of NaY with such narrow pores at low pressure condition. This also applied to 13X support which shows slightly decreased adsorption capacity at 162.02 mg/g sorbent. However, after the modification using MEA was grafted onto these supports, the adsorption capacity significantly decreased by up to 60% of its original adsorption capacity. This phenomenon is due to pore blockage by the amine molecules since the pore size of microporous supports (cages ~ 0.74 nm, supercages ~ 1.3 nm) is smaller than the

approximately larger radius of the amine (~1.4 nm) (Weitkamp, 2000; Inoue *et al*., 1991). When using MEA to modify microporous supports, the amine tends to disperse on the surface of the zeolite framework hence covering the pore of the support. Although MEA itself does provide additional CO_2 adsorption site, but adsorption in the pore of the zeolite framework seem to be the more significant role affecting the adsorption capacity. Furthermore, the crystalline phase of NaY and 13X decreased after modification by MEA as calculated in Table 4.2. The relative intensity for MEA NaY sample is 78.74 which is higher than MEA 13X sample at 68.93. The higher relative intensity for MEA NaY indicated that the sample has better crystalline phase than MEA 13X which explained the higher CO_2 adsorption capacity for MEA modified NaY. Besides, the decreased crystalline phase for both NaY and 13X after MEA modification clarify the decreased adsorption capacity of the MEA modified microporuos supports.

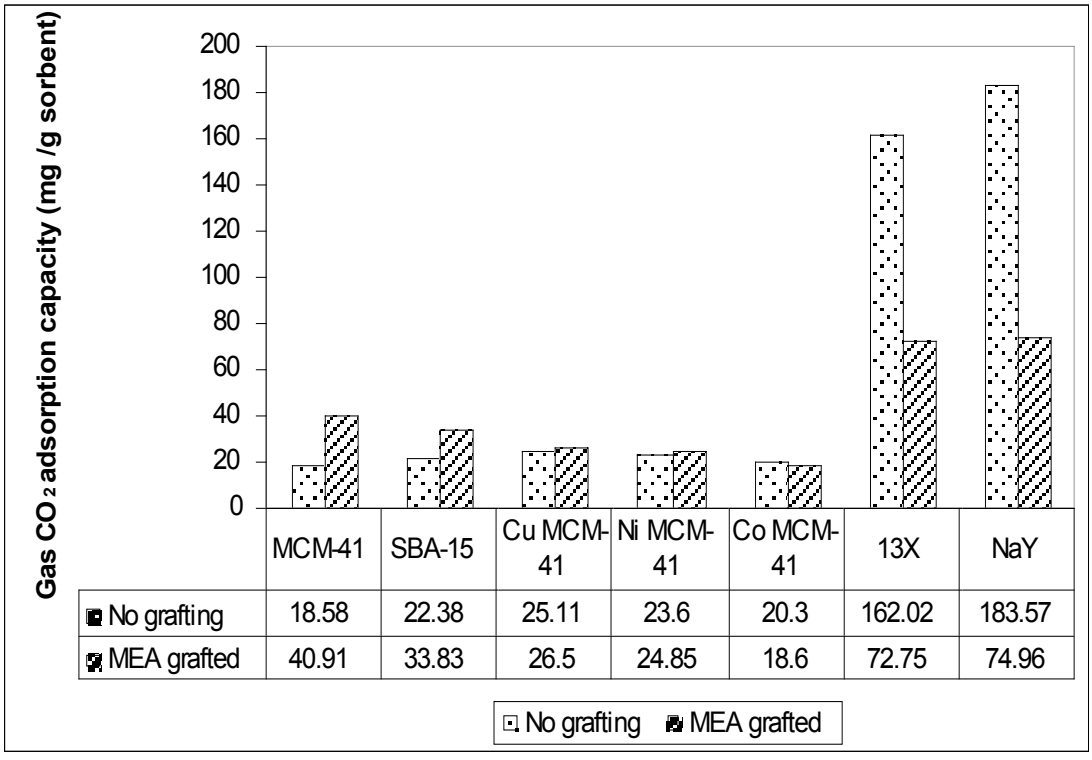

	MCM-41	SBA-15	Cu MCM-41	Ni MCM-41	Co MCM-41	13X	NaY
No grafting	18.58	22.38	25.11	23.6	20.3	162.02	183.57
MEA grafted	40.91	33.83	26.5	24.85	18.6	72.75	74.96

Figure 7.13: Gas CO_2 adsorption capacity for various mesoporous and microporous supports and MEA modified supports.

Meanwhile, as for mesoporous supports, all MEA grafted mesoporous supports show increment in CO_2 adsorption capacity except for MEA modified Co MCM-41 sample. Base on Table 7.1, cobalt oxide has the largest particle size compare to the other two metal oxides. Co_3O_4 particle size is 1.4 times larger than NiO particle size and 3.9 times larger than CuO particle size. The large particle size of Co_3O_4 formed on the surface of the support after calcination proved to be the cause of low adsorption capacity by blocking the pores of the support. As for Cu MCM-41 and Ni MCM-41 supports, after grafting of MEA shows only a small increase in adsorption capacity. The results show that MEA is not the appropriate modify agent to improve adsorption capacity for metal modified supports.

From Figure 7.13, the CO_2 adsorption capacity for SBA-15 is 1.2 times higher than MCM-41 support without MEA grafted. The slightly higher adsorption of SBA-15 is due to larger pore size poses by SBA-15 support. Besides, there were also micropores within the wall of SBA-15 structure contribute to the higher adsorption capacity. The existences of micropores in SBA-15 also provide higher total pore volume at 1.164 cm^3/g compare to 1.0 cm^3/g for MCM-41 (Klimova *et al.*, 2006; Zhou *et al*., 2005; Fulvio *et al*., 2005). These interesting characteristics of SBA-15 proved to be advantageous towards increasing the adsorption capacity. However, after MEA had been grafted into both MCM-41 and SBA-15 supports, the MEA modified MCM-41 shows even higher adsorption capacity compares to MEA modified SBA-15. This is caused by the intrusion of MEA molecules into the pores of SBA-15 and blocked the micropores on the surface of the walls. The blocked micropores will resulted in reduced total pore volume of SBA-15 support and apparently decreasing the adsorption capacity.

TGA curves of CO_2 adsorption capacity for MEA modified on different mesoporous and microporous supports are shown in Figure 7.14. Averagely, mesoporous supports shows more rapid uptake in the early period compares to microporous supports. This is evidently shown in the Figure 7.14 especially for MEA grafted metal modified MCM-41. For instance, MEA Cu MCM-41 sample has the fastest uptake which reaches 85% of the total CO_2 uptake in less than 50 minutes.

However, at the same time period the MEA modified microporous supports only reached about 76% of the total CO_2 uptake averagely. Although the CO_2 uptake is faster for MEA modified mesoporous supports, the total amount of CO_2 uptake for MEA modified microporous supports is much higher with an average of 73 mg/g sorbent adsorption capacity compare to 29 mg/g sorbent of adsorption capacity for MEA modified mesoporous supports.

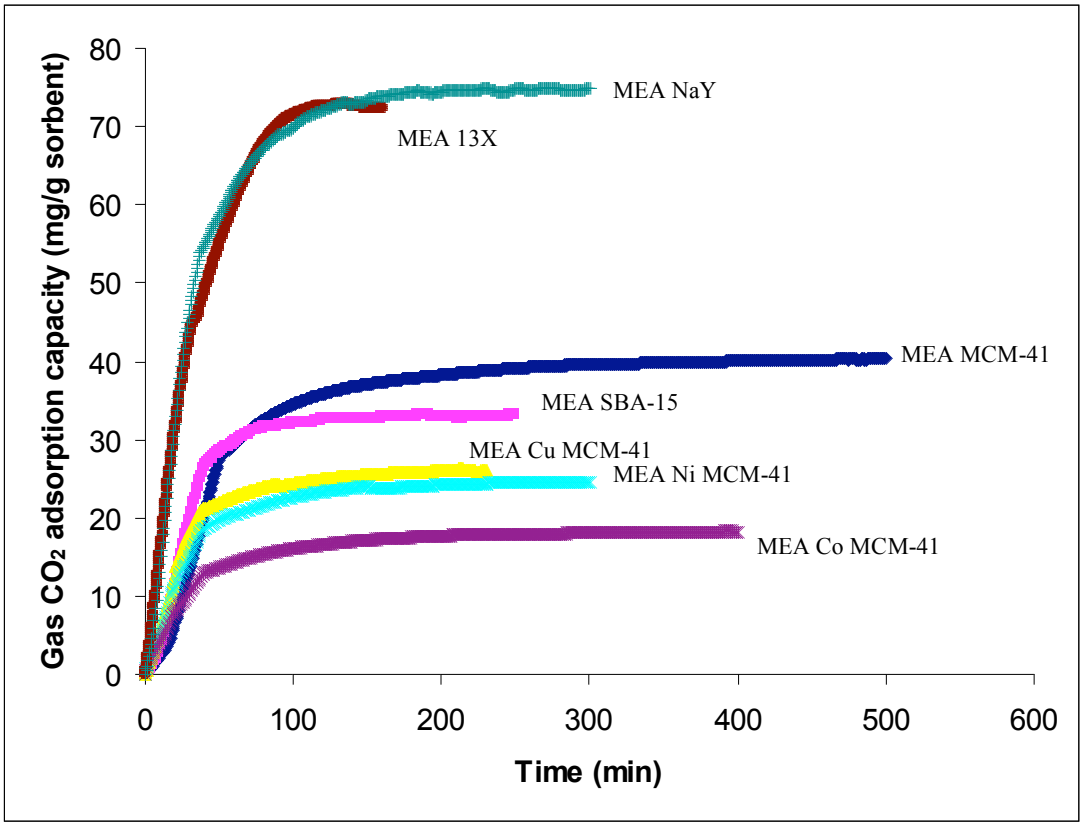

Figure 7.14: TGA curves of CO_2 adsorption capacity for MEA modified mesoporous and microporous supports.

The adsorption time that required for CO_2 adsorbate to reach equilibrium for MEA modified on different mesoporous and microporous supports was shown in Table 4.4. Generally MEA MCM-41 sample has the longest time to reach equilibrium compared to other samples. The fastest to reach equilibrium adsorption time would be MEA 13X in just 160 minutes. However, the adsorption characteristic results shows that even though the CO_2 adsorption process for several types of

samples studied reached the saturation condition faster than others, does not necessarily mean higher adsorption capacity. This is evidently shown in Table 7.4 as MEA NaY sample equilibrium adsorption time is about 300 minutes compared to 230 minutes for MEA Cu MCM-41 sample. However, the adsorption capacity of MEA NaY is 74.96 mg/g sorbent which is 65% more compare to adsorption capacity of MEA Cu MCM-41 at 26.5 mg/g sorbent.

Table 7.4: Equilibrium adsorption time requirement for MEA modified on different mesoporous and microporous supports.

Samples	CO_2 adsorption time required (min)
MEA MCM-41	500
MEA SBA-15	250
MEA Cu MCM-41	230
MEA Ni MCM-41	305
MEA Co MCM-41	400
MEA 13X	160
MEA NaY	300

7.3.3 Effects of amine concentration

To investigate the effects of amine concentration on the gas CO_2 adsorption capacity, MEA amine had been used to modified MCM-41 support at concentration of 10 wt%, 20 wt%, 50 wt% and 75 wt%. The results are shown in Figure 4.15. Generally, at low MEA loading, the MEA amine had little contribution on CO_2 adsorption capacity as can be observed in the case of 10 wt% MEA MCM-41 sample. The adsorption capacity of 23.93 mg/g sorbent is only about 29% increase compare to the parent MCM-41 support. The highest adsorption capacity was reached at 20 wt% of MEA. The 20 wt% MEA MCM-41 shows high adsorption

capacity at 40.91 mg/g sobent which is 120% higher than the parent MCM-41 support.

The pore channels of MCM-41 play an important role on the increase of CO_2 adsorption capacity. When the channels of the MCM-41 are filled with MEA, the apparent pore size of the MCM-41 will be decreased. At the same time, more CO_2 affinity sites are introduced into the channel. These two effects may combine together and result in further increment of the adsorption capacity. In the case of MEA modified MCM-41, physisorption and chemisorption take place at the same time. Physisorption on the MEA MCM-41 sample occur mainly in the pore channels of MCM-41 support, while chemisorption involve the reaction of CO_2 and MEA in the channels of MCM-41 as well as on the external surface of MCM-41.

When the channels of MCM-41 are fully filled with MEA, the highest adsorption capacity can be obtained. When MEA concentration was further increased and the MEA begin to coat on the external surface of MCM-41, the adsorption capacity starting to decrease (Xu *et al*., 2002; Xu *et al*., 2003). Therefore, as can be observed from Figure 7.15, higher MEA concentration at 50 wt% and 75 wt% resulted in reduced adsorption capacity as more pore channel of MCM-41 being filled with MEA hence blocking the pore channels for physisorption to occur resulting in steric hindrance (McKittrick and Jones, 2003).

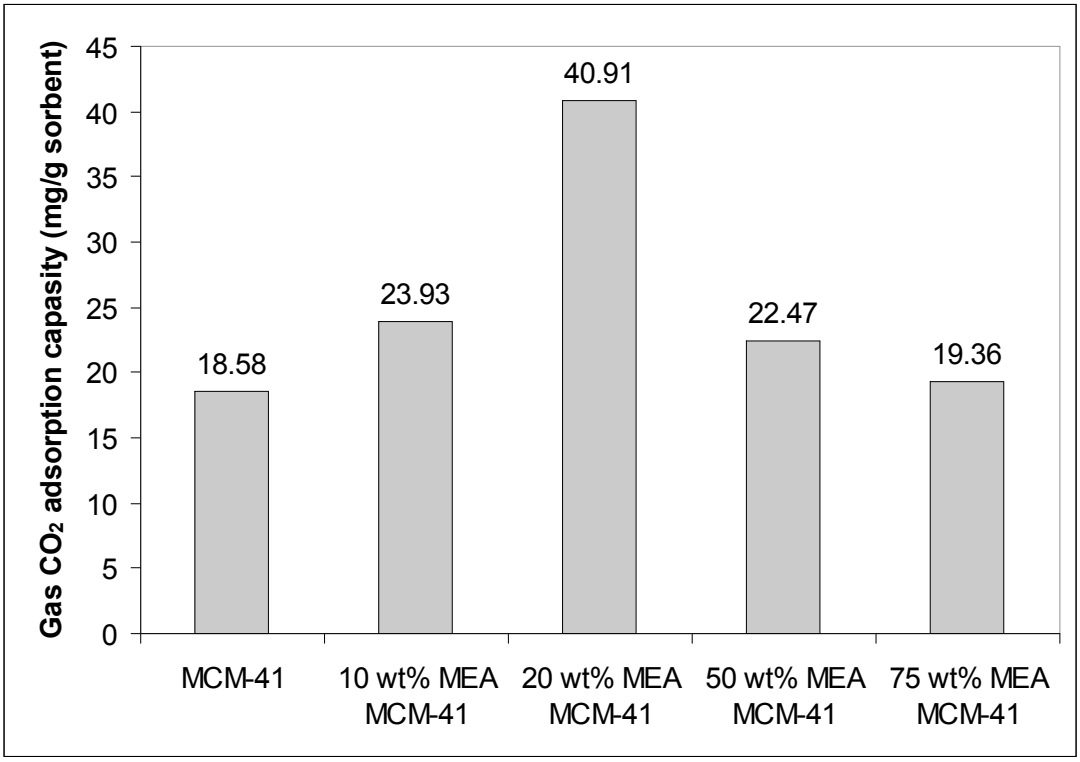

Figure 7.15: CO_2 adsorption capacity for MEA modified MCM-41 at different concentration.

Figure 7.16 presents the TGA curves of CO_2 adsorption capacity for MEA modified MCM-41 at MEA concentration of 10 wt%, 20 wt%, 50 wt% and 75 wt%. There is no specific trend in CO_2 uptake rate when increasing the MEA concentration. The fastest uptake is achieved by 50 wt% MEA MCM-41 sample which reached 90% of total CO_2 uptake in 50 minutes. Moreover, 50 wt% MEA MCM-41 sample also achieved the shortest equilibrium adsorption time at 200 minutes. Sample 20 wt% MEA MCM-41 still the slowest to reach equilibrium adsorption time at 500 minutes but was able to reach the highest adsorption capacity compare to other concentration.

The results show that at 20 wt% of MEA concentration, physisorption and chemisorption were able to occur synergeticly. The MEA amine occupied the pore channels of MCM-41 but still leave some space adequate enough for CO_2 molecules to physisorp added by chemisorption on the external surface of MCM-41 produced

the highest adsorption capacity. The amine concentration higher than 50 wt% would cause blockage of the pore channels hence making the CO_2 penetration into the channels harder and consequently lower adsorption capacity.

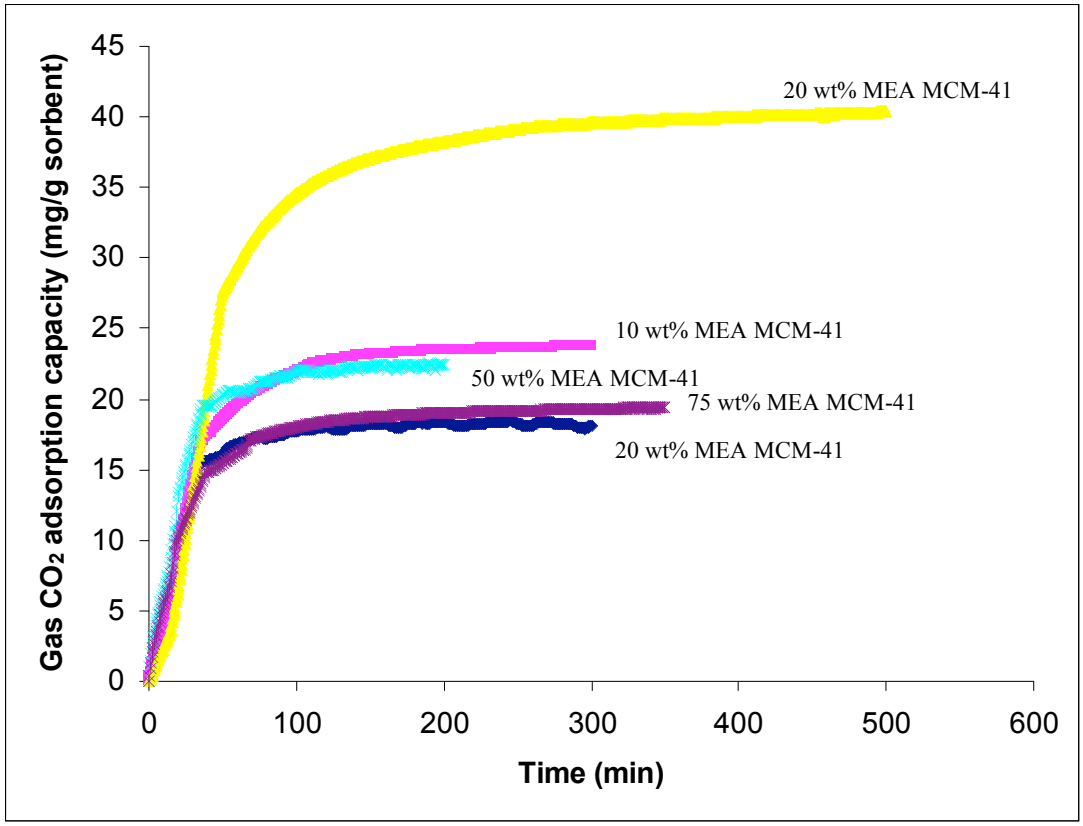

Figure 7.16 TGA curves of CO_2 adsorption capacity for MEA modified MCM-41 at different concentration.

7.3.4 Effect of temperature

The procedure of operating the TGA equipment involved heating and cooling steps that may affects the CO_2 adsorption capacity results. Before CO_2 gas being introduce into the TGA for adsorption by the samples, heating step is required to remove water vapor and other impurities. By observing the results of adsorption

capacity at a range of heating and adsorption temperatures, the influence of different operating temperatures of TGA on CO_2 adsorption capacity can be study. The experiments run at standard 138 kPa of pure CO_2 pressure and in a range of temperatures from as low as 25˚C up to 150˚C.

7.3.4.1 Adsorption temperature

The adsorption of CO_2 by porous materials or amines is an exothermic process. Accordingly, the adsorption capacity should decrease with the increase of temperature. However, study in Xu et al. (2002) shows the otherwise that the CO_2 adsorption capacity increased with increasing temperature. In the end, it is stated that the adsorption capacity at low temperature will eventually be larger than at high temperature if the adsorption time is long enough to ensure that it reached equilibrium state. As in this study, there is no such issue as contradicting the exothermic process theory as the adsorption time is long enough (24 hours) for the samples to reach equilibrium state with the CO_2 adsorbate. The results are evidently shown in Figure 4.17, as the adsorption capacity decreased when the temperature is increased.

The effects of different adsorption temperatures on gas CO_2 adsorption capacity for 20 wt% MEA modified MCM-41 are presented in Figure 7.17. As expected, the CO_2 adsorption capacity at adsorption temperature 25˚C (room temperature) shows the highest value at 82.30 mg/g sorbent. When the adsorption temperature increased to 50˚C, the adsorption capacity decreased to 40.91 mg/g sorbent which is 50.3% reduced in total amount CO_2 adsorbed. When the adsorption temperature is further increased to 75˚C, the adsorption capacity is the lowest at 17.00 mg/g sorbent which is about 58% decrease compare to amount adsorbed at 50˚C. These results indicated that for each 25˚C increment in adsorption temperature, about half of the adsorption capacity is reduced. At higher temperature the adsorbate

CO_2 molecules tend to be in active energized form and are harder to adsorb compare to molecules at lower temperature which has lower activation energy to be adsorbed.

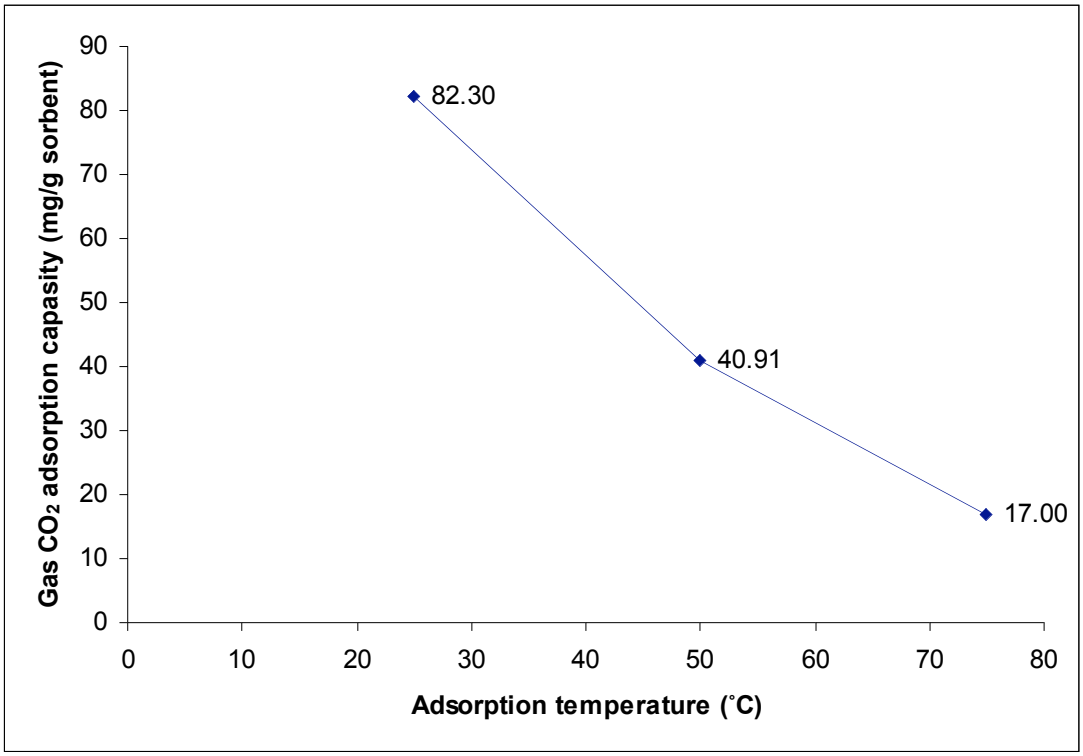

Figure 7.17: Gas CO_2 adsorption capacity for 20 wt% MEA modified MCM-41 at different adsorption temperatures.

The adsorption temperature not only affected the adsorption capacity but also the CO_2 gas uptake rate of 20 wt% MEA MCM-41 sample. Figure 7.18 represents the TGA curves of CO_2 adsorption capacity for 20 wt% MEA modified MCM-41 at the adsorption temperatures of 25˚C, 50˚C and 75˚C. Although the adsorption capacity at adsorption temperature 25˚C is the highest, the CO_2 uptake rate is the slowest. For the first 50 minutes, only about 41% of total uptake is adsorbed by the adsorbent compare to 67% uptake for adsorption temperature at 50˚C. Meanwhile, the fastest CO_2 uptake rate is at adsorption temperature of 75˚C with 84% of total uptake amount for the first 50 minutes.

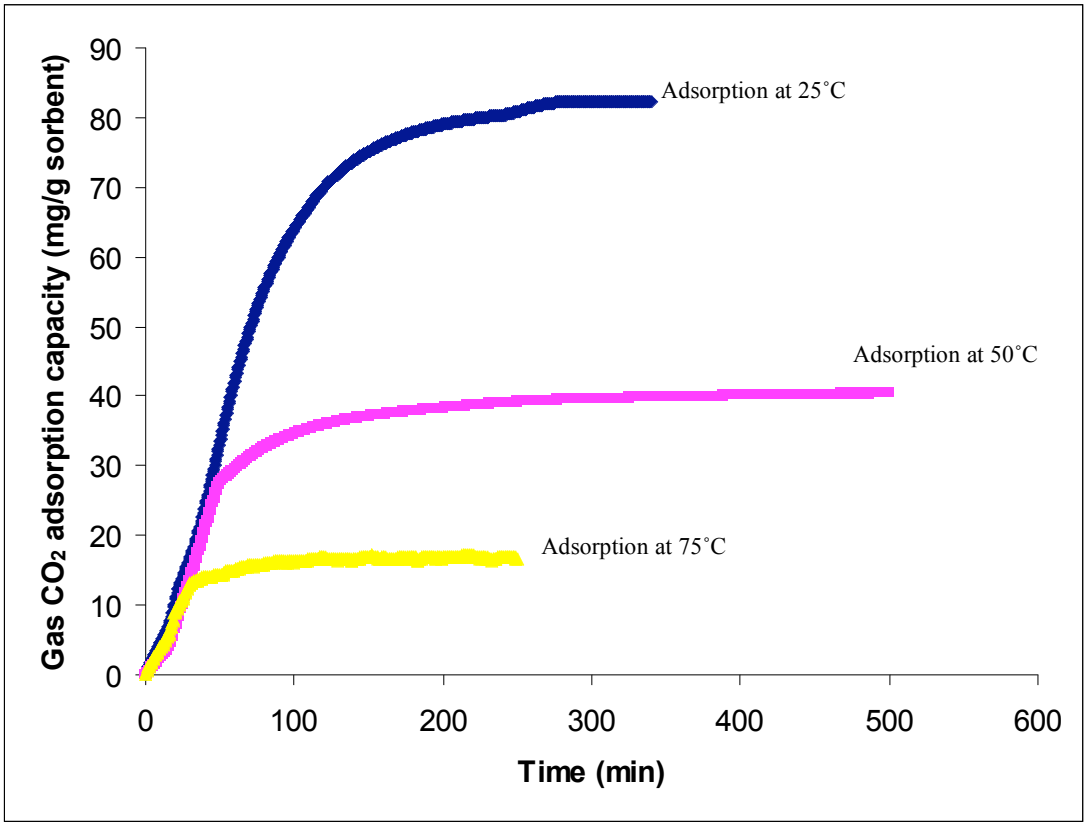

Figure 7.18: TGA curves of CO_2 adsorption capacity for 20 wt% MEA modified MCM-41 at different adsorption temperatures.

4.3.4.2 Heating temperature

The water vapor content in natural gas mixtures can vary from less than 1% to more than 10%. On the other hand, water also plays an important role of proton transfer agent in the reaction of acidic gas and amine solutions (conventional method of removing acidic gas from natural gas). Therefore, it is important to study the effects of water on acidic gas adsorption (Kaggerud *et al.*, 2006; Huang and Yang, 2003).

Through the study by Huang and Yang, they indicated that water vapor actually enhanced CO_2 adsorption on the amine modified samples. Quantitative analysis of the CO_2 desorption amount according to the peak area indicates that the amount of CO_2 desorbed is twice when the water was present during the adsorption. Their result is consistent with the fact that the mechanism for CO_2 removal using amines is dependent on the presence of water. Two moles of amine groups are required to remove every one mol of CO_2 molecules in order to form carbamate when water vapor is absent from the reaction. Whereas, one mol of amine groups is effective enough in removing one mol of CO_2 to form bicarbonate in the presence of water. The study also suggests that the CO_2-amine bonding is enhanced when water vapor is presence during the adsorption (Gray *et al*., 2005; Zhou *et al*., 2005; Khatri *et al.*, 2005; Huang and Yang, 2003).

Since the presence of water affects the CO_2 adsorption capacity, thus it is essential to study the effect of water vapor during gas-solid adsorption interaction. In this study, the main purpose of applying heat to the samples through TGA equipment is to remove impurities and water vapor in order to obtain clean adsorption on the adsorbents. However, since the presence of water proved to be affecting the adsorption capacity, the following experiment was designed to verify the theory. Four different heating temperatures were applied through TGA to investigate the adsorption capacity of 20 wt% MEA modified MCM-41 as shown in Figure 7.19.

The first heating temperature is 25˚C at room temperature (which is without heating). The result shows adsorption capacity of 21.71 mg/g sorbent which is lower than standard experiment temperature at 100˚C with high adsorption capacity of 40.91 mg/g sorbent. The same result is obtained when heating temperature is raised to 50˚C with only a slight increase of adsorption capacity at 23.47 mg/g sorbent. These findings clearly show that although the presence of water does improve adsorption, but without impurities being removed from the pore channels and surface of the adsorbents, it is impossible to achieve maximum CO_2 adsorption capacity. For the last experiment, heating temperature was applied higher than water boiling point at 150˚C since even at 100˚C there still is a small trace of water vapor trapped. This

is to ensure all water vapor is removed from the system, hence the adsorption of CO_2 without the presence of water vapor is able to be confirmed. The CO_2 adsorption capacity at heating temperature 150˚C is 33.11 mg/g sorbent which is about 19% lower than standard at 100˚C. The result further confirm that the presence of water vapor does contribute to CO_2 adsorption capacity by amine modified MCM-41.

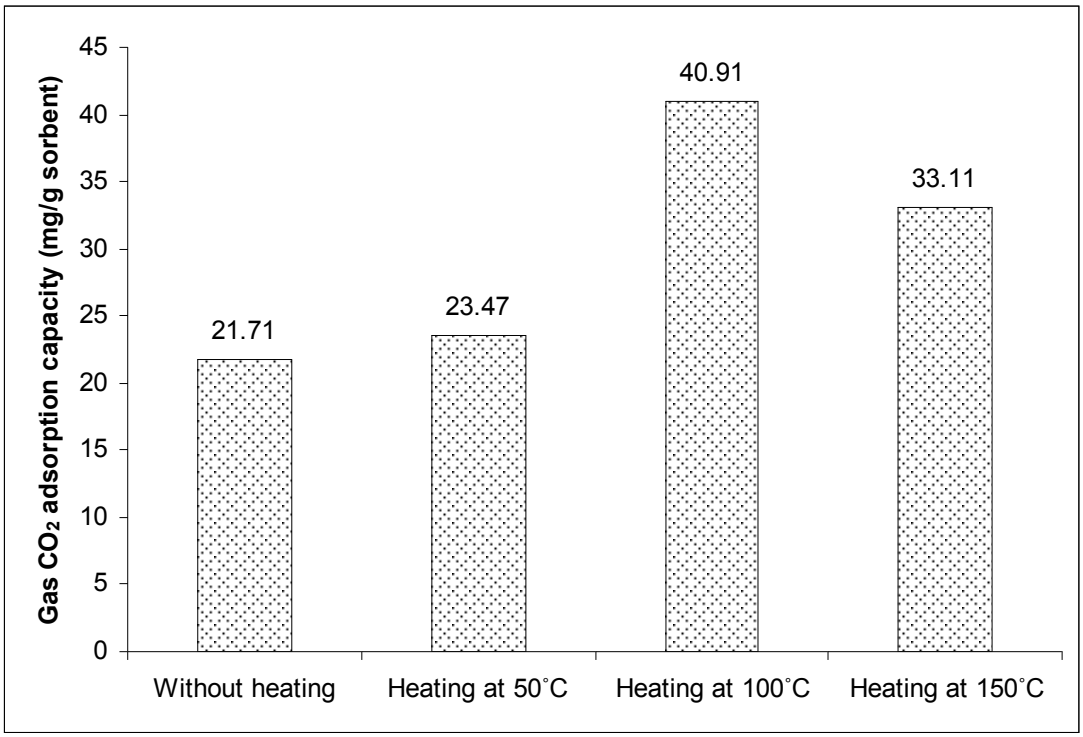

Figure 7.19: CO_2 adsorption capacity for 20 wt% MEA modified MCM-41 at different heating temperatures.

Figure 7.20 presents the effect of heating temperatures on CO_2 uptake rate of 20 wt% MEA modified MCM-41. Surprisingly, although without heating gives the lowest adsorption capacity, the rate of CO_2 adsorption is extremely fast compare to others. For the first 20 minutes, a total of 94% CO_2 uptake is already adsorbed by the adsorbent and the equilibrium is reached by 80 minutes time. As for heating temperature at 50˚C, the uptake rate is a bit slower with 83% of total uptake can be achieved for the first 20 minutes and the equilibrium time required is also quite fast at 110 minutes. Finally, the CO_2 uptake rate shows by 20 wt% MEA modified MCM-41 at heating temperature 150˚C is 78% for the first 50 minutes. The

equilibrium adsorption time is also longer at 350 minutes but is still faster than uptake rate for standard heating temperature at 100˚C.

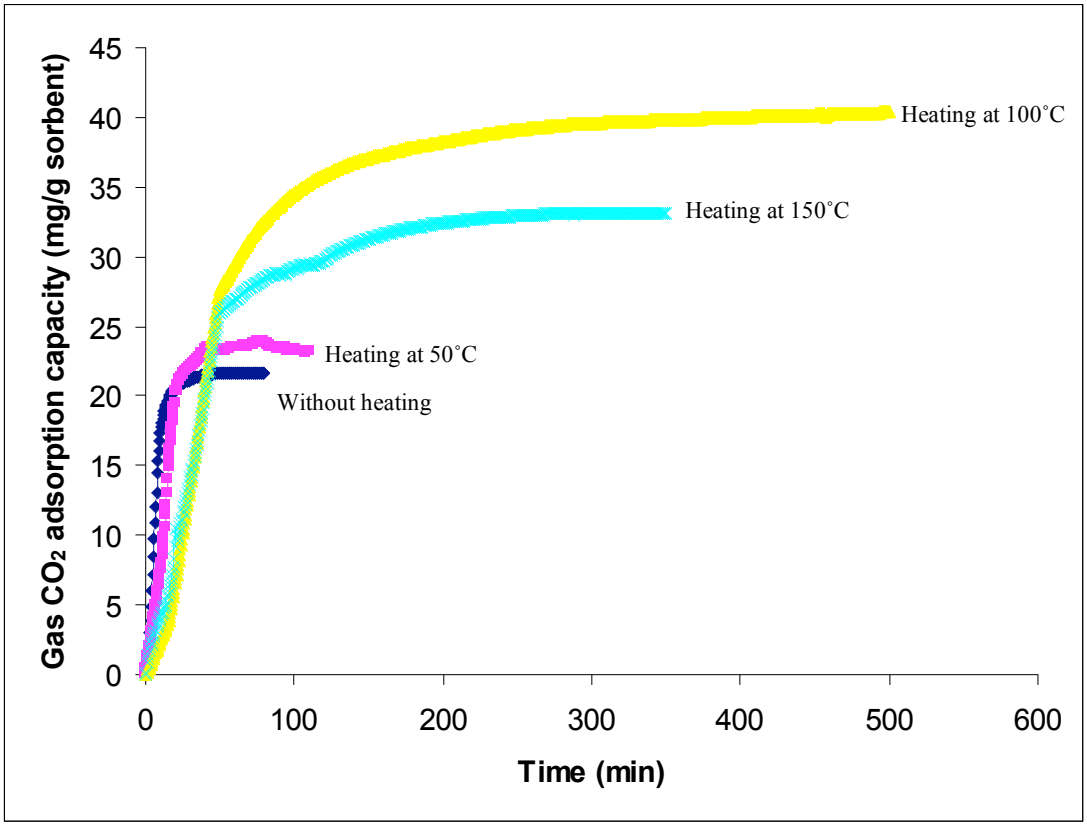

Figure 7.20: TGA curves of CO_2 adsorption capacity for 20 wt% MEA modified MCM-41 at different heating temperatures.

7.4 Gas-Solid Interaction

Interaction between asorbate gas and the solid adsorbent plays an important role in adsorption process. Therefore, it is essential to fully understand the characteristics of interaction between the adsorbed CO_2 gas molecules and the amine modified support materials. In situ FTIR spectroscopy has been utilized for studying the adsorbed species interaction with support materials surface directly and the transport of interacting molecules in pores of the support materials. For this study,

the amine modified samples were activated at 100˚C and vacuum at the same time for 2 hours before the introduction of adsorption gas CO_2 at various pressures. After the adsorption of CO_2 at room temperature for another 1 hour, the samples were studied by transmission FTIR spectroscopy. Thus, the FTIR spectra acquired are the result of solely the interaction of CO_2 gas with the support surface only.

7.4.1 Interaction of CO_2 on various amines modified MCM-41

Carbon dioxide is a linear molecule with four fundamental vibration modes at v_1 1340 cm^{-1}, v_3 2350 cm^{-1} and two bending modes at 666 cm^{-1}, only v_3 and one of the v_2 bending modes that in the plane position are infrared active (Hiyoshi *et al*., 2005; Ingle and Crouch, 1988). The in situ FTIR cell used in this study consists of CaF_2 window which leads to the limitation of wavelength range at 77,000 – 900 cm^{-1}. Hence, the vibration of CO_2 molecules will only be detected at 2350 cm^{-1} region. FTIR spectra of various amines modified MCM-41 after CO_2 adsorption process is presented in Figure 7.21. The spectra are separated into two section which are physisorption section in the region of 2600 – 2000 cm^{-1} and chemisorption section in the region of 1580 – 1350 cm^{-1}.

From Figure 7.21, the band with frequencies around 2350 cm^{-1} is attributed to the v_3 vibration of physisorbed CO_2. It was observed that the FTIR spectra of adsorbed CO_2 in amine modified MCM-41 is similar to the CO_2 band for the parent MCM-41 support. The 2350 cm^{-1} band in the spectra CO_2 appeared at the same location for the pure CO_2 gas phase and the adsorbed physisorbed phase which further confirmed the physisorption of CO_2 molecules on the amine modified MCM-41. Meanwhile, another broader band in the 1580 – 1350 cm^{-1} region was observed for all the amine modified MCM-41 except the MCM-41 support. The peak broad band at around 1455 cm^{-1} represents the C-N stretching vibrations in other word the chemisorbed CO_2 band. The parent MCM-41 spectrum does not exhibit the band at

1455 cm^{-1} region since no amine was detected. This clarify the 1455 cm^{-1} band is attributed to chemisorption of CO_2 reacted with amine of the amine modified MCM-41 to form carbonates and bicarbonates in certain circumstance (Zhao *et al*., 1996; Wakabayashi *et al*., 1997; Khatri *et al*., 2005; Hiyoshi *et al*., 2005).

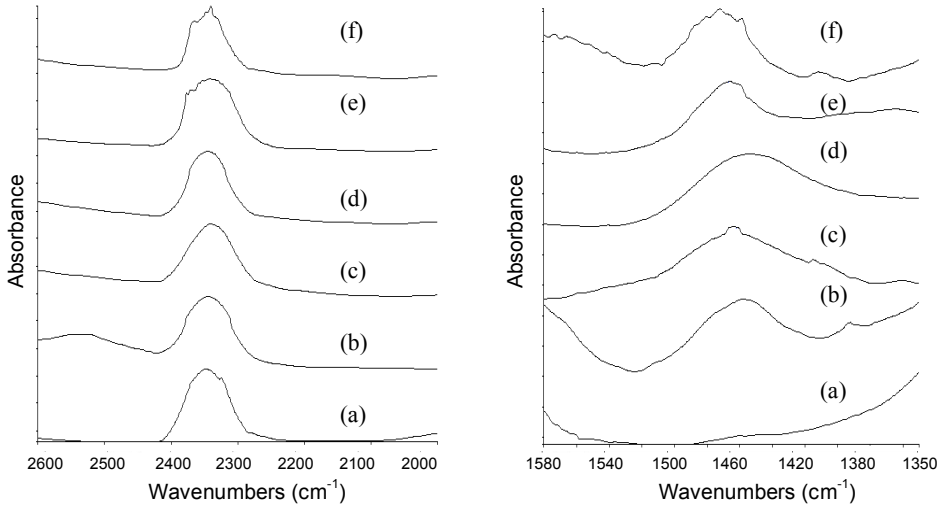

Figure 7.21 FTIR spectra of CO_2 adsorbed on: (a) MCM-41; (b) 20 wt% MEA MCM-41; (c) 20 wt% DEA MCM-41; (d) 20 wt% TEA MCM-41; (e) 20 wt% MDEA MCM-41; and (f) 20 wt% PEI MCM-41 at equilibrium pressures of 138 kPa and room temperature 25˚C.

All amine modified MCM-41 and parent MCM-41 show absorption band at 2350 cm^{-1} region which represent physisorption of CO_2 on the adsorbents as shown in Figure 7.21. All the bands can be observed at around the same region of 2350 cm^{-1}. However, the opposite happen on the chemisorption section which shows inconsistent band and with different absorbance value. The 20 wt% TEA MCM-41 spectrum shows the absorption band at 1456.46 cm^{-1} which is slightly shifted to the lower wavelength compares to others which are more consistent. On the other hand, the parent MCM-41 spectrum does not shows any peak at 1455 cm^{-1} region since there is no amine being modified on the adsorbent.

7.4.2 Interaction of CO_2 on modified MCM-41 at various pressures

In order to investigate the effect of equilibrium pressure to the mechanism of CO_2 gas interaction with MCM-41 surfaces, the adsorption of CO_2 molecules at room temperature (25˚C) with increasing pressure on amine modified MCM-41 was carried out as shown in Figure 7.22. Although the absorbance of the stretching bands changed with increasing pressure, but the band frequencies almost remain unchanged.

By observing the FTIR spectra, increased of the equilibrium pressure would result in an increase of the intensity of the 2350 cm^{-1} absorption band which is assigned to physisorbed CO_2 band. All the bands show consistent frequencies but increased in intensity. As for the chemisorbed band at 1455 cm^{-1} region, the absorption peaks were not consistent especially at high pressure of 414 kPa and 552 kPa. The bands clearly shifted to lower frequencies at around 1420 cm^{-1}.

By increasing the CO_2 equilibrium pressure, the absorbance area for the physisorption peak also increase up to 276 kPa as shown in Figure 7.23. However, further increase in pressure up to 414 kPa and 552 kPa shows decreasing in absorbance area. The peak area in the 2345 – 2335 cm^{-1} region starting to decrease at high pressure as the CO_2 adsorption achieved saturation condition in the case of physisorption. However, in the case of chemisorption, the higher CO_2 equilibrium pressure applied, the more interaction between amine and CO_2 molecules resulting in more chemical reaction and higher chemisorption (Hiyoshi *et al.*, 2000; Zheng *et al.*, 2005; Xu *et al*., 2003; Cheng *et al.*, 2006a). This is evidently shown in Figure 7.24 as the peak area in the 1450 – 1420 cm^{-1} region kept increasing with pressure increment.

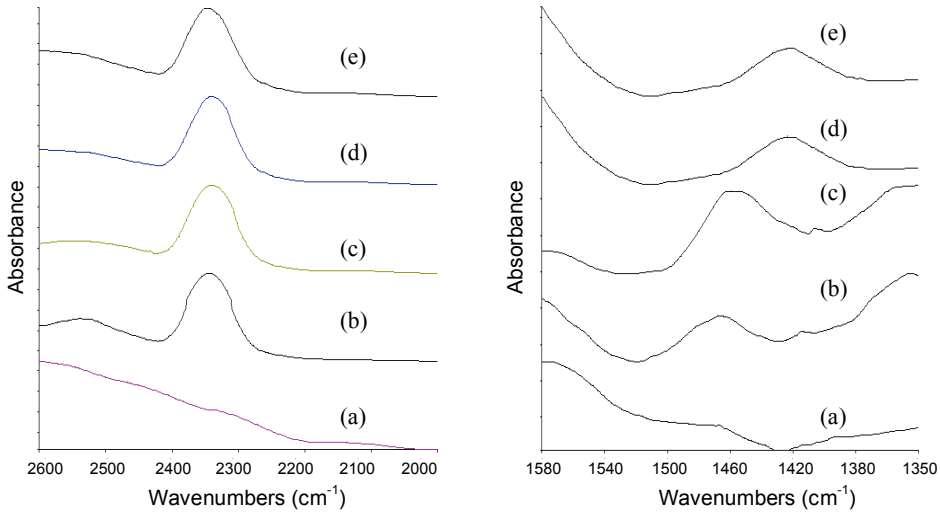

Figure 7.22: FTIR spectra of CO_2 adsorbed on MEA modified MCM-41 at 25˚C and equilibrium pressure: (a) without CO_2; (b) 138 kPa; (c) 276 kPa; (d) 414 kPa and (e) 552 kPa.

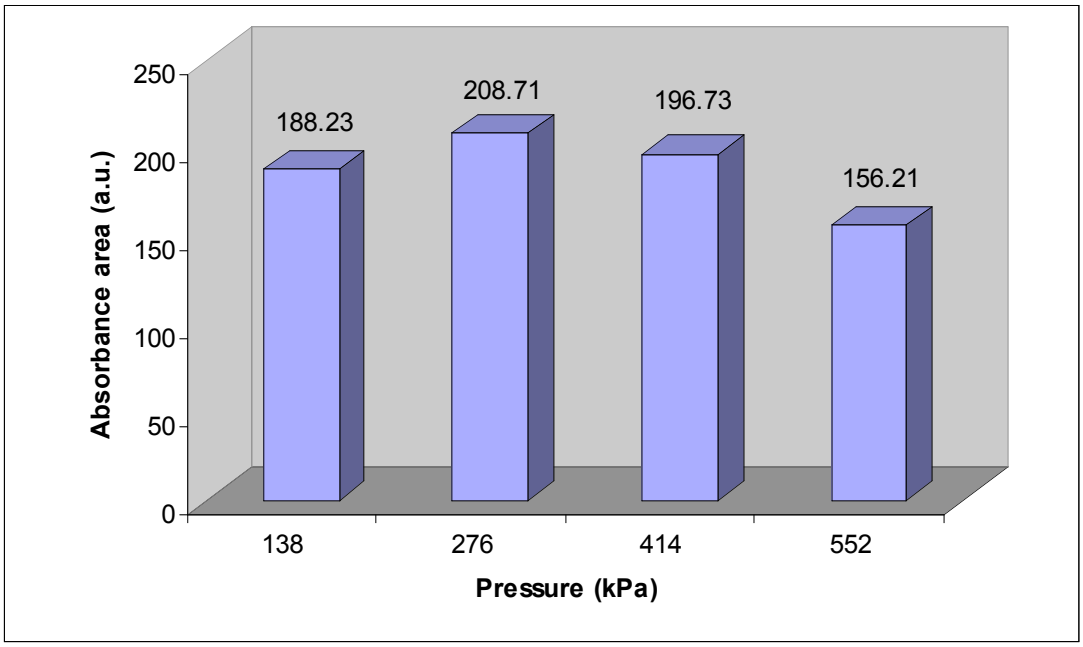

Figure 7.23: Effect of equilibrium CO_2 pressure on the FTIR absorbance areas (2345 – 2335 cm^{-1} region) for the physisorption peak.

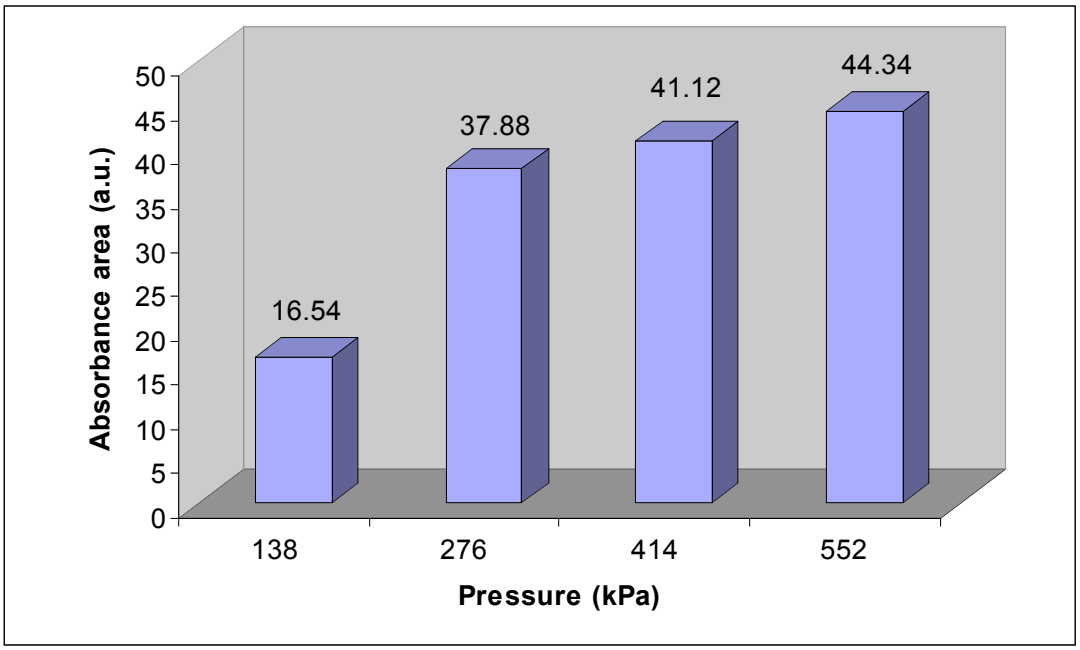

Figure 7.24: Effect of equilibrium CO_2 pressure on the FTIR absorbance areas (1450 – 1420 cm^{-1} region) for the chemisorption peak.

7.5 Summary

The structural characteristics and properties as well as carbon dioxide adsorption characteristics of amine modified mesoporous and microporous materials have been thoroughly studied within the scope of research. The adsorption process of porous materials is generally depends on several parameter such as pore volume, surface area, surface properties and the strength of adsorbate-adsorbent interactions. The incorporation of various alkanoamines on porous materials greatly enhances the CO_2 adsorption performance especially for mesoporous materials. Furthermore, the amines also improved the CO_2-adsorbent bonding and as a result increasing the selectivity of the adsorbent towards CO_2 adsorption. However, effect of amines on porous materials is varying differently towards mesoporous materials and

microporous materials. From the study, mesoporous materials' CO_2 adsorption capacity improved significantly when using monoethanolamine as the modifying agent especially on MCM-41 support. By contrast, monoethanolamine modification on microporous materials shows reduced CO_2 adsorption capacity. In addition, not all amines are suitable for modification on porous materials. Certain amines with large molecules size would actually decrease the CO_2 adsorption performance of the adsorbent. Therefore, this study proved to be important in order to understand the CO_2 adsorption performance of amine modified mesoporous and microporous materials.

CHAPTER 8

ZEOLITE AS ADSORPTIVE METHANE STORAGE ADSORBENT

8.1 Introduction

Porous solid are used technically as adsorbents, catalyst and catalyst supports owing to their structures that give rise high surface area. These structures vary greatly depending on the method of preparation. In particular, they differ in their pore dimensions, which can range from molecular size of 0.5 to 1 nm as in zeolitic materials, to 2-10 nm as in mesoporous MCM-41 type of materials, to large pores as in amorphous silica without a regular structure. Because of the different pore dimensions, these materials have different adsorptive and diffusive properties for organic molecules, which lead to different adsorption behaviors. In this chapter, results for the high pressure methane adsorption on various microporous and mesoporous silica adsorbents will be discussed based on the methane adsorption capacity, and amount of methane adsorbed and desorbed. The effect of adsorbents structure and properties on methane adsorbed and desorbed capacity will be discussed. Effect of metal oxide and metal loading will also be discussed in order to understand how certain metal will affect the adsorbents on methane adsorbed and desorbed capacity. The performance and temperature changes of the adsorbents during charging and discharging will also be discussed.

8.2 Microporous and Mesoporous Silica

8.2.1 Methane Adsorption Characteristics

The methane adsorption capacity of various types of adsorbents for pressure range from 100 to 500 psi is given in Table 8.1. Each adsorbent has different structure and properties such as surface area, micropore volume and packing density that have an influence on the methane adsorption capacity. The methane adsorption capacity of zeolite 13X was found to be comparable with the results reported in the literature. For instance, at 500 psi, the methane storage capacity was found to be 5.0104 mol/kg. While, at the same pressure, Cavenati *et al*. (2004) was reported to be 5.055 mol/kg. This difference might be due to different assumptions and method of calculation used. It is also at 500 psi, the methane adsorption capacity for microporous adsorbents decreases according to the following order: zeolite H-Beta > zeolite 13X > zeolite HY > zeolite ZSM-5.

Table 8.1: Methane adsorption capacity of adsorbents at various pressures.

Adsorbents	**Packing Density (g/cm^3)**	**Methane Adsorption Capacity (mol/kg)**				
		100 psi	**200 psi**	**300 psi**	**400 psi**	**500 psi**
13X	0.56	2.7435	3.3103	3.8769	4.4437	5.0104
ZSM-5	0.53	1.5180	2.0856	2.6531	3.2207	3.7883
H-Beta	0.23	1.6806	2.9347	4.1887	5.4427	6.6967
HY	0.38	0.9089	1.7045	2.5003	3.2960	4.0916
MCM-41	0.14	2.7440	5.0685	7.3932	9.7179	12.0425
SBA-15	0.08	4.3744	7.8300	11.2856	14.7411	18.1967

The methane adsorption capacity for the mesoporous adsorbents (SBA-15 and MCM-41) is higher than microporous adsorbents. Methane adsorption capacity of MCM-41 at 35 bar (508 psi) reported by Duren *et al*. (2004) was 41.57 cm^3/cm^3, which is in good agreement with result obtained in this study. At 35 bar (508 psi), MCM-41 adsorption capacity obtained from this study is 41.32 cm^3/cm^3.

According to Chang and Talu (1996), the most commonly used indicator of the methane delivery is based on the volume of gas discharge at ambient condition over volume of the storage. Table 8.2 shows the volumetric methane adsorption capacity for various adsorbent at pressure from 100 to 500 psi. On volumetric basis, SBA-15 and MCM-41 have lower volumetric adsorption capacity than microporous zeolites understudy.

Table 8.2: Methane adsorption capacity (V/V) of different adsorbents at various pressures.

Adsorbents	**Packing Density (g/cm^3)**	**Methane Adsorption Capacity (V/V)**				
		100 psi	**200 psi**	**300 psi**	**400 psi**	**500 psi**
13X	0.56	37.88	45.71	53.53	61.36	69.18
ZSM-5	0.53	20.03	27.52	35.02	42.50	49.99
H-Beta	0.23	10.29	17.31	24.30	31.35	38.37
HY	0.38	8.56	16.06	23.55	31.05	38.54
MCM-41	0.14	8.03	15.66	23.29	30.92	38.56
SBA-15	0.08	9.17	16.41	23.65	30.89	38.13

Tables 8.1 and 8.2 show that low packing density with high surface area on weight basis will have higher methane capacity per unit mass of adsorbents as pressure increases however the methane capacity at high pressure are less compare to the other adsorbents with higher packing density but lower surface area. Mesoporous silica such as MCM-41 and SBA-15 has higher surface area compare to zeolite but low packing density resulting in higher methane capacity per unit mass of adsorbent. This explains why mesoporous silicas have higher methane capacity per mass adsorbent as pressure increases but in term of volume methane desorbed or store per volume of cell, microporous silicas give better mass methane adsorption capacity.

The adsorbents tested for the high pressure adsorption are expected to experience structure change before and after high pressure adsorption. However, XRD results show that adsorbents before and after high-pressure adsorption do not exhibit any changes in their structure. Salem *et al*. (1998) did high-pressure adsorption on activated carbon and according to their results, there were also no structure changes occur after high pressure adsorption. It is possible to have some changes during adsorption but it is reversible. Although, XRD results show that the structure for microporous and mesoporous adsorbents do not change after high pressure adsorption but studies done by Bai *et al*. (2002) indicate that high pressure between 1000 bar (14503 psi) and 4800 bar (696181 psi) will influence the structure of mesoporous materials. Therefore, one can conclude that adsorption pressure range from 1 bar to 34.47 bars will not change the structure of the adsorbents.

From the literature, one expects that the best material to achieve high methane adsorption per mass of adsorbent would have high accessible surface area, high free volume, low adsorbent framework density and strong energetic interaction with the adsorbed methane (Duren *et al*., 2004). Much attention has focused on the role of surface area so in this study the role of surface area will be analyzed. In order to elucidate the affect of surface area on the amount of methane adsorbed, the amount

methane adsorbed at 500 psi (34.47 bar) was plotted (Figure 8.1). The results show that zeolite 13X, zeolite H-Beta, zeolite ZSM-5 and zeolite HY, which are microporous silica are affected by the surface area. The higher surface area gives higher the methane adsorption capacities. However, MCM-41 and SBA-15 which are mesoporous silica do not affect by the surface area. MCM-41 which has higher surface area has lower methane capacity compare to SBA-15. One factor that may contribute for the difference in term of methane adsorption capacity between SBA-15 and MCM-41 is that in SBA-15 has the presence of specific adsorption sites.

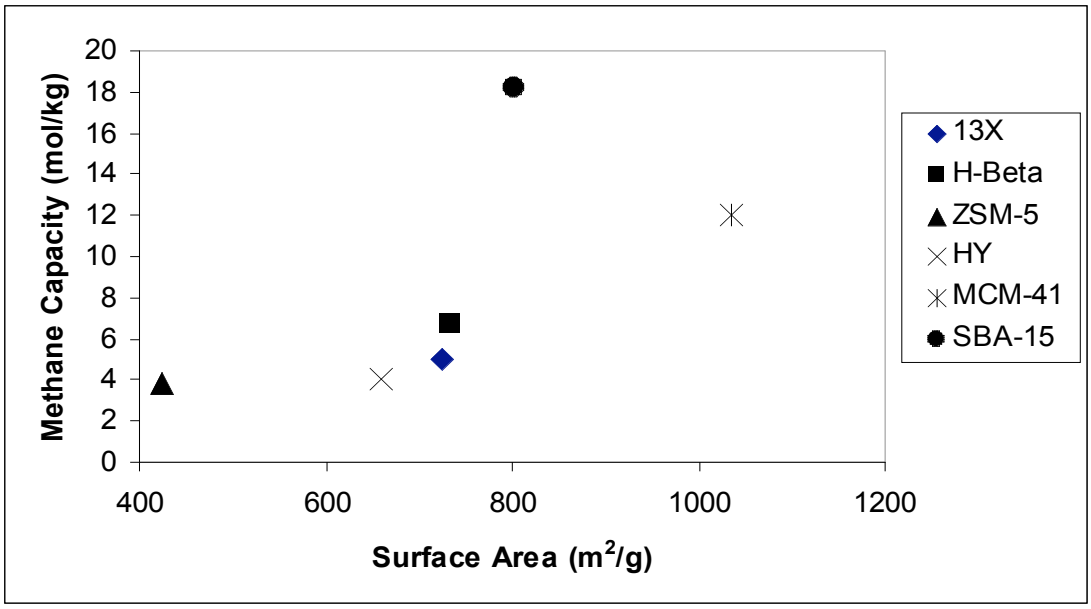

Figure 8.1: Methane adsorption capacity at 500 psi versus adsorbents surface area.

Recently reported structural elucidation studies on SBA-15 indicated the existence of micropores within the pore walls of its mesopores (Fulvio *et al*., 2005; Klimova *et al*., 2006; Newalkar *et al*., 2002). The origin of such micropores is ascribed to the hydrophilic nature of poly (ethylene oxide) (PEO) blocks of the template that are expected to be deeply occluded within the silica walls, which, upon calcination are responsible for the generation of microporosity. Quantitative measurements by X-ray

diffraction have also shown the existence of microporous corona around the mesoporous of SBA-15 (Newalker *et al*., 2002).

In view of this, the SBA-15 framework is visualized as a complex network consisting of an array of mesopore-micropore network instead of uniform mesoporous network like MCM-41. It is expected that with the presence of these micropores, methane molecules will be transported to these sites through mesopores where they are to be adsorbed strongly and due to this, the performance of SBA-15 is better compare to MCM-41. Results presented in Table 8.3 show the amount of gas adsorbed at specific pressure for both MCM-41 and SBA-15. As indicated in the result obtained, SBA-15 is much better than MCM-41. MCM-41 contain large pore that do not adsorb much methane as their interaction potential is too weak.

Table 8.3: Amount of methane adsorbed (mol/kg) for SBA-15 and MCM-41.

	Amount of Methane Adsorbed (mol/kg)				
Adsorbents	**100 psi**	**200 psi**	**300 psi**	**400 psi**	**500 psi**
SBA-15	1.3869	1.7798	2.1063	2.3554	2.5396
MCM-41	0.8782	1.2898	1.6602	1.9823	2.2637

8.2.2 Methane Adsorption Isotherms

Absolute adsorption isotherms for the four zeolites considered are presented in Figure 8.2. At low pressure, materials with the strongest enthalphic interactions with sorbed molecules show the highest level of adsorption (Frost *et al*. 2006). These tend to

be adsorbents with narrow pores because small pores increase the interaction between methane and the framework.

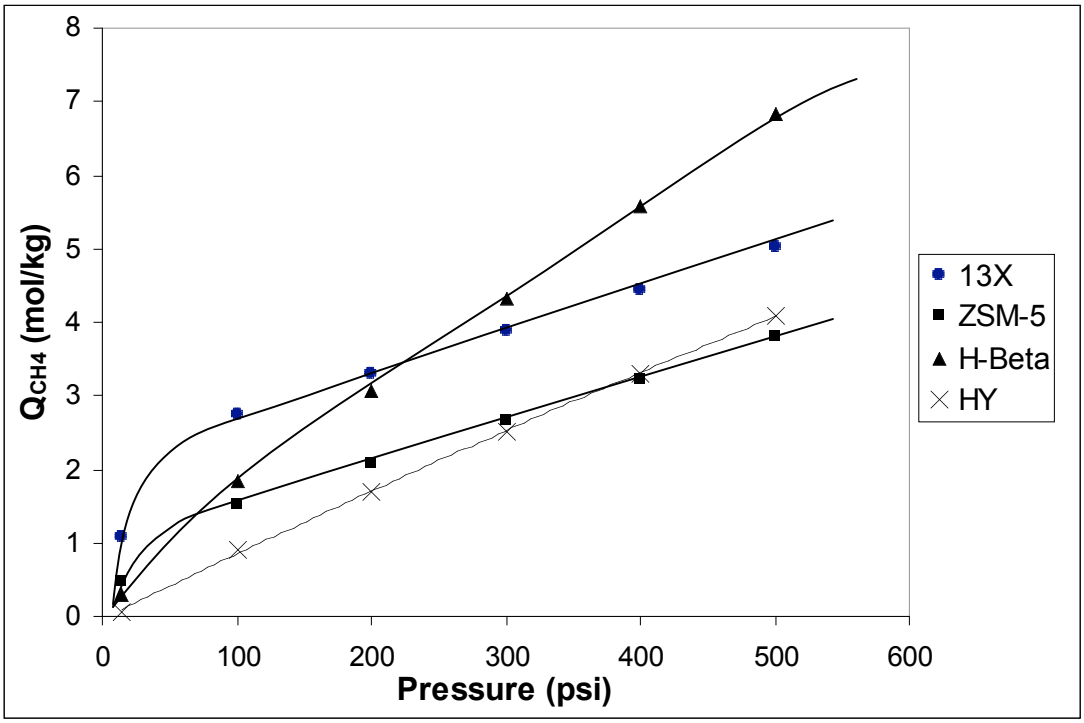

Figure 8.2: Methane adsorption isotherms of various zeolites.

A higher interaction will result higher heat of adsorption. So at low pressure loading, pore size of the adsorbents play an important role but when these pore size are already fill up with methane gas as the pressure increase, the amount of gas adsorbed will then be correlates with the surface area. Frost *et al*. (2006) had identified three adsorption regimes during high pressure adsorption. At low pressure, heat of adsorption will affect the amount methane adsorbed. At intermediate pressures, the amount adsorbed correlates with surface area and at the highest pressure, the amount adsorbed correlates with the free volume.

How the three adsorption regimes connect to each other can be explained using the theory of micropore volume filling. When the methane gas is in contact with the adsorbents, physical adsorption will occur. The pores of the adsorbents will be filled from the smallest pore up to pores of a certain dimension while in larger pores adsorption layer is built up on the pore walls (Nguyen and Do, 2001). As the pressure increases, somewhat wider pores are also filled until at certain pressure a multilayer forms over the filled micropores, which also covers the smooth parts of the surface. These molecules are further pressed against each other as a result of the overlapped potential forces. When the surface area of the adsorbents fill up, adsorbents with free volume will have more room for the guest molecules and consequently will have higher methane gas loading.

The adsorption isotherm (absolute amount adsorbed per kilogram of adsorbent) of methane onto zeolite 13X, zeolite H-beta, zeolite HY, zeolite ZSM-5, SBA-15 and MCM-41 are shown in Figures 8.3 and 8.4. Solid lines in the figures represent the Freundlich isotherm fiting, while the dotted symbols are the experiment data represent each sample tested. The experiment data were well represented by the Freundlich adsorption isotherm model (Choudhary and Mayadevi, 1996), that is

$$q = kP^{1/n} \qquad (4.1)$$

where q is the amount of methane store (mol/kg) at equilibrium pressure P in psi and k and n are the Freundlich constants. The equilibrium adsorption parameters obtained are compiled in Table 8.4. In general, the methane adsorption isotherms were approximately of Type I in nature according to the Brunauer classification, suggesting that physisorption takes place in these materials. Although experiments are extended to relatively high pressure, no maximum was observed in the isotherms.

Table 8.4: Constants of Freundlich isotherm model for methane adsorption onto various adsorbents (0 – 500 psi).

Adsorbents	Freundlich Constants	
	k	n
13X	0.4827	2.6991
ZSM-5	0.1080	1.7683
H-beta	0.0318	1.1650
HY	0.0122	1.0699
MCM-41	0.0395	1.0885
SBA-15	0.0732	1.1297

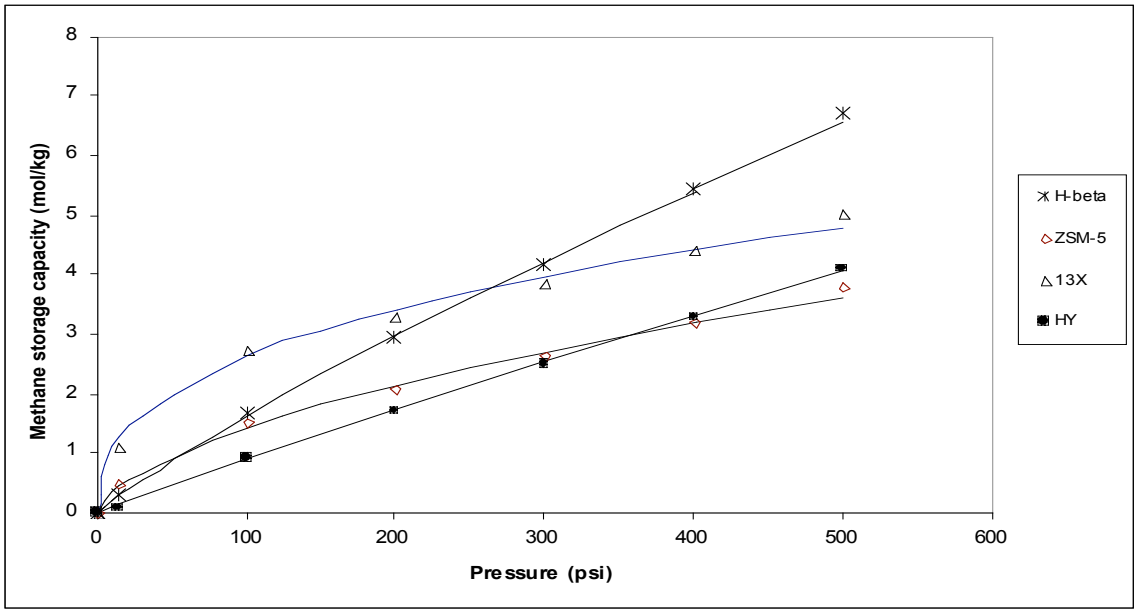

Figure 8.3: Methane adsorption isotherms on various zeolite; solid lines, Freundlich model; dotted symbol, experimental data.

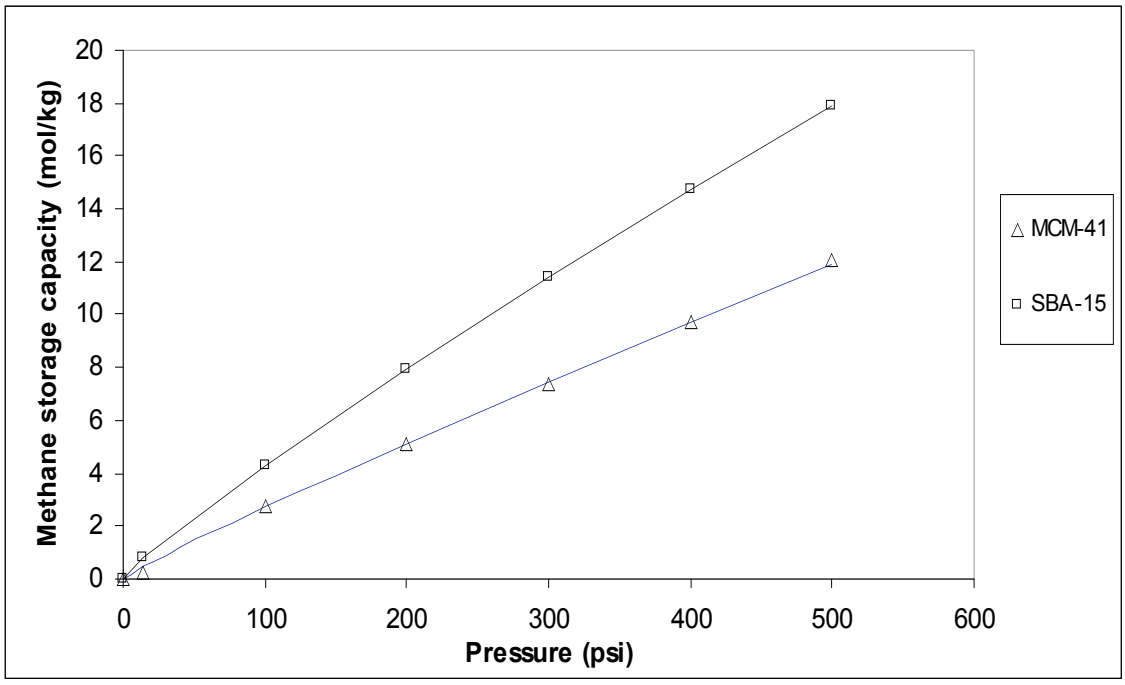

Figure 8.4: Methane adsorption isotherms on MCM-41 and SBA-15; solid lines, Freundlich model; dotted symbol, experimental data.

In order to explore further, a second analysis was performed using the Langmuir model (Ahn *et al*., 2006; Bellat and Grange, 1995; Langmi *et al*., 2005; Huesca *et al*., 1998). In its linear form the Langmuir equation is written as:

$$P/n = 1/(n_m b) + P/n_m \qquad (4.2)$$

Where n is the specific amount of gas adsorbed at the equilibrium pressure P of the gas; n_m the monolayer capacity and b is the adsorption coefficient, which is related to the energy of adsorption (Langmi *et al*., 2005). The Langmuir plots are presented in Figure 8.5 and for all the materials, the plots are nearly linear over the whole pressure range of 0 to 500 psi. This suggests that the Langmuir model may be a valid representation of methane adsorption on these adsorbents and underlying the present observation is physical absorption.

The derived Langmuir parameters are presented in Table 8.5. The data obtain for the amount of gas adsorbed from the experiment are in good agreement with the calculated monolayer capacities except for zeolite HY. Variations in the adsorption coefficient reflect differences in the adsorption energy of the various adsorbents.

Table 8.5: Langmuir parameters for various adsorbents.

Adsorbents	**Experimental Data of CH_4 Adsorbed at 500 psi (mol/kg)**	**Monolayer Capacity, n_m (mol/kg)**	**Adsorption Coefficient, b (psi^{-1})**
13X	3.0222	3.2584	0.0202
ZSM-5	1.5718	1.7746	0.0127
H-beta	0.8957	1.055	0.0106
HY	0.8467	1.4956	0.0020

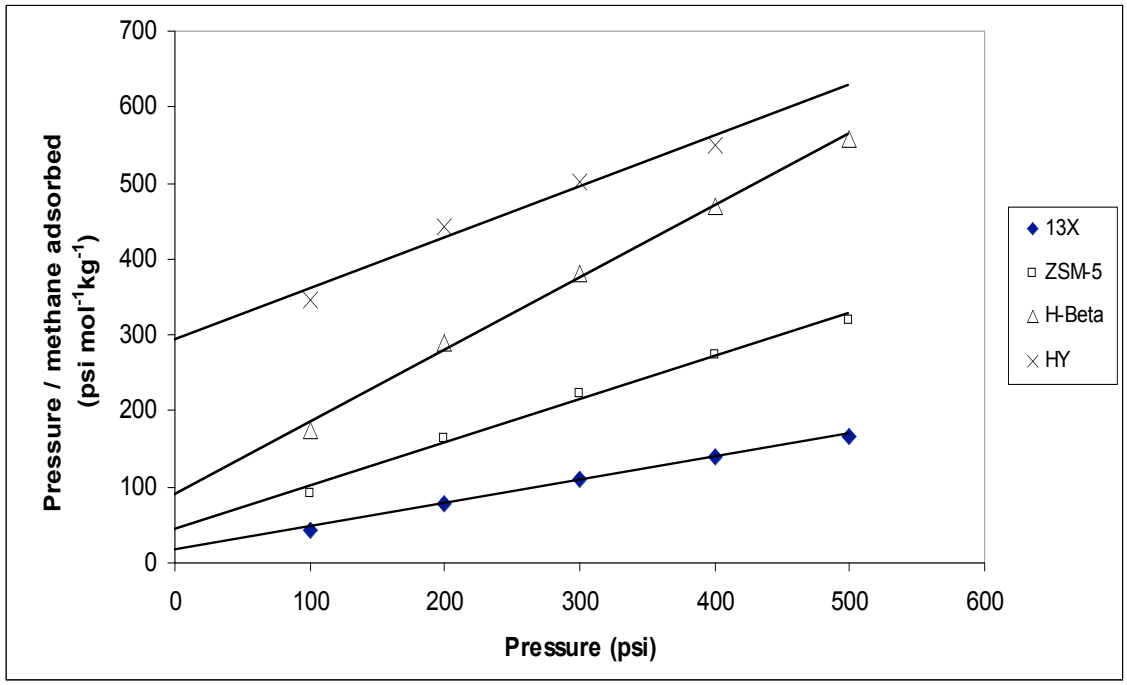

Figure 8.5: Langmuir plots for the adsorption of methane onto various adsorbents.

8.2.3 Methane Adsorptive Storage Characteristics

8.2.3.1 Charging Phase

The temperature profile during methane adsorption onto microporos adsorbents is given in Figure 4.6. Only zeolite H-Beta will be shown here because other adsorbents show similar results to zeolite H-Beta.

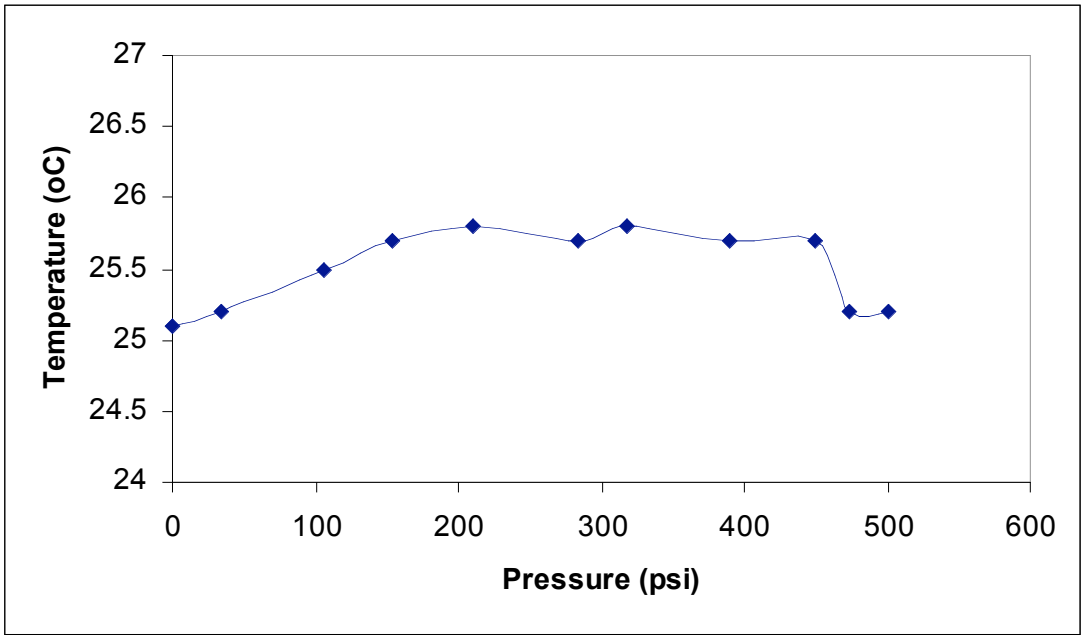

Figure 8.6: Temperature of the adsorption cell during methane adsorption onto H-Beta zeolite at various pressures.

Adsorption is an exothermic process so a rise in temperature occurs (Figure 8.6). The heat is being released is due to the heat of adsorption generated as a result of methane adsorbs on the adsorbent. As the pressure increases, the pore of the adsorbents will fill up until at a certain pressure, so as the heat of adsorption will not influence the

adsorption. This has been explained earlier that high pressure adsorption can be distributed into three regimes which are heat of adsorption, surface area and free volume. As more and more gas is charged into the adsorption cell, the temperature in the cell did not continue to rise instead of the temperature start to fall to ambient temperature. This can be explained that when the temperature starts to fall as pressure increases, all the pore are already being fill, so it is suggest that gas uptake is due mostly to gas compression rather than adsorption (Sejnoha *et al*., 1995).

8.2.3.2 Discharging Phase

The pressure changes that occur in the adsorption cell during discharging is shown only for a typical run with zeolite ZSM-5, discharging the gas from 500 psi to atmospheric pressure. The pressure history is shown in Figure 8.7. The pressure variation with time is nonlinear, since it corresponds to the transformation of a fixed demand rate by the nonlinear isotherm relation.

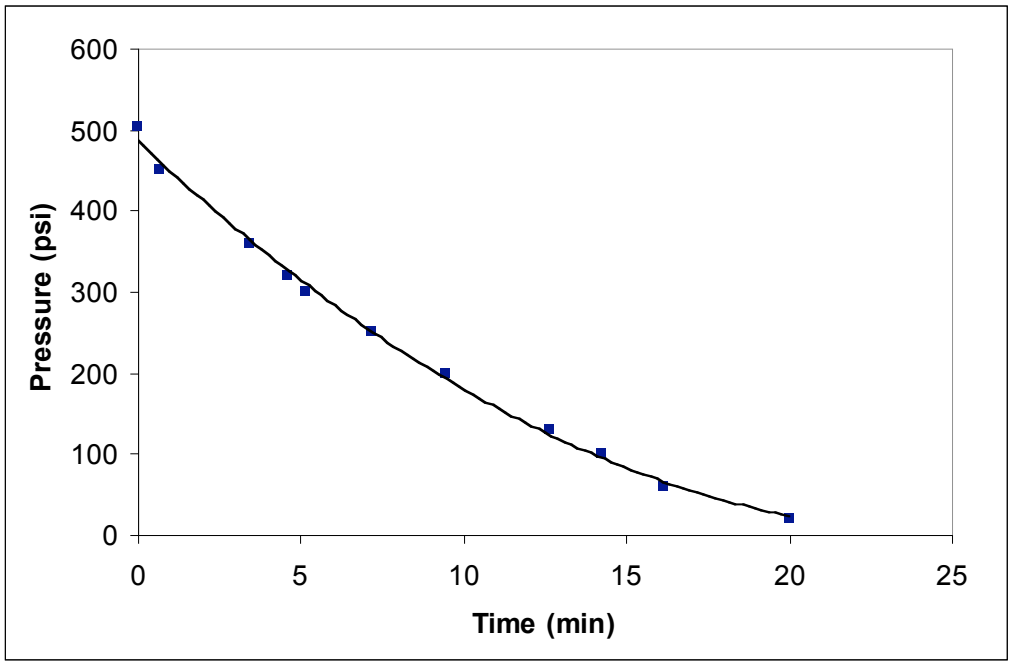

Figure 8.7: A typical transient pressure of the adsorption cell during discharging process.

The behavior of the bed temperature during desorption is rather critical than charging phase. Bed temperature fall with gas exhaustion happens due to the effect of heat of desorption. Variation of the temperature in the very central region of the storage vessel is illustrated in Figure 4.8. Desorption is an endothermic process where heat is used to desorbed the gas. Under natural conditions when no heat is supplied to the system, methane molecules will use heat available within the system to desorb the gas. This will cause the system temperature to fall as the pressure decreases. When the system temperature fall, this will cause some methane gas to be adsorb back into the adsorbent and the larger the temperature drop results the higher the amount of methane retained in the system (Chang and Talu, 1996).

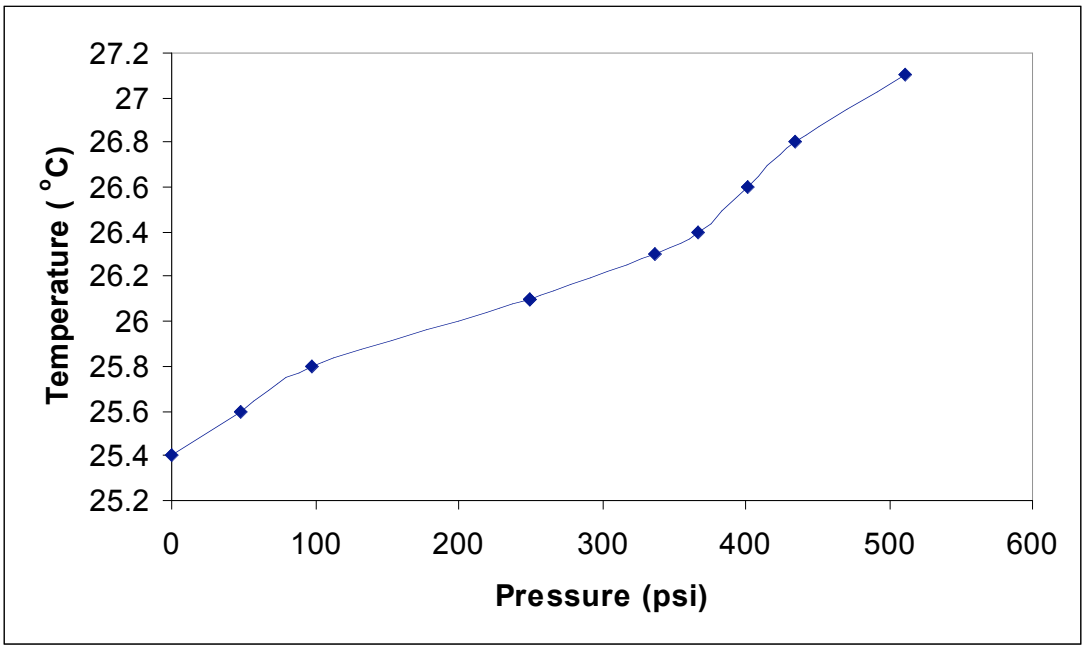

Figure 8.8: Temperature of the adsorption cell during methane desorption from the zeolite H-Beta.

The temperature drop in this experiment is low because heat transfer from the surrounding into the system is easier due to the fact that the adsorption cell used is small. Due to the small dimension of the adsorption cell, heat from the surrounding will encounter little resistance to be adsorbed by the adsorbents.

Tables 8.6 and 8.7 illustrate the amount of gas release and the delivery capacity of different adsorbents at specific pressure respectively. Table 4.6 shows that the zeolite H-Beta, have the highest amount of methane desorbed per gram of adsorbent from pressure 200 psi to 500 psi. At 100 psi, zeolite 13X is much better than H-Beta but as the pressure increases, H-Beta shows higher amount of methane desorbed. The amount of methane desorbed for both zeolite ZSM-5 and zeolite HY were almost the same for pressure ranging from 100 to 300psi. At 200 psi, the methane desorbed for both zeolite ZSM-5 and zeolite HY adsorbents were 1.6104 mol/kg and 1.6479 mol/kg respectively. Meanwhile at 300 psi, the amount of methane desorbed for zeolite ZSM-5 and the

zeolite HY is 2.1779 and 2.4437mol/kg respectively. However, the zeolite HY is much better than zeolite ZSM-5 as the pressure increases. The zeolite HY and zeolite 13X show a similar result at 400 psi and 500 psi. The values for both adsorbents were close for pressure 400 and 500psi. Comparing the results obtain for microporous adsorbents only, the zeolite 13X has the highest amount of methane desorbed per kilogram of adsorbent at 100psi but from 200 psi to 500 psi, H-Beta have the highest amount compare to other adsorbents. The zeolite ZSM-5 shows the lowest amount of methane desorbed although at 100psi it is better than zeolite HY but at pressure 200 psi and above the zeolite HY is better. The mesoporous adsorbents tested in this study have a very high amount of methane desorbed per kilogram of adsorbent compare to the microporous adsorbents. The MCM-41 is 2 times higher than the zeolite H-Beta for all pressure ranges and the SBA-15 has amount of methane desorbed 3 times higher than the zeolite H-Beta. It can also be observed that as the pressure increases, the amount methane release for all adsorbents also increases.

Table 8.6: Amount of methane desorbed at various pressures for different types of adsorbents.

Adsorbents	**Packing Density (g/cm^3)**	**Amount of Methane Desorbed (mol/kg)**				
		100 psi	**200 psi**	**300 psi**	**400 psi**	**500 psi**
13X	0.56	1.6551	2.2219	2.7886	3.3553	3.9220
ZSM-5	0.53	1.0428	1.6104	2.1779	2.7455	3.3131
H-Beta	0.23	1.4673	2.7214	3.9754	5.2294	6.4834
HY	0.38	0.8523	1.6479	2.4437	3.2394	4.0350
MCM-41	0.14	2.5342	4.8589	7.1836	9.5083	11.8329
SBA-15	0.08	3.9150	7.3706	10.8262	14.2817	17.7373

As can be seen in Table 8.7, the volumetric methane delivery capacity was calculated for the adsorbents tested. It can be seen that, even though the sample with the

highest amount of methane release on a gravimetric basis which in this case is SBA-15 (Table 8.6), this sample does not have the highest volumetric delivery capacity. Table 8.7 includes the packing density and volumetric methane delivery values for all the samples used in this study. The zeolite 13X gives the highest value of methane delivery capacity for all pressure range. SBA-15 and zeolite H-Beta have similar values and these two samples have the lowest methane delivery capacity compare to other samples. Zeolite HY and MCM-41 also have similar values but ZSM-5 is better for all pressures. One important parameter that can be taken into account is the packing density. Previously, we find out that packing density also affect the methane adsorption capacity. The zeolite 13X which has the highest packing density gives the highest value of methane delivered in term of volumetric basis and although SBA-15 have the highest methane delivered in gravimetric basis it has the lowest packing density thus resulting lower delivery capacity in volumetric basis. Even though the zeolite HY has higher packing density than MCM-41, their value are almost the same but MCM-41 is better as pressure increases and this is can be due to the large pore volume poses by MCM-41. So in order to get maximum methane delivery, samples with high pore volume and high packing density are needed.

Table 8.7: Methane delivery capacity (V/V) of different adsorbents at various pressures.

Adsorbents	**Packing Density (g/cm^3)**	**Methane Delivery Capacity (V/V)**				
		100 psi	**200 psi**	**300 psi**	**400 psi**	**500 psi**
13X	0.56	22.85	30.68	38.51	46.33	54.16
ZSM-5	0.53	13.76	21.25	28.74	36.23	43.73
H-Beta	0.23	8.66	15.68	22.69	29.71	36.73
HY	0.38	8.02	15.52	23.02	30.51	38.01
MCM-41	0.14	7.83	15.46	23.09	30.72	38.36
SBA-15	0.08	8.20	15.44	22.68	29.92	37.16

Using the measured amount of methane discharge from different adsorbents, a comparison can be made among the adsorbents tested and this is illustrated in Table 8.8. Table 8.8 also includes the amount of methane retained in the cell after discharging at 1 bar. It can be observed that even though the zeolite 13X has the highest methane delivery capacity on volumetric basis, it retains the highest amount of methane at 1 bar, 21.72% of the gas stored still remain in the adsorption cell after discharging. The zeolite ZSM-5 has the second highest of methane retain followed by zeolite H-Beta, SBA-15, MCM-41 and finally zeolite HY. MCM-41 and SBA-15 have lower amount of methane-retained compare to other microporous samples except for the zeolite HY, which has have higher micropore volume compare to other microporous samples.

Table 8.8: Methane adsorption capacity (mol/kg), methane delivery capacity (v/v), and amount of methane retained **(cm^3)** at 500 psi for various adsorbents understudy.

Adsorbents	Packing Density (g/cm^3)	CH_4 Adsorption Capacity, (mol/kg)	CH_4 Adsorption Capacity, (v/v)	CH_4 Delivery Capacity, (v/v)	CH_4 Retained at 1 bar, (cm^3)	% CH_4 Retained
13X	0.56	5.0104	69.18	54.16	225.44	21.72
ZSM-5	0.53	3.7883	49.99	43.73	94.08	12.55
H-Beta	0.23	6.6967	38.37	36.73	24.56	4.27
HY	0.38	4.0916	38.54	38.01	9.03	1.56
MCM-41	0.14	12.0425	38.56	38.36	10.87	1.88
SBA-15	0.08	18.1967	38.13	37.16	14.44	2.52

According to Lozano-Castello *et al*. (2002), samples with too narrow pore size are not suitable for methane storage application because they retain a lot of methane at atmospheric pressure. Mesoporous have high micropore volume and this factor cause the amounts of methane remain in the sample after discharging is low, the value of

1.88% and 2.52% of methane retain in the adsorption cell for MCM-41 and SBA-15 respectively reflects this. Heat of desorption can also causes the methane to be retain in cell due to temperature drop. Discharging is an endothermic process, it has the opposite thermal effect of charging, adsorbents will adsorb heat from the surrounding that cause the temperature in the adsorption cell to drop and thus stop desorption. However in this study, the temperature drop for all the adsorbents tested is not high and the impact on the amount of methane retained after desorption at atmospheric pressure is not significant.

8.3 Modified Microporous and Mesoporous Silica

8.3.1 Methane Adsorption Characteristics

It has been reported that with the introduction of metal into zeolite and mesoporous adsorbents, strong electric field and field gradients will be created that will favor gas adsorption (Li and Yang, 2006).

Thermal dispersion (TD) and incipient wetness impregnation (IWI) methods were employed for the preparation of MgO/H-beta and CuO/H-beta. For the thermal dispersion method, MgO was grinded into powder and mixed uniformly with H-beta at room temperature. The powder mixture was heated up to 873.15 K and held at that temperature for 24 hours. High pressure adsorption until 500 psi was carried out to test this adsorbent and the adsorption performance was compared with that of the adsorbent prepared by the wet impregnation method using $Mg(NO_3)_2$ as magnesium oxide precursor. At 500 psi and room temperature, on thermally dispersed MgO/H-beta, the amount store of CH_4 was 10.8 mol/kg. Similar to MgO/H-beta, CuO/H-beta prepared by thermal dispersion is better than the same adsorbent prepared by wet impregnation

method. The capacity of TD MgO/H-beta and TD CuO/H-beta is 37.4 % and 33.2 % greater than of the same adsorbent prepared by impregnation method respectively. The higher adsorption capacity for the thermal dispersion method was possibly caused by the uniform dispersion of MgO and CuO into the adsorbents channels, the pore sizes that being modified after the dispersion and adding by the moltening effect on the external surfaces, which provides more active sites for CH_4 adsorption. The amount of methane discharge from TD modified adsorbent is also greater than IWI modified samples. Table 8.9 and Figure 8.9 summarize the result obtained.

Table 8.9: Comparison between thermal dispersion (TD) and incipient wetness impregnation (IWI) methods for preparation metal oxide modified zeolites.

Adsorbents	**Methane Adsorption Capacity (mol/kg)**			**Methane Delivery Capacity (mol/kg)**		
	100 psi	**300 psi**	**500 psi**	**100 psi**	**300 psi**	**500 psi**
MgO/H-beta (TD)	2.9044	6.8329	10.7614	2.4343	6.3628	10.2913
MgO/H-beta (IWI)	1.6403	4.1883	6.7363	1.4572	4.0052	6.5532
CuO/H-beta (TD)	2.1298	6.0698	10.0098	2.0499	5.9899	9.9299
CuO/H-beta (IWI)	1.8656	4.2747	6.6839	1.5357	3.9442	6.3534

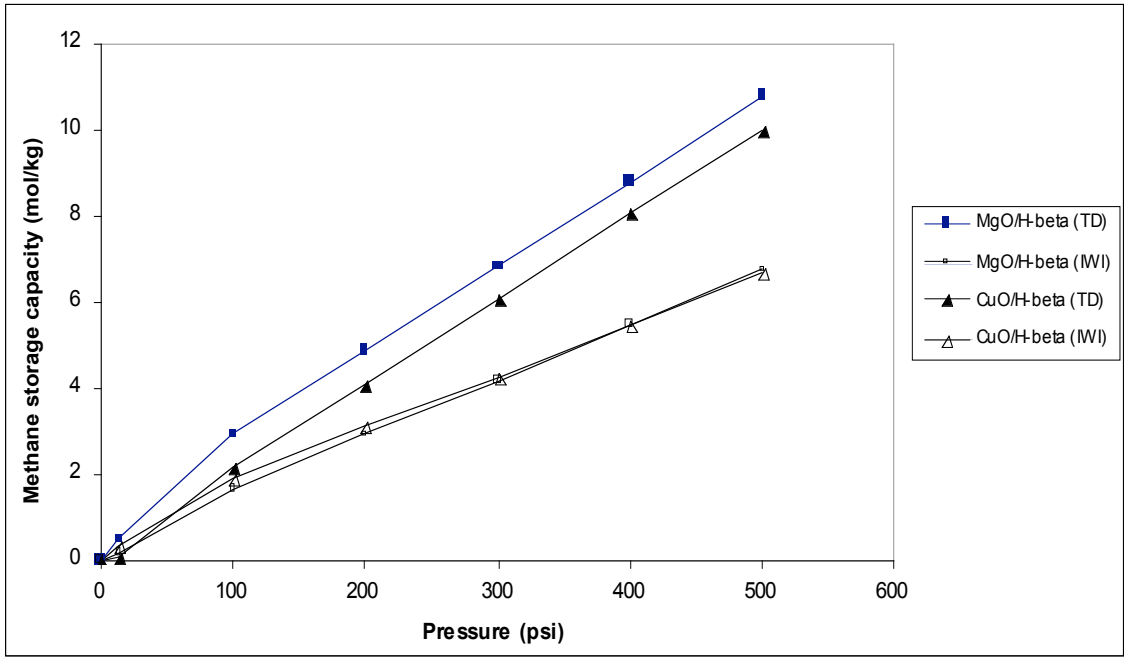

Figure 8.9: Effect of modification techniques on methane adsorption.

Three types of metals were used to disperse onto zeolite H-Beta, 13X and ZSM-5 host matrix system and three types of metal were also used to modify the mesoporous MCM-41 sample. It is suggest that factors such as the pore size of adsorbents, the dynamic diameter of the metal - particle size, and their physicochemical properties play important roles for the dispersion of metal into the adsorbents. The physical properties of the metal used are listed in Table 8.10. Zeolite H-Beta and ZSM-5 was modified using thermal dispersion method by adding metal oxides and results of the XRD show that the peak intensities decreased as compared to unload commercial H-Beta and ZSM-5 which are due to the increase contact matching between the zeolite framework and the present of some metal oxide nanoparticles within the pore of zeolites. Similar XRD results were also obtained for MCM-41. The modified samples surface area and pore volumes will lower compare to the unmodified samples, the decrease in the BET surface area and pore volume could be attributed to the hindrance of the nitrogen molecules into the cavities of zeolite and mesoporous which are occupied by the metal cations (Li and Yang, 2006).

Table 8.10: Physical properties of metal oxides (Náray-Szabo, 1969).

Samples	Particle Size (nm)*	Bond Length (Å)
MgO	39.23	2.10
CaO	92.16	2.40
CuO	25.51	1.84
Co_3O_4	99.13	2.10
NiO	69.91	2.03

* Calculated based on Scherrer equation (Cullity, 1978).

Adsorption capacities were measured for methane on the modified microporous and mesoporous samples. The same experiment procedures were performed for the modified samples until pressure 500 psi. Experimental data are tabulated in Table 8.11. For modified zeolite ZSM-5 samples, all samples showed greater adsorption capacity compare to the unmodified zeolite ZSM-5. For the entire pressure range until 500 psi, zeolite ZSM-5 modified with CuO was found to have the highest methane capacity compare to the other two metals. The zeolite ZSM-5 has a MFI type structure consisting of straight channels and zigzag channels (Figure 8.10). The increase in the gas methane adsorption capacity among the oxides dispersed for the zeolite ZSM-5 was in the following sequences: CuO ~ CaO > MgO.

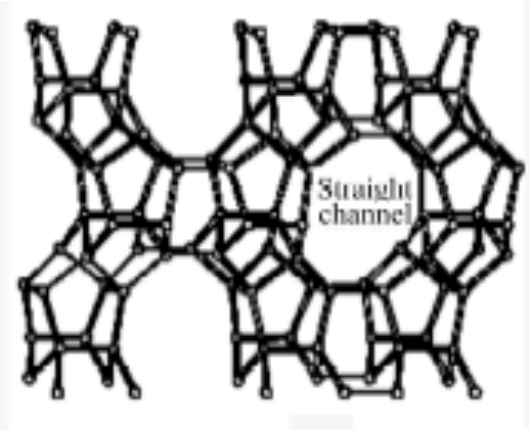

Figure 8.10: ZSM-5 type zeolite (Ming and Wu, 2006).

As for the zeolite H-Beta, all modified samples also showed better methane adsorption capacity compare to the unmodified zeolite H-Beta. Magnesium (II) oxide modified zeolite H-Beta exhibited the most pronounced effect for increasing the capacity nearly up to 60 % higher compare to unloaded zeolite H-Beta. Calsium (II) oxide modified zeolite H-Beta was second best followed by Copper (II) oxide modified zeolite H-Beta.

On the other hand, the methane adsorption capacities of the modified zeolite 13X did not show any improvement compare to the unmodified zeolite 13X. The zeolite 13X has the same framework as the natural mineral faujasite as shown in Figure 8.11. The framework consists of a tetrahedral array of sodalite units interconnected through six membered oxygen bridges. Ten sodalite units form a single large cage-like unit known as supercage. Each supercage is connected to four four neighboring cages through 12-ring windows. According to Langmi *et al* (2005), zeolite type X has very open framework. Since the metal oxides were dispersed instead of ion exchange, some of the

metal ion may have cause pore blocking. The metal loading probably formed agglomeration of bulk metal oxide on the zeolite surfaces and block the pore windows, which restricts the further diffusion of gas CH_4 to adsorb on the active adsorption sites on the zeolite internal surfaces. The ions themselves may occupy significant volumes and affect the methane adsorption capacity. Among the metal oxide used, calcium (II) oxide modified zeolite 13X show the highest methane adsorption capacity compare to the other metal oxides.

Table 8.11: Methane adsorption capacity per kilogram adsorbent onto modified microporous and mesoporous sample.

Adsorbents	**Methane Adsorption Capacity (mol/kg)**				
	100 psi	**200 psi**	**300 psi**	**400 psi**	**500 psi**
ZSM-5	1.5180	2.0856	2.6531	3.2207	3.7883
MgO/ ZSM-5	1.9875	2.6982	3.4089	4.1196	4.8303
CaO/ ZSM-5	1.9978	2.8153	3.6327	4.4501	5.2676
CuO/ ZSM-5	2.0753	2.8792	3.6831	4.4870	5.2909
H-Beta	1.8298	3.0775	4.3253	5.5730	6.8208
MgO/ H-Beta	2.9044	4.8687	6.8329	8.7972	10.7614
CaO/H-Beta	2.4603	4.4329	6.4055	8.3779	10.3506
CuO/H-Beta	2.1298	4.0998	6.0698	8.0398	10.0098
13X	2.7435	3.3103	3.8769	4.4437	5.0104
MgO/13X	0.8029	1.3237	1.8445	2.3653	2.8861
CaO/13X	1.1351	1.6640	2.1929	2.7219	3.2508
CuO/13X	1.1001	1.6683	2.2364	2.8045	3.3726
MCM-41	2.7440	5.0685	7.3932	9.7179	12.0425
MCM-41+Ni	2.6253	5.0599	7.4945	9.9291	12.3637
MCM-41+Co	2.7710	5.3358	7.9007	10.4655	13.0303
MCM-41+Mg	2.0383	3.9381	5.8378	7.7576	9.6373

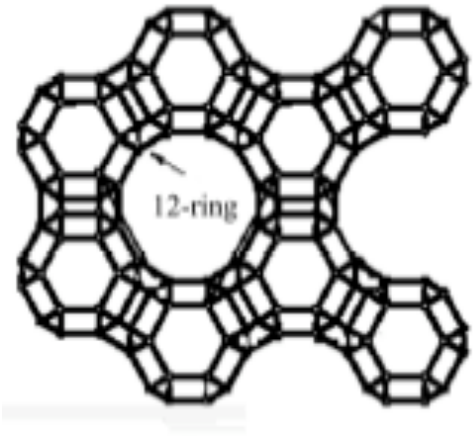

Figure 8.11: X-type zeolite (Ming and Wu, 2006).

Mesoporous samples modified with nickel (II) nitrate and cobalt (III) nitrate showed a slight increase of methane adsorption capacity however magnesium nitrate modified MCM-41 does not showed an improvement instead of having 20% decreasing compare to the unmodified MCM-41. Modified MCM-41 samples using the transition metal nickel nitrate and cobalt nitrate produce the best methane adsorption capacity per kilogram adsorbent compare to other modified adsorbents. However, modified MCM-41 material using magnesium nitrate showed the lowest methane adsorption capacity compare to the other MCM-41 materials. Thus, based on the results obtained in this study, the alkali earth metal seemed to improve the performance of the zeolite H-beta and zeolite ZSM-5 except zeolite 13X and MCM-41.

8.3.2 Methane Adsorption Isotherms

Adsorption capacities were measured for methane on modified ZSM-5, modified H-beta and modified MCM-41 (Table 8.11). The adsorption isotherm for each modified adsorbent is given in Figure 8.12 to Figure 8.14. As shown in Figures 8.12 - 8.14, the Freundlich model fits the data very well. The parameters of the fitting are tabulated in Table 8.12.

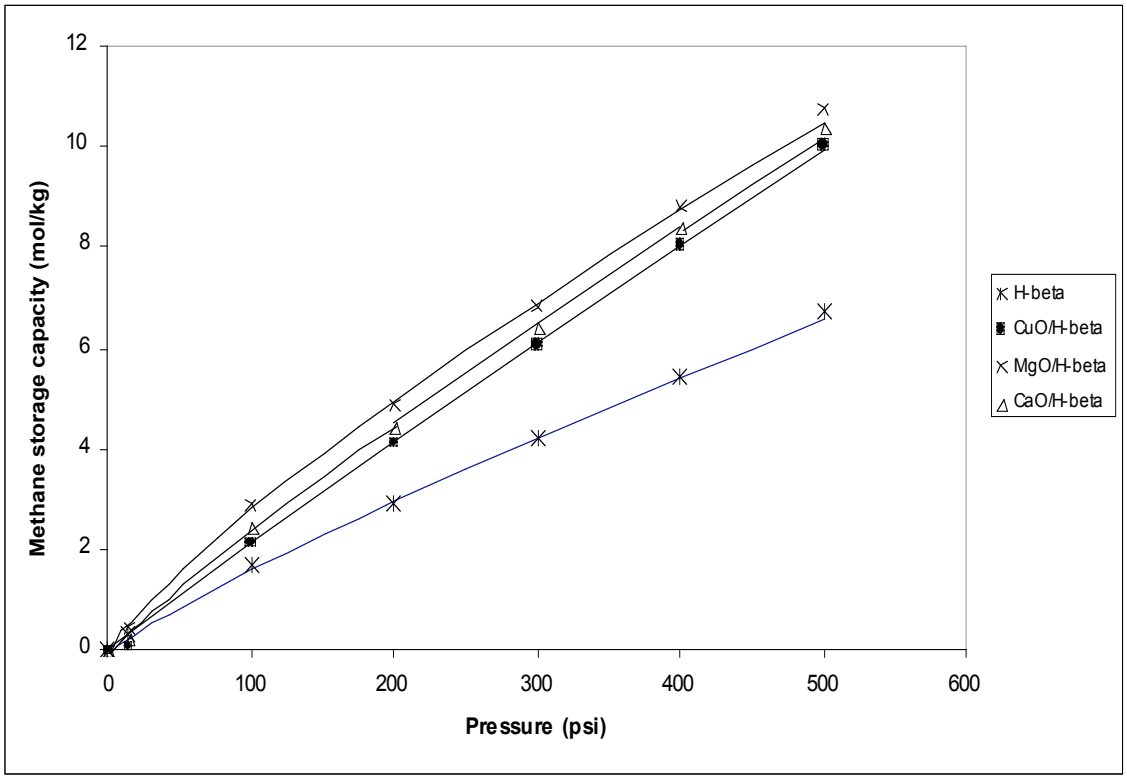

Figure 8.12: Methane adsorption isotherm for modified zeolite H-beta; solid lines, Freundlich model; dotted symbol, experimental data.

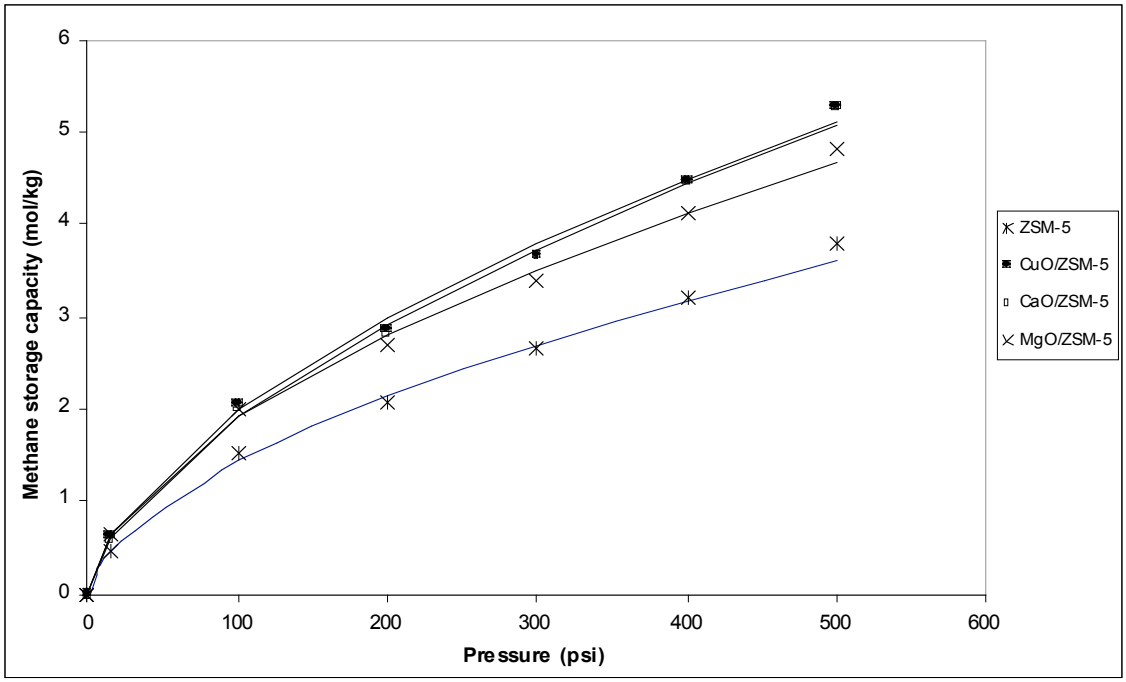

Figure 8.13: Methane adsorption isotherm for modified zeolite ZSM-5; solid lines, Freundlich model; dotted symbol, experimental data.

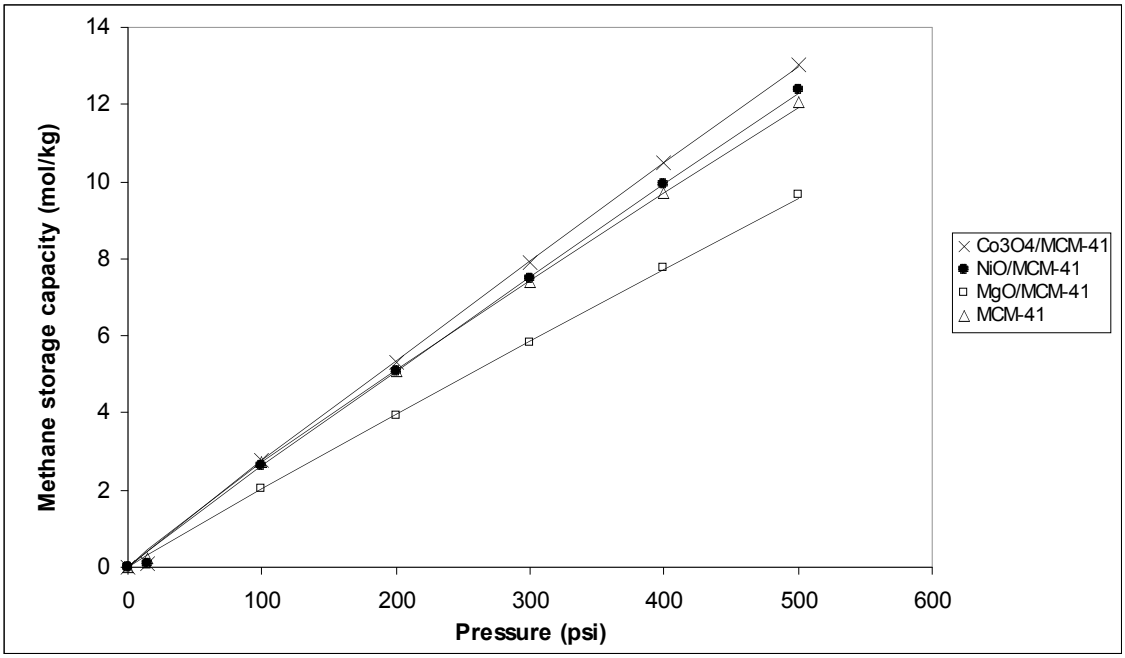

Figure 8.14: Methane adsorption isotherm for modified MCM-41; solid lines, Freundlich model; dotted symbol, experimental data.

Further analysis was performed on the modified zeolites using the linear form of the Langmuir isotherm model. The Langmuir plots are presented in Figures 4.15 and 4.16 and all plots are linear suggest that the Langmuir model may be a valid representation of methane adsorption onto these adsorbents. Based on the adsorption isotherm for the modified samples, no maximum was observed.

Table 8.12: Constants of Freundlich isotherm model for the adsorption of methane in modified adsorbents (0 – 500 psi).

Adsorbents	**Freundlich Constants**	
	k	**n**
H-beta	0.0318	1.1650
MgO/H-beta	0.0674	1.2302
CaO/H-beta	0.0399	1.1207
CuO/H-beta	0.0253	1.0402
ZSM-5	0.1080	1.7683
MgO/ZSM-5	0.1535	1.8218
CaO/ZSM-5	0.1220	1.6670
CuO/ZSM-5	0.1397	1.7274
MCM-41	0.0395	1.0885
MgO/MCM-41	0.0237	1.0354
Co_3O_4/MCM-41	0.0329	1.0397
NiO/MCM-41	0.031	1.0387

When analyzing methane adsorption isotherm for modified zeolite H-beta, the amount methane store for all metal oxide zeolite H-beta is much better than the unmodified H-beta. The largest increase in methane store per kilogram adsorbent was

obtained by MgO modified zeolite H-beta. As for the zeolite ZSM-5, CuO/ZSM-5 gives the most pronounce effect as the zeolite ZSM-5 methane storage capacity increases from 3.7883 mol/kg to 5.2909 mol/kg. The effect of transition metal towards MCM-41 is much higher than alkali earth metal. Both modified MCM-41 with transition earth metal cobalt oxide and nickel oxide increases the methane storage capacity with modified Co_3O_4 modified MCM-41 being the highest amount. However, alkali earth metal MgO modified MCM-41 lower the amount of methane storage compare to unmodified MCM-41.

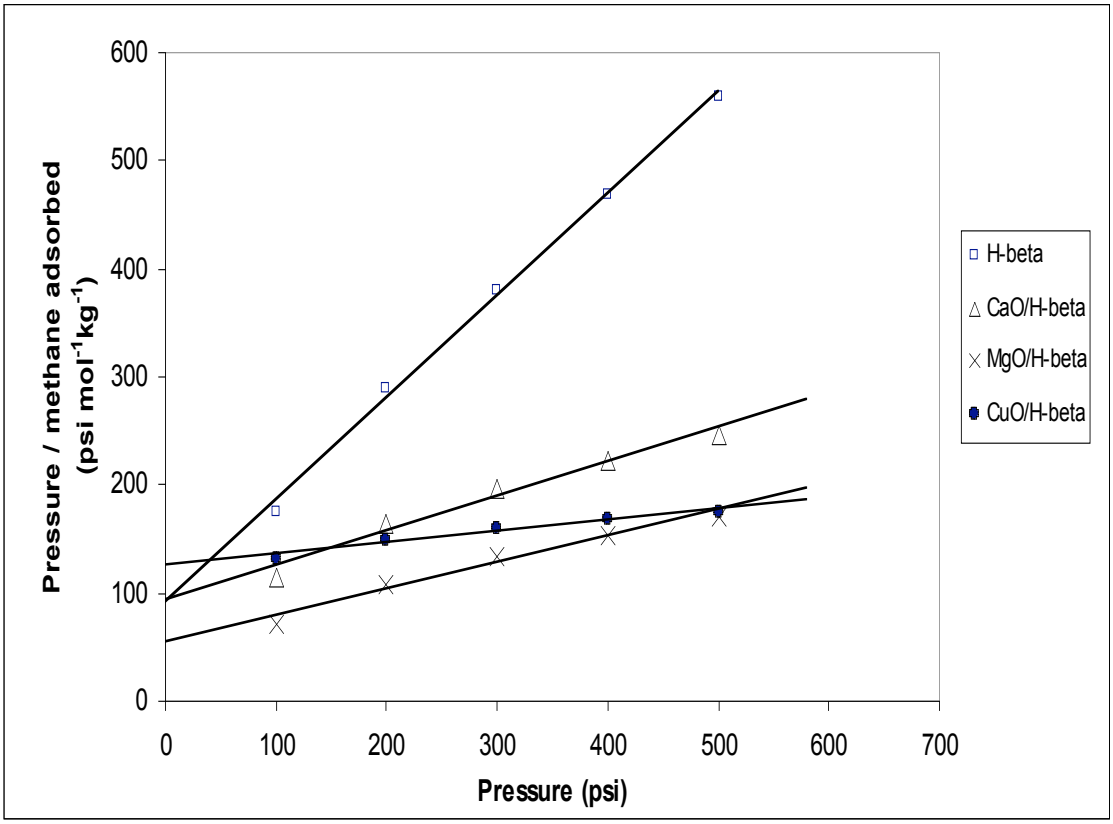

Figure 8.15: Langmuir plots for the adsorption of methane on modified zeolite H-beta.

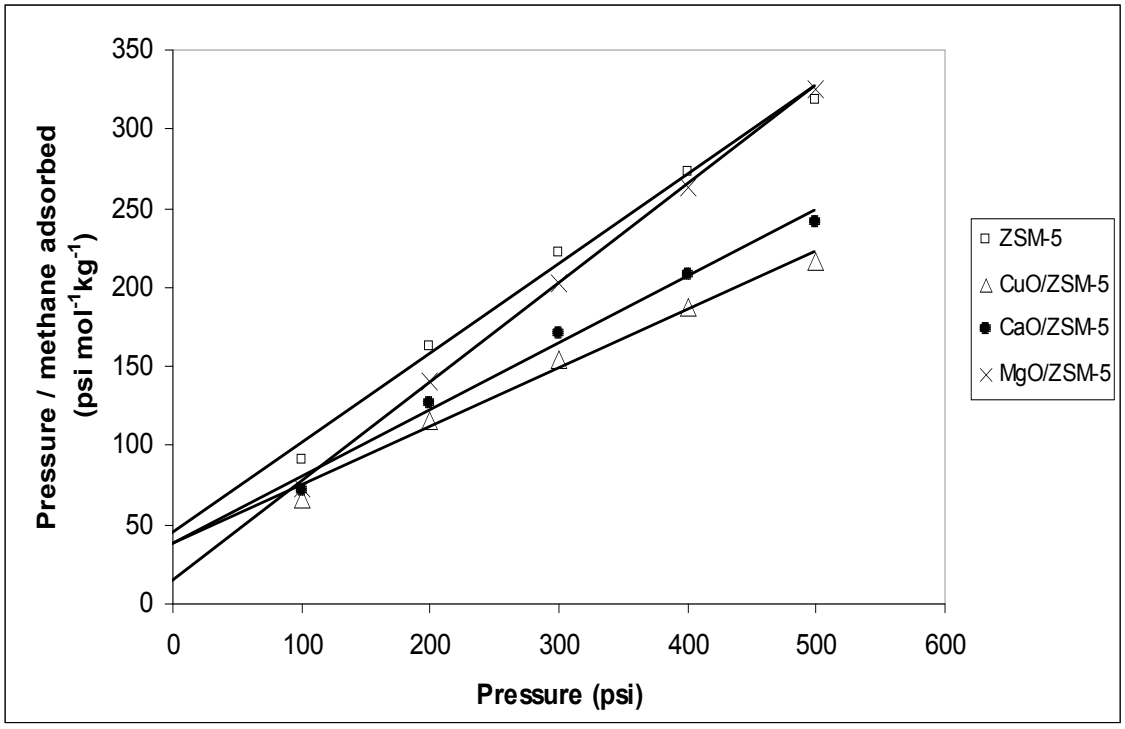

Figure 8.16: Langmuir plots for the adsorption of methane on modified zeolite ZSM-5.

8.3.3 Methane Adsorptive Storage Characteristics

8.3.3.1 Charging Phase

Similar to the result obtained for the unmodified adsorbents, the storage pressure build up is proportional to the amount of gas charged into the vessel. The temperature profile for the modified adsorbents during charging does not affect much. As expected, the temperature reading did showed a slight increase in temperature during charging. However, modified zeolites have higher temperature rising compare to modified MCM-41 samples. This is due to the presence of micropore in the modified zeolite. Materials with smaller pore size have higher heat of adsorption, it increases the interaction

between methane and the framework. According to Frost *et al*. (2006), materials with narrow pores have high framework densities and thus low free void space per gram adsorbent. Therefore, at higher pressure when the pores are nearly filled, the materials with larger free volumes have more room for guest molecules and consequently have higher uptake.

8.3.3.2 Discharging Phase

The quantity of methane effectively released upon discharge is a practical criterion for the evaluation of a method's storage capacity. The amount of methane discharge was measured for different charging pressure in this study. The release of methane was calculated on the basis of unit weight of adsorbent and on the basis of unit volume. Table 8.13 shows the storage and delivery capacities of each modified adsorbents and the effect of charging pressure on amount of methane release is shown in Figure 8.17.

Table 8.13: Methane storage and delivery capacity at 500 psi for modified adsorbents.

	Storage Capacity		Delivery Capacity		Methane Retained at 1
Adsorbents	**mol/kg**	**V/V**	**mol/kg**	**V/V**	**bar (cm^3)**
H-beta	6.82	38.37	6.53	36.73	24.56
MgO/H-beta	10.76	44.74	10.29	42.78	29.32
CaO/H-beta	10.35	43.88	10.11	42.85	15.51
CuO/H-beta	10.01	44.26	9.93	43.90	5.30
ZSM-5	3.79	49.99	3.31	43.73	94.08
MgO/ZSM-5	4.84	49.96	4.19	43.36	99.049
CaO/ZSM-5	5.27	50.32	4.68	44.68	84.57
CuO/ZSM-5	5.29	50.80	4.66	44.70	91.55
MCM-41	12.04	38.56	11.83	38.36	10.87
MgO/MCM41	9.64	41.97	9.57	41.67	4.52
Co_3O_4/MCM41	13.03	42.13	12.93	41.80	5.01
NiO/MCM41	12.36	42.22	12.27	41.90	4.89

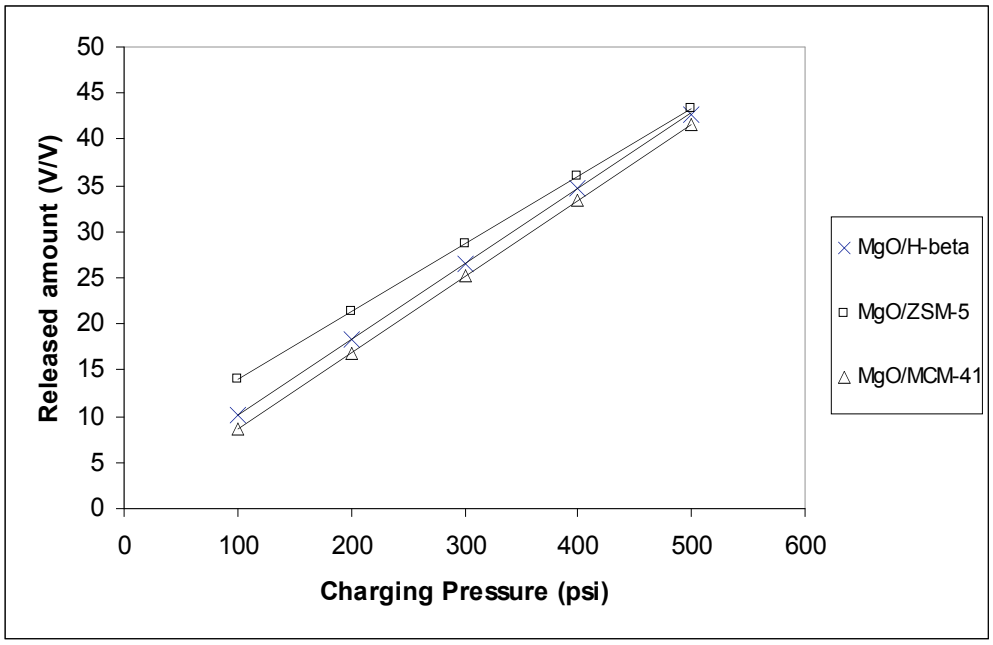

Figure 8.17: Methane release from selected modified adsorbents at different pressures.

Based on Figure 8.17, the amount of methane released from the modified adsorbents increases with increased charging pressure. The metal modified adsorbents not only show improvement in term of storage but also increased the delivery capacity as well. The CuO modified for both ZSM-5 and H-beta showed the highest delivery capacity compare to their other modified samples. Metal oxide modified MCM-41 also show improvement in delivery capacity where NiO/MCM-41 has the best delivery capacity. However, it has to be noted that not all modified adsorbents are better compare to the unmodified one. Magnesium oxide modified ZSM-5 has lower delivery capacity compare to ZSM-5 and even the modified sample has the highest storage capacity, it is not necessary it will have the highest delivery capacity such as the one showed by magnesium oxide modified H-beta. Magnesium oxide modified H-beta has the highest storage capacity among other modified H-beta but its delivery capacity is lower compare to copper oxide modified H-beta which has the storage capacity lower than CaO and MgO modified H-beta.

As can be seen from Table 8.13, with the introduction of metal into the adsorbents the amounts of methane retain in the adsorption cell at 1 bar after discharging is not consistent. The delivered capacity of methane is less than the storage capacity because the adsorbent retains some gas at the exhaustion pressure (Matranga *et al*., 1991). Adsorbents with metal oxide will experience physical properties change based on the type of metal and the amount of metal oxide use. Due to this, the changes in pore size and pore volume will affect the performance of the adsorbent and thus the amount of methane retain after discharging.

8.4 Summary

High pressure methane adsorption isotherms onto various adsorbents were well fitted with the Freunlich model. XRD results indicate that the structure of microporous and mesoporous adsorbents did not change after being tested with methane until pressure up to 500 psi. High pressure methane adsorption can be divided into three regimes. At low pressure, the amount adsorbed correlated with pore size, the surface area at intermediate and free volume at high pressure (35 bar). Adsorbents in addition to having a high micropore surface area that will yield a high adsorption capacity per mass adsorbent; it should also have a high packing density and pore volume. This is to ensure that the methane capacity and the delivery capacity on a volumetric basis would be high. Adding metal oxide into microporous silica will improve its methane capacity and delivery performance and these metal charges will affect the adsorbate/adsorbent interaction even at high pressure adsorption. From the experiment results, in term of mass basis, H-beta has the highest methane adsorption capacity compare to other microporous adsorbents and SBA-15 for the mesoporous adsorbents however in term of volume basis, zeolite 13X is better than the others.

CHAPTER 9

CONCLUSIONS

9.1 Introduction

This chapter summarizes the results of structural and gas adsorption characteristics of adsorbents in order to provide a clearer understanding on the effect of structurally different zeolites and the modified zeolite adsorbents using several modification methods. In order to achieve the objectives and scopes of this study, the synthesis and characterization of zeolites were carried out using methods described in Chapter 3. The gas adsorption measurements have provided some important facts on gas adsorption characteristics of the zeolites. Conclusions are drawn based on the results obtained and the discussions on the effect of structural, physical and chemical properties of zeolite adsorbents on gas adsorption characteristics as presented in Chapters 4, 5, 6, 7, and 8. In addition, this chapter will propose several recommendations for future research direction in order to gain a better understanding of fundamental aspect of gas adsorption.

9.2 Summary of Research Findings

The first part of this study involves gas adsorption characteristics of structurally different zeolite, channel and cage type zeolites. The study shows that gas adsorption characteristics of gas molecules depend mainly on the accessibility of the molecules (pore size or pore opening) to the adsorption sites and pore network systems (one-, two-, or three dimensional pore network system). The presence of zig-zag or sinusoidal channel affects the diffusivity, thus the adsorption of gas molecules. Large pore diameter and three dimensional pore network systems would prevent the occurrences of pore blockage to the adsorption sites. However, in order to obtain high adsorption capacity, surface area and large pore volume are still important requirements for the adsorption of gases.

As the cage structure (cage diameter > 0.11 nm) provides more spaces for gas molecules to adsorb, the presence of cage-like structures in ferrierite structural framework also support the fact that the cages contribute to higher adsorption capacity than ZSM-5, mordenite and zeolite beta. This study also reveals that high crystallinity is not the reason for high adsorption, in fact, it was suggested that some crystalline imperfections, as detected by relative crystallinity of Na-SZ18, creates more adsorption sites that leads to high adsorption capacity. Thus, this study has shown that cage type zeolite represented by faujasite group of zeolites (NaX, NaY and Na-SZ18 (synthesized zeolite)) have higher adsorption capacity than channel type zeolites such as ZSM-5, mordenite, ferrierite and zeolite beta.

The adsorption isotherm data also revealed that dilute form of adsorption occurred due to the absence of specific interaction between adsorbate and adsorbent. However, the presence of quadrapole moment in carbon dioxide molecule initiates Langmuir type adsorption. The rapid increase indicates strong interaction between adsorbates and the adsorption sites. In addition, initial adsorption rate and diffusional time constant also suggested that the properties of adsorbates such as size, charge and the polarity/quadrapole moment influence the characteristics of gas

adsorption. The diffusion in zeolite pore network is the slowest step in the adsorption of carbon dioxide, thus indicate that diffusion is the rate controlling step for carbon dioxide. On the other hand, the rate controlling step for methane, a non-polar molecule, is the interaction between methane and the zeolite.

This study also revealed that modifications greatly influence the physicochemical properties of zeolites and gases adsorptive characteristics. The study on the effect of cations on gas adsorption characteristics of zeolites show that exchanging sodium with other metal cation changed the physicochemical properties of the based zeolite (Na-SZ18). Depending on the size of cation, the crystallinity, Si/Al ratio and unit cell parameter of the zeolites also changed. The surface area, pore volume, and average pore diameter of zeolites also varies as the metal cations replace the Na^{+}. The presence of cations such as Li^{+}, Mg^{2+}, and Ca^{2+} increases the surface area and pore volume of zeolites. Theses changes are due to the reorientation of the atom in zeolite lattice. However, the XRD and FTIR spectra show that the structural framework remains as faujasite type zeolite.

However, the differences brought about by cations were presented by the adsorption isotherm curves even though adsorption of methane on metal cation exchanged zeolites are still at dilute conditions. The calculated model equation constants have shown the effect of cations especially for methane adsorption. The effects of cation, its size and charge are also depicted in the kinetic study of metal cation exchanged zeolites. Since the reported pore diameter of faujasite type zeolite is relatively larger than channel type zeolite (~ 0.74 nm), Knudsen diffusion dominates the methane and carbon dioxide diffusion characteristics in metal cation exchanged zeolite. Again, the initial adsorption rate, diffusional time constant, and equilibrium time also revealed the influence of cation's size and charge on gas adsorption characteristics.

In addition, changes in the FTIR spectroscopy of adsorbed methane and carbon dioxide also indicate the effect of cation in the extra-framework of zeolites. The

changes are more significant in carbon dioxide adsorption since the quadrapole moment of carbon dioxide specifically interacts with the active site (cation) of zeolite. This study reveals that peak positions and the total area change as different cation with different size, charge and position presents as extra-framework cation. Hence, a combination modification on structural properties and physicochemical properties of zeolite can produce a distinctive material that could be used as gas adsorbent. However, further study need to be carried out in order to broaden range of zeolite adsorbent applications.

Again, the study on the effect of metal cation exchanged zeolites on gas adsorption characteristics shows that surface area and pore volume are not the main factors that determine the adsorption capacity of zeolites. The observed different order for gas adsorption characteristics on the metal cation exchanged zeolites is expected to be mostly due to the presence of different cation in the adsorbents. Different cations lead to various degrees of interactions between the adsorbates and adsorbent. The improvement is due to the electrostatic field created by the cations within the pores. In this study, there is evident that the divalent cations such as Ba^{2+}, Mn^{2+}, Ni^{2+}, and Zn^{2+} increase the ratio of surface coverage ratio ($\theta_R > 1.47$), thus suggests that the charge of the cation has great influence on the adsorption process.

This study also revealed that the successive spontaneous dispersion of metal oxides via thermal dispersion and incipient wetness impregnation methods can be used for zeolite surface modification. The dispersed compound is mainly stay on the wall of larger cages in the zeolite and some dispersed on the external surfaces. The dispersion can be in the form of monolayer dispersion or sub-monolayer dispersion depending on the structural properties of metal oxides dispersed.

The metal oxide exists as two-dimensional dispersed species on the surfaces of Na-Y after the calcination when the loading concentration is less than the critical dispersion capacity. When the loading concentration exceeds the threshold value, the heat treatment temperature is too high for an oxide with a zeolite in the calcination

process, or the duration of calcination takes too long period, part of the dispersed species might jostle and migrate to the external surfaces and formed bulk metal oxide compounds. A small part of them will diffuse into the smaller cages of zeolite Na-Y to form inclusion compounds, thus made the pore diameter larger for some types of metal oxide modified zeolite. In addition, when heating a mixture of a metal oxide and Na-Y zeolite in the dispersion process, solid-state ion exchange process might occur at the same time that resulted in the decrease of Si/Al ratio. Moreover, surface area and pore size characterization bring out two main results: the decrease of micropore surface area and micropore volume and the increase of external surface area, which resulted from the dispersion of metal oxide species on Na-Y zeolite surfaces.

On the other hand, adsorption equilibrium results indicated that Group II A metal oxides modified NaY shows the highest adsorption capacity for gas carbon dioxide while Group II B metal oxides give most pronounced effects on gas nitrogen and methane adsorption. In the study, vanadium (V) oxide modified Na-Y decreased the adsorption capacity tentatively for three types of tested gases. This is probably due to the high basicity properties of Group II A metal oxides that improved the interaction of adsorbent with CO_2 acid gas. Meanwhile, the structural and surface properties of NaY after Group II B modification are suitably for dipole adsorbates adsorption. Generally, the specific surface area and micropore volume are not the only determine factors in the gas adsorption processes. The number, types and location of metal oxides on the zeolite surfaces also play the important role in the adsorption equilibrium. The adsorption of gases is influenced by the basicity of oxygen atoms and the Lewis acidity of the counter metal cations of metal oxides existed on zeolite surfaces.

Furthermore, the isosteric heat of adsorption is found increased linearly with the increase of gas adsorption capacity. The heat of adsorption for unmodified Na-Y zeolite is 18.1 kJ/mol, 27.9 kJ/mol and 21.4 kJ/mol for gas CO_2, N_2 and CH_4, respectively. Different types of metal oxide dispersion changes the interaction of adsorbate-adsorbent accordingly in the range of 17.5 – 25.7 kJ/mol for CO_2, 23.1 –

31.3 kJ/mol for N_2 and 17.3 –34.1 kJ/mol for CH_4 adsorption. The higher releasing of heat in the adsorption means higher interaction of adsorbates with adsorbents. Subsequently, the adsorbents have higher gas adsorption capacity.

From the obtained adsorption equilibrium results as well, it is conferred that types of metal oxide (solid state structure, particle size and kinetic diameter), copper oxide loading concentration, calcination temperature, duration of calcination and modification techniques greatly affect the structural properties of modified zeolite adsorbents and its gases adsorptive characteristics. The critical dispersion capacity of CuO onto NaY zeolite as submonolayer dispersion is 2.25 wt.% of CuO loading concentration. Twenty-four hours of calcination process at 873.15 K for copper (II) oxide and NaY zeolite modification enable the uniform dispersion of oxide on the zeolite surfaces and show enhancement in the gas methane adsorption capacity. If these corresponding parametric of modification are well controlled, the desired adsorbent having appropriate physical properties could be prepared for specific gas adsorption application.

Generally, adsorption kinetics of NaY zeolite is improved after some types of metal oxide modification. The mass transfer of gas molecules diffuse into zeolite micropore is following the second law of Fickian diffusion process. The structural and surface properties, metal oxide distribution, particle size and temperature of diffusion are factors that governing the peculiarity of gases diffusion into modified adsorbents. The gas adsorption characteristics presented a rapid initial uptake and slow down of diffusion at higher coverage in the adsorption process. From the characterization results, the zeolite cages after modification are open enough to allow the free diffusion and adsorption of adsorbates. The strength of such interaction depends mainly on the ionic nature, topology of the zeolite framework and the polarity (dipole and quadrupole moments) of the guest molecule. The diffusion rate constant as observed from the results to achieve equilibrium status are following the sequences of $CO_2 > CH_4 > N_2$. This is due to the smallest kinetic diameter of gas CO_2 molecules as well as the largest adsorption energy of CO_2 than that of methane and nitrogen for the adsorption into pores at all size ranges. Gas carbon dioxide is

selectively jumping from one active adsorption site to another that controlled by adsorbate-adsorbent interaction. Gas methane diffusivity is governing both by the size of micropore and gas-zeolite interaction. Meanwhile, gas nitrogen diffusivity is mainly related to the size of micropores. Hence, the diffusion rate constant of nitrogen is relatively slow compared with gas methane and carbon dioxide.

Interaction between different molecules adsorbed on a metal oxide modified NaY zeolite surface are of important in many contexts. The integrated absorbance areas and the intensities of FTIR spectrums reveal that gas CO_2, N_2 and CH_4 interact with metal oxides modified NaY zeolite. For adsorption that is considered in the supercritical adsorption condition in this study, the molecule is free rotating and physically adsorbed on the active adsorption sites on adsorbent surfaces as gas phase molecules. The adsorption sites at smaller pores of NaY also contribute to the strong adsorbate-adsorbent interaction at high temperature adsorption condition. The location and accessibility of active adsorption sites, the pressure and temperature of adsorption are the factors that determine the mechanisms of gases adsorption on the metal oxide modified NaY adsorbents.

Special attention should also be given to the incorporation of amines on porous materials. This study have showed that alkanoamines greatly enhances the CO_2 adsorption performance especially for mesoporous materials. Furthermore, the amines also improved the CO_2-adsorbent bonding and as a result increasing the selectivity of the adsorbent towards CO_2 adsorption. However, not all amines are suitable for modification on porous materials. Certain amines with large molecules size would actually decrease the CO_2 adsorption performance of the adsorbent. Therefore, this study proved to be important in order to understand the CO_2 adsorption performance of amine modified mesoporous and microporous materials.

Furthermore, high pressure adsorption for methane adsorptive gas storage has shown that physicochemical properties of the adsorbents have great influence on the adsorption capacity. The study also proved the earlier suggestion in Chapter 6 about

the role of metal oxide on gas adsorption. The addition of metal oxide into microporous silica improve the methane capacity and delivery performance even at higher pressure.

9.3 **Recommendation for Future Work**

In order to obtain a better understanding of the gas adsorption characteristics in metal oxide modified zeolite adsorbents, the following studies are recommended in future work. For structural and properties characterization, X-Ray Photoelectron Spectroscopy (XPS) is recommended to attain information about the metal oxide dispersion of the adsorbents. Temperature Programmed Reduction (TPR) can provide much information about the reducibility of the deposited metal oxide of the calcined adsorbents. Meanwhile, the Temperature Programmed Desorption (TPD) characterization is highly recommended as well to obtain the acidity and basicity properties of modified zeolites. Besides, one can determine the framework of Si to Al ratio by observing the high-resolution spectra from the solid samples using ^{29}Si and ^{27}Al MAS-NMR Spectroscopy. Apart from that, study on the fundamental aspects of the microwave heating method in the sample preparation for metal oxide dispersion is recommended, since this method has recently attracted increasing interest as an emerging material-processing technique (Deng and Lin, 1997; Yin and Yin, 1998; Han *et al*., 2004).

In general, this study has shown that cage type zeolite is structurally suitable zeolite adsorbent for gas adsorption applications. Since the synthesized zeolite (Na-SZ18) shows a promising performance, a more detailed study on this particular structure need to be carried out especially on parameter that affect the product of zeolite such as temperature, pressure and pH of the gel solution. In addition, it is also worth to investigate the effect different silica and alumina sources in order to minimize the cost of producing zeolite adsorbent. A more economical and

environmental friendly approach would be another advantage in the development of zeolite adsorbent. However, it is also realized that the adsorbent used in this study is limited to several types of zeolites that commercially available in the market. Hence, it is suggested that other types of synthetic zeolites that have been reported by International Zeolite Association-Structure Commission with different structural and physicochemical properties to be used in order to gain a definitive conclusions about on the influence of zeolite structural framework on gas adsorption characteristics.

Other aspects that need further investigation are the effect of adsorption at elevated temperatures and pressures. This is important especially for sub-critical/supercritical adsorbate such as carbon dioxide. Since many studies only involve adsorption at lower temperature (< 273 K), the transition characteristics from sub-critical to supercritical adsorption was not critically addressed. In this case, the model equation that commonly used might need to be extended to take into account the effect of high temperature and pressure adsorption. It is also important to note that cation plays important role in the adsorption of non-polar molecules such as methane. This study have shown that divalent cations in alkaline earth metal group and transition metal are potential candidate as charge balancing cation replacing Na^+ that commonly present in synthetic zeolite. However, the performance of other transition metal cations such as Co^{2+}, Cr^{2+}, Cu^{2+}, Mo^{2+}, Pd^{2+}, Cd^{2+} should be evaluated. Further study should also involve investigation on the optimum amount of cation replacing Na^+. This is rather important since too many cation exchanged could caused the formation of meso- or macropore in zeolite structural framework that can affect the adsorption on zeolite adsorbents.

On the other hand, the gas adsorption isotherms for metal oxide modified NaY in a range of pressure and temperature especially at high temperature and high-pressure conditions can be conducted to get a clear picture of gas adsorption characteristics and equilibrium model. Despite the adsorption process in a pure adsorbate atmosphere, gas mixture adsorption can be carried out to take a look at studied adsorbents selectivity properties. Other types of gases, which are industrial interest

such as gas oxygen, carbon monoxide and sulfur dioxide, are waiting for further extensive investigation.

In addition, the laboratory-made FTIR cell apparatus system in this study could be upgraded for studying the effect of different adsorption temperature on adsorbate-adsorbent interaction. The FTIR study together with ^{1}H and ^{13}C MAS NMR spectroscopy would provide higher resolution information on gas adsorption interaction of metal oxide modified adsorbents. Moreover, from the fundamental screening results obtained in this study, some of the selected metal oxides can disperse into different types of microporous and mesoporous materials to investigate the effect of support to metal oxide modified system as gas adsorbents instead of Na-Y zeolite. The mesoporous materials with high surface area and narrow pore size distribution probably would increase the dispersion capacity of metal oxides and so that providing more active adsorption sites for adsorbate molecules.

Indeed, more knowledge about the implementation of metal oxide modified zeolite for particular application is desirable for further study. The understanding of the basic concepts and gas adsorptive characteristics of the studied adsorbents would give substantial benefit and convenience for the investigation into specific application such as adsorbents for gas separation process, their functionality as catalysts, gas sensor, gas storage, semiconductor and superconductor. The important role of zeolite in the field of catalytic, adsorption and nanoparticle technology therefore would continue to reign supreme in the coming decades.

Finally, it is also suggested that the present model equation need to be extended by taking into account the adsorbate and adsorbent properties, the diffusion in different structural framework and the interaction between adsorbate and adsorbents. The development of a complete model is crucial in predicting the potential adsorbent for specific application. It can be achieved by carrying more measurement on gas adsorption isotherm, gas diffusivity, gas adsorption rate and

gas-zeolite interaction on selected adsorbents in order to gain more data on the effect of various properties on gas adsorption.

9.4 Future Research Direction

In the era of nanotechnology, gas adsorption moves into several new applications such as gas storage, gas sensor, biosensor and semiconductor that involve metal-doped zeolites. At the same time, gas separation and purification require alternative technologies that are more efficient and cost effective. There is also an urgent need for the development of efficient and economically feasible technology for the reduction of gas emission from combustion processes and chemical productions and high temperature solid state gas that capable of making measurements in harsh industrial environment.

Adsorption technology now leads to a new dimension in gas separation and purification and adsorptive gas storage. The use of microporous materials such as zeolite, activated carbon or silica have been started at the beginning of 19^{th} century. Zeolite becomes commercially significant since the discovery of synthetic zeolites. The importance of this materials lies on the fact that zeolite is a microporous material with high surface area and high pore volume capacity. However, there are other features that are equally important in the adsorption that might contribute to the adsorption of gases on zeolite. More researches need to be carried out in order to understand the characteristics of gas adsorption on zeolite adsorbent.

Several factors need to be considered in the study of gas adsorption on zeolites. Structural framework, physicochemical properties of zeolite, adsorbate properties will influence the transfer of adsorbates from the gas phase to the adsorption site and the interaction between the adsorbate and the adsorbent.

Identifying factors that affect the adsorption of gases on zeolite is very crucial in order to optimize the performance of zeolite adsorbent for industrial application. In addition, modification could be carried out to overcome any weaknesses due to pore size, thermal stability, or insufficient active sites. Furthermore, modification could be carried out to achieve high adsorption capacity and selectivity.

To achieve more complete view on the adsorption characteristics of gases onto zeolite, it is important to evaluate the thermodynamic and kinetic parameters using several equation models. At present, thermodynamic models such as Langmuir, Freundlich, Tóth and Dubinin are commonly used to describe the adsorption phenomena on zeolites in a wide range of operating conditions. Other models are usually extended from those models and regarded as development of the classical methods. In addition to that, the kinetics model of adsorption in order to describe the uptake rates of gases. By using the thermodynamic and kinetic models and the experimental data obtained, factors that influence of gas adsorption characteristics could be determined.

REFERENCES

Abdel-Fattah, T. M., Davies, G., Romanovsky, B. V., Shakhanovskaya, O. L., Larin, A. N., Jansen, S. A. and Palmieri, M. J. (1997). Molecular Catalyst Design. Synthesis, Characterization and Properties of Zeolite NaY Catalysts made with A Tetranuclear Copper (II) Complex. *Catal*. *Today*. 33: 313-322.

Ackley, M. W. and Yang, R. T. (1991). Diffusion in Ion-Exchanged Clinoptilolites. *AIChE J*. 37: 1645 – 1656.

Albert, B. R. and Cheetam, A. K. (2000). A Synchotron X-ray Powder Diffraction Study of Highly Crystalline Low-Silica Zeolite P during Na-Ca Ion Exchange. *Micropor. Mesopor. Mater.* 34: 207 – 211.

Ahn, H. W., Moon, J. H., Hyun, S. H. and Lee, C. H. (2004). Diffusion Mechanism of Carbon Dioxide in Zeolite 4A and CaX Pellets. *Adsorption*. 10: 11-128.

Ahn, N. G., Kang, S. W., Min, B. H., and Suh, S. S. (2006). Adsorption Isotherms of Tetrafluoromethane and Hexafluoroethane on Various Adsorbents. *J. Chem. Eng. Data*., 51: 451-456.

Akbar, S. A. and Dutta, P. K. (1999). High-Temperature Ceramic Oxide Gas Sensors. *Surf*. *Eng*. *Sci*. *Technol*. 1: 33-44.

Alcaniz-Monge, J., De La Casa-Lillo, M. A., Cazorla-Amoros, D., and Linares-Solano, A(1997). Methane Storage in Activated Carbon Fibers. *Carbon*, 35: 291-297.

Alkhawaldeh, A., Wu, X. C. and Rayford, G. A. (2003). Conversion of Mixtures of Methane and Acetylene or Ethylene into Higher Molecular Weight Hydrocarbons over Metal-Loaded and Unloaded HZSM-5 Zeolite Catalysts. *Catal*. *Today*. 24: 43-49.

Alyea, E. C. and Bhat, R. N. (1995). Methanol Conversion to Hydrocarbons over WO_3/HZSM-5 Catalysts Prepared by Metal Oxide Vapor Synthesis. *Zeolites*. 15: 318-323.

Anon. A. G. (2005). Foundation Release Natural Gas Outlook to 2020. *Pipeline and Gas Journal*, 232: 6-9.

Anpo, M., Higashimoto, S., Matsuoko, M., Zhanpeisov, N., Shioya, Y., Dzwigaj, S. and Che, M. (2003). The Effect of The Framework Structure on the Chemical

Properties of the Vanadium Oxide Species Incorporated within Zeolites. *Catal. Today*. 78: 211-217.

Aranovich, G. and Donohue, M. (1995). Adsorption Isotherms for Adsorbents Microporous. *Carbon*. 33(10): 1369-1375.

Aranovich, G. and Donohue, M. (1997). Determining Surface Areas from Linear Adsorption Isotherms at Supercritical Conditions. *J. Colloid Interf. Sci.* 194: 392-397.

Arcoya, A., González, J. A., Llabre, G., Seoane, X. L. and Travieso, N. (1996). Role of the Countercations on the Molecular Sieve Properties of A Clinoptilolite. *Microporous Mater.* 7: 1-13.

Areán, C. O., Delgado, M. R. and Palomino, G. T., Rubio, M. T., Tsyganenko, N. M., Tsyganenko, A. A., and Garrone, E. (2005). Thermodynamic Studies on Hydrogen Adsorption on the Zeolites Na-ZSM-5 and K-ZSM-5. *Micropor. Mesopor. Mater*. 80: 247-252.

Arishtirova, K., Kovacheva, P. and Predoeva, A. (2003). Activity and Basicity of BaO Modified Zeolite and Zeolite-Type Catalysts. *Appl. Catal. A: Gen*. 243(1): 191-196.

Armor, J. N. (1998). Metal-Exchanged Zeolites as Catalysts, *Micropor. Mesopor. Mater*. 22: 451 – 456.

Astala, R. and Auerbach, S. M. (2004). The Properties of Methylene- and Amine-Substituted Zeolites from First Principles. *J. AM. CHEM. SOC.*, 126: 1843-1848.

Baciocchi R., Storti G., and Mazzotti M. (2006). Process Design and Energy Requirements for the Capture of Carbon Dioxide, Chemical Engineering and Processing, 45:1047-1058.

Backhaus-Ricoult, M. (2003). Gibbs' Adsorption at α Alumina-Copper Interfaces. *J. Eur. Ceram. Soc*. 23: 2747-2759.

Bae, D. and Seff, K. (2001). Some Chemical Treatments Diminish the Long-Range Ordering in the Aluminosilicate Frameworkof Zeolite X. *Micropor. Mesopor. Mater.* 42: 299 – 306.

Baek, S., Kim, J. and Ihm, S. (2004). Design of Dual Functional Adsorbent/Catalyst System for The Control of VOC's by Using Metal-Loaded Hydrophobic Y-Zeolites. *Catal. Today*. 93-95: 575-581.

Baerlocher, Ch., Meir, W. M. and Olson, D. H. (2001). *Atlas of Zeolite Frame Work Types*. 5th ed. Structure Commission of the International Zeolite Association: Elsevier.

Bailar, J. C., Emeleus, H. J., Nyholm, S. R. and Trotman-Dickenson, A. F. (1973). *Comprehensive Inorganic Chemistry*. Australia: Pergamon Press Ltd.

Balachander, K., Arulkumaran, S., Egawa, T., Sano, Y. and Baskar, K. (2005). Demonstration of AlGaN/GaN Metal-Oxide Semiconductor High-Electron-Mobility Transistors with Silicon-Oxy-Nitride as The Gate Insulator. *Mater. Sci. Eng. B*. 119: 36-40.

Baronskaya, N. A., Woldman, L. S., Davydov, A. A. and Buyevskaya, O. V. (1996). Ethylene Recovery from The Gas Methane Oxidative Coupling by Swing Adsorption Product of Temperature. *Gas. Sep. Purif*. 10(1): 85-88.

Barrer R. M. and Coughlan, B. (1968). *Molecular Sieves Derived From Clinoptilolite: Molecular Sieves*. London: Soc. of Chem. Ind. 141-148.

Barrer, R. M. (1978). Cation-Exchange Equilibria In Zeolites and Feldspathoids. In: Sand, L. B. and Mumpton, F. A. eds. *Natural Zeolites Occurrence, Properties, Use*. New York: Pergamon Press Ltd. 356-371.

Barrer, R. M. and Brook, D.W. (1953). Molecular Diffusion in Chabazite, Mordenite, and Levynite. *Trans. Farad. Soc*. 19:1049-1059.

Barrer, R. M (1982) *Hydrothermal Chemistry of Zeolites*. London: Academic Press.

Barrer, R. M. and Ibbitson, D. A. (1944). Occlusion of Hydrocarbons by Chabazite and Analcite. *Trans. Farad. Soc*. 40: 195-205.

Barton, T. J., Bull, L. M., Klemperer, W. G., Loy, D. A., Mcenaney, B., Misano, M., Monson, P. A., Pes, G., Scherer, G. W., Vartuli, J. C., and Yaghi, O. M. (1999). Tailored Porous Materials. *Chem. Mater*, 11: 2633-2656.

Bastos-Neto, M., Torres, A. E. B., Azevedo, D. C. S., and Cavalcante JR, C. L. (2005). A Theoritical and Experimental Study of Charge and Discharge Cyles in a Storage Vessel for Adsorbed Natural Gas. *Adsorption*, 11: 147-157.

Beck, J. S. and Vartuli, J. C. (1996). Recent Advances in The Synthesis, Characterization and Applications of Mesoporous Molecular Sieves. *Current Opinion in Solid State & Materials Science*, 1: 76-87.

Bellat, J. P. and Simonot-Grange, M. H. (1995). Adsorption of Gaseous p-xylene and m-xylene on NaY, KY, and BaY Zeolites. Part 2: Modeling. Enthalpies and Entropies of Adsorption. *Zeolites*. 15: 219-227.

Bellat, J. P., and Grange, M. H. S. Adsorption of Gaseous p-Xylene and m-Xylene on NaY, KY and BaY zeolites. Part 2: Modeling. Enthalpies and Entropies of Adsorption. University de Bourgogne, Laboratoire de Recherches sur la Reactivite des Solides, Dijon, France.

Belmabkhout, M., Frère, M., and Weireld, G. De. (2004). High Pressure adsorption Measurement. A Comparative Study of the Volumetric and Gravimetric Methods. *Meas. Sci. Technol.*, 15: 848-858.

Bennadja, Y., Beaunier, P., Margolese, and Davidson, A. (2001). Fine Tuning of the Inetraction between Pluronic Surfactant and Silica Walls in SBA-15 Nanostructured Materials. *Micropor. Mesopor. Mater*. 44-45: 147-152.

Bentrup, U., Bruckner, A., Richter, M. and Fricke, R. (2001). NO_x Adsorption on MnO_2/NaY Composite: An In Situ FTIR and EPR Study. *Appl. Catal. B: Environ*. 32: 229-241.

Benvenutti, E. V. and Yoshitaka, G. (1998). Comparative Study of Catalytic Oxidation of Ethanol to Acetaldehyde Using Fe(III) Dispersed on Sb_2O_5 Grafted on SiO_2 and on Untreated SiO_2 Surfaces. *J. Braz. Chem. Soc*. 9: 469-472.

Beyer, H. K., Pál-Borbély, G. and Keindl, M. (1999). Incorporation of Cations into Zeolites by A New Reaction Between Bronsted Acid Zeolites and Metals. I. Zinc into Faujasites and Mordenites. *Micropor. Mesopor. Mater*. 31: 333-341.

Bi, Y. S. and Lu, G. X. (2003). Catalytic CO Oxidation over Palladium Supported NaZSM-5 Catalysts. *Appl. Catal. B: Environ*. 41: 279-286.

Biloe, S., Goetz, V., and Guillot, A. (2002). Optimal Design of an Activated Carbon for an Adsorbed Natural Gas Storage System. *Carbon*, 40: 1295-1308.

Biloe, S., Goetz, V., and Mauran, S. (2001). Characterization of Adsorbent Composite Blocks for Methane Storage. *Carbon*, 39: 1653-1662.

Biloe, S., Goetz, V., and Mauran, S. (2001). Dynamic Discharge and Perforamnce of a New Adsorbent for Natural Gas Storage. *Environmental and Energy Engineering*, 47: 2819-2829.

Bludau, H., Karge, H. G. and Niessen, W. (1998). Sorption, Sorption Kinetics and Diffusion of Pyridine In Zeolites. *Micropor. Mesopor. Mater*. 22: 297-308.

Boger, T., Roesky, R., Gläser, R., Ernst, S., Eigenberger, G., and Weitkamp, J. (1997). Influence of The Aluminum Content on The Adsorptive Properties of MCM-41. *Microporous Materials*, 8: 79-91.

Boger, T., Salden, A. and Eigenberger, G. (1997). A Combined Vacuum and Temperature Swing Adsorption Process for The Recovery of Amine from Foundry Air. *Chem*. *Eng*. *Proc*. 36: 231-241.

Bordawekar, S. V. and Davis, R. J. (2000). Probing The Basic Character of Alkali-Modified Zeolites by CO_2 Adsorption Microcalorimetry, Butene Isomerization, and Toluene Alkylation with Ethylene. *J*. *Catal*. 189: 79-90.

Bordiga, S., Palomino, G. T., Pazé, C. and Zecchina, A. (2000). Vibrational Spectroscopy of H_2, N_2, CO and NO Adsorbed on H, Li, Na, K-exchanged Ferrierite. *Micropor*. *Mesopor*. *Mater*. 34: 67-80.

Bordiga, S., Pazé, C., Berlier, G., Scarano, D, Spoto, G., Zecchina, A. and Lamberti, C. (2001). Interaction of N_2, CO and NO with Cu-exchanged ETS-10: A Compared FTIR Study with Other Cu-Zeolites and with Dispersed Cu_2O. *Catal*. *Today*. 70: 91-105.

Brandt, W. W. and Rudloff, W. (1968). The Concentration Dependence of Zeolite Sorption. *J. Phys. Chem*. 71: 3948-3953.

Braun, S., Appel, L. G., Camorim, V. L. and Schmal, M. (2000). Thermal Spreading of MoO_3 onto Silica Supports. *J. Phys. Chem. B*. 104: 6584-6590.

Breck, D. W. (1974). *Zeolite Molecular Sieves*. Canada: John Wiley & Sons. Inc.

Bulánek, R., Wichterlová, B., Sobalík, Z. and Tichý, J. (2001). Reducibility and Oxidation Activity of Cu Ions In Zeolites Effect of Cu Ion Coordination and Zeolite Framework Composition. *Appl*. *Catal*. *B*: *Environ*. 31: 13-25.

Bülow, M., Dao, L. and Fitch, F. R. (1996). *Removal of Carbon Dioxide from Gas Streams*. (U. S. Patent 5,587,003).

Bülow, M., Shen, D. M. and Jale, S. (2002). Measurement of Sorption Equilibria Under Isosteric Conditions The Principle, Advantages and Limitations. *Appl*. *Surf*. *Sci*. 196: 157-172.

Burchell, T., and Rogers, M. (2000). Low Pressure Storage of Natural Gas for Vehicular Applications. *Society of Automotive Engineers*, Oak Ridge National Laboratory.

Burggraaf, A. J. (1999). Single Gas Permeation of Thin Zeolite (MFI) Membranes: Theory and Analysis of Experimental Observations. *J*. *Membr*. *Sci*. 155: 45-65.

Burggraaf, A. J., Vroonb, Z. A. E. P., Keizera, K. and Verweija, H. (1998). Permeation of Single Gases In Thin Zeolite MFI Membranes. *J*. *Membr*. *Sci*. 144: 77-86.

Burleigh, M. C., Markowitz, M. A., Spector, M. S., and Gaber, B. P. (2001). Amine-Functionalized Periodic Mesoporous Organosilicas. *Chem. Mater.*, 13: 4760-4766.

Calvalho, M. B., Carlvalho, A. P, Ribeiro, F. R., Florentino, A., Gnep, N. S., and Guisnet, M. (1994). Dealumination of Zeolites: Part V. Influence of The Hydrothermal Treatment of Offretite on Its Pore Structure and Acid Properties. *Zeolites* 14: 217 – 224.

Carta, G. and Cincotti, A. (1998). Film Model Approximation for Non-Linear Adsorption and Diffusion in Spherical Particles. *Chem. Eng. Sci.* 53(19): 3483-3488.

Castro, M. S. and Aldao, C. M. (1999). Effects of the Sintering Temperature on the Oxygen Adsorption In ZnO Ceramic. *J. Eur. Ceram. Soc.* 19: 511-515.

Cavenati, S., Grande, C. A. and Rodrigues, A. E. (2006). Separation of $CH_4/CO_2/N_2$ Mixtures by Layered Pressure Swing Adsorption for Upgrade of Natural Gas. *Chem. Eng. Sci.* 61: 3893-3906.

Cavenati, S., Grande, C. A., and Rodrigues, A. E. (2004). Adsorption Equilibrium of Methane, Carbon Dioxide, and Nitrogen on Zeolite 13X at High Pressures. *J. Chem. Eng. Data.* 49: 1095-1101.

Centi, G. and Perathoner, S. (1996). Role and Importance of Oxidized Nitrogen Oxide Adspecies on the Mechanisms and Dynamics of Reaction Over Copper-Based Catalysts. *Catal. Today*. 29: 117-122.

Chang, C. F., Chang, C. Y., Chen, K. H., Tsai, W. T., Shie, J. L. and Chen, Y. H. (2004). Adsorption of Naphthalene on Zeolite From Aqueous Solution. *J. Colloid Interf. Sci.* 277: 29-34.

Chang, C. L., Hsu, C. C. and Huang, T. J. (2003). Cathode Performance and Oxygen-Ion Transport Mechanism of Copper Oxide for Solid-Oxide Fuel Cells. *J. Solid State Electrochem.* 7: 125-128.

Chang, J. S., Park, S. E., Lee, K. W., and Choi, M. J. (1994). Catalytic Reforming of Methane with Carbon Dioxide over Pentasil Zeolite-Supported Nickel Catalyst. In: Weikamp, J., Karge, H. G., Pfeifer, H., and Hölderich, W. eds. *Zeolites and Related Microporous Materials: State of the Art 1994, Stud. Surf. Sci. Catal.* Amsterdam: Elsevier. 84: 1587-1594.

Chang, K. J., and Talu, O. (1996). Behavior and Performance of Adsorptive natural Gas Storage Cylinders during Discharge. *Applied Thermal Engineering*, 16: 359-374.

Chang, M. Y. and Juang, R. S. (2005). Equilibrium and Kinetics Studies on the Adsorption of Surfactant Organic Acids and Dyes from Water onto Natural Biopolymers. *Colloids Surf. A: Physicochemical Engineering Aspects.*269: 35-46.

Chao, C. C. (1989). *Process for Separating Nitrogen from Mixtures Thereof with Less Polar Substances*. (U.S. Patent 4,859,217).

Chao, C. C. (1990). *Selective Adsorption on Magnesium-Containing Clinoptilolites*. (U.S. Patent 4,964,889).

Charmette, C., Sanchez, J., Gramain, Ph. and Rudatsikira, A. (2004). Gas Transport Properties of Poly(ethylene oxide-coepichlorohydrin) Membranes. *J. Membr. Sci*. 230: 161-169.

Chen, H., Matsumoto, A., Nishimiya, N. and Tsutsumi, K. (1999). Preparation and Characterization of TiO_2 Incorporated Y-Zeolite. *Colloids Surf. A: Physicochemical and Engineering Aspects*. 157: 295-305.

Cheng, L. S. and Yang, R. T. (1997). Tailoring Micropore Dimensions In Pillared Clays For Enhanced Gas Adsorption. *Microporous Mater*. 8: 177-186.

Cheng, Q., Pavlinek, V., Lengalova, A., Li, C., He, Y., and Saha, P. (2006b). Conducting Polypyrrole Confined in Ordered Mesoporous Silica SBA-15 channels: Preparation and Its Electrorheology. *Microporous and Mesoporous Materials*: 263-269.

Cheng, Q., Pavlinek, V., Li, C., Lengalova, A., He, Y., and Saha, P. (2006a). Synthesis and Characterization of New Mesoporous Material with Conducting Polypyrrole Confined in Mesoporous Silica. *Materials Chemistry and Physics*, 98: 504-508.

Cheng, Y. S., Huang, Q. L., Eić, M. and Balcom, B. J. (2005). CO_2 Dynamic Adsorption/Desorption on Zeolite 5A studied by ^{13}C Magnetic Resonance Imaging. *Langmuir*. 21: 4376-4381.

Cheung, T., Bhargava, S. K., Hobday, M. and Foger, K. (1996). Adsorption of NO on Cu Exchanged Zeolites, An FTIR Study: Effects of Cu Levels, NO Pressure, and Catalyst Pretreatment. *J. Catal*. 158: 301-310.

Chhatwal, G. R. and Mehra, H. (1974). *Adsorption and Phase Rule*. India: Goel Publishing House.

Choi, E. Y, Kim, Y., and Seff, K. (2000). Structure of a Cyclopropane Sorption Complex of Dehydrated Fully Cd^{2+}-Exchanged Zeolite A. *Micropor. Mesopor. Mater.* 41: 61 – 68.

Choma, J., Jaroniec, M., Burakiewicz-Mortka, W., and Kloske, M. (2002). Critical Appraisal of Classical Methods for Determination of Mesoporous Size Distributions of MCM-41 Materials. *Applied Surface Science*, 196: 216-223.

Choma, J., Kloske, M., and Jaroniec, M. (2003). An Improved Methodology for Adsorption Characterization of Unmodified and Modified Silica Gels. *Journal of Colloid and Interface Science*, 266: 168-174.

Chou, C. T. and Chen, C. Y. (2004). Carbon Dioxide Recovery by Vacuum Swing Adsorption. *Sep. Purif. Technol.* 39: 51-65.

Choudhary, V. R. and Mayadevi, S. (1996). Adsorption of Methane, Ethane, Ethylene, and Carbon Dioxide on Silicalite-1. *Zeolites*. 17: 501-507.

Cizmek, A. , Subotic, B., Eiello, R., Crea, F. , Nastro, A., and Tuoto, C. (1995). Dissolution of High-Silica Zeolites in Alkaline Solutions I. Dissolution of Silicalite-1 and ZSM-5 with Different Aluminum Content. *Micropor. Mater.* 4: 159 – 168.

Coade, R. and Coldham, D. (2006). The Interaction of Mercury and Aluminum in Heat Exchangers in a Natural Gas Plants. *International Journal of Pressure Vessels and Piping*, 83: 336-342.

Coe, C. G., Kirner, J. F., Perantozzi, R. and White, T. R. (1993). *Nitrogen Adsorption with A Divalent Cation Exchanged Lithium X-Zeolite*. (U.S. Patent 5,258,058).

Coluccia, S., Marchese, L. and Martra, G. (1999). Characterization of Microporous and Mesoporous Materials by the Adsorption of Molecular Probes: FTIR and UV-Vis Studies. *Micropor. Mesopor. Mater.*30: 43-56.

Cook, T. L., Komodromos, C., Quinn, D. F., and Ragan, S. (1999). Adsorbent Storage for Natural Gas Vehicles. *Carbon Materials for Advanced Technologies*, 269-301.

Cordeiro, C. N., Rocha, M. S., Faleiros, A. C. and Iha, K. (2005). Analysis of Application of Langmuir Isotherm to Heterogenous Systems: High-Pressure Conditions. *J. Colloid Interf. Sci*. 286: 459-461.

Correa, C. M., Córdoba, F. and Bustamante, F. (2000). The Role of Zeolite Type on The Lean NO_x Reduction by Methane over Pd Loaded Pentasil Zeolites. *Micropor*. *Mesopor*. *Mater*. 40: 149-157.

Cracknell, R. F., Gordon, P., and Gubbins, K. E. (1993). Influence of Pore Geometry on the Design of Micropore Materials for Methane Storage. *J. Phys. Chem.*, 97: 494-499.

Cruccolini, A., Narducci, R. and Palombari, R. (2004). Gas Adsorption Effects on Surface Conductivity of Nonstoichiometric CuO. *Sens*. *Actuators B*. 98: 227-232.

Cui, X. J., Bustin, R. M. and Dipple, G. (2004). Selective Transport of CO_2, CH_4 and N_2 in Coals: Insights from Modeling of Experimental Gas Adsorption Data. *Fuel*. 83: 293-303.

Cullity, B. D. (1978). *Elements of X-Ray Diffraction*. United States of America: Addison-Wesley Publishing Company, Inc. 101-102.

Ćurković, L., Cerjan-Stefanović, Š. and Filipan, T. (1997). Metal Ion Exchange By Natural and Modified Zeolites. *Wat*. *Res*. 31(6): 1379-1382.

Dabrowski, A. (2001). Adsorption- From Theory to Practice. *Advances in Colloid and Interface Science*, 93: 135-224.

Daiminger, U., Lind, W., and Mitariten, M. (2004). Adsorption Added Value. *Hydrocarbon Eng. VII*, 2: 83-86.

Dapurkar, S. E., Badamali, S. K. and Selvam, P. (2001). Nanosized Metal Oxides in the Mesoporous of MCM-41 and MCM-48 Silicates. *Catal*. *Today*. 68: 63-68.

de Sousa, A. and de Sousa, E. M. B. (2005). Ordered Mesoporous Silica Carrier System Applied in Nanobiothecnology. *Brazilian Archieves of Biology and Technology*, 48: 243-250.

Delahay, G., Kieger, S., Neveu, B. and Coq, B. (1998). N_2O origin in NO reduction with NH_3 over copper zeolites. *Surface Chemistry and Catalysis*. 1(2): 229-235.

Deng, S. G. and Lin, Y. S. (1997). Microwave Heating Synthesis of Supported Sorbents. *Chem*. *Eng*. *Sci*. 52(10): 1563-1575.

Deraz, N. A. M. (2001). Surface and Catalytic Properties of Cu/Zn Mixed Oxide Catalysts. *Colloids Surf. A: Physicochemical and Engineering Aspects*. 190: 251-260.

Derouane, E. G. (1998). Zeolites as Solid Solvents. *Journal of Molecular Catalysis A: Chemical*, 134: 29-45.

Desideri, U. and Paolucci, A. (1999). Performance Modelling of A Carbon Dioxide Removal System for Power Plants. *Energy Conversion & Management*, 40: 1899-1915.

Díaz, E., Ordóñez, S., Vega, A. and Coca, J. (2004a). Adsorption Characterisation of Different Volatile Organic Compounds Over Alumina, Zeolites and Activated Carbon Using Inverse Gas Chromatography. *J. Chromatogr. A*. 1049: 139-146.

Díaz, E., Ordóñez, S., Vega, A. and Coca, J. (2004b). Characterization of Co, Fe and Mn-Exchanged Zeolites by Inverse Gas Chromatography. *J. Chromatogr. A*. 1049: 161-169.

Díaz, R. and Lazo, M. F. (2000). Spectroscopic Study of CuO/CoO Catalysts Supported by Si-Al-Y Zeolite Matrices Prepared by Two Sol-Gel Methods. *J. Sol-Gel Sci. Technol*. 17: 137-144.

Ding, W., Meitzner, G. D. and Iglesia, E. (2002). The Effects of Silanation of External Acid Sites on the Structure and Catalytic Behavior of Mo/H-ZSM5. *J. Catal*. 206:14-22.

Ding, Y. and Alpay, E. (2000). Equlibria and Kinetics of CO_2 Adsorption on Hydrotalcite Adsorbent. *Chem. Eng. Sci*. 55: 3461-3474.

Do, D. D. and Do, H. D. (2003). Adsorption of Supercritical Fluids in Non-Porous and Porous Carbons: Analysis of Adsorbed Phase Volume and Density. *Carbon*. 41:1777-1791.

Dong, F., Lou, H. M., Kodama, A., Goto, M. and Hirose, T. (1999). The Petlyuk PSA Process for The Separation of Ternary Gas Mixtures: Exemplification by Separating A Mixture of CO_2-CH_4-N_2. *Sep. Purif. Technol*. 16: 159-166.

Dong, L., Chen, K. and Chen, Y. (1997). Study of the Interactions Between MoO_3 and α-Fe_2O_3. *J. Solid State Chem*. 129: 30-36.

Donohue, M. D. and Aranovich, G. L. (1998). Classification of Gibbs Adsorption Isotherms. *Adv. Colloid Interf. Sci*. 76-77: 137-152.

Doskocil, E. J. and Mankidy, P. J. (2003). Effects on Solid Basicity for Sodium Metal and Metal Oxide Occluded NaX Zeolites. *Appl. Catal. A: Gen*. 252: 119-132.

Dreisbach, F., Staudt, R. and Keller, J. U. (1999). High Pressure Adsorption Data of Methane, Nitrogen, Carbon Dioxide and Their Binary and Ternary Mixtures on Activated Carbon. *Adsorption*. 5: 215-227.

Du, X. M., and Wu, E. D. (2006). Physisorption of Hydrogen in A, X and ZSM-5 Types of Zeolites at Moderately High Pressures. *Chinese Journal of Chemical Physics*, 19.

Duran, T., Sarkisov, L., Yaghi, O. M., and Snurr, R. Q. (2004). Design of New Materials for Methane Storage. *Langmuir*, 20: 2683-2689.

Dutta, P. K. and Vaidyalingam, A. S. (2003). Zeolite-Supported Ruthenium Oxide Catalysts For Photochemical Reduction of Water to Hydrogen. *Micropor. Mesopor. Mater.* 62(1): 107-120.

El-Shobaky, G. A., Hamed, M. N., Abdalla, F. F. and El-Molla, S. A. (2002). Surface and Catalytic Properties of A CuO/MgO System As Influenced by Li_2O-Doping and Exposure to γ–Irradiation. *Colloids Surf. A: Physicochemical and Engineering Aspects*. 207: 293-301.

El-Shobaky, H. G., Mokhtan, M. and El-Shobaky, G. A. (1999). Physicochemical Surface and Catalytic Properties of CuO-ZnO/Al_2O_3 System, *Appl. Catal. A: Gen.* 180: 335-344.

Evans, J., Zaki, A. B., El-Sheikh, M. Y., and El-Safty, S. A. (2000). Incorporation of Transition-Metal Complexes in Functionalized Mesoporous Silica and Their Activity Toward The Oxidation of Aromatic Amines. *J. Phys. Chem. B*, 104: 10271-10281.

Fajula, F., Galarneau, A. and Renzo, F. D. (2005). Advanced Porous Materials: New Developments and Emerging Trends. *Microporous and Mesoporous Materials*, 82.

Feijen, E. J. P., Martens, J. A., and Jacobs, P. A. (1994). Zeolites and Their Mechanism of Synthesis In: *Zeolites and Related Microporous Material: State of Art Studies in Surface Science and Catalysis*. J. Weitkamp J., Karge H. G., Pfeifer H., and Holderich W. (Eds.). 84: 3 – 19.

Fernandez, C., Vedrine, J. C., Grosmangin, J., and Szabo, G. (1986). Dealumination of an Offritite-Type Zeolite: Framework Modifications. *Zeolites*. 6: 484 – 498.

Ferwerda, R. and Van der Maas, J. H. (1995). The Influence of Adsorbed Molecules on the Framework Vibrations of Na-Faujasites Studied with FT Raman Spectroscopy. *Spectrochim. Acta Part A*. 51: 2147-2159.

Firas, N. R., Mat, H. B., and Zakaria, Z. Thermal Behaviour of ANG Tank Loaded with Activated Carbon Under Dynamic Discharge Conditions. *Advance Process*

Engineering (APEN) Research Group, Faculty of Chemical and Natural Resources Engineering, University Technology of Malaysia.

Fitch, F. R., Bülow, M. and Ojo, A. F. (1995). Adsorptive Separation of Nitrogen from Other Gases. (U.S. Patent 5,464,467).

Flanigen E.M., Khatami H. and Szymanski H. A. (1971). Infrared Structural Studies of Zeolite Frameworks. In: Robert F. Gould. ed. *Advanced Chem. Series.* 101: 201-227.

Freitas M.M.A. and Figueiredo J.L. (2001). Preparation of carbon Molecular sieves for Gas separations by Modification of the Pore of Activated carbons, Fuel, 80: 1-6.

Frost and Sullivan. (2001). *Zeolites: Industry Trends and Worldwide Markets In 2010.* New York: Technical Insights.

Frost, H., Duren, T., and Snurr, R. Q. (2006). Effects of Surface Area, Free Volume andHeat of Adsorption on Hydrogen Uptake in Metal-Organic Frameworks. *J. Phys. Chem*., 110; 9565-9570.

Fu, G. and Zhu, H. M. (2003). Neural Network Modeling of Supercritical Adsorption of Methane on Activated Carbon. *Carbon*. 41:2653-2689.

Fulvio, P. F., Pikus, S., and Jaroniec, M. (2005). Short Time Synthesis of SBA-15 Using Various Silica Sources. *J Colloid Interf. Sci.*, 287: 717-720.

Fulvio, P. F., Pikus, S., and Jaroniec, M. (2005). Short-Time Synthesis of SBA-15 Using Various Silica Sources. *J Colloid Interf. Sci.*, 287: 717-720.

Gao, Y., Zhao, H. B. and Zhao, B. Y. (2000). Monolayer Dispersion of Oxide Additives on SnO_2 and Their Promoting Effects on Thermal Stability of SnO_2 Ultrafine Particles. *J. Mater. Sci*. 35: 917-923.

Gardner, T. Q., Falconer, J. L. and Noble, R. D. (2002). Adsorption and Diffusion Properties of Zeolite Membranes by Transient Permeation. *Desalination*. 149: 435-440.

Gaydhankar, T. R., Taralkar, U. S., Jha, R. K., Joshi, P. N., and Kumar, R. (2005). Textural/Structural, Stability and Morphological Properties of Mesostructured Silicas (MCM-41 and MCM-48) Prepared Using Different Silica Sources. *Catal. Comm.*, 6: 361-366.

Gervasini, A. (1999). Characterization of the Textural Properties of Metal Loaded ZSM-5 Zeolites. *Appl. Catal. A: Gen*. 180: 71-82.

Gheno, S. M., Damyanova, S., Riguetto, B. A., Marques, C. M. P., Leite, C. A. P. and Bueno, J. M. C. (2003). CO_2 Reforming of CH_4 Over Ru/Zeolite Catalysts Modified with Ti. *J. Mol. Catal. A: Chem*. 198: 263-275.

Ghobarkar, H., Schaf, O., and Guth, U. (1999). Zeolites- From Kitchen to Space. *Prog. Solid St. Chem.*, 27: 29-73.

Gil, A., and Grange, P. (1996). Application of the Dubinin-Radushkevich and Dubinin-Astakhov equations in the characterization of microporous solids. *A: Physiochemical and Engineering Aspects*, 113: 39-50.

Gomes, V. G. and Yee, K. W. K. (2002). Pressure Swing Adsorption for Carbon Dioxide Sequestration from Exhaust Gases. *Sep. Purif. Tech*. 28: 161-171.

Gray, M. L., Soong, Y., Champagne, K. J., Pennline, H., Baltrus, J. P., Stevens Jr., R. W., Khatri, R.,Chuang, S. S. C., and Filburn, T. (2005). Improved Immobilized Carbon Dioxide Capture Sorbents. *Fuel Proc. Tech.*, 86: 1449-1455.

Gu, J. L., Shi, J. L., Xiong, L. M., Chen, H. R. and Ruan, M. L. (2004). A New Strategy to Incorporate Highly Dispersed Nanoparticles Into the Pore Channels of Mesoporous Silica Thin Films. *Micropor. Mesopor. Mater.*74: 199-204.

Guldur, C. and Balikci, F. (2002). Selective Carbon Monoxide Over Ag-Based Composite Oxides. *J. Hydrogen Energy*. 27(2): 219-224.

Guo, J., Han, A. J., Yu, H., Dong, J. P., He, H., and Long, Y. C. (2006). Base Property of High Silica MFI Zeolites Modified With Various Alkyl Amines. *Micropor. Mesopor. Mater.*: 166-172.

Gupta, J. C., Ma, Y. H. and Sand, L. B. (1971). Diffusion of Sulfur Dioxide In A Synthetic Mordenite and A Natural Erionite. *AICHE Symposium Series*. 67: 51-57.

Gutierrez-Ortiz, J. I., Lopez-Fonseca, R., Aurrekoetxea, U. and Gonzalez-Velasco, J. R. (2003). Low Temperature Deep Oxidation of Dichloromethane and Trichloroethylene By H-ZSM-5 Supported Manganese Oxide Catalysts. *J. Catal*. 218: 148-154.

Hadi Nur, Lau, C. G., Salasiah Endud, and Halimaton Hamdan. (2004). Quantitative Measurement of A Mixture of Mesophases Cubic MCM-48 and Hexagonal MCM-41 by ^{13}C CP/MAS NMR. *Mater. Lett.*, 58: 1971-1974.

Hadjiivanov, K. and Knözinger, H. (1999). FTIR Spectroscopic Evidence of Formation of Geminal Dinitrogen Species During The Low-Temperature N_2 Adsorption on NaY zeolites. *Catal. Lett*. 58: 21-26.

Hadjiivanov, K., Ivanova, E. and Klissurski, D. (2001). Site-Specified and Complex-Specified Formation of Geminal Species During Adsorption of Small Molecules on Cationic Sites. *Catal. Today*. 70: 73-82.

Hadjiivanov, K., Ivanova, E. and Knözinger, H. (2003b). FTIR Study of Low-Temperature CO Adsorption on Y Zeolite Exchanged with Be^{2+}, Mg^{2+}, Ca^{2+}, Sr^{2+} and Ba^{2+} Cations. *Micropor. Mesopor. Mater*. 58: 225-236.

Hadjiivanov, K., Ivanova, E., Kantcheva, M., Ciftlikli, E. Z., Klissurski, D., Dimitrov, L., Knozinger, H. (2002). FTIR Study of Low-Temperature CO Adsorption on Mn-ZSM-5 and MnY Zeolites. Effects of The Zeolite Matrix on the Formation of $Mn^{2+}(CO)_x$ Geminal Species. *Catal. Commun*. 3: 313-319.

Hadjiivanov, K., Tsoncheva, T., Dimitrov, M., Minchev, C. and Knözinger, H. (2003a). Characterization of Cu/MCM-41 and Cu/MCM-48 Mesoporous Catalysts by FTIR Spectroscopy of Adsorbed CO. *Appl. Catal. A: Gen*. 241: 331-340.

Hagen, A., Schneider, E., Kleinert, A., and Roessner, F. (2003). Modification of Acid Supports by Solid-State Redox Reaction. Part I, Preparation and Characterization. *J. Catal*. 222: 227-237.

Hagiwara, Z. and Uchida, M. (1978). Ion-Exchange Reactions of Processed Zeolite and Its Application to the Removal of Ammonia-Nitrogen In Wastes. In: Sand, L. B. and Mumpton, F. A. eds. *Natural Zeolites Occurrence, Properties, Use*. New York: Pergamon Press Ltd. 463-470.

Han, A. J., He, H. Y., Guo, J., Yu, H., Huang, Y. F., and Long, Y. C. (2005). Studies on Structure and acid-base Properties of High Silica MFI-Type Zeolite Modified with Methylamine. *Microporous and Mesoporous Materials*, 79: 177-184.

Han, X. W., Wang, Y., Cao, Y., Yu, Q., Si, L. and Zhou, Y. M. (2004). Characterization The Basicity of Calcium-Modified NaZSM-5 Zeolites. *Proceedings of the 14th International Zeolite Conference*. April 25-30. Cape Town, South Africa: Document Transformation Technologies. 1612-1619.

Harlick, P. J. E. and Tezel, F. H. (2004). An Experimental Adsorbent Screening Study for CO_2 Removal from N_2. *Micropor. Mesopor. Mater*. 76: 71-79.

Hasegawa, Y., Watanabe, K., Kusakabe, K. and Morooka, S. (2001). The Separation of CO_2 Using Y-Type Zeolite Membranes Ion-Exchanged with Alkali Metal Cations. *Sep. Purif. Technol*. 22-23: 319-325.

Hassan, M. H., Way, J. D., Thoen, P. M. and Dillon, A. C. (1995). Single Component and Mixed Gas Transport in A Silica Hollow Fiber Membrane. *J. Membr. Sci*. 104: 27-42.

Hattori, Y., Konishi, T. and Kaneko, K. (2002). XAFS and XPS studies of enhancement of methane adsorption by NiO dispersed ACF with the relevance to structural change of NiO. *Chem. Phys. Lett*. 355: 37-42.

Hayhurst, D. T. (1978). The Potential Use of Natural Zeolites for Ammonia Removal During Coal-Gasification. In: Sand, L. B. and Mumpton, F. A. eds. *Natural Zeolites Occurrence, Properties, Use*. New York: Pergamon Press Ltd. 503-507.

He, J., Duan, X. and Li, C. Y. (2001). Improving The Stability of MCM-41 by Monolayer Dispersion of A Metal Oxide. *Mater. Chem. Phys*. 71: 221-225.

Hegedus, L. L., Aris, R., Bell, A. T., Boudart, M., Chen, N.Y., Gates, B. C., Haag, W. O., Somorjai, G. A. and Wei, J. (1987). *Catalyst Design-Progress and Perspectives.* New York: John Wiley & Sons.

Henriques, C., Ribeiro, M. F., Abreu, C., Murphy, D. M., Poignant, F., Saussey, J. and Lavalley, J. C. (1998). An FT-IR Study of NO Adsorption over Cu-exchanged MFI Catalysts: Effect of Si/Al Ratio, Copper Loading and Catalysts Pretreatment. *Appl. Catal. B: Environ*. 16: 79-95.

Herbst, A. and Harting, P. (2002). Thermodynamics Description of Excess Isotherms in High-Pressure Adsorption of Methane, Argon and Nitrogen. *Adsorption*. 8: 111-123.

Hernández-Huesca, R., Díaz, L., and Aguilar-Armenta, G. (1999). Adsorption Equilibria and Kinetics of CO_2, CH_4 and N_2 In Natural Zeolites. *Sep. Purif. Technol*. 15: 163-173.

Hiyoshi, N., Yogo, K., and Yashima, T. (2005). Adsorption Characteristics of Carbon Dioxide on Organically Functionalized SBA-15. *Microporous and Mesoporous Materials*, 84: 357-365.

Horiuchi, T., Hidaka, H., Fukui, T., Kubo, Y., Horio, M., Suzuki, K. and Mori, T. (1998). Effect of Added Basic Metal Oxides on CO_2 Adsorption on Alumin at Elevated Temperatures. *Appl. Catal. A: Gen*. 167: 195-202.

Hotovy, I., Rehacek, V., Siciliano, P., Capone, S. and Spiess, L. (2002). Sensing Characteristics of NiO Thin Films As NO Gas Sensor. *Thin Solid Films*. 418: 9-15.

Hsu, L. Y., and Teng, H. (2000). Influence of Different Chemical Reagents on the Preparation of Activated Carbons From Bituminous Coal. *Fuel Processing Technology*, 64: 155-166

Hu, Z. S., Wei, L. H., Dong, J. X., Wang, Y. R., Chen, S. Y. and Peng, S. Y. (1999). Modification of The External Surface of ZSM-5 by A Metal Surfactant. *Micropor. Mesopor. Mater.* 28: 49-55.

Huang, H. Y. and Yang, R. T. (2003). Amine-Grafted MCM-48 and Silica Xerogel as Superior Sorbents for Acidic Gas Removal from Natural Gas. *Ind. Eng. Chem. Res,* 42: 2427-2433.

Huang, Y., Paroli, R. M., Delgado, A. H., and Richardson, T. A. (1998). An FT-Raman Study of Solid-State Ion Exchange in Zeolites. *Spectrochimica Acta Part A*. 54: 1347 – 1354.

Huang, Y. J., Wang, H. P., Hsiao, M. C., Tai, C. C., Huang, H. and Liu, S. H. (2004). Speciation of Copper In Micropores. *Water, Air and Soil Pollution*. 153: 187-194.

Huber, S. and Knözinger, H. (1995). FTIR Spectroscopic Studies of Methane Adsorption on Sodium and Cesium Containing Y-Zeolites. *Chem. Phys. Lett.* 244: 111-116.

Hutson, N. D., Rege, S.U., and Yang, R. T. (1999). Mixed Cation Zeolites: Li_xAg_y-X as a Superior Adsorbent for Air Separation. *AIChE J.* 45: 724 –734.

Huwe, H. and Fröba, M. (2003). Iron (III) Oxide Nanoparticles within the Pore System of Mesoporous Carbon CMK-1: Intra-Pore Synthesis and Characterization. *Micropor. Mesopor. Mater.* 60: 151-158.

Impens, N.R.E.N., van der Voort, P., and Vansant, E.F. (1999). Silylation Of Micro-, Meso-, and Nonporous Oxides: A Review. *Micropor. Mesopor. Mater.* 28: 217 – 232.

Ínel, O., Topaloğlu, D., Askin, A. and Tűmsek, F. (2002). Evaluation of The Thermodynamics Parameters for the Adsorption of Some Hydrocarbons on 4A and 13X Zeolites by Inverse Gas Chromatograpghy. *Chem. Eng. J.* 88: 255-262.

Ingle, J. D. and Crouch, S. R. (1988). *Spectrochemical Analysis*. United States of America: Prentice-Hall International Inc. 404.

Inomata, K., Kanazawa, K., Urabe, Y., Hosono, H., and Araki, T. (2001). Natural Gas Storage in Activated Carbon Pellets without a Binder. *Carbon*, 40: 87-93.

Inoue, M., Tanino, H., Kondo, Y., and Inui, T. (1991). Formation of Organic Derivatives of Boehmite by The Reaction of Gibbsite with Glycols and Aminoalcohols. *Clays and Clay Minerals*, 39(2): 151-157.

International Zeolite Association – Structure Commission.Website. *www.iza-structure.org*.

Ishibashi, M., Ota, H., Akutsu, N., Umeda, S., Tajika, M., Izumi, J., Yasutake, A., Kabata, T. and Kageyama, Y. (1996). Technology for Removing Carbon Dioxide from Power Plant Flue Gas by The Physical Adsorption Method. *Energy Convers*. 37(6-8): 929-933.

Itadani, A., Kumashiro, R., Kuroda, Y. and Nagao, M. (2004). Calorimetric Study of N_2 Adsorption on Copper-Ion-Exchanged ZSM-5 Zeolite. *Thermochim. Acta*. 416: 99-104.

Ito, T., Yamaguchi, H., Okabe, K. and Masumi, T. (1998). Single-Crystal Growth and Characterization of Cu2O and CuO. *J. Mater. Sci*. 33: 3555-3566.

Jakubov, T. S., and Mainwaring, D. E. (2002). Modified Dubinin Radushkevich/ Dubinin–Astakhov Adsorption Equations, *J Colloid Interf. Sci.*, 252: 263-268.

Jaroniec, M., Kruk, M., Hyun, J. S., Ryong, R., Sakamoto, Y., and Terasaki, O. (2001). Comprehensive Characterization of Highly Ordered MCM-41 Silicas Using Nitrogen Adsorption, Thermogravimetry, X-ray Diffraction and Transmission Electron Microscopy. *Micropor. Mesopor. Mater.*, 48: 127-134.

Jayaraman, A. and Yang, R. T. (2005). Stable Oxygen-Selective Sorbents for Air Separation. *Chem. Eng. Sci*. 60: 625-634.

Jayaraman, A., Hernandez-Maldonado, A. J., Yang, R. T., Chinn, D., Munson, C. L. and Mohr, D. H. (2004). Clinoptilolites for Nitrogen/Methane Separation. *Chem. Eng. Sci*. 59: 2407-2417.

Jiang, X., Alvarez, D., Tram, J. A. and Aeronex, J. J. S. (2002). *Gas Purification Photolithography Advances Push Purge-Gas Purification.* California: Solid-State Technology.

Joshi, U. D., Joshi, P. N., Tamhankar, S. S., Joshi, V. V. and Shiralkar, V.P. (2001). Adsorption Behavior of N_2, Water, C_6 Hydrocarbons, and Bulkier Benzene Derivative (TMB) on Na-X Zeolite and Its K^+-, Rb^+-, and Cs^+-Exchanged Analogues. *J. Colloid Interf. Sci*. 235: 135-143.

Kaggerud, K. H., Bolland, O., and Gundersen, T. (2006). Chemical and Process Integration: Synergies in Co-Production of Power and Chemicals from Natural Gas With CO_2 Capture. *Appl. Therm. Eng.*, 26: 1345-1352.

Kanazirev, V. and Price, G. L. (1994). Activity of Ga, In and Cu Modified MFI Zeolites for Amine Rections. In: Weikamp, J., Karge, H. G., Pfeifer, H. and Hölderich, W. eds. *Zeolites and Related Microporous Materials: State of the Art 1994, Stud. Surf. Sci. Catal.* Amsterdam: Elsevier. 84: 1935-1942.

Kaneko, K., Murata, K., Shimizu, K., Camara, S., and Suzuki, T. (1993). Enhancement Effect of Micropore Filling for Supercritical Methane by MgO Dispersion. *Langmuir*. 9(5): 1165.

Kaneko, K., Ohta, T., and Ozeki, S. (1988). Chemisorption-Assisted Micropore Filling of NO on Cu, Ni, and Co Oxide-Dispersed Activated Carbon Fibers. *Appl. Surf. Sci*. 33/34: 355-363.

Kang, T., Park, Y., Park, J. C., Cho, Y. S., and Yi, J. (2002). Preparation of Chemically Active Mesoporous Adsorbent for Pt(II) and Pd(II) Adsorption from Aqueous Solutions. *Korean J. Chem. Eng.*, 19(4): 685-687.

Kanô, F., Abeb, I., Kamaya, H. and Uedac, I. (2000). Fractal Model for Adsorption on Activated Carbon Surfaces: Langmuir and Freundlich Adsorption. *Surf. Sci.* 467: 131-138.

Kärger, J. (2003). Measurement of Diffusion In Zeolites – A Never Ending Challenge?. *Adsorption*. 9: 29-35.

Katiyar, A., Yadav, S., Panagiotis, G., Smirniotis, and Pinto, N. G (2006). Synthesis of Ordered Large Pore SBA-15 Sperical Particles for Adsorption of Biomolecules. *J. Chromatogr.* A., 1122: 13-20.

Katoh, M., Yoshikawa, T., Tomonari, T., Katayama, K. and Tomida, T. (2000). Adsorption Characteristics of Ion-Exchanged ZSM-5 Zeolites for CO_2/N_2 Mixtures. *J. Colloid Interf. Sci*. 226: 145-150.

Katsanos, N. A., Rakintzis, N., Roubani-Kalantzaopoulou, F., Arvanitopoulou, E. and Kalantzopoulos, A. (1999). Measurement of Adsorption Energies on Heterogeneous Surfaces by Inverse Gas Chromatography. *J. Chromatogr. A*. 845: 103-111.

Kaushik, V. K, Vijayalakshmi, R. P, Choudry, N. V., and Bhat, S. G. T. (2002). XPS Studies on Cation Exchanged Zeolite A. *Micropor. Mesopor. Mater.* 51: 139 – 144.

Kazansky, V. B., Serykh, A. I. and Pidko, E. A. (2004a). DRIFT Study of Molecular and Dissociative Adsorption of Light Paraffins by HZSM-5 Zeolite Modified with Zinc Ions: Methane Adsorption. *J. Catal*. 225: 269-373.

Kazansky, V. B., Subbotina, I. R., Santen, R. A.V. and Hensen, E. J. M. (2004b). Drifts Study of the Chemical State of Modifying Gallium Ions in Reduced Ga/ZSM-5 Prepared by Impregnation I. Observation of Gallium Hydrides and Application of CO Adsorption as A Molecular Probe for Reduced Gallium Ions. *J. Catal*. 227: 263-269.

Keller, J. U., Dreisbach, F., Rave, H., Staudt, R., and Tomalla, M. (1999). Measurement of Gas Mixture Adsorption Equilibria of Natural Gas Compounds on Microporous Sorbents. *Adsorption*, 5: 199-214.

Khatri, R. A., Chuang, S. S. C., Soong, Y., and Gray, M. (2005). Carbon Dioxide Capture by Diamine-Grafted SBA-15: A Combined Fourier Transform Infrared and Mass Spectrometry Study. *Ind. Eng. Chem. Res.*, 44: 3702-3708.

Khelifa, A., Benchehida, L. and Derriche, Z. (2004). Adsorption of Carbon Dioxide by X Zeolites Exchanged with Ni^{2+} and Cr^{3+}: Isotherms and Isosteric Heat. *J. Colloid Interf. Sci*. 278: 9-17.

Khelifa, A., Derriche, Z. and Bengueddach, A. (1999). Adsorption of Propene on NaX Zeolite Exchanged with Zn^{2+} and Cu^{2+}. *Appl. Catal. A: Gen*. 178: 61-68.

Khouchaf, L., Tuilier, M. H., Wark, M., Soulard, M. and Kessler, H. (1998). Structural Investigation of Zinc Oxide Clustering in Zeolite A and Sodalite. *Micropor. Mesopor. Mater*. 20: 27-37.

Kim, J. H., Ikoma, Y., and Niwa, M. (1999). Control of the Pore Opening Size of HY Zeolite by CVD of Silicon Alkoxide. *Micropor. Mesopor. Mater.* 32: 37 – 44.

Kim, C. J., Kim, H. J., Sun, J. W., Ji, B. K., Kim, H. S., Joo, J. H., Jun, B. H., Jung, C. H., Park, S. D., Park, H. W. and Hong, G. W. (2003). Deposition of CeO_2 and NiO Buffer Layers for YBCO Coated Conductors on Biaxially Textured Ni Substrates by A MOCVD Technique. *Physica C*. 386: 327-332.

Kim, J. H., Kim, E. K., Lee, C. H., Song, M. S., Kim, Y. H. and Kim, J. (2005). Electrical Properties of Metal-Oxide Semiconductor Nano-Particle Device. *Physica E*. 26(1-4): 432-435.

Kington, G. L. and Macleod, A. C. (1959). Heats of Sorption of Gases in Chabazite, Energetic Heterogeneity and The Role of Quadrupoles In Sorption. *Trans. Farad. Soc*. 55: 1799-1814.

Kiyobayashi, T., Takeshita, H. T., Tanaka, H., Takeichi, N., Zuttel, A., Schlapbach, L., and Kuriyama, N. (2002). Hydrogen Adsorption in Carbonaceous Materials - How to determine the Storage Capacity Accurately. *Journal of Alloys and Compounds*, 330-332, 666-669.

Klemm, E., Seitz, M., Scheidat, H., and Emig, G. (1997). Controlling Acidity and Selectivity of HY-Type Zeolite by Silanation. *J Catal*. 173: 177 – 186.

Klimova, T., Esquivel, A., Reyes, J., Rubio, M., Bokhimi, X., and Aracil, J. (2006). Factorial Design for The Evaluation of The Influence of Synthesis Parameters Upon The Textural and Structural Properties of SBA-15 Ordered Materials. *Micropor. Mesopor. Mater.*: 331-343.

Knofel C., Descarpentries J., Benzaouia A., Zelenak V., Monet S., Llewellyn P.L., and Hornebecq V. (2007). Functionalised Micro-/Mesoporous Silica for the Adsorption of Carbon Dioxide, *Micro. Meso. Mater*., 99: 79-85.

Kodde, A. J., Padin, J., Meer, P. J., Mittelmeijer-Hazeleger, M. C., Bliek, A. and Yang, R. T. (2000). $NiCl_2$ on γ-Alumina as Selective Adsorbents for Acetylene Over Ethylene. *Ind. Eng. Chem. Res*. 39: 3108-3111.

Korotcenkov, G., Macsanov, V., Brinzari, V., Tolstoy, V., Schwank, J., Cornet, A. and Morante, J. (2004). Influence of Cu-, Fe-, Co-, and Mn-Oxide Nanoclusters On Sensing Behavior of SnO_2 Films. *Thin Solid Films*. 467(1-2): 209-214.

Kosanović, C., Subotić, B. and Ristić, A. (2002). Structural and Morphological Transformations of the (NH_4, Na)-Exchanged Zeolites 4A, 13X and Synthetic Mordenite by Thermal Treatment. *Croatica Chemica Acta*. 75(3): 783-792.

Kriventsov, V. V. and Kochubey, D. I. (2000). The Determination of Adsorption Site Structures of High Dispersed Oxides by EXAFS Spectroscopy Using Molecules As Probe. *J. Mol. Catal. A: Chem*. 158: 287-291.

Krooss, B. M., van Bergen, F., Gensterblum, Y., Siemons, N., Pagnier, H. J. M., and David, P. (2002). High Pressure Methane and Carbon Dioxide Adsorption on Dry and Moisture Equilibrated Pennsylvanian Coals. *Intl. J Coal Geology*, 51: 69-92.

Kruk, M. and Jaroniec, M. (2001). Characterization of Modified Mesoporous Silicas Using Argon and Nitrogen Adsorption. *Micropor. Mesopor. Mater.*, 44-45: 725-732.

Kruk, M., Jaroniec, M., and Sayari, A. (1999). Influence of Hydrothermal Restructuring Conditions on Structural Properties of Mesoporous Molecular Sieves. *Micropor. Mesopor. Mater.*, 27: 217-229.

Kucherov, A. V., Kucherova, T. N., and Slinkin, A. A. (1998). Modification of zeolites by multi-charged cations by the use of in-situ formed "active gas-phase species". *Micropor. Mesopror. Mater*. 26: 1 – 10.

Kuge, K. and Calzaferri, G. (2003). Gold-Loaded Zeolite A. *Micropor*. *Mesopor*. *Mater*. 66: 15-20.

Kumar, D., Bera, S., Tripathi, A. K., Dey, G. K. and Gupta, N. M. (2003). Uranium Oxide Nanoparticles Dispersed Inside the Mesopores of MCM-48: Synthesis and Characterization. *Micropor*. *Mesopor*. *Mater*. 66: 157-167.

Kumar, D., Schumacher, K., Hohenesche, D. F. V., Grün, M., and Unger, K. K. (2001). MCM-41, MCM-48 and Related Mesoporous Adsorbents: Their Synthesis and Characterisation. *Colloids and Surfaces A: Physicochemical and Engineering Aspects*, 187-188: 109-116.

Kurama, H., Zimmer, A., and Reschetilowski, W. (2002). Chemical Modification Effect on the Sorption Capacities of Natural Clinoptilolite. *Chem. Eng. Tech.* 25: 301 – 305.

Kusakabe, K., Kuroda, T. and Morooka, S. (1998). Separation of Carbon Dioxide From Nitrogen Using Ion-Exchanged Faujasite-Type Zeolite Membranes Formed on Porous Support Tubes. *J*. *Membr*. *Sci*. 148:13-23.

Labidi, A., Jacolin, C., Bendahan, M., Abdelghani, A., Guérin, J., Aguir, K. and Maaref, M. (2004). Impedance Spectroscopy on WO_3 Gas Sensor. *Sens*. *Actuators B*. 106: 713-718.

Langmi, H. W., Book, D., Walton, A., Johnson, S. R., Al-Mamouri, M. M., Speight, J. D., Edwards, P. P., Harris, I. R., and Anderson, P. A. (2005). Hydrogen Storage in Ion-Exchange Zeolites. *J Alloys Comp.*, 404-406, 637-642.

Lau, C., Brück, S., Mai, H. J. and Kynast, U. (2001). Incorporation of Tungsten Trioxide Into Faujasites and Sodalites by Solid-State Reactions. *Micropor*. *Mesopor*. *Mater*. 47: 339-344.

Lavalley, J. C. (1996). Infrared Spectrometric Studies of the Surface Basicity of Metal Oxides and Zeolites Using Adsorbed Probe Molecules. *Catal*. *Today*. 27: 377-401.

Lee, C. K., Kim, W. S., Park, H. H., Jeon, H. and Pae, Y. H. (2005). Thermal-Stress Stability of Yttrium Oxide as A Buffer Layer of Metal-Ferroelectric-Insulator-Semiconductor Field Effect Transistor. *Thin Solid Films*. 473(2): 335-339.

Lee, H., Shim, M., Lee, J. and Kim, S. (1996). Characteristics of CO Gas Adsorption on Modified Natural Zeolite. *Materials Chemistry and Physics*. 44: 79-84.

Lee, J. H., Kim, J. G., Lee, J. K. and Kim, J. H. (2003). NO Removal by CH_4 on Co-NaX-CO and Ag-NaX Catalysts In A Dual-Bed System. *Catal*. *Today*. 87: 35-42.

Lee, S. H., Lee, J. Y., Park, Y. M., Wee, J. H., and Lee, K. Y. (2006). Complete Oxidation of Methane and CO at Low Temperature over $LaCoO_3$ Prepared by Spray-freezing/Freeze-drying Method. *Catalysis Today*. In press.

Lefebvre, F., Mallmann, A. and Basset, J. M. (1999). Modification of the Adsorption and Catalytic Properties of Molecular Sieves by Reaction with Organometallic Complexes. *Eur*. *J*. *Inorg*. *Chem*. 361-371.

Li, G. and Kawi, S. (1999). MCM-41 Modified SnO_2 Gas Sensors: Sensitivity and Selectivity Properties. *Sens*. *Actuators B*. 59: 1-8.

Li, J., Qiu, J., Sun, Y. J., and Long, Y. C. (2000). Studies on Natural STI Zeolite: Modification, Structure, Adsorption and Catalysis. *Micropor*. *Mesopor*. *Mater*. 37: 365-378.

Li, M. and Gu, A. Z. (2004). Determination of The Quasi-Saturated Vapor Pressure of Supercritical Gases In The Adsorption Potential Theory Application. *J*. *Colloid Interf*. *Sci*. 273: 356-361.

Li, M., Gu, A. Z, Lu, X. S. and Wang, R. S. (2003). Determination of the Adsorbate Density from Supercritical Gas Adsorption Equilibrium Data. *Carbon*. 41: 579-625.

Li, Y., and Yang, R. T. (2006). Hydrogen Storage in Low Silica Type X Zeolites. *J. Phys. Chem*., 110: 17175-17181.

Li, Z. P., Gao, L. and Zheng, S. (2002). Investigation of the Dispersion of MoO_3 onto the Support of Mesoporous Silica MCM-41. *Appl*. *Catal*. *A: Gen*. 236: 163-171.

Liang, Z. P., Feng, Y. Q., Liang, Z. Y. and Meng, S. X. (2005). Adsorption of Urea Nitrogen onto Chitosan Coated Dialdehyde Cellulose Under Biocatalysis of Immobilized Urease: Equilibrium and Kinetic. *Biochem*. *Eng*. *J*. 24: 65-72.

Lima, I. M. and Marshall, W. E. (2005). Granular Activated Carbons from Broiler Manure: Physical, Chemical and Adsorptive Properties. *Bioresour*. *Technol*. 96: 699-706.

Lin, H., Kao, S, Lin, K., Chang, J. and Shyu, S. (2004). Grafting TiO_2 on MCM-41 as A Support for Vanadia for Catalytic Oxidation of Ethanol-EXAFS and XANES Analyses of Vanadium. *J*. *Catal*. 224(1): 156-163.

Lin, K. S., Wang, H. P. and Yang, Y. W. (1999). Supercritical Water Oxidation of 2-Chlorophenol Effected by Li^+ and CuO/Zeolites. *Chemosphere*. 39(9): 1385-1396.

Liu X., Li J., Zhou L., Huang D., and Zhou Y. (2005). Adsorption of Carbon Dioxide, Methane and Nitrogen on Ordered Mesoporous Silica Molecular Sieve, Chemical Physics Letters, 415: 198-201.

Liu X.L., Zhou L., Fu X., Sun Y., Su W., and Zhou Y. (2007). Adsorption and Regeneration Study of the Mesoporous Adsorbent SBA-15 Adapted to the Capture/Separation of carbon dioxide and Metahne, Chemical Engineering Science, 62: 1101-1110.

Liu, A. G., Nyavor, K. and Ankumah, R. (2005). Structural and Adsorptive Properties of Ba and Mg Oxide Modified Zirconia. *J. Colloid Interf. Sci*. 284: 66-70.

Liu, B. J. and Ren, Q. L. (2005). Sorption of Levulinic Acid onto Weakly Basic Anion Exchangers: Equlibrium and Kinetic Studies. *J. Colloid Interf. Sci*. 294: 281-287.

Liu, H. M., Li, Y., Shen, W. J., Bao, X. H. and Xu, Y. D. (2004). Methane Dehydroaromatization over Mo/H-ZSM-5 Catalysts In The Absence of Oxygen: Effects of Silanation in HZSM-5 Zeolite. *Catal. Today*. 93-95: 65-73.

Liu, X., Li, J., Zhou, L., Huang, D., and Zhou, Y. (2005). Adsorption of CO_2, CH_4 and N_2 on Ordered Mesoporous Silica Molecular Sieve. *Chem, Phys. Lett.*, 415: 198-201.

Llewellyn, P. L. and Maurin, G. (2005). Gas Adsorption Microcalorimetry and Modeling to Characterise Zeolites and Related Materials. *C. R. Chimie*. 8: 283-302.

Lónyi, F., Valyon, J. and Pál-Borbély, G. (2003). A DRIFT Spectroscopic of the N_2 Adsorption and Acidity of H-Faujasites. *Micropor. Mesopor. Mater*. 66: 273-282.

López-Fonseca, R., Gutiérrez-Ortiz, J. I. and González-Velasco, J. R. (2004). Catalytic Combustion of Chlorinated Hydrocarbons Over H-BETA and PdO/H-BETA Zeolite Catalysts. *Appl. Catal. A*: *Gen*. 271: 39-46.

Lozano-Castelló, D., Alcañiz-Monge, J., de la Casa-Lillo, M. A., Cazorla-Amoros, D., and Linares-Solano, A. (2002). Advances in the Study of Methane Storage in Porous Carbonaceous Materials. *Fuel*, 81: 1777-1803.

Lozano-Castello, D., Cazorla-Amoros, D., Linares-Solano, A., and Quinn, D. F. (2002). Activated Carbon Monolith for Methane Storage: Influence of Binder. *Carbon*, 40: 2817-2825.

Lozano-Castello, D., Cazorla-Amoros, D., Linares-Solano, A., and Quinn, D. F. Micropore Size Distribution Assesed by High Pressure CH_4 (298K) and CO_2 (273K) Adsorption Isotherms. *Department of Chemical and Chemical Engineering, Royal Military College of Canada*.

Lozano-Castelló, D., Cazorla-Amoros, D., Linares-Solano, A., and Quinn, D. F. (2002). Influence of Pore Size Distribution on Methane Storage at Relatively Low Pressure: Preparation of Activated Carbon with Optimum Pore Size. *Carbon*, 40: 989-1002.

Luan, Z. and Fournier, J. A. (2005). In Situ FTIR Spectroscopic Investigation of Active Sites and Adsorbate Interactions in Mesoporous Aluminosilicate SBA-15 Molecular Sieves. *Micropor. Mesopor. Mater.*, 79: 235-240.

Luan, Z., Fournier, J. A., Wooten, J. B., and Miser, D. E. (2005). Preparation and Characterization of (3-aminopropyl)triethoxysilane-Modified Mesoporous SBA-15 Silica Molecular Sieves. *Micropor. Mesopor. Mater.*, 83: 150-158.

Luca, G. D., Pullumbi, P., Barbieri, G., Farma, A. D., Bernardo, P. and Drioli, E. (2004). Gusev and Suter Calculation of The Diffusion Coefficients of Light Gases in Silicalite-1 Membrane and Silica-Sodalite Zeolite. *Sep. Purif. Technol*. 36: 215-228.

Ma, Y. H. and Belmonte, R. P. (1974). Experimental Investigation of Multicomponent Rates of Sorption of SO_2 and CO_2 In Natural Mordenite and Clinoptilolite. Presented at the AICHE 76th National Meeting. March 1974. Tulsa, Oklahoma.

Ma, Y. H. and Lee, T. Y. (1978). Sorption and Diffusion Properties of Natural Zeolites. In: Sand, L. B. and Mumpton, F. A. eds. *Natural Zeolites Occurrence, Properties, Use*. New York: Pergamon Press Ltd. 373-383.

Macdonald, J. A. F., and Quinn, D. F. (1995). The Preparation of Active Carbons from Natural Materials for Use in Gas Storage. *Journal of Porous Materials*, 1: 43-54.

Machado, R. S. A., Fonseca, J. M. G., Arakaki, L. N. H., Espinola, J. G. P. and Oliveira, S. F. (2004). Silica Gel Containing Sulfur, Nitrogen and Oxygen as

Adsorbent Centers on Surface for Removing Copper From Aqueous/Ethanolic Solutions. *Talanta*. 63: 317-322.

Malbrunot, P., Vidal, D., and Vermesse, J. (1997). Adsorbent Helium Density Measurement and Its Effect on Adsorption Isotherms at High Pressure. *Langmuir*, 13: 539-544.

Malyshev, M. E., Paukshtis, E. A. and Malysheva, L. V. (2005b). Interaction of N_2 with the Acid Sites of Oxides. *Kinetics Catal*. 46(1): 107-113.

Malyshev, M. E., Paukshtis, E. A., Malysheva, L. V., Toktarev, A. V. and Vostrikova, L. A. (2005a). N_2 and CO as Probe Molecules for Determining the Properties of Acid Sites on the Surface of Zeolites. *Kinetics Catal*. 46(1): 100-106.

Manoilova, O. V., Mentruit, M. P., Palomino, G. T., Tsyganenko, A. A. and Areán, C. O. (2001). Variable-Temperature Infrared Spectroscopy of Carbon Monoxide Adsorbed on the Zeolite K-ZSM-5. *Vib. Spectrosc*. 26: 107-111.

Marecka, A. and Mianowski, A. (1998). Kinetics of CO_2 and CH_4 Sorption on High Rank Coal at Ambient Temperatures. *Fuel*. 77(14): 1691-1696.

Maroto-Valer M.M., Tang Z., and Zhang Y. (2005). Carbon Dioxide Capture by Activated and impregnated Anthracites, Fuel Processing Technology, 86: 1487-1502.

Massman, W. J. (1998). A Review of the Molecular Diffusivities of H_2O, CO_2, CH_4, CO, O_3, SO_2, NH_3, N_2O, NO, and NO_2 in Air, O_2 and N_2 Near STP. *Atmospheric Environ*. 32(6): 1111-1127.

Masteri-Farahani, M., Farzaneh, F. and Ghandi, M. (2003). Molybdenum Incorporated Silicalite As Catalyst for Epoxidation of Olefins. *J. Mol. Catal. A: Chem*. 192: 103-111.

Matranga, K. R., Myres, A. L., and Glandt, E. D. (1991). Storage of Natural Gas by Adsorption on Activated Carbon. *Chemical Engineering Science*, 47: 1569-1579.

Maurin, G., Llewellyn, P.L., Poyet, Th. and Kuchta, B. (2005). Adsorption of Argon and Nitrogen in X-Faujasites: Relationships for Understanding the Interactions with Monovalent and Divalent Cations. *Micropor. Mesopor. Mater*. 79: 53-59.

Mavrakis, D., Thomaidis, F., and Ntroukas, I. (2006). An Assessment of The Natural Gas Supply Potential of The South Energy Corridor from The Caspian Region to The EU. *Energy Policy*, 34: 1671-1680.

McKittrick, M. W. and Jones, C. W. (2003). Toward Single-Site Functional Materials-Preparation of Amine-Functionalized Surfaces Exhibiting Site-Isolated Behavior. *Chem. Mater*, 15: 1132-1139.

Meier, W. M. and Olson, D. H. (1992). *Atlas of Zeolite Structure Types*. 3rd Edition. Stoneham: Butterworth-Heinemann.

Meisen, A. and Shuai, X. S. (1997). Research and Development Issues in CO_2 Capture. *Energy Convers. Mgmt*, 38: 837-842.

Menon, V. C., and Komarneni, S. (1998). Porous Adsorbents for Vehicular Natural Gas Storage: A Review. *Journal of Porous Materials*, 5: 43-58.

Mercer, B. W. and Ames, L. L. (1978). Zeolite Ion-Exchange In Radioactive and Municipal Wastewater Treatment. In: Sand, L. B. and Mumpton, F. A. eds. *Natural Zeolites Occurrence, Properties, Use*. New York: Pergamon Press Ltd. 451-462.

Mercuri, L. P., Matos, J. R., Li, Z., and Jaroniec, M. (2006). Comparative Thermogravimetric and Adsorption Study of Highly Ordered Mesoporous Materials. *Journal of Colloid and Interface Science*, 296: 377-380.

Mirji, S. A., Halligudi, S. B., Mathew, N., Jacob, N. E., Patil, K. R., and Gaikwad, A. B. (2006). Adsorption of Methanol on Mesoporous SBA-15. *Mater. Lett*.

Mizukami, K., Takaba, H., Kobayashi, Y., Oumi, Y., Belosludov, R. V., Takami, S., Kubo, M. and Miyamoto, A. (2001). Molecular Dynamics Calculations of CO_2/N_2 Mixture through the NaY Type Zeolite Membrane. *J. Membr. Sci*. 188: 21-28.

Mortensen, J. J., Hammer, B. and Nørskov, J. K. (1998). A Theoretical Study of Adsorbate-Adsorbate Interactions on Ru (0001). *Surf. Sci*. 414: 315-329.

Mozgawa, W., Jastrzebski, W. and Handke, M. (2005). Vibrational Spectra of D4R and D6R Structural Units. *J. Mol. Struct*. 744-747: 663-670.

Mugge, J., Bosch, H. and Reith, T. (2001). Measuring and Modeling Gas Adsorption Kinetics In Single Porous Particles. *Chem. Eng. Sci*. 56: 5351-5360.

Muller, M., Harvey, G., and Prins, R. (2000). Comparison of the Dealumination of Zeolites Beta, Mordenite, ZSM-5 and Ferrierite by Thermal Treatment, Leaching with Oxalic Acid and Treatment with $SiCl_4$ By H, Si And Al MAS NMR. *Micropor. Mesopor. Mater.* 34: 135 – 147.

Munson, R. A. (1973). *Properties of Natural Zeolites*. United State: National Technology Information Service.

Murcia, A. B., Fletcher, A. J., Martinez, J. G., Amoros, D. C., Solano, A. L., and Thomas, K. M. (2003). Probe Molecule Kinetic Studies of Adsorption on MCM-41. *J. Phys. Chem. B*, 107: 1012-1020.

Myers, A. L. (2002). Thermodynamics of Adsorption In Porous Materials. *AIChE J*. 48: 145-160.

Náray-Szabó, I. (1969). *Inorganic Crystal Chemistry*. Hungary: Akadémiai Kiadó, Budapest.

Nery, J. G., Mascarenhas, Y. P., and Cheetham, A., K. (2003). A study of the Highly Crystalline, Low-Silica, Fully Hydrated Zeolite P Ion Exchanged with (Mn^{2+}, Cd^{2+}, Pb^{2+}, Sr^{2+}, Ba^{2+}) Cations. *Micropor. Mesopor. Mater.* 57: 229 – 248.

Newalkar, B. L., Choudary, N. V., Kumar, P., Komarneni, S., and Bhat, T. S. G. (2002). Exploring the Potential of Mesophorous Silica, SBA-15, as an Adsorbent for Light Hydrocarbon Separation. *Chem. Mater*. 14: 304-309.

Neyestanaki, A. K., Kumar, N. and Lindfors, L. E. (1995). Catalytic Combustion of Propane and Natural Gas Over Cu and Pd Modified ZSM Zeolite Catalysts. *Appl. Catal. B: Environ*. 7: 95-111.

Nishimaya, N., Kishi, T., Mizushima, T., Matsumoto, A. and Tsutsumi, K. (2001). Hyperstoichiometric Hydrogen Occlusion by Palladium Nanoparticles Included in NaY Zeolite. *J. Alloys Compd*. 319: 312-321.

Niwa, M., Habuta, Y., Okumura, K. and Katada, N. (2003). Solid Acidity of Metal Oxide Monolayer and Its Role In Catalytic Reactions. *Catal. Today*. 87: 213-218.

Njikamp, M. G., Raaymakers, J. E. M. J., Dillen, A. J. V. and Jong, K. P. (2001). Hydrogen Storage Using Physisorption – Materials Demands. *Appl. Phys. A*. 72: 619-623.

Nyquist, R. A. and Kagel, R. O. (1971). *Infrared Spectra of Inorganic Compounds: 3800-45 cm^{-1}*. New York: Academic Press.

Ogura, M, Shinomiya, S., Tateno, J., Nara, Y., Nomura, M., Kikuchi, E., and Matsukata, M. (2001). Alkali-Treatment Technique – New Method for Modification of Structural and Acid-catalytic Properties of ZSM-5 Zeolites. *Appl. Catal. A: General.* 219: 33 – 43.

Oka, N., Izumi, J. and Suzuki, M. (2000). Mechanism of Oxygen Adsorption on Partially K Exchanged Na-A Type Zeolite. *Adsorption*. 6: 149-158.

Okumura, K., Nota, K., Yoshida, K. and Niwa, M. (2005). Catalytic Performance and Elution of Pd In The Heck Reaction Over Zeolite-Supported Pd Cluster Catalyst. *J. Catal*. 231: 245-253.

Oliveira, L. C. A., Petkowicz, D. I., Smaniotto, A., and Pergher, S. B. C. (2004). Magnetic Zeolites: A New Adsorbent for Removal of Metallic Contaminants from Water. *Water Research*. 38: 3699-3704.

Otsuka, K., Kaburagi, T., Yamada, C. and Takenaka, S. (2003). Chemical Storage of Hydrogen By Modified Iron Oxides. *J. Power Sources*. 122(2): 111-121.

Özkan, G. and Özçelik, E. (2005). CO_2 Adsorption on Porous NiO as A Cathode Material for Molten Carbonate Fuel Cells. *J. Power Sources*. 140: 28-33.

Padin, J. and Yang, R. T. (1999). New Sorbents for Olefin/Paraffin Separations By Adsorption Via Π-Complexation: Synthesis and Effects of Substrates. *Chem. Eng. Sci*. 55: 2607-1616.

Pakseresht, S., Kazemeini, M. and Akbarnejad, M. M. (2002). Equilibrium Isotherms for CO, CO_2, CH_4 and C_2H_4 on the 5A Molecular Sieve by A Simple Volumetric Apparatus. *Sep. Purif. Technol*. 28: 53-60.

Philippe, L., Sammon, C., Lyon, S. B., and Yarwood, J. (2004a). An FTIR/ATR in Situ Study of Sorption and Transport in Corrosion Protective Organic Coatings 1. Water Sorption and Role of Inhibitor Anions. *Progress in Organic Coatings*, 49: 302-314.

Philippe, L., Sammon, C., Lyon, S. B., and Yarwood, J. (2004b). An FTIR/ATR in Situ Study of Sorption and Transport in Corrosion Protective Organic Coatings 2. The Effects of Temperature and Isotop Dilution. *Progress in Organic Coatings*, 49: 315-323.

Pohle, R., Fleischer, M. and Meixner, H. (2001). Infrared Emission Spectroscopic Study of the Adsorption of Oxygen on Gas Sensors Based on Polycrystalline Metal Oxide Films. *Sens. Actuators B*. 78: 133-137.

Pohorecki R. and Mozenski C. (1998). A New Adsorbent for Carbon Dioxide and Hydrogen Sulphide Adsorption Process, Chemical Engineering and Processing, 37: 69 – 78.

Polychronopoulou, K., Fierro, J. L. and Efstathiou, A. M. (2005). Novel Zn-Ti Based Metal Oxides for Low-Temperature Adsorption of H2S from Industrial Gas Streams. *Appl. Catal. B: Environ*. 57: 125-137.

Ponce, M. A., Castro, M. S. and Aldao, C. M. (2004). Influence of Oxygen Adsorption and Diffusion On the Overlapping of Intergranular Potential Barriers In SnO_2 Thick Films. *Mater. Sci. Eng. B*. 111: 14-19.

Pröckl., S. S., Kleist, W. and Köhler, K. (2005). Design of Highly Active Heterogeneous Palladium Catalysts for The Activation of Aryl Chlorides In Heck Reactions. *Tetrahedron*. 61: 9855-9859.

Pupier, O., Goetz, V., and Fiscal, R. (2005). Effect of Cycling Operations on an Adsorbed Natural Gas Storage. *Chemical Engineering and Processing*, 44: 71-79.

Qian, L. and Yan, Z. F. (2001). Micropore Modification of Zeolites With Transition-Metal Oxides. *Colloids Surf. A: Physicochemical and Engineering Aspects.* 180: 311-316.

Quinn, D. F., and Macdonald, J. A. (1992). Natural Gas Storage. *Carbon*, 30(7): 1097-1103.

Quinn, D. F., and Ragan, S. (2000). Carbons Suitable for Medium Pressure (6.9 MPa) Methane Storage. *Adsorption Science and Technologies*, 18: 515-527.

Raaen, S. and Ramstad, A. (2005). Monte-Carlo Simulations of Thermal Desorption of Adsorbed Molecules from Metal Surfaces. *Energy*. 30: 821-830.

Radovic, M. and Lara-Curzio, E. (2004). Mechanical Properties of Tape Cast Nickel-Based Anode Materials for Solid Oxide Fuel Cells Before and After Reduction In Hydrogen. *Acta Materialia*. 52: 5747-5756.

Radwan, N. R. E., Mokhtar, M. and El-Shobaky, G. A. (2003). Surface and Catalytic Properties of CuO and Co_3O_4 Solids as Influenced by Treatment with Co^{2+} and Cu^{2+} Species. *Appl. Catal. A: Gen*. 241: 77-90.

Rakić, V. M., Hercigonja, R. V. and Dondur, V. T. (1999). CO Interaction with Zeolites Studied by TPD and FTIR: Transition-Metal Ion-Exchanged FAU-Type Zeolites. *Micropor. Mesopor. Mater*. 27: 27-39.

Rantala, T. S., Golovanov, V. and Lantto, V. (1995). A Cluster Approach for the Adsorption of Oxygen and Carbon Monoxide on SnO_2 and CdS Surfaces. *Sens. Actuators B*. 24-25: 532-536.

Rao, S. N. R., Waddell, E., Mitchell, M. B. and White, M. G. (1996). Selective Sulfur Dioxide Adsorbents Prepared from Designed Dispersions of Groups IA and IIA Metal Oxides on Alumina. *J. Catal*. 163: 176-185.

Rege, S. R., Yang, R. T. and Buzanowski, M. A. (2000). Sorbents for Air Prepurication in Air Separation. *Chem*. *Eng*. *Sci*. 55: 4827-4838.

Rege, S. U. and Yang, R. T. (1997). Limits of Air Separation by Adsorption with LiX Zeolite. *Industrial and Engineering Chemical Research*. 36: 5358-5365.

Rege, S. U. and Yang, R. T. (2001). A Novel FTIR Method for Studying Mixed Gas Adsorption at Low Concentrations: H_2O and CO_2 on NaX Zeolite and γ-Alumina. *Chem*. *Eng*. *Sci*. 56: 3781-3796.

Remillard J. T. (1999). Materials Advances for Chemical Sensing Applications. Fiber-Optic Exhaust-Gas Sensor Based On the Fluorescence Characteristics of Cu Containing Zeolites. *Appl*. *Opt*. 38: 5306.

Ribeiro, F. R., Alvarez, F., Henriques, C., Lemos, F., Lopes, J. M. and Ribeiro, M. F. (1995). Structure-Activity Relationship In Zeolites. *J*. *Mol*. *Catal*. *A: Chem*. 96: 245-270.

Rodriguez, A. (1995). Vibrational Spectroscopy and Structural Analysis of Na-Y Zeolite. *Vib*. *Spectrosc*. 9: 225-258.

Romanovsky, B. V. (2001). Zeolite-Based Nanocomposites: Synthesis, Characterization and Catalytic Applications. In: Galarneau, A., Di-Renzo, F., Fajula, F. and Vedrine, J. eds. *Zeolites and Mesoporous Materials at the Dawn of the 21st Century*. *Stud*. *Surf*. *Sci*. *Catal*. Amsterdam: Elsevier. 135: 103-112.

Roque-Malherbe, R. (2000). Complementary Approach to the Volume Filling Theory of Adsorption in Zeolites. *Micropor*. *Mesopor*. *Mater*. 41: 227-240.

Rutherford, S. W. and Coons, J. E. (2005). Adsorption Equilibrium and Transport Kinetics for A Range of Probe Gases in Takeda 3A Carbon Molecular Sieve. *J*. *Colloid Interf*. *Sci*. 284: 432-439.

Rutherford, S. W. and Do, D. D. (2000). Adsorption Dynamics of Carbon Dioxide on A Carbon Molecular Sieve 5A. *Carbon*. 38: 1339-1350.

Ruthven, D. M. (1984). *Principles of Adsorption and Adsorption Processes*. New York: John Wiley and Sons.

Ruthven, D. M. (2001). Short Communication: Diffusion of Simple Molecules in 4A Zeolite. *Adsorption*. 7: 301-304.

Ruthven, D. M. (2004). Sorption Kinetics for Diffusion-Controlled Systems with A Strongly Concentration-Dependent Diffusivity. *Chem*. *Eng*. *Sci*. 59: 4531-4545.

Ruthven, D. M. and Derrah, R. I. (1978). Sorption and Diffusion In Natural Erionite. In: Sand, L. B. and Mumpton, F. A. eds. *Natural Zeolites Occurrence, Properties, Use*. New York: Pergamon Press Ltd. 403-409.

Salama, T. M., Mohamed, M. M., Othman, I. and El-Shobaky, G. A. (2005). Structural and Textural Characteristics of Ce-Containing Mordenite and ZSM-5 Solids and FTIR Spectroscopic Investigation of the Reactivity of NO Gas Adsorbed on Them. *Appl. Catal. A: Gen*. 286: 85-95.

Salem, M. M. K., Braeur, P., Szombathely, M. v., Heuchel, M., Harting, P., Quitzsch, K., and Jaroneic, M. (1998). Thermodynamics of High Pressure Adsorption of Argon, Nitrogen and Methane on Microporous Adsorbents. *Langmuir*, 14: 3376-3389.

Sand, L. B. and Mumpton, F. A. (1978). *Natural Zeolites Occurrence, Properties, Use*. New York: Pergamon Press Ltd.

Sangwichien, C., Aranovich, G. L. and Donohue, M. D. (2002). Density Functional Theory Predictions of Adsorption Isotherms with Hysteresis Loops. *Colloids Surf. A: Physicochem. Eng. Aspects*. 206: 313-320.

Sárkány, J. (1997). FTIR Study on the Interaction of O_2 and CO with Cu^+ ions in Zeolite ZSM-5 Formation and Reactivity of Superoxide. *J. Mol. Struct*. 410-411: 95-98.

Sasse, A. and Förster, H. (1995). Adsorption of Homonuclear Diatomics In Zeolites at Low Temperature Studied by FTIR Spectroscopy. *J. Mol. Struct.* 349: 97-100.

Sato, K., Nishimura, Y., Matsubayashi, N., Imamura, M., and Shimada, H. (2003). Structural Changes of Zeolite Y During Ion Exchange Treatment; Effect of Si/Al Ratio of the Starting NaY. *Micropor. Mesopor. Mater.* 59: 133 – 146.

Savitz, S., Myers, A. L. and Gorte, R. J. (2000). A Calorimetric Investigation of CO, N_2 and O_2 In Alkali-Exchanged MFI. *Micropor. Mesopor. Mater*. 37: 33-40.

Scarano, D., Bertarione, S., Spoto, G., Zecchina, A. and Areán, C. O. (2001). FTIR Spectroscopy of Hydrogen, Carbon Monoxide, and Methane Adsorbed and Co-Adsorbed on Zinc Oxide. *Thin Solid Films*. 400: 50-55.

Schüth, F. and Schmidt, W. (2002). Microporous and Mesoporous Materials. *Adv. Eng. Mater*. 4(5): 269-279.

Schüth, F., Wingen, A. and Sauer, J. (2001). Oxide Loaded Ordered Mesoporous Oxides for Catalytic Applications. *Micropor. Mesopor. Mater*. 44-45: 465-476.

Seidel, U., Koch, M., Brunner, E., Staudte, B.and Pfeifer, H. (2000). NMR and IR Studies on The Adsorption of Methane and Trimethylgallium on Zeolite HY. *Micropor*. *Mesopor*. *Mater*. 35-36: 341-347.

Shaheen, W. M. and Ali, A. A. (2001). Thermal Solid-Solid Interaction and Physicochemical Properties of CuO-Fe_2O_3 System. *J. Inorg*. *Mater*. 3: 1073-1081.

Shen, D. M. and Bülow, M. (1998). Isosteric Study of Sorption Thermodynamics of Single Gases and Multi-Component Mixtures on Microporous Materials. *Micropor*. *Mesopor*. *Mater*. 22: 237-249.

Shen, D. M., Bülow, M., Siperstein, F., Engelhard, M. and Myers, A. L. (2000). Comparison of Experimental Techniques for Measuring Isosteric Heat of Adsorption. *Adsorption*. 6: 275-286.

Sherman, J. D. (1999). Synthetic Zeolites and Other Microporous Oxide Molecular Sieves. *Proc. Natl. Acad. Sci.*, 96: 3471-3478.

Siantar, D. P., Millman, W., and Fripiat, J. F. (1995). Structural Defect and Cation Exchange Capacity in Dealuminated Y Zeolites. *Zeolites*. 15: 556 – 560.

Sierraalta, A., Anez, R. and Brussin, M. (2002). Theoretical Study of NO2 Adsorption on A Transition-Metal Zeolite Model. *J. Catal*. 205: 107-114.

Sing, K. (2001). The Use of Nitrogen Adsorption For The Characterization of Porous Materials. *Colloid and Surface A: Physicochem. Eng. Aspects*, 187-188: 3-9.

Sing, K. S. W. (1989). Characteristic of Adsorbents. In: Rodrigues, A. E., Levan, M. D. and Tondeur, D. eds. *Adsorption: Science and Technology*. Dordrecht: Kluwer Academic. 3 -14.

Sing, K. S. W. (1998). Adsorption Methods for the Characterization of Porous Materials. *Adv*. *Colloid Interf*. *Sci*. 76-77: 3-11.

Sing, K. S. W. (2004). Characterization of Porous Materials: Past, Present and Future. *Colloid Surf. A: Physicochem. Eng. Aspects*, 241: 3-7.

Siriwardane R.V., Shen M.S., Fisher E.P., and Poston J.A. (2001). Adsorption of Carbon Dioxide on Molecular Sieves and Activated Carbon, Energy & Fuel, 15: 279-284.

Šlijivančanin, Ž. and Pasquarello, A. (2004). Nitrogen Adsorption on A Supported Iron Nanocluster. *Vacuum*. 74: 173-177.

Song C. (2006). Global Challenges and Strategies for Control, Conversion and utilization of Carbon Dioxide for Sustainable Development Involving Energy, Catalysis, Adsorption and Chemical Processing, *Catal. Today*, 115: 2-32.

Sonwane, C. G. and Bhatia, S. K. (1998). Adsorption in Mesopores: A Molecular-Continuum Model with Application to MCM-41. *Chem*. *Eng*. *Sci*. 53(17): 3143-3156.

Sosin, K. A., and Quinn, D. F. (1995). Using the High Pressure Methane Isotherm for Determination of Pore Size Distribution of Carbon Adsorbents. *J Porous Mater.*, 1: 111-119.

Sosin, K. A., Quinn, D. F., and Macdonald, J. A. F. (1996). Changes in PSD of Progressively Activated Carbons Obtained from Their Supercritical Methane Isotherm. *Carbon*, 34: 1335-1341.

Sousa-Aguiar, E. F., Camorim, V. L. D., Zotin, F. Z. and Santos, R. L. C. (1998). A Fourier Transform Infrared Spectroscopy Study of La-, Nd-, Sm-, Gd- and Dy-Containing Y Zeolites. *Micropor*. *Mesopor*. *Mater*. 25: 25-34.

Srdić, V. V., Omorjan, R. P. and Seydel, J. (2005). Electrochemical Performances of (La, Sr)CoO_3 Cathode For Zirconia-Based Solid Oxide Fuel Cells. *Mater*. *Sci*. *Eng*. *B*. 116(2): 119-124.

Srivastava, R., Srinivas, D., and Ratnasamy, P. (2006). Sites for CO2 Activation Over Amine-Functionalized Mesoporous Ti(Al)-SBA-15 Catalysts. *Microporous and Mesoporous Materials*, 90: 314-326.

Steel, K. M. and Koros, W. J. (2003). Investigation of Porosity of Carbon Materials and Related Effects on Gas Separation Properties. *Carbon*. 41: 253-266.

Stelzer, J., Paulus, M., Hunger, M. and Weitkamp, J. (1998). Hydrophobic Properties of All-Silica Zeolite Beta. *Micropor*. *Mesopor*. *Mater*. 22: 1-8.

Stuart, B. (2004). *Infrared Spectroscopy: Fundamentals and Application*. England: John Wiley and Sons, Ltd.

Stucky, G. D., Zhao, D. Y., Feng, J. L., Huo, Q. S., Melosh, N., Fredrickson, G. H., and Chmelka, B. F. (1998). Triblock Copolymer Syntheses of Mesoporous Silica with Periodic 50 to 300 Angstrom Pores. *Science*, 279: 548-552.

Sultana, A., Habermacher, D. D., Kirschhock, C. E. A. and Martens, J. A. (2004). Adsorptive Separation of NO_x In Presence of SO_x from Gas Mixture Simulating Lean Burn Engine Exhaust by Pressure Swing Process on Na-Y Zeolite. *Appl*. *Catal*. *B: Environ*. 48: 65-76.

Sun Y., Liu X.W., Su W., Zhou Y., and Zhou L. (2007). Studies on Ordered Mesopoorus Materials for Potential Environmental and Clean Energy Applications, Applied Surface Science, 253: 5650-5655.

Sun, J., Brady, A., Rood, M. J., and Lehmann, C. M. (1997). Adsorbed Natural Gas Storage with Activated Carbons Made from Illinois Coals and Scrap Tires. *Energy and Fuels*, 11: 316-322.

Suzuki, M. (1990). *Adsorption Engineering*. New York: Elsevier Science Publishing.

Suzuki, T., Kobori, R. and Kaneko, K. (2000). Grand Canonical Monte Carlo Simulation-Assisted Pore-Width Determination of Molecular Sieve Carbons by Use of Ambient Temperature N_2 Adsorption. *Carbon*. 38: 623-641.

Szabo, N. F. (2003). *Development of Harsh Environmental Nitrogen Oxide Solid-State Gas Sensors*. Stuttgart: Ohio State University.

Szanyi, J. and Paffett, M. T. (1996). The Adsorption of NO and Reaction of NO with O_2 on H-, NaH-, CuH-, and Cu-ZSM-5: An In Situ FTIR Investigation. *J. Catal*. 164: 232-245.

Szostak, R. (1992). *Handbook of Molecular Sieves*. New York: Van Nostrand Reinhold.

Takagi, H., Hatori, H., Yamada, Y., Matsuo, S. And Shiraishi, M. (2004). Hydrogen Adsorption Properties of Activated Carbon with Modified Surfaces. *Journal of Alloys and Compounds*, 385: 257-263.

Takamura, Y., Narita, S., Aoki, J., Hironaka, S. and Uchida, S. (2001). Evaluation of Dual-Bed Pressure Swing Adsorption for CO_2 Recovery from Boiler Exhaust Gas. *Sep. Purif. Technol*. 24: 519-528.

Tallon, C., Moreno, R., and Nieto, M. I. (2006b). Synthesis of γ-Al_2O_3 Nanopowders by Freeze-drying. *Materials Research Bulletin*, 41: 1520-1529.

Tallon, C., Yates, M., Moreno, R., and Nieto, M. I. (2006a). Porosity of Freeze-dried γ-Al_2O_3 Powders. *Ceramics International*. In press.

Tallon, J. (2000). *Industry Warms to Superconductors*. Physics World March 2000.

Tan, O. K., Cao, W., Hu, Y. and Zhu, W. (2004). Nanostructured Oxides by High-Energy Ball Milling Technique: Application as Gas Sensing Materials. *Solid State Ionics*. 172(1-4): 309-316.

Terry Anak George Paou (2002). Storage Capacity and Delivery Performance of Commercial Adsorbents for Adsorbed Methane Storage. Universiti Teknologi Malaysia: Master Thesis.

Thommes, M., Köhn, R., and Fröba, M. (2002). Sorption and Pore Condensation Behavior of Pure Fluids in Mesoporous MCM-48 Silica, MCM-41 Silica, SBA-

15 Silica and Controlled-Pore Glass at Temperatures Above and Below The Bulk Triple Point. *Appl. Surf. Sci.*, 196: 239-249.

Thoret, J., Man, P. P. and Fraissard, J. (1997). Solid-Solid Interaction and Reaction Between Antimony Oxide, Sb_2O_3, and NaY or LaNaY Zeolites. Comparison with V_2O_5 and MoO_3. *Zeolite*. 18(2-3): 152-161.

Tomchenko, A. A., Harmer, G. P. and Marquis, B. T. (2005). Detection of Chemical Warfare Agents Using Nanostructured Metal Oxide Sensors. *Sens*. *Actuators B*. 108: 41-55.

Tongpool, R. and Yoriya, S. (2005). Kinetics of Nitrogen Dioxide Exposure In Lead Phthalocyanine Sensors. *Thin Solid Films*. 477: 148-152.

Torre-Abreu, C., Ribeiro, M. F., Henriques, C. and Delahay, G. (1997). Characterization of CuMFI Catalysts by Temperature Programmed Desorption of NO and Temperature Programmed Reduction. Effect of The Zeolite Si/Al Ratio and Copper Loading. *Appl*. *Catal*. *B*: *Environ*. 12: 249-262.

Tóth, J. (2000). An Opportunity to Develop Software for Gas/Solid Adsorption Measurements. *J. Colloid Interf*. *Sci*. 225: 191-195.

Tóth, J. (2004). On Thermodynamics Inconsistency of Isotherm Equations: Gibbs's Thermodynamics. *J. Colloid Interf*. *Sci*. 262: 25-31.

Triantafillidis, C. S., Vlessidis, A.G., and Evmiridis, N. P. (2000). Dealuminated H-Y Zeolites: Influence of The Degree and The Type Of Dealumination Method on The Structural and Acidic Charcteristics of H-Y Zeolites. *Ind. Eng. Chem. Res.* 39: 307 – 319.

Triebe, R. W. and Tezel, F. H. (1995). Adsorption of Nitrogen, Carbon Monoxide, Carbon Dioxide and Nitric Oxide on Molecular Sieves. *Gas Sep*. *Purif*. 9(4): 223-230.

Triebe, R. W., Tezel, F. H., and Khulbe, K. C. (1996). Adsorption of Methane, Ethane and Ethylene on Molecular Sieve Zeolites. *Gas Sep. Purif*. 10: 81-84.

Trigueiro, F. E., Monteiro, D. F. J., Zotin, F. M. Z., and Sousa-Aguiar, E. F. (2002). Thermal Stability of Y Zeolites Containing Different Rare Earth Cations. *J. Alloys and Compounds*. 344: 337 – 341.

Tseng, H. H. and Wey, M. Y. (2004). Study of SO_2 Adsorption and Thermal Regeneration over Activated Carbon-Supported Copper Oxide Catalysts. *Carbon*. 42: 2269-2278.

Tuel, A. (1999). Modification of Mesoporous Silicas by Incorporation of Heteroelements In the Framework. *Micropor. Mesopor. Mater.* 27 :151–169.

Turky, A. E. M. M., Radwan N. R. E. and El-Shobaky, G. A. (2001). Surface and Catalytic Properties of CuO Doped with MgO and Ag_2O. *Colloid Surf. A: Physicochemical and Engineering Aspects*. 181: 57-68.

Ustinov, E. A., Do, D. D. and Jaroniec, M. (2005). Application of Density Functional Theory to Equilibrium Adsorption of Argon and Nitrogen on Amorphous Silica Surface. *Appl. Surf. Sci*. 252: 548-561.

Ustinov, E. A., Do, D. D., and Jaroniec, M. (2005). Adsorption of Argon and Nitrogen in Cylindrical Pores of MCM-41 Materials: Application of Density Functional Theory. *Applied Surface Science*.

Ustinov, E. A., Do, D. D., Herbst, A., Staudt, R. and Harting, P. (2002). Modeling of Gas Adsorption Equilibrium Over A Wide Range of Pressure: A Thermodynamic Approach Based on Equation of State. *J. Colloid Interf. Sci*. 250: 49-62.

Valente Nabais J.M., Carrott P.J.M., Ribeiro Carrott M.M.L., Padre-Eterno A.M., Menendez J.A., Dominguez A., and Ortiz A.L. (2006). New Acrylic Monolithic Carbon Molecular Sieves for Carbon Dioxide/Nitrogen and Carbon Dioxide/Methane Separations, Carbon 44: 1158-1165.

Valtchev, V. and Mintova, S. (1995). The Effect of the Metal Substrate Composition on the Crystallization of Zeolite Coatings. *Zeolites*. 15: 171-175.

Valyon, J., Lónyi, F., Onyestyák, G. and Papp, J. (2003). DRIFT and FR Spectroscopic Investigation of N_2 and O_2 Adsorption on Zeolites. *Micropor. Mesopor. Mater*. 61: 147-158.

Valyon, J., Onyestyák, G. and Rees, L. V. C. (2004). Adsorption and Diffusion of Nitrogen and Oxygen In Natural Mordenites. *Proceedings of the 14th International Zeolite Conference*. April 25-30. Cape Town, South Africa: Document Transformation Technologies. 2078-2085.

van Bekkum, H., Flanigen, E. M., and Jansen, J. C. (Eds.). (1991). Introduction to Zeolite Science and Practice: *Studies in Surface Science and Catalysis*, Vol 58. Amsterdam: Elsevier.

van Mao, L. R., Le S. T., Ohayon, D., Caillibot, F., Gelebert, L., and Denes, G. (1997). Modification of the Micropore Characteristics of the Desilicated ZSM-5 Zeolite by Thermal Treatment. *Zeolites* 19: 270 –278.

Vansant, E. F. (1987). Pore Size Engineering in Zeolites. In: Grobet P. J., Mortier W. J., Vansat E. F, and Schulz-Ekloff G. (Eds.). *Innovation in Zeolite Material Science*. Nieuwpoort. Belgium: Elsevier.

Vartuli, J. C., Malek, A., Roth, W. J., Kresge, C. T., and McCullen, S. B. (2001). The Sorption Properties of As-Synthesized and Calcined MCM-41 and MCM-48. *Microporous and Mesoporous Materials*, 44-45: 691-695.

Vasiliev, L. L., Kanonchik, L. E., Mishkinis, D. A., and Rabetsky, M. I. (2000). Adsorbed Natural Gas Storage and Transportation Vessels. *Int. J. Therm. Sci.*, 39: 1047-1055.

Vaughan, D. E. W. (1978). Properties of Natural Zeolites. In: Sand, L. B. and Mumpton, F. A. eds. *Natural Zeolites Occurrence, Properties, Use*. New York: Pergamon Press Ltd. 356-371.

Vayssilov, G. N., Hu, A., Birkenheuer, U. and Rosch, N. (2000). Dinitrogen As Probe Molecule of Alkali-Exchanged Zeolites A Density Functional Study. *J. Mol. Catal. A: Chem*. 162: 135-145.

Wakabayashi, F., Kondo, J. N., Domen, K. and Hirose, C. (1997). FT-IR Study of the Interaction of Oxygen, Argon, Helium, Nitrogen and Xenon with Hydroxyl Groups in H-Y zeolite at Low Temperatures. *Micropor. Mater*. 8: 29-37.

Wang, Y. D., Chen, Q. L., Yang, W. M., Xie, Z. K., Xu, W. and Huang, D. Y. (2003). Effect of Support Nature on WO_3/SiO_2 Structure and Butene-1 Metathesis. *Appl. Catal. A: Gen*. 250: 25-37.

Wang, Z. M., Wang, Z. X., Yamashita, N., Hoshinoo, K., and Kanoh, H. (2004). Changes in Microporosity and CH_4 Adsorptivity of Preoxidized Ptch-Based Activated Carbon Fibres by Mg Deposition. *J. Colloid Interf. Sci*. 276: 151-158.

Warmuziński, K. and Sodzawiczny, W. (1999). Effect of Adsorption Pressure on Methane Purity During PSA Separations of CH_4/N_2 Mixtures. *Chem. Eng. Proc*. 38: 55-60.

Watanabe, M., Osada, M., Inomata, H., Arai, K. and Kruse, A. (2003). Acidity and Basicity of Metal Oxide Catalysts for Formaldehyde Reaction In Supercritical Water at 673 K. *Appl. Catal. A: Gen*. 245: 333-341.

Webb, S. W. and Pruess, K. (2003). The Use of Fick's Law for Modeling Trace Gas Diffusion in Porous Media. Transport in Porous Media. 51: 327-341.

Webster, C. E., and Drago, R. S. (1999). The Multiple Equilibrium Analysis Quantitative Prediction of Single and Multi Component Adsorption Isotherms on Carbonaceus and Zeolite Solids. *Micropor. Mesopor. Mater.*, 33: 291-306.

Weh, K., Noack, M., Sieber, I. and Caro, J. (2002). Permeation of Single Gases and Gas Mixtures Through Faujasite-Type Molecular Sieve Membranes. *Micropor. Mesopor. Mater.* 54: 27-36.

Weikamp, J. (1996). *Zeolite as Media for Hydrogen Storage.* Stuttgart: Institute for Thermodynamic and Warmetechnic, University Stuttgart.

Weitkamp, J. (2000). Zeolites and Catalysis. *Solid State Ionics*, 131: 175-188.

Winter, M. (2004). *Chemistry: Webelements Periodic Table*. United Kingdom: The University of Sheffield and Web elements Ltd.

Wöllenstein, J., Burgmair, M., Plescher, G., Sulima, T., Hildenbrand, J., Böttner, H. and Eisel, I. (2003). Cobalt Oxide Based Gas Sensors on Silicon Substrate for Operation at Low Temperatures. *Sens. Actuators B*. 93: 442-448.

Wu, R., Hu, C., Yeh, C. and Su, P. (2003). Nanogold on Powdered Cobalt Oxide for Carbon Monoxide Sensor. *Sens. Actuators B*. 96(3): 596-601.

Xiao, F. S., Zheng, S., Sun, J. M., Yu, R. B., Qiu, S. L. and Xu, R. R. (1998). Dispersion of Inorganic Salts into Zeolites and Their Pore Modification. *J. Catal*. 176: 474-487.

Xie, Y. C. and Tang, Y. Q. (1990). Spontaneous Monolayer Dispersion of Oxides and Salts onto Surfaces of Supports: Application to Heterogeneous Catalysis. *Adv. Catal*. 37: 1-43.

Xie, Y., Bu, N., Liu, J., Yang, G., Qiu, J., Yang, N. and Tang, Y. (1990). *Adsorbents for Used In The Separation of Carbon Monoxide and/or Unsaturated Hydrocarbons From Mixed Gases*. (U.S. Patent 4917711).

Xu, B., Dong, L., Fan, Y. N. and Chen, Y. (2000), A Study on the Dispersion of NiO and/or WO_3 on Anatase. *J. Catal*. 1936: 88-95.

Xu, X. W., Wang, J. and Long, Y. C. (2005). Nano-Tin Dioxide/NaY Zeolite Composite Material: Preparation, Morphology, Adsorption and Hydrogen Sensitivity. *Micropor. Mesopor. Mater*. 83: 60-66.

Xu, X., Song, C., Andresen, J. M., Miller, B. G., and Scaroni, A. W. (2002). Novel Polyethylenimine-Modified Mesoporous Molecular Sieve of MCM-41 Type as High-Capacity Adsorbent for CO_2 Capture. *Energy & Fuels*, 16: 1463-1469.

Xu, X., Song, C., Andrésen, J. M., Miller, B. G., and Scaroni, A. W. (2003). Preparation and Characterization of Novel CO_2 "Molecular Basket" Adsorbents Based on Polymer-Modified Mesoporous Molecular Sieve MCM-41. *Microporous and Mesoporous Materials*, 62: 29-45.

Xu, X., Song, C., Miller, B. G., and Scaroni, A. W. (2005). Adsorption Separation of Carbon Dioxide From Flue Gas of Natural Gas-Fired Boiler by A Novel Nanoporous "Molecular Basket" Adsorbent. *Fuel Processing Technology*, 86: 1457-1472.

Yamazaki, T., Nishimura, H. and Ozawa, S. (2000). Adsorption Behavior of Some Gas Molecules in Ω-Zeolite Pores. *Micropor. Mesopor. Mater.* 38: 187-196.

Yang Q. and Lin Y.S. (2006). Kinetics of Carbon Dioxide Sorption on Perovskite-Type Metal Oxides, *Ind. Eng. Chem. Res.*, 45: 6302-6310.

Yang, R. T. (1997). *Gas Separation by Adsorption Process*. London: Imperial College Press.

Yang, X. D., Zheng, Q. R., Gu, A. Z., and Lu, X. S. (2005). Experimental Studies of the Performance of Adsorbed Natural Gas Storage System during Discharge. *Applied Thermal Engineering*, 25: 591-601.

Yermakov, A.Y., Feduschak, T.A., Uimin, M.A., Mysik, A.A., Gaviko, V.S., Chupakhin, O.N., Shishmakov, A.B., Kharchuk, V.G., Petrov, L.A., Kotov, Y.A., Vosmerikov, A.V. and Korolyov, A.V. (2004). Reactivity of Nanocrystalline Copper Oxide and Its Modification under Magnetic Field. *Solid State Ionics*. 172: 317-323.

Yin, D. H. and Yin, D. L. (1998). The Dispersion and Solid-State Ion Exchange of $ZnCl_2$ onto the Surface of NaY Zeolite Using Microwave Irradiation. *Micropor. Mesopor. Mater.* 24: 123-126.

Yong Z., Mata V., and Rodrigues A.E. (2002). Adsorption of carbon dioxide at high Temperature – A Review, Sep. Purif. Technol., 26: 195-205.

Yong, S. K. and Wha, S. A. (1999). Synthesis and Characterization of Zeolite L. *Bull. Korean Chem. Soc.* 20 (2): 1-6.

Yong, Z., Mata, V. and Rodrigues, A. E. (2002). Adsorption of Carbon Dioxide at High Temperature – A Review. *Sep. Purif. Technol.* 26: 195-205.

Yoshida, H., Murata, C. and Hattori, T. (2000). Screening Study of Silica-Supported Catalysts for Photoexpoxidation of Propene by Molecular Oxygen. *J. Catal.* 194: 364-372.

Yoshida, S., Hirano, S., Harada, A. and Nakano, M. (2001). Nitrogen Adsorption Properties of Cubic and Orthorhombic Li-exchanged Low Silica X. *Micropor. Mesopor. Mater.* 46: 203-209.

Yu, H., Fung, K., Guo, T. and Chang, W. (2004). Syntheses of Perovskite Oxides Nanoparticles $La_{1-x}Sr_xMO_{3-\delta}$ (M = Co and Cu) as Anode Electrocatalyst for Direct Methanol Fuel Cell. *Electrochim. Acta.* 50(2-3): 811-816.

Yu, X. F., Wu, N. Z., Xie, Y. C., Tang, Y. Q. (2001). The Monolayer Dispersion of V_2O_5 and Its Influence on the Anatase-Rutile Transformation. *J. Mater. Sci. Lett.* 20: 319-321.

Yun, Z. Y., Xu, Y., Xu, J. H., Wu, Z. Y., Wei, Y. L., Zhou, Z. P. and Zhu, J. H. (2004). In Situ FTIR Investigation on the Adsorption of Nitrosamines In Zeolites. *Micropor. Mesopor. Mater.* 72: 127-135.

Zhang, C., Liu, Q., Xu, Z. and Wan, K. S. (2003). Synthesis and Characterization of Composite Molecular Sieves with Mesoporous and Microporous Structure from ZSM-5 Zeolites by Heat Treatment. *Micropor. Mesopor. Mater.* 62: 157-163.

Zhang, C., Lu, X. S., and Gu, A. Z. (2004). How to Accurately Determine the uptake of Hydrogen in Carbonaceous Materials. *International Journal of Hydrogen Energy*, 29: 1271-1276.

Zhang, S., Talu, O., and Hathurst, D. T. (1990). High Pressure Adsorption of Methane in NaX, MgX, CaX, SrX and BaX. Department of Chemical Engineering, *Cleveland State University*, *Cleveland*. 95: A22-A26.

Zhang, X., Schubert, S., and Agar, D. W. (2005). Studies on The Kinetics of Carbon Dioxide Absorption With Immobilised Amines (IA). *Chemical Enginering Journal,* 107: 97-102.

Zhang, Y., Anderson, S. and Muhammed, M. (1995). Nanophase Catalysis Oxides: I. Synthesis of Doped Cerium Oxides as Oxygen Storage Promoters. *Appl. Catal. B: Environ.* 6(4): 325-337.

Zhang, Z., Chen, H. and Sachtler, W. M. H. (1991). Migrationand Coalescence of Pd Carbonyl Clusters in Zeolite Y. *J. Chem. Soc. Faraday Trans.* 87: 1413-1418.

Zhao, D. (1998). Triblock Copolymer Synthesis of Mesoporous Silica with Periodic 50 to 300 Angstrom Pores. *Science*. 279: 548-552.

Zhao, X. S., Lu, G. Q., and Hu, X. (2000). Characterization of The Structural and Surface Properties of Chemically Modified MCM-41 Material. *Microporous and Mesoporous Materials*, 41: 37-47.

Zhao, X. S., Lu, G. Q., and Hu, X. (2001). Organophilicity of MCM-41 Adsorbents Studied by Adsorption and Temperature-Programmed Desorption. *Colloids and Surfaces A: Physicochemical and Engineering Aspects*, 179: 261-269.

Zhao, X. S., Lu, G. Q., and Millar, G. J. (1996). Advances in Mesoporous Molecular Sieve MCM-41. *Ind. Eng. Chem. Res.*, 35: 2075-2090.

Zhao, X. S., Lu, M. G. Q., and Song, C. (2003). Immobilization of Aluminum Chloride on MCM-41 as A New catalyst System for Liquid-Phase Isopropylation of Naphthalene. *J. Mol. Catal. A: Chem*. 191: 67-74.

Zheng, F., Tran, D. N., Busche, B. J., Fryxell, G. E., Addleman, R. S., Zemanian, T. S., and Aardahl, C. L. (2005). Ethylenediamine-Modified SBA-15 as Regenerable CO_2 Sorbent. *Ind. Eng. Chem. Res.*, 44: 3099-3105.

Zheng, S. R., Jentys, A. and Lercher, J. A. (2003). On the Enhanced Para-Selectivity of HZSM-5 Modified by Antimony Oxide. *J. Catal*. 219: 310-319.

Zhou, L. and Zhou, Y. P. (1998). Linearization of Adsorption Isotherms for High-Pressure Applications. *Chem. Eng. Sci*. 53(14): 2531-2536.

Zhou, L., and Zhou, Y. (2001). Determination of Compressibility Factor and Fugacity Coefficient of Hydrogen in Studies of Adsorptive Storage. *International Journal of Hydrogen Energy*, 26: 597-601.

Zhou, L., Liu, X., Sun, Y., Li, J., and Zhou, Y. (2005). Methane Sorption in Ordered Mesoporous Silica SBA-15 in The Presence of Water. *J. Phys. Chem. B*, 109: 22710-22714.

Zhou, L., Wu, J. Q., Li, M., Wu, Q., Zhou, Y. P. (2005). Prediction of Multicomponent Adsorption Equilibrium of Gas Mixtures Including Supercritical Components. *Chem. Eng. Sci*. 60: 2833-2844.

Zhou, L., Wu, J., Li, M., Wu, Q., and Zhou, Y. (2005). Prediction of Multicomponent Adsorption Equilibrium of Gas Mixtures including Supercritical Components. *Chemical Engineering Science*, 60: 2833-2844.

Zhou, L., Zhou, Y. P., Bai, S. P. and Yang, B. (2002). Studies on the Transition Behavior of Physical Adsorption from the Sub-to the Supercritical Region: Experiments on Silica Gel. *J. Colloid Interf. Sci*. 253: 9-15.

Zhou, Q. and Gould, R. D. (1998). A Study of the Response Rate to Nitrogen Dioxide Exposure In Metal Phthalocyanine Thin Film Sensors. *Thin Solid Films*. 317: 436-439.

Zhou, Y., Wang, Y., Chen, H., and Zhou, L. (2005). Methane Storage in Wet Activated Carbon: Studies on the Charging/ Discharging Process. *Carbon*, 43: 2007-2012.

Zhu, S. M., Zhou, H. S., Hibino, M., and Honma, I. (2003). Metallic Ruthenium Incorporation in The Porous Structure of SBA-15 Using a Sonochemical method. *J. Mater. Chem.*, 13: 1115-1118

Zhu, Y., Mimura, K. and Isshiki, M. (2005). Influence of Oxide Grain Morphology on Formation of the CuO Scale During Oxidation of Copper at 600 –1000 ^{0}C. *Corros*. *Sci*. 47: 537-544.

Zhu, Y., Tang, W., Zhao, B., Cai, X. and Xie, Y. (2004). Spontaneous Dispersion of Salts and Oxides Onto Surfaces of Zeolites and Its Applications. *Proceedings of the 14th International Zeolite Conference*. April 25-30. Cape Town, South Africa: Document Transformation Technologies. 3021-3027.